**Department of Chemical Engineering**

**Faculty of Engineering University of Porto**




# Hydrogen Production by Catalytic Decomposition of Methane

**Adelino Filipe Carrapatoso Cunha**

A thesis submitted for the Degree of

Doctor of Philosophy (Ph.D)

Supervisor: J.L.C.C. Figueiredo (Full Professor)

Co-Advisor: J.J.M. Órfão (Associate Professor)

**Porto 2009**

O trabalho constante na seguinte Tese de Doutoramento foi elaborado no Laboratório de Catálise e Materiais da Faculdade de Engenharia Universidade do Porto, sob orientação do Prof. José Luís Cabral Conceição Figueiredo e co-orientação de Prof. José Joaquim de Melo Órfão entre 01 de Outubro de 2004 e 15 de Maio de 2009.

Os meus agradecimentos dirigem-se ao Professor Doutor Eng.º José Luís C. C. Figueiredo pelo seu constante incentivo e por me permitir total liberdade para a concretização deste projecto.

Ao Prof. Doutor Eng.º José Joaquim de Melo Órfão expresso os meus agradecimentos pela sua disponibilidade para a resolução de questões científicas.

Quero agradecer também aos meus colegas de laboratório e restantes membros do grupo de trabalho do Laboratório de Catálise e Materiais pela sua colaboração.

Quero expressar os meus especiais agradecimentos e elevadíssima consideração ao Doutor Rainer-Leo Meisel e à H.C. Starck GmbH, Bayer Material Science Company, Alemanha, pelo fornecimento de material, catalisadores e intercâmbio técnico-científico.

Ao Estado Português, agradeço o seu esforço financeiro e incentivo à fomentação científica no nosso país, nomeadamente à Fundação para a Ciência e Tecnologia, pela Bolsa de Doutoramento (BD/16035/2004) concedida.

Aos meus pais uma especial saudação de enorme agradecimento, elevadíssimo respeito e consideração, bem como um grande muito obrigado.

*"Ipsa scientia potestas est."*

*"Knowledge itself is Power."*

**Sir Francis Bacon**

# *Resumo*

Este trabalho teve por objectivo o desenvolvimento de catalisadores para produção de hidrogénio e nanofibras/nanotubos de carbono a partir de metano.

O hidrogénio é o combustível de excelência para utilização em células de combustível, sendo o gás natural a matéria-prima ideal para produzir hidrogénio. Convencionalmente usam-se processos como o steam-reforming ou a oxidação parcial, que produzem também óxidos de carbono. Uma vez que os catalisadores usados em *células de combustível* não toleram a presença de CO, convém explorar vias alternativas para produção de hidrogénio puro. O cracking catalítico do metano ($CH_4 \rightarrow C + 2H_2$) é interessante neste contexto, já que em determinadas condições se podem produzir também nanofibras e/ ou nanotubos de carbono, que são materiais de elevado valor agregado. Assim, os objectivos do projecto foram:

a) Desenvolver catalisadores e optimizar as condições experimentais, visando a produção de hidrogénio isento de CO por decomposição do metano;
b) Produzir simultaneamente fibras de carbono (nanotubos e/ou nanofibras), e caracterizar esses materiais tendo em vista eventuais aplicações.

Estudou-se a decomposição de metano em catalisadores de níquel, cobalto e ferro, do tipo Raney, e optimizaram-se as condições para produzir hidrogénio e carbono filamentar.

Usaram-se técnicas de caracterização dos catalisadores tais como: análise do tamanho de partículas por LASER (LPSA), morfologia por microscopia electrónica de varrimento (SEM), análise de textura por adsorção de azoto a 77 K (método de BET), determinação de composição química por microanálise de raios X (EDX) e da química superficial por espectroscopia de fotoelectrões de raios X (XPS), transformações de fases por calorimetria diferencial de varrimento (DSC), natureza e estrutura das fases sólidas por difracção de raios X (XRD), e reacções a temperatura programada (TPRe).

Os ensaios cinéticos foram executados num reactor (integral) tubular de quartzo em leito fixo. Os resultados foram interpretados com base em um mecanismo anteriormente proposto, de ampla aceitação. Analisou-se a influência da temperatura, massa do catalisador, caudal volumétrico, composição inicial da fase gasosa, presença de hidrogénio em pré-tratamentos dos catalisadores e o efeito dos ciclos sucessivos de deposição/gasificação sobre a mesma amostra, das misturas físicas entre os vários catalisadores do tipo Raney e da adição de óxido de lantânio e da adição de cobre de Raney.

Os depósitos formados foram caracterizados por meio das seguintes técnicas de análise físico-química: morfologia por SEM, topologia por TEM e tamanho de cristais assim como o grau de grafitização por difracção de raios X (XRD).

Verificou-se que os catalisadores do tipo Raney são extremamente activos, selectivos e estáveis. Após pré-tratamento em hidrogénio observou-se, na maior parte dos casos, um aumento significativo da rugosidade das superfícies relativamente às estruturas iniciais, originando estabilidade adicional, tal como absoluta ausência de $CO_x$ na produção de hidrogénio e carbono. A presença de Cu Raney nos sistemas catalíticos do Ni Raney aumenta claramente a estabilidade do catalisador para a decomposição do metano. A adição de $La_2O_3$ em concentrações adequadas aumenta a estabilidade dos catalisadores como também a selectividade para a formação de depósitos de carbono filamentar. Observou-se a formação de nanofibras e nanotubos de carbono (CNF/CNT), de acordo com o mecanismo proposto na literatura.

## *Summary*

The goal of this Dissertation was the development of catalysts for the production of pure Hydrogen and carbon nanofibers/carbon nanotubes from methane.

Hydrogen is well known to be the preferred energy carrier for fuel cells. Natural gas is the ideal source for its production. Nowadays, hydrogen is produced mostly by Steam Reforming and Partial Oxidation processes which generate appreciable amounts of carbon oxide by-products. In particular, carbon monoxide is a catalyst poison for the application of hydrogen in fuel cells. Therefore alternative routes are needed for hydrogen production. Catalytic methane decomposition is of interest because under certain conditions carbon nanofibers and carbon nanotubes are simultaneously synthesized, which have interesting applications. Therefore, the objectives of this work are:

a) Pure hydrogen production by catalytic methane decomposition at optimal conditions, and
b) Simultaneous synthesis of carbon nanotubes/carbon nanofibers and respective characterisation, in order to find eventual applications.

The catalytic methane decomposition was studied on Raney-type Ni, Co and Fe catalysts. Under optimal conditions, hydrogen and filamentous carbon species are generated.

For catalyst characterization the following techniques were used: Particle size by LASER, morphology by scanning electron microscopy (SEM), texture by nitrogen adsorption at 77K (BET-Method), chemical composition by energy dispersive x-ray spectroscopy (EDX), chemical surface composition by X-ray photoelectron spectroscopy (XPS), phase transformations by differential scanning calorimetry (DSC), nature and structure of the solid by X-ray diffraction (XRD) and catalysts activity and selectivity by temperature programmed reactions (TPRe).

Kinetic studies where made in an integral reactor (fixed bed quartz tubular reactor). The results were discussed based on the well known reaction mechanism reported in the literature. The influence of temperature, catalyst mass, gas flow rate, gas phase composition, hydrogen pre-treatment, presence of hydrogen during reaction as well as successive cycles of carbon deposition and gasification on the catalyst were studied. Moreover, the influence of physical Raney-type catalyst mixtures, such as Lanthanum(III)-oxide and Raney-Cu, were also studied.

For the characterization of the carbon deposits the following techniques where used: Morphology by scanning electron microscopy (SEM), topology by transmission electron microscopy (TEM), crystal sizes and degree of graphitization by X-ray diffraction (XRD).

Raney-type catalysts showed high activities, selectivities as well as stabilities. The catalyst pre-treatment with hydrogen originates in most cases a rough surface when compared with the original catalyst. Furthermore, the stability could be increased coupled with absolute absence of carbon oxides during hydrogen generation.

The presence of Raney-Cu increases significantly the catalyst stability for methane decomposition. The introduction of $La_2O_3$ in adequate quantities increases not only the stability, but also the selectivity towards filamentous carbon deposits. It was observed that mostly carbon nanofibers (CNF) and carbon nanotubes (CNT) are generated, in agreement with the reaction mechanism reported in the literature.

# *Résumé*

Cet´ étude a pour objectif de développer des catalyseurs pour la production d'hydrogène et de nanofibres/nanotubes de carbone à partir du méthane.

L'hydrogène est le combustible par excellence pour une utilisation en cellules à combustible, le gaz naturel étant la matière première pour produire l'hydrogène. De façon conventionnelle, il est obtenu via des procédés tels que le vaporeformage (*steam reforming*) ou l'oxydation partielle, qui produisent également des oxydes de carbone. Dans la mesure où les catalyseurs utilisés dans les cellules à combustibles ne tolèrent pas la présence de CO, il convient alors d'explorer des voies alternatives pour produire de l'hydrogène pur. Le craquage catalytique du méthane ($CH_4 \rightarrow C + 2H_2$) est dans ce contexte particulièrement intéressant puisque dans certaines conditions, il peut également produire des nanofibres et/ou nanotubes de carbone, qui sont des matériaux de haute valeur ajoutée. Les objectifs de ce projet sont donc les suivants:

a) Développer des catalyseurs et optimiser les conditions expérimentales en vue de produire de l'hydrogène exempt de CO par décomposition du méthane ;
b) Produire simultanément des fibres de carbone (nanotubes et/ou nanofibres) et caractériser ces matériaux dans la perspective des éventuelles applications.

Nous avons ainsi étudié la décomposition du méthane sur des catalyseurs de nickel, cobalt et fer, de type Raney, dans des conditions permettant la production d'hydrogène et d'espèces variées de carbone filamentaire.

Nous avons surtout utilisé des techniques de caractérisation des catalyseurs tels que : l´analyse de la taille des particules par LASER (LPSA), la morphologie par microscopie électronique à balayage (MEB), analyse de texture par adsorption d'azote à 77 K (méthode BET), détermination de la composition chimique via microanalyse, par dispersion d'énergie des photons X (EDX), de transformation de phases par calorimétrie différentielle à balayage (CDB), nature et structure des phases par diffraction des rayons X (DRX), et des réactions à température programmée (RTP).

Les essais cinétiques ont été réalisés dans un réacteur (intégral) tubulaire de quartz en lit fixe. Les résultats ont été interprétés en vue du mécanisme proposé. Nous avons ensuite analysé l'influence de la température, de la masse de catalyseur, du débit volumétrique, de la composition initiale de la phase gaz, de la présence d'hydrogène en prétraitement des catalyseurs durant la réaction, et l'effet des cycles successifs de dépôt/gazéification sur le même échantillon, des mélanges physiques entre les différentes catalyseurs de type Raney et de l'addition d'oxyde de lanthane et de l'addition de cuivre de Raney.

Les caractérisations des dépôts formés ont été effectués avec les techniques suivantes d'analyse physico-chimiques : la morphologie par MEB, la topologie par MET et la taille des cristaux ainsi que le degré de graphitisation par diffraction des rayons X (DRX).

Nous avons vérifié que les catalyseurs de type Raney sont extrêmement actifs, sélectifs et stables. Après le prétraitement en hydrogène, nous avons observé dans la plupart des cas, une augmentation significative de la rugosité des surfaces par rapport à ses structures initiales conférant une stabilité additionnelle, ainsi qu'une absence absolue de $CO_x$ dans la production d'hydrogène et de carbone. La présence de Cu de Raney sur les systèmes catalytiques de Ni Raney augmente clairement la stabilité pour la décomposition du méthane. L'addition de $La_2O_3$ en concentrations adéquates augmente aussi bien la stabilité des catalyseurs que la sélectivité pour la formation des dépôts de carbone filamentaire. Nous avons confirmé la formation des nanofibres et nanotubes de carbone (NFC/NTC), confirmant de façon claire le mécanisme proposé dans la littérature.

# *Zusammenfassung*

Ziel dieser Dissertaion war es Katalysatoren für die Herstellung von hochreinem Wasserstoff sowie Kohlestoffnanofasern und –nanoröhrschen ausgehend von Methan zu entwickeln.
Wasserstoff ist bekannterweise der bevorzugte Energieträger für Brennstoffzellen. Erdgas ist der ideale Rohstoff für dessen Herstellung. Wasserstoff wird großtechnisch über Wasserdampfreformierung oder Partialoxidation gewonnen, welche in grossen Maßstab Kohlenoxide als Nebenprodukte frei setzen. In der Brennstoffzellentechnik ist vor allem Kohlenmonoxid bekannt als Katalysatorgift, deshalb ist es von Bedeutung alternative Wege für die Wasserstofferzeugung zu finden. Die katalytische Methanzersetzung kann hierbei von Interesse sein, da unter bestimmten Bedingungen gleichzeitig Kohlestoffnanofasern und -nanoröhrschen synthetisiert werden können, die vom Standpunkt der Wissenschaft und Technik erhebliches Anwendungspotential aufweisen. Die Zielsetzungen sind:

a) Herstellung von hochreinem Wasserstoff, ausgehend von der katalytischen Methanzersetzung, unter optimalen Bedingungen, sowie
b) die gleichzeitige Synthese von Kohlestoffnanofasern und –nanoröhrschen, und dessen Charakterizierung mit dem Ziel potentielle Anwendungen zu verfolgen.

Die katalytische Methanzersetung wurde an Ni, Co und Fe Katalysatoren vom Typ Raney untersucht. Unter bestimmten Bedingungugen werden Wasserstoff sowie Kohlefasern erzeugt.
Folgende Methoden wurden für die Katalysatorcharakterizierung verwendet: Partikelgrößen mittels LASER, Morphologie mittels Rasterelektronenmikroskopie (REM), Textur über Sorptionsgleichgewichtsisothermen in Stickstoff bei 77 K (BET-Methode), Chemischen Zusammensetzung mittels Energie Dispersiver Röntgenstrahlung (EDR), Chemischen Oberflächenzusammensetzung mittels Röntgenphotoelektronenspectroskopie (RPS), Phasenumwandlungen mittels Diffentieller Kalorimetrie (DSC), Chemische- und strukturelle Phasenumwandlungsprozesse mittels Röntgenpulverdiffraktometrie (RPD) sowie Katalysatoraktivitäten und -selektivitäten über Temperatur Programmierte Reaktionen (TPR).
Kinetischen Untersuchungen wurden in einem Integral Reaktor (Quarzglass Strömungsrohr mit einem Katalysatorfestbett) durchgeführt. Die Ergebnisse wurden anhand des bekannten Reaktionsmechanismus erklärt. Einflüsse der Temperatur, Katalysatormasse, Gasströmungsgeschwindigkeit, Gasphasenzusammenseztung, Wasserstoffvorbehandlungen, Wasserstoff während des Reaktionsablaufs sowie Regenerierungsprozesse, d.h. Ablagerung von Kohlenstoff und dessen Vergasung am selben Katalysator, wurden untersucht. Der Einfluß von physischen Raney-Typ Katalysatorenmischungen, Lanthan(III)-Oxid und Raney-Kupfer wurde ebenfalls untersucht.
Für die Untersuchung des Kohlenstoffs wurden folgende Charakterisierungsmethoden verwendet: Morphologie mittels Rasterelektronenmikroskopie (REM), Topologie mittels Transmissionselektronenspektroskopie und Kristallgröße sowie Graphitisierungsgrad mittels Röntgenpulverdiffraktometrie (RPD).
Raney-Typ Katalysatoren weisen starke Aktivitäten auf, sind sehr selektiv und stabil. Die Katalysatorvorbehandlung mittels Wasserstoff ruft in den meisten Fällen eine Erhöhung der Oberflächenrauhigkeit hervor. Eine zusätzliche Stabilität wie auch absolute kohlenoxidfreie Wasserstoff darstellung wird hervorrufen. Die Anwesenheit von Raney-Cu erhöht die operatorische Stabilität der Methanzersetzung. Der Zusatzt von $La_2O_3$, in angemessenen Proportionen, erhöht nicht nur die Stabilität sowie auch die selektive Darstellung von Kohlenstoff. Es wurde eindeutig Kohlestoffnanofasern und –nanoröhrschen (CNF/CNT) nachgewiesen, so daß der literarische bekannte Reaktionsmechanismus bekräftig wird.

# *Index*

# *Chapter I*

***Introduction***


| | | |
|---|---|---|
| **1.1** | **Motivation and Objectives** | 3 |
| **1.2** | **Energy and Raw material demands** | 5 |
| **1.3** | **From hydrocarbons to hydrogen economy** | 8 |
| **1.4** | **Catalytic methane cracking as alternative process** | 11 |
| **1.4.1** | **Methane conversion** | 11 |
| **1.4.2** | **Catalysts** | 12 |
| **1.4.3** | **Deactivation** | 14 |
| **1.4.4** | **Carbon products** | 17 |
| **1.5** | **Raney-type catalysts** | 20 |
| | **References** | 26 |

# *Chapter II*

**Catalytic Decomposition of Methane on Raney-type Catalysts**


**Abstract**

**2.1 Introduction** 38

**2.2 Experimental** 38

**2.2.1 Catalysts** 38

**2.2.2 Reaction studies** 39

**2.2.3 Characterization of catalysts and carbon deposits** 39

**2.3 Results** 40

**2.3.1 Catalysts characterization** 40

**2.3.2 Catalysts performance** 44

*2.3.2.1 Preliminary tests* 44

*2.3.2.2 Isothermal tests* 45

**2.3.3 Characterization of the carbon deposits** 53

**2.4 Discussion** 55

**2.5 Conclusions** 60

**References** 61


# *Chapter III*

**Carbon deposits on Raney-type Catalysts**


**Abstract**

**3.1 Introduction** 68

**3.2 Experimental** 69

**3.3 Characterization of the carbon deposits containing metal nanoparticles** 69

**3.3.1 Carbon deposits obtained on Ni50 catalysts** 69

**3.3.2 Carbon deposits obtained on Ni30 catalysts** 76

**3.3.3 Carbon deposits obtained on Co50 and Co30 catalysts** 82

**3.3.4 Carbon deposits obtained on Fe50 and Fe35 catalysts** 86

**3.4 Conclusions** 91

**References** 92

# *Chapter IV*

**Methane Decomposition on Ni-Cu alloyed and Fe-Cu Raney-type Catalysts**

**Part A**
**Methane Decomposition on Ni-Cu alloyed Raney-type Catalysts**


Abstract

4.1 Introduction 100

4.2 Experimental 101

4.2.1 Catalysts preparation 101

4.2.2 Catalyst testing 102

4.2.3 Characterization of catalysts and carbon deposits 102

4.3 Results 103

4.3.1 Catalysts characterization 103

4.3.2 Catalysts performance 108

4.3.3 Characterization of the carbon deposits 114

4.4 Discussion 117

4.5 Conclusions 119

References 120


**Part B**
**Methane Decomposition on Fe-Cu Raney-type Catalysts**


Abstract

4.6 Introduction 126

4.7 Experimental 128

4.7.1 Catalysts preparation 128

4.7.2 Catalysts testing 128

4.7.3 Characterization of catalysts and carbon deposits 129

4.8 Results and Discussion 129

4.8.1 Catalysts characterization 129

4.8.2 Catalysts performance 136

4.8.3 Characterization of the carbon deposits 138

4.9 Conclusions 140

References 141

# *Chapter V*

**Methane Decomposition on $La_2O_3$ promoted Raney-type Catalysts**

**Part A**
**Methane Decomposition on $La_2O_3$ promoted Raney-Fe Catalysts**


Abstract

5.1 Introduction 148

5.2 Experimental 149

5.2.1 Catalysts preparation 149

5.2.2 Catalysts characterization 149

5.2.3 Catalysts testing 150

5.3 Results and Discussion 150

5.3.1 Catalysts characterization 150

5.3.2 Catalysts performance 154

5.4 Conclusions 156

References 157


**Part B**
**Methane Decomposition on $La_2O_3$ promoted Ni and Ni-Cu Raney-type Catalysts**


Abstract

5.5 Introduction 162

5.6 Experimental 163

5.6.1 Catalysts preparation 163

5.6.2 Reaction studies 164

5.6.3 Characterization of catalysts and carbon deposits 164

5.7 Results and Discussion 165

5.7.1 Catalysts characterization 165

5.7.2 Catalysts performance 177

*5.7.2.1 Preliminary tests* 177

*5.7.2.2 Isothermal tests* 178

5.7.3 Characterization of the carbon deposits 185

5.7.4 Comparison with other catalysts reported 190

5.8 Conclusions 192

References 193

# *Chapter VI*

**Summary**


**6.1 Energy, Materials and Catalysis** 197

**6.2 CDM on Raney-type Catalysts** 198

**6.3 Carbon deposits on Raney-type Catalysts** 200

**6.4 Effect of promoters on Raney-type Catalysts** 200

**6.4.1 Effects of Raney-Cu as structural promoter on Raney-type Catalysts** 201

**6.4.2 Effect of $La_2O_3$ as electronic promoter on Raney-type Catalysts** 202

**6.5 Conclusions and Suggestions for Future Work** 202

**References** 205


# Appendix

Supporting Information Available: CD-ROM

**Acronyms**

| | |
|---|---|
| BET | Brunnauer Emmett Teller |
| CAEM | Controlled atmosphere electron microscopy |
| CCVD | Catalytic chemical vapour deposition |
| CMD | Catalytic methane decomposition |
| CNF | Carbon nanofibers |
| CNT | Carbon nanotubes |
| DSC | Differential scanning calorimetry |
| EDX | Energy dispersive spectroscopy |
| FC | Filamentous carbon |
| FWHM | Full-width at half maximum |
| HPT | Hydrogen pre-treatment |
| ICDD | International Centre for Diffraction Data |
| IR | Infrared |
| ITT | In situ thermal treatment |
| Me | Active metal |
| MWCNT | Multiwall carbon nanotubes |
| SEM | Scanning electron microscopy |
| SWCNT | Singlewall carbon nanotubes |
| TEM | Transmission electron microscopy |
| TPD | Temperature programmed desorption |
| TPR | Temperature programmed reduction |
| TPRe | Temperature programmed reaction |
| XAFS | X-ray absorption fine structure spectroscopy |
| XPS | X-ray photoelectron spectroscopy |
| XRD | X-ray diffraction |

# *Chapter I*

## *INTRODUCTION*

*"There is no existence of a greater force in nature*

*which time has arrived."*

**Victor Hugo**

## 1.1 Motivation and Objectives

The fossil fuel resources (hydrocarbons) are the most important raw materials for the industrial production of hydrogen used in the chemical industry and for energy demands [1]. Apart from ammonia synthesis, the production of methanol and oxo-synthesis products are of particular importance. Large quantities of hydrogen are needed in refineries for hydrotreating, and also in the production of several important organic products, e.g. aniline and diaminotoluenes from nitrotoluenes (starting material for dyes, pharmaceuticals, isocyanate polymers and solvents) [2]. The hydrogen consumed worldwide in 1986 exceeded 500 billion $Ncm^3$ and for the future (year of 2025) it is expected that the consumption will increase up to 1500-2000 billion $Ncm^3$ [3]. However, reserves of fossil fuels, in particular oil, are limited [4]. This led to the idea that hydrogen could be used economically as a substitute energy form. A review dealing with the perspectives and planning of the utilization of hydrogen as a major universal energy carrier has been published [5]. In addition to economic reasons for the introduction of new energy sources and new energy carriers, ecological reasons are becoming increasingly important [6-8]. The increase in $CO_2$ content of the atmosphere, caused by the use of fossil energy sources is predicted to lead to extensive climatic changes associated to a gradual warming up [9]. The utilization of the traditional energy carriers, e.g. coal, oil (in the form of gasoline, diesel, kerosene, etc.) and natural gas, leads to emissions of $SO_2$, $NO_x$ and hydrocarbons, which cause the destruction of the environment. Hydrogen competes with the conventional energy carriers namely hydrocarbons (methane, LPG, gasoline, etc.), coal, electric power and regenerable sources. Since only water is obtained as a product of the combustion, emissions such as CO, $SO_2$, incompletely combusted hydrocarbons, particles, soot and ash are avoided. Apart from the direct utilization of hydrogen for heating purposes, the generation of electricity is important in the hydrogen energy concept [10,11]. In the reverse reaction of the water electrolysis process, the chemical energy of hydrogen can be converted directly into electrical energy. This takes place in fuel cells by allowing the cold combustion of hydrogen with oxygen to occur electrochemically [12]. Fuel cell technology has seen a rapid development in the past decade, driven primarily by the fact that fuel cells are environmentally more desirable and have high efficiencies [13,14]. This technology generates electricity "just in time" and at desired locations. As a result, this process becomes attractive for the automobile and power plant industry. Vehicles can be propelled by electricity produced by an on-board fuel cell which substitutes the conventional combustion engines. At room temperature the maximum possible voltage of the $H_2$-$O_2$ system is 1.23 V. In practice, cell voltages of 0.7 V are reached. Since heat power conversions are avoided, efficiencies of 40 – 60 % can be attained

[15]. The most developed versions are the low-temperature fuel cells. Without exception, they have a high specific energy density (7.2 kWh/kg) and a long lifetime. In practice, residual CO is unacceptable for the current fuel cells. The stringent requirement (10-100 ppm of CO) in the hydrogen stream adds to costs [16,17].

Hydrogen is typically produced through steam reforming [18,19]. Methane represents the principal component in natural gas, its abundance and high H/C ratio is ideal for hydrogen production [20-22]. However, CO is an undesirable co-product, which has to be converted into $CO_2$ in subsequent steps; therefore it implicates additional costs in separation processes. In this context, as an alternative path, it appears logical to use the direct catalytic decomposition of methane from natural gas into hydrogen and carbon:

$$CH_4 \rightleftharpoons C + 2\,H_2 \qquad \Delta_r H^o\,(298.15K) = 74.6\ kJ/mol$$

This process is of special interest since the formation of $CO_x$ is avoided [23,24]. Combined with the possible formation of carbon nanofibers (CNF) and carbon nanotubes (CNT), this process can be of high economic interest [25,26].

Recently, the applications of CNT and CNF for electronic parts, materials and catalysis have been investigated [27,28]. To obtain high conversions of methane to pure hydrogen and carbon materials with commercial value it is essential to find adequate catalysts. A bibliographic search shows that supported catalysts such as $Ni/Al_2O_3$ have moderate activities, but generally they are not very stable. The best results have been obtained with high metal loaded catalytic systems [29,30]. Therefore, massive catalysts might show better performances for the defined task.

Therefore, in this thesis, we examine the catalytic decomposition of methane using Raney-type catalysts as a potential process for ultra pure hydrogen production, at economically moderate conditions, with high activities and long catalytic life-time, together with the formation of high value carbon materials such as CNF/CNT. The aim of this study is to understand the behavior of Raney-type catalysts and promoters for the cracking of methane, studying the influence of the operating conditions on catalysts activity, selectivity and stability. The properties of the carbon deposits have also been examined. It was found that most of the catalysts used have high performance for the conversion of methane at moderated temperatures, and allow the production of high purity hydrogen. Moreover, a large amount of CNF is obtained as co-product, and in some cases CNT are clearly identified.

## 1.2 Energy and Raw Materials

Since the last century, both population and technological development grew up exponentially; and faith in progress had no restrictions. The advances in the last century were, in fact, greater than in the previous history of mankind. Until now the exorbitant economical growth seemed to have no limitations. Mankind assumed that natural resources were infinite and that the environment had unlimited capacity to accommodate wastes.

Science provides an illusion similar to someone in paradise, blessed by fortune. People often associate science and technology with human- and social progress and believe that wellbeing for all is only a question of time. Unfortunately, no medal of honour is obtained without suffering, and all illusions are lost after some time. "Sustainable development" became the new paradigm, but what does this mean? The last Conferences in Rio de Janeiro (Brazil), Kioto (Japan) or Toronto (Canada) illustrate that the situation is serious; the scenario is of alert and if nothing changes our society will soon collapse.

It is necessary to analyse the origin of the problems; there are three main traps which require adequate solutions, as shown in Figure 1.1.

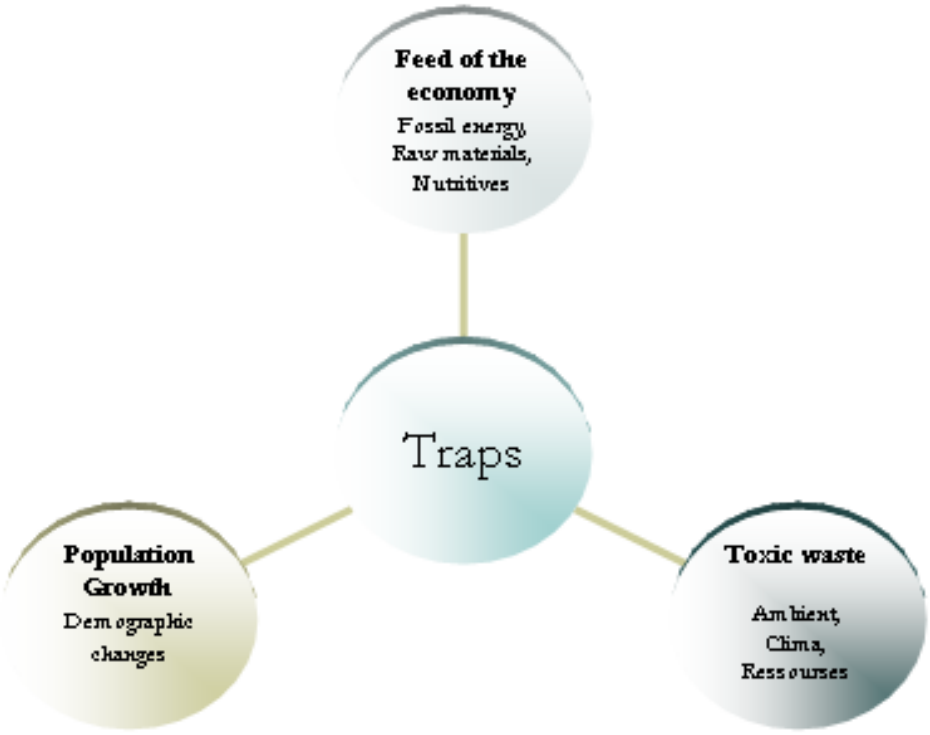



Fig. 1.1 The three overall traps of our global society [31]

In the beginning, energy sources were limited to human- and animal work. Fire was produced by wood combustion, and wind and water were used for propulsion. Two hundred years ago, with the advent of the industrial revolution, coal started to be used as primary energy source. Since the beginning of the 20$^{th}$ century, and especially after the Second World War, industry turned to the cheaper and widely available crude oil, which is still the most important source of the present economy. Natural gas and nuclear power appeared in the last 50 years. The primary energy consumption in the last century has grown up more than 13 times since the year 1900 when it was 29.309 EJ (Exa Joule ≡ $10^{18}$) to the year 2000, in which the value increased to 381.017 EJ. It is expected that the energy consumption will increase 50 % more in the following 20 years [31].
According to the available data, over 90 % of the worldwide energy demands are covered by the fossil energy sources, 5 % by nuclear power and 5 % by renewable energies (Fig. 1.2). It is worth noting that only 7 % of the used oil is transformed by the chemical industry, since major amounts are exclusively used for energy demands [1]. While nature took thousands of years to accumulate resources in the form of coal, oil and natural gas, it will possibly take only a few years for mankind to destroy such reserves. Fossil fuels are produced by solar energy, by the so-called "Photosynthesis" or "Carbon Assimilation", in the plants, with the assistance of Chlorophyll (Mg-Porphyrin complex).

$$CO_2 + H_2 \quad \underset{\leftarrow}{\overset{h \cdot \nu}{\rightleftharpoons}} \quad \text{hydrocarbons} + O_2 \qquad \text{(eq. 1.2)}$$

Anaerobic decomposition of the organic material results into fossil sources. This process is very slow. The main source of energy for the production of organic raw material is solar energy. The yearly carbon uptake from the atmosphere is about $120 \cdot 10^9$ tonnes [32].
After the oil crises in the 1970´s decade, a change in the attitude of industry occurred, and alternative energy sources started to be sought. It is expected that coal reserves will only last for ~200 years and oil ~50 years, if the consumption levels continue as they are today [33]. Briefly explained, the fossil sources on which our society depends are limited, and time is running out. Everybody agrees that we need to have a structural change in our energy system. However, it can be difficult to preview or choose the way. A healthy alternative is the use of an energy and raw material mixture to avoid dependency of only one source. Figures 1.3 and 1.4 explain the present energy and raw materials system. Coal, oil, natural gas and uranium are obtained from the ground, via appropriate transformation processes (which also consume energy).

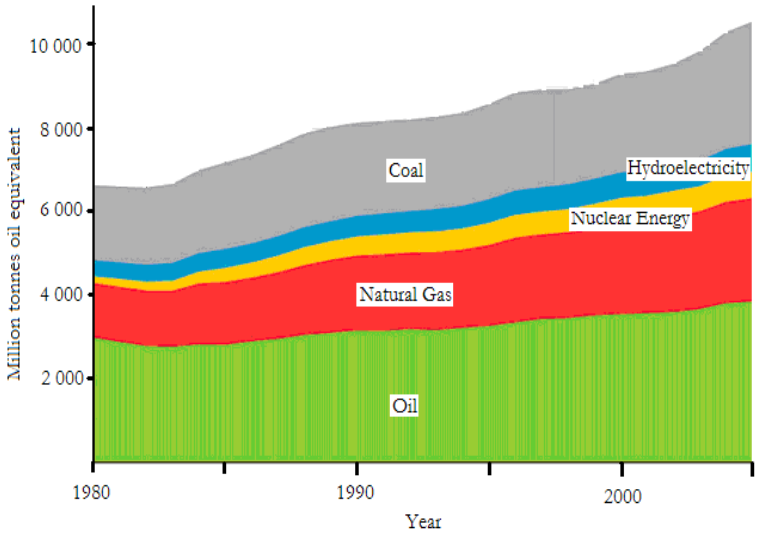



Fig. 1.2 World consumption of primary energy, million tons oil equivalent [33]

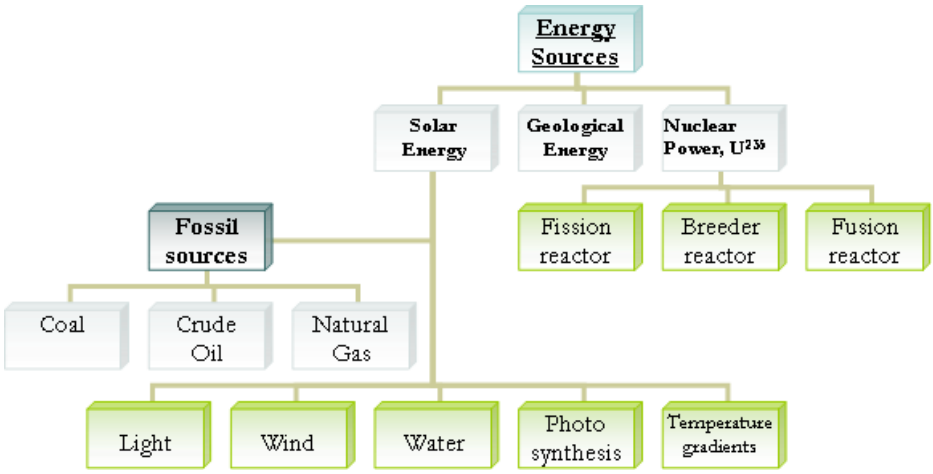



Fig. 1.3 Primary energy and raw material sources

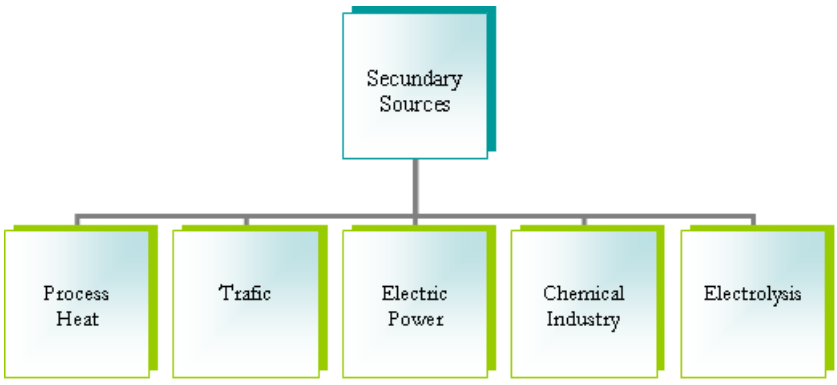



Fig. 1.4 Secondary sources and their applications

The secondary energy and higher value materials are used for the most specific applications. After use, appropriate treatments are required for the residual by-products such as toxic wastes, waste water, ashes, heat and dust, before returning them to the environment. This open system fails if the inlet- and output system are not working properly. Since 1850, the $CO_2$ concentration in the atmosphere has raised up strongly [34]. The $CO_2$ molecule is suitable for IR absorption and enhances the greenhouse effect. The contribution of methane for the greenhouse effect is ~2 % and it is IR-radiation active just like $CO_2$. The continuous increase of $CO_2$ and $CH_4$ emissions in the atmosphere caused a temperature increase [35]. The vast majority of the simulated scenarios preview a temperature increase between 1.1 to 6.4 ºC during the twenty-first century [36], depending on the emission quantities and their effect, as well as interactions with other environmental parameters.

## 1.3 From hydrocarbons to hydrogen economy

Hydrogen appears in nature only chemically bonded. To produce non bonded hydrogen, external energy sources are needed and depend exclusively on economic criteria. The availability and price of the feedstock, and the investment costs for a plant are the most important aspects. Most of the hydrogen is produced from natural gas, oil and coal, either as a main product or as a by-product. The main sources of hydrogen are [37]:

- Coke oven gas
- Coal gasification
- Gasification of liquid and gaseous hydrocarbons
- Steam reforming of hydrocarbons
- Hydrogen from hydrogen sulphide
- Refinery or petrochemical processes (catalytic reforming, catalytic and thermal cracking)
- Electrolysis
- Hydrogen as by-product of the organic chemicals industry

Figure 1.5 shows the main industrial processes for hydrogen production. The preference for hydrocarbon feedstocks, if available, is due to the fact that the energy demand is much lower than for electrolysis of water [38,39]. Vacuum residue, naphtha or hydrogen-rich off-gases are

also important sources. In autothermal reformers, the energy for hydrogen production is generated by the catalytic partial oxidation of part of the feedstock.

Due to the strong correlation between energy and hydrocarbon prices, it is not expected that the situation might change in the near future. The cost structure indicates that hydrogen will still be preferentially produced from hydrocarbons [40]. However, limited hydrocarbon reserves and increasing environmental problems will force the development of a new hydrogen economy [10].

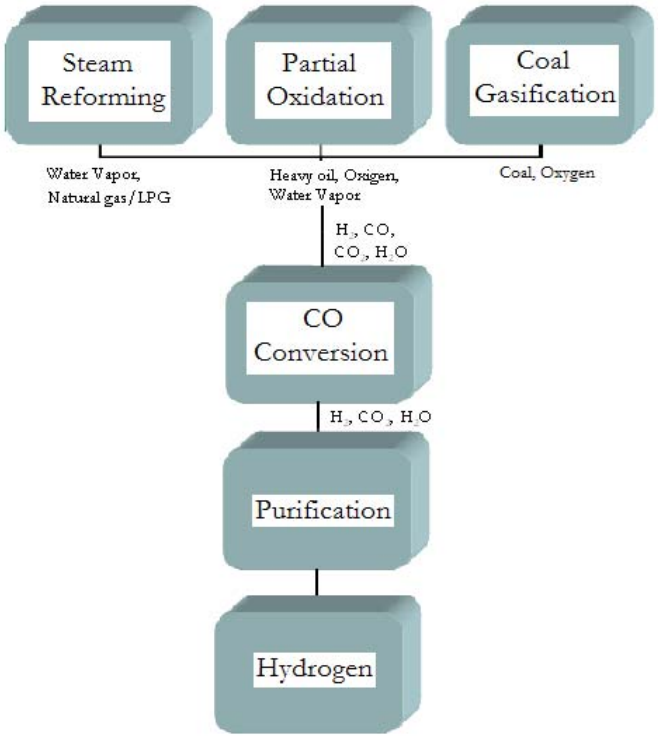



Fig. 1.5 Main hydrogen production processes

It is difficult to implement hydrogen as energy source, since it has to compete with other energy carriers: conventional energy sources (fossil fuels and nuclear energy), electric power from geothermal sources, solar energy (photovoltaic, solar thermal plants), energy gradients induced by the climatic changes (wind, waves, heat), water power and the upcoming regenerable sources such as biogas (biomass fermentation), bioalcohols (ethanol from sugarcane or other carbohydrates), vegetable oils (rapeseed oil for biodiesel production) [33,41]. A hydrogen energy concept has to be based on a clean form of energy, with minimum effect on the environment, improved economic advantages and socially acceptable [31,42-44]. The feasibility of hydrogen as energy carrier depends on price advantage, production costs, transport, logistic and storage [45]. The concept of a hydrogen economy is not new; indeed, many scientists in the beginnings of the

20th century, in particular J.B.S. Haldane (Scotland), described in a theoretical way the production, storage and application possibilities of hydrogen [46-48].

Hydrogen is an indirect source of energy, not a resource, but it can be used as a suitable substitute for fossil fuels. All primary energy sources can be used to generate hydrogen (see Fig. 1.3) [49-53].

The use of hydrogen as an energy carrier in electrochemical energy conversion with new fuel cell technologies is also of great relevance. Fuel cells produce electrical power by "cold combustion" of hydrogen and oxygen, an inverse reaction of the electrolysis process. The chemical energy is thus converted directly into electrical energy [54,55]. Fuel Cells require extremely low levels of CO (100 ppm or less of CO in hydrogen) [56-59]. The essence of this process is that heat-power conversions are avoided and that high efficiencies can be obtained depending on the version of the fuel cell. Normally, there are two types of fuel cells [60,61]:

- High-temperature fuel cells
  - ⇒ Molten Carbonate Fuel Cell (MCFC)
  - ⇒ Solid-oxide Fuel Cell (SOFC).
- Low-temperature fuel cells
  - ⇒ Alkaline Fuel Cell
  - ⇒ Proton Exchange Membrane Fuel Cell (PEMFC)
  - ⇒ Phosphoric acid fuel cell
  - ⇒ Direct Methanol Fuel Cell (DMFC)

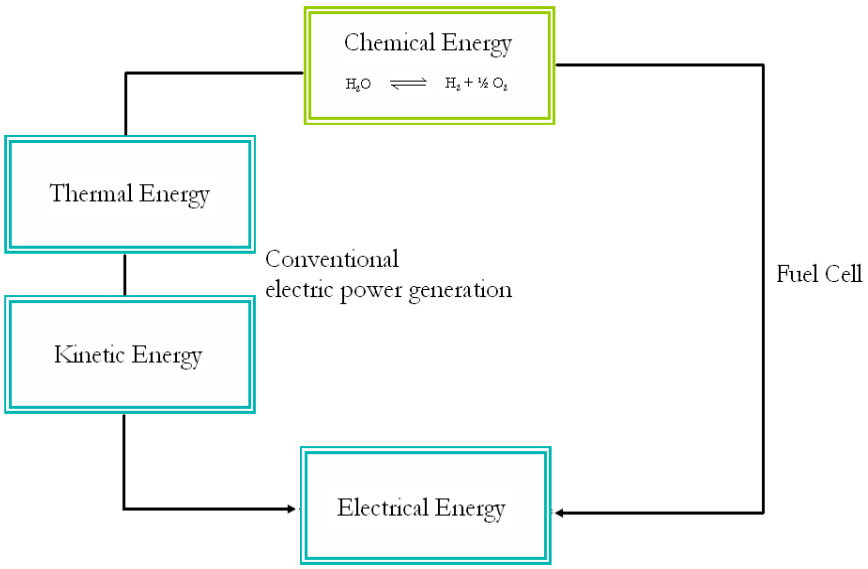



Fig. 1.6 Energy transformation diagram

Figure 1.6 compares the conventional and the direct energy transformation processes. The former one requires at least two steps before the energy is converted into electricity. The latter pathway converts directly the chemical energy into electricity; therefore, the energy conversion efficiency is higher due to less entropy effects.

## 1.4 Catalytic methane cracking as an alternative process

### 1.4.1 Methane conversion

Methane conversion into higher value chemicals has been the subject of many studies since the second half of the last century. Theoretically, methane can be used as raw material in several synthesis processes, such as aromatisation, direct methanol synthesis, oxidative coupling, indirect conversion into syngas in auto-thermal steam-reforming, dry reforming, partial oxidation, etc.
More recently, it has been proposed to crack methane, at moderate temperatures, into hydrogen and carbon, followed by gasification of carbon with steam, oxygen or carbon dioxide [62-67].

$$CH_4 \rightleftharpoons 2\,H_2 + C \qquad \text{(eq. 1.3)}$$

$$C + H_2O \rightleftharpoons CO + H_2 \qquad \text{(eq. 1.4)}$$

$$C + \tfrac{1}{2}\,O_2 \rightleftharpoons CO \qquad \text{(eq. 1.5)}$$

$$C + CO_2 \rightleftharpoons 2CO \qquad \text{(eq. 1.6)}$$

Earlier, methane decomposition was studied as one of the side reactions in the steam reforming process. The aim was to eliminate/reduce the formation of carbon deposits on catalysts [68] which were a source of deactivation. More recently, however, catalytic carbon formation attracted a lot of attention for the production of carbon materials with a high commercial value, such as carbon nanofibers and nanotubes.
Several new processes have been suggested for high purity hydrogen production, such as the fossil fuel decarbonisation process at temperatures above 800 ºC [69-71], catalytic methane cracking [72-80], methane cracking combined with steam regeneration in distinct steps [81-83], and stepwise cyclic steam reforming of methane into hydrogen and carbon dioxide at 500 ºC [65]. The main purpose is to produce hydrogen with less possible energy input (operating conditions) and to fulfil some criteria, such as no $CO_x$ emissions and producing CNF/CNT with appropriate physical and chemical properties for further technological applications.
There is still some controversy about the detailed growth mechanism of CNF/CNT from hydrocarbons, but most features of the process can be understood in terms of the original proposals of Baker et al. [81] and Lobo et al. [82]. Hydrocarbons are dissociatively adsorbed over metal catalysts; in the case of Fe, Co, Ni, the process leads to adsorbed carbon atoms (carbidic

carbon), which have been identified by temperature-programmed surface reaction [83]. Carbon can then diffuse on the surface or through the metal, to form filamentous carbon (CNF/CNT), as observed by controlled atmosphere electron microscopy (CAEM). During the process, metal particles may be lifted up from the catalyst surface and taken away on top of the growing fibers. This is called "tip growth" mode. Alternatively, the metal particles stay on the surface, leading to the "base growth" mode. This depends on the strength of the metal-support interaction [84]. The adsorbed carbon species are also able to react on the surface, forming the so-called "encapsulating" carbon, which may be avoided if the active metal is able to catalyse the hydrogenation of intermediates along the reaction path on the surface [68].

The kinetics of carbon formation from olefins on Ni, Co and Fe has been explained in terms of carbon diffusion through the metal as the rate determining step [82,85]. However, the possible role of metal carbides, especially in the initial phases preceding the steady-state growth of carbon filaments, is still unclear [86-89].

The kinetics of carbon deposition on iron from methane/hydrogen mixtures was studied extensively by Grabke [90,91], and a mechanism based on the dissociative adsorption of methane followed by stepwise dehydrogenation of the adsorbed methyl species was found to be the rate-limiting step.

Alstrup and Tavares showed that the steady-state rate of carbon deposition from $CH_4$+$H_2$ mixtures on silica supported Ni and Ni-Cu alloy catalysts could be described by a similar mechanism [92,93]. However, in this case the adsorption of methane could not be assumed to be close to equilibrium. In any case, these authors demonstrated that the rates of carbon formation on metals, at constant temperature, cannot be determined only by the carbon activity of the gas.

### 1.4.2 Catalysts

Some authors have proposed the use of carbon-based catalysts for the catalytic decomposition of methane [94,95]. Unfortunately, carbon materials show low activities, they require high temperatures, and their stability is not very good. Kim et al. tested several activated carbons in a fixed-bed reactor, between 750-900 ºC, where only hydrogen was found as final product [96]. The activity of the catalyst was found to vary inversely with the particle size. Moliner et al. studied coal-derived activated carbons [97]. The results, obtained in a fixed-bed reactor between 850-950 ºC, showed high initial activities, but rapid catalyst deactivation after 8 h of time on stream. However, the higher the contact time, the lower was the conversion rate. Muradov et al. also studied the catalytic methane decomposition on carbon-based materials; activated carbons

were found to be most active, and the methane decomposition was dependent on the surface structure [98]. The experiments were conducted in a fixed-bed at 850 ºC, traces of CO being detected. Not surprisingly, the activation energies determined were between those of the non-catalytic (370-433 kJ/mol) and metal-catalysed reactions (60 kJ/mol). Dunker et al. conducted reactions with and without catalysts in a fluidized-bed reactor [99]. In the absence of a catalyst, only traces of hydrogen were found at temperatures between 789-918 ºC. The introduction of carbon-based catalysts increased slightly the methane conversion rates.

Until now, the best results for the catalytic methane decomposition were achieved with nickel phases. Silica supported Ni catalysts were intensively studied by many groups, the catalytic cracking of methane being performed at temperatures higher than 400 ºC [100]. Otsuka et al. reported that $Ni/SiO_2$ was the most active phase among all supported transition and precious metal catalysts tested. The addition of $CaNi_5$, a hydrogen-absorbing alloy, enhanced the conversion of methane beyond thermodynamic limits [101-103]. Ermakova et al. tested nickel catalysts in a vibrofluidized bed between 500-600 ºC [104]. Rapid catalyst deactivation was observed above 600ºC, due to pore plugging by carbon formation. The support effect was studied by Otsuka et al. [80]. It was reported that, among all used carbon supports, the most promising ones were carbon fibers synthesized via methane, because of the relative low production temperature (500-550 ºC) and regeneration during methane decomposition. However, low methane conversions (~10 %) were reached. $Ni/SiO_2$, $Ni/Al_2O_3$, $Ni/TiO_2$ and $Pd\text{-}Ni/SiO_2$ catalysts were also studied, and fast catalyst deactivation was observed. The introduction of regeneration cycles with oxygen could increase the catalyst lifetime. The catalyst performance was found to depend on the support according to the sequence: $SiO_2 < TiO_2 < Al_2O_3$. It was speculated that catalyst deactivation was due to Ni sintering. Takenaka et al. used silica-supported nickel catalysts, but conversions below 30 % were reached at 700 ºC, accompanied by fast deactivation. By using X-ray Absorption Fine Structure Spectroscopy (XAFS), nickel carbides were detected at the deactivation stage. The introduction of Pd into $Ni/SiO_2$ increased the catalytic lifetime at temperatures higher than 600 ºC [105]. Zein and Mohamed used three different methods for the preparation of a catalyst consisting of 15 mol % $MnO_x$/20 mol % $Ni/TiO_2$ catalyst: impregnation, poly-vinyl method (polyvinyl alcohol as solvent) and sol-gel method. At 725 ºC, methane conversions around 58 % were observed for 5 hours. The use of regeneration cycles did not affect the catalyst activity [106]. The introduction of Cu on Ni-alumina catalysts improved the methane conversion and catalyst lifetime, as observed by Chen et al. in the temperature range between 500-900 ºC [107]. Experiments conducted at 700 ºC yielded methane conversions ~54 % with stabilities of 20 hours.

Cobalt as active phase is generally not chosen due to its lower activity for methane conversion, together with higher price and toxicity. Only a few studies were made focusing on hydrogen production. A Co/MgO catalyst was tested at 900 ºC by Wang and Ruckenstein in a fixed bed, without any significant success [108]. Takenaka et al. used several supports for cobalt, finding that the activity was hardly dependent on the catalytic supports and crystallite size [109].

Due to the larger abundance and economic cost, it was interesting to test iron as active phase for the catalytic decomposition of methane. Muradov used iron oxide catalysts and observed the formation of large amounts of $CO_x$ during the first two hours, resulting in low hydrogen yields. However, after this induction period, high catalytic activities were observed above 600 ºC [110,111]. Shah et al. tested alumina supported iron catalysts at temperatures between 400-1200 ºC. The conclusion was that molybdenum or palladium doped iron catalysts showed better activities, ~67 %, but the catalyst was strongly deactivated by sintering above 800 ºC [112]. Murata et al. showed that the stability of Fe-based catalysts increased in the presence of $O_2/CO_2$. The methane conversion on $Fe/Al_2O_3$ decreased from 95 to 79 % after 6 hours of testing, while the conversions remained constant with $Fe/Mg/Al_2O_3$. Nevertheless, some CO was detected, together with encapsulating carbon [113]. Reshetenko et al., using co-precipitated $Fe/Al_2O_3$, Fe-$Co/Al_2O_3$ and Fe-$Ni/Al_2O_3$ catalysts between 600-650 ºC, concluded that deactivation was caused by graphite-like carbon layers formed on the metal particles, phase composition changes, metal particles dispersion and their blocking inside multiwall CNT [114].

### 1.4.3 Deactivation

The mechanism of catalyst deactivation during methane decomposition is very complex. Shah et al. observed that the active metal phases do not deactivate due to surface re-crystallization or poisoning, and that the metals remain in their zero-valent state even after being encapsulated by graphitic layers [112]. The build up of carbon on a catalyst surface depends on various factors: nature of the active metal phase, metal particle size, metal-support interaction, carbon removal rate by diffusion through the metal particle, gasification rate due to the presence of hydrogen, $CH_x$ bond breaking and the formation of different carbon deposits due to parallel reactions.

The ferrous metals Ni, Co and Fe are, by far, the most active phases for methane decomposition into hydrogen and filamentous carbon, due to their ability to dissolve carbon and/or to form metal carbides, Ni being the best.

TEM and SEM examinations generally show that the diameters of the carbon filaments formed on supported metal catalysts are in the same range of the metal particle sizes. Rostrup-Nielsen

postulated that the metal particle size can be correlated to the thermodynamic properties, thus the carbon growth process is dependent on the particle size [115]. Baker reported that the Ni particle diameter is critical for carbon growth, sizes between 60-100 nm being most effective [116]. Takenaka et al. observed that the active Ni phase will be encapsulated by carbonaceous deposits when the particle sizes are larger than 200 nm, thus preventing the access of methane to the active sites [117].

Unsupported Ni powders go through strong sinterization process in hydrocarbon atmosphere. Kim et al. reported that Ni particles with diameters of 10-50 nm were good for the initial growth of the carbon filaments, but sizes below 7 nm were useless [118]. Baker [116] and Bartholomew [119] reported that the inverse square root of the carbon filaments growth rate is proportional to the metal particle size, the carbon diffusion rate being faster on small particles due to shorter diffusion paths. The formation of carbon involves C-C bond additions and, therefore, the orientation of the atoms in the active metal phases is sensitive towards the morphologies of the formed carbon species, a so-called "epitaxial effect" [116]. An elegant way to reduce the formation of encapsulating carbon is to dilute the Ni surfaces with much less reactive atoms, such as copper, as reported by Alstrup and Tavares [93]. Solymosi et al. reported that the turnover frequency (TOF) for methane decomposition on Pd supported catalysts decreases with the support type in the following order: $TiO_2 > Al_2O_3 > SiO_2 > MgO$ [120]. This phenomenon has been explained either in terms of particle size or carbon migration from the metal to the support.

So far, the effect of the metal loading has not been clarified. A variety of metal loadings have been used in literature. Most of the works used low metal loads. However, some researchers tried to use high loaded nickel catalysts to increase carbon formation, as Shaikhutdinov et al. [121]. These studies on high loaded Ni catalysts were reported not to be good due to fast deactivation, active site blocking by carbon and particle sinterization resulting in large sizes between 100-300 nm [122,123].

Nevertheless, researchers from the Institute of Carbon Chemistry in Zaragoza, Spain reported good results for methane conversion using high nickel contents on support materials. High loaded nickel catalysts were tested by Suelves et al. at temperatures between 550-700 ºC, using a pure methane feed [124]. Methane conversions near 25 % at 550 ºC, 54 % at 650 ºC and 67 % at 700 ºC were observed, without catalyst deactivation during the 8 hour tests. Higher operation temperatures resulted in closer approach to thermodynamic values. Important conclusions were reported, namely that the deactivation of the catalyst is dependent on catalyst mass and particle size.

Another important aspect is the effect of the metal-support interaction on catalyst deactivation. It was reported by Demicheli et al. that the presence of some potassium at the interface between nickel and carbon lowers the adhesion strength of graphite to the metal particle, and that was confirmed by TEM-EDX examinations on a Ni-alumina catalyst [125]. It was also suggested by Snoeck et al. that the metal-support interaction explains the formation of full or hollow carbon filaments [126]. At low temperatures, the formation of encapsulating carbon is slow, so that the carbon atoms have full access to the entire metal-support interface via diffusion, and full filament nucleation is observed. At higher temperatures, nucleation starts before the entire metal-support interface is saturated with carbon atoms, so the metal/support interaction is more relevant and the particles are lifted up to places where no carbon is precipitated. The suggested mechanism is based on the observation that the formation of hollow filaments is always accompanied by particles with structures similar to drops or pear-shaped cones. Tavares et al. also suggested that, in a similar way, those small particles are held in the support due to enhanced metal-support interaction, therefore, the so-called 'octopus' carbon is observed during methane decomposition over Ni–Cu–Al catalysts at 550 ºC and above, when several filaments grow from one metal particle, and graphite layers are stacked perpendicular to the filament axis [127]. Ermakova and Ermakov have shown that the interaction between metal and silica influences the yields of carbon formation. In fact, 90 % Ni in 10 % $SiO_2$, resulted in fast deactivation. In the case of Fe, silica can either inhibit or promote carbon formation [128].

The operating conditions significantly affect catalyst stability. Depending on the method used (hydrogen pre-treatments or hydrogen in the inlet feedgas), hydrogen always promotes gasification of the carbon deposits. The evolution of hydrogen is dependent on the methane decomposition rate. If the concentration of methane in the feedstream is raised, macroscopically less reactant will be converted, but at the same time more hydrogen is generated so that the metal catalyst will adsorb hydrogen and promote gasification. The same effect can be observed when hydrogen is directly introduced into the methane feed gas, hereby the equilibrium is shifted to the left. Nolan et al. reported that the presence of hydrogen influences the carbon morphologies [129]. Shah et al. reported that, for the same catalyst, the decay constant or respective activity profile is different and depends mainly on the $p_{H_2}^2 / p_{CH_4}$ ratio [112]. On the other hand, Rodriguez et al. reported that CO has a promoting effect on ethylene decomposition over Fe catalysts. It can be concluded that the gas phase components strongly influence the catalyst performance [130].

The morphology and amount of carbon deposited is mostly influenced by the reaction temperature [131]. This is originated by the ability of Ni, Co and Fe to dissolve carbon in a

certain temperature range. On one hand, these active phases are unable to dissolve carbon below 350 ºC, but on the other hand the methane decomposition rate is faster than bulk and surface diffusion of carbon above 900 ºC. Therefore, the metal surface becomes rapidly covered with encapsulating carbon, which stops the reaction.

The performance of catalysts for methane decomposition is limited when used in fixed beds. Therefore, space limitations and the formation of carbon in the reactor must be seen as limiting issues.

### 1.4.4 Carbon products

For a successful $CO_x$-free hydrogen production via catalytic decomposition of methane, the carbon by-product should, if possible, appear as high-value product for further synthesis with appropriate chemical or physical treatments towards the development of new materials with unique properties. In the worst scenario the obtained carbon product can be burned off for energy supply, or used for partial oxidation or in Boudouard-reaction for CO generation. In the luckiest case high value carbon deposits such as CNF/CNT will be obtained.

Carbon exists in several allotropic forms, as shown in Figure 1.7; they differ from one another in the arrangement of the carbon atoms in their lattice [132]. The structure of these materials determines their physical and mechanical properties [133].

Graphite (word meaning old greek "to write") is thermodynamically the most stable allotrope of carbon at standard conditions. Graphitic carbon is characterized by $sp^2$-hybridization. Due to its associated π-bonds, perpendicular to the σ-bond layers, graphite forms a layered lattice. Only some natural graphites and heat-treated samples are nearly perfect crystals. Most of the carbon materials deviate from the perfect crystal structure, therefore other terms are used to characterize the less perfect graphite carbon structures (coke, charcoal, activated carbon, polycrystalline graphite, carbon blacks, carbon fibres, pyrocarbon, etc.).

Carbon fibers are among the most important materials used in technical applications, consisting of at least 92 wt. % of regularly ordered carbon. In the two-dimensional long-range order the carbon atoms are in planar hexagonal networks without any measurable crystallographic order in the third direction.

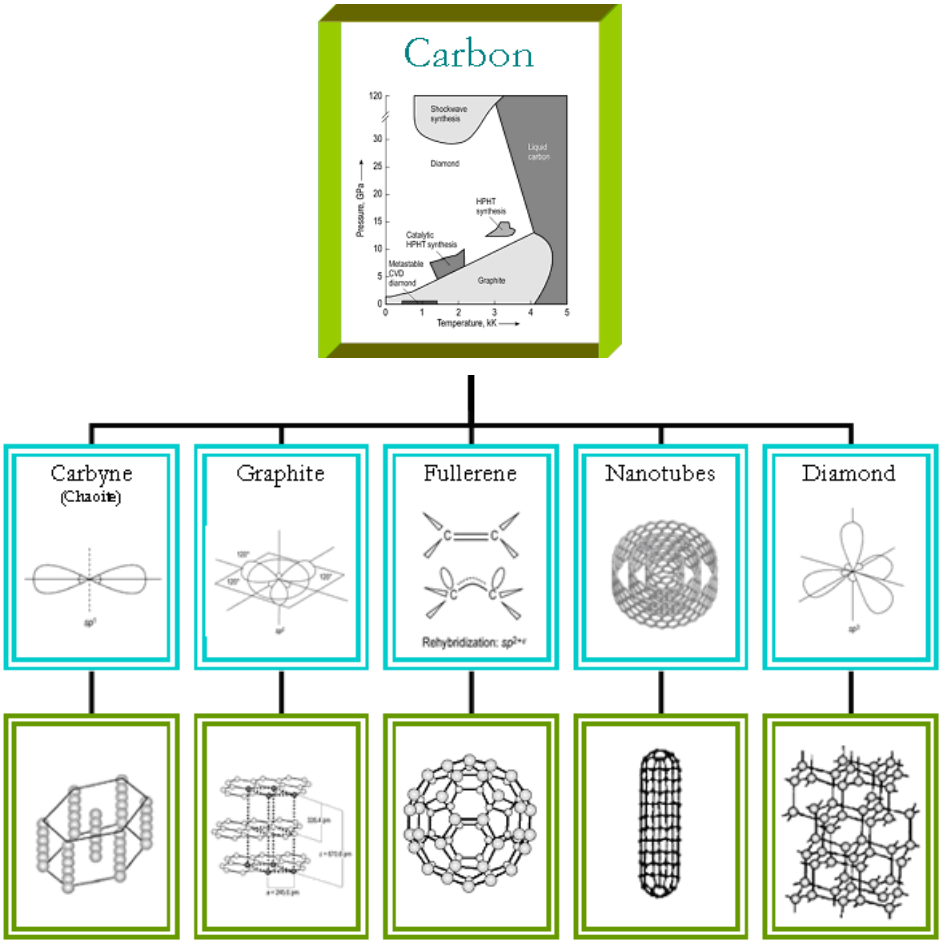



Fig. 1.7 Allotropic forms of carbon

Depending on the production process, several types of carbon fibers can be obtained. The properties of the carbon fibres depend strongly on the used raw material (organic polymers or hydrocarbons), stabilization treatment, carbonization, graphitization and final heat treatment, e.g. polyacrylnitrile (PAN)-based carbon fibres, pitch based carbon fibres or rayon-based carbon fibres.

Normally, the carbon fibers are classified in high modulus (HM), where the graphitic layers have a parallel orientation to the fibre axis, and high tensile (HT) carbon fibres without any well defined orientation. Anisotropic fibres have a high degree of order; they are mainly used as reinforcement in composite materials with organic polymer matrices. Typical end products are textiles, yarns, nets, thread, ropes, etc. Isotropic carbon fibres have a low crystalline order; therefore they have less suitable mechanical properties. The potential technological applications can be catalyst supports, isolation and filtration materials.

The recently discovered new forms of carbon are the nanotubes. Single-wall carbon nanotubes (SWCNT) can be described as rolled up graphene sheets which are closed at each end with half

of a fullerene [134]. Multi-wall carbon nanotubes (MWCNT) consist of various concentric graphene layers.

Different methods are used to produce carbon nanotubes, particularly to synthesize the SWCNT, such as laser evaporation, electric arc discharge and the solar method [135-137]. The catalytic chemical vapour deposition (CCVD) method is known to be an efficient process to produce MWCNT on a large scale [138]. Furthermore, reports have shown that this method can also be efficient to produce SWCNT [139]. The CCVD methods may be based on the pyrolysis of organometallic compounds (metallocenes or $Fe(CO)_5$) [140], or on the catalytic decomposition of hydrocarbons [101].

However, the CCVD technique may originate different carbon products, depending mainly on the catalytic metal and hydrocarbon used, such as carbon nanofibers (CNF), carbon nanotubes (CNT) and encapsulating carbon. The catalytically formed CNF and CNT are generally cylindrical or tubular with radii in nanometer scale and lengths up to several micrometers. The main differences between these three carbon types are described in Table 1.1. The CNF can be divided in two types, a parallel type and a fishbone type (Fig. 1.8).

Table 1.1

Chemical vapour deposited carbon allotropes

| Type | Shape | Graphite layer orientation | Catalyst particle position |
|---|---|---|---|
| CNF | Stacked carbon cones | # $\Theta \leq 90^o$ | At their tip |
| CNT | | $\Theta = 0^o$ | At their tip |
| Encapsulating carbon | Multilayer shells or "carbon onions" | N/A | Surrounded by graphite carbon |

The orientation angle $\Theta$ is the graphite layer orientation between the graphite basal planes and the tube axis.

# The higher the orientation the less the possibility that the fibers are hollow.

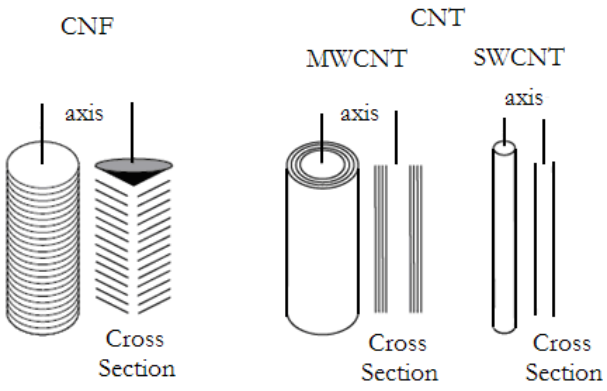



Fig. 1.8 Schematic representation of CNF, MWCNT and SWCNT

## 1.5 Raney-type catalysts

In this work, the catalytic performance of Raney-type catalysts (unsupported catalysts) for methane decomposition was examined. The active phases are nickel, cobalt and iron. To understand the nature and properties of these materials a short overview is given below.

Raney-type catalysts are solid composites [141]. Fine grains in the form of bimetallic alloys are used to synthesize the Raney-type catalysts. The alloys, containing an active metal (Cu, Fe, Co, Ni, Pt, Ru, and Pd) and a second alloy component such as Si, Zn, Mg, or preferentially Al, are prepared by a melting process. During this process the metal phase mixture can also be rapidly quenched using liquid nitrogen or water. Hereafter, the cooled alloy block is then crushed into a fine powder. The particle sizes of the powders are adjusted to the required catalytic applications. Economic reasons play also a role; small particle sizes lead to higher surfaces areas but implicate higher costs in the crushing process. During the melting procedure, small amounts of a third metal, such as zinc, molybdenum, tungsten or chromium, may be added. This is done to enhance catalytic activity, and as such this third metal is called a "promoter" [142]. The addition of a promoter changes the alloy, leading to different properties. The alloy powder is treated with an alkali, usually with a concentrated NaOH solution, which removes selectively the less noble component from the alloy [143]. This leaching treatment is called "activation".

The temperature used to leach the alloy has a marked effect on the surface properties of the catalyst. Commonly used is the temperature range from 70 to 100 °C. The surface areas of the catalysts tend to decrease with increasing leaching temperature [141]. This is due to structural re-arrangements within the alloy that may be considered analogous to sintering, where alloy elements start adhering to each other, leading to the loss of the porous structure.

Alternatively, the more generic terms "skeletal catalysts" or "sponge-metal catalysts" are also used for catalysts which have physical (porous nature) and chemical properties similar to those of Raney nickel, e.g. cobalt, iron, copper, etc. The most common alloy used in industry contains an equal amount (mass) of nickel and aluminium. It was developed in 1926 by the American engineer Murray Raney as an alternative catalyst for the hydrogenation of vegetable oils in industrial processes [142].

After activation, the catalyst shows the presence of residual quantities of $\alpha$-$Al_2O_3$, which help to preserve the pore structure of the catalyst. The porous microstructure of the catalyst arises from the outgoing hydrogen forming free spaces in the Ni crystal. The simplified leaching process is described by the following chemical equations:

$$Al + NaOH + 3H_2O \rightarrow Na[Al(OH)_4] + 3/2\ H_2 \quad \text{(eq. 1.7)}$$

$$Al + 3NaOH + 3H_2O \rightarrow Na_3[Al(OH)_6] + 3/2\ H_2 \quad \text{(eq. 1.8)}$$

If $K_s$ is the constant of product solubility of the ions $Al^{3+}$ and $OH^-$, and $K_c$ is the constant of $Al(OH)_4^-$ complex formation, then the following relations are valid:

$$K_s = [Al^{3+}] \cdot [OH^-]^3 \quad \text{(eq. 1.9)}$$

$$K_c = \frac{[Al(OH)_4^-]}{[Al^{3+}] \cdot [OH^-]^4} \quad \text{(eq. 1.10)}$$

The final conclusion is

$$[Al(OH)_4^-] = K_c \cdot [Al^{3+}] \cdot [OH^-]^4$$

$$= K_c \cdot \frac{K_s}{[OH^-]^3} \cdot [OH^-]^4 = K_c \cdot K_s \cdot [OH^-] \quad \text{(eq. 1.11)}$$

The saturation concentration of Al in NaOH is proportional to the hydroxide concentration. Theoretically, it is possible to dissolve completely the Al using a supersaturated concentration of NaOH [144]. To avoid the formation of aluminium hydroxide in the form of hydragillite or bayerite, it is required to work with high concentration of NaOH [145-148]. During the leaching process, hydragillite and bayerite may cause blocking of the pores, with subsequent loss of surface area and therefore loss of catalyst efficiency.

Nickel is an excellent catalyst for hydrogenation/dehydrogenation reactions. It is important to obtain a high surface area and fine dispersion. Depending on the preparation mode, Ni catalysts often have a sufficiently high surface area and open pore structure to be employed directly.

This type of catalyst is used in a variety of organic synthesis because of their stability and high catalytic activity even at room temperature [149,150]. An overview of the applications of Raney-type catalysts in organic chemistry was published by Schröter [151], but only in the 1960´s the systematic research of these materials, was started.

It is mainly used in the reduction of compounds that have multiple bonds, such as alkines, alkenes, nitrils, dienes, aromatics and carbonyls [152,153]. The reduction of a C=C double bond with Raney-Ni results in a syn fashion [154]. Additionally, Raney-Ni will reduce hetero-hetero atoms bonds such as nitro groups or nitrosamines [155]. The reductive alkylation of amines and the amination of alcohols are also reported [156]. Practical examples for the use of Raney-Ni in chemical industry are e.g.

- Hydrogenation of Glucose into Sorbitol [157]
- Desulfurization of a thioacetal [158]
- Hydrogenation of benzene into cyclohexane [159].

Raney-type catalysts show different properties which depend mostly on the initial alloy composition and preparation method. During the cooling or quenching process, several different Me-Al phases are produced. These Me-Al phases have different leaching properties. Murray Raney described in his first Patent a process for the production of porous Ni by leaching Si from a Ni-Si alloy with NaOH [160]. In a second Patent he found that a better catalyst could be obtained by the leaching of a Ni-Al alloy [142]. In 1940 Murray Raney reported that alumina rich alloys with a composition in the range of 50-70 wt. % of Al are adequate for the production of Ni catalysts [161]. Bradley and Taylor showed that these alloys have different compositions. Depending on the cooling process, different phases such as the Al-$NiAl_3$-eutectic, $NiAl_3$ and $Ni_2Al_3$ where found [162]. The fast quenching of an alloy shows also the presence of a fine dendritic NiAl microstructure [163]. The existence of another $Ni_2Al$ phase in the mentioned compound range was also found by Gwyer [164] and Reynaud [165]. This phase was not included in the phase diagram. The phases are shown in the phase-diagram of Massalski (Figure 1.9) [166,168]. In Figure 1.10 the crystallographic structures for the Ni-Al system according to the International Centre for Diffraction Data (ICDD) are shown.

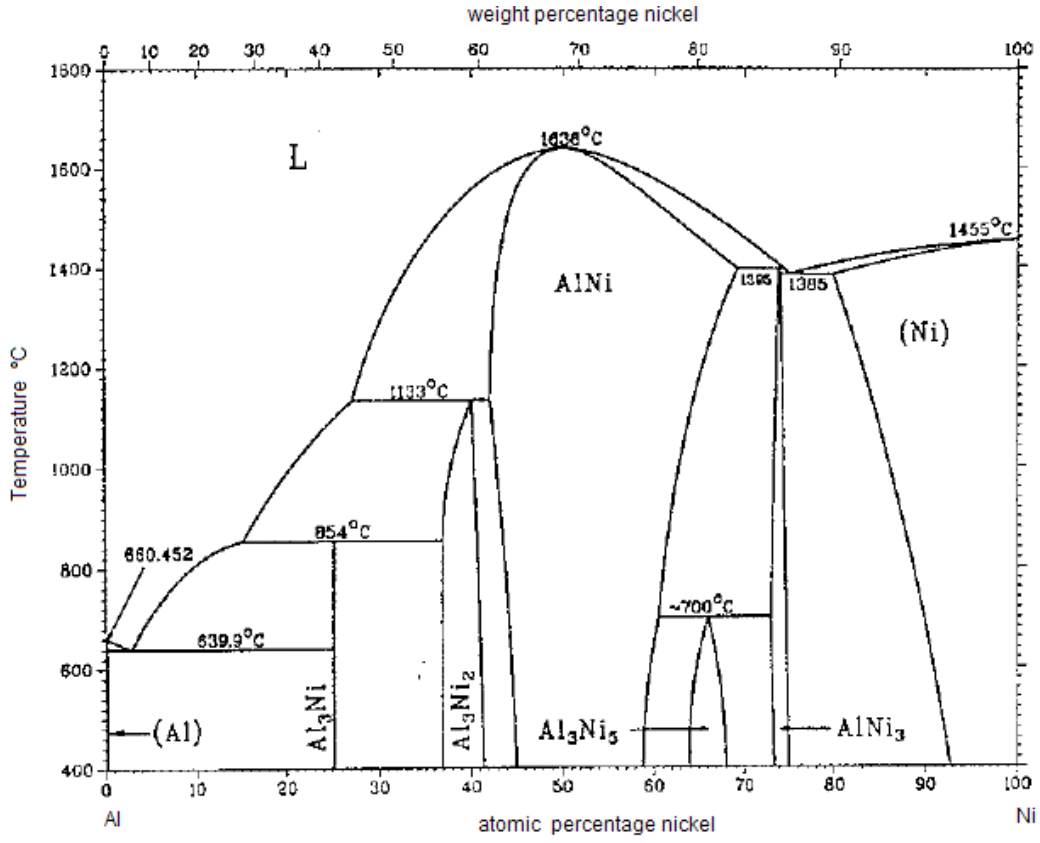
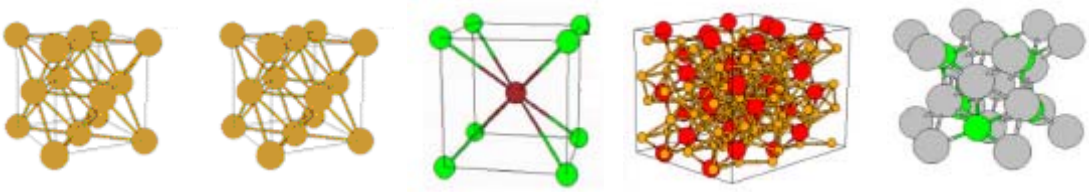



Fig. 1.9 Phase diagram of Ni-Al according to Massalski [168]



Ni Al NiAl $Ni_3Al$ $Al_3Ni_2$

Fig. 1.10 Crystal structures of Ni-Al phases.

Surface analysis of Ni-Al intermetallic phases shows the presence of Al on the surface (Al rich phase) as well as the partial oxidation of Al into Al(III)-oxide. The higher the Al content in the alloy, the higher is the content of segregated Al and the larger is the Al(III)-oxide layer [165].

The reactivity of the Ni-Al phases versus NaOH increases with the Al content [167]. The Al-$NiAl_3$-eutectic, which has 95 wt. % of Al, reacts immediately with the alkali. Al is dissolved from the alloy leaving inner space. The $NiAl_3$ phase reacts also quickly with NaOH, but the $Ni_2Al_3$ phase takes longer to be leached. The Ni-rich phases NiAl and $Ni_3Al$ are not adequate to form Raney-Ni catalysts [168,169]. They react very slowly with the alkali and only the surface Al reacts to form small quantities of Al(III)-oxide [167].

According to the results of Presnyakov et al., the first activation step of an Ni-Al alloy into Raney-Ni is the leaching of Al from the Al-$NiAl_3$-Eutectic and then the removal of Al atoms from the crystal grid in the intermetallic phases, called phase transformation, in the following order [170]:

$$\text{Al-NiAl}_3\text{-Eutectic} \rightarrow \text{NiAl}_3 \rightarrow \text{Ni}_2\text{Al}_3 \rightarrow \text{NiAl} \rightarrow \text{Ni}_3\text{Al} \rightarrow \text{Ni}$$

The transformation of the Al-$NiAl_3$ alloy occurs directly into Ni, the leaching of the $Ni_2Al_3$ alloy passes through different phase transformations; $Ni_2Al_3$ , NiAl, $Ni_3Al$ and Ni [171]. During the leaching process of the $Ni_2Al_3$ alloy the formation of a NiAl phase is observed in the interphase between the unleached $Ni_2Al_3$ and the Ni dispersed in NaOH. The Ni atoms diffuse from the leached Ni area into the boundary area where NiAl is formed [172]. The kinetic of the leaching process is described by Presnyakov et al. [170].

The diffusion of the alkali in the pores of the reaction layer is the rate controlling process [173]. Choudhary et al. state that the initial leaching rate is directly proportional to the outer particle surface area; diffusion effects in the pores do not have any influence [174]. The activation energy is 60 kJ/mol.

Macroscopically, the shape of the particles from the original alloy during the leaching process is kept [175-177]. Microscopically, fine spaces are formed and the particles show smaller sizes originated by the leaching process [180].

Raney-Ni has a face centered cubic structure (fcc), lattice constant is 0.353 nm and hard shifted [181]. The crystal size is in the range of 5-20 nm. EXAFS-examinations show that the coordination number of Ni is 6 [180,181]. The low coordination number is typical for high dispersed catalysts and the Ni-atoms probably take predominantly positions at the surface [182]. XPS-examinations show that Ni is chemically in the oxidation state 0, present as metallic Ni [166,183,184].

During the reaction of Al with NaOH, the hydrogen formed is partially stored in the Ni. The amount of the hydrogen stored depends on the pre-treatment of the catalyst [185]. The hydrogen is partially adsorbed at the surface of the Ni lattice [186-193].

The reversible bonded/dissolved $H_2$ is responsible for the catalytic activity in hydrogenation reactions [194-196]. If the Raney-Ni is heated, hydrogen desorbs and the activity of the catalyst is reduced [197]. Re-adsorption experiments of hydrogen after desorption of the stored hydrogen show that only 10 percent of the former amount is adsorbed [198].

Residual dissolved quantities of Al in the Ni grid are able to expand the fcc-lattice. According to the phase-diagram it is possible to dissolve 7 at. % (4 wt. %) of Al in the fcc Ni-lattice. This concentration corresponds to a lattice-constant of 0.353 nm (Ni mixed crystal) [199].

The residual quantity of Al in Raney-Ni is dependent on the original alloy [163]. The higher the content of $Ni_2Al_3$ in the alloy, the higher is the residual quantity of Al in the catalyst due to the poor leaching of this phase. Raney-Ni catalysts from a $Ni_2Al_3$ phase have a residual quantity of Al in the order of 23 at. %, and catalysts from $NiAl_3$ phase have only 5 at. % of residual Al [163,178]. Surface analysis show that residual Al is present both in the metallic form and in the oxide form [200-202]. XPS-examinations performed on Raney-Ni from the intermetallic phases $Ni_2Al_3$ and $NiAl_3$ as well as from the alloys which contain the two phases, show that Al is only found in the metallic form [203]. Birkenstock et al. reports that Al(III)-oxide is only present in the surface [184]. It is supposed that the metallic Al is dissolved in the lattice of Ni and that there is a possibility of unleached Al in the centre of the catalyst phase.

It was found that residual Al is responsible for a higher activity during hydrogenation processes. The texture and the specific surface area of Ni is stabilized, thus residual $Al/Al^{3+}$ acts as structural promoter and therefore the activity increases [200]. Al in the grain boundaries prevents the sinterization of the Ni-particles and stabilizes the structure [204]. The high defect density in Raney-Ni has its origin in the residual Al [205].

Several studies were made for the surface and porous structure in Raney-Ni. Schmidt published an overview of the different techniques for the characterization of the Raney-Ni surface and presented an optimal method for chemisorptions of hydrogen [206]. It is shown that there is a linear correlation between surface area and the crystallite size [207]; the smaller the Ni-crystallites are the higher is the surface area. At low leaching temperatures the amount of small Ni-crystallites increases. It is also observed that there is a linear correlation between the particle size and the activity [208]. The total surface area of Raney-Ni is between 80-100 $m^2/g$ [207]. It is possible to measure the Ni content on surface by chemisorption of CO [210]. Assuming that CO is not adsorbed by $Al^{3+}$, the total amount of Ni exposed on surface (BET-method) is around 70 %. Similar results were obtained by Fouilloux et al. [211]. They analyzed a Raney-Ni catalyst produced from a Ni-Al alloy with 46 wt. % of Ni. The surface area was around 80 $m^2/g$ and the average pore diameter was 0.3 nm. It was reported from electrochemical measurements that the activity of the catalyst increases linearly with the surface area, because of the corresponding larger amount of active sites [212]. The heating of Raney-Ni results in sintering of the Ni particles [213], because the Ni particles increase their size due to re-crystallization and the defect order in the grids is diminished. A treatment of Raney-Ni in hydrogen atmosphere activates the sintered catalyst again [214].

The use of silicon, magnesium or zinc instead of Al in an alloy results in a non-pyrophoric Raney-Ni [215-219]. These catalysts have a higher content of un-leached phases than the pyrophoric Ni-catalysts from Ni-Al alloys. Normally, they have a lower surface area and less adsorbed hydrogen which desorbs at room temperature (weak bonds). Also the metallic Ni content is lower. Curiously, the activity in the hydrogenation of nitrobenzene was found to be higher than for Raney-Ni from Ni-Al alloys. During the application of the Raney-Ni catalysts, deactivation is observed. The reason for the deactivation is the re-orientation of Al [220]. During the reaction, Al is enriched on the surface, which results in blockage of the active Ni sites. However, it is also possible that adsorbed organic molecules may be responsible for the blockage of the active sites [184].

Raney-type catalysts are highly pyrophoric, as a result of their large surface area and adsorbed hydrogen. When exposed to air it will ignite or burn, producing hazardous fumes, forming NiO. Therefore, Raney-Ni should be handled under an inert atmosphere ($N_2$-atmosphere, $H_2O_{(l)}$ or $EtOH_{(l)}$) during laboratory preparation. The acute exposure to Raney-Ni may cause irritation of the respiratory tract (causes pulmonary fibrosis if inhaled), convulsions, intestinal disorders, eye and skin irritation. Raney-Ni is carcinogenic and teratogenic.

## References


[1] J.-D. Arndt, S. Freyer, R. Geier, O. Machhammer, J. Schwartze, M. Volland, R. Diercks, *Chem. Ing. Technik* **5** (2007) 521.

[2] K. Weissermel, H.J. Arpe, *Industrial Organic Chemistry*, 4th ed. Wiley-VCH 2002.

[3] M. Fischer, G. Kreysa, G. Sandstede, *Int. J. Hydrogen Energy* **12** (1987) 39.

[4] D.S. Scott, *Int. J. Hydrog. Energy* **30** (2005) 1.

[5] A.-S. Rühle: *Wasserstoff und Wirtschaft*, Hydrogeit Verlag, Kremmen 2005.

[6] W. Seifritz, *Int. J. Hydrog. Energy* **30** (2005) 45.

[7] N.Z. Muradov, Hydrogen from Fossil Fuels without $CO_2$ Emission: Perspectives and Applications, *Hydrogen Power System International Symposium*, Cassino-Gaeta, Italy, 1995.

[8] T.R.C. Fernandes, F. Chen, M.G. Carvalho, *Int. J. Hydrog. Energy* **30** (2005) 239.

[9] K.E. Lonngren, E.-W. Bai, *Energy Policy* **36** (2008) 1567.

[10] N. Muradov, T.N. Veziroglu, *Int. J. Hydrog. Energy* **30** (2005) 225.

[11] J.R. Rostrup-Nielson, *Cat. Rev.* **46** (2004) 247.

[12] H. Liebhafsky, E. J. Cairns: *Fuel Cells and Fuel Cell Batteries*, Wiley, New York 1968.

[13] EU: *European Fuel Cell and Hydrogen Projects*, EU, 2003.

[14] M.G. Poirier, C. Sapundzhiev, *Int. J. Hydrog. Energy* **22** (1997) 429.

[15] H. Wendt, W. Jenseit, *Chem. Ing. Tech.* **60** (1988) 180.

[16] T.J. Schmidt, Z. Jusys, H.A. Gasteiger, R.J. Behm, U. Endruschat, H. Boennemann, *J. Electroanalytical Chem.* **501** (2001) 132.

[17] C.-H. Wan, Q.-H. Zhuang, *Electrochimica Acta* **52** (2007) 4111.

[18] J.A. Moulijin, M. Makee, A. van Diepen, *"Chemical Process Technology"*, Wiley, Chichester 2001.

[19] J.R. Rostrup-Nielson, *Catal. Today* **18** (1993) 305.

[20] J.N. Armor, *Appl. Catal. A: Gen.* **176** (1999) 159.

[21] Y. Yürüm, in *"Hydrogen Energy System"*, Kluver Academic Publishers, Dordrecht, (1995), 15.

[22] M. Ota, Y. Abe, M. Watanabe, R.L. Smith Jr., H. Inomata, *Fluid Phase Equilibria* **228-229** (2005) 553.

[23] P. Ferreira-Aparicio, I. Rodriguez-Ramos, A. Guerrero-Ruiz, *Appl. Catal. A: Gen.* **148** (1997) 343.

[24] T.V. Choudhary, D.W. Goodman, *J. Catal.* **192** (2000) 316.

[25] J.L. Figueiredo, C.A. Bernardo, R.T.K. Baker, K.J. Huttinger, *Carbon Fibers Filaments and Composites*, Kluwer Academic Publisher, 1990.

[26] M. Endo, Y.A. Kim, T. Matusita, T. Hayashi, in *Carbon Filaments and Nanotubes*, Kluwer Academic Publisher, Dordrecht, (2001), 5161.

[27] M.F.R. Pereira, J.L. Figueiredo, J.J.M. Órfão, P. Serp, P. Kalck, Y. Kihn, *Carbon* ***42*** (2004) 2807.

[28] P. Serp, M. Corrias, P. Kalck, *Appl. Catal. A: Gen.* **253** (2003) 337.

[29] I. Suelves, M.J. Lázaro, R. Moliner, B.M. Corbella, J.M. Palácios, *Int. J. Hydrog. Energy* **30** (2005) 1555.

[30] G. Bonura, O. Di Blasi, L. Spadaro, F. Arena, F. Frusteri, *Catal. Today* **116** *(2006)* 298.

[31] M.F. Fischa, *Chem. Ing. Tech.* **79** (2007) 29.

[32] R.K. Clayton: *Photosynthesis*, Cambridge University Press (1981).

[33] N. Lior, *Energy* **33** (2008) 842.

[34] H. Römpp, *Römpp Lexikon Chemie*, Verlag: Thieme, Stuttgart, 10 Aufl. 1996.

[35] M. Tomkiewicz, *C.R. Chimie* **9** (2006) 172.

[36] Climate Change 2007: *The Physical Science Basis. Contribution of Working Group I to the Fourth Assessment Report of the Intergovernmental Panel on Climate Change.* Intergovernmental Panel on Climate Change (2007-02-05).

[37] P. Häussinger, R. Lohmüller, A.M. Watson, *Hydrogen*, Ullmann's Encyclopedia of Industrial Chemistry (2000).

[38] F. Joensen, J. R. Rostrup-Nielsen, *J. Power Sources* **105** (2002) 195.

[39] J.R. Rostrup-Nielsen, *Catal. Today* **71** (2002) 243.

[40] J.R. Rostrup-Nielsen, *Catal. Today* **63** (2000) 159.

[41] J.O'M. Bockris, in "*Energy options"*, Wiley, New York, 1985, 185.

[42] J.O'M. Bockris, *Int. J. Hydrog. Energy* **33** (2008) 2129.

[43] S. Blanchette Jr., *Energy Policy* **36** (2008) 522.

[44] A.L. Dicks, *J. Power Sources* **61** ( 1996 ) 113.

[45] S. Dunn, *Int. J. Hydrog. Energy* **27** (2002) 235.

[46] Jules Verne, *The Mysterious Island*, (http://www.literature-web.net/verne/mysteriousisland, 1874).

[47] P. Hoffmann: *The Forevel Fuel: The Story of Hydrogen*, Westview Press, Boulder, 1981.

[48] D. Gregory, *Sci. Am.* **228** (1973) 13.

[49] J.O'M. Bockris, in "*Energy: the solar hydrogen alternative",* Wiley, New York, 1980, 181.

[50] R. Sternberg, *Renewable & Sustainable Energy Reviews* **12** (2008) 1588.

[51] G.M.J. Herbert, S. Iniyan, E. Sreevalsan, S. Rajapandian, *Renewable & Sustainable Energy Reviews* **11** (2007) 1117.

[52] H.Z. Wang, D.Y.C. Leung, M.K.H. Leung, M. Ni, A review on hydrogen production using aluminum and aluminum alloys, *Renewable & Sustainable Energy Reviews* (2008).

[53] N. Lior, *Energy* **33** (2008) 842.

[54] K.V. Kordesch, G.R. Simader, *Chem. Rev.* **95** (1995) 191.

[55] C.H. Hamann, W. Vielstich, *Elektrochemie*, 3. Aufl., Wiley-VCH 1998.

[56] D.L. Trimm, Z.I. Önsan, *Catal. Rev.* **43** (2001) 31.

[57] A.F. Ghenciu, *Curr. Opin. Solid State Mater. Sci.* **6** (2002) 389.

[58] A. Qi, B. Peppley, K. Karan, *Fuel Process. Technol.* **88** (2007) 3.

[59] D.L. Trimm, *Appl. Catal. A: Gen.* **296** (2005) 1.

[60] M. Cappadonia, U. Stimming, K.V. Kordesch, J.C.T. de Oliveira, *Fuel Cells*, Ullmann's Encyclopedia of Industrial Chemistry (2000).

[61] S. Prakash, W. Mustain, P.A. Kohl, *J. Power Sources* **185** (2008) 392.

[62] T.V. Choudhary, D.W. Goodman, *Catal. Letters* **59** (1999) 93.

[63] T.V. Choudhary, D.W. Goodman, *Catal. Today* **77** (2002) 65.

[64] V.R. Choudhary, S. Banejee, A.M. Rajput, *J. Catal.* **198** (2001) 136.

[65] V.R. Choudhary, S. Banejee, A.M. Rajput, *Appl. Catal. A: Gen.* **234** (2002) 259.

[66] T.V. Choudhary, E. Aksoyln, D.W. Goodman, *Catal. Rev.* **45** (2003) 151.

[67] T.V. Choudhary, C. Sivadinarayana, D.W. Goodman, *Chem. Eng. J.* **93** (2003) 69.

[68] J.L. Figueiredo, *Erdöl & Kohle, Erdgas, Petrochemie* **42** (1989) 294.

[69] M. Steinberg, *Energy Conver. & Manag.* **36** (1995) 791.

[70] M. Steinberg, *Int. J. Hydrog. Energy* **23** (1998) 419.

[71] M. Steinberg, *Int. J. Hydrog. Energy* **24** (1999) 771.

[72] N.Z. Muradov, *Energy & Fuels* **12** (1998) 41.

[73] N.Z. Muradov, *Int. J. Hydrog. Energy* **26** (2001) 1165.

[74] M.G. Poirier, C. Sapundzhiev, *Int. J. Hydrog. Energy* **22** (1997) 429.

[75] G.G. Kuvshinov, Y.I. Mogilnykh, D.G. Kuvshinov, *Catal. Today* **42** (1998) 357.

[76] M.A. Ermakova, D.Yu. Ermakov, G.G. Kuvshinov, L.M. Plyasova, *J. Catal.* **187** (1999) 77.

[77] M.A. Ermakova, D.Yu. Ermakov, G.G. Kuvshinov, *Appl. Catal. A : Gen.* **201** (2000) 61.

[78] L.B. Avdeeva, D.I. Kochubey, S.K. Shaikhutdinov, *Appl. Catal. A: Gen.* **177** (1999) 43.

[79] K. Otsuka, T. Seino, S. Kobayashi, *Chem. Letters* **11** (1999) 1179.

[80] K. Otsuka, H. Ogihara, S. Takenaka, *Carbon* **41** (2003) 223.

[81] R.T.K. Baker, M.A. Barber, P.S. Harris, F.S. Feates, R.J. Waite, *J. Catal.* **26** (1972) 51.

[82] L.S. Lobo, D.L. Trimm, J.L. Figueiredo, Proc. 5th Int. Congr. Catal., Palm Beach, 1972, (J.W. Hightower, editor) vol. 2, p. 1125, North-Holland, Amsterdam (1973).

[83] J.G. McCarty, H.J. Wise, *J. Catal.* **57** (1979) 406.

[84] R.T.K. Baker, in J. L. Figueiredo, C. A. Bernardo, R. T. K. Baker, K. J. Huttinger, (eds.), *Carbon Fibers Filaments and Composites*, Kluwer Academic Publishers, pp. 405-439, 1990.

[85] C.A. Bernardo, L.S. Lobo: in: *Catalyst Deactivation*, B. Delmon, G.F. Froment (Editors), p. 409, Elsevier, Amsterdam, 1980.

[86] D.L. Trimm: in: Progress in Catalyst Deactivation, J.L. Figueiredo (Editor), p. 31, Martinus Nijhoff Publishers, The Hague, 1982.

[87] J.L. Figueiredo, D.L. Trimm, *J. Appl. Chem. Biotechnol.* **28** (1978) 611.

[88] M.S. Hoogenraad, *Growth and utilization of carbon fibrils*. Ph.D. thesis, Utrecht University, The Netherlands, 1995.

[89] I. Alstrup, *J. Catal.* **109** (1988) 241.

[90] H.J. Grabke, *Metall. Trans.* **1** (1970) 2872.

[91] H.J. Grabke, *Ber. Bunsenges. Phys. Chem.* **69** (1965) 409.

[92] I. Alstrup, M.T. Tavares, *J. Catal.* **135** (1992) 147.

[93] I. Alstrup, M.T. Tavares, *J. Catal.* **139** (1993) 513.

[94] I. Suelves, J.L. Pinilla, M.J. Lázaro, R. Moliner, *Chem. Eng. J.* **140** (2008) 432.

[95] J. Ashok, S.N. Kumar, A. Venugopal, V.D. Kumari, S. Tripathi, M. Subrahmanyam, *Catal. Comm.* **9** (2008) 164.

[96] M.H. Kim, E.K. Lee, J.H. Jun, S.J. Kong, G.Y. Han, B.K. Lee, T.-J. Lee, K.J. Yoon, *Int. J. Hydrog. Energy* **29** (2004) 187.

[97] R. Moliner, I. Suelves, M.J. Lázaro, O. Moreno, *Int. J. Hydrog. Energy* **30** (2005) 293.

[98] N. Muradov, F. Smith, A. T-Raissi, *Catal. Today* **102-103** (2005) 225.

[99] A.M. Dunker, S. Kumar, P.A. Mulawa, *Int. J. Hydrog. Energy* **31** (2006) 473.

[100] B. Monnerat, L. Kiwi-Minsker, A. Renken, *Chem. Eng. Sci.* **56** (2001) 633.

[101] K. Otsuka, S. Kobayashi, S. Takenaka, *Appl. Catal. A: Gen.* **210** (2001) 371.

[102] K. Otsuka, S. Kobayashi, S. Takenaka, *Appl. Catal. A: Gen.* **190** (2000) 261.

[103] K. Otsuka, T. Seino, S. Kobayashi, S. Takenaka, *Chem. Lett.* **28** (1999) 1179.

[104] M.A. Ermakova, D. Yu, G.G. Kuvshinov, *Appl. Catal. A: Gen.* **201** (2000) 61.

[105] S. Takenaka, Y. Shigeta, E. Tanabe, K. Otsuka, *J. Phys. Chem. B.* **108** (2004) 7656.

[106] S.H.S. Zein, A.R. Mohamed, *Energy & Fuels* **18** (2004) 1336.

[107] J. Chen, Y. Li, Z. Li, X. Zhang, *Appl. Catal. A: Gen.* **269** (2004) 179.

[108] H.Y. Wang, E. Ruckenstein, *Carbon* **40** (2002) 1911.

[109] S. Takena, M. Ishida, M. Serizawa, E. Tanabe, K. Otsuka, *J. Phys. Chem. B.* **108** (2004) 11464.

[110] N.Z. Muradov, *Int. J. Hydrog. Energy* **18** (1993) 211.

[111] N.Z. Muradov, *Energy & Fuels* **12** (1998) 41.

[112] N. Shah, D. Panjala, G.P. Huffman, *Energy & Fuels* **15** (2001) 1528.

[113] K. Murata, M. Inaba, M. Saito, I. Takahara, N. Mimura, *React. Kinet. Catal. Lett.* **80** (2003) 39.

[114] T.V. Reshetenko, L.B. Avdeeva, V.A. Ushakov, E.M. Moroz, A.N. Shmakov, V.V. Kriventsov, D.I. Kochubey, Yu. T. Pavlyukhin, A.L. Chuvilin, Z.R. Ismagilov, *Appl. Catal. A: Gen.* **270** (2004) 87.

[115] J.R. Rostrup-Nielsen, *J. Catal.* **27** (1972) 343.

[116] R.T.K. Baker, *Carbon* **27** (1989) 315.

[117] S. Takenaka, E. Kato, Y. Tomikubo, K. Otsuka, *J. Catal.* **219** (2003) 176.

[118] J.H. Kim, D.J. Suh, T.J. Park, K.L. Kim, *Appl. Catal. A: Gen.* **197** (2000) 191.

[119] C.H. Bartholomew, *Appl. Catal. A: Gen.* **212** (2001) 17.

[120] F. Solymosi, A. Erdohelyi, J. Cserenyi, *Abstracts of Papers of the Am. Chem. Soc.* **207** (1994) 28.

[121] S.K. Shaikhutdinov, L.B. Avdeeva, D.V. Goncharova, D.I. Kochubey, B.N Novgorodov, *Appl. Catal. A: Gen.* **126** (1995) 125.

[122] M. Matsukata, T. Matsushita, K. Ueyama, *Chem. Eng. Sci.* **51** (1996) 2769.

[123] E.G.M. Kuijpers, J.W. Jansen, A.J. van Dillen, J.W. Geus, *J. Catal.* **72** (1981) 75.

[124] I. Suelves, M.J. Lázaro, R. Moliner, B.M. Corbella, J.M. Palacios, *Int. J. Hydrog. Energy* **30** (2005) 1555.

[125] M.C. Demicheli, D. Duprez, J. Barbier, O.A. Ferretti, E.N. Ponzi, *J. Catal.* **145** (1994) 437.

[126] J.W. Snoeck, G.F. Froment, M. Fowles, *J. Catal.* **169** (1997) 240.

[127] M.T. Tavares, C.A. Bernardo, I. Alstrup, J.R. Rostrup-Nielson, *J. Catal.* **100** (1986) 545.

[128] M.A. Ermakova, D.Yu. Ermakov, *Catal. Today* **77** (2002) 225.

[129] P.E. Nolan, M.J. Schabel, D.C. Lynch, A.H. Cutter, *Carbon* **33** (1995) 79.

[130] N.M. Rodriguez, M.S. Kim, R.T.K. Baker, *J. Catal.* **144** (1993) 93.

[131] P.K. de Bokx, A.J.H.M. Kock, E. Boellaard, W. Klop, J.W. Geus, *J. Catal.* **96** (1985) 454.

[132] A. Krüger, *Neue Kohlenstoffmaterialien*, Teubner Verlag 2006.

[133] U. Müller, *Anorganische Strukturchemie*, Teubner Verlag 1996.

[134] M.S. Dresselhaus, G. Dresselhaus, R. Saito, *Carbon* **33** (1995) 883.

[135] A. Thess, R. Lee, P. Nikolaev, H.J. Dai, P. Petit, J. Robert, C.H. Xu, Y.H. Lee, S.G. Kim, A.G. Rinzler, D.T. Colbert, G.E. Scuseria, D. Tomanek, J.E. Fisher, R.E. Smalley, *Science* **273** (1996) 483.

[136] C. Journet, W.K. Maser, P. Bernier, A. Loiseau, M.L. De La Chapelle, S. Lefrant, P. Deniart, R. Lee, J.E. Fisher, *Nature* **388** (1997) 756.

[137] D. Laplaze, P. Bernier, W.K. Maser, G. Flamant, T. Guillard, A. Loiseau, *Carbon* **36** (1998) 685.

[138] V. Ivanov, A. Fonseca, J. B. Nagy, A.A. Lucas, D. Bernaerts, X.B. Zhang, *Carbon* **33** (1995) 1727.

[139] J.-F. Colomer, C. Stephan, S. Lefrant, G. Van Tendeloo, I. Willems, Z. Kónya, A. Fonseca, Ch. Laurent, J. B. Nagy, *Chem. Phys. Lett.* **317**(2000) 83.

[140] J.J. Schneider, J. Engstler, *Deutsches Bundespatentamt* **DE** 100 09 991. A1.

[141] A.J. Smith, D.L. Trimm, *Annu. Rev. Mater. Res.* **35** (2005) 127.

[142] M. Raney, *US Patent* 1,628,190 (1927).

[143] Becker, H.G.O., Berger, W., Domschke, G., *„Organikum"* Wiley-VCH, 2004.

[144] M. Boll, S. Völkening, *DE Patent* 10 330 636, (2005).

[145] Z. Csürös, J. Petró, V. Kalman, L. Erdey, F. Paulik, *Chem. Eng.* **10** (1966) 27.

[146] A.F.Holleman, E. Wiberg, *„Lehrbuch der Anorganischen Chemie"* deGruyter, Berlin 1985.

[147] S. Nishimura, S. Ikeda, M. Kinoshita, M. Kawashina, *Bulletin of the Chemical Society of Japan* **58** (1985) 391.

[148] S.D. Robertson, J. Freel, R.B. Anderson, *J. Catal.* **24** (1972) 130.

[149] H.C. Robinson, H.R. Snyder, *Org. Synth.* **3** (1955) 720.

[150] E. Schwenk, D. Papa, H. Hankin, , M. Ginsberg, *Org. Synth.* **3** (1955) 742.

[151] R. Schröter, *Angew. Chemie* **54** (1941) 229.

[152] G. Ertl, H. Knözinger, *Preparation of Solid Catalysts*, Wiley-VCH 1997.

[153] G.A. Page, D.S. Tarbell, *Org. Synth.* **4** (1963) 136.

[154] T.W.G. Solomons, C.B. Frykle, *Org. Chemistry*, Wiley-VCH 2004.

[155] D. Enders, R. Pieter, B. Renger, D. Seebach, *Org. Synth.* **6** (1988) 542.

[156] R.G. Rice, E.J. Kohn, *Org. Synth.* **4** (1963) 283.

[157] S. Schimpf, C. Louis, P. Claus, *Appl. Catal. A: Gen.* **318** (2007) 45.

[158] P.G. Gassman, T.J. van Bergen, *Org. Synth.* **6** (1988) 601.

[159] T.W.G. Solomons, C.B. Fryhle, *Organic Chemistry* 8th Ed (2004), Wiley Int. Ed.

[160] M. Raney, *US Patent* 1,563,787 (1925).

[161] M. Raney, *Ind. Eng. Chem.* **32** (1940) 1199.

[162] A.J. Bradley, A. Taylor, *Proceedings of the Royal Society London A* **159** (1937) 56.

[163] S. Hamar-Thibault, J. Gros, J.C. Joud, J. Masson, J.P. Damon, J.M. Bonnir, in: *Preparation of Catalysts V*, Poncelet, Jacobs et al. (eds), Elsevier, Amsterdam 1991, 601.

[164] A. Gwyer, *Zeitschrift für Anorganische Chemie* **57** (1908) 113.

[165] F. Reynaud, *J. Appl. Crystallography* **9** (1976) 263.

[166] W.O. Alexander, N.B. Vaughan, *J. Inst. Metals* **61** (1937) 247.

[167] J. C. Klein, D. Hercules, *Analytical Chemisry* **53** (1981) 754.

[168] T.-B. Massalski, *Binary Alloy Phase Diagrams*, ASM International 1996.

[169] G. Stempel, *Nickel-Berichte* **24** (1966) 221.

[170] A.A. Presnyakov, K.T. Chernousova, T. Kabiev, A.B. Fasman, T.T. Bocharova, *J. Appl. Chemistry of the USSR* **40** (1967) 929.

[171] V.N. Ermolaev, A.B. Fasman, S.A. Semiletov, V.I. Khitova, *Bulletin of the Academy of Sciences of the USSR*, *Physical Series* **7** (1983) 1218.

[172] F. Delannay, *Reactivity of Solids* **2** (1986) 235.

[173] S.D. Mikkailenko, G.N. Baeva, B.F. Petrov, A.B. Fasman, *Soviet Powder Metallurgy and Metal Ceramics* **25** (1986) 537.

[174] V.R. Choudhary, S.K. Chaudhari, M.G. Sane, *Proceedings of the 7th National Symposium on Catalysis*, Wiley Eastern Ltd., New Delhi (1985) 171.

[175] C.S. Brooks, F.D. Lenkey, G.S. Golden, *Surf. Tecnol.* **16** (1982) 67.

[176] C.S. Brooks, F.D. Lemkey, G.S. Golden, *Rapidly Solidification Amorphous and Crystalline Alloys*, Proceedings of the Materials Research Society Annual Meeting, North-Holland Publ., New York 1982, 397.

[177] P. Colin, S. Hamar-Thibault, J.C. Joud, *J. Mater. Sci.* **27** (1992) 2326.

[178] J. Freel, W. J. Pieters, R. B. Anderson, *J. Catal.* **16** (1970) 281.

[179] A. Knappworst, K.-H. Mader, *Naturwissenschaften* **52** (1965) 590.

[180] I. Nakabayashi, E. Nagav, K. Miyata, T. Moriga, T. Ashida, T. Tomida, M. Hyland, J. Metson, *J. Mater. Chem.* **5** (1995) 737.

[181] B. Frenzel, J. Rothe, J. Hornes, P. Fornasini, *J. de Physique IV* **7** (1997) 273.

[182] G.H. Via, J.-H. Sinfelt, F.W. Lytle, *J. Chem. Phys.* **71** (1979) 690.

[183] F. Delannay, J.P. Damon, J. Masson, B. Delmon, *Appl. Cat.* **4** (1982) 169.

[184] U. Birkenstock, R. Holm, B. Reinfandt, S. Storp, *J. Catal.* **93** (1985) 55.

[185] G.L. Paduykova, G.A. Pushkauva, A.B. Fasman, *Soviet Electrochem.* **20** (1984) 891.

[186] S.Sh. Schilstein, E.A. Vishnevetskii, V.A. Somenkov, A.B. Fasman, *Inorganic Mater.* **16** (1981) 1466.

[187] J. Heiszman, J. Petró, A. Tungler, T. Máthé, Z. Csürös, *Acta Chimica Academiae Scientiarum Hungaricae* **89** (1976) 31.

[188] J. Heiszman, S. Békássy, J. Petró, *Proceedings of the 4th Int. Conference on Thermal Analysis*, 3, Heyden, London 1975, p. 193.

[189] A. Tungler, J. Petró, T. Máthé, J. Heiszman, S. Békássy, Z. Csürös, *Acta Chimica Academiae Scientiarum Hungaricae* **89** (1976) 31.

[190] I. Nicolau, R.B. Anderson, *J. Catal.* **68** (1981) 339.

[191] R.J. Kokes, P.H. Emmett, *J. Am. Chem. Society* **81** (1959) 5032.

[192] P. Fouilloux, G.A. Martin, A.J. Renouprez, B. Moraweck, B. Imelik, M. Prettre, *J. Catal.* **25** (1972) 212.

[193] G.A. Martin, P. Fouilloux, *J. Catal.* **38** (1975) 231.

[194] F. Hochard, H. Jobic, J. Massardier, A. Renouprez, *J. Mol. Catal.* **95** (1995) 165.

[195] J. Heiszman, S. Békássy, A. Tungler, J. Petró, *Proceedings of the 2nd Int. Congress on Hydrogen in Metals*, 2, Pergamon Press, Oxford, Paper No. 4A13, 1995.

[196] A.D. Johnson, S.P. Daley, A.L. Utz, S.T. Ceyer, *Science* **257** (1992) 223.

[197] A. Tungler, J. Petró, T. Máthé, J. Heiszman, F. Buella, Z. Csürös, *Acta Chimica Academiae Scientiarum Hungaricae* **89** (1976) 151.

[198] A. Tungler, S. Békássy, J. Petró, T. Máthé, *Acta Chimica Academiae Scientiarum Hungaricae* **105** (1980) 73.

[199] A. Taylor, R. Floyd, *J. Institute of Metals* **81** (1952) 5.

[200] G. Bayer, H.G. Fitzky, R. Holm, *Forschungsberichte Rohstofforschung*, Bundesministerium für Forschung und Technologie, Bonn 1982.

[201] F. Hochard-Poncet, P. Delichère, B. Moraweck, M. Jobic, A.J. Renouprez, *J. Chem. Society Faraday Transactions* **91** (1995) 2891.

[202] P. Fouilloux, *Appl. Cat.* **8** (1983) 1.

[203] F. Delannay, J.P. Damon, J. Masson, B. Delmon, *Appl. Catal.* **4** (1982) 169.

[204] J.-P. Candy, P. Fouilloux, J. Vedrine, B. Imelik, *Compte Rendue Academie de Science Paris* **288** (1979) 97.

[205] C.E. Pearce, D. Lewis, *J. Catal.* **26** (1972) 318.

[206] S.R. Schmidt, *Catalysis of Organic Reactions*, Dekker, New York, 45.

[207] S.D. Robertson, R.B. Anderson, *J. Catal.* **41** (1976) 405.

[208] E. Hofer, H. Hintermann, *Transactions of the Faraday Society* **60** (1964) 1457.

[209] S.D. Robertson, R.B. Anderson, *J. Catal.* **41** (1976) 405.

[210] J. Freel, S.D. Robertson, R.B. Anderson, *J. Catal.* **18** (1970) 249.

[211] P. Fouilloux, G.A. Martin, A.J. Renouprez, B. Moraweck, B. Imelik, M. Prettre, *J. Catal.* **25** (1972) 212.

[212] O. Markolová, K. Smrcek, Z. Ministr., Z. Spitzer, *Chem. Commun.* **47** (1982) 1695.

[213] J. Yasamura, *Nature* **173** (1954) 80.

[214] S.D. Mikkailenko, T.A. Khodareva, E.V. Leongardt, *J. Catal.* **141** (1993) 699.

[215] S. Békassy, J. Petró, G. Liptay, J. Heiszman, A. Tungler, *Proceedings of the 4th Int. Conference of Thermal Analysis*, Vol. 3, Heyden, London, 1975, 221.

[216] S. Békassy, J. Petró, E. Kristyák, A. Csamáky, A. Kálmán, *Acta Chimica Academiae Scientiarum Hungaricae* **88** (1976) 375.

[217] J. Heiszman, S. Békássy, J. Petró, *Acta Chimica Academiae Scientiarum Hungaricae* **86** (1975) 347.

[218] J. Heiszman, K. Payer, S. Békássy, J. Petró, *Acta Chimica Academiae Scientiarum Hungaricae* **84** (1975) 431.

[219] A. Tungler, S. Békássy, J. Petró, *Acta Chimica Academiae Scientiarum Hungaricae* **86** (1975) 359.

[220] D.F. Allgeyer, *Industrial Research & Development* **23** (1981) 118.

# *Chapter II*

## Catalytic Decomposition of Methane on Raney-type Catalysts

Published in

Applied Catalysis A: General 348 (2008) 103

*"Progress is the way from the primitive through the complicated to the simple."*

**Werner von Braun**

## Abstract

The catalytic decomposition of methane into $CO_x$-free hydrogen and filamentous carbon was investigated on Raney-type catalysts. Catalysts performance was assessed by comparing the measured conversions with the equilibrium values and with selected results reported recently. The activity, selectivity and stability were dependent on the alloy composition and preparation method (conventional or quenched alloy types), as well as the operating conditions. Textural properties, chemical compositions and catalyst performances were determined, and the carbon deposits were characterized by different techniques. Ni and Co catalysts obtained from Raney-type alloys prepared by quenching showed better performance for methane decomposition than conventional systems, with conversions approaching equilibrium. The stability of the catalysts could be extended by increasing the contact time and by hydrogen pre-treatment of the catalysts. The carbon deposits consist mostly of carbon nanofibres and carbon nanotubes. In addition to the high activity and stability for methane decomposition, there was no generation of carbon oxides, which makes these catalysts suitable for the production of pure hydrogen for fuel cells.

## 2.1 Introduction

Concerns over the environment and depletion of fossil fuels led to the concepts of "hydrogen-energy system" and "hydrogen economy". Hydrogen is a convenient energy carrier which can be used efficiently and without any emissions in fuel cells. Hydrogen is mostly produced by steam reforming of methane, which also yields CO and $CO_2$. For fuel cell applications, however, very low levels of carbon oxides are tolerated. An interesting alternative process is the catalytic decomposition of methane ($CH_4 \rightleftharpoons C + 2\ H_2$), especially if the carbon by-product can be obtained in suitable form for practical applications, such as carbon nanofibers or nanotubes [1]. Thus, there has been an intense research effort on this topic in recent years. Various types of carbon materials (activated carbons, carbon blacks) have been used as catalysts for this purpose [2–6]. However, in general, carbon materials perform rather poorly, since the methane conversions reported are quite low, and there is strong deactivation due to carbon deposition. It also became clear that the carbon deposits are not catalytically active themselves for further methane decomposition [4]. Metal catalysts for this reaction are usually based on Ni, Co or Fe [7–27], which is not surprising, since these are well known active catalysts for hydrocarbon decomposition and carbon formation [28,29]. Supported catalysts such as $Ni/Al_2O_3$ have moderate activities, but generally they are not very stable. The best results have been obtained with high metal loaded catalyst systems [7,16]. Therefore, massive catalysts seem to be a good choice for the proposed task. In the present work we report promising results obtained with massive skeletal catalysts (Raney-type Ni, Co and Fe). The effect of the operating conditions on the activity, selectivity and stability of these catalytic systems, and on the type of carbon formed, was investigated in detail. To our knowledge there is only one very recent report on this type of catalyst for methane decomposition, where the emphasis was on carbon nanofibre formation [30].

## 2.2 Experimental

### 2.2.1 Catalysts

The skeletal (Raney-type) catalysts used in this work were prepared from Me–Al alloys (Me = Ni, Co or Fe) obtained from two different sources. The nominal active metal mass content in the alloys are 50 and 30 wt. % for Ni, 50 and 30 wt. % for Co, 50 and 35 wt. % for Fe. The Ni 50 wt. % alloy is a commercial product from Fluka Chemie Gmbh. The remaining alloys used were supplied by H.C. Starck GmbH (Amperkat® SK alloys). The Ni30, Co30 and Fe35 alloys are

obtained by a fast quenching method [31], and the remaining alloys are conventional products [32]. Prior to the reaction tests, the Raney-type alloys were activated by leaching out the aluminium with a concentrated NaOH solution at room temperature for 2 h [33]. The catalysts were subsequently washed several times with distilled water and kept in a flask with ethanol as required by their pyrophoric nature. In this work, the catalysts are designated by the original composition of the alloys. Thus, catalyst Ni30 is the catalyst obtained by leaching out the Al from the 30 % Ni – 70 % Al alloy.

### 2.2.2 Reaction studies

Temperature programmed reaction (TPRe) experiments were carried out with a custom built setup, consisting of a U-shaped tubular micro-reactor, placed inside an electrical furnace. The flow rate of methane (2.5 $Ncm^3$/min) diluted in helium carrier gas (25 $Ncm^3$/min) and a temperature program from room temperature to 800 ºC at a heating rate of 5 ºC/min was controlled with appropriate equipment. The amounts of $H_2$ (m/z = 2), $CH_4$ (m/z = 16), $C_2H_2$ (m/z = 26), CO or $C_2H_4$ (m/z = 28), NO or $C_2H_6$ (m/z = 30), and $CO_2$ (m/z = 44) were monitored with a quadrupole mass spectrometer.

For the isothermal reaction studies, the catalysts were loaded into a tubular reactor, and dried overnight at 78 ºC in a nitrogen stream of 100 $Ncm^3$/min. In some cases, the catalysts were pretreated in hydrogen for 2 h at 600 ºC with a total gas flow rate of 110 $Ncm^3$/min and a composition corresponding to a $H_2/N_2$ molar ratio of 1:10. This treatment is hereafter referred to as HPT.

The continuous-flow reactor was a 75 cm long silica tube with 2.7 cm i.d., inserted into a furnace with a PID temperature controller. The flow rates of methane (99.999 %), nitrogen (99.995 %) and hydrogen (99.999 %) were controlled by mass flow controllers. In most of the experimental runs the feed composition was a gas mixture of methane and nitrogen (molar ratio of 1:10) with a total gas flow rate of 110 $Ncm^3$/min. During the reaction, the composition of the outgoing gas stream was determined with a gas chromatograph equipped with a capillary column (Carboxen 1010 Plot, Supelco) and a thermal conductivity detector.

### 2.2.3. Characterization of catalysts and carbon deposits

The particle size distributions of the alloys and the corresponding catalysts were measured with a laser particle size analyzer Coulter LS 230.

The specific surface areas of the fresh catalysts were calculated by the BET method from the $N_2$ equilibrium adsorption isotherms at 77 K, determined with a Coulter Omnisorp 100 CX apparatus.

The alloys, catalysts and carbon deposits were examined with a JEOL JCM-35C scanning electron microscope (SEM) associated with an energy dispersive X-ray analyzer (EDX) Tracor TN-2000.

A high-resolution transmission electron microscopy (TEM) study of the carbon deposits was carried out with a Phillips CM12 instrument.

X-ray photoelectron spectra (XPS) of the alloys and catalysts were acquired in a VG Scientific Escalab 200A apparatus. Quantitative results were obtained by fitting the experimental peaks to Gaussian–Lorentzian curves, measuring the spectral areas corresponding to each chemical element of interest and applying their respective empirical sensitivity factors.

## 2.3 Results

### 2.3.1 Catalysts characterization

The properties of the Raney-type alloys and their corresponding catalysts are collected in Table 2.1.

Table 2.1

Characterization of the Raney-type alloys and corresponding catalysts

| Sample | Alloy | | | Catalyst | | |
|---|---|---|---|---|---|---|
| | $\bar{d}$ [μm] | $R^a_{n,alloy}$ | $R^a_{eff,alloy}$ | $\bar{d}$ [μm] | $R^a_{eff,catalyst}$ | $S_{BET}$ [$m^2/g$] |
| Ni50 | 36 | 0.315 | 0.39 ± 0.06 | 21 | 0.72 ± 0.07 | 82 |
| Ni30 | 285 | 0.165 | 0.17 ± 0.02 | 156 | 0.85 ± 0.07 | 64 |
| Co50 | 62 | 0.314 | 0.30 ± 0.05 | 59 | 0.85 ± 0.16 | 41 |
| Co30 | 372 | 0.164 | 0.17 ± 0.02 | 211 | 0.94 ± 0.06 | 26 |
| Fe50 | 86 | 0.326 | 0.35 ± 0.09 | 43 | 0.95 ± 0.05 | 62 |
| Fe35 | 51 | 0.206 | 0.23 ± 0.06 | 63 | 0.95 ± 0.19 | 24 |

$\bar{d}$ : average particle size of the powders;

$R^a_{n,alloy}$ : nominal atomic ratio active metal/total metals;

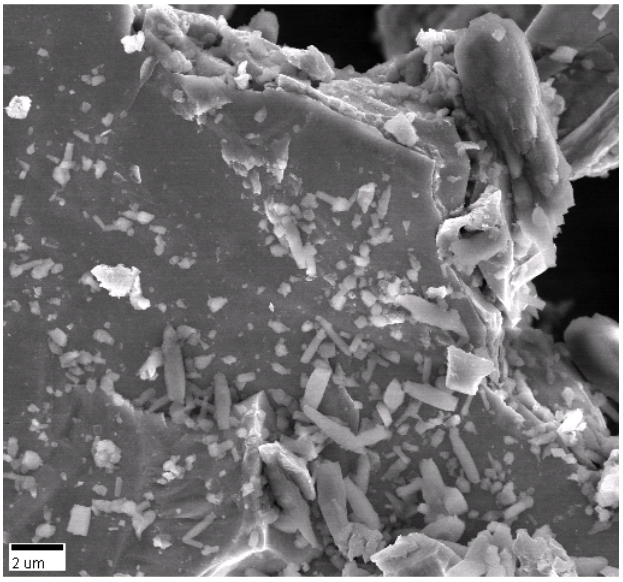
$R^a_{eff,alloy}$ : determined effective atomic ratio active metal/alloy metals;

$R^a_{eff,catalyst}$ : determined effective atomic ratio active metal/catalyst metals;

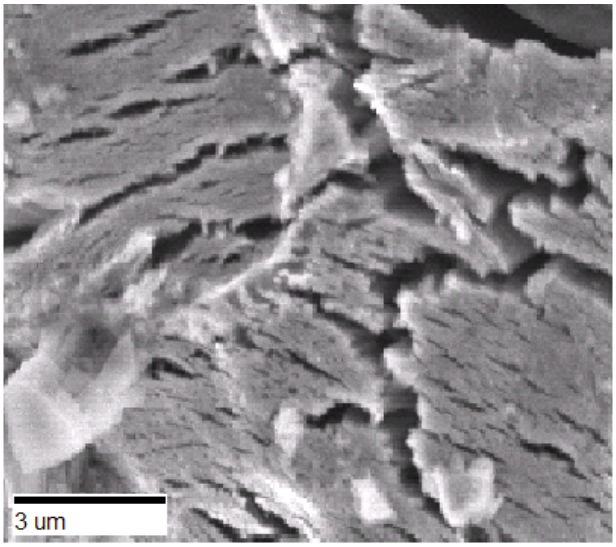
$S_{BET}$: specific surface area.

It is observed that the particle sizes of the Ni50, Ni30, Co30 and Fe50 catalysts are approximately half of those of the original alloys, while Co50 and Fe35 kept approximately their original size. The BET surface areas of the catalysts are within the range of reported values for this type of catalysts [34].

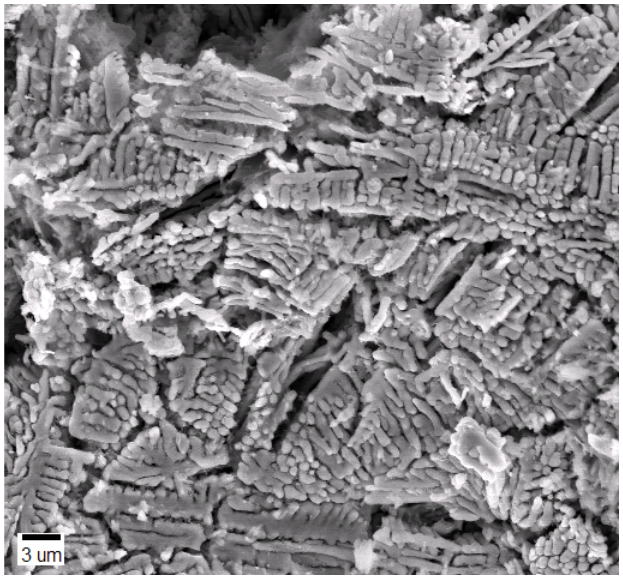
It is also observed that the catalysts Ni30, Co30 and Fe35 exhibit lower surface areas and higher particle sizes than Ni50, Co50 and Fe50, respectively, most probably as a result of the different preparation methods of the original alloys. For the alloys, the atomic ratios $R^{a}_{eff,alloy}$ = (active metal/total metal) determined by EDX are in good agreement with the nominal values $R^{a}_{n,alloy}$. Upon activation, the corresponding atomic ratios in the catalysts $R^{a}_{eff,catalyst}$ are much higher, due to the removal of most of the Al. The residual Al left is present as $Al_2O_3$, as confirmed by EDX. It should be noticed that the residual amount of Al is higher in the Ni50 catalyst, all other catalysts being richer in the active metal. The residual alumina left after leaching will act as a structural promoter, stabilizing the catalyst structure against sintering, in a similar way as for other massive catalysts reported in the literature [14,24,35]. The residual quantity of Al in Raney-type Ni catalysts depends on the original alloy [36]. Various phases may be present, such as $NiAl_3$, $Ni_2Al_3$ and NiAl. The higher the content of Ni in these intermetallic phases, the lower is their reactivity towards leaching by NaOH. The Ni50 and Ni30 alloys have different amounts of these phases. For instance, the Ni50 alloy contains both $Ni_2Al_3$ and $NiAl_3$, while Ni30 contains mostly $NiAl_3$. Therefore, the residual amount of Al in the Ni50 catalyst is larger, due to the lower leaching rate of the $Ni_2Al_3$ phase relatively to $NiAl_3$ [37,38]. Fig. 2.1(a–c) shows SEM micrographs of the catalysts Ni50 (Fig. 2.1a), Ni50 pre-treated in hydrogen (Fig. 2.1b) and Ni30 (Fig. 2.1c). Comparison of these micrographs shows that the microstructure of Ni50 becomes similar to that of Ni30 upon hydrogen treatment (HPT). Catalysts Co50, Fe50 and Fe35 show nearly the same morphology as Ni50, and the catalyst Co30 is similar to Ni30. The Co50, Fe50 and Fe35 catalysts pre-treated with hydrogen show morphologies similar to Ni30 (or Co30). The more fragmented microstructure of Ni30 and Co30 is typical of alloys which have been quenched rapidly during the production process, and this microstructure is kept also after leaching with an alkaline solution [31].




a)




b)




c)

Fig. 2.1 SEM micrographs of Ni50 (a), Ni50 (HPT) (b), Ni30 (c) catalysts.

Table 2.2 shows the surface characterization of the Me–Al alloys and the corresponding catalysts, obtained by XPS.

Table 2.2

Surface characterization of Raney-type alloys and corresponding catalysts

| | Me $2p^3$ [eV] | $Al/Al_2O_3$ 2p [eV] | $R^a_{surface}$ |
|---|---|---|---|
| Alloy | | | |
| Ni50 | 853.5 | 76.0 | 0.06 |
| Ni30 | 854.0 | 75.9 | 0.01 |
| Co50 | 779.6 | 76.9 | 0.03 |
| Co30 | 780.7 | 78.0 | 0.01 |
| Fe50 | 709.0 | 76.1 | 0.07 |
| Fe35 | 709.5 | 77.5 | 0.02 |
| | | | |
| Catalyst | | | |
| Ni50 | 853.5 | 74.0 | 0.75 |
| Ni30 | 854.0 | 73.9 | 0.80 |
| Co50 | 784.0 | 71.1 | 0.43 |
| Co30 | 781.1 | 70.6 | 0.58 |
| Fe50 | 713.1 | 71.7 | 0.49 |
| Fe35 | 710.3 | 69.9 | 0.05 |

$R^a_{surface}$ : determined atomic ratio active metal on surface/total metals.

In the case of the alloys, the results show that the particles are mostly covered with an $Al_2O_3$ layer. The higher the Al content in the original alloy, the higher is the amount of $Al_2O_3$ found on the surface [38,39]. Upon activation, the XPS spectra of the catalysts show that Ni and Co are mostly in the zero-valent state, confirming that there is no formation of oxides or hydroxides when the corresponding alloys are attacked by NaOH, in agreement with the literature [33,39–41]. Thus, any oxygen remaining in the catalyst must be bound to Al, or is present as adsorbed species. The presence of residual Al or alumina was detected and also reported by other authors [42–44]. The XPS spectra for the Fe catalysts show clearly that their surface is partially oxidized into Fe(II) and/or Fe(III), in agreement with other authors [41].

As shown in Table 2.2, the values for the exposed Ni atoms on the surface of the respective catalysts are in good agreement with the values obtained by EDX analysis. For the Co and Fe catalysts, the concentrations of active atoms exposed on the surface are lower than those indicated by the EDX values, showing that there is enrichment of Al on the surface. The very low $R^a_{surface}$ found for catalyst Fe35 indicates that Fe must be almost completely covered with Al. This is possibly related to the method of preparation of the original alloy, and will reflect upon the catalytic behavior of this sample, as will be shown in Section 2.3.2.2.

### 2.3.2 Catalysts performance

*2.3.2.1 Preliminary tests*

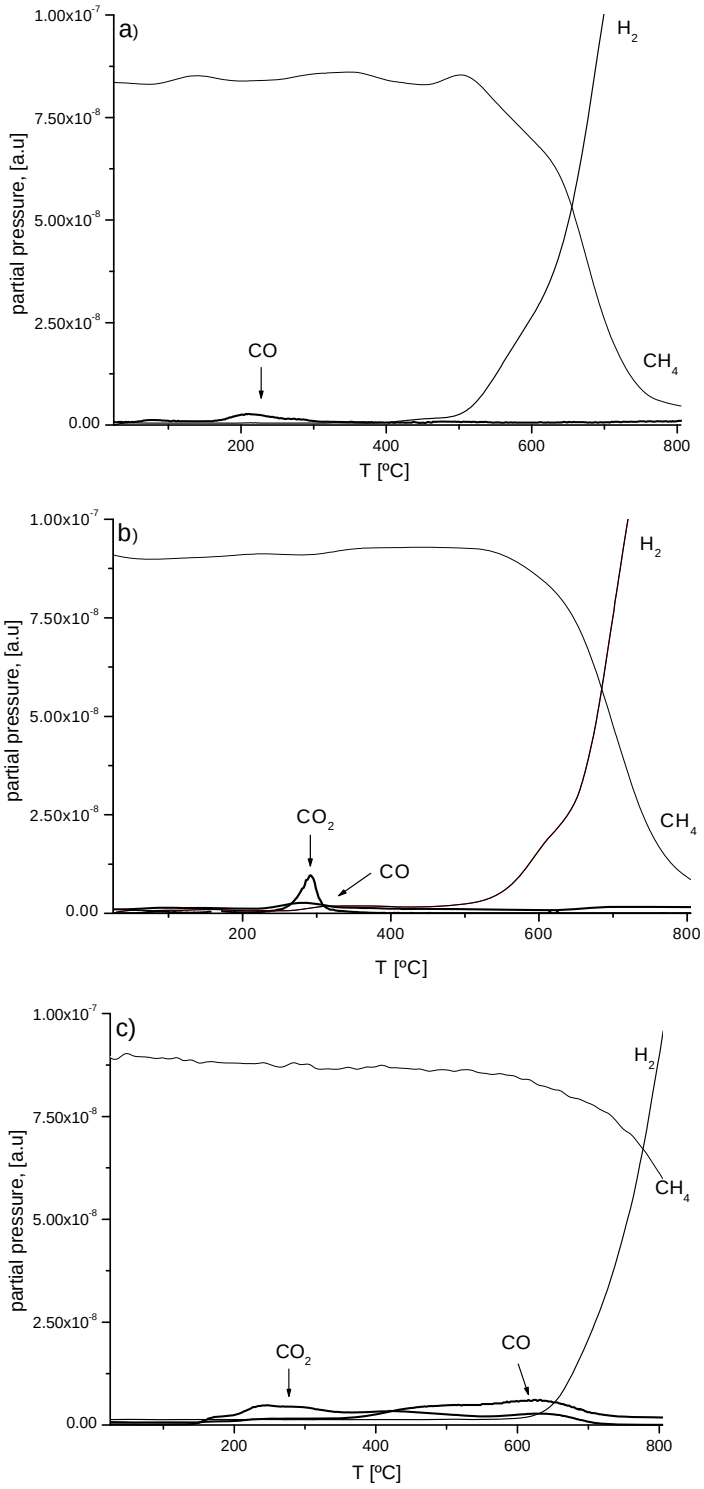



Fig. 2.2 TPRe with Ni30 (a), Co30 (b) and Fe50 (c). Experimental conditions: 0.1 g catalyst, heating rate 5 ºC/min, temperature range 25-1000 ºC and flow rate of 27.5 $Ncm^3/min$ ($CH_4$/He = 0.1).

Temperature programmed reaction experiments were carried out first, mainly in order to determine the temperature ranges where the Raney-type catalysts were active for methane decomposition. The results are shown in Fig. 2.2. It may be observed that the catalytic activity of Ni30 (Fig. 2.2a) starts at about 500 ºC, traces of CO being observed in the range of 150–300 ºC. Co30 shows similar behavior to Ni30 (Fig. 2.2b). Small amounts of CO and $CO_2$ were produced between 250 and 350 ºC. With Fe50 (Fig. 2.2c), hydrogen production starts at about 625 ºC and larger amounts of CO and/or $CO_2$ were evolved in the range of 200–800 ºC. This is an indication that Fe was oxidized by NaOH during the Al leaching step.

#### *2.3.2.2 Isothermal tests*

Based on the results of the previous section, it was decided to carry out the isothermal catalytic tests in the temperature range of 400–700 ºC. The catalysts were evaluated for 5 h on stream, and the effects of catalyst mass and volumetric flow rate (contact time), temperature, feed composition and hydrogen pre-treatment of the catalysts were investigated. The activity of the catalysts is assessed by comparing the maximum conversions obtained with the equilibrium conversions calculated for each set of experimental conditions. The stability of the catalysts is assessed by comparing the maximum conversions with the residual conversions at the end of the 5 h tests. The carbon yields obtained in all the experiments were in agreement with the corresponding evolutions of the methane conversion. The molar ratio of hydrogen and carbon produced was always close to 2, except with the Fe catalysts. Fig. 2.3a and b shows the conversion of methane at 600 ºC over a 5 h run with Ni50, using different catalyst masses and feed flow rates, respectively. Under these conditions, the equilibrium conversion is 88 %, as indicated by the dotted line. Higher contact times (higher catalyst masses or lower flow rates) lead to higher methane conversions. As shown in Fig. 2.3a, a mass of 1.0 g of Ni50 is needed for stable operation with a flow rate of 110 $Ncm^3/min$. The highest methane conversion (approximately 80 %) was recorded with 2.5 g of catalyst, while the use of catalysts masses lower than 1.0 g is found to result in rapid deactivation. Similar effects are observed in Fig. 2.3b, where results corresponding to different flow rates are presented. The effect of contact time on conversion was expected; however, a clear stabilizing effect was additionally observed, which will be addressed in Section 2.4.

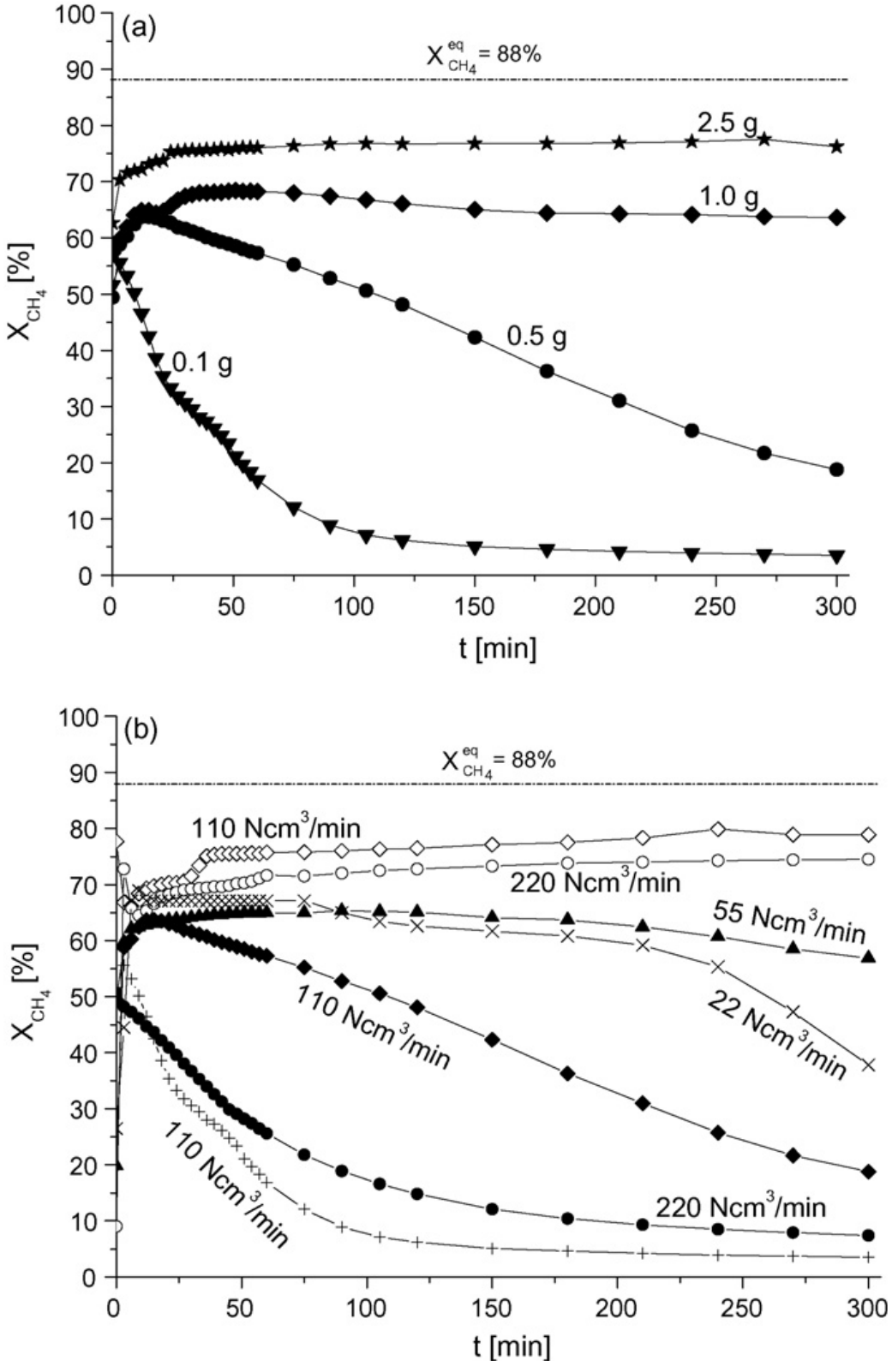



Fig. 2.3 Methane conversion as function of reaction time with Ni50 catalyst and $CH_4/N_2$ = 0.1: (a) catalyst mass effect at 600 ºC and flow rate of 110 $Ncm^3/min$; (b) volumetric flow-rate effect at 600 ºC, with 2.5 g (open symbols), 0.5 g (filled symbols) or 0.1 g (other symbols) of catalyst.

The effect of temperature in the performance of the Ni50 catalyst is shown in Fig. 2.4. It may be observed that the maximum methane conversion increases with the temperature. In particular, it is important to mention that the value obtained at 700 ºC is near the conversion corresponding to thermodynamic equilibrium (96 %). However, deactivation occurs above a certain temperature. For example, with a catalyst mass of 0.5 g and a flow rate of 110 $Ncm^3/min$, stable operation is only possible at temperatures lower than 580 ºC (see Fig. 2.4). Additionally, it was demonstrated that this deactivation phenomenon starts to occur at lower temperatures when using lower catalyst masses. For instance, with a Ni50 catalyst mass of 0.1 g, it was experimentally verified that a significant deactivation arises near 550 ºC (results shown in the Appendix). Moreover, the deactivation is highly sensitive to small changes of temperature; under the previous conditions and at 555 ºC, residual methane conversions (≈5%) were attained after 3.5 h, but at 560 ºC the catalyst is almost completely deactivated after 2.5 h. The effect of the methane concentration is shown in Fig. 2.5. It may be observed that higher methane concentrations in the feed stream lead to lower conversions, in agreement with what would be expected for this reversible reaction. The stability observed at higher methane concentrations, and also at low temperatures (Fig. 2.4), will be discussed in Section 2.4. The effect of the presence of hydrogen in the feed stream on the performance of the Ni50 catalyst is shown in Fig. 2.6 (filled symbols). It may be observed that the addition of hydrogen to the feed stream (keeping the total volumetric flow rate constant) lowers the conversion of methane; however, a certain level of hydrogen in the feed stream is beneficial, as it helps to maintain stable operation. A stabilizing effect may also be achieved by pre-treatment of the catalyst with hydrogen (open symbols). This is most certainly related to the microstructure changes induced on the catalyst, as can be observed by comparing Fig. 2.1a and b. Fig. 2.7 shows the performance of the Ni30 catalyst. Under the same conditions, the results are better than those reported above for Ni50. The conversions recorded at 700 ºC are very close to the calculated equilibrium conversion (96 %). It may be also observed that stable operation is possible at 600 ºC with 1 g of catalyst, whereas similar methane conversions with Ni50 were only possible with a catalyst mass of 2.5 g. Long duration tests with 2.5 g of Ni30 at 600 ºC showed stable operation at least up to 12 h; then, it was necessary to stop the experiment, because the accumulation of carbon in the catalyst bed originated an excessive pressure drop. The better performance of Ni30 compared to Ni50 is related to the specific microstructure of this catalyst, shown in Fig. 2.1c. These microstructure effects will be further discussed in Section 2.4.

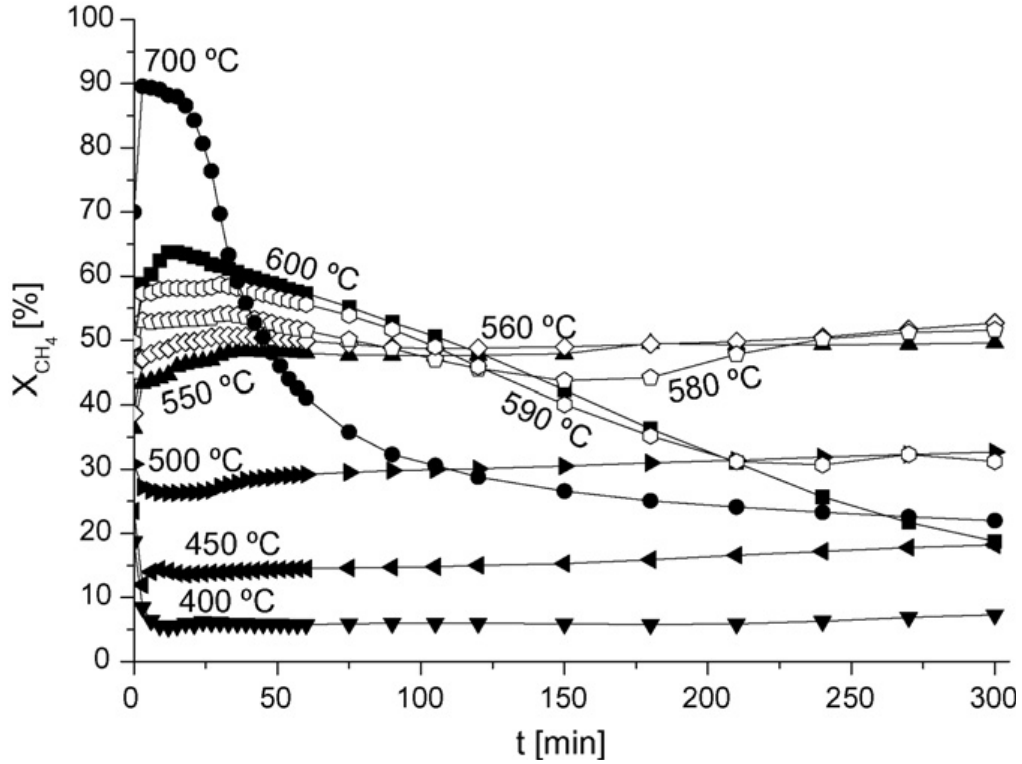



Fig. 2.4 Methane conversion as function of reaction time with Ni50 catalyst: temperature effect with 0.5 g of catalyst and flow rate of 110 $Ncm^3$/min ($CH_4/N_2$ = 0.1).

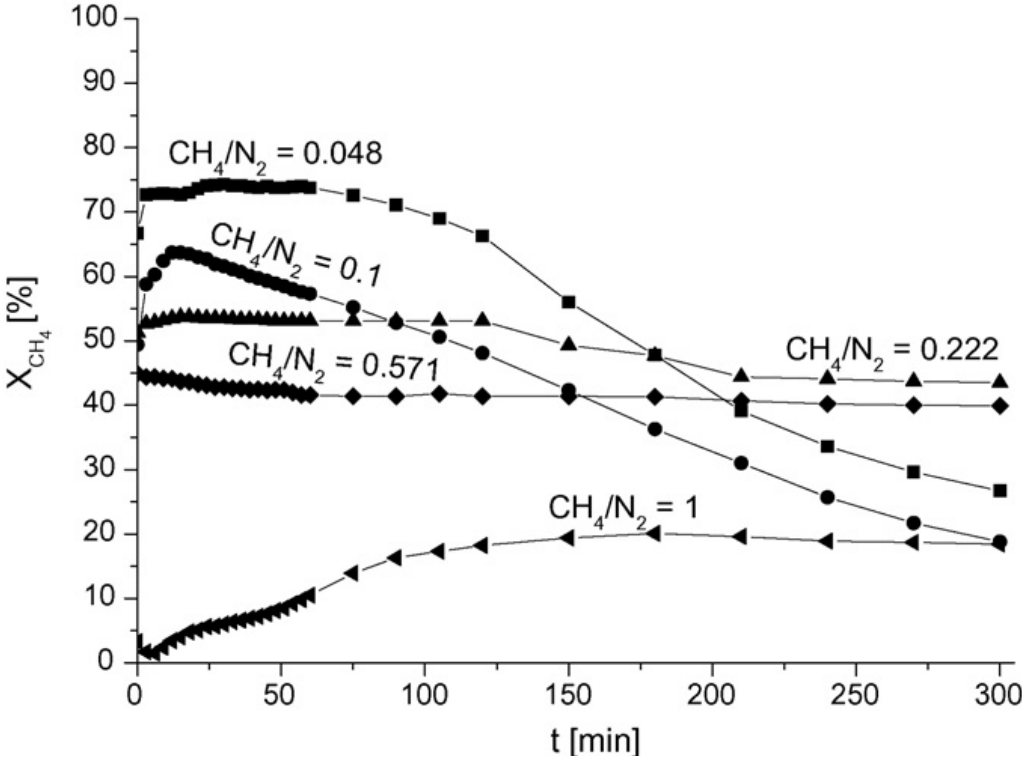



Fig. 2.5 Methane conversion as function of reaction time with Ni50 catalyst: feed composition effect with 0.5 g of catalyst at 600 ºC and flow rate of 110 $Ncm^3$/min.

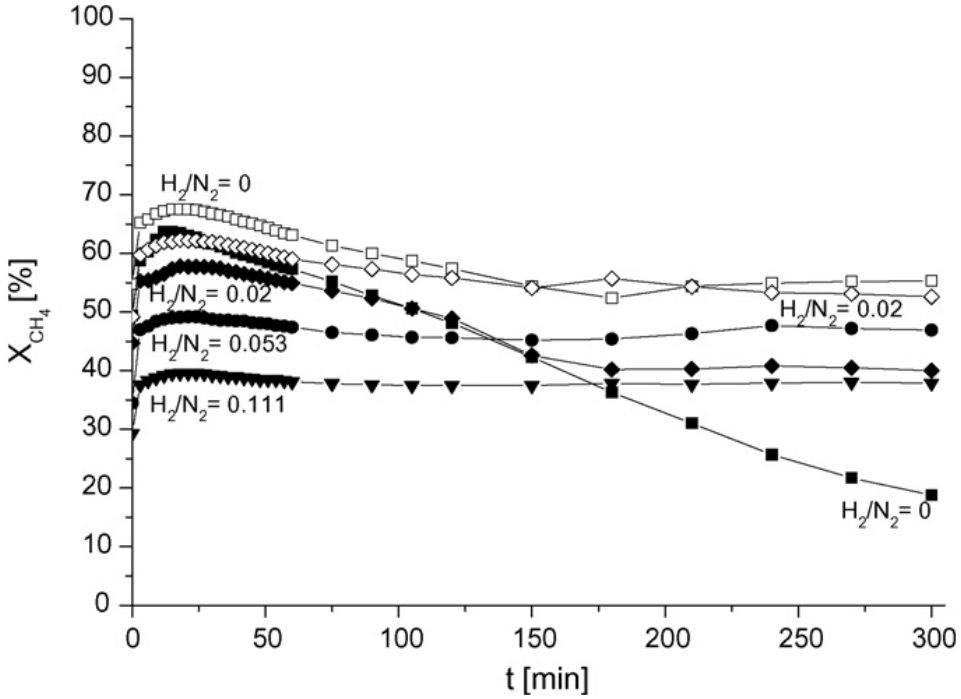



Fig. 2.6 Methane conversion as function of reaction time with Ni50 catalyst: effect of hydrogen with 0.5 g of catalyst, at 600 ºC and flow rate of 110 $Ncm^3/min$ of $CH_4/(N_2+H_2)$=0.1 (filled symbols), or HTP (open symbols).

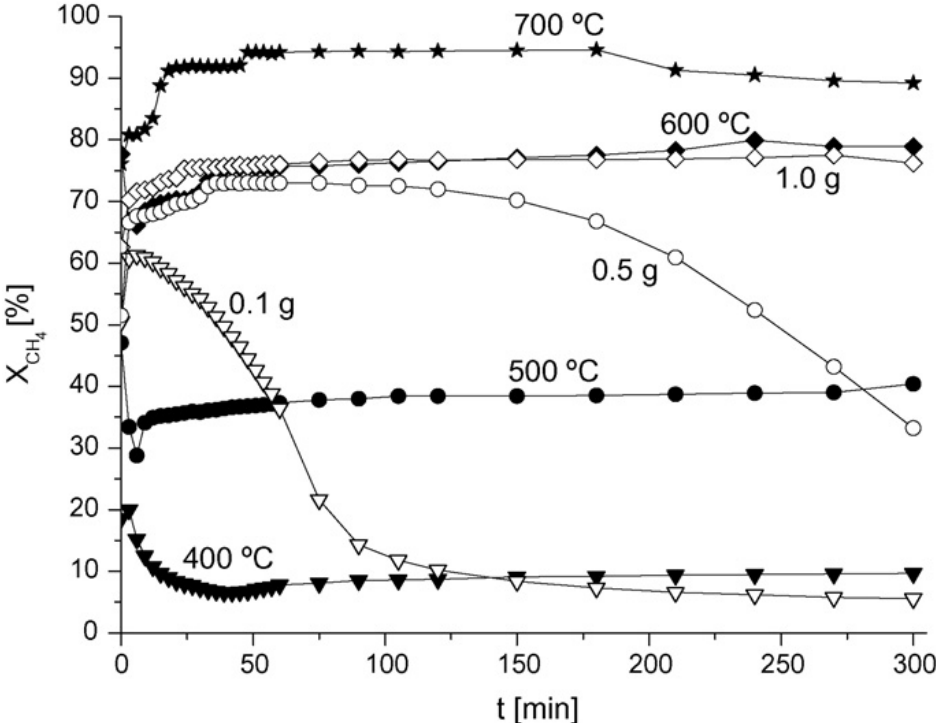



Fig. 2.7 Methane conversion as function of reaction time with Ni30 catalyst: catalyst mass effect at 600 ºC (open symbols), and temperature effect with 2.5 g catalyst (filled symbols). Flow rate of 110 $Ncm^3/min$ ($CH_4/N_2$ = 0.1).

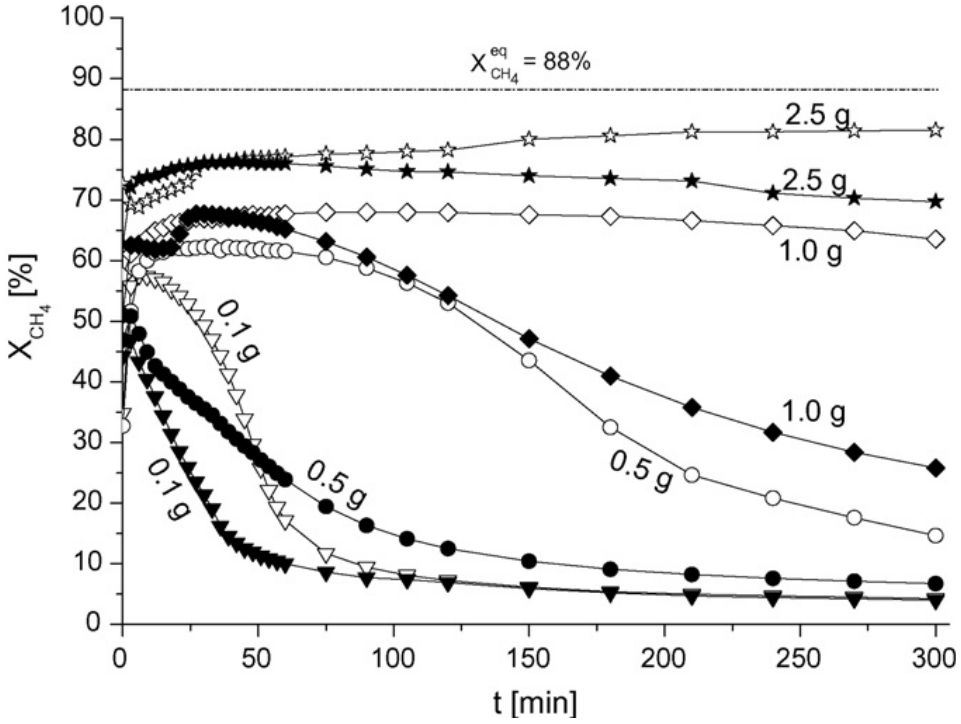



Fig. 2.8 Methane conversion as function of reaction time with catalysts Co50 (filled symbols) and Co30 (open symbols): catalyst mass effect at 600 ºC and flow rate of 110 $Ncm^3/min$ ($CH_4/N_2$ = 0.1).

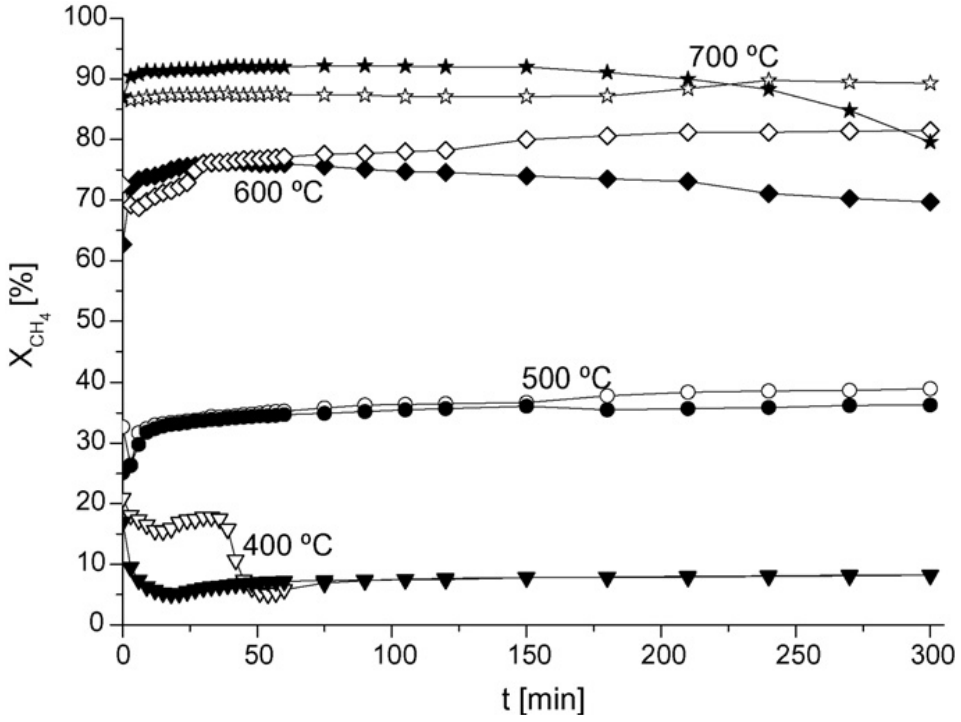



Fig. 2.9 Methane conversion as function of reaction time with catalysts Co50 (filled symbols) and Co30 (open symbols): temperature effect with 2.5 g and flow rate of 110 $Ncm^3/min$ ($CH_4/N_2$ = 0.1).

Figs. 2.8 and 2.9 show the evolution of methane conversions with time on stream, obtained with Co50 and Co30 catalysts, using different catalyst masses or temperatures, respectively. The behavior is similar to that reported above for the Ni catalysts: higher catalyst masses lead to higher conversions and extended stability, and higher temperatures result in higher conversions. Additionally, it may be observed that Co30 performs better than Co50. At 600 ºC, 1.0 g of the Co30 catalyst is enough to achieve a performance similar to that recorded with 2.5 g of Co50 (Fig. 2.8). Stable operation at 600 ºC was demonstrated with 2.5 g of Co30 for 10 h, with measured methane conversions around 80 %.

As shown in Figs. 2.10 and 2.11, the results obtained with the Fe50 and Fe35 catalysts are quite different from those reported for the Ni and Co catalysts. The methane conversions are usually low at the beginning of the experiments, and increase during a large period of time before the catalysts eventually deactivate or attain apparent steady-state behavior. This initial activation period is explained by the reduction of the iron oxides present on the surface of these catalysts, which were detected by EDX and XPS. As a consequence, the molar ratio between hydrogen and carbon formed is different from 2, and large amounts of carbon oxides are produced (also observed in the TPRe tests) in this reduction process. Similar behavior was reported by Muradov for methane decomposition on $Fe_2O_3/Al_2O_3$ [19]. The catalyst mass effect was studied at 600 ºC (Fig. 2.10). Similarly to the other catalysts studied, higher catalysts masses lead to higher stability. Stable operation was achieved with 2.5 g of catalyst, after the initial activation period. With lower masses of Fe50, there is an initial increase in activity (as a result of the reduction of iron oxides, as discussed before) followed by some deactivation (curves for 0.1, 0.5 and 1.0 g of Fe50). It is also instructive to compare the curves obtained with 0.5 g of catalysts Fe50 and Fe35. The Fe35 catalyst does not activate at all, which can be explained by the very low surface contents of metallic iron (cf. Table 2.2). However, when submitted to the hydrogen pre-treatment (HPT), this catalyst (Fe35) behaves similarly to Fe50 (cf. curves for 0.5 g in Fig. 2.10). The effect of temperature was investigated between 500 and 700 ºC (Fig. 2.11). It may be observed that the activation period (corresponding to the reduction of surface oxides) decreases as the temperatures increases. Thereafter, stable operation was demonstrated at 700 ºC with 2.5 g Fe50 at least up to 12 h (when the experiment had to be interrupted due to the accumulation of carbon in the catalyst bed).

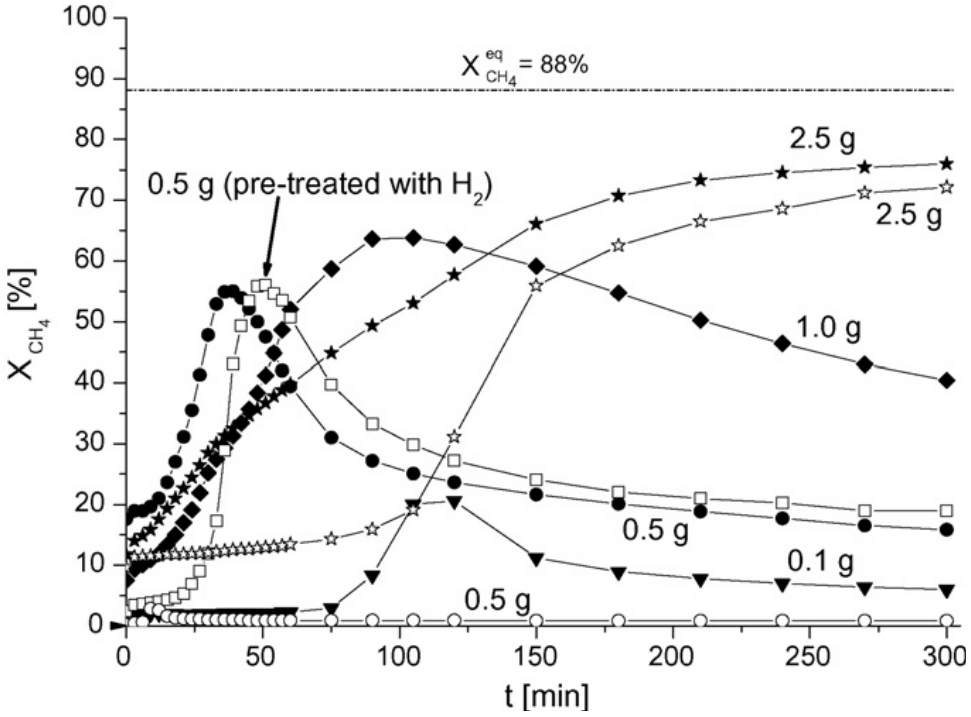



Fig. 2.10 Methane conversion as function of reaction time with catalysts Fe50 (filled symbols) and Fe35 (open symbols): catalyst mass effect at 600 ºC and flow rate of 110 $Ncm^3$/min ($CH_4/N_2$ = 0.1).

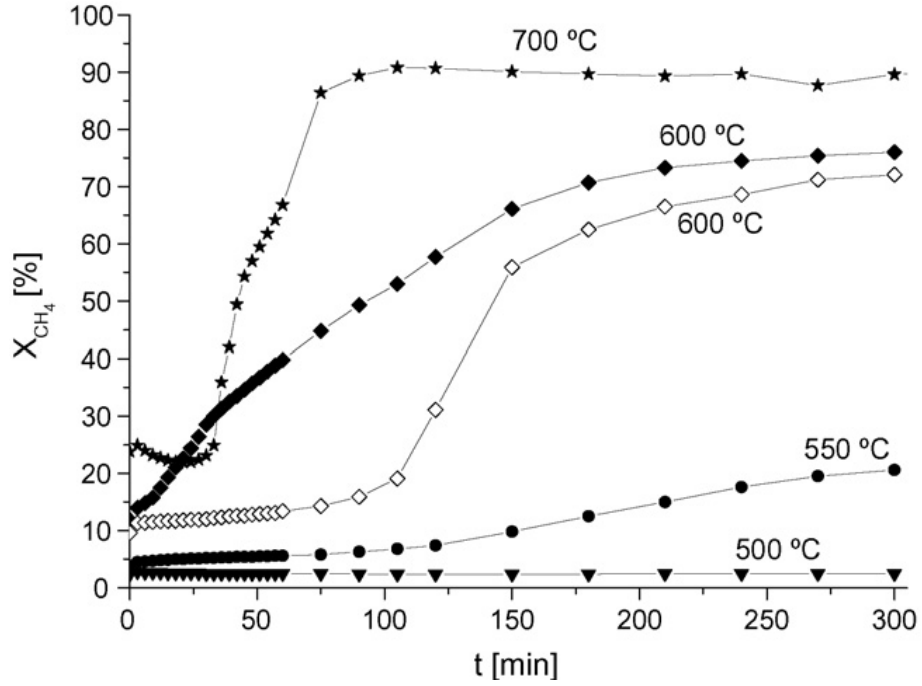



Fig. 2.11 Methane conversion as function of reaction time with catalysts Fe50 (filled symbols) and Fe35 (open symbols): temperature effect with 2.5 g and flow rate of 110 $Ncm^3$/min ($CH_4/N_2$ = 0.1).

### 2.3.3 Characterization of the carbon deposits

Fig. 2.12 shows SEM micrographs of carbon deposits obtained on the Ni catalysts. In all cases, carbon filaments were observed, consisting mostly of carbon nanofibres (CNF) associated with metal particles of the same diameter, which are clearly visible in some of the micrographs (Fig. 2.12a).

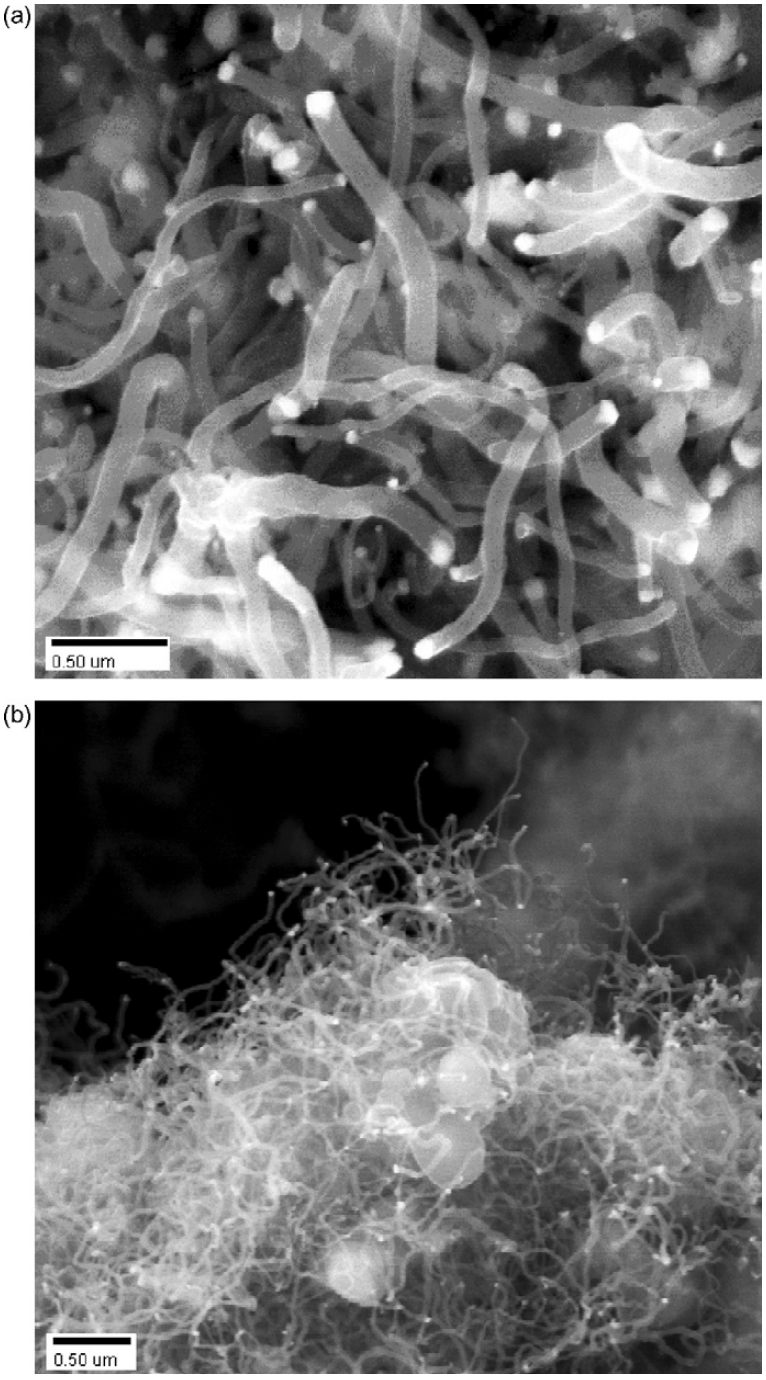



Fig. 2.12 SEM micrographs of carbon deposits obtained on Ni50 (a) at 400 ºC and (b) at 600 ºC.

The deposits were also examined by TEM, in order to get more information on the carbon structure. A typical example is shown in Fig. 2.13, giving evidence for the presence of multiwall carbon nanotubes (MWCNT). In general, it was observed that the carbon deposits obtained at low temperatures contained mostly CNF, while MWCNT were predominantly formed at higher temperatures. A more detailed characterization of the carbon deposits will be the object of a separate chapter. Nevertheless, it should be noted that the carbon filaments produced had diameters in the range of 20–200 nm, while the particle size of the catalysts was 3 orders of magnitude higher (20–200 μm).

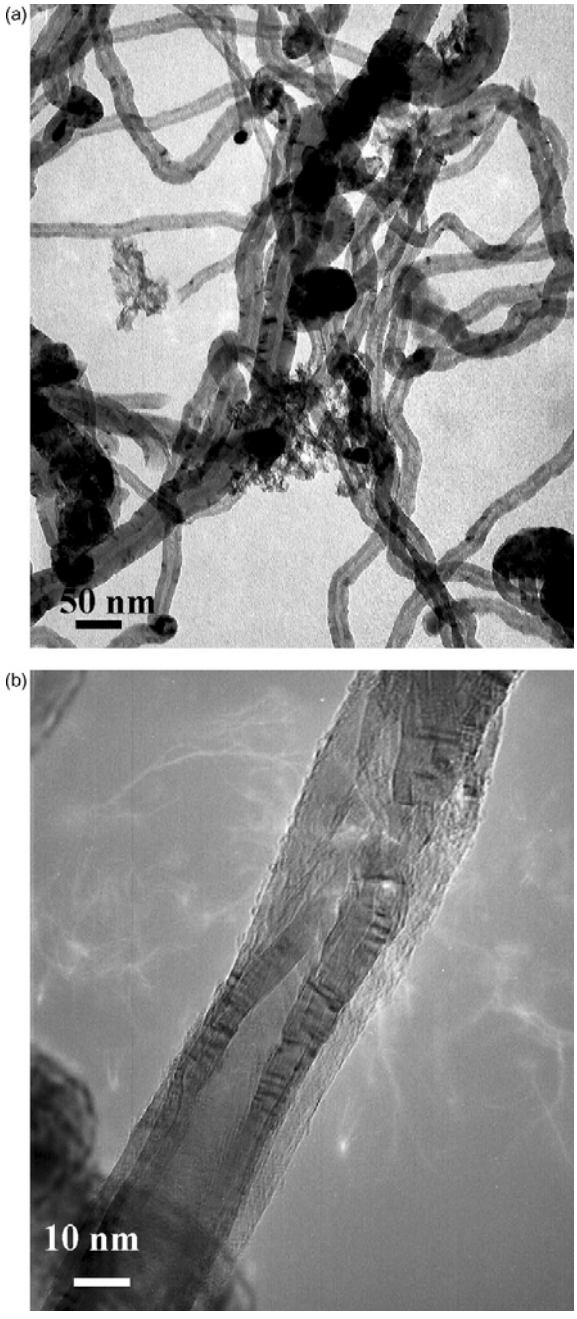



Fig. 2.13 TEM micrographs of carbon deposits obtained on Ni30 at 600 ºC.

## 2.4 Discussion

Methane decomposition into hydrogen and carbon on metal catalysts can be adequately described by the mechanism proposed in 1972 [28,45]. In their original work, Baker et al. [45] studied the formation of filamentous carbon on supported metal crystallites, while Lobo et al. [28] used pure metal foils. The situation is basically the same in both cases, involving the dissociative adsorption of the hydrocarbon on the metal surface, the dissolution and subsequent diffusion of the adsorbed carbon atoms through the metal, and the precipitation of carbon at the backside of the metal particles originating carbon filaments. However, there is an additional stage in the case of pure metals, whereby crystallites are detached from the metal surface. This initial step is responsible for the eventual observation of induction periods, and for the effect of some pre-treatments on the rates of carbon formation [46]. Nevertheless, once metal crystallites are detached, carbon filaments grow for extended periods of time, until the metal crystallites become deactivated by encapsulating carbon. The reaction steps involved are summarized in Fig. 2.14 [47].

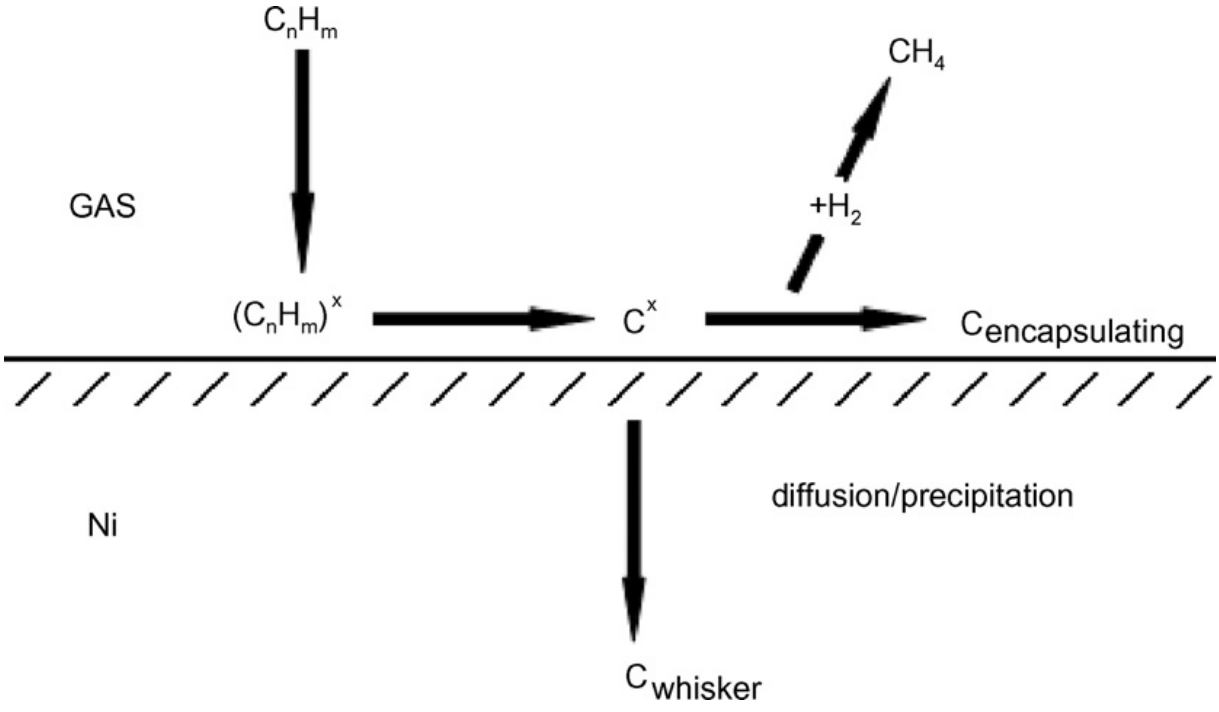



Fig. 2.14 Mechanism proposed for hydrocarbon decomposition on Ni catalysts (reproduced from Ref. [47]).

Nickel, cobalt and iron, and their alloys, are the most active catalysts for this process. However, in the case of iron, the reaction mechanism cannot be described only by the steps shown in Fig. 2.14, because the formation of iron carbide, $Fe_3C$, must be accounted for [48].

More recent studies by in situ high-resolution electron microscopy allowed for the direct observation of surface structures in the catalyst nanoparticles and their modifications under reaction conditions [49]. In particular, the role of surface diffusion of Ni and C atoms was highlighted, as well as the spontaneous formation of Ni step-edges at the Ni–C interface, where the precipitation of graphite occurs [50].

In any case, the relative rates of the processes shown in Fig. 2.14 determine whether the catalyst deactivates or not. This will depend on the nature of the reactants, temperature, hydrogen concentration and catalyst activity. At low temperatures, nucleation and growth of surface carbon are slow, and filamentous carbon formation predominates. At high temperatures, the presence of hydrogen is needed to hydrogenate surface intermediates, thereby preventing the formation of encapsulating carbon [51]. It should be emphasized that while filamentous carbon is being formed, the catalyst remains active. Thus, this is an essential feature for the sustained decomposition of the hydrocarbon.

It is perhaps appropriate at this stage to refer the observations of Figueiredo and Trimm, concerning the gasification of carbon deposits obtained on nickel foils by hydrocarbon decomposition. It was indeed found that the amount of metal in such carbon deposits was proportional to the weight of the deposit, an average concentration of Ni of 1.6 wt. % being reported [52]. The process of carbon formation is akin to the metal dusting phenomenon [53], and in fact similar concentrations of Ni were reported in this context, implying that the rate of nickel detachment from the surface is proportional to the rate of carbon formation [54,55]. The relationships between metal dusting corrosion and the growth of carbon nanotubes and carbon nanofibres are discussed in a recent article [56].

With this background in mind, we can now proceed to analyse the results reported in Section 2.3.2.2, starting with the Ni50 catalyst.

As shown in Fig. 2.3, a minimum amount of catalyst seems to be required for stable operation, at a given set of reaction conditions. In order to explain this result, we recall that unsupported metal catalysts must first disintegrate to produce in situ small metal crystallites, which will then be active for the growth of carbon filaments. Deactivation may occur as a result of encapsulation of metal crystallites, but new crystallites can be formed from the bulk metal, if a minimum amount is present. Similar effects of the catalyst mass were reported in the context of carbon formation from CO disproportionation [57].

Stable operation is then the net result of in situ generation of metal crystallites, and deactivation by encapsulating carbon. When using a powder, as in the present case, it is not possible to separate the carbon deposit from the catalyst particles in order to check for the presence of such crystallites, as was done in the case of metal foils [52]. However, it seems reasonable to accept that disintegration occurs, especially when one compares the diameters of the carbon filaments formed, and those of the associated metal crystallites (20–200 nm), with the particle size of the original catalyst (20–200 μm, as shown in Table 2.1).

Although we have presented our results in terms of methane conversion versus time, it is also important to consider the rates of carbon formation. The mass of carbon deposited can be calculated by integration of the methane conversion curves. For instance, from the data in Fig. 2.3a, with 1 g of catalyst, we calculate 1.14 g of carbon deposited, while the experimental value, determined by weighing the catalyst before and after the run, was 1.04 g. Taking into account the inevitable losses while removing catalyst plus carbon from the reactor, we can conclude that the carbon balance is essentially correct. Therefore, the calculated average rate of carbon formation was only 0.23 gC/(gcat h). However, one should consider that this rate is based on the total mass of catalyst needed for stable operation, while the amount of metal involved in carbon formation (metal crystallites produced in situ) is much lower. For instance, if one takes the Ni concentration reported for carbon deposits on Ni, namely 1.6 wt. % [52], the effective rate of carbon formation will be of the order of 13 gC/(gNi h).

Figs. 2.4 to 2.6 show the effects of temperature and feed composition. A quantitative interpretation of the behaviour of these curves would require a detailed model taking into account the hydrodynamics of the reactor, as well as the specificities of the reactions involved (see Fig. 2.14): formation of filamentous and encapsulating carbon, reverse reaction, role of $H_2$ (produced by reaction or added to the feed) in preventing the formation of encapsulating carbon, in situ formation of the metal crystallites which are active for reaction. The formulation of such a model is outside the scope of the present investigation. However, from a qualitative point of view, we can offer some explanations for the observed behaviour. For instance, in the curve for $CH_4/N_2 = 1$, Fig. 2.5, we observe an extensive induction period, before reaching a stable conversion. Induction periods have been reported during carbon formation on metals [46,57]. In the present case, we may assume that the initial rate of in situ crystallite production is too low to cope with so much methane in the feed. This does not occur for the next two curves (corresponding to $CH_4/N_2 = 0.571$ and 0.222), where there is no significant induction period. In any case, a more or less stable methane conversion was reached in these three runs (there is only a slight deactivation in the third curve, corresponding to $CH_4/N_2 = 0.222$).

This stability may be achieved because the amount of hydrogen produced from methane decomposition is sufficient to avoid the formation of encapsulating carbon. It should be recalled that the hydrogen concentration in the reactor depends on the conversion and also on the methane concentration in the feed: $[H_2] = 2\,[CH_4]_{in}\,X_{CH_4}$, so that lower conversions do not imply necessarily lower concentrations of hydrogen produced. For instance, under the conditions of Fig. 2.5, the concentration of hydrogen in the reactor (hydrogen produced) is about 0.01mol/dm$^3$, for these three runs. When the $[CH_4]_{in}$ is further decreased (curves for $CH_4/N_2$ = 0.1 and 0.048) we reach higher conversions initially, but less hydrogen is produced (for $CH_4/N_2$ = 0.1, the $H_2$ concentration can be estimated as 0.005 mol/dm$^3$), which apparently is not sufficient to avoid deactivation (by encapsulating carbon). To obviate this situation, we can increase the mass of catalyst in order to have a continuous source of new crystallites, as shown in Fig. 2.3a, or we can add hydrogen to the feed, as shown in Fig. 2.6.

Bearing in mind the above discussion, it is easy to understand that catalysts with the microstructure of Fig. 2.1b and 2.1c will be more active, since this particular microstructure will favour disintegration and the in situ generation of metal crystallites. This explains the better results obtained with Ni30, and also the effect of HPT on Ni50 (Fig. 2.6, open symbols). The Co catalysts behaved similarly to Ni, while the different behaviour of Fe was already explained in Section 2.3.2.2, in terms of the presence of surface oxides formed during the Al leaching process.

We are now able to compare the results obtained in the present study with those previously reported for the catalytic decomposition of methane on Ni, Co and Fe catalysts [7–10,12,13,15–17,19–25], as shown in Table 2.3. The experimental conditions are listed, together with the equilibrium methane conversion, the maximum conversion reported, and the final conversion measured after several hours on stream. Catalyst activity can be assessed by comparing $X_{CH_4}^{\max}$ with $X_{CH_4}^{eq}$, while catalyst stability can be assessed by comparing $X_{CH_4}^{\max}$ with $X_{CH_4}^{t}$. Among the supported metals, high loaded catalysts show the best performances. Even better performances, in terms of activity and stability, are those exhibited by unsupported catalysts, such as NiCuAl [13,22] and NiCuMg [23,24], as well as the skeletal catalysts reported in the present study. Therefore, supported metal catalysts, especially those with low metal loads, are not adequate for the sustained production of hydrogen by methane decomposition. Indeed, in such catalyst systems there will be a finite number of metal crystallites, all of which will become deactivated by encapsulating carbon in due course. On the contrary, unsupported metals (or high metal loaded supported catalysts) will provide for an in situ generation of metal crystallites, which will be able to carry on the reaction for extended periods of time.

Table 2.3

Selected results for the catalytic decomposition of methane

| Catalyst [Reference] | $m_{cat}$ [g] | T [ºC] | $F^{inlet}_{CH_4+N_2}$ [$\frac{Ncm^3}{min}$] | $F^{inlet}_{CH_4}$ [$\frac{Ncm^3}{min}$] | $X^{eq}_{CH_4}$ [%] | $X^{max}_{CH_4}$ [%] | $X^{t}_{CH_4}$ [%] | t [h] |
|---|---|---|---|---|---|---|---|---|
| 16.4 wt.% $Ni/SiO_2$ [8] | 0.2 | 550 | n.a. | 20 | 68.5 | 35 | 0 | 3.2 |
| 10% wt $Ni/SiO_2$ [9] | 0.1 | 550 | 25 | 20 | 68.5 | 45 | 5 | 12 |
| 16% wt $Ni/SiO_2$ [16] | 0.05 | 550 | 60 | 10 | 79.6 | 35 | 0 | 3.5 |
| 48% wt Ni/MgO [16] | 0.05 | 550 | 60 | 10 | 79.6 | 38 | 0 | 4.5 |
| CRG-F (60% wt Ni) [16] | 0.05 | 550 | 60 | 10 | 79.6 | 52 | 52 | 6 |
| 30% wt Ni/HY [20] | 0.05 | 550 | 60 | 33.3 | 60.9 | 27 | 2 | 12 |
| 65% wt $Ni/SiO_2$-$Al_2O_3$ [7] | 0.3 | 700<br>550 | 20 | 100 | 80.8<br>45.6 | 63<br>32 | 42<br>32 | 16<br>16 |
| Ni-Cu-$Nb_2O_5$ [15] | 0.05 | 600 | 40 | 100 | 59.3 | 43 | 3 | 45 |
| Ni-Cu-alumina [10] | 0.1 | 750 | 68 | 37 | 92.6 | 70 | 70<br>0 | 10<br>17 |
| Ni-Cu-MgO [12] | 0.05 | 700 | 60 | 100 | 80.8 | 47 | 45<br>0 | 10<br>20 |
| Ni-Cu-Al [13] | 0.3 | 700 | 20 | 100 | 80.8 | 65 | 65 | 8 |
| Ni-Al [22] | 0.3 | 700 | 20 | 100 | 80.8 | 67 | 60 | 8 |
| Ni-Cu-Al [22] | 0.3 | 700 | 20 | 100 | 80.8 | 75 | 75 | 8 |
| Ni-Mg [23] | 0.3 | 700 | 20 | 100 | 80.8 | 50 | 43 | 8 |
| Ni-Cu-Mg [23] | 0.3 | 700 | 20 | 100 | 80.8 | 71 | 67 | 8 |
| Ni-Mg [24] | 0.3 | 700 | 20 | 100 | 80.8 | 67 | 50 | 8 |
| Ni-Cu-Mg [24] | 0.3 | 700 | 20 | 100 | 80.8 | 67 | 67 | 8 |
| Ni-Si [21] | 0.3 | 700 | 20 | 100 | 80.8 | 52 | 45 | 8 |
| Ni-Cu-Si [21] | 0.3 | 700 | 20 | 100 | 80.8 | 71 | 65 | 8 |
| Ni30 [This work] | 2.5 | 700 | 110 | 10 | 95.9 | 95 | 89 | 5 |
| Ni30 [This work] | 2.5 | 600 | 110 | 10 | 88.0 | 83 | 80 | 12 |
| Ni30 [This work] | 1.0 | 600 | 110 | 10 | 88.0 | 78 | 76 | 5 |
| Ni30 [This work] | 0.5 | 600 | 110 | 10 | 88.0 | 73 | 33 | 5 |
| Ni50 [This work] | 2.5 | 600 | 110 | 10 | 88.0 | 78 | 76 | 5 |
| Ni50 [This work] | 0.5 | 600 | 110 | 10 | 88.0 | 64 | 19 | 5 |
| Ni50 (HPT) [This work] | 0.5 | 600 | 110 | 10 | 88.0 | 68 | 55 | 5 |
| Ni50 [This work] | 0.5 | 550 | 110 | 10 | 79.6 | 50 | 50 | 5 |
| Pd-Co/$Al_2O_3$ [17] | 0.03 | 700 | 80 | 100 | 80.8 | 29 | 3 | 33 |
| 9% wt Co/$Al_2O_3$ [25] | 0.05 | 700 | 35 | 14.3 | 94.1 | 32 | 23 | 4 |
| Co30 [This work] | 2.5 | 700 | 110 | 10 | 95.9 | 90 | 89 | 5 |
| Co30 [This work] | 1.0 | 600 | 110 | 10 | 88.0 | 68 | 64 | 5 |
| Co30 [This work] | 0.5 | 600 | 110 | 10 | 88.0 | 62 | 15 | 5 |
| Co50 [This work] | 2.5 | 600 | 110 | 10 | 88.0 | 76 | 70 | 5 |
| Co50 [This work] | 1.0 | 600 | 110 | 10 | 88.0 | 68 | 26 | 5 |
| $Fe_2O_3/Al_2O_3$ [19] | 2.0 | 850 | n.a. | n.a. | n.a. | 95 | 30<br>10 | 1<br>10 |
| Fe50 [This work] | 2.5 | 700 | 110 | 10 | 95.9 | 91 | 91 | 12 |
| Fe50 [This work] | 1.0 | 600 | 110 | 10 | 88.0 | 64 | 40 | 5 |
| Fe50 [This work] | 0.5 | 600 | 110 | 10 | 88.0 | 55 | 16 | 5 |
| Fe35 [This work] | 0.5 | 600 | 110 | 10 | 88.0 | 3 | 1 | 5 |
| Fe35 (HPT) [This work] | 0.5 | 600 | 110 | 10 | 88.0 | 56 | 19 | 5 |

$F_{CH_4+N_2}^{inlet}$ : inlet flow rate of methane and nitrogen;

$F_{CH_4}^{inlet}$ : inlet flow rate of methane;

$X_{CH_4}^{eq}$ : equilibrium methane conversion;

$X_{CH_4}^{max}$ : maximum methane conversion during reaction;

$X_{CH_4}^{t}$ : methane conversion at time t.

It is now clear that stable operation demands a certain amount of catalyst for a continuous supply of metal crystallites. It is also evident that the more fragmented microstructure of the catalysts obtained from alloys produced by fast quenching (Ni30 and Co30), or submitted to hydrogen pre-treatments, will facilitate the detachment of metal crystallites, leading to better performances in methane decomposition.

## 2.5 Conclusions

It has been shown that Raney-type catalysts are quite good catalysts for the decomposition of methane into hydrogen and filamentous carbon (CNF or MWCNT). The excellent performance of these catalysts has been explained in terms of a continuous supply of metal crystallites, which are detached from the metal surface. The influence of the operating variables was investigated in detail. Higher contact times favour stability, and higher temperatures increase activity. Higher methane concentrations in the feed stream lead to lower conversions, but improve stability, due to higher hydrogen production. The presence of hydrogen in the feed stabilizes the catalyst, but reduces the methane conversion. In general, catalyst pre-treatment with hydrogen increases the activity and stability. Ni and Co catalysts perform better than Fe, the best results being obtained with the Ni30 catalyst. This was interpreted in terms of the microstructure of these materials.
SEM and TEM examinations show that the carbon deposits on Ni and Co catalysts consist mainly of CNF and MWCNT. A lot of encapsulating carbon was frequently observed with the Fe catalysts.

## Appendix

Additional results obtained for this Chapter II can be consulted in the Appendix.

## References


[1] N. Muradov, T.N. Veziroglu, *Int. J. Hydrogen Energy* **30** (2005) 225.

[2] N. Muradov, *Catal. Commun.* **2** (2001) 89.

[3] E.K. Lee, S.Y. Lee, G.Y. Han, B.K. Lee, T.J. Lee, J.H. Jun, K.J. Yoon, *Carbon* **42** (2004) 2641.

[4] N. Muradov, F. Smith, A.T. Raissi, *Catal. Today* **102**/103 (2005) 225.

[5] I. Suelves, M.J. Lázaro, R. Moliner, J.L. Pinilla, H. Cubero, *Int. J. Hydrogen Energy* **32** (2007) 3320.

[6] J. Ashok, S.N. Kumar, A. Venugopal, V.D. Kumari, S. Tripathi, M. Subrahmanyam, *Catal. Commun.* **9** (2008) 164.

[7] I. Suelves, M.J. Lázaro, R. Moliner, B.M. Corbella, J.M. Palacios, *Int. J. Hydrogen Energy* **30** (2005) 1555.

[8] T. Zhang, M.D. Amiridis, *Appl. Catal. A: Gen.* **167** (1998) 161.

[9] T.V. Choudhary, C. Sivadinarayana, C.C. Chusuei, A. Klinghoffer, D.W. Goodman, *J. Catal.* **199** (2001) 9.

[10] Y. Li, J. Chen, Y. Qin, L. Chang, *Energy & Fuels* **14** (2000) 1188.

[11] S.H.S. Zein, A.R. Mohamed, *Energy & Fuels* **18** (2004) 1336.

[12] H. Wang, R.T.K. Baker, *J. Phys. Chem. B* **108** (2004) 20273.

[13] I. Suelves, M.J. Lázaro, R. Moliner, Y. Echegoyen, J.M. Palacios, *Catal. Today* **116** (2006) 271.

[14] T.V. Reshetenko, L.B. Avdeeva, V.A. Ushakov, E.M. Moroz, A.N. Shmakov, V.V. Kriventsov, D.I. Kochubey, Yu.T. Pavlyukhin, A.L. Chuvilin, Z.R. Ismagilov, *Appl. Catal. A: Gen.* **270** (2004) 87.

[15] J. Li, G. Lu, K. Li, W. Wang, *J. Mol. Catal. A: Chem.* **221** (2004) 105.

[16] G. Bonura, O. Di Blasi, L. Spadaro, F. Arena, F. Frusteri, *Catal. Today* **116** (2006) 298.

[17] H. Ogihara, S. Takenaka, I. Yamanaka, E. Tanabe, A. Genseki, K. Otsuka, *J. Catal.* **238** (2006) 353.

[18] Y. Zhang, K.J. Smith, *J. Catal.* **231** (2005) 354.

[19] N.Z. Muradov, *Energy & Fuels* **12** (1998) 41.

[20] J. Ashok, S.N. Kumar, A. Venugopal, V.D. Kumari, M. Subrahmanyam, *J. Power Sources* **164** (2007) 809.

[21] M.J. Lázaro, Y. Echegoyen, I. Suelves, J.M. Palacios, R. Moliner, *Appl. Catal. A: Gen.* **329** (2007) 22.

[22] Y. Echegoyen, I. Suelves, M.J. Lázaro, R. Moliner, J.M. Palacios, *J. Power Sources* **169** (2007) 150.

[23] Y. Echegoyen, I. Suelves, M.J. Lázaro, M.L. Sanjuán, R. Moliner, *Appl. Catal. A: Gen.* **333** (2007) 229.

[24] R. Moliner, Y. Echegoyen, I. Suelves, M.J. Lázaro, J.M. Palacios, *Int. J. Hydrogen Energy* **33** (2008) 1719.

[25] G.B. Nuernberg, H.V. Fajardo, D.Z. Mezalira, T.J. Casarin, L.F.D. Probst, N.L.V. Carreño, *Fuel* **87** (2008) 1698.

[26] J. Ashok, S.N. Kumar, M. Subrahmanyam, A. Venugopal, *Catal. Lett.* **121** (2008) 283.

[27] M.E. Rivas, J.L.G. Fierro, R. Guil-López, M.A. Peña, V. La Parola, M.R. Goldwasser, *Catal. Today* **133–135** (2008) 367.

[28] L.S. Lobo, D.L. Trimm, J.L. Figueiredo, in: J.W. Hightower (Ed.), Proceedings of the 5th International Congress on Catalysis 1972, vol. 2, North-Holland, Amsterdam, 1973, pp. 1125.

[29] P. Ferreira-Aparicio, I. Rodríguez-Ramos, A. Guerrero-Ruiz, *Appl. Catal. A: Gen.* **148** (1997) 343.

[30] J. Highfield, Y.S. Loo, Z. Zhong, B. Grushko, *Carbon* **45** (2007) 2597.

[31] U. Birkenstock, J. Scharschmidt, P. Kunert, H. Meinhardt, P. Hausel, P. Maier, U.S. Patent 5,090,997 (1992).

[32] M. Raney, U.S. Patent 1,628,190 (1927).

[33] U. Birkenstock, R. Holm, B. Reinfandt, S. Storp, *J. Catal.* **93** (1985) 55.

[34] J. Rothe, J. Hormes, C. Schild, B. Pennemann, *J. Catal.* **191** (2000) 294.

[35] M.A. Ermakova, D.Yu. Ermakov, G.G. Kuvshinov, L.M. Plyasova, *J. Catal.* **187** (1999) 77.

[36] S. Hamar-Thibault, J. Gros, J.C. Joud, J. Masson, J.P. Damon, J.M. Bonnier, in: G. Poncelet, P. Jacobs, P. Grange, B. Delmon (Eds.), Preparation of Catalysts V, Elsevier, Amsterdam, 1991, pp. 601.

[37] T.B. Massalski, Binary Alloy Phase Diagrams, ASM International, 1996.

[38] A.J. Smith, D.L. Trimm, *Ann. Rev. Mater. Res.* **35** (2005) 127.

[39] J.C. Klein, D.M. Hercules, *Anal. Chem.* **53** (1981) 754.

[40] F. Dellannay, J.P. Damon, J. Masson, B. Delmon, *Appl. Catal.* **4** (1982) 169.

[41] C.D. Wagner, W.M. Riggs, L.E. Davis, J.F. Moulder, in: G.E. Muilenberg (Ed.), Handbook of X-ray Photoelectron Spectroscopy, PerkinElmer Corporation, Physical Electronics Division, Eden Prairie, MN, 1979.

[42] F. Hochard-Poncet, P. Delichère, B. Moraweck, H. Jobic, A.J. Renouprez, *J. Chem. Soc., Faraday Trans.* **91** (1995) 2891.

[43] P. Fouilloux, *Appl. Catal.* **8** (1983) 1.

[44] M. Boll, S. Volkening, Deutsch Patent DE 10,330,636 A1 (2005).

[45] R.T.K. Baker, M.A. Barber, P.S. Harris, F.S. Feates, R.J. Waite, *J. Catal.* **26** (1972) 51.

[46] L.S. Lobo, D.L. Trimm, *J. Catal.* **29** (1973) 15.

[47] J.L. Figueiredo, in: J.L. Figueiredo (Ed.), Progress in Catalyst Deactivation, Martinus-Nijhoff, The Hague, 1982, pp. 45.

[48] B.J. Cooper, D.L. Trimm, *J. Catal.* **62** (1980) 35.

[49] S. Helveg, C. López-Cartes, J. Sehested, P.L. Hansen, B.S. Clausen, J.R. Rostrup-Nielsen, F. Abild-Pedersen, J.K. Nørskov, *Nature* **427** (2004) 426.

[50] S. Helveg, P.L. Hansen, *Catal. Today* **111** (2006) 68.

[51] J.L. Figueiredo, D.L. Trimm, in: Proceedings of the 4th London International Carbon and Graphite Conference, Soc. Chem. Industry, London, (1974), p. 314.

[52] J.L. Figueiredo, D.L. Trimm, *J. Catal.* **40** (1975) 154.

[53] H.J. Grabke, *Mater. Corros.* **49** (1998) 303.

[54] E. Pippel, J. Woltersdorf, R. Schneider, *Mater. Corros.* **49** (1998) 309.

[55] J. Zhang, P. Munroe, D.J. Young, *Acta Mater.* **56** (2008) 68.

[56] Z. Zeng, K. Natesan, *Chem. Mater.* **17** (2005) 3794.

[57] J. Guinot, M. Audier, M. Coulon, L. Bonnetain, *Carbon* **19** (1981) 95.

# Chapter III

## Carbon deposits on Raney-type Catalysts

Partially published in

Applied Catalysis A: General 351 (2008) 204

Catalysis Communications 10 (2009) 1203

*"Ideas are investments*

*the remaining is only money."*

**Eric Singer**

## Abstract

Simultaneous generation of filamentous carbon and nickel, cobalt or iron nanoparticles was achieved by methane decomposition over Raney-type skeletal catalysts. The nanoparticles were generated by metal disintegration and stabilized by filamentous carbon. These composite materials were characterized, and part of them tested as catalysts for hydrogenation reactions. The Ni nanoparticles in reduced form showed superficial oxide layers that contribute to protect them from bulk oxidation by air. They exhibit excellent catalytic properties for liquid phase hydrogenation reactions. The analysis of Fe nanoparticles showed the presence of iron carbide.

## 3.1 Introduction

$CO_x$-free hydrogen production via catalytic methane decomposition (CMD) [1] may only be applicable in an industrial process if the produced carbon by-products hold potential for wide technological applications.

On the other hand, nanocrystalline materials, typically less than 100 nm in size, are highly interesting scientifically. Due to the very small grain size, a significant volume of the microstructure is composed of interfaces/grain boundaries and hence a large fraction of the atoms resides in grain boundaries. Consequently, they often exhibit superior properties in comparison to their conventional coarse-grained polycrystalline counterparts [2]. Nanoscale materials have attracted interest for applications in various fields, such as optoelectronics and magnetic devices, biosensors, nanomachines, etc.

One of the possibilities is to use the produced carbon deposits, which contain metal nanoparticles, as catalysts, particularly for hydrogenation reactions. For example, the catalytic hydrogenation of aromatic nitro compounds is usually catalysed by supported noble metals (Pt, Pd, and Ru) or Raney-Ni.

The exposed surface area plays a major role in catalysis, and the large specific surface area of nanomaterials can be used for this purpose. Moreover, the influence of particle size on the activity and selectivity is a well known fact in several catalytic reactions. Ni, Co and Fe are widely used in catalytic hydrogenation/dehydrogenation reactions. Several reports on the preparation and catalytic application of nickel nanoparticles can be found in the literature [3–12]. In heterogeneous catalysis, nanomaterials are usually dispersed on supports. The support materials stabilize the nanoparticles, preventing surface migration and coalescence during reaction at high temperatures. Sometimes they influence the course of the reaction too. Recently, there has been a growing interest in filamentous carbon, or carbon nanofibres (CNF). CNF are produced by decomposing carbonaceous gases on iron, cobalt or nickel catalysts. The growth of CNF is accompanied by the disintegration of the active metal; metal particles are located on top of carbon filaments. There are many reports available in the literature on the use of CNF, after purification, as catalyst supports and adsorbents [13–19]. The mechanism of growth of carbon filaments catalysed by metal particles has been discussed in the literature [20–26].

In the context of by-product applications, e.g. as catalyst, the carbon deposits containing metal nanoparticles, obtained in the experiments described in Chapter II, were subjected to additional characterizations, using different physico-chemical techniques. These studies are presented in the following pages. Most of the produced nanomaterials [1] exhibit excellent stability under air, no

special care being required for their storage. The corresponding catalytic results were published in references [3,4].

## 3.2 Experimental

Raney-type skeletal nickel, cobalt and iron catalysts were prepared from Me–Al alloys (Me = Ni, Co and Fe) as already reported in Chapter II. CMD was carried out over the skeletal catalysts in order to generate hydrogen and carbon deposits with metal nanoparticles, since the growth of carbon filaments is accompanied by the disintegration of skeletal metal [1]. Carbon filaments held the metal nanoparticles on the top, which were thereby stabilized. The reactor was subsequently cooled to room temperature; the carbon deposits with metal nanoparticles were recovered and stored in covered bottles under air.

## 3.3 Characterization of the carbon deposits containing metal nanoparticles

The carbon deposits with metal nanoparticles were characterized by applying different physicochemical techniques. The contents of nickel and aluminium in the catalysts were determined by ICP-AES analysis. SEM examination was carried out using an electron beam of 20 kV. For TEM analysis, specimens were prepared by ultrasonic dispersion of the carbon deposits with metal nanoparticles in ethanol, evaporating a drop of the resultant suspension onto a copper grid covered with a formvar film. The analyses were carried out at an accelerating voltage of 120 kV. XRD measurements were conducted using Cu $K_\alpha$ radiation ($\lambda$ = 0.154 nm). Intensity was measured by step scanning in the 2$\theta$ range of 10º – 90º. The average metal crystallite size was calculated using the Scherrer equation. XPS analysis was performed using Mg $K_\alpha$ radiation (1253.6 eV). Charging effect was corrected using the C 1s level (285.0 eV) as reference.

### 3.3.1 Carbon deposits obtained on Ni50 catalyst

Table 3.1 shows the detailed conditions used to prepare the nickel nanoparticles stabilized by filamentous carbon.

The nickel and aluminium contents of the nanoparticles stabilized by filamentous carbon were determined by ICP-AES analysis. The results are listed in Table 3.2.

Table 3.1

Conditions of CMD for the preparation

of filamentous carbon stabilized nickel nanoparticles

| Original catalyst | Pre-treatment | $CH_4$ space velocity [$cm^3$ $min^{-1}$ $g^{-1}$ Ni] | $T_{reaction}$ [a] [ºC] | Time [h] | Resulting product |
|---|---|---|---|---|---|
| Raney-Ni (Ni50) | – | 20 | 400 | 40 | NiFC1 |
| | – | 20 | 600 | 5 | NiFC2 |
| | HPT | 20 | 600 | 5 | NiFC3 |
| | – | 4 | 600 | 5 | NiFC4 |

Feed: methane diluted in nitrogen ($CH_4/N_2$ ratio = 0.1). Total flow-rate: 110 $cm^3$ (STP) $min^{-1}$.

HPT: pre-treatment at 600 ºC for 2 h under hydrogen diluted in nitrogen ($H_2/N_2$ = 0.1) with a total gas flow-rate of 110 $cm^3$ (STP) $min^{-1}$.

[a] Reactor heated up to reaction temperature under nitrogen flow (100 $cm^3$ (STP) $min^{-1}$), heating rate 25 ºC $min^{-1}$.

Table 3.2

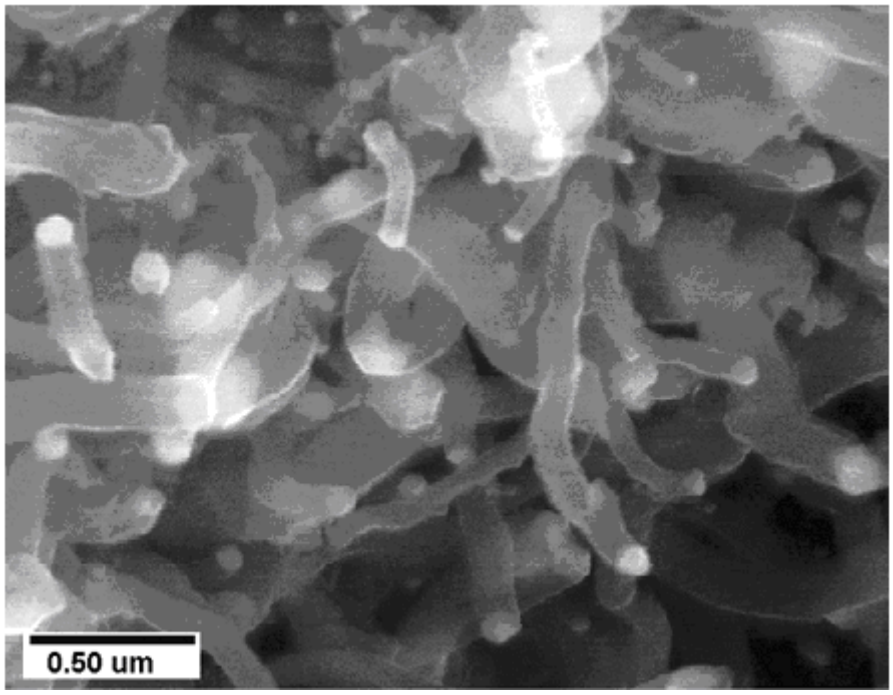
ICP-AES analysis results (wt. %) and

C and Ni crystal sizes of the samples

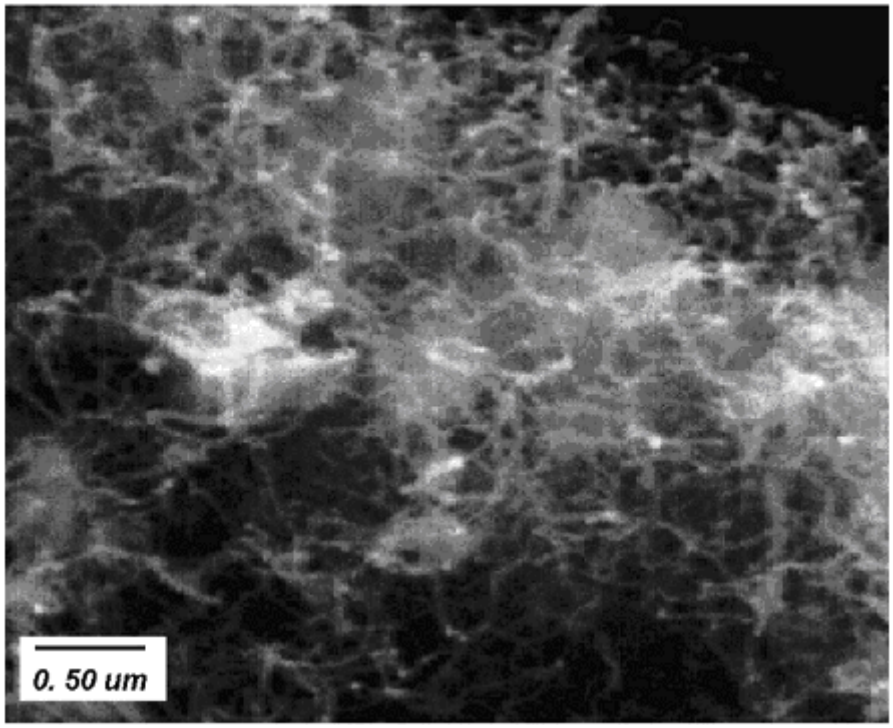
| Catalyst | Ni (±0.5%) | Al (±0.5%) | $d_{Ni}$ [nm] | $d_{Carbon}$ [nm] | $D_{(002)}$ [nm] |
|---|---|---|---|---|---|
| NiFC1 | 33.0 | 5.0 | 19 | 5 | / |
| NiFC2 | 35.6 | 3.4 | 19 | 9 | 0.339 |
| NiFC3 | 24.1 | 8.0 | 30 | 13 | 0.338 |
| NiFC4 | 59.7 | 10.7 | 24 | 6 | 0.340 |

$D_{(002)}$: interplanar distance of carbon.

The morphology of the nickel nanoparticles stabilized by filamentous carbon was examined by SEM and some micrographs are shown in Fig. 3.1. Carbon filaments, holding Ni nanoparticles on top, are clearly visible. In most cases, the diameter of the Ni particle is the same as that of the carbon filament.




NiFC1




NiFC3

Fig. 3.1 SEM images of the carbon deposits with nickel nanoparticles.

Fig. 3.2 shows TEM micrographs of the nickel nanoparticles stabilized by filamentous carbon. The carbon deposit on NiFC1 consists mostly of nanofibres, whereas carbon nanotubes predominate in samples NiFC2, NiFC3 and NiFC4. This is in agreement with Chapter II, where it was observed that carbon deposits generated by methane decomposition at low temperature contained mostly nanofibres, carbon nanotubes being predominantly formed at high temperature. Ni nanoparticles on the tip of carbon filaments are clearly visible in all the samples. Some of the Ni particles in sample NiFC3 are situated at the middle. Bi-directional growth is well documented in the literature [27,28], and is frequently observed with metal alloy catalysts. It is generally explained by reconstruction of the catalyst particles. Apparently, this phenomenon can also be promoted by the hydrogen pre-treatment, as in the present case. Even though the carbon deposits mostly consist of nanofibres and nanotubes, they are mixed with fragments of the original catalyst. Moreover, the carbon filaments (and therefore the associated nickel particles) are not uniform in diameter. Diameter of carbon filaments in the catalysts covers a wide range (NiFC1: 20-200 nm, NiFC2: 20-120 nm, NiFC3: 20-70 nm and NiFC4: 20-60 nm).

The XRD patterns of the samples are shown in Fig. 3.3. Sharp diffraction peaks present at 2θ values of 44.5º, 51.7º and 76.3º clearly indicate the presence of crystalline metallic nickel [29–31]. None of the patterns displays the NiO peak. A very small amount of NiO may be present on the uppermost layers (evidenced by XPS), which is below the detection limit of XRD. This clearly indicates that nickel is well stabilized by the carbon filaments. Higher intensities of diffraction peaks of catalysts NiFC2, NiFC3 and NiFC4 can be related to the higher temperature of methane decomposition reaction. It may be recalled that the temperature of carbon deposition by methane decomposition leading to catalysts NiFC2, NiFC3 and NiFC4 was 600 ºC, whereas catalyst NiFC1 was obtained at 400 ºC (Table 3.1). The nickel crystallite size was calculated applying the Scherrer equation, and is shown in Table 3.2. The crystallites are well in the nanometer scale region (19-30 nm). Comparatively larger Ni crystallites are observed in catalyst NiFC3. Hydrogen pre-treatment of the Ni skeletal catalyst before methane decomposition seems to be responsible. Diffraction peaks at a 2θ value of 26.3º, present in all the XRD patterns, can be assigned to carbon [31].

The carbon crystal sizes are approximately between 5-13 nm. However, it seems that the C and Ni crystal sizes are dependent on the reaction temperature, hydrogen pre-treatment of the catalyst and Raney-Ni catalyst mass used. The interlayer distance between basal planes of ideal graphite (0.3354 nm) is used to compare with those of the produced carbon deposits. The carbon deposits produced on monometallic Ni show in all cases deviations from perfect graphite.

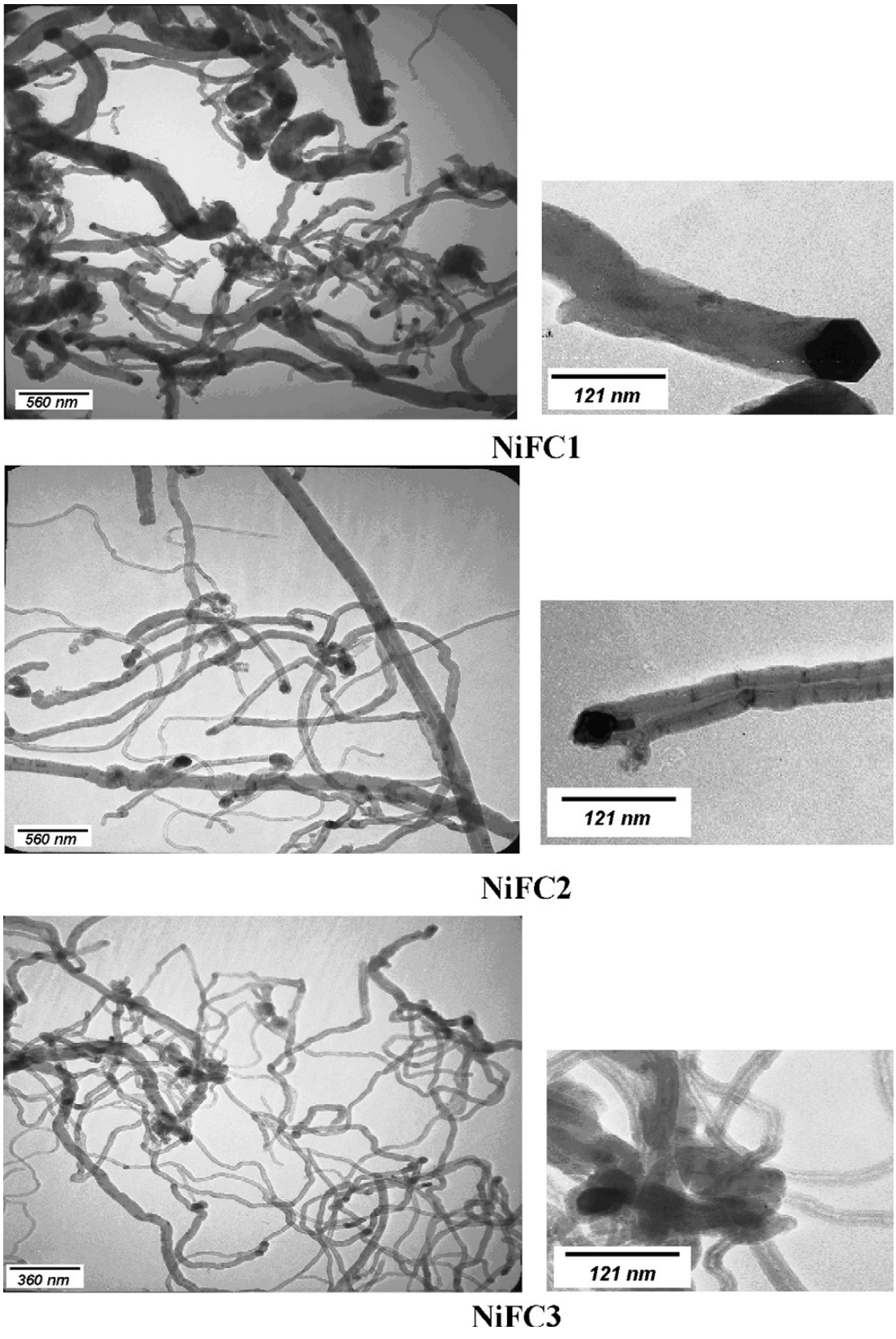



Fig. 3.2 TEM images of the carbon deposits with nickel nanoparticles.

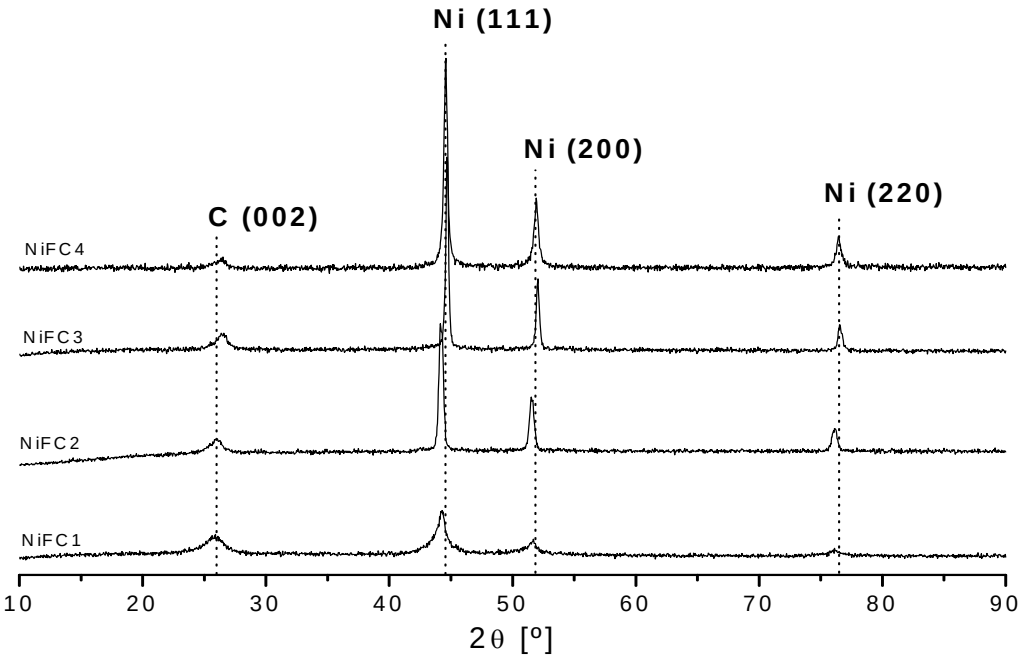
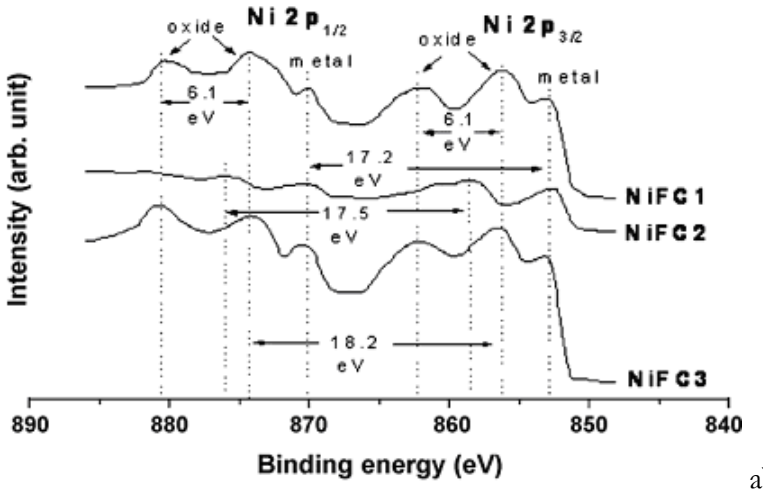
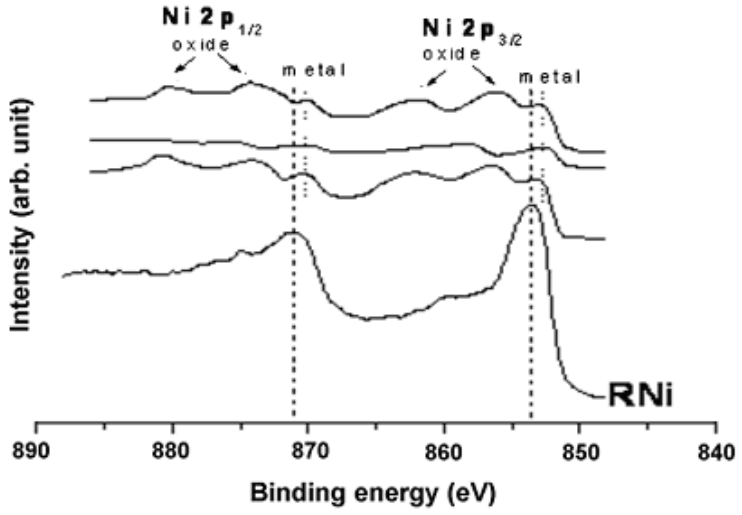



Fig. 3.3 XRD patterns of the carbon deposits with nickel nanoparticles.

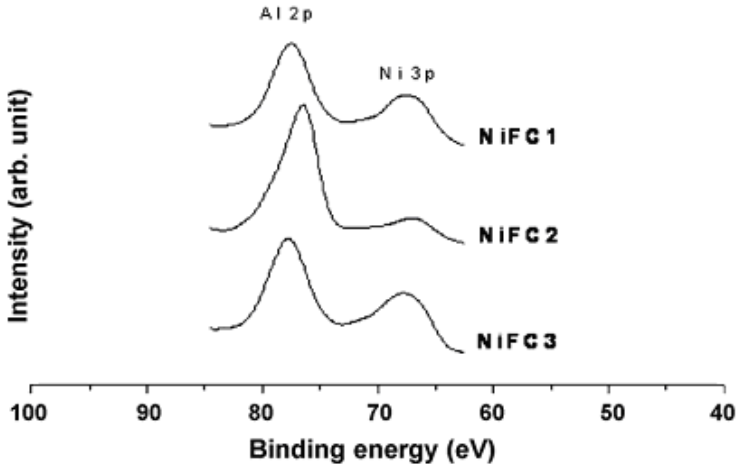
XPS spectra of Ni 2p region of the stabilized catalysts are shown in Fig. 3.4a and 3.4b. The spectra in Fig. 3.4a clearly reveal the presence of surface nickel in metallic as well as in oxidised states in all the catalysts. The $2p^{3/2}$ photoelectron peak observed at 852.8 ± 0.1 eV corresponds to metallic nickel [29,30]. A typical doublet (separated by 17.2 eV) can be also observed [29]. The emission line at 856.2 eV observed in samples NiFC1 and NiFC3 corresponds to nickel oxide/hydroxide, with a doublet separation of about 18.2 eV [29,32]. Besides, shake-up (satellite) peaks can also be seen in the region at about 6.1 eV higher than the normal $2p^{3/2}$ and $2p^{1/2}$ bands [33]. Unlike samples NiFC1 and NiFC3, sample NiFC2 showed a band at about 858.5 eV. Hoffer et al. [29] also observed this kind of phenomena with high binding energy of Ni $2p^{3/2}$. According to them, the high binding energy is related to a $Ni^{2+}$ containing species, which strongly interacts with its environment. Comparison of the spectra of the NiFC catalysts with that of Raney-Ni (RNi, see Fig. 3.4b) clearly shows a negative shift of the binding energy (BE) of Niº in the NiFC samples, indicating charge transfer from carbon filaments to nickel. Table 3.3 summarises the $2p_{3/2}$ BE values along with fractional amount of Niº. Al 2p and Ni 3p XPS spectra are shown in Fig. 3.4c. Aluminium is mostly present in oxide/hydroxide form in all the samples, showing 2p binding energy of 77.2 ± 0.6 eV. Binding energy of Al 2p in $Al_2O_3$ or $NaAlO_2$ is reported to be 74.2 ± 0.3 eV [34]. The high binding energy of Al 2p suggests that aluminium present in the form of $Al^{3+}$ may be in strong interaction with the surroundings.




a)




b)




c)

Fig. 3.4 XPS spectra of the samples: (a-b) Ni 2p; (c) Al 2p and Ni 3p.

Even though nickel oxide/hydroxide and aluminium oxide/ hydroxide are below the detection limit of XRD (Fig. 3.3), XPS analyses confirm their presence on the surface. The small amount of thin oxide/hydroxide layers together with filamentous carbon seems to be protecting nickel particles from bulk oxidation by air.

Table 3.3

Analysis of XPS spectra of the Ni $2p_{3/2}$ region

| Sample | $Ni^o$ | |
|---|---|---|
| | BE [eV] | Fractional amount |
| RNi | 853.58 | 0.78 |
| NiFC1 | 852.94 | 0.22 |
| NiFC2 | 852.66 | 0.29 |
| NiFC3 | 852.95 | 0.22 |

### 3.3.2 Carbon deposits obtained on Ni30 catalyst

Table 3.4 shows the conditions used to obtain the carbon deposits on Raney-Ni30.

Table 3.4

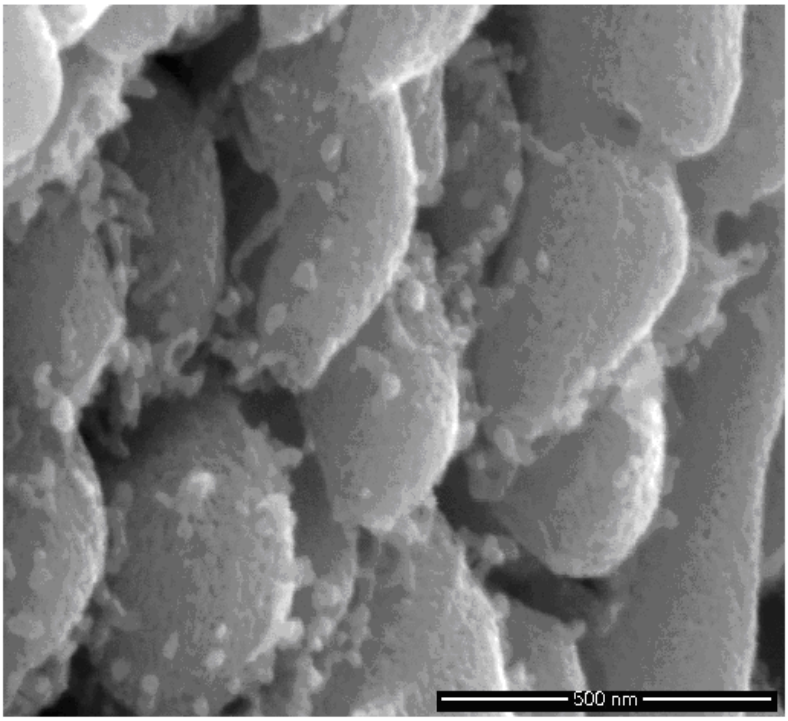
Conditions of CMD for the preparation

of filamentous carbon stabilized nickel nanoparticles

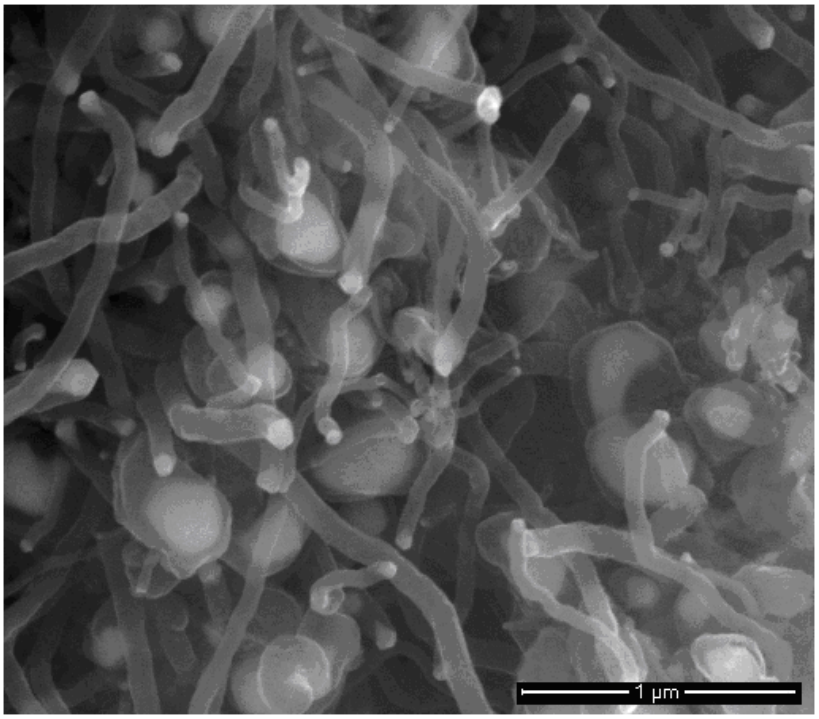
| Original catalyst | $CH_4$ space velocity [$cm^3$ $min^{-1}$ $g^{-1}$ Ni] | $T_{reaction}$ [a] [ºC] | Time [h] | Resulting product |
|---|---|---|---|---|
| Raney-Ni (Ni30) | 20 | 400 | 5 | NiFC5 |
| | 20 | 500 | 5 | NiFC6 |
| | 20 | 600 | 5 | NiFC7 |
| | 20 | 700 | 5 | NiFC8 |

Feed: methane diluted in nitrogen ($CH_4/N_2$ ratio = 0.1). Total flow-rate: 110 $cm^3$ (STP) $min^{-1}$.

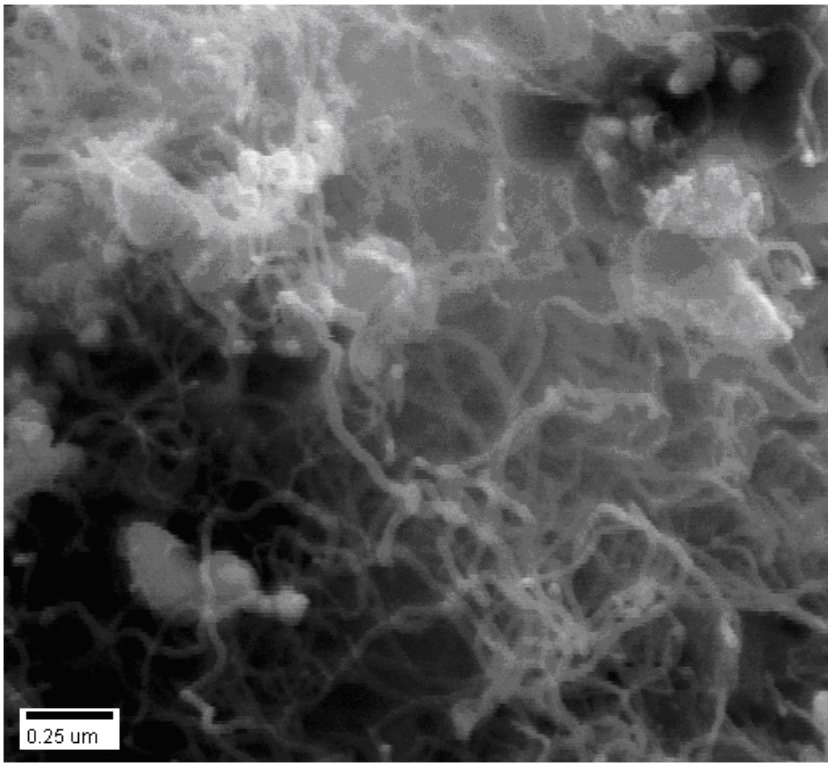
[a] Reactor heated up to reaction temperature under nitrogen flow (100 $cm^3$ (STP) $min^{-1}$), heating rate 25 ºC $min^{-1}$.



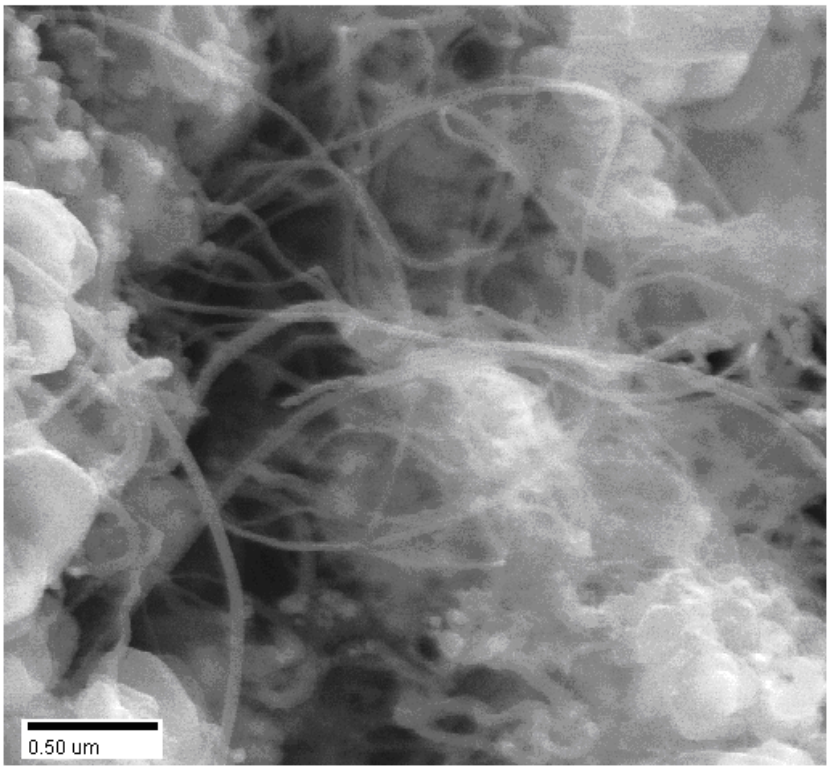

NiFC5




NiFC6

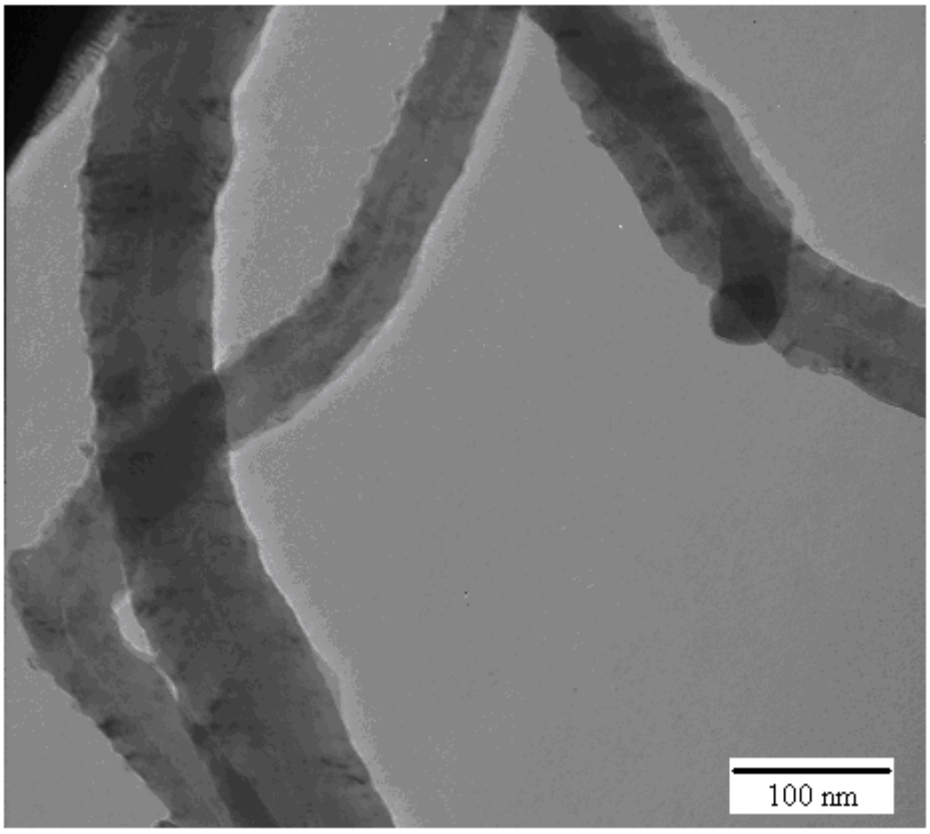



NiFC7

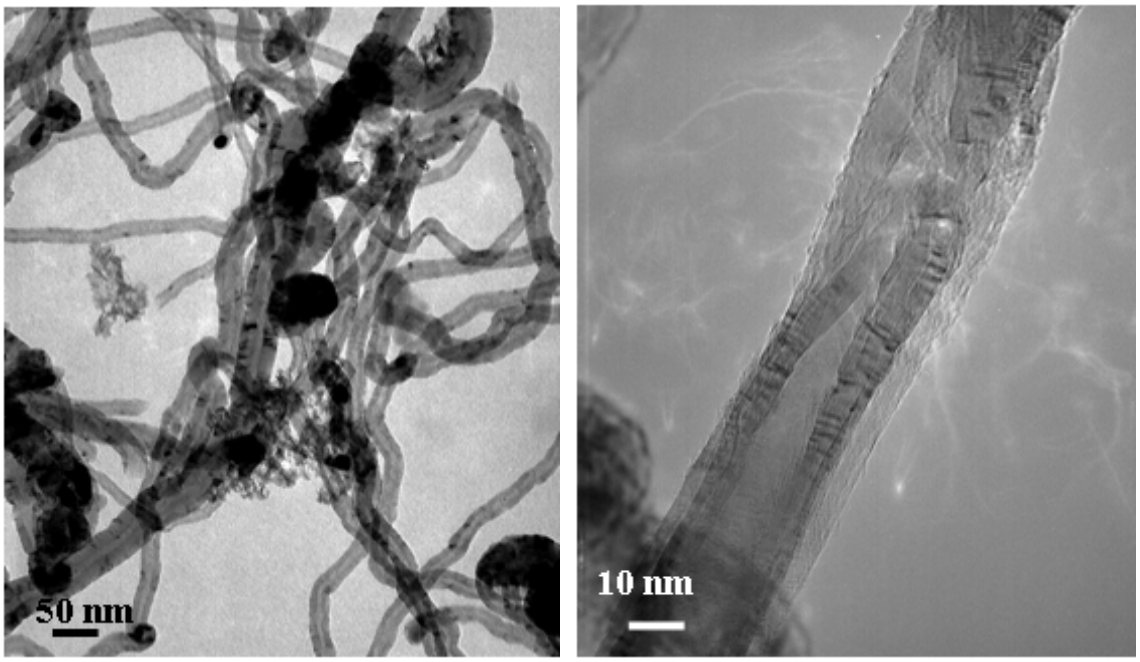



NiFC8

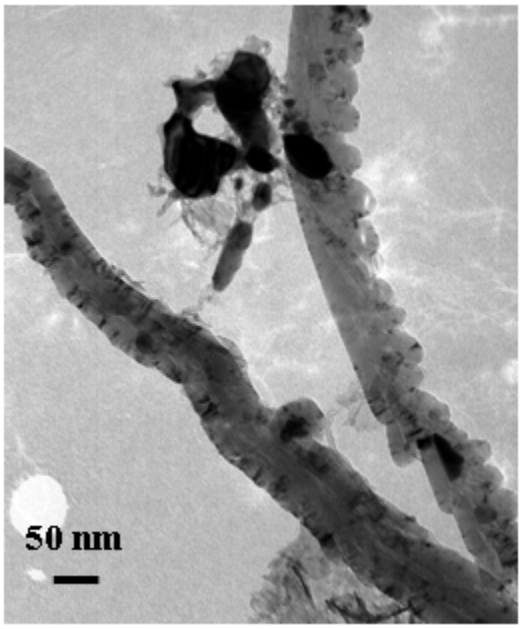
Fig. 3.5 SEM images of the carbon deposits obtained on Raney-Ni30.




NiFC6




NiFC7




NiFC8

Fig. 3.6 TEM images of the carbon deposits obtained on Raney-Ni30.

The morphology of the carbon deposits obtained on Ni30 was examined by SEM and the images are shown in Figure 3.5. According to the low temperature and short reaction time used, only incipient carbon filaments (spots-like) were found in sample NiFC5. Instead, the dendritically amorphous structure of the Ni30 catalyst is kept. On the other hand, carbon filaments holding Ni nanoparticles on top are clearly visible in NiFC6. In most cases, the diameters of the Ni particles correspond to those of the carbon filaments. For NiFC7, carbon filaments and some encapsulating carbon surrounding the Ni particles are visible. The amount of encapsulating carbon increases in NiFC8, according to the higher reaction temperature. Nevertheless, the higher the reaction temperature the narrower are the diameters and the longer are the CNF.

TEM micrographs of the catalysts with carbon deposits are shown in Figure 3.6. In most cases the carbon deposits in NiFC6 are present as CNF with thick walls. At 600 ºC, MWCNT are observed for NiFC7, and the carbon filaments are less thick than for NiFC6. A large amount of graphitic deposits and only few fibres were observed in NiFC8. Ni particle sizes were estimated from the TEM images, and the particles are well in the nanometer scale region (diameters are in the range of 10-100 nm).

The average Ni crystallite sizes were determined by XRD and the patterns of the carbon deposits associated with the Ni30 catalysts are shown in Figure 3.7. Sharp diffraction peaks present at 2θ values of ~44.7º, ~51.8º and ~76.4º indicate the presence of crystalline nickel in oxidation state 0 [29-31]. No NiO was detected. Larger Ni crystallites (sharp diffraction peaks) are observed for

NiFC6, NiFC7 and NiFC8, which may be an evidence of metal particle agglomeration/sinterization at higher reaction temperatures. Diffraction peaks at a 2θ value of ~26.2º, present in most of the XRD patterns, are assigned to graphitic carbon [35].

The qualitative discussion of the crystallinity of the carbon deposits is based on the dominant reflection line assigned to graphite: the (002) plane. Here, it is essential to recall that the carbon reflection line is a contribution of many possible carbon allotropes [35]. Depending on the catalytic system and operating conditions, the respective carbon reflection (002) is different. The quality of the carbon deposits was interpreted in terms of interplanar distances, compared to the value of graphite (0.3354 nm). In all cases the formation of graphitic carbon is observed.

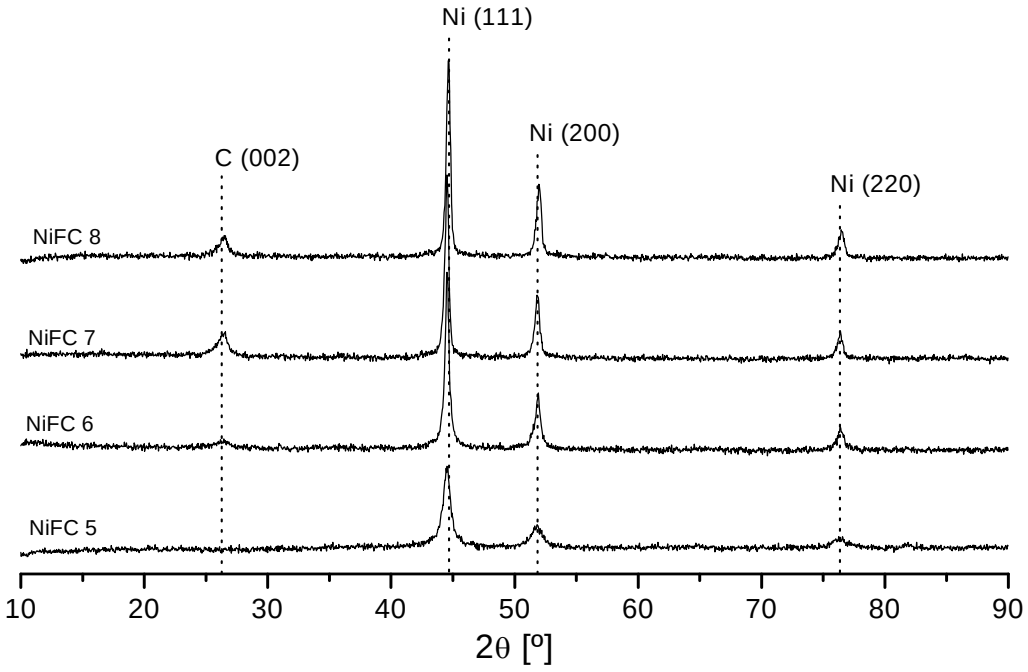



Fig. 3.7 XRD patterns of the catalysts with carbon deposits.

In Table 3.5 the crystal sizes of the carbon deposits and metallic Ni particles are collected. The carbon crystal sizes are approximately between 5-8 nm. Moreover, they show deviations from the interplanar distances of ideal graphite.

Table 3.5

C and Ni crystal sizes of the samples

| Sample | $d_{Ni}$ [nm] | $d_{Carbon}$ [nm] | $D_{(002)}$ [nm] |
|---|---|---|---|
| NiFC5 | 11.6 | / | / |
| NiFC6 | 23.0 | 5.6 | 0.340 |
| NiFC7 | 22.2 | 7.5 | 0.339 |
| NiFC8 | 22.5 | 6.4 | 0.337 |

$D_{(002)}$: interplanar distance of carbon.

### 3.3.3 Carbon deposits obtained on Co50 and Co30 catalysts

Table 3.6 shows the conditions used to prepare the carbon deposits on Raney-Co catalysts.

Table 3.6

Conditions of CMD for the preparation

of filamentous carbon stabilized cobalt nanoparticles

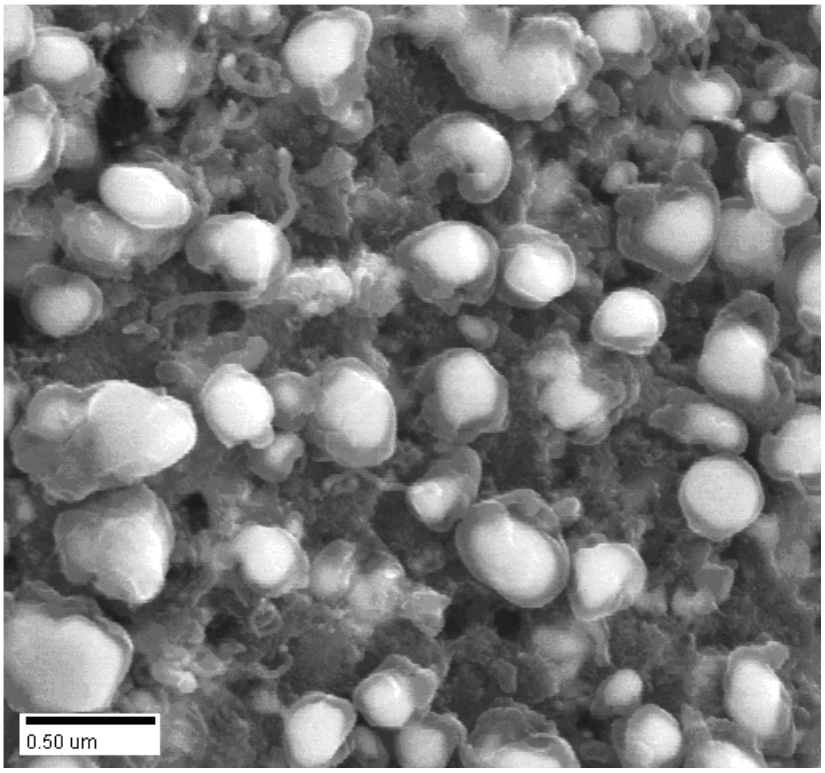
| Original catalyst | $CH_4$ space velocity [$cm^3$ $min^{-1}$ $g^{-1}$ Ni] | $T_{reaction}$ [a] [ºC] | Time [h] | Resulting product |
|---|---|---|---|---|
| Raney-Co (Co50) | 4 | 500 | 5 | CoFC1 |
| | 20 | 600 | 5 | CoFC2 |
| | 4 | 700 | 5 | CoFC3 |
| Raney-Co (Co30) | 4 | 600 | 5 | CoFC4 |

Feed: methane diluted in nitrogen ($CH_4/N_2$ ratio = 0.1). Total flow-rate: 110 $cm^3$ (STP) $min^{-1}$.

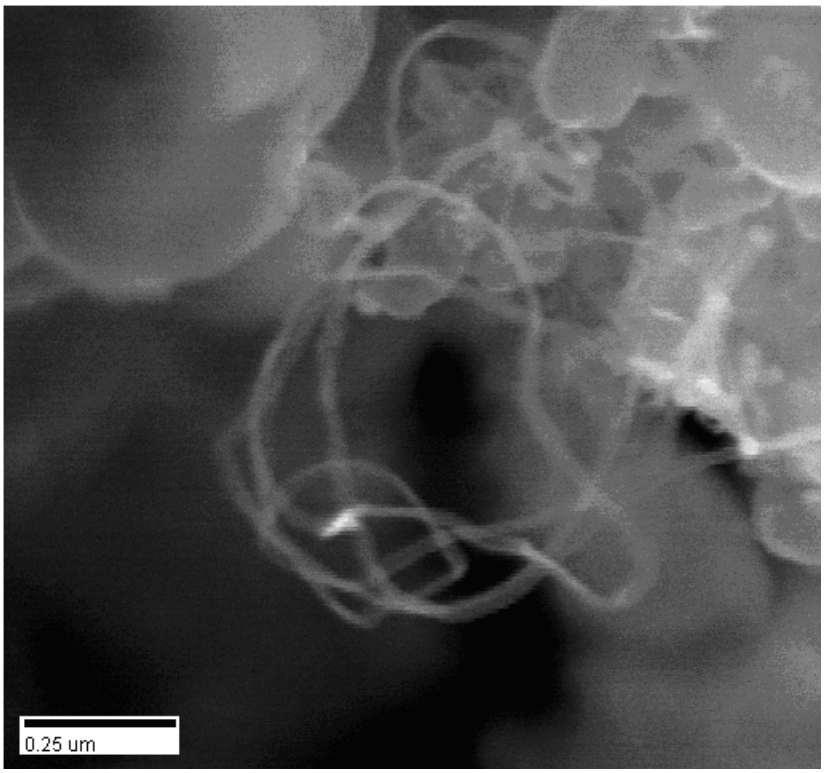
[a] Reactor heated up to reaction temperature under nitrogen flow (100 $cm^3$ (STP) $min^{-1}$), heating rate 25 ºC $min^{-1}$.

In principle, the carbon deposits obtained on Raney-Co catalysts are expected to be similar to those obtained for Raney-Ni catalysts.

SEM micrographs of samples CoFC1 and CoFC3 are depicted in Figure 3.8. The formation of filamentous carbon can be observed. The CNF obtained on Co50 show diameters in the same range as those observed for Ni50. As reaction temperatures used in the CMD increase, higher amounts of encapsulating carbon are formed.



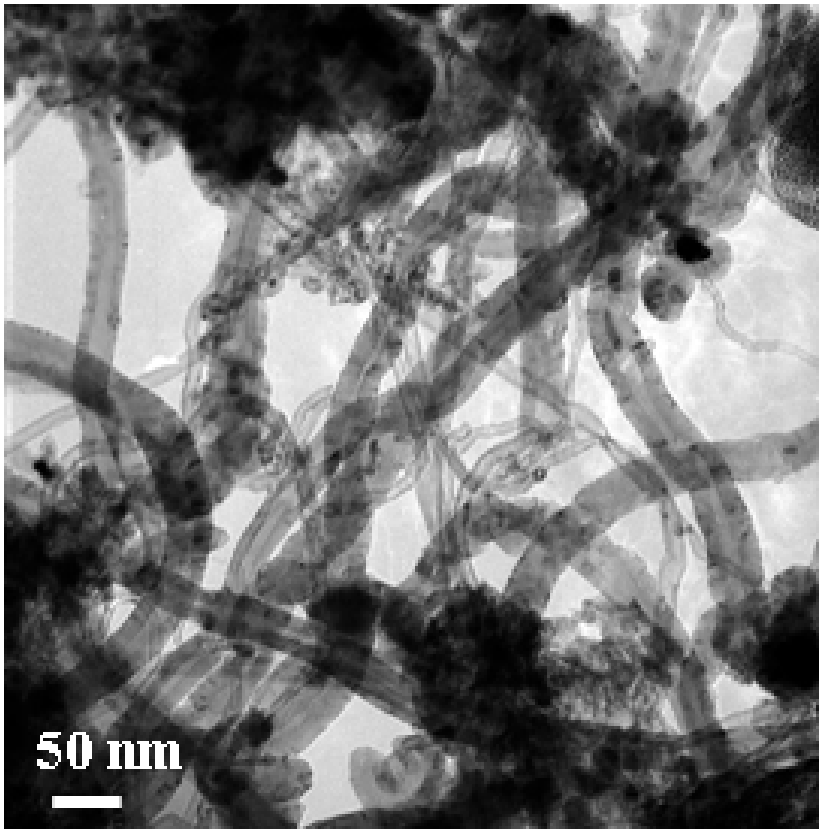

CoFC1




CoFC3

Fig. 3.8 SEM images of the carbon deposits obtained on Raney-Co50.

A TEM micrograph of sample CoFC4 is shown in Figure 3.9. The presence of carbon filaments consisting mainly of MWCNT is detected. The Co particles are mostly found on top of the fibers and show similar diameters as the CNF (10-100 nm).




CoFC4

Fig. 3.9 TEM image of the carbon deposits obtained on Raney-Co30.

The bulk properties of CoFC2 and CoFC4 were studied with XRD in Figure 3.10. The obtained patterns reveal that cobalt is in the metallic form and no CoO is found. The Co reflections show that the most intensive signal is observed for the (111) plane, whereas the other planes, (220) and (222), show very small intensities and are very broad.

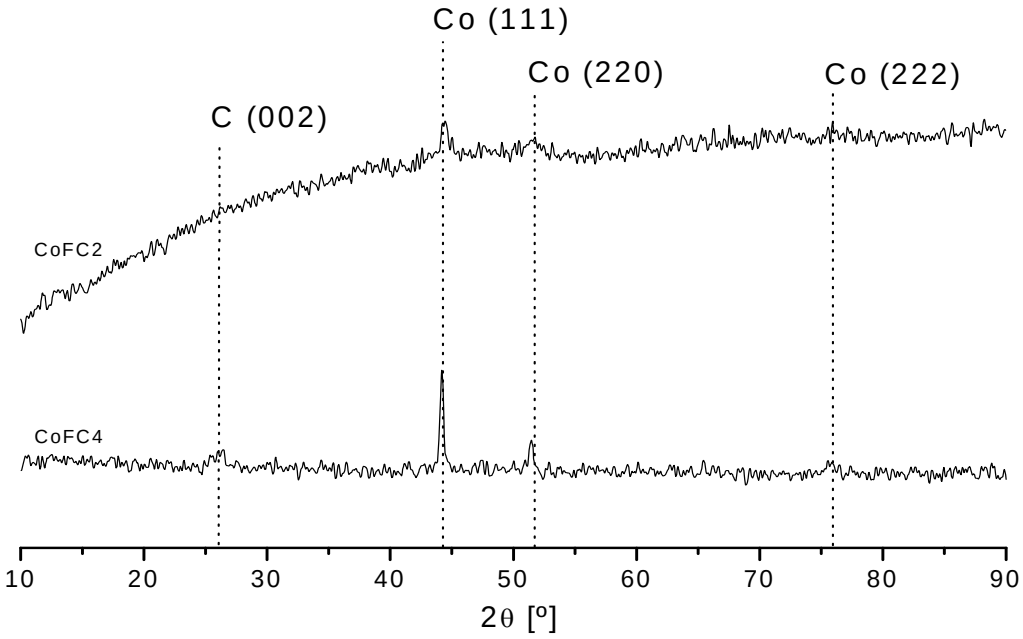



Fig. 3.10 XRD patterns of the catalysts with carbon deposits.

In Table 3.7 the crystal sizes of C and Co for CoFC2 and CoFC4 are collected; they were calculated according to the most intensive (002) and (111) diffraction planes, respectively. Interesting is the fact that the Co crystal sizes are smaller than those obtained for the deposits containing Ni. The smallest size is found for CoFC4 with a dimension of ~10 nm, whereas CoFC2 shows a crystal size of ~16 nm. The corresponding carbon deposits on CoFC4 show an average carbon crystal size of ~17 nm. The interplanar distance of carbon in CoFC4 is closer to that of ideal graphite than in CoFC2.

Table 3.7

C and Co crystal sizes of the samples

| Sample | $d_{Co}$ [nm] | $d_C$ [nm] | $D_{(002)}$ [nm] |
|---|---|---|---|
| CoFC2 | 16 | 15 | 0.341 |
| CoFC4 | 10 | 17 | 0.337 |

$D_{(002)}$: interplanar distance of carbon.

### 3.3.4 Carbon deposits obtained on Fe50 and Fe35catalysts

Table 3.8 shows the conditions used to prepare the carbon deposits obtained on Raney-Fe.

Table 3.8
Conditions of CMD for the preparation
of filamentous carbon stabilized iron nanoparticles

| Original catalyst | Pre-treatment | $CH_4$ space velocity [$cm^3\ min^{-1}\ g^{-1}$ Ni] | $T_{reaction}$ [a] [ºC] | Time [h] | Resulting product |
|---|---|---|---|---|---|
| Raney-Fe | – | 4 | 550 | 5 | FeFC1 |
| (Fe50) | – | 4 | 600 | 5 | FeFC2 |
| | – | 4 | 700 | 5 | FeFC3 |
| | – | 20 | 600 | 5 | FeFC4 |
| | HPT | 20 | 600 | 5 | FeFC5 |
| (Fe35) | – | 20 | 600 | 5 | FeFC6 |
| | HPT | 20 | 600 | 5 | FeFC7 |

Feed: methane diluted in nitrogen ($CH_4/N_2$ ratio = 0.1). Total flow-rate: 110 $cm^3$ (STP) $min^{-1}$.

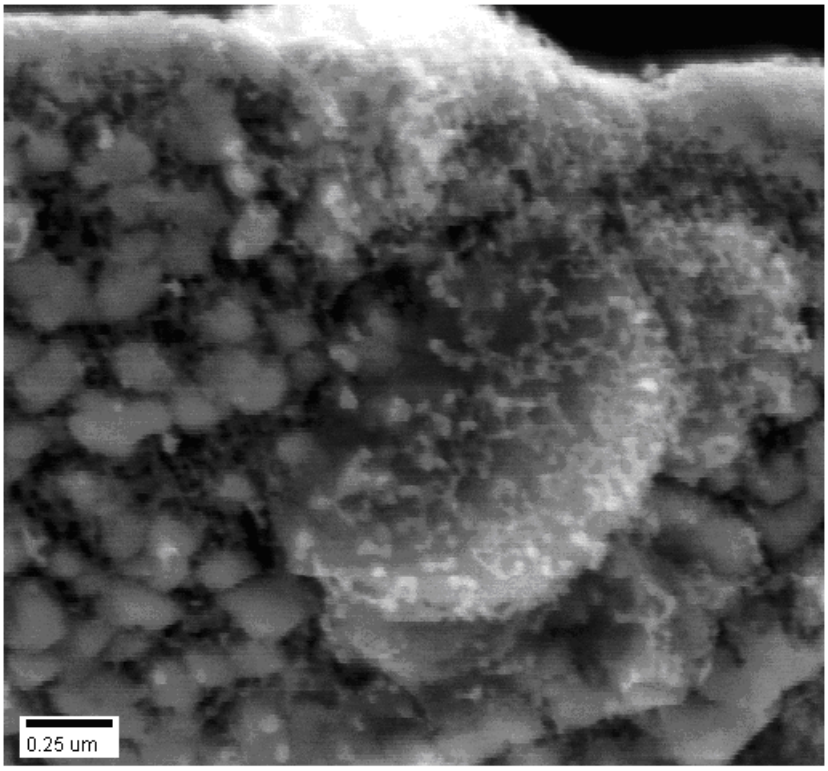
HPT: pre-treatment at 600 ºC for 2 h under hydrogen diluted in nitrogen ($H_2/N_2$ = 0.1) with a total gas flow-rate of 110 $cm^3$ (STP) $min^{-1}$.

[a] Reactor heated up to reaction temperature under nitrogen flow (100 $cm^3$ (STP) $min^{-1}$), heating rate 25 ºC $min^{-1}$.

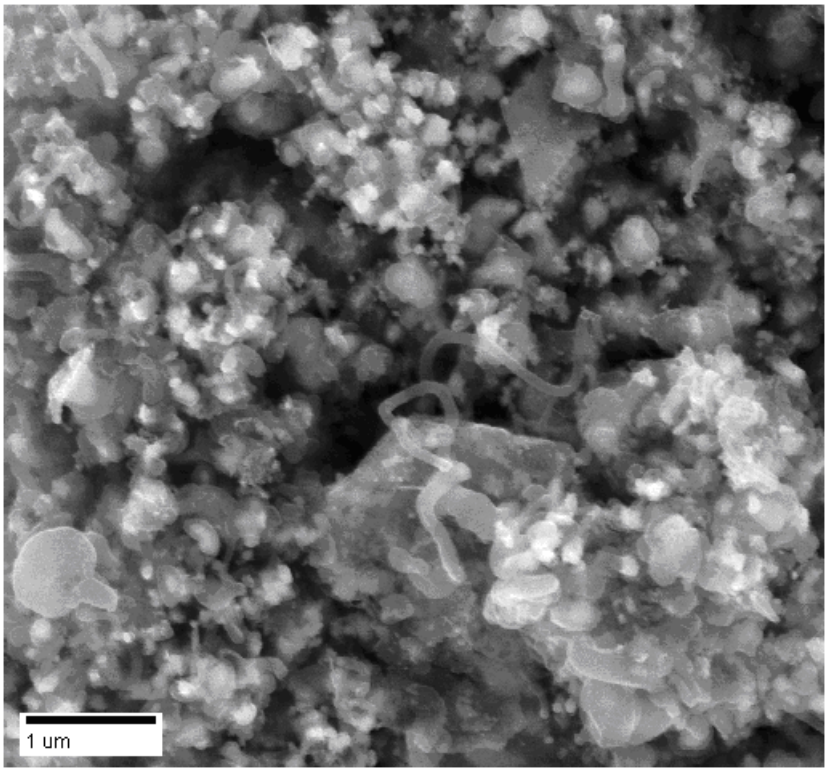
The properties of the carbon deposits obtained on Fe catalysts are quite different from those produced on Ni or Co Raney-type catalysts. This behavior was already observed in Chapter II, and will be discussed below.

SEM micrographs of FeFC1, FeFC2 and FeFC3 were acquired and are shown in Figure 3.11. Large amounts of encapsulating carbon are observed at all temperatures tested. Some CNF are also visible, but the diameters are much larger than those produced on Ni or Co catalysts, and these fibers are generally very short. Agglomerates of metal particles are also frequently observed.

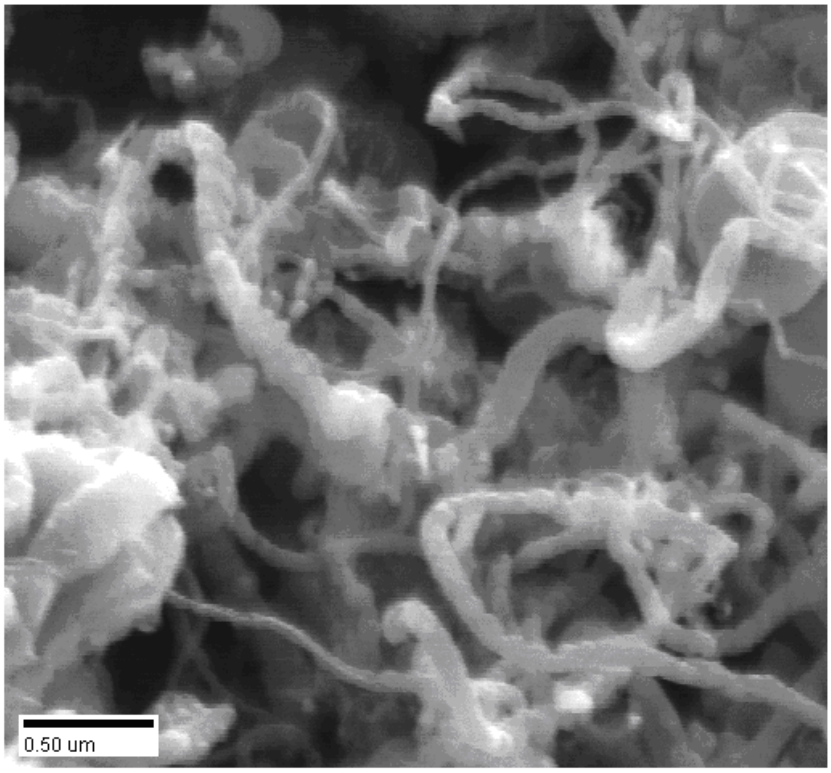
TEM micrographs of the carbon deposits obtained on FeFC2 and FeFC3 are shown in Figure 3.12. It can be seen that higher reaction temperatures (700 ºC) generate few nanofibers and some nanotubes, accompanied by large amounts of encapsulating carbon and particle agglomerates. At lower reaction temperatures (600 ºC) a large amount of encapsulated particles is also observed, but only very few CNT (bamboo-like) are formed.




FeFC1

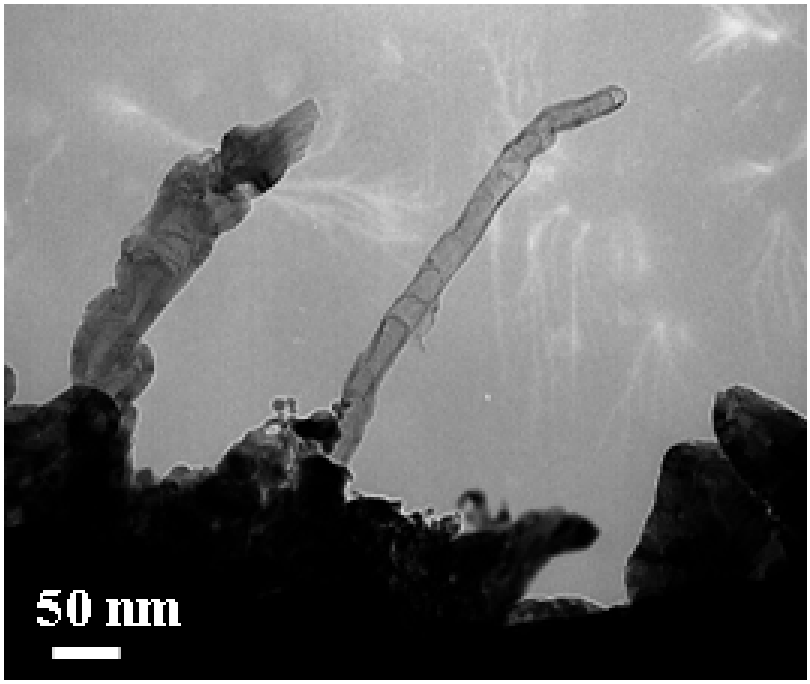



FeFC2

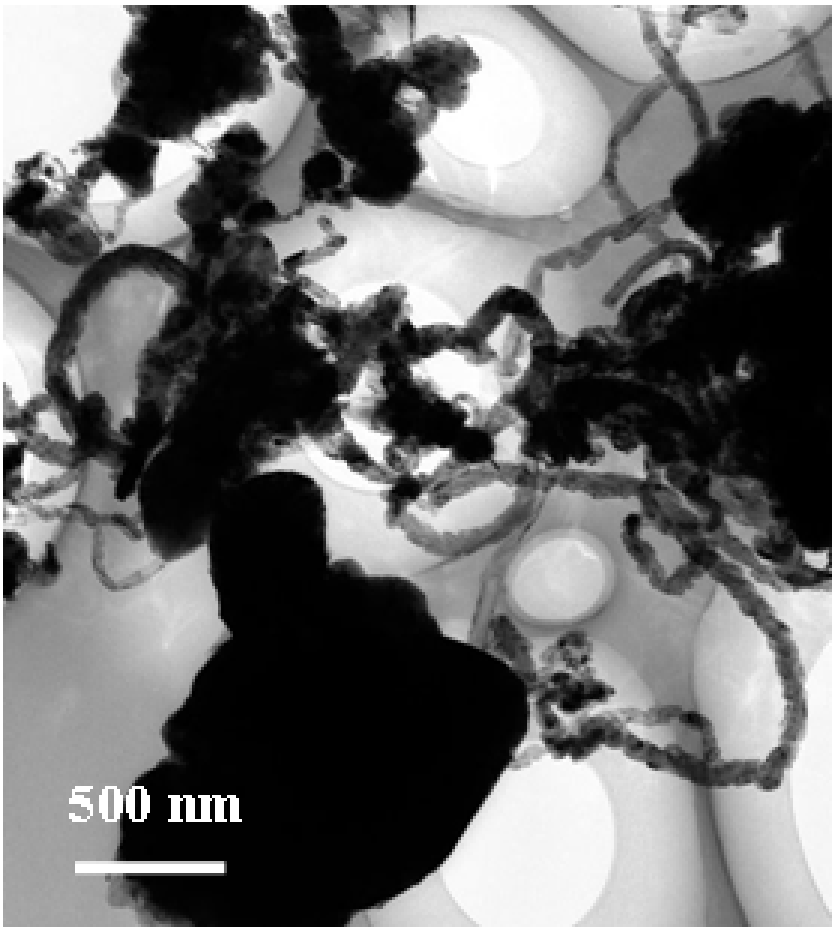



FeFC3

Fig. 3.11 SEM images of the carbon deposits obtained on Raney-Fe50.




FeFC2




FeFC3

Fig. 3.12 TEM images of the carbon deposits obtained on Raney-Fe50.

The XRD patterns of the deposits containing Fe are shown in Figure 3.13. FeFC4 shows the presence of three phases: graphite like carbon at the 2θ position 26.2º, Fe at 2θ = 44.7º, 65.4º and 82.5º as well as $Fe_3C$ (Cementite or Cohemite) at 2θ = 26.2º, 37.7º, 39.7º, 43.0º, 43.8º, 44.7º, 45.0º, 45.9º, 48.7º, 49.4º, 51.9º, 54.5º, 61.7º, 78.4º and 80.6º. For FeFC5 only two phases were detected: a Fe phase at the 2θ positions 44.6º, 65.1º and 82.3º as well as a graphite-like carbon phase at the 2θ position of 26.6º. No iron carbide was found.

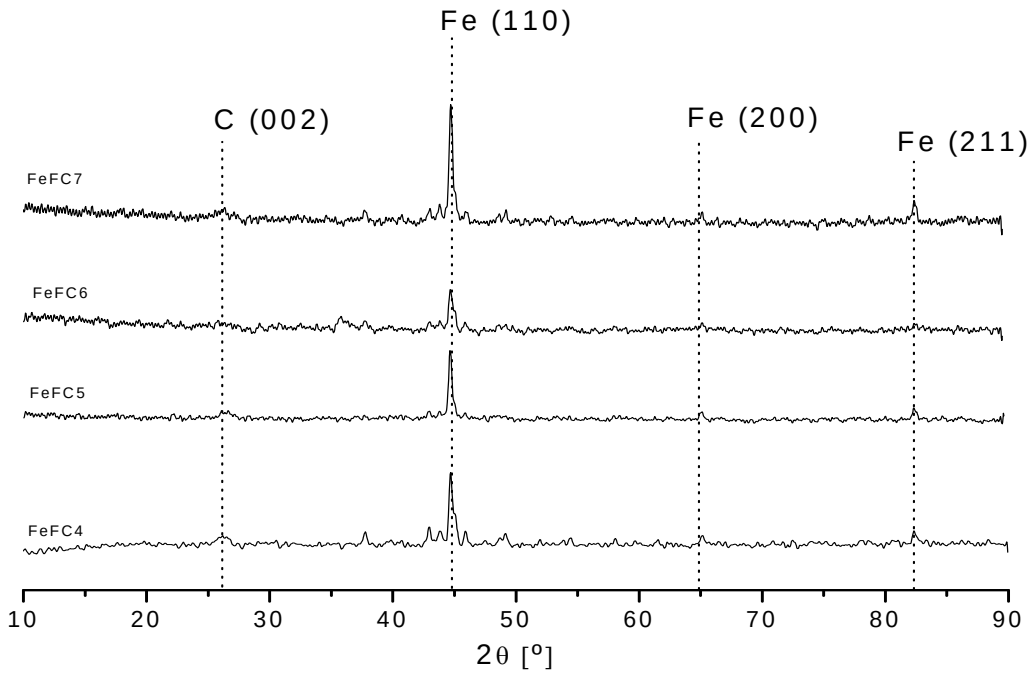



Fig. 3.13 XRD patterns of the carbon deposits obtained on Raney-Fe.

The XRD results for FeFC6 catalyst show the presence of carbon. The presence of a Fe phase at the 2θ positions of 44.7º, 65.1º and 82.4º was found, but the signals are weak. A $Fe_3C$ (Cementite) phase was also detected at 2θ = 37.8º, 43.0º, 43.8º, 44.7º, 45.9º, 48.3º and 49.0º. Important to mention is that a $Fe_2O_3$ phase, as Maghemite, was recognized at 2θ = 30.6º, 32.5º, 35.8º, 44.7º and 65.1º. Finally, FeFC7 was identified with a α-Fe phase at the 2θ positions 44.7º, 65.1º, and 82.3º), a $Fe_3C$ (Cementite) phase at 2θ = 37.8º, 43.0º, 44.7º, 46.0º and 49.2º, and a graphite-like (002) pattern at 2θ = 26.3º.

The interplanar distance of carbon shows in all cases strong deviations relatively to ideal graphite. Table 3.9 collects the results calculated for these samples.

Table 3.9

C, Fe and $Fe_3C$ crystal sizes of the samples

| Sample | $d_{Fe}$ [nm] | $d_C$ [nm] | $D_{(002)}$ [nm] |
|---|---|---|---|
| FeFC4 | 52.1 | 42.4 | 0.341 |
| FeFC5 | 41.0 | / | 0.339 |
| FeFC6 | 32.6 | 46.4 | 0.346 |
| FeFC7 | 52.1 | / | 0.339 |

$D_{(002)}$: interplanar distance of carbon.

## 3.4 Conclusions

Nickel nanoparticles on filamentous carbon can be generated by decomposing methane over Raney-type skeletal nickel catalysts. Nickel particles are stabilized by the carbon filaments. Stabilized nanocatalysts consist of nickel particles in metallic form with superficial oxide layers on top of carbon filaments. Oxide layers together with filamentous carbon protect nickel particles from bulk oxidation by air. Catalysts are stable under air. The main characteristics of cobalt nanoparticles stabilized by carbon filaments are similar to nickel. The nickel nanoparticles on filamentous carbon exhibit excellent performance in the liquid phase hydrogenation of nitrobenzene and chloronitrobenzenes. The iron nanoparticles show the presence of iron carbide.

## Appendix

Additional results obtained for this Chapter III can be consulted in the Appendix.

## References


[1] A.F. Cunha, J.J.M. Órfão, J.L. Figueiredo, *Appl. Catal. A: Gen.* **348** (2008) 103.

[2] C. Suryanarayana, *Int. Mater. Rev.* **40** (1995) 41.

[3] N. Mahata, A.F. Cunha, J.J.M. Órfão, J.L. Figueiredo, *Appl. Catal. A: Gen.* **351** (2008) 204.

[4] N. Mahata, A.F. Cunha, J.J.M. Órfão, J.L. Figueiredo, *Catal. Commun.* **10** (2009) 1203.

[5] M. Watanabe, H. Yamashita, X. Chen, J. Yamanaka, M. Kotobuki, H. Suzuki, H. Uchida, *Appl. Catal. B: Environ.* **71** (2007) 237.

[6] A.P. Weber, P. Davoodi, M. Seipenbusch, G. Kasper, *J. Nanopart. Res.* **8** (2006) 445.

[7] J. Zhang, H. Xu, W. Li, *Appl. Catal. A: Gen.* **296** (2005) 257.

[8] M.M. Selim, I.H. Abd El-Maksoud, *Micropor. Mesopor. Mater.* **85** (2005) 273.

[9] Y. Du, H. Chen, R. Chen, N. Xu, *Appl. Catal. A: Gen.* **277** (2004) 259.

[10] J. Gao, F. Guan, Y. Zhao, W. Yang, Y. Ma, X. Lu, J. Hou, J. Kang, *Mater. Chem. Phys.* **71** (2001) 215.

[11] S. Kapoor, H.G. Salunke, A.K. Tripathi, S.K. Kulshreshtha, J.P. Mittal, *Mater. Res. Bull.* **35** (2000) 143.

[12] D. Zuo, Z. Zhang, Z. Cui, L. Dong, *Chin. J. Catal.* **17** (1996) 166.

[13] P. Serp, M. Corrias, P. Kalck, *Appl. Catal. A: Gen.* **253** (2003) 337.

[14] K.P. De Jong, J.W. Geus, *Catal. Rev. Sci. Eng.* **42** (2000) 481.

[15] J.-K. Chang, H.-Y. Tsai, W.-T. Tsai, *J. Power Sources* **182** (2008) 317.

[16] T.V. Reshetenko, L.B. Avdeeva, Z.R. Ismagilov, A.L. Chuvilin, V.B. Fenelonov, *Catal. Today* **102–103** (2005) 115.

[17] M.N. Timofeeva, M.M. Matrosova, T.V. Reshetenko, L.B. Avdeeva, A.A. Budneva, A.B. Ayupov, E.A. Paukshtis, A.L. Chuvilin, A.V. Volodin, V.A. Likholobov, *J. Mol. Catal. A: Chem.* **211** (2004) 131.

[18] G.A. Kovalenko, E.V. Kuznetsova, Yu.I. Mogilnykh, I.S. Andreeva, D.G. Kuvshinov, N.A. Rudina, *Carbon* **39** (2001) 1033.

[19] Sh.K. Shaikhutdinov, L.B. Avdeeva, B.N. Novgorodov, V.I. Zaikovskii, D.I. Kochubey, *Catal. Lett.* **47** (1997) 35.

[20] J. Highfield, Y.S. Loo, Z. Zhong, B. Grushko, *Carbon* **45** (2007) 2597.

[21] J.L. Figueiredo, in: J.L. Figueiredo (Ed.), Progress in Catalyst Deactivation, Martinus-Nijhoff, The Hague, 1982, pp. 45.

[22] S. Helveg, C. López-Cartes, J. Sehested, P.L. Hansen, B.S. Clausen, J.R. Rostrup-Nielsen, F. Abild-Pedersen, J.K. Nørskov, *Nature* **427** (2004) 426.

[23] M.A. Ermakova, D.Yu. Ermakov, L.M. Plyasova, G.G. Kuvshinov, *Catal. Lett.* **62** (1999) 93.

[24] R.T. Yang, J.P. Chen, *J. Catal.* **115** (1989) 52.

[25] J. Rostrup-Nielsen, D.L. Trimm, *J. Catal.* **48** (1977) 155.

[26] R.T.K. Baker, M.A. Barber, P.S. Harris, F.S. Feates, R.J. Waite, *J. Catal.* **26** (1972) 51.

[27] M.S. Kim, N.M. Rodriguez, R.T.K. Baker, *J. Catal.* **131** (1991) 60.

[28] W.B. Downs, R.T.K. Baker, *Carbon* **29** (1991) 1173.

[29] B.W. Hoffer, E. Crezee, F. Devred, P.R.M. Mooijman, W.G. Sloof, P.J. Kooyman, A.D. van Langeveld, F. Kapteijn, J.A. Moulijn, *Appl. Catal. A: Gen.* **253** (2003) 437.

[30] M. Wang, H. Li, Y. Wu, J. Zhang, *Mater. Lett.* **57** (2003) 2954.

[31] A.K. Chatterjee, M. Sharon, R. Banerjee, *J. Power Sources* **117** (2003) 39.

[32] B.W. Hoffer, A.D. van Langeveld, J.-P. Janssens, R.L.C. Bonné, C.M. Lok, J.A. Moulijn, *J. Catal.* **192** (2000) 432.

[33] P. Lu, T. Teranishi, K. Asakura, M. Miyake, N. Toshima, *J. Phys. Chem. B* **103** (1999) 9673.

[34] F. Hochard-Poncet, P. Delichere, B. Moraweck, H. Jobic, A.J. Renouprez, *J. Chem. Soc., Faraday Trans.* **91** (1995) 2891.

[35] T. Belin, F. Epron, *Mater. Sci. & Eng. B* **119** (2005) 105.

# *Chapter IV*

## Methane Decomposition on Ni-Cu alloyed and Fe-Cu Raney-type Catalysts

Published in

International Journal of Hydrogen Energy (2009), in press

Fuel Processing Technology (2009), submitted

*"The progress is the labor of nagger,*

*Satisfied people do not want any change."*

**H.G. Wells**

# *Part A*

## Methane Decomposition on Ni-Cu alloyed Raney-type catalysts

## Abstract

In the present work, we report on the performance of Ni-Cu alloyed Raney-type catalysts for the production of hydrogen by catalytic methane decomposition. The activity of the catalysts was assessed by comparing the experimental conversions with the calculated equilibrium conversions for each set of experimental conditions. The stability of the catalysts was assessed by comparing the maximum conversions with the conversions at the end of 5 hour tests. Comparison with monometallic Ni Raney-type catalytic systems shows that Cu addition significantly improves catalyst stability. Excellent results were obtained when the Ni-Cu Raney-type system was thermally treated in situ at 600 ºC, as a result of incipient alloy formation.

## 4.1 Introduction

Catalytic methane decomposition (CMD) into $CO_x$-free hydrogen and carbon is an attractive reaction for the hydrogen energy system ($CH_4 \rightleftharpoons C + 2H_2$) [1-5]. The feasibility of the above mentioned reaction depends mainly on the operating conditions and the catalyst itself. In a previous work, it was shown that the use of Fe, Co or especially Ni as active phases in Raney-type catalysts provided very good catalytic performances in comparison with other catalysts reported in the literature [6].

Stable operation of the CMD mostly depends on avoiding the formation of encapsulating carbon species on active metal particles surfaces, while filamentous carbon does not necessarily deactivate the catalyst [7,8]. Therefore it is necessary to find suitable promoters. Several authors have reported that bimetallic systems can improve methane conversion. A variety of promoters have been suggested, such as alloyed metals (Cu, Rh, Pt, Ru and Pd) in Ni, or the use of Mn and Mo [9-12]. It has been found that the addition of Pd or Cu increases the stability of $Ni/SiO_2$ at 550 ºC due to a synergistic effect [9,13]. Li et al. have found that Cu addition to $Ni/Al_2O_3$ increases the performance of the catalyst for methane decomposition [14].

An elegant method to improve stability is the control of ensemble size, i.e. the number of adjacent active sites, which is achieved by dilution with an inert metal [15,16]. The introduction of copper as promoter on nickel catalysts is not a novelty, as filamentous carbon formed from benzene by chemical vapor deposition (CVD) on Ni-Cu alloys was reported by Nishiyama and Tamai already in 1974 [17]. The performance of Ni-Cu alloys in many hydrocarbon reactions was reviewed by Ponec [18]. The changes in activity and selectivity are ascribed to the dilution of the nickel surface atoms (geometric effect), rather than an electronic effect. The formation of smaller ensembles of nickel surface atoms minimizes the interactions of adsorbed carbon species, thus reducing the rate of encapsulating carbon formation, which is responsible for catalyst deactivation [19-21]. In this way, Ni-Cu alloys are more efficient for filamentous carbon formation than the pure active Ni phase. For instance, Baker and col. studied the formation of carbon filaments from ethylene decomposition over unsupported Ni and Ni-Cu catalysts [22-24]. With pure Ni, the presence of hydrogen was required for the formation of filamentous carbon, while this was not necessary with Ni-Cu. It was suggested that adsorbed hydrogen might perform the same function as Cu, namely to limit the size of Ni ensembles, thereby inhibiting the formation of encapsulating carbon [22]. They found that catalyst stability was dependent on catalyst mass, and that the maximum ethylene conversion over a Ni-Cu (30 wt. % Cu) catalyst occurred in the temperature range 600-700 ºC.

Good results were also reported for CMD on supported and unsupported Ni-Cu catalysts [14,25-45], showing that higher activities and stabilities could be achieved with smaller amounts of catalyst.

Many different methods of catalyst preparation are described in the literature, such as direct fusion, co-precipitation, impregnation, etc. To the best of our knowledge, the incipient alloying by in-situ thermal treatment of Raney-type catalyst mixtures based on Ni and Cu, used in the present work, was never reported before. In this work, we examine physical mixtures of Ni and Cu Raney-type catalysts, with residual alumina as textural promoter, prepared with or without an in situ thermal treatment (ITT), as catalysts for methane decomposition in a fixed-bed reactor. The performance of the bimetallic Raney catalysts, either as a physical mixture or as an incipient alloyed system, in different compositions and operating conditions, was compared with the monometallic Raney-Ni catalysts used in our previous work [6]. In addition, the carbon deposits were also analyzed and found to include carbon nanofibers (CNF)/multiwall carbon nanotubes (MWCNT) and/or encapsulating carbon, depending on the operating conditions used.

## 4.2 Experimental

### 4.2.1 Catalysts preparation

The skeletal (Raney-type) catalysts used in this work were prepared from Me-Al alloys (Me = Ni or Cu) obtained from two different sources. The nominal active metal mass content in the alloys are 50 wt. % for Cu, and 50 or 30 wt. % for Ni. The Ni50 wt. % alloy is a commercial product from Fluka Chemie Gmbh and is a conventional alloy [46]. The remaining Ni30 and Cu50 alloy powders were supplied by H.C. Starck GmbH (Amperkat® SK alloys). Ni30 is obtained by a fast quenching method and Cu50 is a conventional alloy [47]. The Cu50 and Ni30 (or Ni50) alloys were mixed and Al was leached using a concentrated NaOH solution at room temperature, forming a heterogeneous mixture of catalyst particles. Details of the Raney-type catalysts preparation are largely documented in literature [48,49]. The catalysts are named by their original alloy composition, e.g. Ni30Cu50 is the catalyst obtained by leaching out the Al from a mixture of the Ni-Al (30 wt. %/70 wt. %) and Cu-Al (50 wt. %/50 wt. %) alloys. Except where noted, the catalysts were prepared with equal amounts of Ni and Cu. So, to prepare Ni50Cu50 1 g of each alloy was used, while for Ni30Cu50 1.67 g of Ni30 was mixed with 1 g of Cu50 [50-52].

Other Cu containing compounds such as $Cu(OH)_2{\cdot}CuCO_3$ or $Cu(acac)_2$ were also tested; the corresponding results are included in the Appendix.

### 4.2.2 Catalyst testing

The procedure is similar to that described in Chapter II. Depending on the desired effect, the catalysts went through different pre-treatment procedures. In most cases, the physically mixed Ni-Cu catalytic systems were subjected to an in situ thermal treatment at 600 ºC with a pure nitrogen flow rate of 100 $Ncm^3/min$ for two hours. This treatment is hereafter referred to as ITT. Except where noted, the performance of the Ni30Cu50 (ITT) catalytic system was studied with 1.0 g (0.5 g Cu +0.5 g Ni) of catalyst mass at different operating conditions.

For the isothermal reaction studies, the catalysts were loaded into a tubular reactor, and dried overnight at 78 ºC in a nitrogen stream of 100 $Ncm^3/min$. The continuous-flow reactor was a 75 cm long silica tube with 2.7 cm i.d., inserted into a furnace with a PID temperature controller. The flow rates of methane (99.999 %), nitrogen (99.995 %) and hydrogen (99.999 %) were controlled by mass flow controllers. In most of the experimental runs the feed composition was a gas mixture of methane and nitrogen (molar ratio of 1:10) with a total gas flow rate of 110 $Ncm^3/min$. During the reaction, the composition of the outgoing gas stream was analyzed with a gas chromatograph equipped with a capillary column (Carboxen 1010 Plot, Supelco) and a thermal conductivity detector.

### 4.2.3 Characterization of catalysts and carbon deposits

The used techniques are similar to that described in Chapter II. The particle size distributions of the alloys and the corresponding catalysts were measured with a laser particle size analyzer. The specific surface areas of the fresh catalysts were calculated by the BET method from the $N_2$ equilibrium adsorption isotherms at 77 K. The alloys, catalysts and carbon deposits were examined with a JEOL JCM-35C scanning electron microscope (SEM) associated with an energy dispersive X-ray analyzer (EDX). A transmission electron microscopy (TEM) study of the carbon deposits was carried out with a Phillips CM12 instrument. X-ray photoelectron spectra (XPS) of the alloys and catalysts were acquired in a VG Scientific Escalab 200A apparatus. Quantitative results were obtained by fitting the experimental peaks to Gaussian–Lorentzian curves, measuring the spectral areas corresponding to each chemical element of interest and applying their empirical sensitivity factors. Powder X-ray diffraction (XRD) measurements were carried out in a PANalytical's X'Pert PRO diffractometer, using $CuK_\alpha$ radiation. The crystallite sizes of metals and carbon in catalysts were calculated by the Scherrer equation.

## 4.3 Results

### 4.3.1 Catalysts characterization

The properties of the Cu50, Ni30 and Ni50 alloys and corresponding catalysts, as well as the Ni30Cu50 (ITT) and Ni50Cu50 (ITT) catalytic systems are shown in Table 4.1.

Table 4.1

Characterization of the Raney-type alloys and catalysts

| Sample | Alloy | | | Catalyst | | |
|---|---|---|---|---|---|---|
| | $\bar{d}$ [μm] | $R^a_{n,alloy}$ | $R^a_{eff,alloy}$ | $\bar{d}$ [μm] | $R^a_{eff,catalyst}$ | $S_{BET}$ [$m^2/g$] |
| Cu50 | 50 | 0.299 | 0.35 ± 0.05 | 46 | 0.95 ± 0.10 | 17 |
| Ni30 | 285 | 0.165 | 0.17 ± 0.02 | 156 | 0.85 ± 0.07 | 64 |
| Ni50 | 36 | 0.315 | 0.39 ± 0.06 | 21 | 0.72 ± 0.07 | 82 |
| Ni30Cu50 (ITT) | / | / | / | 83 | 0.90 ± 0.09 | 36 |
| Ni50Cu50 (ITT) | / | / | / | 53 | 0.84 ± 0.09 | 13 |

$\bar{d}$ : average particle size of the powders;

$R^a_{n,alloy}$ : nominal atomic ratio active metal/total metals;

$R^a_{eff,alloy}$ : determined effective atomic ratio active metal/alloy metals;

$R^a_{eff,catalyst}$ : determined effective atomic ratio active metal/catalyst metals;

$S_{BET}$: specific surface area.

The average particle size ($\bar{d}$) of Cu50 was found to be ~46 μm. The BET surface area of this catalyst is in the range of values reported in literature [50]. The properties of the nickel alloys and catalysts were already discussed in a previous article [6].

The atomic ratios of the alloys determined by EDX, $R^a_{eff,alloy}$ = (active metal/total metal), are in reasonable agreement with the nominal values, $R^a_{n,alloy}$. Upon activation, the atomic ratios in the corresponding catalysts are much larger, as expected. Residual $Al_2O_3$ is present, due to incomplete leaching of Al. The Cu50 catalyst has the highest atomic ratio while Ni50 has the lowest. Additionally, it should be mentioned that copper may not be uniformly distributed in the Ni-Cu ITT systems.

The average particle sizes of the Ni-Cu catalytic systems change after ITT. In the case of Ni30Cu50 (ITT), the average particle size is lower than that of the Ni30 catalyst, and higher than

that of Cu50; however, it is lower than the average particle sizes of the two single catalysts. For the Ni50Cu50 (ITT) catalytic system, the opposite is observed; the average particle size is higher than the average of the two individual Ni50 and Cu50 catalyst phases. This may result from catalyst particle agglomeration.

The BET surface areas of Ni30 (quenched catalyst) and especially Ni50 (conventional catalyst) are significantly reduced when Cu50 is added and the resulting mixture goes through an in situ thermal treatment (ITT). All isotherms show hysteresis loops characteristic of capillary condensation in mesoporous materials. However, the isotherms of Ni30 and Ni50 indicate the presence of smaller pores.

The physicochemical surface properties of the Me-Al alloys, the corresponding monometallic catalysts and bimetallic Ni-Cu (ITT) catalytic systems are collected in Table 4.2.

Table 4.2

Surface characterization of the Raney-type alloys and catalysts

| Sample | Ni $2p^3$ [eV] | Cu $2p^3$ [eV] | $Al/Al_2O_3$ 2p [eV] | $R^a_{Ni}$ | $R^a_{Cu}$ |
|---|---|---|---|---|---|
| Alloy | | | | | |
| Cu50 | / | 932.9 | 74.7 | / | 0.03 |
| Ni30 | 854.0 | / | 75.9 | 0.01 | / |
| Ni50 | 853.5 | / | 76.0 | 0.06 | / |
| | | | | | |
| Catalyst | | | | | |
| Cu50 | / | 931.2 | 73.5 | / | 0.43 |
| Ni30 | 854.0 | / | 73.9 | 0.80 | / |
| Ni50 | 853.5 | / | 74.0 | 0.75 | / |
| Ni30Cu50 (ITT) | 856.5 | 932.0 | 74.2 | 0.10 | 0.13 |
| Ni50Cu50 (ITT) | 856.4 | 932.5 | 74.2 | 0.10 | 0.14 |

$R^a_{Ni}$ : determined atomic ratio nickel on surface/total metals;

$R^a_{Cu}$ : determined atomic ratio copper on surface/total metals.

The XPS spectra obtained for the Cu-Al alloy and the corresponding Cu50 catalyst show that the majority of the alloy particles are covered with an $Al_2O_3$ layer. After activation, copper is found to be mainly present in the zero-valent state. The XPS spectra of the Ni-Cu (ITT) catalytic systems (Figure 4.1), with a mass composition of 50 wt. % of Cu, show that both Ni and Cu are mainly in the oxidation state zero. The presence of $Cu_2O$ was detected, since it may be formed during leaching with NaOH. The amounts of Ni and Cu atoms exposed on the Ni-Cu (ITT) catalytic surfaces are very low. Instead, most of the alumina (~80 %) is exposed. This suggests that alumina segregates to the catalyst surface. Moreover, the atomic ratios of Ni and Cu on the

catalyst surface are similar, indicating that the surface dilution is in agreement with the amounts of Me-Al alloys (Me = Ni, Cu) used.

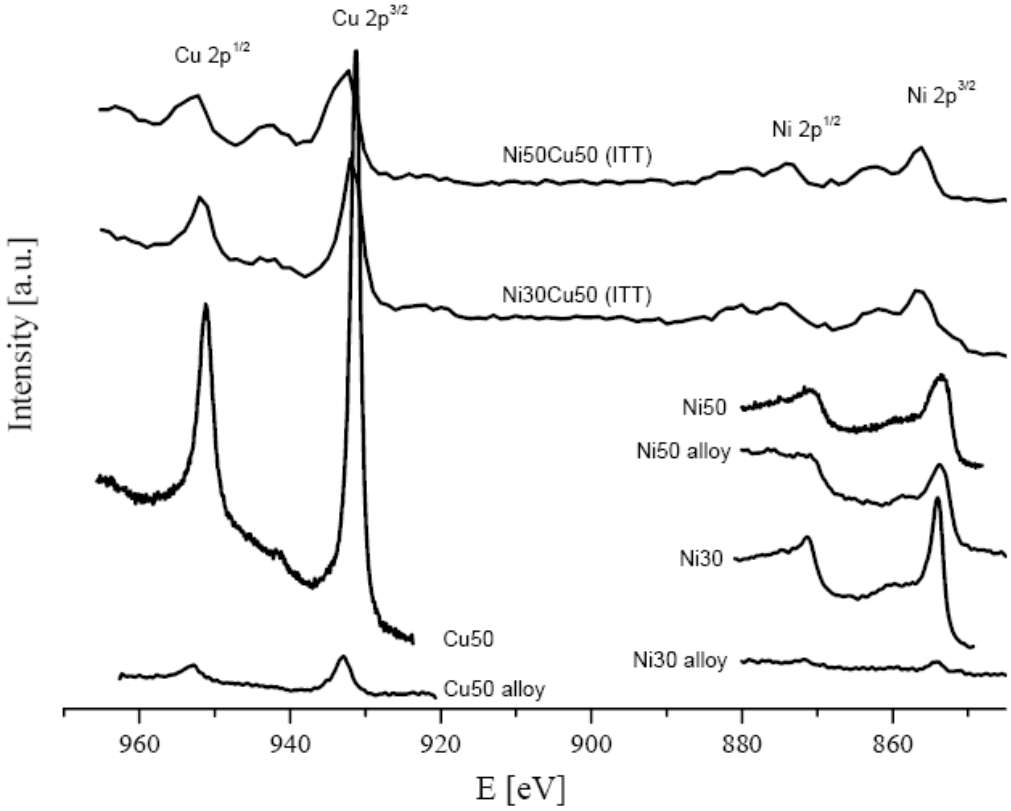



Fig. 4.1 XPS spectra of Ni, Cu and NiCu alloys and catalysts.

X-ray diffraction patterns were obtained for the alloys (results shown in the Appendix). The Cu50 alloy was clearly identified as syn-Khatyrkite ($Al_2Cu$). The Ni30 alloy showed mainly the presence of an $Al_3Ni$ phase. Two phases were found in the Ni50 alloy: $Al_3Ni_2$ and $Al_3Ni$. Some unsolved Al was also detected.

Figure 4.2 shows the X-ray diffraction patterns of the catalysts Cu50, Ni30, Ni50 as well as Ni30Cu50 and Ni50Cu50 at 30 ºC, 600 ºC and after 2 h of thermal treatment at 600 ºC (ITT). The Ni30 and Ni50 catalysts show, at 30 ºC and 600 ºC, the typical Ni reflection planes (111), (200) and (220) with the respective 2θ angles, assigned to metallic face centered cubic (fcc) Ni0. The Cu detected in Cu50 shows similar reflection planes as Ni due to the same crystal lattice structure and approximately the same atomic radius. The presence of cuprite ($Cu_2O$) at 30 ºC was also detected. However, at 30 ºC, the Ni and Cu reflections are broader than at 600 ºC. The patterns of the Ni30Cu50 and Ni50Cu50 catalysts at 30 ºC are a sum of the two separated phases. At 600 ºC, a slight modification of the full-width at half maximum (FWHM) is observed. The Cu reflection planes decrease while those of Ni increase.

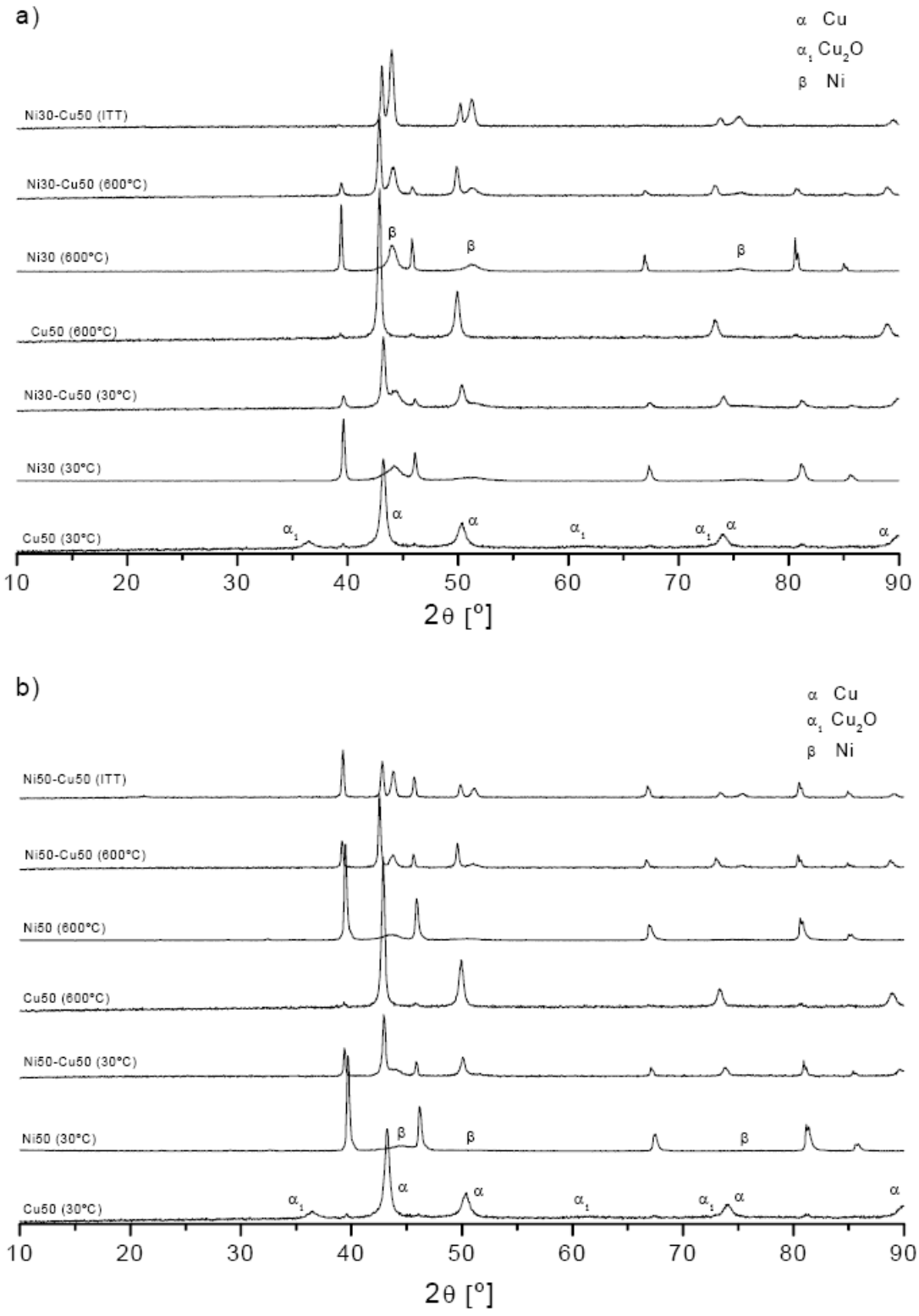



Fig. 4.2 XRD patterns of mono- and bimetallic catalysts measured at 30 ºC, 600 ºC and after 2 h of thermal treatment at 600 ºC: (a) Ni30Cu50, and (b) Ni50Cu50.

This phenomenon is related to the agglomeration of particles. After two hours of thermal treatment at 600 ºC, the intermetallic phase transformation in Ni30Cu50 and Ni50Cu50 catalyst is clearly visible. Both systems show the formation of an intermetallic alloy phase with fcc structure and composition equivalent to $Ni_{0.48}Cu_{0.52}$. Cu is incorporated in the Ni lattice and the incipient formation of this Ni-Cu alloy is confirmed by the observation of sharper Ni diffraction lines at 2θ ~44º and 51º, which increase with temperature and time, and broader Cu diffraction lines at 2θ ~43º and 50º, which decrease instead. Both the Ni and Cu diffraction lines overlap after the ITT process. For a well defined Ni-Cu alloy, the presence of single diffraction lines should be expected. This means that some of the copper is segregated simultaneously with Ni-Cu alloy particles.

Table 4.3

Ni and Cu crystal sizes of the Raney-type alloys and catalysts

| Sample | T [ºC] | $d_{Ni}$ [nm] | $d_{Cu}$ [nm] |
|---|---|---|---|
| Alloy | | | |
| Cu50 | 30 | / | 53.8 |
| Ni30 | 30 | 52.9 | / |
| Ni50 | 30 | 85.2 | / |
| Monometallic Catalyst | | | |
| Cu50 | 30 | / | 17.2 |
| Cu50 | 600 | / | 23.8 |
| Ni30 | 30 | 10.7 | / |
| Ni30 | 600 | 10.1 | / |
| Ni50 | 30 | 13.6 | / |
| Ni50 | 600 | 10.2 | / |
| Bimetallic Catalyst | | | |
| Ni30Cu50 | 30 | 6.7 | 23.9 |
| Ni30Cu50 | 600 | 18.1 | 14.1 |
| Ni30Cu50 (ITT) | 600 | 15.8 | 15.7 |
| Ni50Cu50 | 30 | 13.7 | 17.2 |
| Ni50Cu50 | 600 | 14.5 | 67.4 |
| Ni50Cu50 (ITT) | 600 | 26.3 | 39.2 |

The Ni and Cu crystal sizes of the Raney-type alloys and catalytic systems are shown in Table 4.3. It is observed that the sizes of the Ni crystals are relatively independent of temperature, while the Cu crystal size seems to increase with temperature. At 600 ºC, the Ni and Cu crystal particle sizes of Ni30Cu50 and Ni50Cu50 catalytic systems suffer significant changes, which are especially marked in the case of Ni50Cu50 after two hours treatment (ITT).

### 4.3.2 Catalysts performance

Having in mind the results of the previously tested monometallic Ni30 and Ni50 catalysts [6], it was decided to carry out the isothermal tests for the Cu and Ni-Cu catalytic systems in the temperature range 400-900 ºC. The catalysts were evaluated for 5 hours on stream. The effects of the catalyst composition, volumetric flow-rate (contact time), temperature, feed composition and hydrogen pre-treatment of the catalysts were investigated. The carbon yields obtained in all the experiments are in agreement with the corresponding evolution of the methane conversions.

The effect of catalyst composition (keeping the total metal mass equal to 0.5 g) in Ni-Cu systems, at 600 ºC and with a volumetric flow rate of 110 $Ncm^3$/min, is shown in Figure 4.3. Figure 4.3a shows the behaviour of physical catalyst mixtures of Ni30 and Cu50. The results for the single Cu and Ni phases are also included, together with a sample containing 1.0 g of catalyst mixture. As we can see, copper is not active for methane decomposition. When the Cu content is 20 % (curve 0.4 g Ni + 0.1 g Cu) it may be observed that the methane conversion reaches ~70 % after a few minutes, and then decreases to reach a constant level of ~30 % after 180 min. The conversions are lower when the content of Cu50 increases (curves for 0.25 g Ni + 0.25 g Cu and 0.1 g Ni + 0.4 g Cu), because the amount of the active phase (Ni30) is lower.

The results are quite different with the incipient alloyed catalyst mixtures, Ni30Cu50 (ITT), as shown in Figure 4.3b. The initial conversions are slightly lower (in the range 60-70 %), but catalyst deactivation is not so important. Therefore, the performances after 5 hours are better. The best result was recorded with a mass content of 20 wt. % of Cu50 on 0.5 g of Ni30Cu50 (ITT). The final conversion was approximately 58 %.

It must be realized that some alloying may also occur during reaction at 600 ºC (the catalytic tests lasting 5 hours). This accounts for some stabilization of the catalyst obtained by physical mixture when compared to the monometallic Ni catalysts previously reported [6]. However, the ITT treatment seems to be most effective when performed on the catalyst before reaction, that is, before carbon starts to be formed, as can be observed by comparing Figures 4.3a and 4.3b.

The effect of catalyst composition (keeping the Ni mass equal to 0.5 g) of the Ni30Cu50 (ITT) and Ni50Cu50 (ITT) catalytic systems is shown in Figure 4.4. It is observed (Figure 4.4a) that a mass content of 67 wt. % Cu in 1.5 g of Ni30Cu50 (ITT) shows the best performance (curve +1.0 g Cu). Stable operation without significant deactivation and methane conversions near 70 % are obtained.

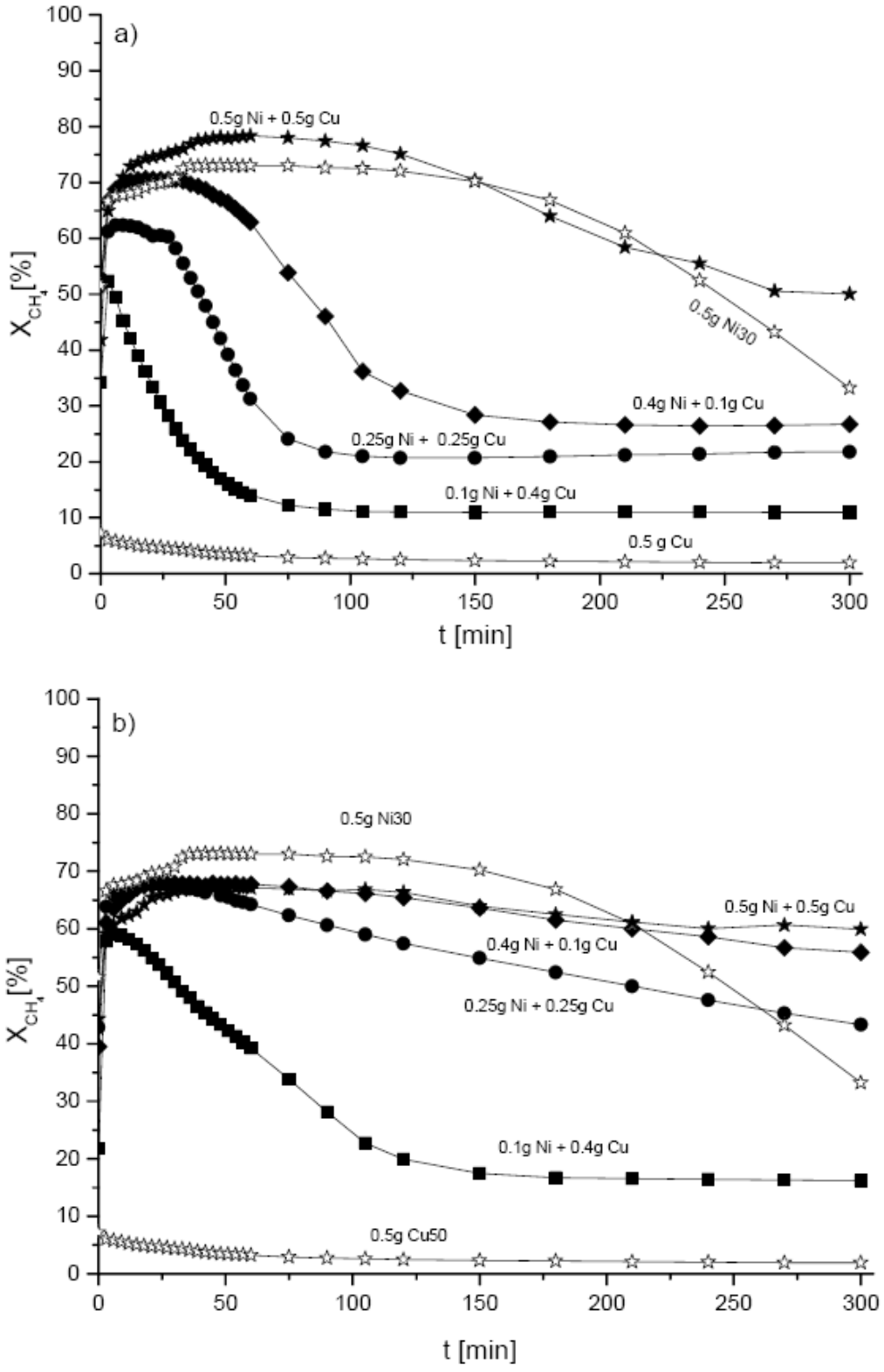



Fig. 4.3 Methane conversion as function of reaction time at 600 ºC and a flow rate of 110 $Ncm^3/min$ ($CH_4/N_2$ = 0.1). Composition effect, keeping the total metal mass equal to 0.5 g on Ni30Cu50: a) physical mixtures; b) ITT catalysts.

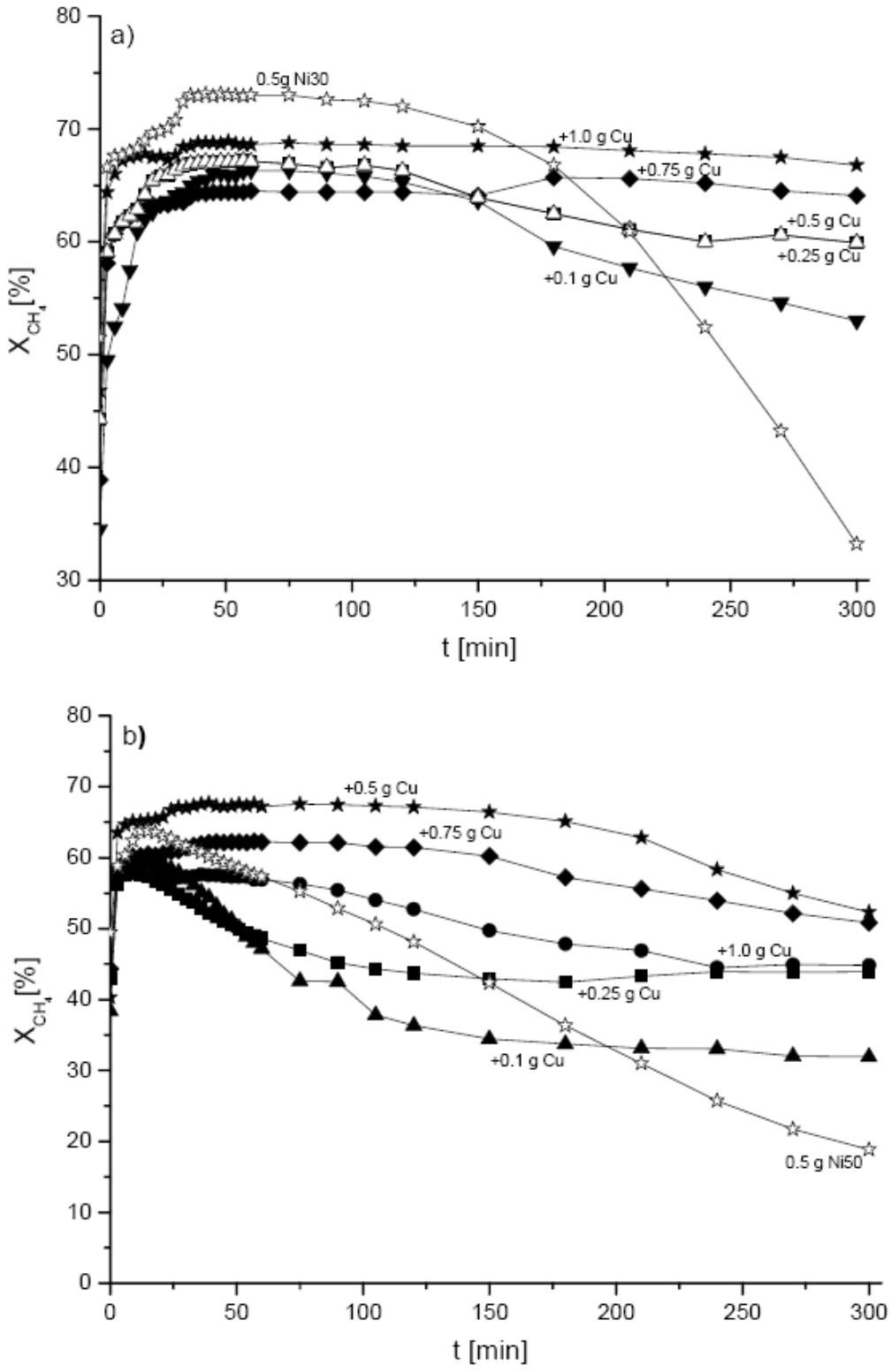



Fig. 4.4 Methane conversion as function of reaction time at 600 ºC and a flow rate of 110 $Ncm^3/min$ ($CH_4/N_2$ = 0.1). Composition effect, keeping the Ni mass equal to 0.5 g, on: a) Ni30Cu50 (ITT) catalysts; b) Ni50Cu50 (ITT) catalysts.

It is worth noting that for the same stable performance 1.0 g of Ni30 was necessary under the same conditions [6]. Below a certain copper content, slight deactivation is observed; this is particularly notorious in the catalytic system with 17 wt. % of Cu in 0.6 g of Ni30Cu50 (ITT) (curve +0.1 g Cu).

The same effect was also studied for different Ni50Cu50 (ITT) catalytic systems (Figure 4.4b). The best results were obtained with 50 wt. % of copper, but in general the Ni50Cu50 (ITT) system performs worse than the Ni30Cu50 (ITT) one. Nevertheless, the performances are better than those obtained with 0.5 g of the monometallic Ni50 [6].

The effect of the volumetric flow rate (contact time) was investigated between 55-220 $Ncm^3/min$, at 600 ºC and with a feed composition of $CH_4/N_2$ = 0.1, using 1.0 g of Ni30Cu50 (ITT), the results being shown in Figure 4.5. Higher contact times (55 $Ncm^3/min$) were found to be beneficial for a stable run, while lower contact times resulted in significant activity losses and irregular operation (220 $Ncm^3/min$). This result is similar to what was observed with monometallic catalysts [6].

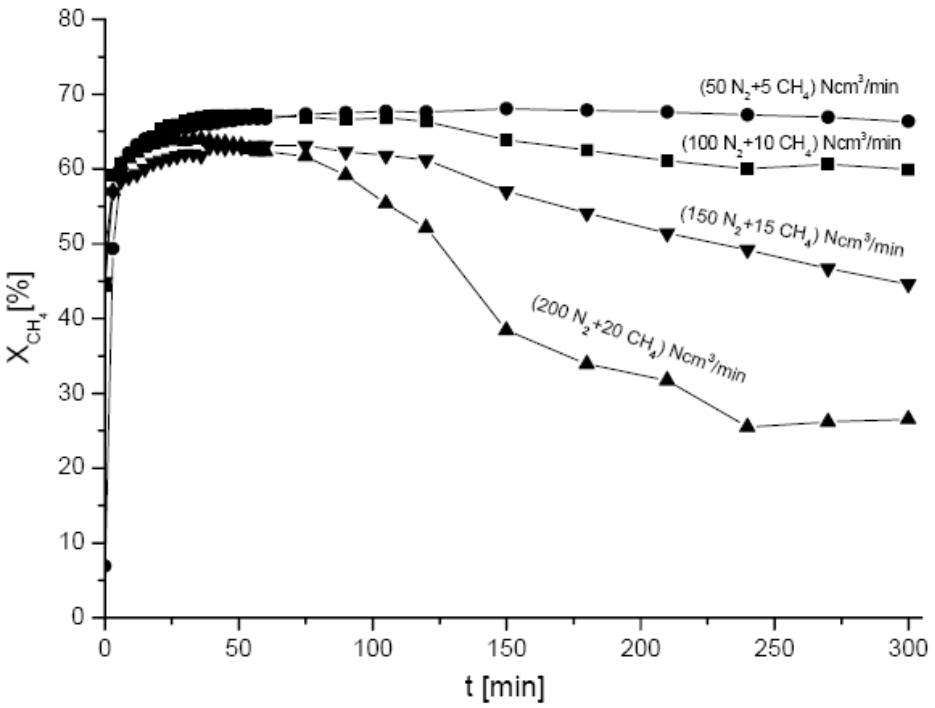



Fig. 4.5 Methane conversion as function of reaction time with Ni30Cu50 (ITT) catalyst. Volumetric flow rate effect ($CH_4/N_2$ = 0.1) with 1.0 g of catalyst at 600 ºC.

The effect of the reaction temperature was studied between 400-900 ºC using 1.0 g of Ni30Cu50 (ITT). As shown in Figure 4.6, stable operation is observed below 700 ºC. At 700 ºC and above, the deactivation process is significant. At 700 ºC, the catalyst runs more or less stable at ~90 % for one hour. Afterwards, slow deactivation occurs until 2.5 h of reaction time, followed by an important deactivation that leads to a steady-state value of ~40 %. It may be recalled that for stable operation at 700 ºC, 2.5 g of Ni30 were required [6].

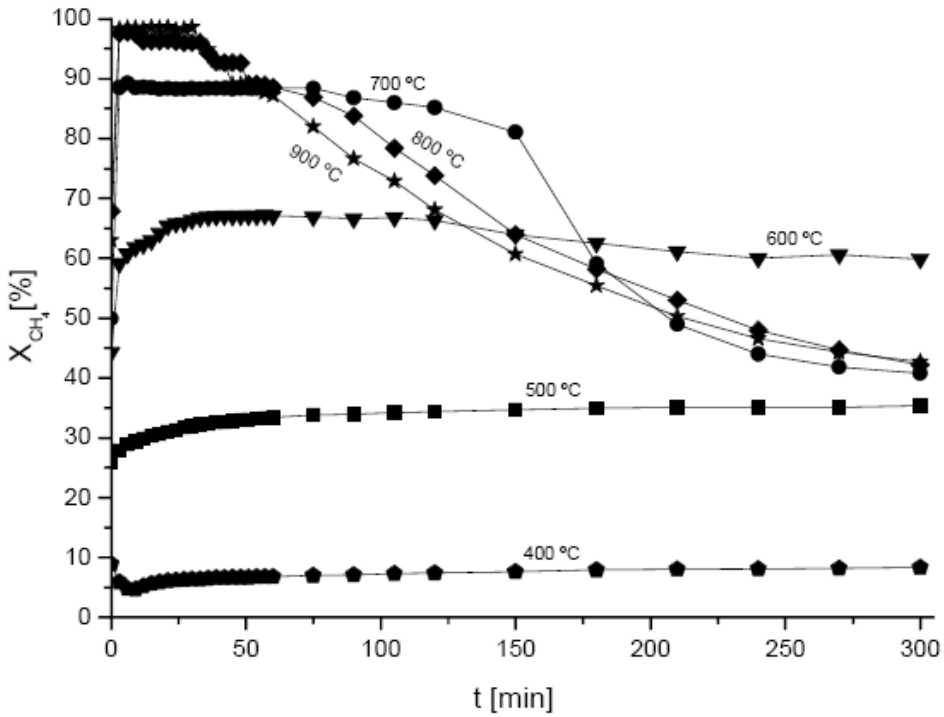



Fig. 4.6 Methane conversion as function of reaction time with Ni30Cu50 (ITT) catalyst. Temperature effect with 1.0 g of catalyst and a flow rate of 110 $Ncm^3/min$ ($CH_4/N_2$ = 0.1).

The effect of the feed methane concentration using 1.0 g of Ni30Cu50 (ITT) is shown in Figure 4.7. The best results are obtained for a low methane/nitrogen ratio of 0.023. It can be observed that for this feed composition the methane conversion is more or less stable at around 85 %. The compositions in the range $CH_4/N_2$ = 0.023-0.222 show moderate deactivation, and lower conversions, as expected for a reversible reaction. The stability observed for high methane concentrations ($CH_4/N_2 \geq 0.571$) may be ascribed to the high amounts of hydrogen produced, which are probably sufficient to avoid the formation of encapsulating carbon. The conversions measured are significantly higher than those reported previously for the Ni50 catalyst [6], and suggest a good promotion effect of copper.

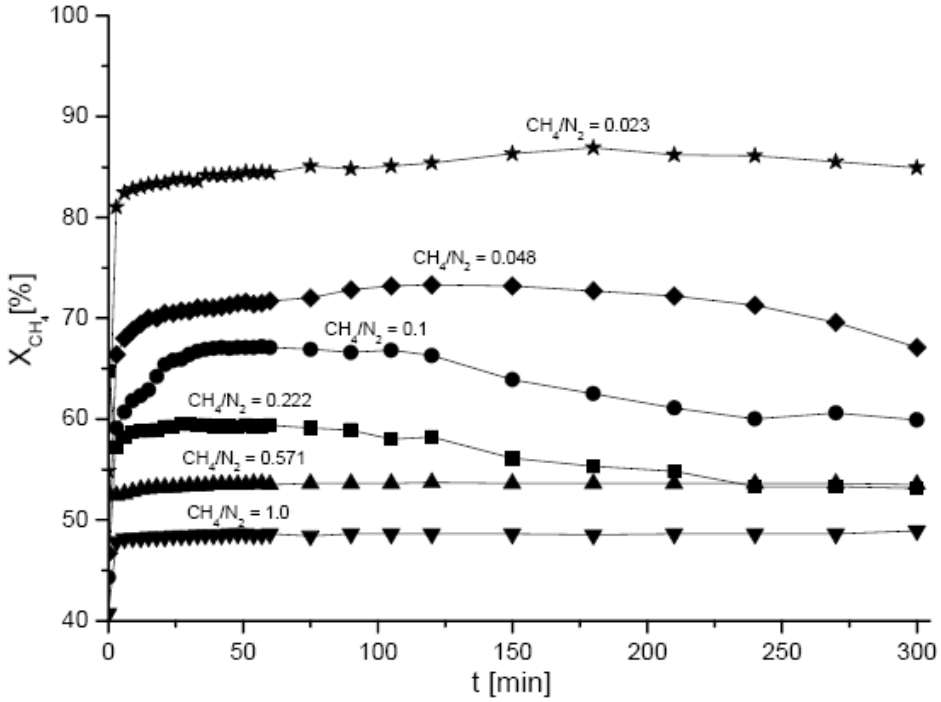



Fig. 4.7 Methane conversion as function of reaction time with Ni30Cu50 (ITT) catalyst. Feed composition effect with 1.0 g of catalyst at 600 ºC and a flow rate of 110 $Ncm^3$/min.

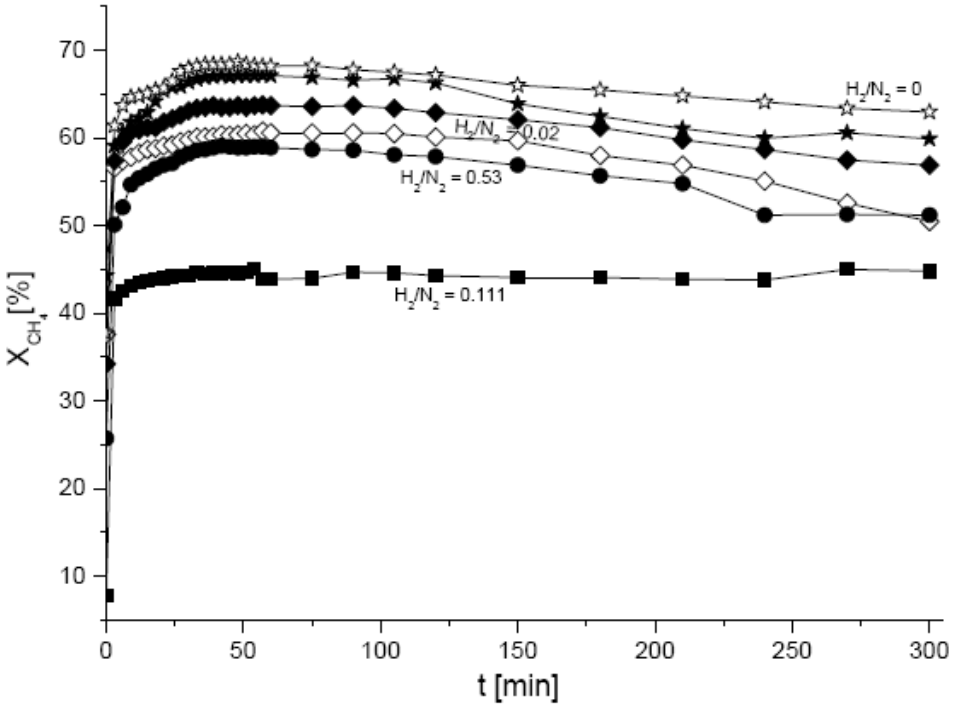



Fig. 4.8 Methane conversion as function of reaction time with Ni30Cu50 (ITT) catalyst: effect of hydrogen with 1.0 g of catalyst at 600 ºC and flow rate of 110 $Ncm^3$/min of $CH_4/(H_2+N_2)$ = 0.1 (filled symbols), or HPT (open symbols).

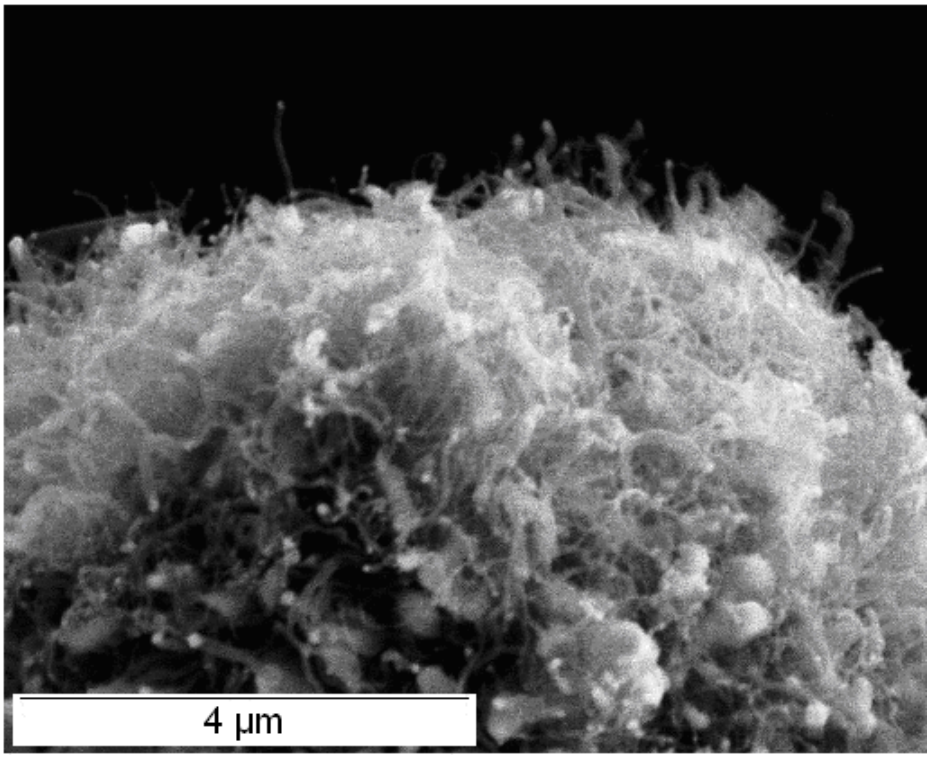
Introduction of hydrogen in the feed (Figure 4.8) reduces methane conversion, because it decreases the net rate; nevertheless, this seems to be beneficial for a stable run, similarly to the case of monometallic Raney catalysts, as previously discussed [6].

### 4.3.3 Characterization of the carbon deposits

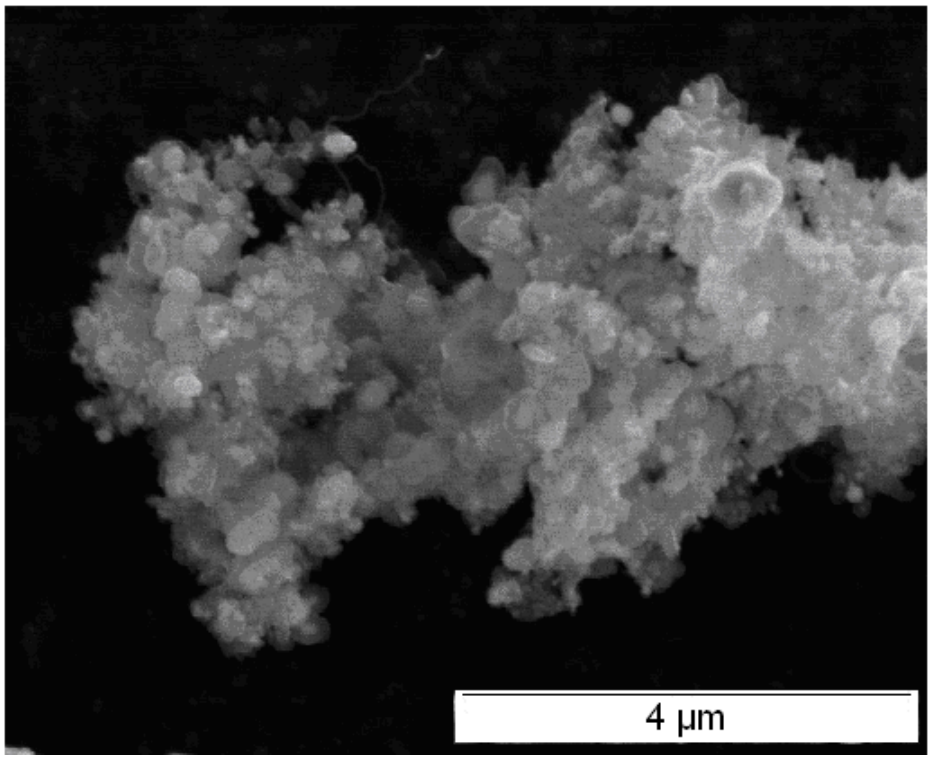
Figure 4.9 shows the morphology of the carbon deposited on Ni30Cu50 (ITT) catalysts at 600 ºC (a), and 700 ºC (b). The carbon deposits differ in their structure as a consequence of the different active phases. There are no carbon filaments on the deposits obtained on the Cu50 catalyst, as previously reported [53]. The SEM micrographs of the Ni30Cu50 (ITT), and also Ni50Cu50 (ITT), clearly show very long carbon nanofibers (CNF) after CMD at 600 ºC. The diameters of the CNF and metal particles (seen as bright spots) on the top of the formed fibers are in the range of 10-100 nm. The Ni30Cu50 (ITT) catalyst, after reaction at 700 ºC, shows the presence of carbon layers which encapsulate the catalyst particles.

For a more detailed characterization of the formed CNF at 600 ºC on Ni30Cu50 (ITT) catalysts, a TEM picture is presented in Figure 4.10, showing filaments with narrow hollow cores. In some cases, fishbone CNF have been detected. Also the fiber cores are not totally straight; some irregularities can be found, indicating the possibility of particle motion (rotation, vibration and translation) during carbon precipitation, thus forming angles <90º with the fiber axis. TEM micrographs of carbon deposits after reaction at 700 ºC (not included here) show the presence of large amounts of encapsulating carbon (graphitic carbon layers around the metal particles).

Table 4.4 collects the crystal sizes of carbon as well as those of Ni and Cu in the deposits after reaction. The carbon crystal sizes are between 8 and 24 nm. The carbon deposits obtained on the monometallic Ni catalysts show the smallest crystal sizes. The carbons obtained on the bimetallic Ni-Cu catalysts exhibit approximately twice as large crystal size when produced at 600 ºC, whereas the carbon crystal sizes of the monometallic Ni catalysts are similar to that produced on bimetallic Ni-Cu catalyst at 700 ºC. The interlayer distance between basal planes of ideal graphite is 0.3354 nm, which can be compared with those of the produced carbons (Table 4.4). Carbon produced on monometallic Ni and bimetallic Ni-Cu catalysts at 700 ºC deviate more from ideal graphite than the carbon produced with bimetallic Ni-Cu catalysts at 600 ºC. From these observations, we can conclude that the presence of Cu in the incipient alloyed Ni-Cu Raney-type catalysts is beneficial for the formation of more ordered graphitic carbon at 600 ºC.




a)




b)

Fig. 4.9 SEM micrographs of carbon deposits obtained on Ni30Cu50 (ITT) at 600 ºC (a) and 700 ºC (b).

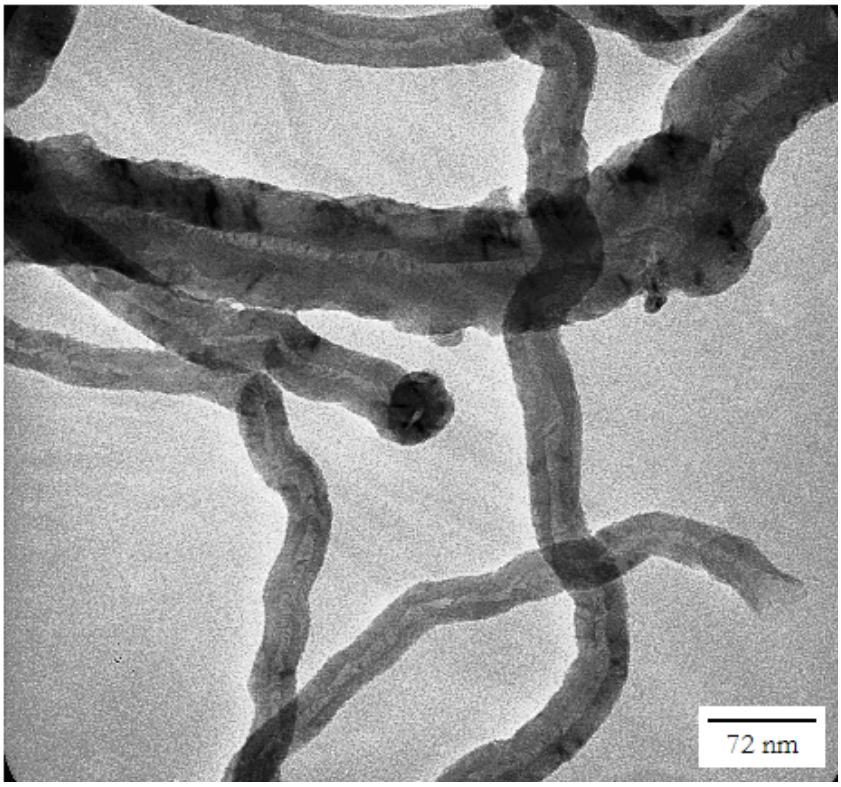



Fig. 4.10 TEM micrograph of the carbon deposit obtained on Ni30Cu50 (ITT) at 600 ºC.

Table 4.4

C, Ni and Cu crystal sizes of carbon and metals in the deposits after reaction

| Catalyst | $T^{reaction}$ [ºC] | $d_{Ni}$ [nm] | $d_{Cu}$ [nm] | $d_{Carbon}$ [nm] | $D_{(002)}$ [nm] |
|---|---|---|---|---|---|
| Cu50 | 600 | / | 48.8 | / | / |
| Ni30 | 600 | 22.2 | / | 7.5 | 0.339 |
| Ni50 | 600 | 18.2 | / | 8.8 | 0.339 |
| Ni30Cu50 (ITT) | 600 | 38.9 | 53.1 | 23.7 | 0.337 |
| Ni30Cu50 (ITT) | 700 | 20.4 | 32.5 | 9.3 | 0.339 |
| Ni50Cu50 (ITT) | 600 | 17.6 | 15.3 | 17.1 | 0.338 |

$D_{(002)}$ : interplanar distance of carbon.

For comparison purposes, diffraction patterns of the previously used Raney-Ni catalysts (Ni30 and Ni50) and catalysts used in this work with corresponding carbon deposits are shown in Figure 4.11.

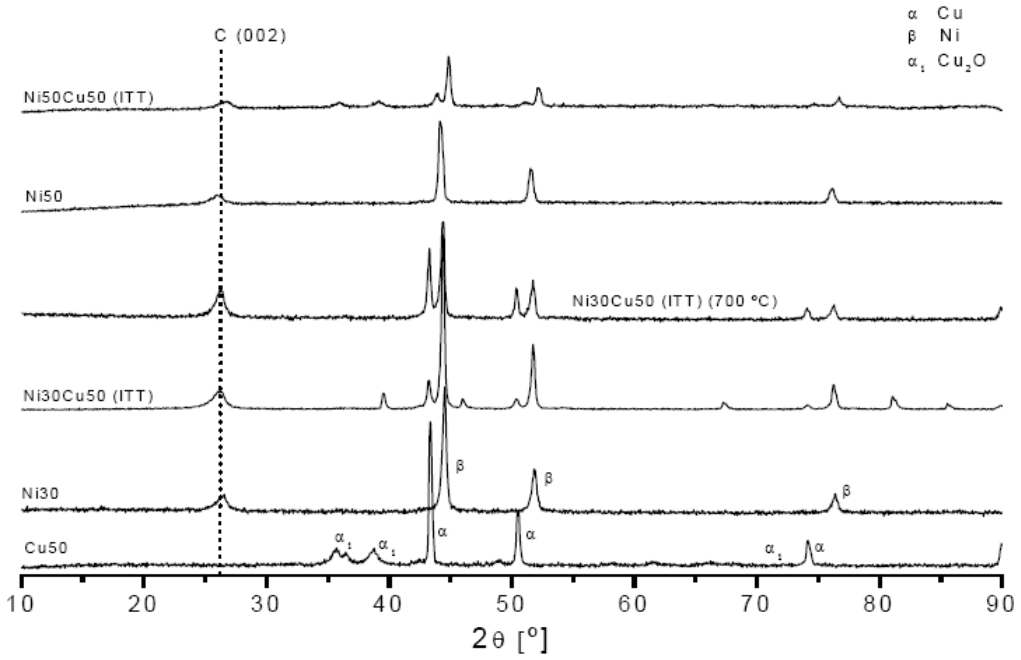



Fig. 4.11 XRD patterns of carbon deposits obtained on Ni and Ni-Cu (ITT) catalysts at 600 ºC and 700 ºC.

## 4.4 Discussion

The mechanism of hydrocarbons decomposition into hydrogen and filamentous carbon on metals, proposed in 1972 and largely documented in the literature [7,8,54], may be recalled here. The dissociative adsorption of hydrocarbons on metals such as Ni, Co or Fe, and the dissolution and subsequent diffusion of adsorbed carbon atoms through the metal, leads to carbon precipitation at the rear of the metal particles forming filamentous carbon. Catalyst deactivation is originated by the formation of encapsulating carbon species on the metal surface, thus blocking the access of methane to the active sites. Copper shows only a low activity for methane decomposition, but it cannot dissolve carbon or form filaments; therefore, encapsulating carbon is formed exclusively.

The formation of encapsulating carbon on nickel can be prevented by "ensemble control". This consists in diluting the active metal phase with an inactive one, for instance, by introduction of copper, eventually forming Ni-Cu alloys. This will separate the active Ni sites from each other, so that the adsorbed carbon-containing species will have more difficulty to react with each other on the surface. Therefore, lower amounts of encapsulating carbon will be formed and the stability of the catalyst is improved.

Table 4.5

Selected results for the catalytic decomposition of methane on Ni and Ni-Cu catalysts

| Catalyst [Reference] | $m_{cat}$ [g] | T [°C] | $\dot{V}_{total}$ [$\frac{Ncm^3}{min}$] | $\dot{n}_{CH_4}$ [$\frac{mmol}{min}$] | $X_{CH_4}^{eq}$ [%] | $X_{CH_4}^{max}$ [%] | $X_{CH_4}^{t}$ [%] | t [h] |
|---|---|---|---|---|---|---|---|---|
| Ni-Cu-MgO [27] | 0.3 | 700 | 20 | 0.893 | 80.8 | 67 | 67 | 8 |
| Ni-Cu-MgO [28] | 0.3 | 700 | 20 | 0.893 | 80.8 | 71 | 67 | 8 |
| Ni-Cu-$Al_2O_3$ [29] | 0.3 | 700 | 20 | 0.893 | 80.8 | 75 | 75 | 8 |
| Ni-Cu-$SiO_2$ [30] | 0.3 | 700 | 20 | 0.893 | 80.8 | 71 | 65 | 8 |
| Ni-Cu-$Al_2O_3$ [31] | 0.3 | 700 | 20 | 0.893 | 80.8 | 65 | 65 | 8 |
| Ni-Cu-$Nb_2O_5$ [36] | 0.05 | 600 | 20 | 0.893 | 59.3 | 43 | 3 | 80 |
| Ni-Cu-MgO [39] | 0.05 | 665 | 60 | 2.68 | 74.6 | 54 | 0 | 11 |
| | 0.05 | 750 | 60 | | 87.4 | 31 | 0 | 45 |
| Ni-Cu-$Al_2O_3$ [14] | 0.1 | 600 | 68 | 3.04 | 59.3 | 22 | 0 | 100 |
| | 0.1 | 750 | 68 | 1.12 | 92.7 | 70 | 0 | 17 |
| Ni30 [6] | 0.5 | 600 | 110 | 0.446 | 88.0 | 73 | 33 | 5 |
| Ni30Cu50 (ITT) | *1.0 | 700 | 110 | 0.446 | 95.9 | 89 | 41 | 5 |
| Ni30Cu50 (ITT) | *1.0 | 600 | 110 | 0.112 | 96.2 | 87 | 85 | 5 |
| Ni30Cu50 (ITT) | *1.0 | 600 | 110 | 0.223 | 93.1 | 73 | 67 | 5 |
| Ni30Cu50 (ITT) | *1.0 | 600 | 110 | 0.446 | 88.0 | 67 | 60 | 5 |
| Ni30Cu50 (ITT) | *1.0 | 600 | 110 | 0.893 | 80.9 | 60 | 54 | 5 |
| Ni30Cu50 (ITT) | *1.0 | 600 | 110 | 1.79 | 72.3 | 54 | 54 | 5 |
| Ni30Cu50 (ITT) | *1.0 | 600 | 110 | 2.46 | 68.1 | 49 | 49 | 5 |
| Ni30Cu50 (ITT) | **0.5 | 600 | 110 | 0.446 | 88.0 | 68 | 56 | 5 |
| Ni50 [6] | 0.5 | 600 | 110 | 0.446 | 88.0 | 64 | 19 | 5 |
| Ni50Cu50 (ITT) | *1.0 | 600 | 110 | 0.446 | 88.0 | 68 | 52 | 5 |

*(50wt% Cu); **(20wt% Cu).

$\dot{V}_{total}$ : total volumetric flow rate;

$\dot{n}_{CH_4}$ : molar flow rate of methane;

$X_{CH_4}^{eq}$ : equilibrium methane conversion;

$X_{CH_4}^{max}$ : maximum methane conversion during reaction;

$X_{CH_4}^{t}$ : methane conversion at time t.

We can now compare the results obtained in the present study with selected data previously reported for CMD on Ni-Cu catalysts [14,27-31,36,39], which are included in Table 4.5. The experimental conditions are listed, together with the equilibrium methane conversion, the maximum conversion reported, and the final conversion measured after several hours on stream. Catalyst activity can be assessed by comparing the maximum conversion, $X_{CH_4}^{\max}$, with the equilibrium conversion, $X_{CH_4}^{eq}$, while catalyst stability is assessed by comparing $X_{CH_4}^{\max}$ with the final conversion, $X_{CH_4}^{t}$ and with the previously tested Raney-Ni catalysts [1]. It has already been noted that high loaded or unsupported catalysts show the best performances [1]. Even better performances, in terms of activity and stability, are those of copper containing catalysts, such as NiCuAl [29,31] and NiCuMg [27,28]. The Ni-Cu incipient alloyed skeletal catalysts reported in the present study are also quite good, showing stable operation at relatively low temperatures.

## 4.5 Conclusions

It has been found that addition of copper significantly improves the stability of Raney-Ni catalysts for methane decomposition. This has been explained in terms of an ensemble effect, which decreases the rate of formation of encapsulating carbon. In particular, excellent results were obtained when the Ni-Cu Raney-type system was thermally treated in situ at 600 ºC, as a result of incipient alloy formation.

## References


[1] N.Z. Muradov, T.N. Veziroglu, *Int. J. Hydrogen Energy* **30** (2005) 225.

[2] N. Muradov, *Int. J. Hydrogen Energy* **26** (2001) 1165.

[3] I. Suelves, M.J. Lázaro, R. Moliner, B.M. Corbella, J.M. Palacios, *Int. J. Hydrogen Energy* **30** (2005) 1555.

[4] A. M. Dunker, S. Kumar, P. A. Mulawa, *Int. J. Hydrogen Energy* **31** (2006) 473.

[5] J.L. Pinilla, R. Moliner, I. Suelves, M.J. Lázaro, Y. Echegoyen, J.M. Palacios, *Int. J. Hydrogen Energy* **32** (2007) 4821.

[6] A.F. Cunha, J.J.M. Órfão, J.L. Figueiredo, *Appl. Catal. A: Gen.* **348** (2008) 103.

[7] J.L. Figueiredo, in: J.L. Figueiredo (Ed.), Progress in Catalyst Deactivation, Martinus-Nijhoff, The Hague, 1982, pp. 45.

[8] R.T.K. Baker, M.A. Barber, P.S. Harris, F.S. Feates, R.J. Waite, *J. Catal.* **26** (1972) 51.

[9] S. Takenaka, Y. Shigeta, E. Tanabe, K. Otsuka, *J. Catal.* **220** (2003) 468.

[10] S. Takenaka, Y. Shigeta, E. Tanabe, K. Otsuka, *J. Phys. Chem. B* **108** (2004) 7656.

[11] S.H.S. Zein, A.R. Mohamed, *Energy & Fuels* **18** (2004) 1336.

[12] N. Shah, D. Panjala, G.P. Huffman, *Energy & Fuels* **15** (2001) 1528.

[13] K. Otsuka, S. Takenaka, H. Ohtsuki, *Appl. Catal. A: Gen.* **273** (2004) 113.

[14] Y. Li, J. Chen, Y. Qin, L. Chang, *Energy & Fuels* **14** (2000) 1188.

[15] J.R. Rostrup-Nielsen, *J. Catal.* **85** (1984) 31.

[16] N.T. Andersen, F. Topsøe, I. Alstrup, J.R. Rostrup-Nielsen, *J. Catal.* **104** (1987) 454.

[17] Y. Nishiyama, Y. Tamai, *J. Catal.* **33** (1974) 98.

[18] V. Ponec, *Adv. Catal.* **32** (1983) 149.

[19] C.A. Bernardo, I. Alstrup, J.R. Rostrup-Nielson, *J. Catal.* **96** (1985) 517.

[20] G.A. Martin, *Catal. Rev.-Sci. Eng.* **30** (1988) 519.

[21] I. Alstrup, *J. Catal.* **109** (1988) 241.

[22] M.S. Kim, N.M. Rodriguez, R.T.K. Baker, *J. Catal.* **131** (1991) 60.

[23] N.M. Rodriguez, M.S. Kim, R.T.K. Baker, *J. Catal.* **140** (1993) 16.

[24] M.S. Kim, N.M. Rodriguez, R.T.K. Baker, *J. Catal.* **134** (1992) 253.

[25] T.V. Reshetenko, L.B. Avdeeva, Z.R. Ismagilov, A.L. Chuvilin, V.A. Ushakov, *Appl. Catal. A: Gen.* **247** (2003) 51.

[26] L. Dussault, J.C. Dupin, C. Guimon, M. Monthioux, N. Latorre, T. Ubieto, E. Romeo, C. Royo, A. Monzón, *J. Catal.* **251** (2007) 223.

[27] Y. Echegoyen, I. Suelves, M.J. Lázaro, M.L. Sanjuán, R. Moliner, *Appl. Catal. A: Gen.* **333** (2007) 229.

[28] Y. Echegoyen, I. Suelves, M.J. Lázaro, R. Moliner, J.M. Palácios, *J. Power Sources* **169** (2007) 150.

[29] M.J. Lázaro, Y. Echegoyen, I. Suelves, J.M. Palácios, R. Moliner, *Appl. Catal. A: Gen.* **329** (2007) 22.

[30] I. Suelves, M.J. Lázaro, R. Moliner, Y. Echegoyen, J.M. Palácios, *Catal. Today* **116** (2006) 271.

[31] R. Moliner, Y. Echegoyen, I. Suelves, M.J. Lázaro, J.M. Palacios, *Int. J. Hydrogen Energy* **33** (2008) 1719.

[32] A. Monzón, N. Latorre, T. Ubieto, C. Royo, E. Romeo, J.I. Villacampa, L. Dussault, J.C. Dupin, C. Guimon, M. Montioux, *Catal. Today* **116** (2006) 264.

[33] L. Dussault, J.C. Dupin, N. Latorre, T. Ubieto, L. Noé, M. Monthioux, E. Romeo, C. Royo, A. Monzón, C. Guimon, *J. Phys. & Chem. Solids* **67** (2006) 1162.

[34] A.R. Naghash, Z. Xu, T.H. Etsell, *Chem. Mater.* **17** (2005) 815.

[35] J. Chen, Y. Li, Z. Li, X. Zhang, *Appl. Catal. A: Gen.* **269** (2004) 179.

[36] J. Li, G. Lu, K. Li, W. Wang, *J. Molec. Catal. A: Chem.* **221** (2004) 105.

[37] Q. Weizhong, L. Tang, W. Zhanwen, W. Fei, L. Zhifei, L. Guohua, L. Yongdan, *Appl. Catal. A: Gen.* **260** (2004) 223.

[38] W. Qian, T. Liu, F. Wei, Z. Wang, Y. Li, *Appl. Catal. A: Gen.* **258** (2004) 121.

[39] H. Wang, R.T.K. Baker, *J. Phys. Chem. B.* **108** (2004) 20273.

[40] V.B. Fenelonov, A.Y. Derevyankin, L.G. Okkel, L.B. Avdeeva, V.I. Zaikovskii, E.M. Moroz, A.N. Salanov, N.A. Rudina, V.A. Likholobov, S.K. Shaikhutdinov, *Carbon* **35** (1997) 1129.

[41] S.K. Shaikhutdinov, L.B. Avdeeva, O.V. Goncharova, D.I. Kochubey, B.N. Novgorodov, L.M. Plyasova, *Appl. Catal. A: Gen.* **126** (1995) 125.

[42] L.B. Avdeeva, O.V. Goncharova, D.I. Kochubey, V.I. Zaikovskii, L.M. Plyasova, B.N. Novgorodov, S.K. Shaikhutdinov, *Appl. Catal. A: Gen.* **141** (1996) 117.

[43] S.K. Shaikhutdinov, V.I. Zaikovskii, L.B. Avdeeva, *Appl. Catal. A: Gen.* **148** (1996) 123.

[44] J.L. Pinilla, I. Suelves, M.J. Lázaro, R. Moliner, J.M. Palacios, *Int. J. Hydrogen Energy* **33** (2008) 2515.

[45] M.J. Lázaro, Y. Echegoyen, C. Alegre, I. Suelves, R. Moliner, J.M. Palácios, *Int. J. Hydrogen Energy* **33** (2008) 3320.

[46] M. Raney, U.S. Patent 1,628,190 (1927).

[47] U. Birkenstock, J. Scharschmidt, P. Kunert, H. Meinhardt, P. Hausel, P. Maier, U.S. Patent 5,090,997 (1992).

[48] U. Birkenstock, R. Holm, B. Reinfandt, S. Storp, *J. Catal.* **93** (1985) 55.

[49] J. Rothe, J. Hormes, C. Schild, B. Pennemann, *J. Catal.* **191** (2000) 294.

[50] E.H. Schreiber, M.D. Rhodes, G.W. Roberts, *Appl. Catal. B: Environ.* **23** (1999) 9.

[51] D.J. Young, M.S. Wainwright, R.B. Anderson, *J. Catal.* **64** (1980) 116.

[52] S.R. Montogomery, Functional Group Activity of Promoted Raney Nickel Catalysts, Catalysis of Organic Reactions, Vol. 5, Dekker, New York 1981, 382.

[53] P. Ammendola, L. Lisi, G. Ruoppolv, G. Russo, *J. Mol. Catal. A: Chem.* **266** (2007) 31.

[54] L.S. Lobo, D.L. Trimm, J.L. Figueiredo, in: J.W. Hightower (Ed.), Proceedings of the 5$^{th}$ Int. Congress on Catalysis 1972, North-Holland, Amsterdam, 1973, Vol. 2, pp. 1125.

# *Part B*

## Methane Decomposition on Fe-Cu Raney-type catalysts

## Abstract

The decomposition of methane into hydrogen and carbon was studied on Fe-Cu catalysts of Raney-type. The activity of the catalysts was assessed by comparing the experimental conversions with the calculated equilibrium conversions for each set of experimental conditions. The stability of the catalysts was assessed by comparing the maximum conversions with the conversions at the end of 5 hour tests. The carbon deposits obtained consist mostly of carbon nanofibers. Good results were obtained when the Fe-Cu Raney-type systems were thermally treated in situ at 600 ºC, as a result of incipient alloy formation. These catalysts showed higher stability than the monometallic Raney-Fe catalysts.

## 4.6 Introduction

Hydrogen production via catalytic methane decomposition (CMD), $CH_4 \rightleftharpoons C + 2H_2$ is an interesting alternative to conventional processes, such as steam-reforming and partial oxidation, which result in high $CO_2$ emissions [1-4].

Although the reaction can be catalyzed by carbon materials [5,6], the most effective catalysts are high-loaded or unsupported Ni, Co or Fe catalysts [4,7-10]. High methane conversions have been reported with these systems in the temperature range from 500 to 800 ºC. Hydrogen is produced together with filamentous carbon (carbon nanofibers and/or carbon nanotubes), thus ensuring that the catalyst is not deactivated by carbon deposition on the active metal surface (encapsulating carbon) [11]. Nickel has been most extensively studied, since it leads to the best performances; however, iron based catalysts would provide for a cheaper alternative, if some operational problems could be solved, such as the need for higher temperatures and larger amounts of the active phase, which are required for stable operation [12]. These problems can be solved in part by the use of suitable promoters.

Muradov studied CMD over iron oxide, appreciable catalytic activity being found at temperatures above 600 ºC after some induction period [13]. In a later work [14], the activity of alumina-supported $Fe_2O_3$ (10 wt. %) catalyst was investigated over a wider temperature range (up to 900 ºC). Hydrogen production at 850 °C could be broken down into several steps: an induction period corresponding to the reduction of iron oxide, then the Fe-catalyzed decomposition of methane followed by a deactivation period leading to a low residual activity. This behavior is typical of supported (low metal loaded) catalysts. Much better results have been obtained with high loaded metal catalysts in the presence of textural promoters such as alumina. For instance, Avdeeva et al. reported high carbon capacities during CMD for catalysts with 90 wt. % Ni, 60–75 wt. % Co, and 50–80 wt. % Fe [15].

The nature of the textural promoter on iron catalysts was found to affect both the carbon yields as well as the structure and morphology of the carbon filaments produced [16]. In addition, a sharp acceleration of the reaction was observed above 680 ºC. This temperature corresponds to the point of transition of $Fe_3C$ from a stable to a metastable state. Takenaka et al. studied CMD over $Fe_2O_3/Al_2O_3$ and $Fe_2O_3/SiO_2$ at 800 ºC [17]. They observed that the rates of hydrogen production were higher on the unsupported or higher loaded catalysts. In addition, $Fe_2O_3$ was found to be reduced stepwise with methane during the reaction ($Fe_2O_3 \rightarrow Fe_3O_4 \rightarrow FeO \rightarrow \alpha$-Fe and $Fe_3C$), $Fe_3C$ and α-Fe being identified as the catalytically active species. These results seem to

support the mechanism proposed by Ermakova et al. [16], whereby $Fe_3C$ decomposes into Fe and filamentous carbon.

It has been reported that Fe-Me (Me = Mg, Mo, Pd, Co, Ni) bimetallic systems can improve methane conversion. Shah et al. reported that alumina supported bimetallic Fe-Mo and Fe-Pd catalysts showed better activity than monometallic iron at 700-800 ºC [18-20]. Ogihara et al. also tested Fe-Pd, among other Pd-based alloys catalysts [21]. Reshetenko et al. [15,22,23] investigated CMD on high metal loaded $Fe/Al_2O_3$, $Fe\text{-}Co/Al_2O_3$ and $Fe\text{-}Ni/Al_2O_3$ catalysts in the temperature range 600-650 ºC. The introduction of small amounts of Co or Ni into $Fe/Al_2O_3$ was found to increase the production of carbon nanotubes, the highest carbon capacity being obtained with a composition of 50-65 % Fe, 5-10 % Co (or Ni) and 25-45 % of $Al_2O_3$. The higher efficiency of the bimetallic Fe catalysts was explained in terms of crystal structure and size distribution of the alloy particles. Moreover, the results suggested that during CMD the catalyst particle consists of a carbon solution in the metal, which forms $Fe_3C$ and $Fe_xC_y$ upon cooling.

It is known that the introduction of Cu into high Ni loaded catalysts with $Al_2O_3$, $SiO_2$, $TiO_2$ and MgO as textural promoters increases their catalytic performance for CMD [7-10]. The effect of Cu may be explained by the formation of small ensembles of surface Ni atoms (geometric effect), thus minimizing the interactions of adsorbed carbon species which might lead to the formation of encapsulating carbon [24-26]. Although copper and iron exhibit only limited miscibility (in contrast to copper and nickel, which can form alloys over the whole composition range), Krishnankutty et al. reported a large increase in the amount of filamentous carbon produced from ethylene on an unsupported iron catalyst doped with 2 wt. % Cu at 600 ºC [27,28]. This result was interpreted in terms of an electronic effect, the presence of Cu facilitating the dissociative chemisorption of ethylene.

We have previously reported on the performance of monometallic Ni, Co and Fe Raney-type catalysts for CMD [4]. Raney-Ni was the best of these catalysts. Raney-Fe, after an initial activation period (similar to the induction period reported by Muradov [14]), reached high methane conversions, but its stability was poor, unless large amounts of catalyst were used. In a subsequent study, we showed that alloying with copper significantly improved the stability of the Raney-Ni catalyst [29]. Based on these findings, we set about to study also the effect of copper addition to the Raney-type iron catalysts.

Several methods of catalyst preparation have been reported in the literature, but the incipient alloying of Raney-type catalysts based on Fe and Cu, used in the present work, was not yet published. The physical mixtures of Fe-Cu Raney-type catalysts were prepared by an in situ thermal treatment (ITT). The effect of Raney-Cu on Raney-Fe as incipient alloyed system with

different catalyst mass compositions was studied and compared with the monometallic Raney-Fe catalysts used in our previous work [4]. The carbon deposits formed contained carbon nanofibers (CNF) as well as encapsulating carbon.

## 4.7 Experimental

### 4.7.1 Catalysts preparation

The skeletal (Raney-type) catalysts used in this work were prepared from Me-Al alloys (Me = Fe or Cu). The nominal active metal mass contents in the alloys are 50 wt. % for Cu, and 50 or 35 wt. % for Fe. The Fe50, Fe35 and Cu50 alloy powders were supplied by H.C. Starck GmbH (Amperkat® SK alloys). Fe35 [30] was obtained by a fast quenching method, while Fe50 and Cu50 are conventional alloys [31]. The Cu50 and Fe50 (or Fe35) alloy powders were mixed and Al was leached using a concentrated NaOH solution at room temperature, forming a heterogeneous mixture of catalyst particles. Details of the Raney-type catalysts preparation are largely documented in the literature [32]. The catalysts are named by their original alloy composition, e.g. Fe50Cu50 is the catalyst obtained by leaching out Al from the Fe-Al (50 wt. %/50 wt. %) and Cu-Al (50 wt. %/50 wt. %) alloys. Except where noted, the catalysts were prepared with 40 wt. % of Fe and 60 wt. % Cu. So, to prepare the Fe50Cu50 catalyst, 1 g of Fe50 alloy and 1.5 g of Cu50 alloy were used, while for Fe35Cu50, 1.43 g of Fe35 was mixed with 1.5 g of Cu50.

### 4.7.2 Catalyst testing

For the isothermal reaction studies, the catalysts were loaded into a tubular reactor, and dried overnight at 78 ºC in a nitrogen stream of 100 $Ncm^3$/min. In some cases, the catalysts were pretreated in hydrogen for 2 h at 600 ºC with a total gas flow rate of 110 $Ncm^3$/min and a composition corresponding to a $H_2/N_2$ molar ratio of 1:10. This treatment is hereafter referred to as HPT.

The continuous-flow reactor was a 75 cm long silica tube with 2.7 cm i.d., inserted into a furnace with a PID temperature controller. The flow rates of methane (99.999 %), nitrogen (99.995 %) and hydrogen (99.999 %) were controlled by mass flow controllers. In most of the experimental runs the feed was a gas mixture of methane and nitrogen (molar ratio of 1:10) with a total gas flow rate of 110 $Ncm^3$/min. During the reaction, the composition of the outgoing gas stream was

analyzed with a gas chromatograph equipped with a capillary column (Carboxen 1010 Plot, Supelco) and a thermal conductivity detector.

Depending on the desired effect, the catalysts went through different treatment procedures. In most cases, the physically mixed Fe-Cu catalytic systems were subjected first to a reduction treatment with a pure hydrogen flow of 10 $Ncm^3$/min for 30 min, to remove most of the oxidized layers of the Fe catalysts, and then to an in situ thermal treatment at 600 ºC with a pure nitrogen flow rate of 100 $Ncm^3$/min for two hours. This treatment is hereafter referred to as ITT. The performance of the bimetallic Fe-Cu (ITT) catalytic systems was compared to the results obtained with monometallic Fe catalysts (0.5 g of catalyst mass).

### 4.7.3 Characterization of catalysts and carbon deposits

The particle size distributions of the alloys and the corresponding catalysts were measured with a laser particle size analyzer. The specific surface areas of the fresh catalysts were calculated by the BET method from the $N_2$ equilibrium adsorption isotherms at 77 K. The alloys, catalysts and carbon deposits were examined with a JEOL JCM-35C scanning electron microscope (SEM) associated with an energy dispersive X-ray analyzer (EDX). X-ray photoelectron spectra (XPS) of the alloys and catalysts were acquired in a VG Scientific Escalab 200A apparatus. Quantitative results were obtained by fitting the experimental peaks to Gaussian–Lorentzian curves, measuring the spectral areas corresponding to each chemical element of interest and applying their empirical sensitivity factors. Powder X-ray diffraction (XRD) measurements were conducted on a PANalytical's X'Pert PRO diffractometer, using $CuK_\alpha$ radiation. The metal crystallite sizes were calculated by the Scherrer equation.

## 4.8 Results and Discussion

### 4.8.1 Catalysts characterization

A summary of the alloys used and corresponding catalysts (Cu50, Fe50 and Fe35), hydrogen pre-treated monometallic Fe catalysts, as well as in situ thermally treated bimetallic Fe-Cu catalytic systems is shown in Table 4.6.

The average particle size ($\bar{d}$) of the Cu50 catalyst was found to be ~46 μm, and its BET surface area is in the range of values reported in literature [33].

Table 4.6

Characterization of the Raney-type alloys and catalysts

| Sample | Alloy | | | Catalyst | | |
|---|---|---|---|---|---|---|
| | $\bar{d}$ [μm] | $R^a_{n,alloy}$ | $R^a_{eff,alloy}$ | $\bar{d}$ [μm] | $R^a_{eff,catalyst}$ | $S_{BET}$ [$m^2/g$] |
| Cu50 | 50 | 0.299 | 0.35 ± 0.05 | 46 | 0.95 ± 0.10 | 17 |
| Fe50 | 86 | 0.326 | 0.35 ± 0.09 | 43 | 0.95 ± 0.05 | 62 |
| Fe35 | 51 | 0.206 | 0.23 ± 0.06 | 63 | 0.95 ± 0.19 | 24 |
| Fe50 (HPT) | / | / | / | 13 | 0.95 ± 0.05 | 5 |
| Fe35 (HPT) | / | / | / | 29 | 0.95 ± 0.19 | 6 |
| Fe50Cu50 (ITT) | / | / | / | 21 | 0.95 ± 0.08 | 11 |
| Fe35Cu50 (ITT) | / | / | / | 15 | 0.95 ± 0.15 | 12 |

$\bar{d}$ : average particle size of the powders;

$R^a_{n,alloy}$ : nominal atomic ratio active metal/total metals;

$R^a_{eff,alloy}$ : determined effective atomic ratio active metal/alloy metals;

$R^a_{eff,catalyst}$ : determined effective atomic ratio active metal/catalyst metals;

$S_{BET}$: specific surface area.

The atomic ratios of the alloys determined by EDX, $R^a_{eff,alloy}$ = (active metal/total metal), are in reasonable agreement with the nominal values, $R^a_{n,alloy}$. Upon activation, the atomic ratios in the corresponding catalysts are much larger, as expected. Residual $Al_2O_3$ is present, due to incomplete leaching of Al. All catalytic systems show an atomic ratio of active metal/catalyst metals of ~0.95. However, it should be mentioned that Cu may not be uniformly distributed in the Fe-Cu ITT systems.

The untreated monometallic catalysts have two to three times larger particle sizes than the HPT Fe or ITT Fe-Cu catalysts. This phenomenon is related to particle fragmentation during hydrogen treatment (embrittlement effect) as well as Fe-Cu particle fusion (crystal reorientation). The introduction of Cu increases the average particle size from 13 μm in the Fe50 (HPT) catalyst to 21 μm in the Fe50Cu50 (ITT) system, whereas in the case of Fe35Cu50 (ITT) the opposite situation is observed, the average particle size decreasing from 29 μm in Fe35 (HPT) to 15 μm in Fe35Cu50 (ITT). This observation is probably explained by the amorphous structure of the Fe35 alloy and respective catalyst, which permits better contact between Fe and Cu particles.

The BET surface areas decrease significantly when the monometallic Fe catalysts are subjected to HPT. However, if Cu is introduced, the bimetallic catalysts show smaller BET surface area losses

(the values are nearly twice as big). Moreover, the HPT Fe catalysts show nearly the same BET surface areas (5-6 $m^2/g$). The same situation is also observed for the bimetallic Fe-Cu ITT systems (11-12 $m^2/g$). The corresponding $N_2$ isotherms show that the materials are essentially mesoporous. The isotherms also indicate that the monometallic Fe catalysts have larger pore sizes after HPT. Similarly, the isotherms obtained on the Fe-Cu (ITT) catalytic systems indicate large pores.

Table 4.7 presents the XPS results of the catalytic systems, as well as the exposed surface atomic ratios, which were measured at room temperature. Comparison of the Fe and Fe-Cu catalytic systems shows that a higher binding energy (713.1 eV) is observed in the case of the Fe50 catalyst; all other systems show surface iron mainly in zero-valent state.

Table 4.7

Surface characterization of the Raney-type alloys and catalysts

| Sample | Fe $2p^3$ [eV] | Cu $2p^3$ [eV] | Al/$Al_2O_3$ 2p [eV] | $R^a_{Fe}$ | $R^a_{Cu}$ |
|---|---|---|---|---|---|
| Alloy | | | | | |
| Cu50 | / | 932.9 | 74.7 | / | 0.03 |
| Fe50 | 709.0 | / | 76.1 | 0.07 | / |
| Fe35 | 709.5 | / | 77.5 | 0.02 | / |
| Catalyst | | | | | |
| Cu50 | / | 931.2 | 73.5 | / | 0.43 |
| Fe50 | 713.1 | / | 71.7 | 0.49 | / |
| Fe35 | 710.3 | / | 69.9 | 0.05 | / |
| Fe50 (HPT) | 710.0 | / | 73.8 | 0.25 | / |
| Fe35 (HPT) | 709.9 | / | 73.8 | 0.24 | / |
| Fe50Cu50 (ITT) | 710.7 | 932.8 | 74.7 | 0.15 | 0.14 |
| Fe35Cu50 (ITT) | 710.4 | 932.4 | 74.7 | 0.14 | 0.22 |

$R^a_{Fe}$: determined atomic ratio iron on surface/total metals;

$R^a_{Cu}$: determined atomic ratio copper on surface/total metals.

In all catalytic systems, aluminium is mostly present as Al(III) surface species ($Al(OH)_3$, $Al_2O_3$ and $Na_2Al_2O_4$). A strong presence of aluminium on catalyst surface is observed, even after HPT or ITT of the mono- and bimetallic systems (atomic fractions between 0.64 and 0.76).

Before HPT of Fe50 and Fe35, the catalysts show Fe surface atomic fractions of 0.49 and 0.05, respectively, whereas after the treatment both Fe50 (HPT) and Fe35 (HPT) present values near 0.25. The former surface decrease in Fe can be explained by the segregation of $Al_2O_3$ to the surface, thus less amounts of Fe atoms are exposed. The latter surface increase in Fe is an evidence of the reduction process with hydrogen. Fe35 shows mainly $Fe_2O_3$ in the bulk structure,

which segregates partially to the surface during HPT and is then reduced to Fe°. The different behaviour of Fe50 and Fe35 probably stems from the different microstructures of the original alloys.

The surface concentrations change significantly for the Fe50Cu50 (ITT) catalytic system. The surface value decreases to 0.15 for Fe and to 0.14 for Cu, meaning a Fe:Cu surface dilution ratio of ~1:1. In the case of the Fe35Cu50 (ITT) catalytic system, the surface concentration of Fe is practically the same (0.14), but Cu is 50 % higher (0.22). Thus, the surface dilution ratio is around 2:3, corresponding to the mole ratio input of Fe35 (0.5 g of Fe) and Cu50 (0.75 g of Cu), i.e., ~3:4 mol/mol.

In Figure 4.12 SEM examinations showed that the Fe50 (HPT) particles present a conventional morphology, but the Fe35 (HPT) particles resemble the formerly discussed rough surface morphology of Ni50 (HPT) [4].

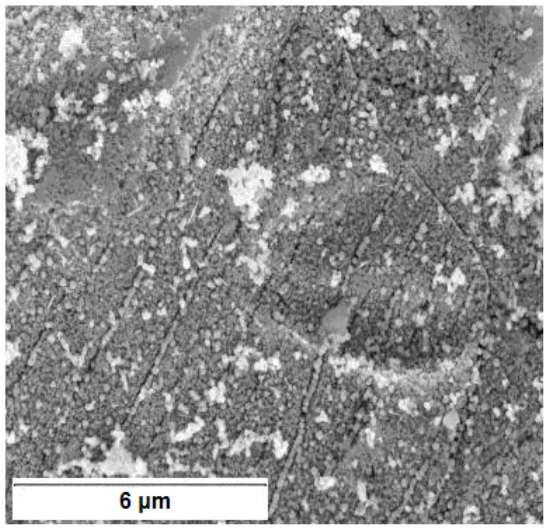



Fig. 4.12 SEM micrographs on Fe50 (HPT) (a) and Fe35 (HPT) (b).

X-ray diffraction patterns of the Fe-Al alloys were identified for Fe35 as monoclinic $FeAl_{3.2}$ together with fcc Al (results shown in the Appendix). The identified phases in Fe50 are triclinic $FeAl_2$ and orthorhombic $Fe_2Al_5$, as well as $Fe_4Al_{13}$.

Figure 4.13 shows the X-ray diffraction patterns of the Fe-Cu catalytic systems taken at 30 ºC, 600 ºC and after 2 h of in situ thermal treatment under vacuum at 600 ºC. Before measurement the bimetallic catalysts were submitted to a reduction treatment at 600 ºC with a pure $H_2$ flow of 10 $Nm^3$/min. Thereafter the catalysts were in situ thermally treated at 600 ºC under a pure $N_2$ flow of 100 $Nm^3$/min (ITT).

The catalyst Cu50 (HPT) was used as reference, instead of Cu50 [27], in order to avoid overlapping with diffraction patterns of metal oxides. Indeed, CuO and $Cu_2O$ can be easily reduced by $H_2$ at 300 ºC, as confirmed by TPD, TPRe and DSC experiments (results shown in the Appendix). For Cu-Fe alloy formation the two elements must be mainly in the zero valent state. Therefore, the XRD patterns of Fe50 (HPT) and Fe35 (HPT) were taken for comparison purposes. The identified phases and corresponding 2θ positions can be consulted in Table 4.8.

In all cases, the involved species show the presence of a fcc crystal structure, except where noted. The presence of $Fe^o$, $Fe_2O_3$ and $Fe_3O_4$ was detected in the untreated Fe50 catalyst at 600 ºC. In the case of Fe35 at 600 ºC, only $Fe_2O_3$ is found. After HPT (and also ITT), these catalysts show only the presence of $Fe^o$ and $Fe_3O_4$. However, the proportion of $Fe_3O_4$ is higher in the Fe35 (HPT) catalyst, in accordance with the reduction sequence $Fe_2O_3 \rightarrow Fe_3O_4 \rightarrow FeO \rightarrow Fe^o$.

The reflection patterns for the Fe-Cu (ITT) catalysts, at 30 ºC can be considered as a sum of the two individual ones, Fe50 (HPT) or Fe35 (HPT) and Cu50 (HPT). At 600 ºC, the FWHM changes, the Cu peaks loose on sharpness while the Fe peaks in return increase. This is an indication of particle agglomeration between Fe and Cu, meaning that the chemical heterogeneity decreases. There is no evidence for the formation of an intermetallic phase after the 2 h thermal treatment at 600 ºC, but the crystal sizes of Fe and Cu show nearly the same values. This observation can be interpreted as an indication for the incipient formation of a Fe-Cu alloy.

As shown in Table 4.9, Fe35Cu50 (ITT) has crystal sizes of 22 nm, whereas the crystal sizes of Fe50Cu50 (ITT) are 21 nm for Fe and 18 nm for Cu. It may be recalled that the Fe35 alloy has an amorphous nature, and therefore the exchange of atom positions will be facilitated.

Fe-Cu alloy formation requires higher treatment temperatures than for instance the Ni-Cu alloy formation. Moreover, Fe-Cu alloy formation is only possible in certain composition ranges, whereas Ni-Cu alloy formation spans the whole composition range above 700K [34].

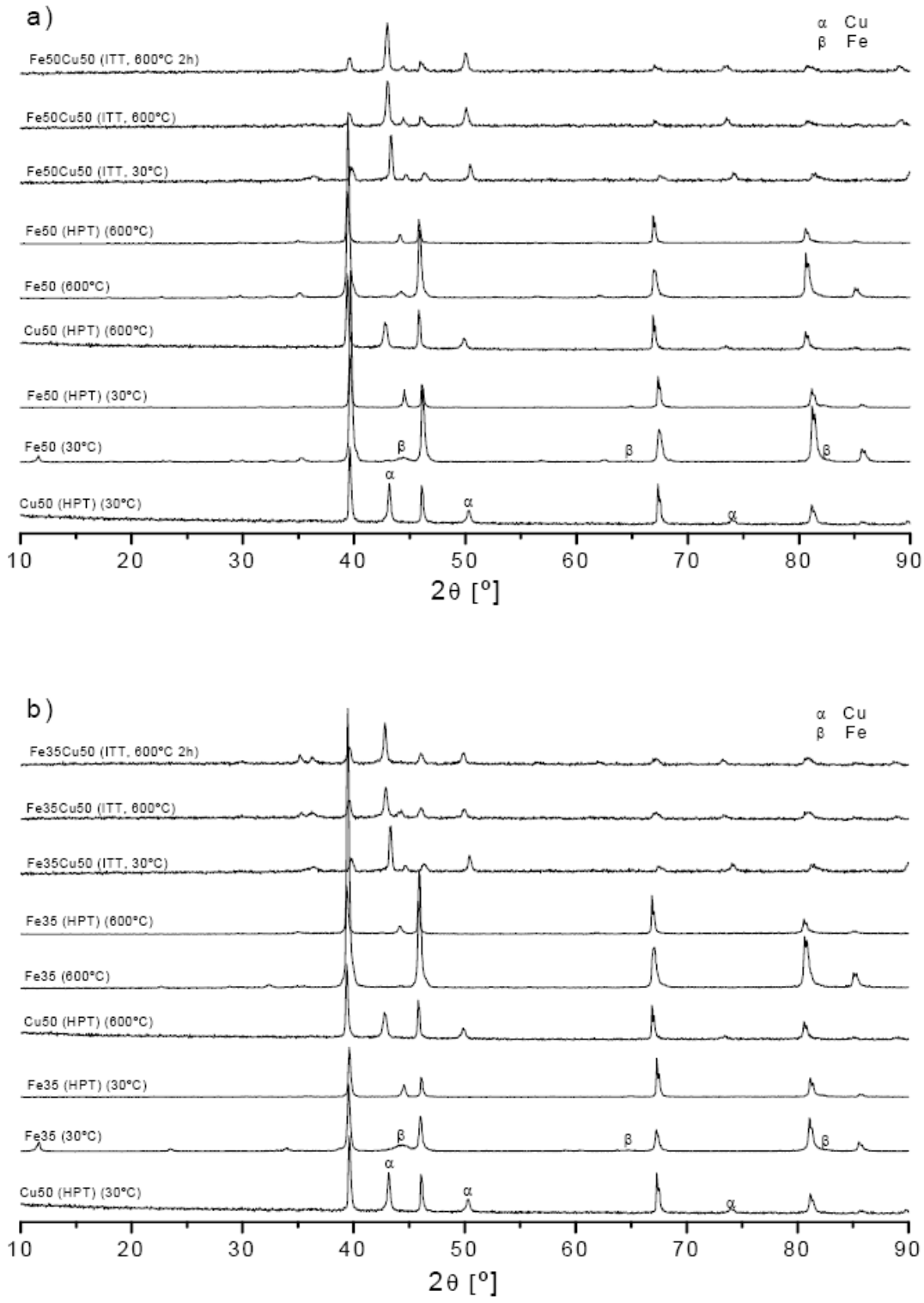



Fig. 4.13 XRD patterns of the Fe50-Cu50 (a) and Fe35-Cu50 (b) mono- and bimetallic catalysts measured at 30 ºC, 600 ºC and after 2 h of thermal treatment at 600 ºC.

Table 4.8

Phases identified in the catalysts and corresponding 2θ positions (at 30 and 600 ºC)

| Sample | T [ºC] | Phase | 2θ positions |
|---|---|---|---|
| Cu50 (HPT) | 30 | Cuº | 43.2º (111)*, 50.3º (200)*, 73.9º (220)* |
| | 600 | Cuº | 42.8º (111)*, 49.9º (200)*, 73.4º (220)* |
| Fe50 | 30 | Feº | 44.5º (110)* |
| | | $Fe_2O_3$[$] | 18.2º, 23.5º, 30.0º, 35.3º, 56.9º, 62.5º, 64.8º, 81.2º |
| | 600 | Feº | 44.2º (110)* |
| | | $Fe_2O_3$ | 22.7º, 32.5º, 67.0º |
| | | $Fe_3O_4$ | 29.9º, 35.1º, 53.0º, 56.4º |
| Fe50 (HPT) | 30 | Feº | 44.2º (110)*, 65.0º (200)*, 82.2º (211)* |
| | | $Fe_3O_4$ | 35.6º, 62.8º |
| | 600 | Feº | 44.2º (110)*, 65.0º (200)*, 82.2º (211)* |
| | | $Fe_3O_4$ | 29.9º, 34.9º, 62.0º, 67.5º, 72.8º, 78.5º, 80.7º, 85.5º |
| Fe50Cu50 (ITT) | 30 | Cuº | 43.3º (111)*, 50.5º (200)*, 74.1º (220)* |
| | | Feº | 44.7º (110)*, 64.5º (200)*, 82.3º (211)* |
| | | $Fe_3O_4$ | 35.5º, 36.4º, 67.9º, 74.1º, 86.1º |
| | 600 | Cuº | 43.0º (111)*, 50.1º (200)*, 73.6º (220)*, 89.2º |
| | | Feº | 44.4º (110)*, 64.5º (200)*, 82.3º (211)* |
| | | $Fe_3O_4$ | 35.5º, 36.1º, 67.1º, 85.3º, 89.2º |
| | 600[#] | Cuº | 43.0º (111)*, 50.0º (200)*, 73.5º (220)*, 89.0º |
| | | Feº | 44.4º (110)* |
| | | $Fe_3O_4$ | 35.2º, 36.7º, 67.0º, 73.5º, 81.1º, 89.9º |
| Fe35 | 30 | Feº | 44.5º (110)*, 65.0º (200)*, 82.3º (211)* |
| | 600 | $\alpha$-$Fe_2O_3$ | 22.7º, 28.6º, 29.7º, 32.5º, 34.8º, 35.6º, 67.0º, 80.7º |
| Fe35 (HPT) | 30 | Feº | 44.5º (110)*, 64.9º (200)*, 82.2º (211)* |
| | | $Fe_3O_4$ | 36.1º, 57.8º, 82.2º |
| | 600 | Feº | 44.5º (110)*, 64.9º (200)*, 82.2º (211)* |
| | | $Fe_3O_4$ | 17.9º, 29.7º, 35.0º, 42.5º, 62.0º |
| Fe35Cu50 (ITT) | 600[#] | Cuº | 42.8º (111)*, 49.9º (200)*, 73.3º (220)*, 88.7º |
| | | $Fe_3O_4$ | 30.0º, 35.2º, 36.7º, 62.1º, 67.3º, 73.3º, 77.7º, 80.9º, 85.5º |

[#]in situ thermal treated under vacuum during 2 h before measurement

*reflection plane

[$]$Fe_2O_3$ syn-Maghemite

Table 4.9

Fe and Cu crystal sizes of Raney-type catalysts

| Sample | T [ºC] | $d_{Fe}$ [nm] | $d_{Cu}$ [nm] |
|---|---|---|---|
| Alloy | | | |
| Fe50 | 30 | 53 | / |
| Fe35 | 30 | 53 | / |
| Monometallic Catalyst | | | |
| Cu50 (HPT) | 600 | / | 21 |
| Fe50 (HPT) | 600 | 31 | / |
| Fe35 (HPT) | 600 | 29 | / |
| Bimetallic Catalyst | | | |
| Fe50Cu50 (ITT) | 30 | 7 | 36 |
| Fe50Cu50 (ITT) | 600[#] | 21 | 18 |
| Fe35Cu50 (ITT) | 30 | 17 | 22 |
| Fe35Cu50 (ITT) | 600[#] | 22 | 22 |

[#]in situ thermal treated under vacuum during 2h before measurement

### 4.8.2 Catalysts performance

Keeping in mind the results of the previously tested monometallic Fe50 and Fe35 catalysts [4], it was decided to carry out isothermal catalytic tests for the Fe-Cu catalytic systems at 600 ºC. The catalysts were evaluated for 5 hours on stream and the effects of the incipient alloyed catalysts composition were investigated.

The carbon yields obtained in all the experiments are in agreement with the corresponding evolution of the methane conversions.

Figure 4.14 shows the mass composition effect of the FeCu (ITT) catalytic systems. All the curves show an initial activation period, which corresponds to the reduction of $Fe_xO_y$ formed during the preparation of the catalysts (leaching by NaOH) as previously discussed [4].

Before reaction, only the presence of $Fe_2O_3$ is detected by XRD in Fe35. $Fe_2O_3$ is reduced stepwise by methane during the reaction, according to Takenaka et al. [17]. However, Fe35 shows very poor catalytic performance. For reasonable catalytic performance, induction periods of more than 5 h are required (not shown here). In spite of the different surface areas (Table 4.6), the performances of Fe35 (HPT) (Fig. 4.14b) and Fe50 (Fig. 4.14a) are similar, as expected from the phases detected by XRD. The catalyst Fe50 (HPT) shows a very short induction period compared to Fe50 (Fig. 4.14a), because this sample contains very low levels of $Fe_3O_4$ (Table 4.8). Both Fe50 (HPT) and Fe35 (HPT) show also more or less the same activities, which can be explained by the similar atomic ratios of Fe atoms exposed on surface (Table 4.7).

It may be observed (Figure 4.14a) that the best catalytic performance corresponds to a mass content of 60 wt. % of Cu50 in Fe50Cu50 (ITT) (curve +0.75 g Cu50). The highest recorded methane conversion is 51 %, which decreases to 32 % after 5 h of testing (Table 4.10).

Table 4.10

Selected results for the catalytic decomposition of methane on Fe and Fe-Cu catalysts

| Catalyst | $m_{cat}$ [g] | $X_{CH_4}^{max}$ [%] | $X_{CH_4}^{5h}$ [%] |
|---|---|---|---|
| Fe50 | 0.5 | 55 | 17 |
| Fe50 (HPT) | 0.5 | 56 | 23 |
| Fe50Cu50 (ITT) | 1.25 | 51 | 32 |
| Fe35 | 0.5 | 4 | 1 |
| Fe35 (HPT) | 0.5 | 56 | 19 |
| Fe35Cu50 (ITT) | 1.25 | 40 | 35 |

Operating conditions: temperature of 600 ºC, total flow rate of 110 $Ncm^3$/min, molar methane flow rate of 0.446 mmol/min, and corresponding methane equilibrium conversion of 88.0 %.

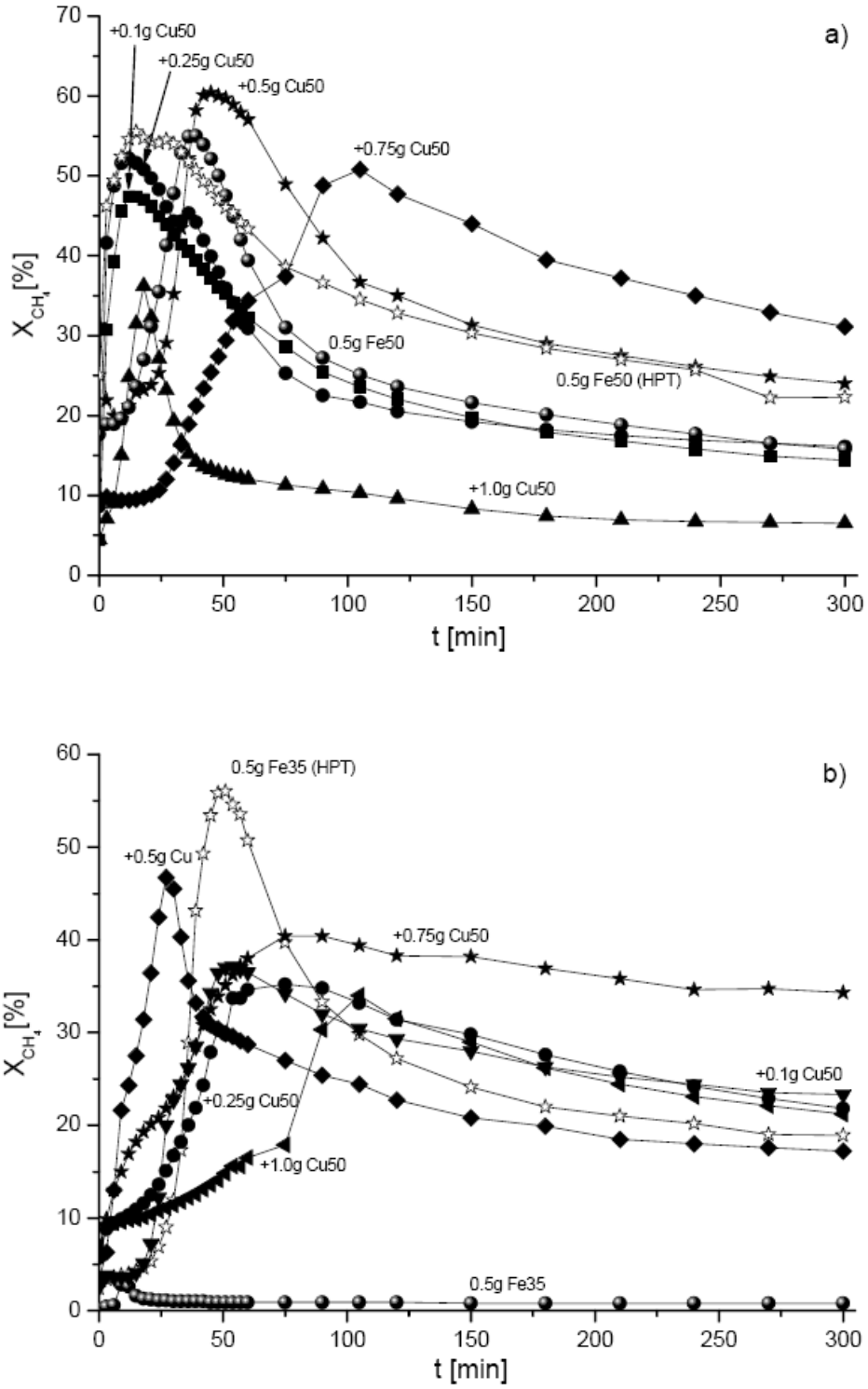



Fig. 4.14 Methane conversion as function of reaction time at 600 ºC, flow rate of 110 $Ncm^3$/min and methane molar flow rate of 0.446 mmol/min: a) Mass composition effect on Fe50Cu50 (ITT) catalyst with 0.5 g of Fe50; b) Mass composition effect on Fe35Cu50 (ITT) catalyst with 0.5 g of Fe35.

The deactivation process was significantly reduced in comparison to the monometallic Fe50 and Fe50 (HPT) catalysts, which show conversions after 5 h of 17 % and 23 %, respectively. It is also observed that addition of Cu decreases the catalyst activity to a certain level.

However, catalyst deactivation cannot be avoided completely. This is most probably related to the surface dilution ratio of the Fe50Cu50 (ITT) catalytic system (Fe:Cu ~ 1:1). The surface dilution with copper atoms is probably not sufficient for ensemble control [29]. It should also be recalled that the results obtained by XRD indicate crystal size deviations (21 nm for Fe and 18 nm for Cu).

The same experimental procedure was also applied for different Fe35Cu50 (ITT) catalytic mass compositions (Figure 4.14b). An optimum mass composition was again found for a Cu50 content of 60 wt. %. It is evident that the Fe35Cu50 (ITT) catalytic system performs similarly to the Fe50Cu50 (ITT), but with better stability, although with lower activity, as expected from the higher proportion of surface copper, which is inactive [29]. Here the surface dilution of copper atoms is higher (Table 4.7), so that the presence of smaller ensembles will improve catalyst stability. It is also important to stress that the crystal sizes of both Fe and Cu are equal (Table 4.9). Therefore, the incipient formation of a Fe-Cu alloy was proposed (section 4.8).

### 4.8.3 Characterization of the carbon deposits

Figure 4.15 shows the morphology of the carbon deposits produced at 600 ºC on Fe35Cu50 (ITT) catalysts, where the presence of carbon nanofibers (CNF) may be observed. The diameters of the CNF and metal particles on the top of them are mostly in the range 100-200 nm. The Fe-Cu (ITT) catalysts seem to be effective for the production of CNF.

For comparison purposes, the diffraction patterns of the previously used Raney-Fe catalysts (Fe50, Fe50 (HPT), Fe35 and Fe35 (HPT)) [4] and FeCu (ITT) catalysts, together with the corresponding carbon deposits, are depicted in Figure 4.16.

In all cases, the formation of graphitic carbon is observed. After methane decomposition, the monometallic Fe50, Fe50 (HPT), Fe35 and Fe35 (HPT) catalysts show the presence of cementite Fe3C, while no cementite was found in the incipiently alloyed Fe50Cu50 (ITT) and Fe35Cu50 (ITT) catalysts. The XRD spectra of both FeCu (ITT) catalysts show signs of a $Fe_{0.7}Cu_{0.3}$ alloy accompanied with segregated Fe in the bulk structure.

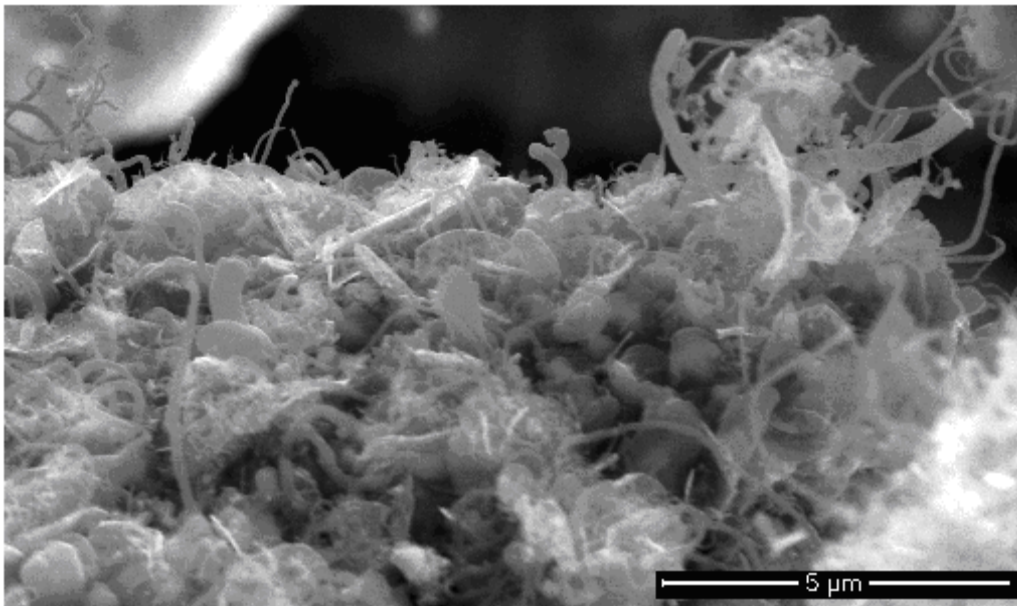



Fig. 4.15 SEM micrograph of the carbon deposit obtained at 600 ºC on Fe35Cu50 (ITT).

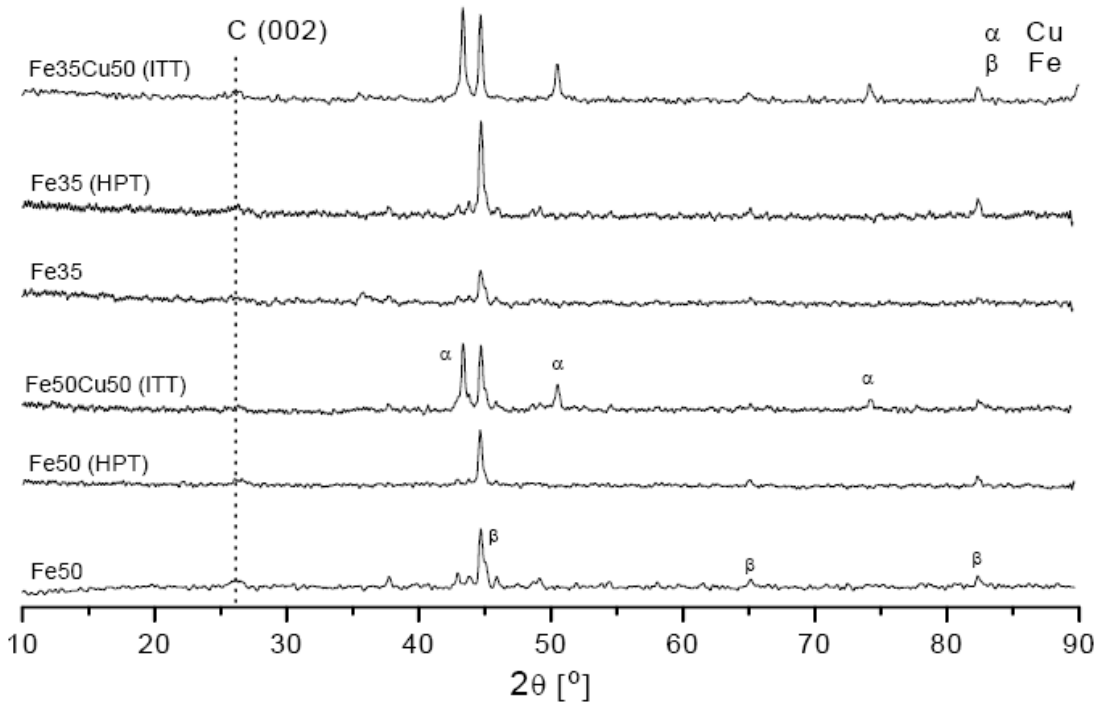



Fig. 4.16 XRD patterns of carbon deposits obtained on Fe and FeCu (ITT) catalysts at 600 ºC.

## 4.9 Conclusions

It has been shown that incipiently alloyed Fe-Cu Raney-type catalysts exhibit increased stability for the decomposition of methane into hydrogen and filamentous carbon (CNF). The stability of these catalysts has been explained by ensemble control, which decreases deactivation by encapsulating carbon. The optimum mass content of Raney-Cu in the Fe-Cu catalytic systems was determined.

## Appendix

Additional results obtained for this Chapter IV can be consulted in the Appendix.

## References


[1] Y. Yürüm, in Hydrogen Energy System, Y. Yürüm (ed.), Kluwer Academic Publishers (1995), 15.

[2] N. Muradov, T.N. Veziroglu, *Int. J. Hydrogen Energy* **30** (2005) 225.

[3] M. Steinberg, *Int. J. Hydrogen Energy* **23** (1998) 419.

[4] A.F. Cunha, J.J.M. Órfão, J.L. Figueiredo, *Appl. Catal. A: Gen.* **348** (2008) 103.

[5] N. Muradov, F. Smith, A. T-Raissi, *Catal. Today* **102-103** (2005) 225.

[6] M.J. Lázaro, J.L. Pinilla, I. Suelves, R. Moliner, *Int. J. Hydrogen Energy* **33** (2008) 4104.

[7] I. Suelves, M.J. Lázaro, R. Moliner, Y. Echegoyen, J.M. Palácios, *Catal. Today* **116** (2006) 271.

[8] M.J. Lázaro, Y. Echegoyen, I. Suelves, J.M. Palácios, R. Moliner, *Appl. Catal. A: Gen.* **329** (2007) 22.

[9] R. Moliner, Y. Echegoyen, I. Suelves, M.J. Lázaro, J.M. Palacios, *Int. J. Hydrogen Energy* **33** (2008) 1719.

[10] M.J. Lázaro, Y. Echegoyen, C. Alegre, I. Suelves, R. Moliner, J.M. Palácios, *Int. J. Hydrogen Energy* **33** (2008) 3320.

[11] J.L. Figueiredo, Filamentous carbon, *Erdöl & Kohle Erdgas Petrochemie* **42** (1989) 294.

[12] A. Konieczny, K. Mondal, T. Wiltowski, P. Dydo, *Int. J. Hydrogen Energy* **33** (2008) 264.

[13] N.Z. Muradov, *Int. J. Hydrogen Energy* **18** (1993) 211.

[14] N.Z. Muradov, *Energy & Fuels* **12** (1998) 41.

[15] L.B. Avdeeva, T.V. Reshetenko, Z.R. Ismagilov, V.A. Likholobov, *Appl. Catal. A: Gen.* **228** (2002) 53.

[16] M.A. Ermakova, D.Y. Ermakov, A.L. Chuvilin, G.G. Kuvshinov, *J. Catal.* **201** (2001) 183.

[17] S. Takenaka, M. Serizawa, K. Otsuka, *J. Catal.* **222** (2004) 520.

[18] N. Shah, D. Panjala, G.P. Huffman, *Energy & Fuels* **15** (2001) 1528.

[19] N. Shah, S. Pattanaik, F. E. Huggins, D. Panjala, G. P. Huffman, *Fuel Process. Technol.* **83** (2003) 163.

[20] A. Punnoose, N. Shah, G.P. Huffman, M.S. Seehra, *Fuel Process. Technol.* **83** (2003) 263.

[21] H. Ogihara, S. Takenaka, I. Yamanaka, E. Tanabe, A. Genseki, K. Otsuka, *J. Catal.* **238** (2006) 353.

[22] T.V. Reshetenko, L.B. Avdeeva, Z.R. Ismagilov, V.A. Ushakov, A.L. Chuvilin, Y.T. Pavlyukhin, *Chem. Sustain. Develop.* **11** (2003) 239.

[23] T.V. Reshetenko, L.B. Avdeeva, V.A. Ushakov, E.M. Moroz, A.N. Shmakov, V.V. Kriventsov, D.I. Kochubey, Y.T. Pavlyukhin, A.L. Chuvilin, Z.R. Ismagilov, *Appl. Catal. A: Gen.* **270** (2004) 87.

[24] M.S. Kim, N.M. Rodriguez, R.T.K. Baker, *J. Catal.* **131** (1991) 60.

[25] C.A. Bernardo, I. Alstrup, J.R. Rostrup-Nielsen, *J. Catal.* **96** (1985) 517.

[26] M.T. Tavares, I. Alstrup, C.A.A. Bernardo, *Mater. & Corr.* **50** (1999) 681.

[27] N. Krishnankutty, N.M. Rodriguez, R.T.K. Baker, *J. Catal.* **158** (1996) 217.

[28] N. Krishnankutty, C. Park, N.M. Rodriguez, R.T.K. Baker, *Catal. Today* **37** (1997) 295.

[29] A.F. Cunha, J.J.M. Órfão, J.L. Figueiredo, in press. doi: Int. J. Hydrogen Energy 10.1016/j.ijhydene.2009.03.040.

[30] U. Birkenstock, J. Scharschmidt, P. Kunert, H. Meinhardt, H. Paul, P. Meier, U.S. Patent 5,090,997 (1992).

[31] M. Raney, U.S. Patent 1,628,190 (1927).

[32] U. Birkenstock, R. Holm, B. Reinfandt, S. Storp, *J. Catal.* **93** (1985) 55.

[33] E.H. Schreiber, M.D. Rhodes, G.W. Roberts, *Appl. Catal. B: Environ.* **23** (1999) 9.

[34] http://www.crct.polymtl.ca/FACT/documentation/SGTE/SGTE_Figs.htm. Scientific Group Thermodata Europe - SGTE Alloy Phase Diagrams.

# *Chapter V*

## Methane Decomposition on $La_2O_3$ promoted Raney-type Catalysts

Published in

Energy & Fuels (2009), submitted

Applied Catalysis A: General (2009), to be submitted

*"Imagination is more important than knowledge,*

*because imagination spans the whole world."*

**Albert Einstein**

# *Part A*

## Methane Decomposition on $La_2O_3$ promoted Raney-Fe Catalysts

## Abstract

The catalytic decomposition of methane into hydrogen and carbon was studied on $La_2O_3$ promoted Raney-type Fe catalysts. Promoted catalysts were synthesised by in situ thermal treatment of physical mixtures of Raney Fe and $La_2O_3$. The catalysts were characterised by particle size measurement, BET, XRD, XPS and SEM. $La_2O_3$ acts as textural promoter. XPS reveals charge transfer from $La_2O_3$ to Fe. Promoted Raney Fe catalyst with an optimum loading of $La_2O_3$ exhibited good performance in methane decomposition.

## 5.1 Introduction

The catalytic decomposition of methane is an interesting route to the production of hydrogen ($CH_4 \rightarrow C + 2H_2$) [1-3]. One mole of methane produces two moles of hydrogen together with one mole of carbon. Methane is the preferred reactant among the hydrocarbons since the hydrogen to solid carbon ratio is in large favour to hydrogen. Production of hydrogen by catalytic decomposition of methane does not release any harmful products to the atmosphere. Hence, it is environmentally preferable over conventional processes, such as steam reforming of natural gas or coal gasification. Furthermore, this process produces $CO_x$ free hydrogen, which can be used in fuel cell systems to produce energy, avoiding cumbersome and expensive purification process. Besides, the formation of carbon in the form of carbon nanofibers (CNF) and carbon nanotubes (CNT) makes this process more interesting, since these materials hold scientific and technological potential [4-6].

Fe, Co and Ni, being elements of the groups 8-10 in the periodic table, show nearly the same physical and chemical properties, which reflects also on the catalytic decomposition of methane [3,7-9]. Nevertheless, some differences are there, especially with Fe. Fe shows quite different properties in methane decomposition [10-13]. It has been observed in our previous work that Co or Fe perform worse than Ni [3]. Relatively high masses of Co or Fe are required to maintain catalyst stability. In the case of Fe, a hydrogen pre-reduction process is also required to avoid large induction periods, corresponding to the reduction of iron oxides. However, because of low cost and wide availability, Fe can be an attractive alternative to Ni. Also, the application of suitable promoters can enhance the activity of Fe.

Several reports are available where $La_2O_3$ has been applied as promoter for Ni catalysts in methane decomposition [14,15]. Rivas et al. also observed that in-situ generated $La_2O_3$ acts as excellent stabilizer for nickel particles in the same reaction [16].

The objective of this work is to study the promotional effect of $La_2O_3$ on Raney type Fe skeletal catalysts during catalytic decomposition of methane at well defined operating conditions. Physical mixtures of Raney Fe and $La_2O_3$ were subjected to in situ thermal treatment under diluted hydrogen to facilitate close interaction between the active phase and the promoter.

## 5.2 Experimental

### 5.2.1 Catalysts preparation

Raney-type catalysts were prepared from Fe-Al alloys of two types, supplied by H.C. Starck GmbH (Amperkat® SK alloys). The nominal Fe content in the alloys was 35 or 50 wt. %. The alloy containing 50 % Fe was conventional [17]. Whereas, the alloy powder containing 35 % Fe was obtained by fast quenching method [18].

The Raney-type catalysts were prepared by leaching out Al with a concentrated NaOH solution at room temperature [19]. The obtained samples were subsequently washed several times with distilled water. The catalysts were doped with $La_2O_3$ (Merck). In a typical procedure, a calculated amount of $La_2O_3$ was suspended in 50 ml distilled water, added to the Raney catalyst and left on an ultrasonicator for 1 h. Subsequently the sample was transferred carefully to a tubular reactor avoiding exposure to air and dried under $N_2$ flow (100 $Ncm^3$ $min^{-1}$) at 100 ºC for 3 h. The sample was then pretreated at 600 ºC for 2 h under 10 % $H_2$ in $N_2$ prior to each run, in order to facilitate close interaction between active metal and $La_2O_3$. For direct comparison, unpromoted Raney Fe catalysts were also pretreated under the same conditions. Two series of catalysts having 5, 10, 20 and 50 wt. % $La_2O_3$ loadings, along with unpromoted ones, were prepared starting both types of Fe-Al alloys. The unpromoted catalysts were designated as xFe and the promoted catalysts were designated as xFeLa(y). x stands for Fe wt. % value in the original alloy and y stands for wt. % of $La_2O_3$ in the catalysts.

### 5.2.2 Catalyst characterization

The particle size distributions of the catalysts were measured with a laser particle size analyzer. Surface areas were calculated by the BET method from the $N_2$ adsorption isotherms at 77 K. XRD measurements were conducted using Cu $K_\alpha$ radiation ($\lambda$ = 0.154 nm). Intensity was measured by step scanning in the 2θ range of 10º-90º. Crystallite size was calculated applying Scherrer equation. XPS analysis was performed using Mg $K_\alpha$ radiation (1253.6 eV). Charging effect was corrected using C 1s level (285.0 eV) as reference. Quantitative results were obtained by fitting the experimental peaks to Gaussian–Lorentzian curves with Shirley background, measuring the spectral areas corresponding to each chemical element of interest and applying their empirical sensitivity factors. SEM examination was carried out using an electron beam of 20 kV.

### 5.2.3 Catalyst testing

As described in the catalyst preparation section, the catalysts were pretreated in situ before actual reaction run. The catalysts were evaluated in the decomposition of methane in a continuous-flow reactor consisting of a 75 cm long silica tube with 2.7cm i.d., inserted into a furnace with a PID temperature controller. The flow rates of methane (99.999 %), nitrogen (99.995 %) and hydrogen (99.999%) were controlled by mass flow controllers. The feed consisted of a mixture of methane and nitrogen (molar ratio of 1:10) with a total gas flow rate of 110 $Ncm^3$ $min^{-1}$. During the reaction, the composition of the outgoing gas stream was analyzed with a gas chromatograph equipped with a capillary column (Carboxen 1010 Plot, Supelco) and a thermal conductivity detector.

## 5.3 Results and discussion

### 5.3.1 Catalysts characterization

Table 5.1 lists average particle sizes and BET surface areas of some selected catalysts.

Table 5.1

Average particle sizes ($\bar{d}$) and BET surface areas ($S_{BET}$) of selected catalysts

| Catalyst | $\bar{d}$ [μm] | $S_{BET}$ [$m^2/g$] |
|---|---|---|
| 50Fe | 13 | 5 |
| 50FeLa(20) | 13 | 11 |
| 35Fe | 29 | 6 |
| 35FeLa(20) | 12 | 11 |

The average particle size of catalysts originating from the alloy containing 35 % Fe decreases upon $La_2O_3$ promotion, whereas it remains constant in the catalysts originating from the alloy containing 50 % Fe. The BET surface areas of the unpromoted catalysts, obtained from both alloys, are pretty low (5-6 $m^2$ $g^{-1}$), which indicates that the catalysts went through a sinterization process during hydrogen pretreatment. Untreated Raney Fe catalysts exhibited BET areas in the range 25–60 $m^2$ $g^{-1}$ [3]. Addition of $La_2O_3$ avoids sinterization to a certain extent, and the promoted catalysts exhibit comparatively higher BET areas (11 $m^2$ $g^{-1}$). It can be inferred that $La_2O_3$ acts as a textural promoter.

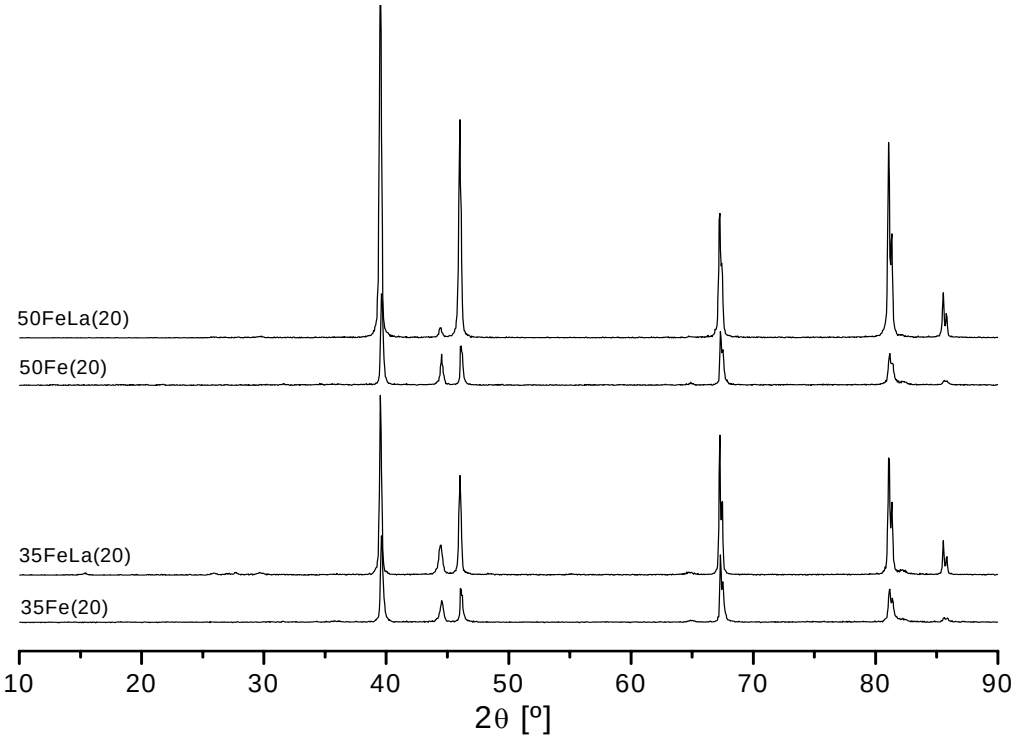



Fig. 5.1 XRD patterns of selected catalysts.

XRD spectra of representative samples are shown in Figure 5.1. All the catalysts show a sharp diffraction line at 2θ value of ~44.5º corresponding to Fe (100) [20,21]. Minor peaks are also observed at 2θ values of ~65º and ~82º corresponding to Fe (200) and Fe (211) diffraction planes, respectively. Only very weak diffraction lines corresponding to $La_2O_3$ or $La(OH)_3$ are observed with the $La_2O_3$ promoted catalysts. Both 50FeLa(20) and 35FeLa(20) show presence of $La_2O_3$ (101) at 2θ value of ~29º. In addition, 35FeLa(20) shows diffraction lines at 2θ values of ~16º, ~27º and ~28º corresponding to (100), (110), and (101) planes of $La(OH)_3$. Crystallite size of Fe was calculated applying Scherrer equation. Most intensive peak was considered for calculation, and the obtained crystallite size was considered as an average crystallite size. The catalysts obtained from the alloy containing 50 % Fe exhibited Fe crystallite size of ~15 nm, whereas the catalysts obtained from the alloy containing 35 % Fe exhibited Fe crystallite size of ~ 25 nm. The crystallite size of Fe in the catalysts is well in the optimum range for filamentous carbon formation during hydrocarbon decomposition [22,23].

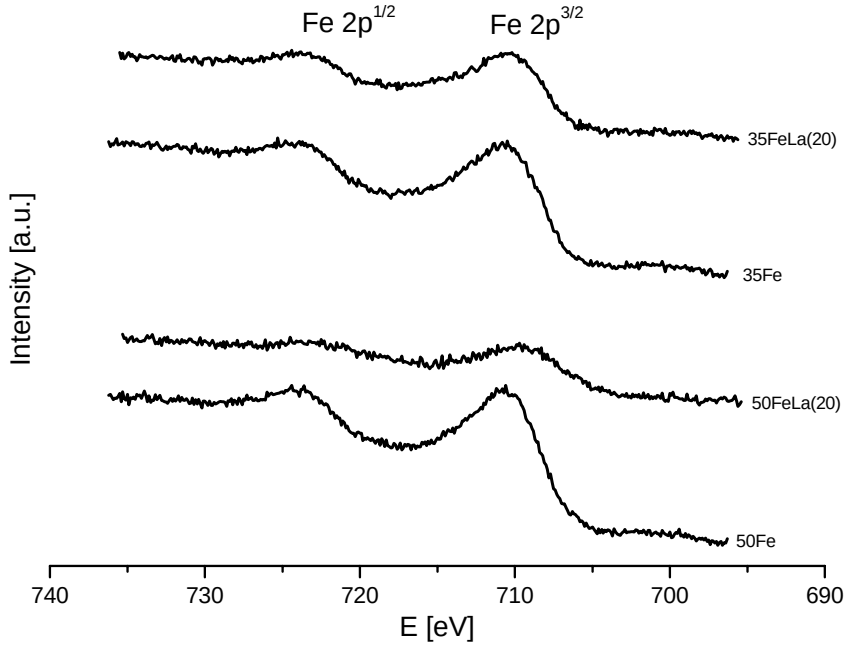



Fig. 5.2 Fe 2p XPS spectra of selected catalysts.

The catalysts were subjected to Fe 2p, La 3d, and Al 2p XPS analysis. Figure 5.2 shows XPS spectra of the Fe 2p region of some selected samples. The spectra clearly reveal that surface Fe is mainly present in the oxidised state. The $2p^{3/2}$ photoelectron peak observed at 710.2 ± 0.5 eV can be assigned to a combination of $Fe^{2+}$ and $Fe^{3+}$. Reported binding energy (BE) values of Fe $2p^{3/2}$ in FeO and $Fe_2O_3$ are 709.5 ± 0.3 eV and 710.5 ± 0.1 eV, respectively [24-26]. Hence, surface iron mainly consists of FeO and $Fe_2O_3$ in the present catalysts. Comparison of the spectra of $La_2O_3$ promoted catalysts with those of unpromoted catalysts shows a negative shift of BE in the promoted catalysts, indicating charge transfer from $La_2O_3$ to iron.

Table 5.2 summarises the Fe $2p^{3/2}$, La $3d^{5/2}$ and Al 2p BE values along with surface concentration of iron.

Table 5.2

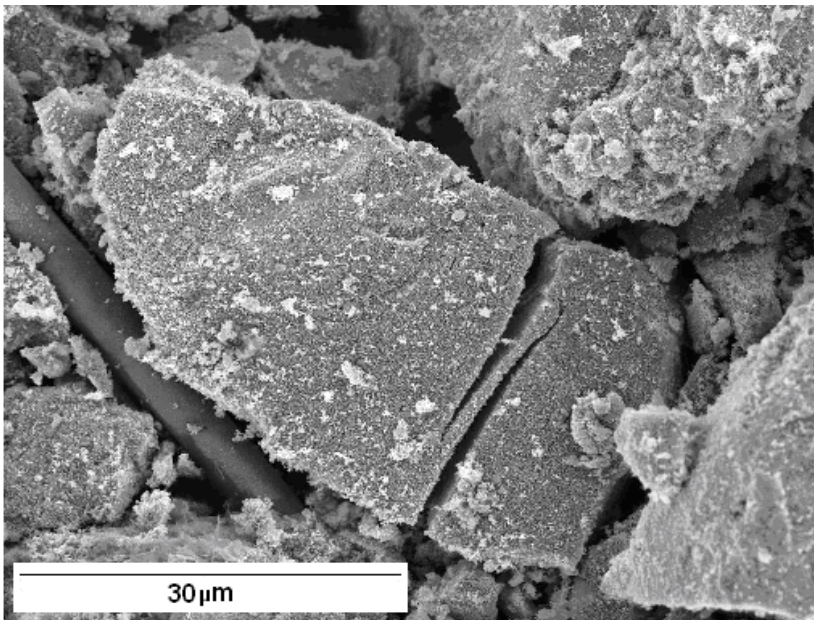
XPS results of selected catalysts

| Catalyst | Fe $2p^{3/2}$ [eV] | La $3p^{5/2}$ [eV] | Al/$Al_2O_3$ 2p [eV] | $R^a_{Fe}$ | $R^a_{La}$ |
|---|---|---|---|---|---|
| 50Fe | 710.0 | / | 73.8 | 0.25 | / |
| 50FeLa(20) | 709.1 | 835.1 | 72.6 | 0.15 | 0.41 |
| 35Fe | 709.9 | / | 73.8 | 0.24 | / |
| 35FeLa(20) | 709.7 | 835.6 | 73.5 | 0.18 | 0.22 |

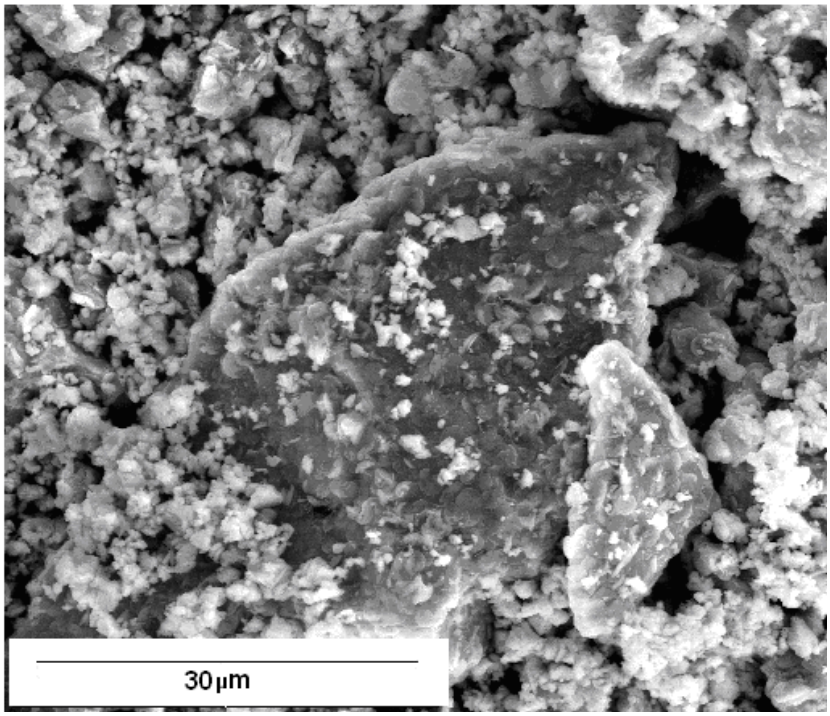
$R^a_{Fe}$ : Fractional amount of Fe.

$R^a_{La}$ : Fractional amount of La.

The catalysts were also characterised by SEM, typical micrographs being shown in Figure 5.3. Both promoted and unpromoted catalysts exhibit rough surfaces. The bright points, observed in 50Fe, indicate the presence of $Fe_xO_y$ on the surface. $La_2O_3$ agglomerates on iron surface are clearly visible in the promoted catalyst.




a)




b)

Fig. 5.3 SEM images of catalysts a) 50Fe and b) 50FeLa(20).

### 5.3.2 Catalyst performance

Catalytic decomposition of methane was carried out isothermally at 600 ºC. The results are shown in Figure 5.4. The catalysts were evaluated for 5 hours on stream. The carbon yields obtained in all the experimental runs are in agreement with the methane conversion values. Figure 5.4a shows the effect of $La_2O_3$ loading on Raney Fe obtained from Fe-Al alloy containing 50 % Fe, while Figure 5.4b shows the effect of $La_2O_3$ loading on Raney Fe obtained from Fe-Al alloy containing 35 % Fe. The methane conversion increases initially, attains a maximum value, and then drops down over all the catalysts. The initial induction period is related to the reduction of surface $Fe_xO_y$. XPS analysis confirms that surface layers mainly consist of Fe in oxidised states, even though XRD reveals that bulk Fe is mainly in metallic state. Conversion maxima over all the catalysts are in the range 50–55 %. Rapid deactivation beyond conversion maxima is not unexpected, as blocking of active sites by initial carbon deposition can be significant. However, the drop in methane conversion is much slower at later stages of the reaction. This performance of the catalysts, with very slow deactivation, implies that deposited carbon is mainly filamentous (nanofibre or nanotube) rather than encapsulating carbon. In fact, SEM analysis of catalysts after reaction confirms that a large fraction of deposited carbon is filamentous (results shown in the Appendix). Comparison between Figures 5.4a and 5.4b reveals that catalysts from the 50/50 Fe/Al alloy exhibited better performance than those obtained from the 35/65 Fe/Al alloy. Also, it is evident that $La_2O_3$ promotes the activity of Raney iron up to a certain loading. However, excess $La_2O_3$ decreases the activity, by blocking active Fe sites. Among the selected samples, Raney Fe promoted with 20 wt. % $La_2O_3$, is the best catalyst for decomposition of methane to hydrogen and carbon. After 5 h on stream, 50FeLa(20), obtained from the 50/50 Fe/Al alloy and promoted by 20 wt. % $La_2O_3$, exhibited nearly stable performance with 42 % methane conversion. However, 35FeLa(20), the analog system obtained from the 35/65 Fe/Al alloy, showed inferior performance with 28 % methane conversion and not reaching steady state after 5 h on stream. $La_2O_3$ enhances the activity of Raney iron in two ways. First, it acts as good textural promoter, $La_2O_3$ promoted catalysts showing higher BET surface areas than the unpromoted catalysts (Table 5.1). Secondly, it acts as an electronic promoter, as shown by a negative shift of BE of iron in the promoted catalysts, indicating charge transfer from $La_2O_3$ to iron (Figure 5.2 and Table 5.2). An increased electron density over iron seems to enhance electron transfer to σ* antibonding orbital of adsorbed methane thereby facilitating C-H bond splitting. This argument is further supported by the fact that the enhancement of the activity after 5 h, compared to the respective unpromoted counterparts, is more pronounced in 50FeLa(20) than in 35FeLa(20).

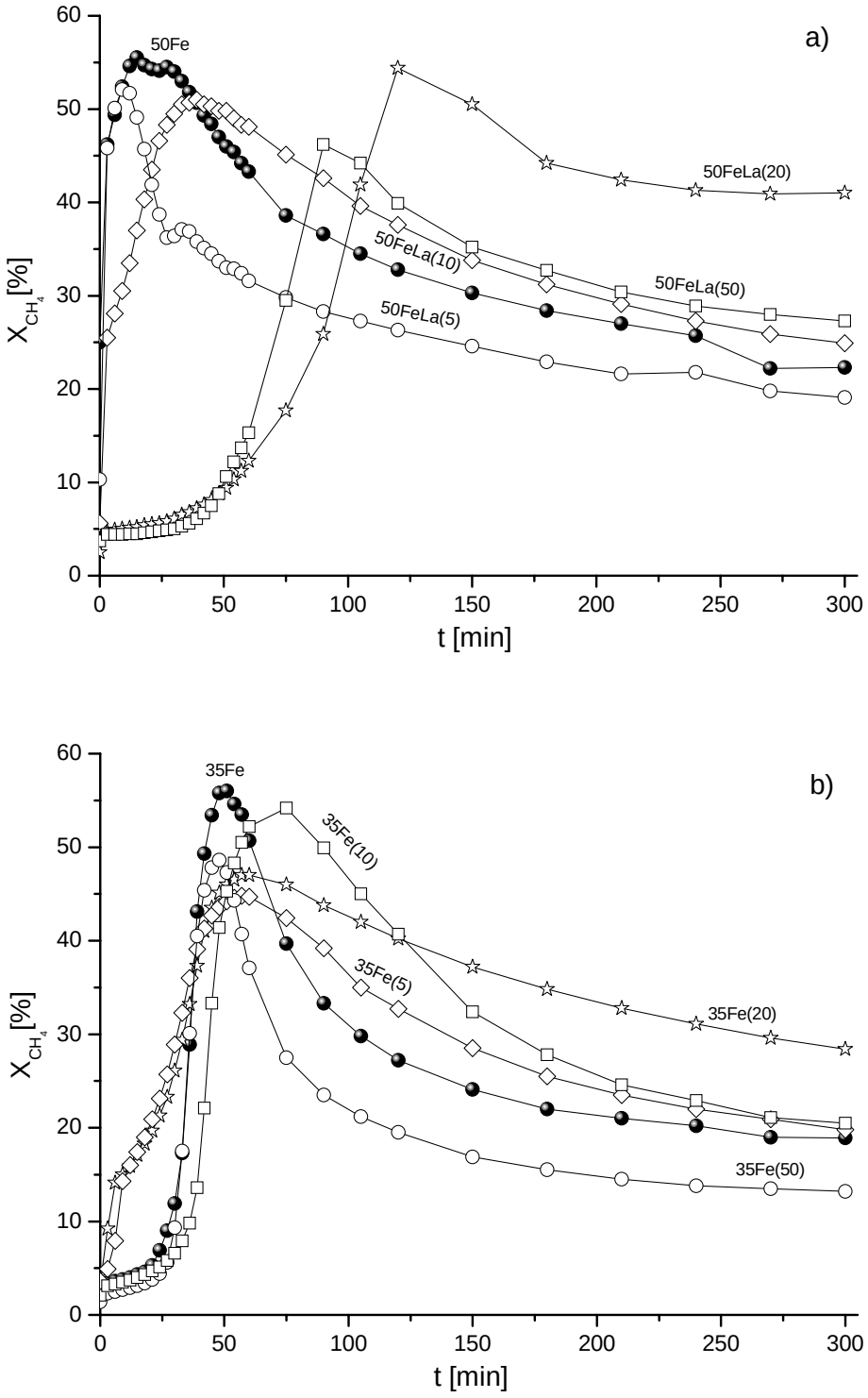



Fig. 5.4 Performance of the catalysts in methane decomposition. a) Catalysts - originated from 50/50 Fe/Al alloy, b) Catalysts originated from 35/65 Fe/Al alloy. Reaction conditions: amount of catalysts - 0.5g Raney Fe (+ promoter), total flow-rate of $CH_4$ + $N_2$ gas mixture - 110 $Ncm^3$ $min^{-1}$ ($CH_4/N_2$ = 0.1), temperature - 600 ºC.

After 5 h on stream, 50FeLa(20) exhibited 20 % higher methane conversion than 50Fe, whereas 35FeLa(20) exhibited only 9 % higher conversion than 35Fe. Table 5.2 shows that Fe $2p^{3/2}$ BE shift in 50FeLa(20) is -0.9 eV compared to -0.3 eV in 35FeLa(20), meaning higher electron density over Fe in 50FeLa(20) than 35FeLa(20).

## 5.4 Conclusions

$La_2O_3$ promoted Raney Fe catalysts for methane decomposition can be synthesised by in situ thermal treatment of physical mixtures of Raney Fe and $La_2O_3$.

$La_2O_3$ acts as a textural promoter by increasing BET surface area. It also acts as an electronic promoter by transferring charge to iron. The activity and stability of Raney Fe can be improved by adequate loading of $La_2O_3$. However, excess $La_2O_3$ blocks the active sites. The best systems, among those tested, corresponds to 20 wt. % $La_2O_3$ promoted Raney Fe.

## References


[1] N.Z. Muradov, T.N. Veziroglu, *Int. J. Hydrogen Energy* **30** (2005) 225.

[2] P. Häussinger, R. Lohmüller, A.M. Watson, Hydrogen, Ullmann's Encyclopedia of Industrial Chemistry, 7th Edition (2000).

[3] A.F. Cunha, J.J.M. Órfão, J.L. Figueiredo, *Appl. Catal. A: General* **348** (2008) 103.

[4] N. Mahata, A.F. Cunha, J.J.M. Órfão, J.L. Figueiredo, *Appl. Catal. A: General* **351** (2008) 204.

[5] N. Mahata, A.F. Cunha, J.J.M. Órfão, J.L. Figueiredo, *Catal. Commun.* **10** (2009) 1203.

[6] P. Serp, J.L. Figueiredo (editors), Carbon Materials for Catalysis, Wiley, Hoboken 2009.

[7] R.T. Yang, J.P. Chen, *J. Catal.* **115** (1989) 52.

[8] T. Koertz, R.A. van Santen, *J. Mol. Catal.* **74** (1992) 185.

[9] L.B. Avdeeva, D.I. Kochubey, Sh.K. Shaikhutdinov, *Appl. Catal. A: General* **177** (1999) 43.

[10] N.Z. Muradov, *Energy & Fuels* **12** (1998) 41.

[11] M.A. Ermakova, D.Y. Ermakov, A.L. Chuvilin, G.G. Kuvshinov, *J. Catal.* **201** (2001) 183.

[12] H. Ogihara, S. Takenaka, I. Yamanaka, E. Tanabe, A. Genseki, K. Otsuka, *J. Catal.* **238** (2006) 353.

[13] R. Sharma, E. Moore, P. Rez, M.M.J. Treacy, *Nano Letters* **9** (2009) 689.

[14] J. Gao, Z. Hou, J. Guo, Y. Zhu, X. Zheng, *Catal. Today* **131** (2008) 278.

[15] P. Jiang, Y. Shang, T. Cheng, Y. Bi, K. Shi, S. Wei, G. Xu, K. Zhen, *J. Natur. Gas Chem.* **12** (2003) 183.

[16] M.E. Rivas, J.L.G. Fierro, R. Guil-López, M.A. Peña, V. La Parola, M.R. Goldwasser, *Catal. Today* **133-135** (2008) 367.

[17] M. Raney, U.S. Patent 1,628,190 (1927).

[18] U. Birkenstock, J. Scharschmidt, P. Kunert, H. Meinhardt, P. Hausel, P. Maier, U.S. Patent 5,090,997 (1992).

[19] U. Birkenstock, R. Holm, B. Reinfandt, S. Storp, *J. Catal.* **93** (1985) 55.

[20] S. Yin, C. Li, Q. Blan, M. Lu, *Mater. Sci. Eng. A* **496** (2008) 362.

[21] B.N. Mondal, A. Basumallick, P.P. Chattopadhyay, *J. Magn. Magn. Mater.* **309** (2007) 290.

[22] D. Chen, K.O. Christensen, E. Ochoa-Fernández, Z. Yu, B. Tøtdal, N. Latorre, A. Monzón, A. Holmen, *J. Catal.* **229** (2005) 82.

[23] Y. Li, B. Zhang, X. Xie, J. Liu, Y. Xu, W. Shen, *J. Catal.* **238** (2006) 412.

[24] M. Aronniemi, J.Sainio, J. Lahtinen, *Surf. Sci.* **578** (2005) 108.

[25] D.H. Lee, S.Y.Yoon, J.H. Kim, S.J. Suh, *Thin Solid Films* **475** (2005) 251.

[26] P. Keller, H-H. Strehblow, *Corros. Sci.* **46** (2004) 1939.

# *Part B*

## Methane Decomposition on $La_2O_3$ promoted Ni and Ni-Cu Raney-type Catalysts

## Abstract

The catalytic decomposition of methane into hydrogen and carbon was studied on $La_2O_3$ doped Raney-type catalysts. The performance of these catalysts was assessed by comparing with previously used Raney-type catalysts and other results reported recently. The performances were dependent on the amount of promoter used, good incorporation onto the catalyst surface, and operating conditions. $La_2O_3$ was responsible for enhanced catalyst stability, and high selectivity towards the formation of filamentous carbon, including carbon nanofibers and multiwalled carbon nanotubes. The promoted catalysts are suitable for ultra pure hydrogen production.

## 5.5 Introduction

Clean sources of energy are currently one of the most important research topics, due to the raw materials situation and environmental impacts. Conventional fossil fuels are becoming scarce, and hydrogen is predicted to be the fuel of the future [1].

The goal is to use hydrogen in low temperature proton exchange membrane fuel cells (PEMFC), but they tolerate CO only in the 10-100 ppm range [2].

Hydrogen is typically produced by auto-thermal steam reforming or partial oxidation of methane. Separation and purification processes are required, such as the water-gas shift and methanation reactions. Pressure swing adsorption (PSA) can also be coupled for hydrogen purification [3,4].

More recently, the production of hydrogen by catalytic methane decomposition (CMD) has attracted a lot of attention, as an alternative route to avoid $CO_x$ formation when appropriate catalysts are used [5-7].

It is known that metals such as Ni, Co or Fe are active for CMD. In particular, nickel is able to decompose methane at moderate conditions forming filamentous carbon. The stability and activity of the catalysts as well as filamentous carbon growth and their morphology depend on the catalytic active sites, catalyst structure, texture, particle sizes, support nature and operating conditions. However, the catalysts require not only an active phase, but also promoters to maintain long time activity. Indeed, it is well known that catalyst stability requires the formation of filamentous carbon (which does not deactivate the catalyst), while graphitic overlayers (encapsulating carbon) are responsible for catalyst deactivation [8].

So, most of the efforts made in CMD were focused on Ni and Ni-Cu phases with textural promoters [9-13]. In a recent work, it was found that incipient alloyed Ni-Cu Raney-type catalysts are also quite effective for CMD [14].

Support materials may affect the catalytic properties. Most of the published works related with this topic refer mainly to Ni catalysts supported in a variety of carbon materials or metal oxides, such as $Al_2O_3$, $SiO_2$, $TiO_2$, MgO, ZnO, $Nb_2O_5$, $CeO_2$ and Zeolites [15-19].

Recently, Rivas et al. have communicated that a mixed oxide, $LaNiO_3$ showed stable catalytic properties for methane decomposition [20,21]. The stability of this catalyst may be ascribed to the formation of highly dispersed Ni crystallites, obtained upon hydrogen reduction, in close contact with the $La_2O_3$ substrate [22]. Other authors also used $La_2O_3$ as an additive for Ni catalysts [23,24]. It is reported that catalytic sites for carbon growth are provided, because very small particles are produced during the reduction process of the perovskite-type oxides.

The present work is aimed to develop a suitable catalyst for methane decomposition, with activities near equilibrium, high stability, no formation of $CO_x$, and production of high added-value carbon by-products. Therefore, we discuss the effect of Lanthanum (III)-oxide in unsupported Ni and Ni-Cu skeletal phases of Raney-type. Raney-type catalysts with several dopants were previously reported for other catalytic reactions [25], but not for CMD. $La_2O_3$ doped Ni and Ni-Cu phases of Raney-type were prepared with or without an in situ hydrogen pre-treatment (HPT). The influence of the promoter is compared with the Raney-type catalysts used under different operating conditions in previous works [9,14]. It will be shown that these newly developed catalysts are by far the most efficient ever reported. Moreover, the carbon by-product has been found to consist of carbon nanofibers (CNF) and multiwall carbon nanotubes MWCNT; encapsulating carbon was found only when the operating conditions were not appropriate.

## 5.6 Experimental

### 5.6.1 Catalysts preparation

Skeletal Raney-type catalysts were prepared from Me-Al alloys (Me = Ni or Cu), obtained from two different sources. The nominal active metal mass content in the alloys were 30 and 50 wt. % for Ni and 50 wt. % for Cu. The Ni50 conventional alloy is a commercial product from Fluka Chemie Gmbh [26]. The remaining Ni30 and Cu50 alloy powders were supplied by H.C. Starck GmbH (Amperkat® SK alloys). Ni30 is obtained by a fast quenching method [27] whereas Cu50 is a conventional alloy [26].

The Raney-type alloys (Ni50 or Ni30) were activated by leaching out the aluminium with a concentrated NaOH solution at room temperature [28]. Cu50 and Ni30 alloys were mixed before activation, thus forming a heterogeneous mixture of catalyst particles after leaching. The mass content of the active Ni phase was the same as the Cu one (Ni/Cu mass ratio = 1). The Ni30, Ni50 catalysts as well as Ni30Cu50 physical catalyst mixtures were subsequently washed several times with distilled water and doped with Lanthanum (III)-oxide in 50 ml of distilled water. $La_2O_3$ was obtained from Merck Gmbh, Darmstadt. The Ni- $La_2O_3$ and the Ni-Cu- $La_2O_3$ mixtures were stirred in ultrasonic bath for 1 h or 2 h, respectively.

Typically $La_2O_3$ loads of 19.4 wt. % for Ni50 and 10.7 wt. % for Ni30 were used and the catalysts are designated as Ni50La and Ni30La, respectively. The mass fraction of $La_2O_3$ used in the Ni30-Cu50-$La_2O_3$ catalytic system was 0.057. This catalytic system is referred hereafter as NiCuLa. $La_2O_3$ doped Cu50 is abbreviated as Cu50La.

### 5.6.2 Catalyst testing

Temperature programmed reaction (TPRe) experiments were carried out with a custom made set-up, consisting of a U-shaped tubular micro-reactor, placed inside an electrical furnace. Methane (5 $Ncm^3$/min) was diluted in helium carrier gas (50 $Ncm^3$/min). A temperature program from room temperature to 1000 ºC, at a heating rate of 5 ºC/min, was carried out using appropriate equipment. The amounts of $H_2$ (m/z = 2), $CH_4$ (m/z = 16), CO (m/z = 28), and $CO_2$ (m/z = 44) were monitored using a Spectramass Dataquad quadrupole mass spectrometer.
For the isothermal reaction studies, the catalysts were loaded into a tubular reactor, and dried overnight at 100 ºC in a nitrogen stream of 100 $Ncm^3$/min. In most cases, the catalysts were pretreated in hydrogen for 2 h (4 h for NiCuLa) at 600 ºC with a total gas flow rate of 110 $Ncm^3$/min and a composition corresponding to a $H_2/N_2$ molar ratio of 1:10. This treatment is hereafter referred to as HPT.
The continuous-flow reactor was a 75 cm long silica tube with 2.7 cm i.d., inserted into a furnace with a PID temperature controller. The flow rates of methane (99.999 %), nitrogen (99.995 %) and hydrogen (99.999 %) were controlled by mass flow controllers. In most of the experimental runs the feed was a gas mixture of methane and nitrogen (molar ratio of 1:10) with a total gas flow rate of 110 $Ncm^3$/min. During the reaction, the composition of the outgoing gas stream was analyzed with a gas chromatograph equipped with a capillary column (Carboxen 1010 Plot, Supelco) and a thermal conductivity detector.

### 5.6.3 Characterization of catalysts and carbon deposits

The particle size distributions of the alloys and the corresponding catalysts were measured with a laser particle size analyzer. The specific surface areas of the fresh catalysts were calculated by the BET method from the $N_2$ equilibrium adsorption isotherms at 77 K. The alloys, catalysts and carbon deposits were examined with a JEOL JCM-35C scanning electron microscope (SEM) associated with an energy dispersive X-ray analyzer (EDX). A high-resolution transmission electron microscopy (TEM) study of the carbon deposits was carried out with a Phillips CM12 instrument. X-ray photoelectron spectra (XPS) of the alloys and catalysts were acquired in a VG Scientific Escalab 200A apparatus. Quantitative results were obtained by fitting the experimental peaks to Gaussian–Lorentzian curves, measuring the spectral areas corresponding to each chemical element of interest and applying their empirical sensitivity factors. Powder X-ray diffraction (XRD) measurements were conducted on a PANalytical's X'Pert PRO diffractometer,

using $CuK_\alpha$ radiation. The crystallite sizes of catalysts and carbon deposits were calculated by the Scherrer equation.

## 5.7 Results and Discussion

### 5.7.1 Catalysts characterization

The properties of the Raney-type catalysts used are collected in Table 5.3. The average particle sizes of the catalysts are in the range 20-156 μm.

Table 5.3

Characterization of the Raney-type catalysts

| Catalyst | $\bar{d}$ [μm] | $R^a_{eff}$ | $S_{BET}$ [$m^2/g$] |
|---|---|---|---|
| $La_2O_3$ | 15 | / | 2 |
| Cu50 | 46 | 0.95 ± 0.10 | 17 |
| Ni50 | 21 | 0.72 ± 0.07 | 82 |
| Ni50 (HPT) | 85 | 0.72 ± 0.07 | 9 |
| Ni50La | 20 | 0.68 ± 0.07 | 19 |
| Ni50La (HPT) | 34 | 0.68 ± 0.07 | 18 |
| Ni30 | 156 | 0.85 ± 0.07 | 64 |
| Ni30 (HPT) | 38 | 0.85 ± 0.07 | 22 |
| Ni30La | 141 | 0.82 ± 0.07 | 43 |
| Ni30La (HPT) | 38 | 0.82 ± 0.07 | 31 |
| Ni30Cu50 (TT) | 83 | 0.43 ± 0.09 | 36 |
| NiCuLa | 33 | 0.37 ± 0.08 | 21 |
| NiCuLa (HPT) | 23 | 0.37 ± 0.08 | 27 |

$\bar{d}$ : average particle size of the powders;

$R^a_{eff}$ : effective atomic ratio (active Ni atoms/total atoms);

in the case of the sample Cu50 the value indicated refers to Cu atoms;

$S_{BET}$: specific surface area.

The average particle size of Ni50 increases strongly after hydrogen pre-treatment, while the opposite is observed for Ni30. The average particle sizes are kept small, upon addition of $La_2O_3$ followed by hydrogen pretreatment, showing that $La_2O_3$ acts as a good structural promoter. The NiCuLa (HPT) catalyst shows the lowest value (23 μm), which can be explained by particle fragmentation (effect of HPT), phase transformation (Ni-Cu alloy formation), and texture reorientation ($La_2O_3$ incorporation) during HPT process. A slightly higher value (33 μm) was found for the untreated physical mixture of NiCuLa.

$La_2O_3$ shows a small BET surface area. The Ni50 (HPT) and Ni30 (HPT) catalysts show BET surfaces areas smaller than the respective untreated catalysts, due to sinterization.

The addition of $La_2O_3$ to Ni50 decreases strongly the BET surface area, while the $La_2O_3$ doped Ni30 catalyst is less sensitive to that. After a hydrogen treating procedure of the same catalyst, the surface area is more or less half of the untreated Ni30. The surface area of the Ni50La (HPT) system is similar to that of the same untreated catalyst, but higher than the Ni50 (HPT) one.

The surface area of NiCuLa is 21 $m^2/g$. The Ni30 (HPT), Ni30Cu50 (ITT) and the Ni30La (HPT) catalysts show BET values near to the measured value for NiCuLa (HPT). Thus, the hydrogen pre-treatment, the alloy formation between Ni and Cu and the physical interactions of the involved phases reduce the BET surface areas and average particle sizes.

Table 5.4 collects the XPS data of the catalytic systems used. It has been reported by Cesteros et al., that in Ni catalysts, lanthanum migrates from the bulk to the surface [29]. The XPS spectra show overlapping of Ni $2p^{3/2}$ and La $3d^{5/2}$ levels in the Raney-Ni catalysts doped with $La_2O_3$. Therefore, quantification was only possible by the use of the less intensive Ni $3p^{3/2}$ singlet energy level [30,31]. The bond energies of Ni are in the region of zero valent state, meaning that Ni was not oxidized by $La_2O_3$. The XPS spectra obtained for Ni50 (HPT) and Ni30 (HPT) show significant losses of Ni atoms exposed on surface. Nevertheless, Ni30 (HPT) exhibits nearly twice as many Ni atoms on surface than Ni50 (HPT), which is probably related to the microstructure. A lot of aluminium (>80 %) is found on catalyst surface due to phase segregation.

Table 5.4

Surface characterization of the Raney-type catalysts

| Catalyst | Ni | | Cu | La | $Al^{3+}$ | | | | |
|---|---|---|---|---|---|---|---|---|---|
| | $2p^{3/2}$ [eV] | $3p^{3/2}$ [eV] | $2p^{3/2}$ [eV] | $3d^{5/2}$ [eV] | 2p [eV] | $R^a_{Ni}$ | $R^a_{Cu}$ | $R^a_{La}$ | $R^a_{Al}$ |
| Ni50 | 853.5 | / | / | / | 74.0 | 0.75 | / | / | 0.25 |
| Ni50 (HPT) | 852.5 | / | / | / | 74.5 | 0.09 | / | / | 0.91 |
| Ni50La | / | 67.1 | / | 834.6 | 73.4 | 0.28 | / | 0.48 | 0.24 |
| Ni50La (HPT) | / | 64.1 | / | 834.7 | 74.1 | 0.08 | / | 0.05 | 0.87 |
| Ni30 | 854.0 | / | / | / | 73.9 | 0.80 | / | / | 0.20 |
| Ni30 (HPT) | 852.2 | / | / | / | 74.3 | 0.17 | / | / | 0.83 |
| Ni30La | / | 67.4 | / | 834.8 | 73.6 | 0.45 | / | 0.06 | 0.49 |
| Ni30La (HPT) | / | 65.2 | / | 834.7 | 73.7 | 0.13 | / | 0.07 | 0.80 |
| Cu50 | / | / | 931.2 | / | 73.5 | / | 0.43 | / | 0.57 |
| Ni30Cu50 (ITT) | 856.5 | / | 932.0 | / | 74.2 | 0.10 | 0.13 | / | 0.77 |
| NiCuLa (HPT) | / | 64.5 | 932.3 | 835.4 | 74.3 | 0.04 | 0.11 | 0.12 | 0.73 |

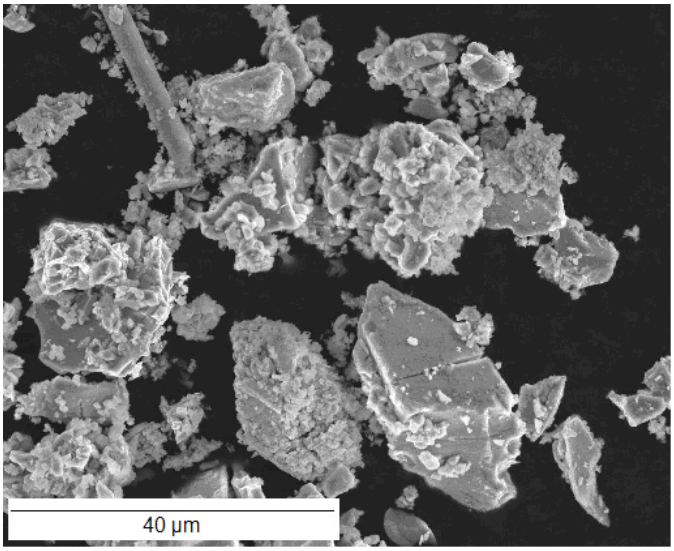
$R^a$ : atomic fraction on catalyst surface.

The Ni atoms exposed on the surface of Ni30La corresponds to an atomic fraction of 0.45, higher than for the Ni50La system (0.28). On the other hand, the exposed La atoms on the surface of Ni50La are 8 times higher than for Ni30La, suggesting that $La_2O_3$ is better incorporated on Ni30. The Ni atoms exposed on the catalyst surface, after hydrogen pre-treatment of the Ni-$La_2O_3$ catalytic systems are in the range of the above discussed Ni30 (HPT) and Ni50 (HPT) catalysts. A significant reduction of La exposed on the surface, associated with a strong presence of $Al_2O_3$ is observed for Ni50La (HPT), suggesting that $La_2O_3$ promotes the segregation of $Al_2O_3$ to the surface.

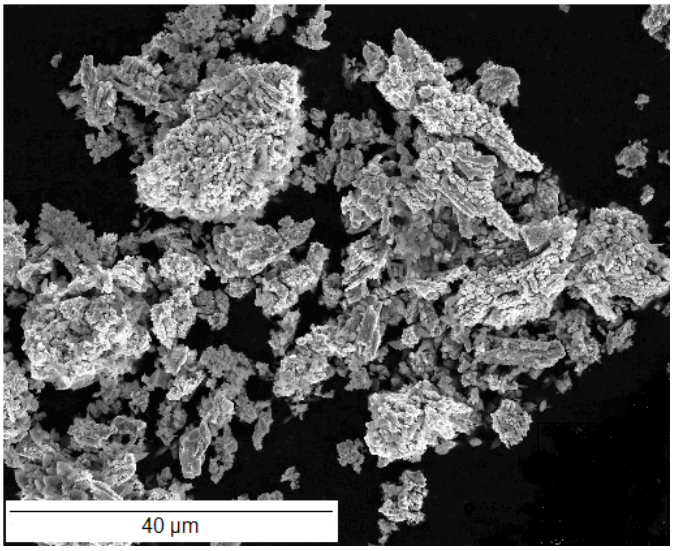
Nickel and Copper in NiCuLa (HPT) are mostly in the valent state, meaning that these metals were not significantly oxidized by $La_2O_3$.

Phase segregation of $Al_2O_3$ is observed after HPT or ITT treating processes in all catalytic systems, and the surface atomic fractions of aluminium are always between 0.73 and 0.91. Comparing Ni30La and Ni30La (HPT) shows that the lanthanum exposed on the surface does not change; however, an increase from 0.06 to 0.12 in lanthanum is observed for NiCuLa (HPT), showing higher segregation of $La_2O_3$. We suggest that $La_2O_3$ was mostly incorporated in the monometallic Ni30 texture, but less well incorporated in the bimetallic Ni-Cu one. The atomic fractions of Ni and Cu exposed on catalyst surface in the Ni30Cu50 (ITT) are very low, 0.10 for each metal, in good agreement with the mass input ratio of the used Me-Al alloys (Me = Ni and Cu). The NiCuLa (HPT) shows a surface concentration of Cu atoms which is higher than Ni. Lower amounts of Ni atoms are exposed on surface (0.04), when comparing Ni30Cu50 (ITT) with NiCuLa (HPT).

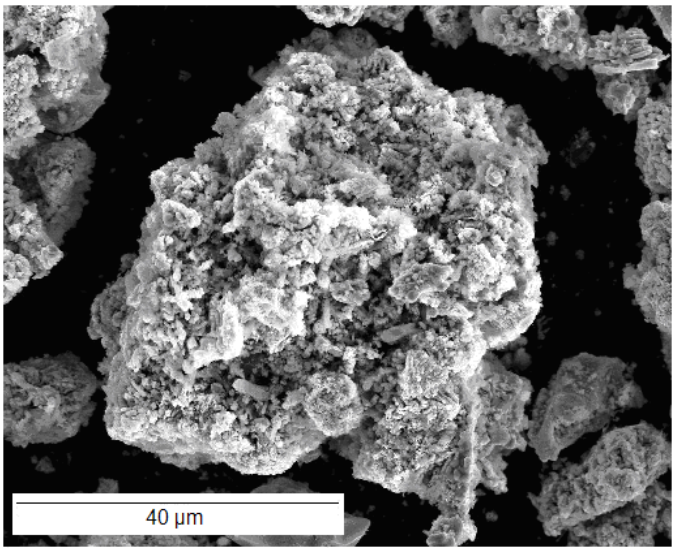
Figure 5.5 shows SEM micrographs of Ni50La (HPT), Ni30La (HPT) and NiCuLa (HPT) catalysts. The Ni catalysts are covered by a thin layer of $La_2O_3$. Apart from that layer, the presence of $La_2O_3$ agglomerates is clearly visible in the Ni50La (HPT) system. The original morphology of the Ni30 catalyst has been kept after hydrogen pre-treatment, and for Ni50 the surface became rougher [9]. It is interesting to observe that the NiCuLa (HPT) particles have a strongly amorphous structure. Moreover, the solid compound shows a phase distribution, where some particles are richer in Ni while others are richer in copper. The $La_2O_3$ phase is in most cases segregated from the metal compounds (observed in the backscattered image as bright points). The formerly dendritic structure of Ni30, and the flat structure of Cu50, are not present any more.




a)




b)




c)

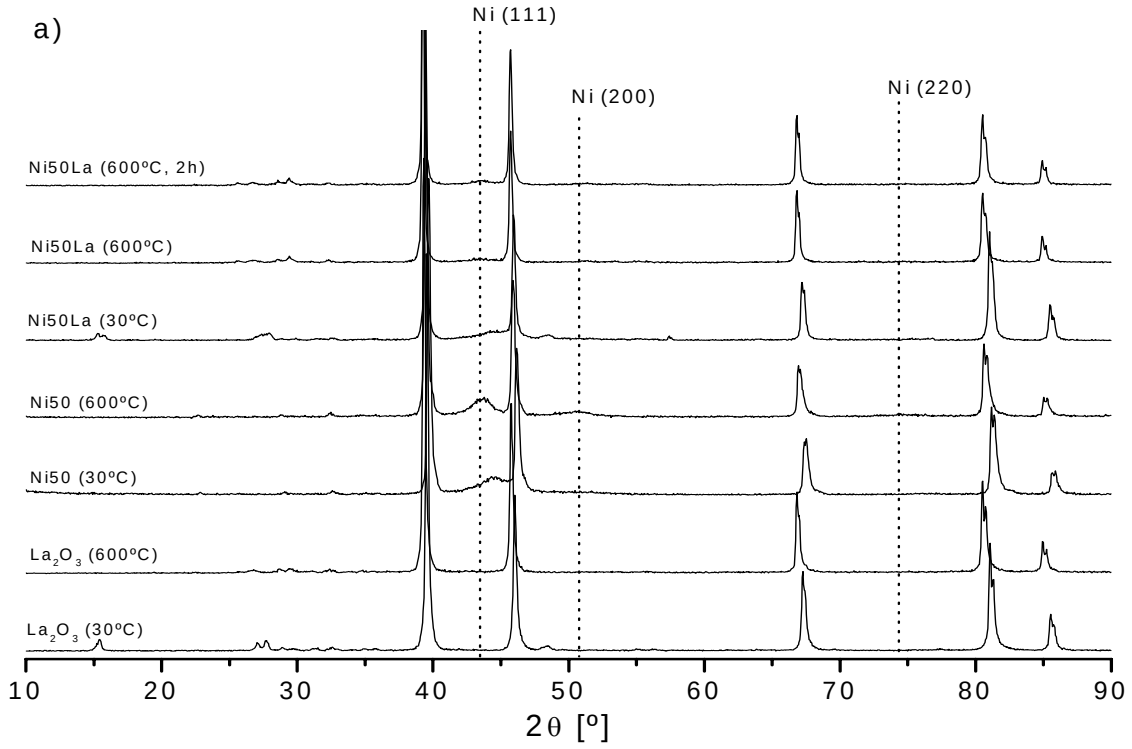
Fig. 5.5 SEM micrographs of Ni50La (HPT) (a), Ni30La (HPT) (b) and NiCuLa (HPT) (c) catalysts.

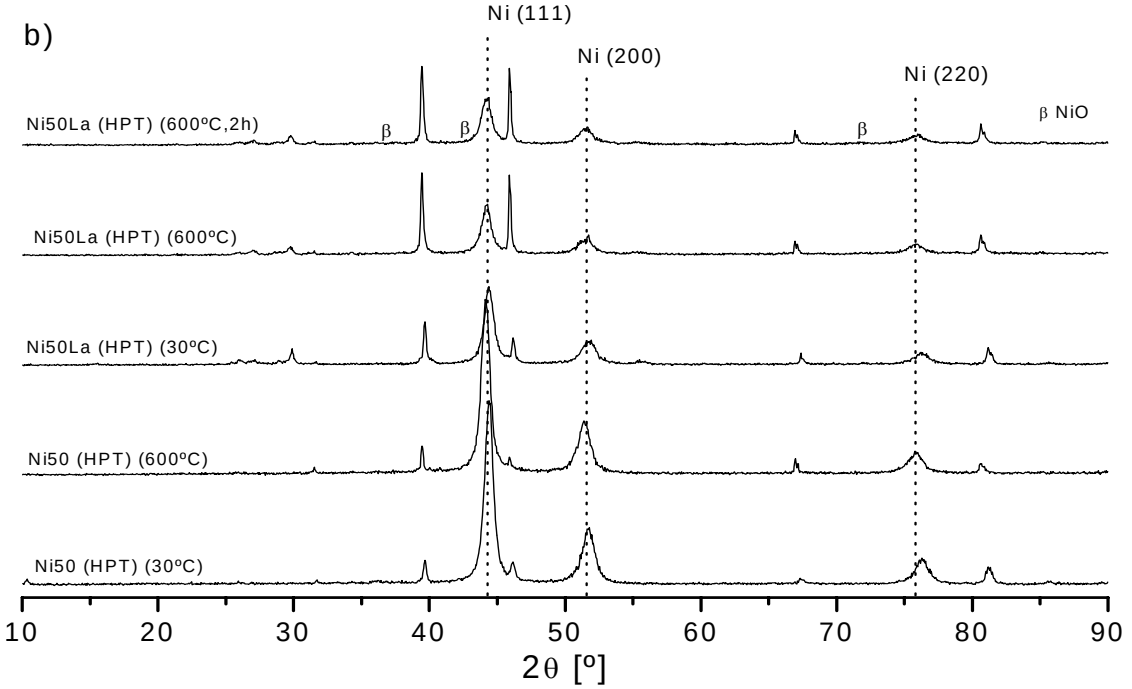
Figure 5.6 depicts the X-ray diffraction patterns of $La_2O_3$, untreated Ni and Cu Raney-type catalysts, hydrogen pre-treated Ni and Cu Raney-type catalysts, simple and hydrogen pre-treated Ni- $La_2O_3$ catalyst mixtures, at 30 ºC, 600 ºC and after treatment at 600 ºC for 2 hours, as well as the untreated physical catalyst mixture NiCuLa, and NiCuLa (HPT). The formation of any Perovskite- or Spinel-type phase has not been detected for the used catalytic systems [32-35]. Table 5.5 summarizes the phases identified by XRD.

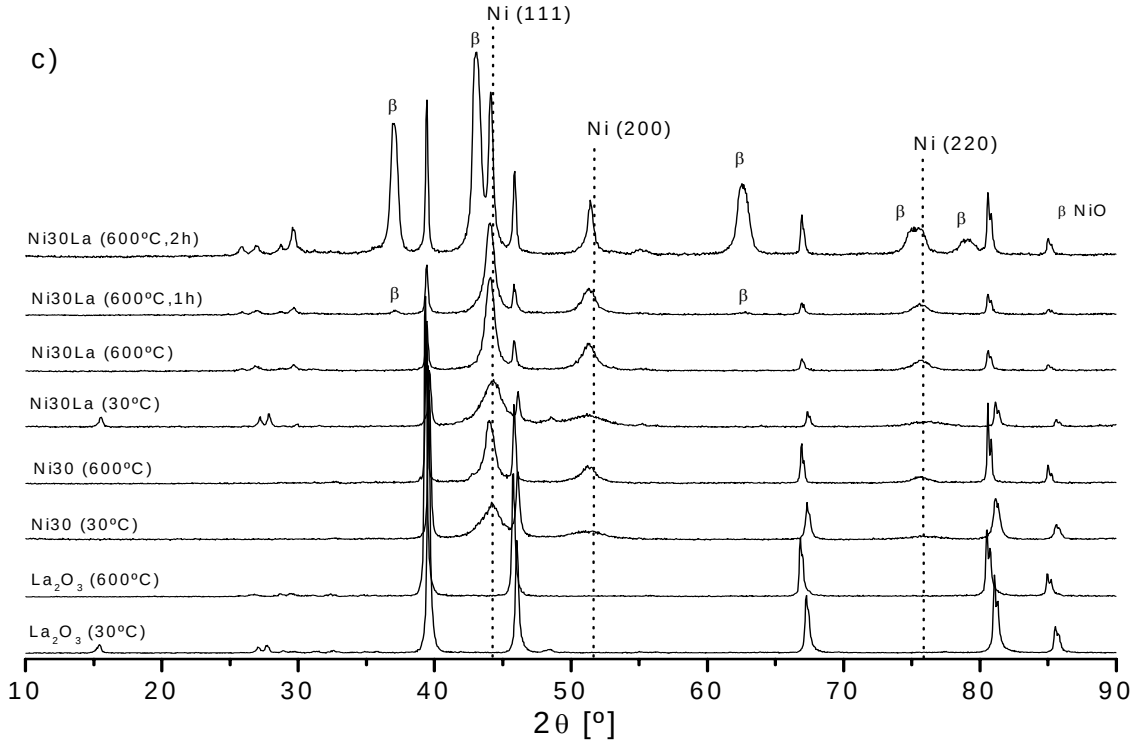
Table 5.6 collects the crystal sizes of $La_2O_3$, Ni50, Ni50 (HPT), Ni30, Ni30 (HPT), Cu50 and Cu50 (HPT) samples, as well as the crystal sizes of the $La_2O_3$ doped catalysts Ni50La, Ni50La (HPT), Ni30La, Ni30La (HPT), Cu50La, Cu50La (HPT), NiCuLa and NiCuLa (HPT) taken at 30 ºC, 600 ºC and after thermal treatment procedure at 600 ºC.

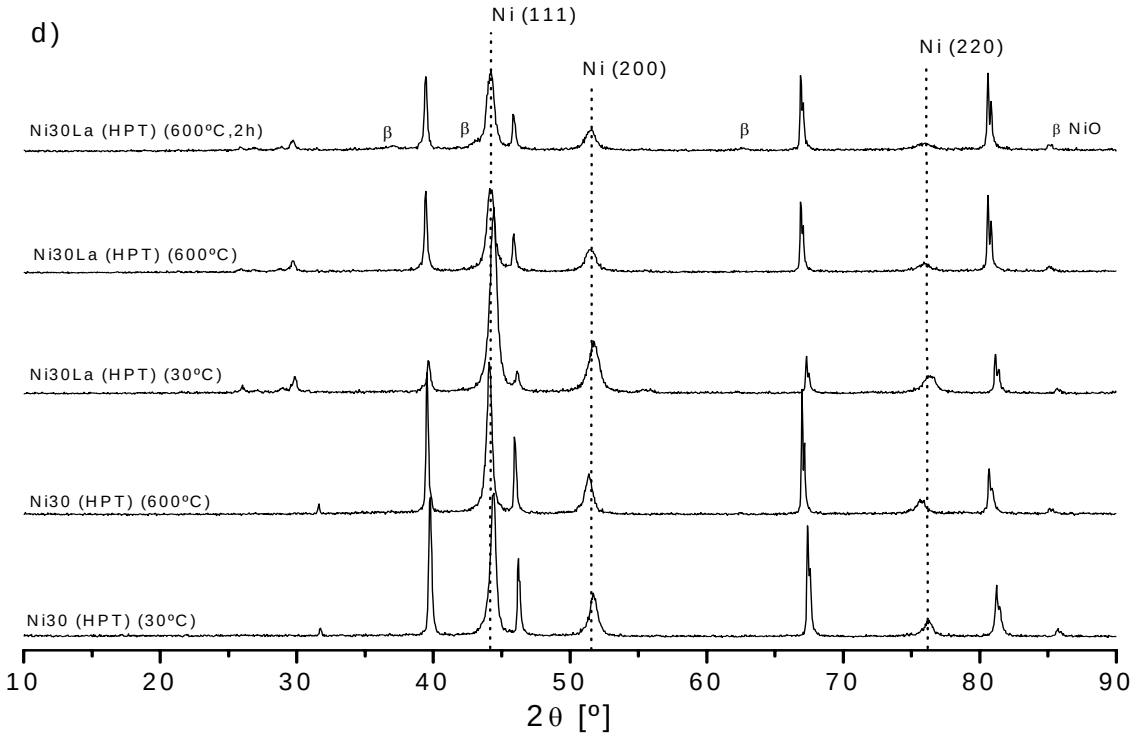
It has been reported that the crystal size influences the growth of CNF [36]. On one hand, large Ni crystals reduce the growth rate due to lower surface area exposition. On the other hand, too small sizes (≤3 nm) result in a "non metal-like state" due to the conducting band splitting into discrete energy levels, charge or electron transfers between particles and support. An optimum growth rate and yield of CNF can be achieved with Ni crystal sizes between 11-34 nm [37,38]. The crystal size of $La_2O_3$, at 600 ºC is approximately half of the value recorded at 30 ºC, due to the phase transformation of $La(OH)_3$ and $La_2O_3CO_2$ into $La_2O_3$. Cu50 (HPT) shows a crystal size of ~53 nm for Cu at 30 ºC. All other values for Cu in the Cu50 additive are in the range of 17-26 nm. Except for Ni30 (HPT) catalyst, which shows crystal sizes of ~31 nm, all other Raney-Ni systems (Ni50, Ni50 (HPT) and Ni30) have crystal sizes in a narrow range between 10-14 nm. The hydrogen pre-treatment of Ni30 increases its crystal sizes more than 3 times.

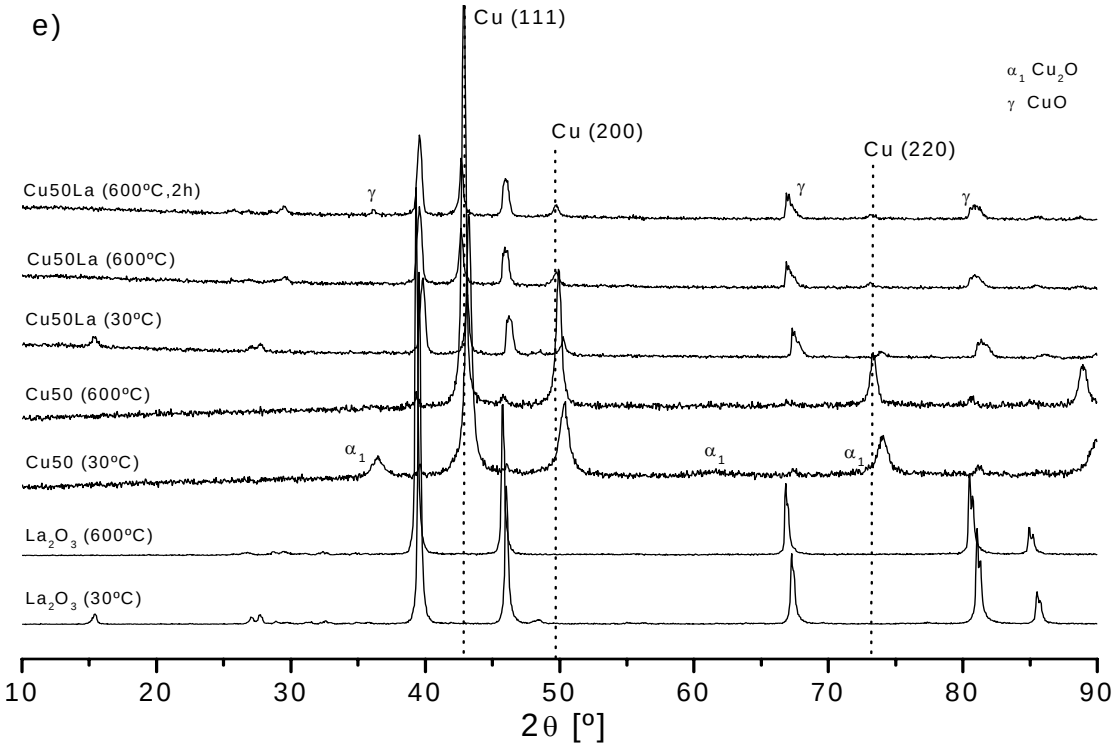
The introduction of $La_2O_3$ as promoter plays an important role in the crystal sizes of the metals. At 30 ºC, the crystal sizes of Ni are between 9 to 15 nm. In the case of Ni30 the Ni crystal size increases to ~31 nm upon HPT. For the Ni50La system the values of Ni50 and $La_2O_3$ are close at 600 ºC. However, at 600 ºC the crystal size of Ni increases substantially to ~52 nm, simultaneously some losses are observed for $La_2O_3$ (~35 nm). After 2h of thermal treatment a slight decrease is found for Ni (~49 nm), while for $La_2O_3$ an increase to ~ 43 nm is found. The same phenomenon is observed for the Ni50La (HPT) system, however after 2 h of thermal treatment, a new NiO phase appears, with an approximately crystal size value of 35 nm and near the Ni value of ~31 nm.

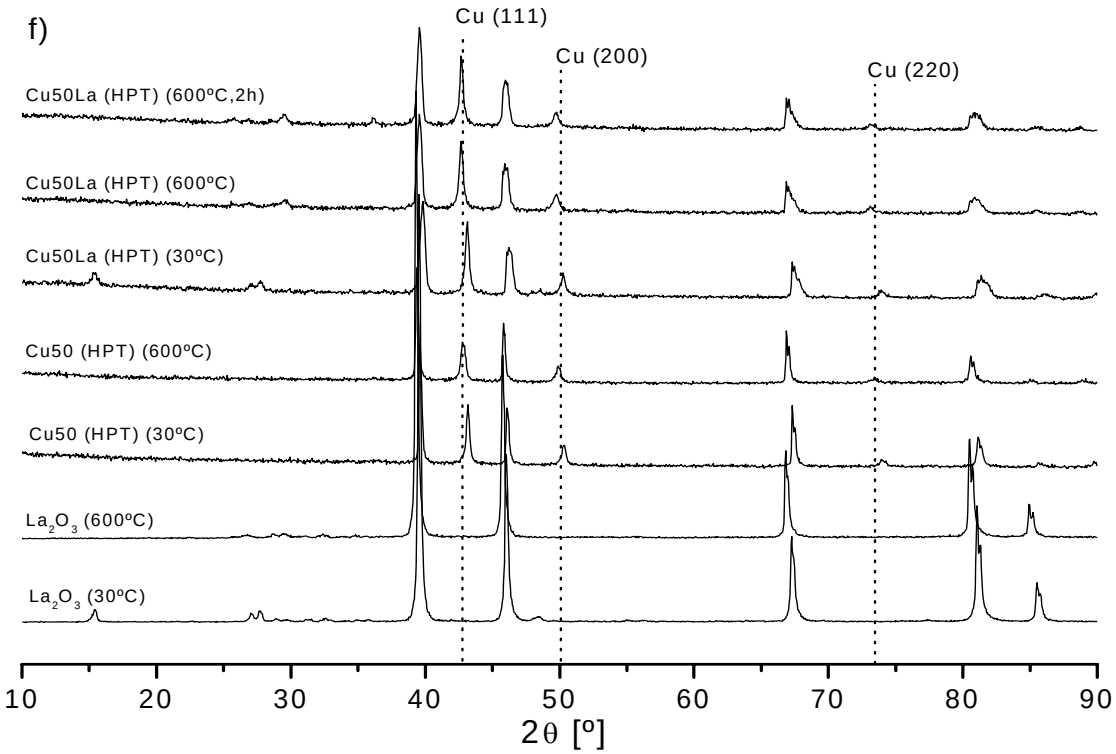

a)
Ni (111)
Ni (200)
Ni (220)
Ni50La (600ºC, 2h)
Ni50La (600ºC)
Ni50La (30ºC)
Ni50 (600ºC)
Ni50 (30ºC)
La2O3 (600ºC)
La2O3 (30ºC)
10 20 30 40 50 60 70 80 90
2θ [º]


b)
Ni (111)
Ni (200)
Ni (220)
β
β
β
β NiO
Ni50La (HPT) (600ºC,2h)
Ni50La (HPT) (600ºC)
Ni50La (HPT) (30ºC)
Ni50 (HPT) (600ºC)
Ni50 (HPT) (30ºC)
10 20 30 40 50 60 70 80 90
2θ [º]


c)
Ni (111)
Ni (200)
Ni (220)
β
β NiO
Ni30La (600ºC,2h)
Ni30La (600ºC,1h)
Ni30La (600ºC)
Ni30La (30ºC)
Ni30 (600ºC)
Ni30 (30ºC)
La2O3 (600ºC)
La2O3 (30ºC)
10 20 30 40 50 60 70 80 90
2θ [º]


d)
Ni (111)
Ni (200)
Ni (220)
β
β NiO
Ni30La (HPT) (600ºC,2h)
Ni30La (HPT) (600ºC)
Ni30La (HPT) (30ºC)
Ni30 (HPT) (600ºC)
Ni30 (HPT) (30ºC)
10 20 30 40 50 60 70 80 90
2θ [º]


e)
Cu (111)
Cu (200)
Cu (220)
α1 Cu2O
γ CuO
Cu50La (600ºC,2h)
Cu50La (600ºC)
Cu50La (30ºC)
Cu50 (600ºC)
Cu50 (30ºC)
La2O3 (600ºC)
La2O3 (30ºC)
γ
α1
10 20 30 40 50 60 70 80 90
2θ [º]


f)
Cu (111)
Cu (200)
Cu (220)
Cu50La (HPT) (600ºC,2h)
Cu50La (HPT) (600ºC)
Cu50La (HPT) (30ºC)
Cu50 (HPT) (600ºC)
Cu50 (HPT) (30ºC)
La2O3 (600ºC)
La2O3 (30ºC)
10 20 30 40 50 60 70 80 90
2θ [º]

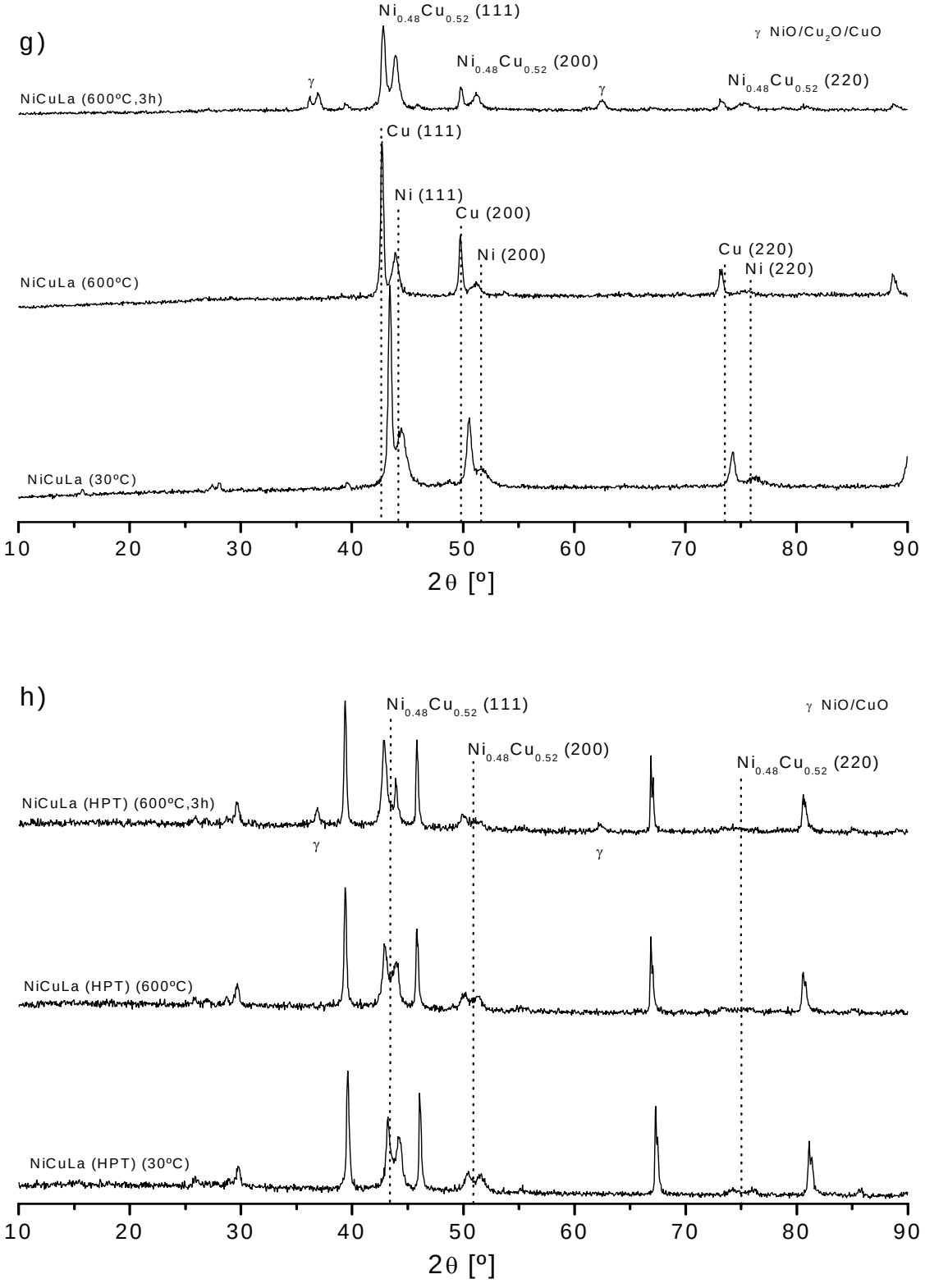



Fig. 5.6 XRD patterns of Ni50La (a), Ni50La(HPT) (b), Ni30La (c), Ni30La (HPT) (d), Cu50La (e), Cu50La (HPT) (f), NiCuLa (g) and NiCuLa (HPT) measured at 30 ºC, 600 ºC and after thermal treatment at 600 ºC.

Table 5.5

Phases identified in the catalysts (at 30, 600 ºC and after 2 h of in situ thermal treatment in vacuum 600 ºC) and corresponding 2θ positions

| Sample | T [ºC] | Phase | 2θ positions |
|---|---|---|---|
| $La_2O_3$ | 30 | hcp $La_2O_3$ | 27.7º (002)*, 28.9º (101)*, 49.5º (103)* |
| | | hcp $La(OH)_3$ | 15.5º (100)*, 27.1º (110)*, 27.7º (101)*, 31.4º (200)*, 35.8º (111)*, 39.6º (211)*, 48.1º (300)*, 48.5º (211)*, 56.1º (220)*, 63.7º (311)* |
| | | monoclinic $La_2O_3CO_2$ | 29.7º (013)*, 31.4º (-111)*, 34.2º (112)* |
| | 600 | hcp $La_2O_3$ | 29.7º (101)*, 39.4º (102)*, 55.7º (112)*, 80.5º (212)*, 85.0º (204)* |
| Ni50 | 30 | fcc Ni | 44.3º (111)* |
| | 600 | fcc Ni | 43.7º (111)*, 50.5º (200)*, 74.6º (220)* |
| | | α-$Al_2O_3$ | 39.5º (222)*, 45.7º (400)*, 67.0º (440)*, 80.7º (622)*, 85.0º (444)* |
| Ni50La | 30 | fcc Ni | 44.2º (111)* |
| | | fcc $La_2O_3$ | 27.5º (222)*, 29.9º (321)*, 39.5º (422)*, 55.5º (631)*, 81.1º (754)*, 85.7º (358)* |
| | | α-$Al_2O_3$ | 46.0º (400)*, 57.4º (422)*, 67.3º (440)* |
| | 600 | fcc Ni | 43.2º (111)* |
| | | hcp $La_2O_3$ | 25.7º (100)*, 28.6º (002)*, 29.4º (011)*, 51.6º (013)*, 55.3º (112)*, 80.5º (122)*, 84.9º (024)* |
| | 600# | fcc Ni | 45.7º (111)* |
| | | hcp $La_2O_3$ | 25.7º (100)*, 28.5º (011)* |
| Ni50 (HPT) | 30 | fcc Ni | 44.4º (111)*, 51.7º (200)*, 76.3º (220)* |
| | 600 | fcc Ni | 44.2º (111)*, 51.4º (200)*, 75.9º (220)* |
| Ni50La (HPT) | 30 | fcc Ni | 44.4º (111)*, 51.8º (200)*, 76.4º (220)* |
| | | hcp $La_2O_3$ | 14.9º (001)*, 25.8º (100)*, 28.8º (002)*, 29.9º (011)*, 45.9º (110)* |
| | 600 | fcc Ni | 44.2º (111)*, 51.7º (200)*, 75.8º (220)* |
| | | hcp $La_2O_3$ | 25.8º (100)*, 28.8º (002)*, 29.8º (011)*, 55.3º (112)*, 62.0º (202)* |
| | 600# | fcc Ni | 44.0º (111)*, 51.3º (200)*, 75.7º (220)* |
| | | rhombohedral NiO | 37.5º (003)*, 44.0º (202)*, 71.8º (214)* |
| | | fcc $La_2O_3$ | 27.0º (222)*, 28.8º (321)*, 31.5º (400)*, 55.3º (444)* |
| Ni30 | 30 | fcc Ni | 44.2º (111)*, 51.6º (200)*, 75.7º (220)* |
| | 600 | fcc Ni | 44.0º (111)*, 51.4º (200)*, 75.7º (220)* |
| Ni30La | 30 | fcc Ni | 44.3º (111)*, 51.5º (200)*, 76.3º (220)* |
| | | hcp $La(OH)_3$ | 15.5º (100)*, 27.2º (110)*, 27.8º (101)*, 31.4º (200)*, 48.6º (211)*, 64.1º (311)* |
| | 600 | fcc Ni | 44.1º (111)*, 51.3º (200)*, 75.6º (220)* |
| | | hcp $La_2O_3$ | 25.9º (100)*, 28.8º (002)*, 29.6º (101)*, 62.0º (202)* |
| | 600[1h] | fcc Ni | 44.1º (111)*, 51.3º (200)*, 75.8º (220)* |
| | | hcp $La_2O_3$ | 26.0º (100)*, 28.8º (002)*, 29.7º (101)* |
| | | rhombohedral NiO | 37.0º (101)*, 62.7º (104)* |
| | 600# | fcc Ni | 44.1º (111)*, 51.5º (200)*, 75.6º (220)* |
| | | hcp $La_2O_3$ | 25.9º (100)*, 28.7º (002)*, 29.7º (101)*, 74.8º (211)*, 78.7º (114) |
| | | rhombohedral NiO | 37.2º (101)*, 62.9º (104)*, 75.6º (113)*, 79.2º (202)* |
| Ni30 (HPT) | 30 | fcc Ni | 44.4º (111)*, 51.7º (200)*, 76.3º (220)* |
| | 600 | fcc Ni | 44.1º (111)*, 51.4º (200)*, 75.7º (220)* |

| | | | |
|---|---|---|---|
| Ni30La (HPT) | 30 | fcc Ni | 44.4º (111)*, 51.7º (200)*, 76.3º (220)* |
| | | hcp $La_2O_3$ | 25.8º (100)*, 28.9º (002)*, 29.8º (011)*, 55.3º (112)*, 56.0º (201)*, 62.0º (202)*, 72.3º (023)* |
| | 600 | fcc Ni | 44.2º (111)*, 51.5º (200)*, 76.0º (220)* |
| | | $La_2O_3$ | 25.7º (100)*, 28.5º (002)*, 29.7º (011)*, 55.7º (201)* |
| | 600# | fcc Ni | 44.2º (111)*, 51.5º (200)*, 76.0º (220)* |
| | | hcp $La_2O_3$ | 25.7º (100)*, 28.6º (002)*, 29.7º (011)*, 55.2º (112)* |
| | | NiO | 37.0º (021)*, 62.8º (024)* |
| Cu50 | 30 | fcc Cu | 43.2º (111)*, 50.4º (200)*, 74.0º (220)* |
| | | fcc $Cu_2O$ | 36.9º (111)*, 61.5º (220)*, 74.0º (311)* |
| | 600 | fcc Cu | 42.9º (111)*, 49.9º (200)*, 73.3º (220)*, 88.9º (311)* |
| Cu50La | 30 | fcc Cu | 43.5º (111)*, 50.7º (200)*, 74.0º (220)* |
| | | fcc $Cu_2O$ | 36.2º (111)*, 61.4º (220)* |
| | | hcp $La(OH)_3$ | 15.6º (100)*, 27.1º (110)*, 39.5º (201)*, 48.8º (211)*, 76.1º (222)* |
| | 600 | fcc Cu | 42.8º (111)*, 49.8º (200)*, 73.3º (220)*, 88.9º (311)* |
| | | CuO | 36.2º (-111)*, 39.7º (200)*, 67.0º (310)*, 80.7º (-114)*, 88.9º (130)* |
| | | fcc $La_2O_3$ | 26.9º (222)*, 29.7º (321)*, 61.3º (246)* |
| | 600# | fcc Cu | 42.8º (111)*, 49.8º (200)*, 73.2º (220)* |
| | | CuO (Tenorite) | 36.2º (-111)*, 39.8º (200)*, 62.5º (-113)*, 67.2º (-311)*, 73.2º (311)*, 80.7º (-204)* |
| | | $Cu_2O$ (Cuprite) | 37.0º (111)*, 62.5º (220)*, 78.5º (222)* |
| | | $La_2O_3$ | 27.1º (222)* |
| Cu50 (HPT) | 30 | fcc Cu | 43.2º (111)*, 50.3º (200)*, 73.9º (220)* |
| | 600 | fcc Cu | 42.8º (111)*, 49.9º (200)*, 73.4º (220)* |
| Cu50La (HPT) | 30 | fcc Cu | 43.1º (111)*, 50.2º (200)*, 74.0º (220)* |
| | | hcp $La(OH)_3$ | 15.4º (100)*, 27.1º (110)*, 27.8º (101)*, 39.8º (201)*, 48.5º (211)*, 77.9º (321)* |
| | 600 | fcc Cu | 42.7º (111)*, 49.7º (200)*, 73.1º (220)* |
| | | hcp $La_2O_3$ | 25.7º (100)*, 28.7º (002)*, 29.6º (101)*, 55.3º (112)* |
| | 600# | fcc Cu | 42.7º (111)*, 49.7º (200)*, 73.2º (220)* |
| | | CuO | 36.2º (-111)*, 67.0º (310)* |
| | | hcp $La_2O_3$ | 25.8º (100)*, 28.5º (002)*, 29.5º (101)*, 55.8º (112)* |
| NiCuLa | 30 | fcc Cu | 43.4º (111)*, 50.6º (200)*, 74.3º (220)* |
| | | fcc Ni | 44.5º (111)*, 51.7º (200)*, 76.4º (220)* |
| | | hcp $La(OH)_3$ | 15.9º (100)*, 27.2º (110)*, 28.0º (101)*, 39.6º (201)*, 49.0º (211)* |
| | 600 | fcc Cu | 42.7º (111)*, 49.7º (200)*, 73.3º (220)*, 88.7º (311)* |
| | | fcc Ni | 43.9º (111)*, 51.3º (200)*, 75.3º (220)* |
| | | hcp $La_2O_3$ | 27.4º (002)*, 53.8º (20-1)* |
| | 600# | fcc $Ni_{0.48}Cu_{0.52}$ | 43.1º & 44.3º (111)*, 50.2º & 51.5º (200)*, 73.6º & 75.9º (220)*, |
| | | fcc Cu | 89.2º (311)* |
| | | NiO (Bunsenite) | 37.0º (111)*, 43.1º (200)*, 62.5º (220)* |
| | | fcc $La_2O_3$ | 27.2º (222)*, 36.8º (332)* |
| NiCuLa (HPT) | 30 | fcc $Ni_{0.48}Cu_{0.52}$ | 43.2º & 44.2º (111)*, 50.4º & 51.5º (200)*, 74.2º & 76.3º (220)* |
| | | hcp $La_2O_3$ | 25.9º (100)*, 28.5º (002)*, 29.8º (011)*, 55.2º (112)* |
| | 600 | fcc $Ni_{0.48}Cu_{0.52}$ | 43.0º & 44.0º (111)*, 50.1º & 51.3º (200)*, 73.5º & 75.9º (220)* |
| | | hcp $La_2O_3$ | 25.8º (100)*, 28.8º (002)*, 29.7º (011)*, 55.2º (112)* |
| | 600# | fcc $Ni_{0.48}Cu_{0.52}$ | 42.9º & 43.9º (111)*, 50.0º (200)*, 73.5º (220)* |
| | | fcc Cu | 88.9º (311)* |
| | | rhombohedral NiO | 36.9º (101)*, 62.5º (110)* |
| | | fcc $Cu_2O$ | 36.9º (101)*, 62.5º (220)* |
| | | hcp $La_2O_3$ | 25.9º (100)*, 29.1º (002)*, 29.6º (011)*, 51.8º (013)*, 55.5º (112)* |

#in situ thermal treated under vacuum during 2h before measurement;

*reflection plane.

Table 5.6

Average crystal sizes of the prepared samples

| Sample | T [°C] | $d_{Ni}$ [nm] | $d_{NiO}$ [nm] | $d_{Cu}$ [nm] | $d_{CuO}$ [nm] | $d_{La_2O_3}$ [nm] |
|---|---|---|---|---|---|---|
| $La_2O_3$ | 30 | / | / | / | / | 106.0 |
| $La_2O_3$ | 600 | / | / | / | / | 46.7 |
| Cu50 | 30 | / | / | 17.2 | / | / |
| Cu50 | 600 | / | / | 23.8 | / | / |
| Cu50 (HPT) | 30 | / | / | 53.1 | / | / |
| Cu50 (HPT) | 600 | / | / | 26.0 | / | / |
| Ni50 | 30 | 13.6 | / | / | / | / |
| Ni50 | 600 | 10.2 | / | / | / | / |
| Ni50 (HPT) | 30 | 11.2 | / | / | / | / |
| Ni50 (HPT) | 600 | 11.2 | / | / | / | / |
| Ni30 | 30 | 10.7 | / | / | / | / |
| Ni30 | 600 | 10.1 | / | / | / | / |
| Ni30 (HPT) | 30 | 31.3 | / | / | / | / |
| Ni30 (HPT) | 600 | 31.3 | / | / | / | / |
| Ni50La | 30 | 14.2 | / | / | / | 46.9 |
| Ni50La | 600 | 51.6 | / | / | / | 35.3 |
| Ni50La | 600# | 49.4 | / | / | / | 42.5 |
| Ni30La | 30 | 12.4 | / | / | / | 48.0 |
| Ni30La | 600 | 14.9 | / | / | / | 48.3 |
| Ni30La | 600# | 31.3 | 41.5 | / | / | 27.9 |
| Cu50La | 30 | / | / | 13.6 | / | 134.6 |
| Cu50La | 600 | / | / | 16.5 | 35.3 | 37.1 |
| Cu50La | 600# | / | / | 22.6 | 6.3 | 37.0 |
| NiCuLa | 30 | 9.4 | / | 36.6 | / | 97.5 |
| NiCuLa | 600 | 13.9 | / | 30.8 | / | 15.3 |
| NiCuLa | 600* | 39.0 | 33.1 | 39.0 | 33.1 | 31.4 |
| Ni50La (HPT) | 30 | 11.1 | / | / | / | 47.6 |
| Ni50La (HPT) | 600 | 38.9 | / | / | / | 23.4 |
| Ni50La (HPT) | 600# | 31.3 | 34.5 | / | / | 48.2 |
| Ni30La (HPT) | 30 | 14.9 | / | / | / | 43.4 |
| Ni30La (HPT) | 600 | 11.6 | / | / | / | 43.8 |
| Ni30La (HPT) | 600# | 43.1 | 34.7 | / | / | 24.6 |
| Cu50La (HPT) | 30 | / | / | 90.2 | / | 15.0 |
| Cu50La (HPT) | 600 | / | / | 69.8 | / | 16.0 |
| Cu50La (HPT) | 600# | / | / | 26.7 | 30.4 | 34.1 |
| NiCuLa (HPT) | 30 | 13.3 | / | 22.3 | / | 19.3 |
| NiCuLa (HPT) | 600 | 16.1 | / | 16.1 | / | 15.2 |
| NiCuLa (HPT) | 600* | 60.7 | 28.6 | 60.7 | 28.6 | 20.9 |

#in situ thermal treated under vacuum during 2 h before measurement;

*in situ thermal treated under vacuum during 3 h before measurement.

The Ni30La and Ni30La (HPT) systems show similar crystal sizes for Ni, NiO and $La_2O_3$ at the respective temperatures and treating conditions. At 30 ºC and 600 ºC, the crystal sizes of both Ni (12-15 nm) and $La_2O_3$ (43-48 nm) are similar. After 2 h of catalyst treating at 600 ºC, the values of the Ni crystal sizes increase to ~31 nm (Ni30La) and ~43 nm in Ni30La (HPT), while the new NiO phase shows nearly the same crystal sizes as for Ni, ~42 nm for Ni30La and ~35 nm for Ni30La (HPT). However, marked crystal size losses are detected for $La_2O_3$ (25-28 nm).

For the Cu50La and Cu50La (HPT) system the crystal sizes of the respective compounds show significant variations. At 30 ºC, 600 ºC and after 2 h of thermal treatment at 600 ºC the Cu crystals in the Cu50La system show a size increase from ~14 to 23 nm. For the Cu50La (HPT) the opposite case is observed where the Cu crystal sizes decrease from ~90 nm to ~27 nm when the temperature increases from 30 ºC to 600 ºC and is maintained for 2 h at 600 ºC. At the same time the crystallite size of $La_2O_3$ increases from ~15-16 nm to ~34 nm, and the appearance of CuO with a crystal size of ~30 nm is observed.

Finally, the crystal sizes of the NiCuLa system as well as the NiCuLa (HPT) were also analyzed. The sizes of the Ni-Cu alloy crystallites in the NiCuLa (HPT) catalytic system increase from ~13 nm to 61 nm when the temperature is increased from 30 ºC to 600 ºC and stabilized during 3 h. After the thermal treatment procedure, the NiO and CuO crystallites grow up to ~29 nm.

For the untreated NiCuLa system, the crystal sizes show similar behavior, but during the heating process from 30 ºC to 600 ºC, the crystal sizes of Ni (9-14 nm) and Cu (31-37 nm) differ due to the starting process of Ni-Cu alloy formation. Upon three hours of thermal treatment at 600 ºC, the crystal sizes of Ni and Cu are nearly equal due to the formation of a $Ni_{0.48}Cu_{0.52}$ alloy. Again, NiO and CuO appear after this thermal treating process, with crystal sizes of ~33 nm.

### 5.7.2 Catalysts performance

#### *5.7.2.1 Preliminary tests*

The desorption of water, chemically incorporated in $La_2O_3$ as $La(OH)_3$, was evaluated by temperature programmed desorption (TPD) and differential scanning calorimetry (DSC). The first $H_2O$ peak (m/z = 18) is observed in the temperature range between 220 and 320 ºC, and a second less intense one between 350 and 480 ºC. The DSC test shows also two peaks corresponding to $H_2O$ as observed above. The first one, between 275 and 350 ºC, is stronger than the second, which has been detected between 450 and 520 ºC. The process of $H_2O$ release is endothermic, as expected. Since two peaks were observed, we can assume that two processes of water release take place. The first step is a chemical reaction of the type:

$La(OH)_3 \rightleftharpoons LaOOH + H_2O(g)$ and the second is, most probably, the removal of adsorbed traces of water $2LaOOH \rightleftharpoons La_2O_3 + H_2O(g)$.

Prior to the isothermal runs, temperature programmed reaction experiments (TPRe) were carried out in order to determine the temperature range where the NiCuLa (HPT) is active for methane decomposition. The results showed that the catalyst is active above 400 ºC, without any $CO_x$ formation.

#### *5.7.2.2 Isothermal tests*

Bearing in mind previously reported results [9,14], it was decided to carry out isothermal catalytic tests in the temperature range of 400-900 ºC. Catalysts were evaluated on stream and the effects of the physical catalyst mixtures, mass composition, hydrogen pre-treating temperature, catalyst mass, temperature and feed gas composition were investigated.

Activities of catalysts are assessed by comparing the maximum conversions with the calculated equilibrium conversions. Stability is assessed by comparing the maximum conversions with the conversions at the end of at least 5 hours on stream.

The carbon yields obtained in all the experiments were in good agreement with the methane conversion values.

The effect of catalyst composition in Ni-$La_2O_3$ systems, at 600 ºC and with a volumetric flow rate of 110 $Ncm^3/min$ is shown in Figure 5.7.

Figure 5.7a depicts the mass ratio effect of the Ni50La catalyst mixture for methane decomposition as function of the reaction time at 600 ºC. It is observed that $La_2O_3$ itself shows residual activities of ~2 %. The Ni50 catalyst, without $La_2O_3$ as promoter, shows high methane conversions initially, but is quickly deactivated. The addition of $La_2O_3$ increases the catalyst stability, especially when the Ni50La catalytic system went through an in situ pre-treatment in hydrogen. However, smaller amounts of the more active Ni phase lead to earlier catalyst deactivation and smaller activities.

Figure 5.7b shows the mass composition effect of the Ni50La catalyst system, at 600 ºC with a total Ni50 mass of 0.5 g. It is observed that the Ni50La (HPT) catalyst has a certain optimum $La_2O_3$ mass content in the range of 0.06-0.586 g in which it performs significantly better than Ni50 or Ni50 (HPT) catalysts. The untreated Ni50La catalyst shows similar or slightly worse catalytic behaviour than the Ni50 catalyst.

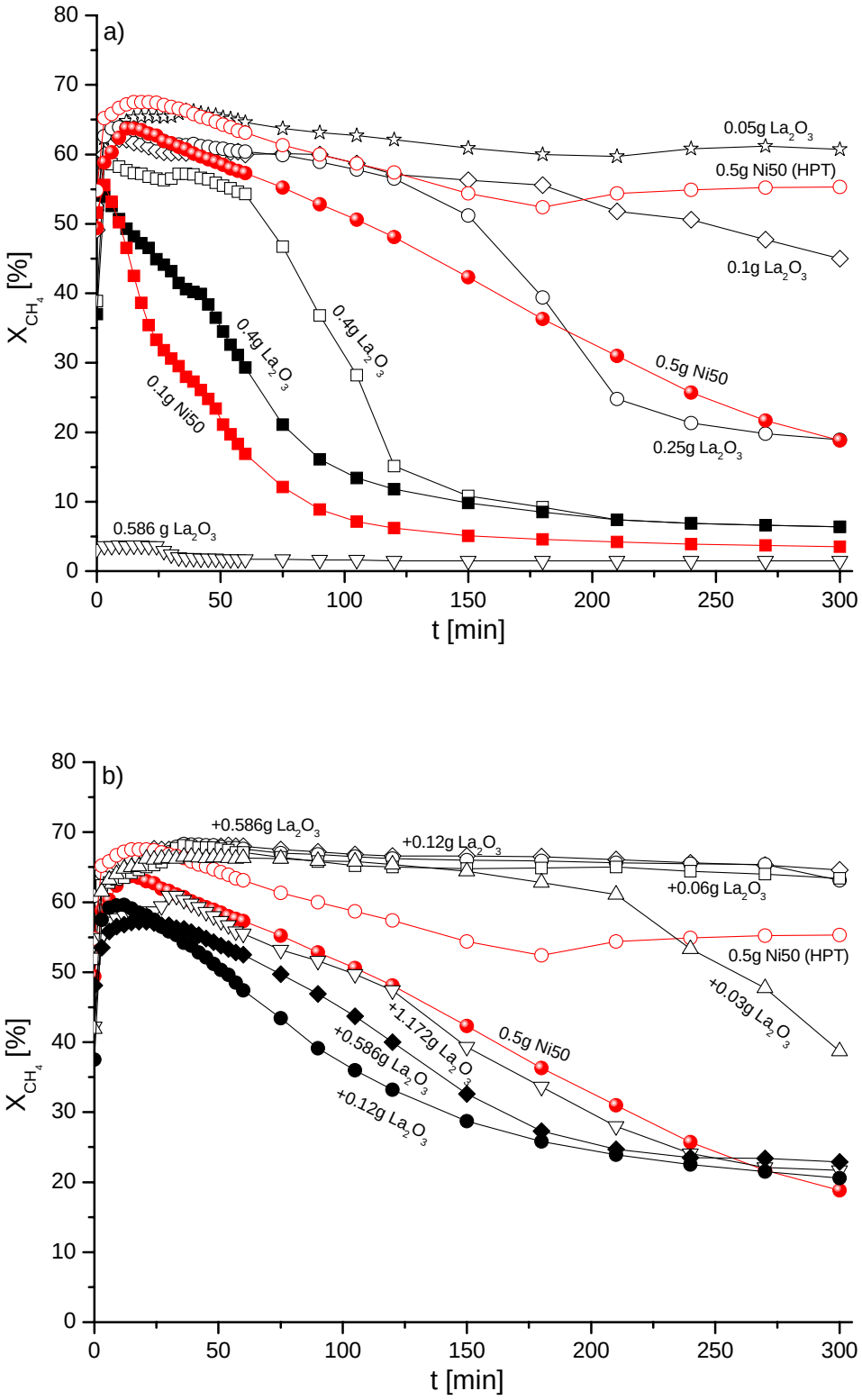



Fig. 5.7 Methane conversion as function of reaction time with Ni50La (filled symbols) and Ni50La (HPT) (open symbols) at 600 ºC and a flow-rate of 110 $Ncm^3$/min: a) Composition effect, keeping the total mass equal to 0.5 g; b) Composition effect, keeping the Ni mass equal to 0.5 g.

Figure 5.8 shows the mass ratio effect on the Ni30La system with a total Ni mass of 0.5 g at 600 ºC. It is shown that an optimum $La_2O_3$ content in Ni30, between 0.03-0.06 g, performs a stable operation, when the catalyst has been in situ hydrogen pre-treated. Above these amounts of $La_2O_3$, there is no significant stabilizing effect.

The Ni30 (HPT) catalyst shows less decrease in activity than the untreated Ni30 system. It may be also observed that the untreated Ni30La catalytic system (with 10.7 wt. % of $La_2O_3$) has a similar performance to the hydrogen pre-treated catalyst. This phenomenon was not observed for the untreated Ni50La catalytic system (cf. Fig. 5.7b).

The effect of the in situ hydrogen pre-treating temperature on 0.62 g of Ni50La catalytic system (19.4 wt % $La_2O_3$) was studied. It was observed that the ideal hydrogen pre-treating temperature is 600 ºC, when the reaction also proceeds at the same temperature and flow-rate. The catalytic system shows fast deactivation when the treatment temperature is raised above 600 ºC, most probably due to sinterization. Below hydrogen pre-treating temperatures of 600 ºC the catalyst is not effective enough for reaction stabilization, especially under a treating temperature of 500 ºC.

Figure 5.9 shows the effect of the reaction temperature which was tested between 400 and 900 ºC for 0.62 g of Ni50La (HPT). Below 600 ºC, the system is quite stable, but with low catalytic activities. Above 600 ºC, rapid catalyst deactivation is observed, and the higher the reaction temperature, the faster the deactivation process is, except at a reaction temperature of 900 ºC where high conversion are observed during the first hour, followed by a strong decay period between 60-180 min, and then a less pronounced deactivation. Most probably this is related to the very high reaction temperature and promoter effect of $La_2O_3$.

Figure 5.10 shows the effect of the feedstream composition for 0.62 g of the Ni50La (HPT) at 600 ºC and with a total flow-rate of 110 $Ncm^3$/min. For a small methane ratio of 0.048, the 2 h hydrogen pre-treated catalyst performs significantly better than the others. However, during the experimental run the activities approach the values measured with a methane/nitrogen ratio of 0.1. Curiously, if the catalyst has been treated with hydrogen only for 1 h, the system shows an activity drop after the first minutes of testing, and an increase until almost a constant level of ~80 % is achieved. This activity drops may be originated by another parallel reaction, perhaps the reaction between LaOOH with methane forcing the formation of $CO_x$. The higher the methane ratio in the feedstream, the greater is the stability at the expense of activity, which decreases. However, the activities recorded for methane ratios of 0.222, 0.571 and 1.0 show similar values and are higher than for Ni50 [9]. Hence, the promoting effect of $La_2O_3$ is here clearly visible.

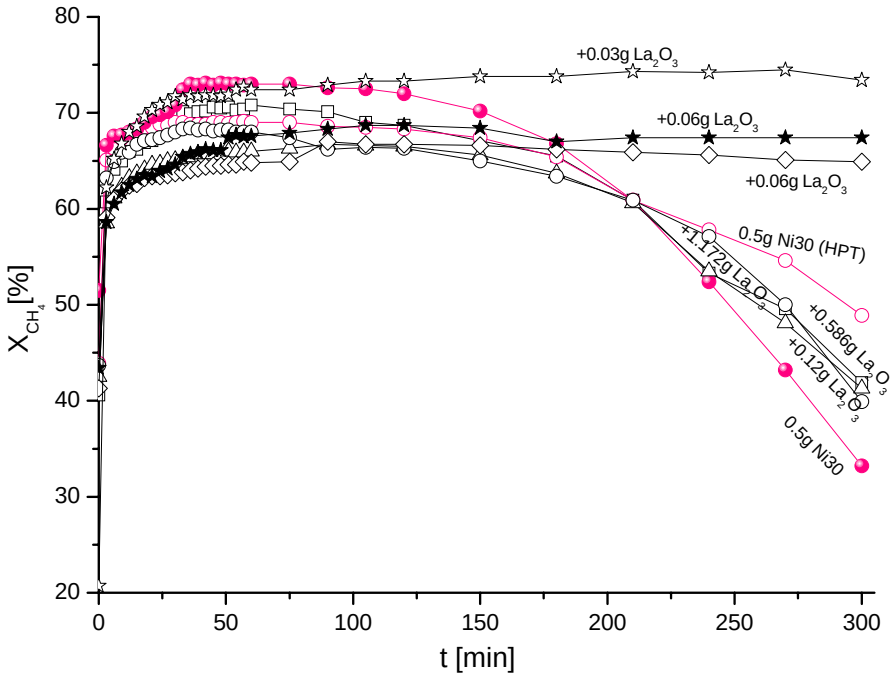



Fig. 5.8 Methane conversion as function of reaction time with Ni30La (filled symbols) and Ni30La (HPT) (open symbols) at 600 ºC and a flow-rate of 110 $Ncm^3/min$ ($CH_4/N_2$ = 0.1): Composition effect, keeping the Ni mass equal to 0.5 g.

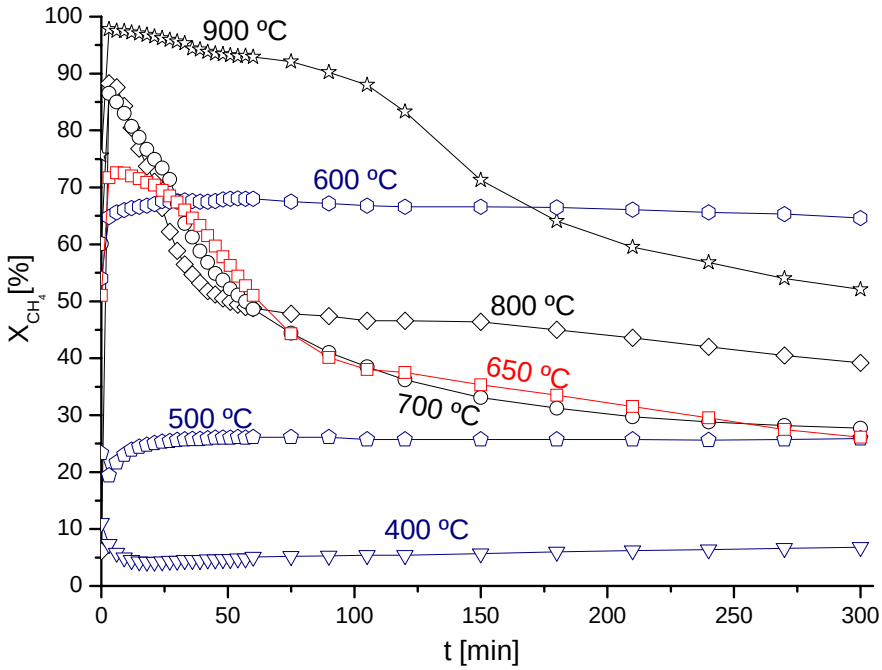



Fig. 5.9 Methane conversion as function of reaction time with Ni50La (HPT): Temperature effect with 0.62 g of catalyst and a flow-rate of 110 $Ncm^3/min$ ($CH_4/N_2$ = 0.1).

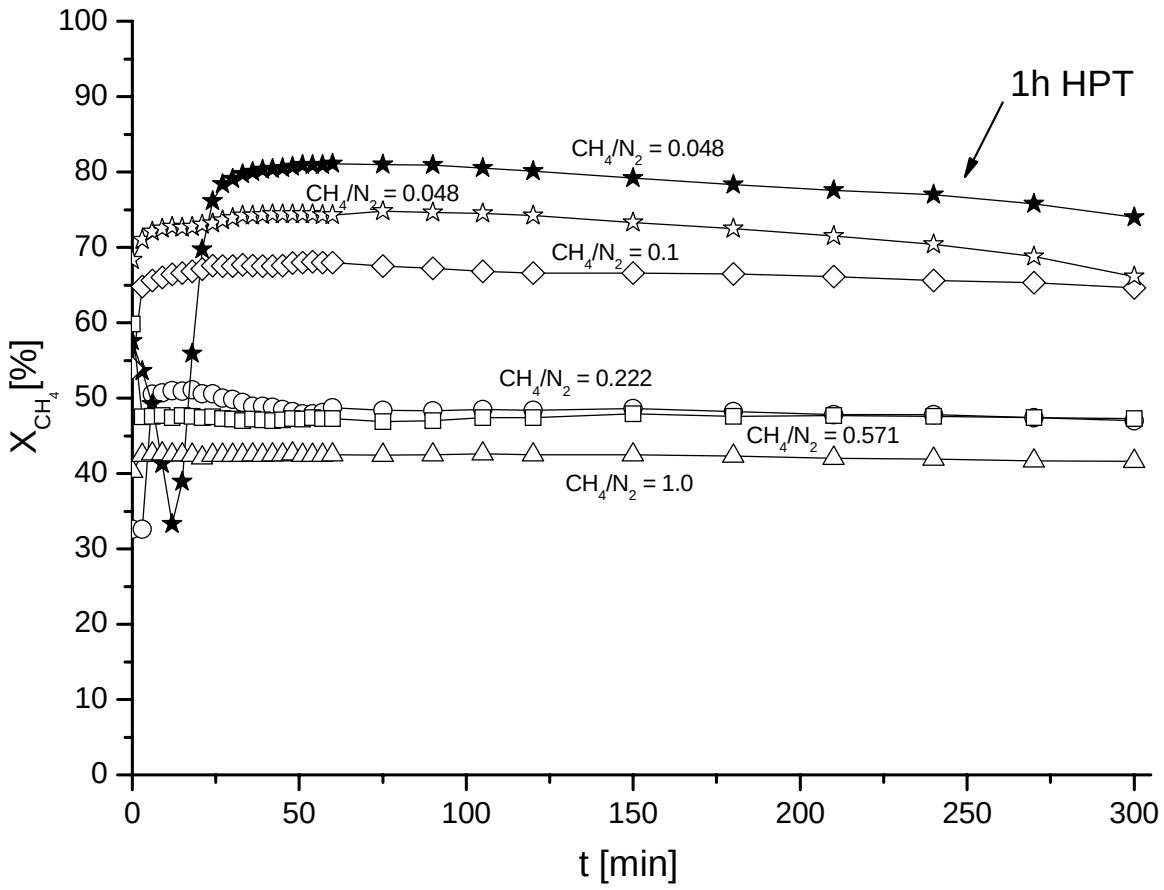



Fig. 5.10 Methane conversion as function of reaction time with Ni50La (HPT): Feed composition effect with 0.62 g (0.5 g Ni + 0.12 g $La_2O_3$) of catalyst, at 600 ºC and flow-rate of 110 $Ncm^3$/min.

Figure 5.11 shows the catalyst mass effect on NiCuLa (HPT) for methane conversion at 600 ºC. Not surprisingly, the higher the catalyst mass the higher the methane conversion. The four phase catalytic system requires less catalyst mass for stable run than the systems used previously, e.g., only 0.1 g of the most active nickel phase and 0.224 g overall catalyst mass is required for a stable run, while the Ni30 [9], Ni30Cu50 (ITT) [14] and Ni30La (HPT) phases require at least catalyst masses of 2.5 g, 1.0 g and 0.56 g, respectively. The highest methane conversion (~80 %) was obtained with 5.6 g of NiCuLa (HPT), which is close to the thermodynamic value of 88 %. It is also observed that the introduction of the Cu and $La_2O_3$ promoters decreases catalyst activity compared with that of the monometallic Ni30. The more phases are introduced, the lower is the catalyst activity; in return, the larger is the stability effect.

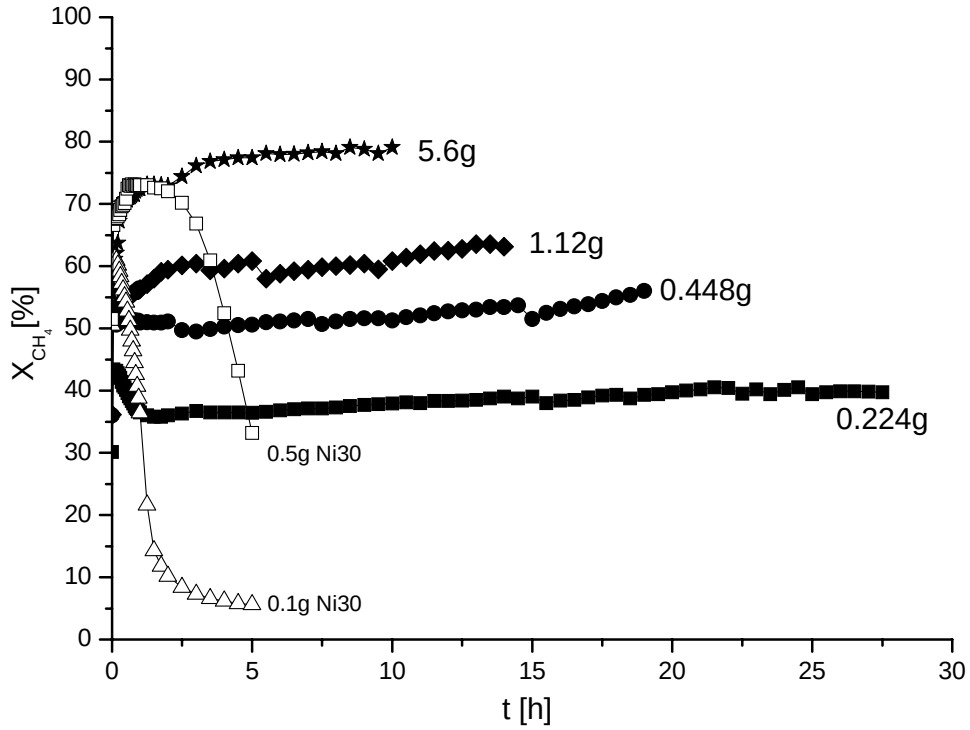



Fig. 5.11 Methane conversion as function of reaction time with NiCuLa (HPT): Catalyst mass effect at 600 ºC and a flow-rate of 110 $Ncm^3/min$ ($CH_4/N_2$ = 0.1).

Figure 5.12 depicts the effect of the temperature between 400-900 ºC on 1.12 g of NiCuLa (HPT). The catalyst is quite stable until 600 ºC, but rapid catalyst deactivation occurs at 700 ºC, and above. However, the higher the applied reaction temperature, the faster is the approximation of the initial conversions to thermodynamic values and the higher are the activities at steady-state. Not shown here is the effect of the methane concentration on 1.12 g of NiCuLa (HPT). At 700 ºC, the increase of methane in the feed brought a significant increase in catalyst stability, due to higher quantities of generated hydrogen during the reaction process. Unfortunately, the same effect could not be observed at 800 ºC. Possibly, the quantities of encapsulating carbon formed are too high to be re-hydrogenated by the hydrogen produced [9,39].

Figure 5.13 illustrates the effect of the catalyst mass on NiCuLa (HPT) in a pure methane flow rate of 10 $Ncm^3/min$ at 700 ºC. It is clearly shown that the use of a pure methane feed stabilizes significantly the performance of the catalyst. Moreover, 0.224 g of catalyst mass is enough for stable running and a catalyst mass of 1.12 g is sufficient to achieve methane conversions near to equilibrium. The catalyst runs for at least 22 h with stable performance.

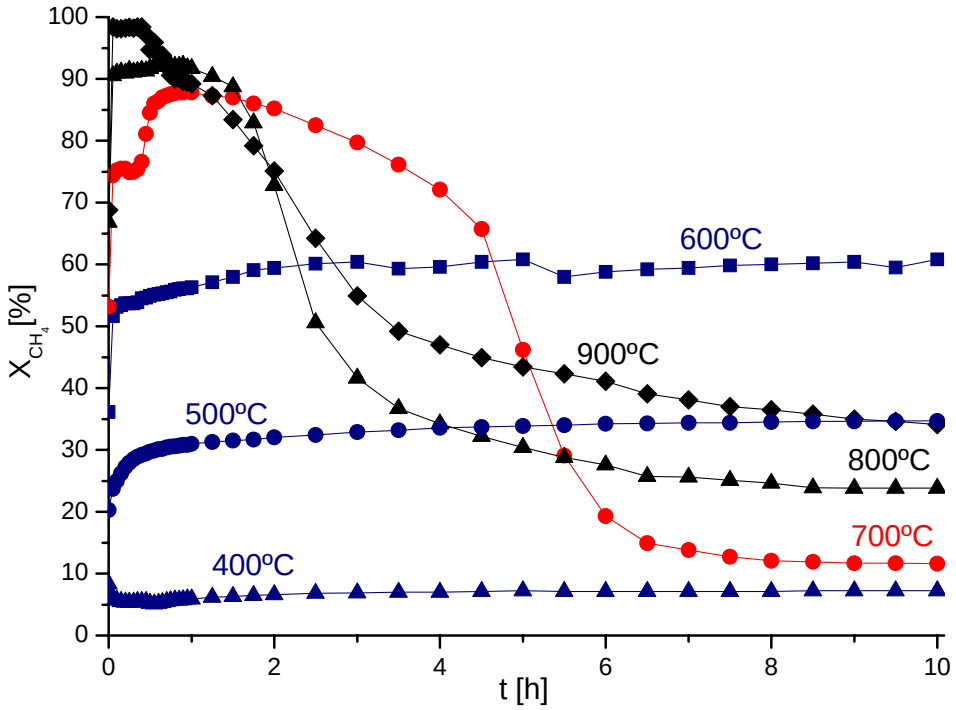



Fig. 5.12 Methane conversion as function of reaction time with NiCuLa (HPT): Temperature effect with 1.12 g of catalyst and a flow-rate of 110 $Ncm^3/min$ ($CH_4/N_2$ = 0.1).

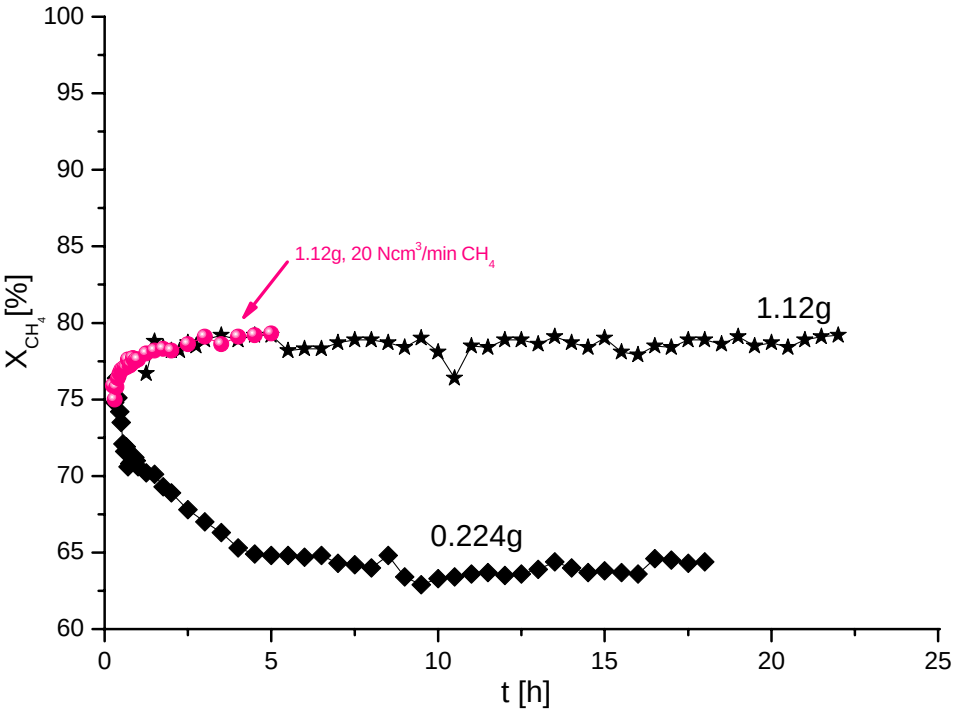
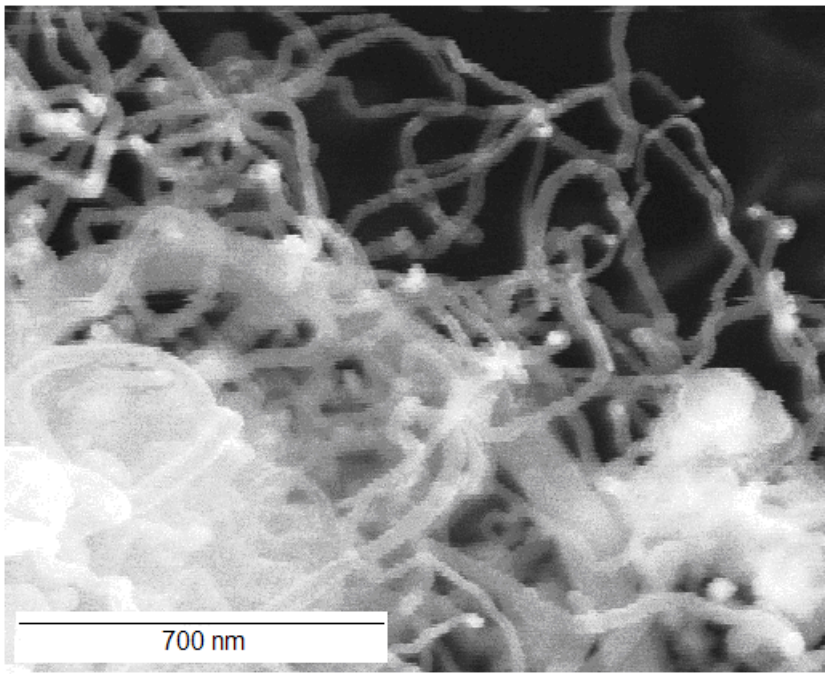


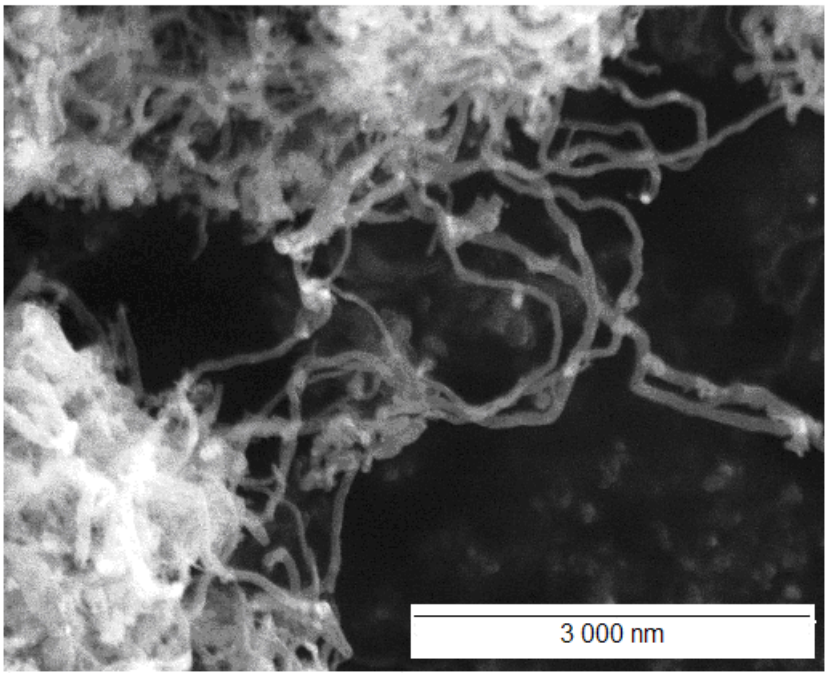

Fig. 5.13 Methane conversion as function of reaction time with NiCuLa (HPT): Catalyst mass effect at 700 ºC and pure $CH_4$ at flow-rates of 10 or 20 $Ncm^3/min$.

### 5.7.3 Characterization of the carbon deposits

The Ni50 (HPT) catalyst produces long and thin carbon filaments. Similar carbon filaments are also observed at 600 ºC on Ni50La (HPT). This catalyst, used at a reaction temperature of 700 ºC, suffers a strong deactivation as a result of large amounts of encapsulating carbon formed.




a)




b)

Fig. 5.14 SEM micrographs of carbon deposits obtained at 600 ºC on Ni30La (a) and NiCuLa (HPT) (b).

Ni30 (HPT) produces less amounts of filamentous carbon than Ni50 (HPT). The Ni particles are mostly encapsulated by the carbon deposits. The introduction of the $La_2O_3$ promoter into Ni30 changes the morphologies of the carbon deposits, as shown in Figure 5.14.

The Ni30La (HPT) system yields more filaments; however, some encapsulating carbon is obtained. A lot of filamentous carbon was obtained on the Ni30La system. The filaments are very long and thin with diameters between 10-100 nm (Fig. 5.14a).

Carbon deposits obtained on NiCuLa (HPT) at 600 ºC consist mainly of filaments with diameters also in the range of 10-100 nm (Fig. 5.14b). The active Ni particles have similar diameters to those of the filaments. At a reaction temperature of 700 ºC and with a flow-rate of 110 $Ncm^3/min$ ($CH_4/N_2$ = 0.1) the formation of encapsulating carbon was clearly observed. This type of carbon is responsible for catalyst deactivation (see Fig. 5.14b). Some CNF were also detected.

Figure 5.15 shows TEM micrographs of the carbon deposits obtained on Ni50La (HPT) catalyst, at 600 ºC. The cores of the filaments are straight, well formed, hollow channels. The borders show the presence of multiple layers. MWCNT are clearly identified. The MWCNT layers show a high degree of order, with more than 20 layers with a thickness of around 10 nm. The CNT itself has a diameter of around 30 nm (see Fig. 5.15). $La_2O_3$ as promoter influences strongly the formation of well-formed MWCNT. Gao et al. has also found that CNT are formed when a $LaNi_5$ alloy is leached in KOH. The topologies of the CNT obtained on $La_2O_3$ doped Raney-Ni catalysts are in good agreement with those reported by the above author [23]. The results were similar for the Ni30La catalysts after reaction at 600 ºC.

TEM micrographs of the carbon deposits produced on NiCuLa (HPT) at 600 ºC and at 700 ºC in a pure methane flow-rate of 10 $Ncm^3/min$ were also taken (not shown here). In both cases, the presence of large amounts of MWCNT is detected. The outer carbon layers are thicker than the narrow hollow cores. At a reaction temperature of 600 ºC, the produced CNT show generally smaller diameters (~18 nm) than those produced at a reaction temperature of 700 ºC (~34 nm). Inside some parts of the CNT, catalyst particles may be observed, especially at 700 ºC. This observation suggests that, during the reaction, the catalyst is in a molten state. The hollow channels inside the CNT are not uniformly straight, suggesting that during the growth process, the active phase particles perform not only translations, but also rotations and/or vibrations, due to the quasi-liquid state. Nevertheless, at a reaction temperature of 600 ºC, nearly perfect carbon layers are clearly visible. This phenomenon may be attributed to the presence of $La_2O_3$ in the catalytic system.

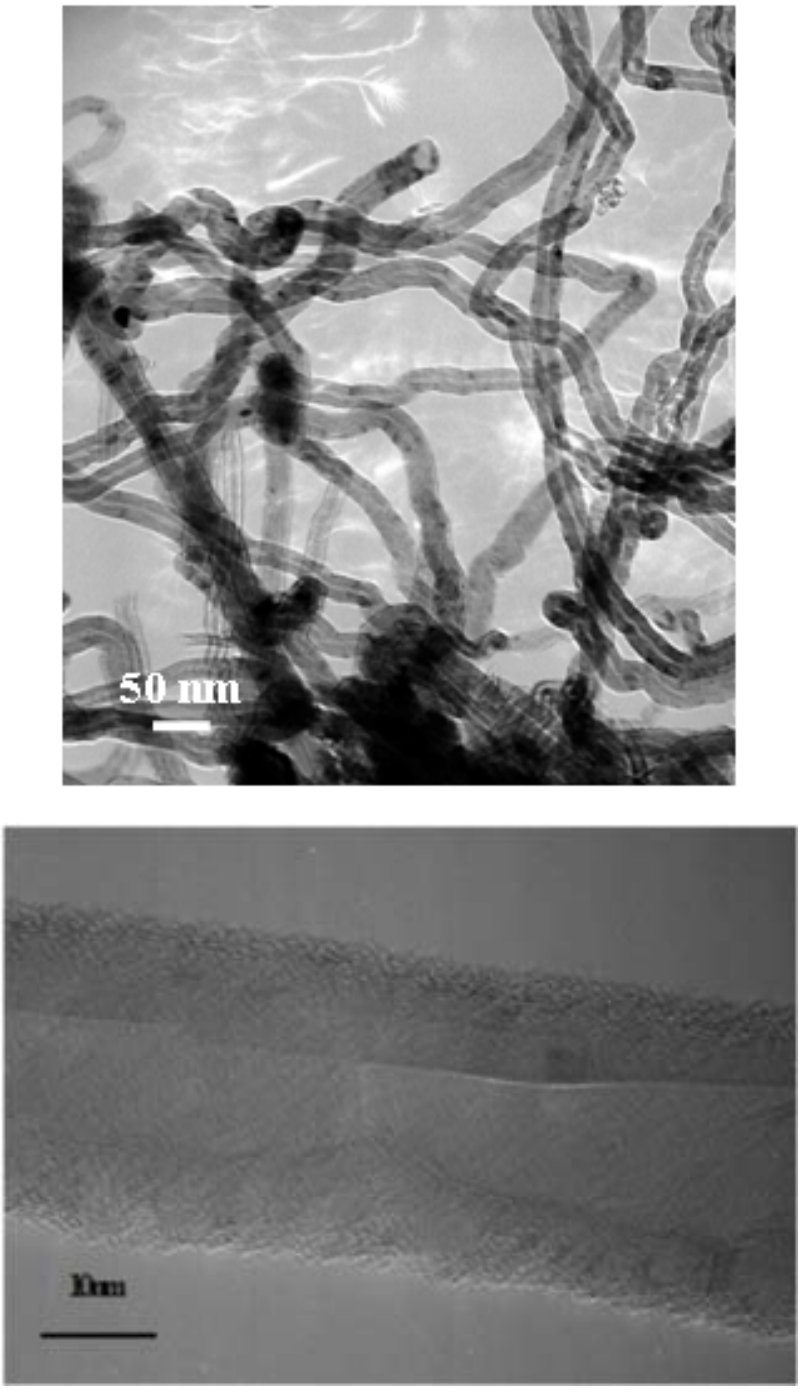



Fig. 5.15 TEM micrographs of carbon deposits obtained on Ni50La (HPT) at 600 ºC.

Diffraction patterns of the carbon deposits with the corresponding catalysts are depicted in Figure 5.16. The crystallinity of these carbon deposits is assigned to the dominant (002) reflection plane of graphite and has the advantage to compare qualitatively the produced carbon deposits on the used catalysts at 600 ºC and at 700 ºC.

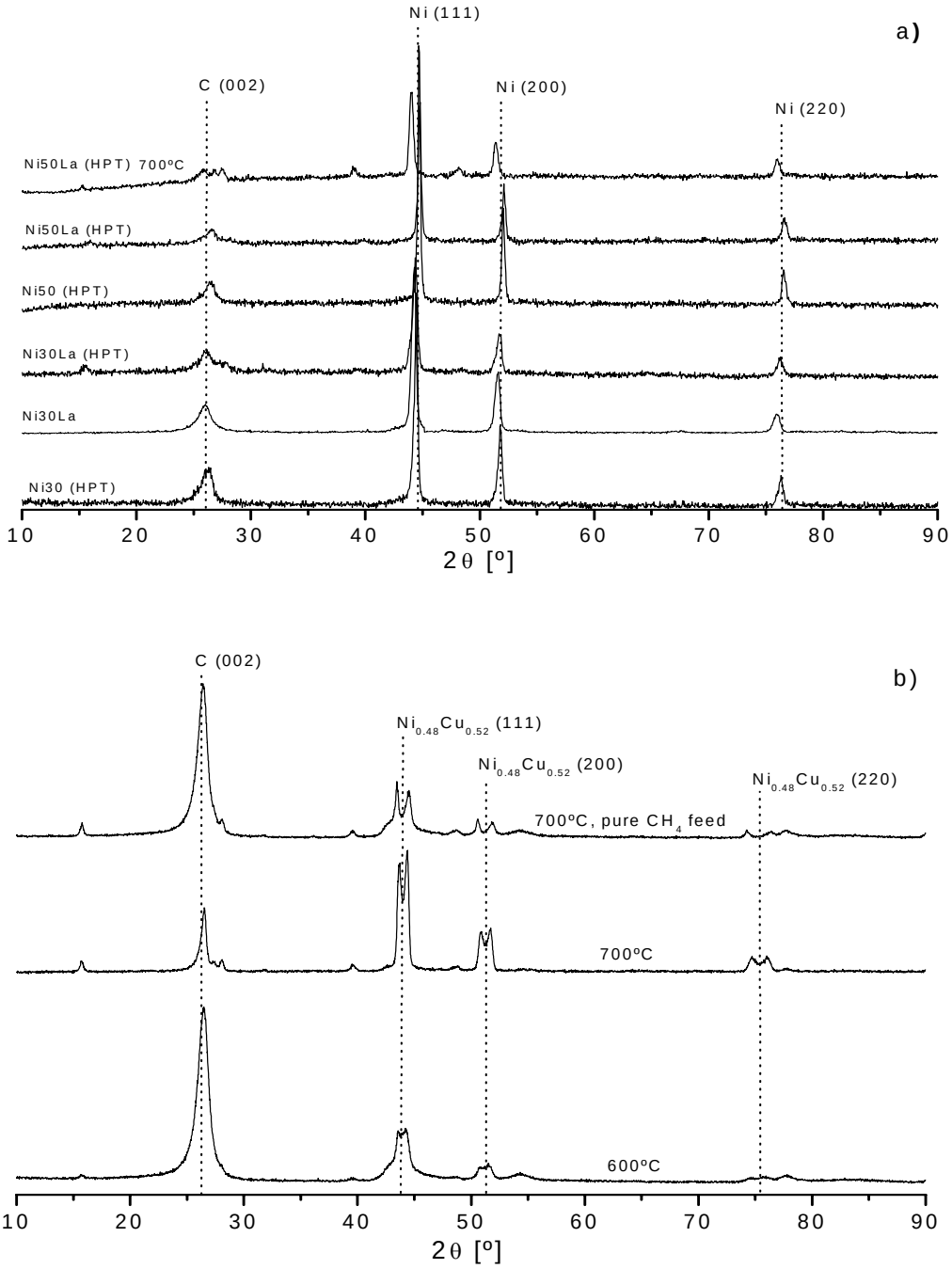



Fig. 5.16 XRD patterns of carbon deposits obtained on Ni and Ni-$La_2O_3$ catalysts (a) and on NiCuLa (HPT) (b) at 600 ºC and 700 ºC.

The pre-treatment of the Ni catalysts and the $La_2O_3$ promoter have a certain influence on the carbon crystallinity. When the Ni- $La_2O_3$ catalysts are pre-treated with hydrogen, the sharpness of the (002) graphite planes decreases; however, the peaks are still less sharp than those of the used Ni (HPT) catalysts. The reflection planes of the carbon deposits obtained on Ni30 (HPT) catalysts show that the produced graphitic carbon has a relatively smaller crystallinity than the other used catalytic systems. The introduction of $La_2O_3$ into the Ni30 catalysts decreases the

sharpness of the (002) graphite peaks; as a result they become broader and larger. Depending on the operating conditions used in the CMD on NiCuLa (HPT), the sharpness of the (002) reflection plane shows variations. The (002) reflections obtained for the used operating conditions at 600 ºC, and at 700 ºC with a pure methane flow, show a stronger sharpness than for the carbon deposits produced at 700 ºC, with a total flow-rate of 110 $Ncm^3/min$ ($CH_4/N_2$ = 0.1).

Table 5.7 collects the crystal sizes of the produced carbon deposits and respective $La_2O_3$ doped Ni and Ni-Cu catalysts of Raney-type. The Ni crystal sizes are between 17 and 52 nm. The crystal sizes of the Ni particles in Ni50La (HPT) are smaller than in the Ni50 (HPT). The crystal sizes of carbon are similar for Ni50 (HPT) and Ni50La (HPT) catalysts. For the Ni50La (HPT) system at a reaction temperature of 700 ºC, the crystal size is 23.6 nm. The Ni and produced carbon crystallites from Ni30 (HPT), Ni30La and Ni30La (HPT) catalysts are similar, but the carbon crystallites are slightly smaller than those of the Ni50 (HPT) and Ni50La (HPT) catalytic systems. The crystal sizes of Ni in Ni30 (HPT), Ni30La and Ni30La (HPT) catalysts are similar to the Ni50 (HPT) and larger than those of the Ni50La (HPT) catalyst. The crystal sizes of carbon obtained on NiCuLa (HPT) at 600 ºC, as well as 700 ºC and 10 $Ncm^3/min$ of pure methane are very small and show sizes of ~14 nm and ~20 nm, respectively. The crystal sizes of Ni and Cu are similar in both cases for the carbon deposits, 21-22 nm and 14-17 nm, respectively. This is a clear indication of a real $Ni_{0.48}Cu_{0.52}$ alloy formation. The carbon solid produced at 700 ºC and a flow-rate of 110 $Ncm^3/min$ ($CH_4/N_2$ = 0.1) shows a carbon crystal size of ~35 nm. The values for Ni (~52 nm) and Cu (~37 nm) show that the process of alloy formation was less well succeeded. However, it can be seen that $La_2O_3$ acts as a structural promoter.

The interplanar distances between the basal planes of perfect graphite (0.3354 nm) were also compared with those of the produced carbon deposits. The use of Ni50La (HPT) produces at 600 ºC, carbon very close to perfect graphite, while the same catalyst used at 700 ºC produces carbon far away from the perfect graphitic structure. Also Ni30La and especially Ni30La (HPT) produce carbon which is not in the range of perfect graphite. Hydrogen pre-treated Ni catalysts produce, at 600 ºC, carbon closer to perfect graphite than untreated Ni catalysts. It can be concluded that a hydrogen pre-treatment as well as the presence of $La_2O_3$ is of advantage for the formation of well-ordered graphitic carbon layers, while the absence of this electronic promoter and/or hydrogen pre-treatment leads to the production of more disordered carbon layers, especially at reaction temperatures higher than 600 ºC.

Table 5.7

Crystal sizes of carbon and metals in the deposits

| Catalyst | $T^{reaction}$ [°C] | $d_C$ [nm] | $d_{Ni}$ [nm] | $d_{Cu}$ [nm] | $D_{(002)}$ [nm] |
|---|---|---|---|---|---|
| Ni50 | 600 | 8.8 | 18.2 | / | 0.339 |
| Ni50 (HPT) | 600 | 13.3 | 30.8 | / | 0.338 |
| Ni50La (HPT) | 600 | 11.2 | 17.9 | / | 0.335 |
| Ni50La (HPT) | 700 | 23.6 | 17.9 | / | 0.345 |
| Ni30 | 600 | 10.6 | 22.6 | / | 0.339 |
| Ni30 (HPT) | 600 | 6.2 | 24.2 | / | 0.337 |
| Ni30Cu50 (ITT) | 600 | 23.7 | 38.9 | 53.1 | 0.337 |
| Ni30La | 600 | 9.5 | 28.1 | / | 0.340 |
| Ni30La (HPT) | 600 | 8.5 | 30.3 | / | 0.342 |
| NiCuLa (HPT) | 600 | 14.2 | 21.3 | 21.8 | 0.337 |
| NiCuLa (HPT) | 700 | 34.9 | 51.7 | 37.1 | 0.337 |
| NiCuLa (HPT) | *700 | 20.2 | 17.0 | 14.2 | 0.337 |

* pure inlet methane feed (10 $Ncm^3$/min).

### 5.7.4 Comparison with other catalysts reported

The results obtained in this chapter can now be compared with those previously reported for CMD [9-14,21]. In Table 5.8 are summarized the experimental conditions together with the equilibrium methane conversion, the maximum recorded conversion as well as the final conversion measured after some time on stream. The catalyst stability is assessed by comparing $X_{CH_4}^{\max}$ with $X_{CH_4}^{t}$.

Catalysts with a low load of $La_2O_3$ are adequate for long time stability in methane decomposition. The main advantage of NiCuLa (HPT) is that low amounts of catalyst mass are required for stable CMD run when catalyst deactivation does not occur. The most obvious explanation is that the hydrogen formed during the CMD has a much higher contact time with the catalyst and the formed carbon. Therefore, higher rates of hydrogenation and dehydrogenation can be expected in a reversible reaction.

We believe that the promoting effect of $La_2O_3$ is related to electron transfer to nickel, as discussed in the case of the Raney-Fe catalysts.

Table 5.8

Selected results for the catalytic decomposition of methane on $La_2O_3$ promoted Ni and Ni-Cu catalysts

| Catalyst [Reference] | $m_{cat}$ [g] | T [°C] | $\dot{V}_{total}$ $[\frac{Ncm^3}{min}]$ | $\dot{n}_{CH_4}$ $[\frac{mmol}{min}]$ | $X_{CH_4}^{eq}$ | $X_{CH_4}^{max}$ | $X_{CH_4}^{t}$ | t [h] |
|---|---|---|---|---|---|---|---|---|
| Ni-Cu-MgO [10] | 0.3 | 700 | 20 | 0.893 | 80.8 | 71 | 67 | 8 |
| Ni-Cu-$Al_2O_3$ [11] | 0.3 | 700 | 20 | 0.893 | 80.8 | 75 | 75 | 8 |
| Ni-Cu-$SiO_2$ [12] | 0.3 | 700 | 20 | 0.893 | 80.8 | 71 | 65 | 8 |
| Ni-Cu-$TiO_2$ [13] | 0.3 | 700 | 20 | 0.893 | 80.8 | 54 | 54 | 8 |
| $LaNiO_3$ [21] | 0.06 | 650 | 100 | 0.134 | 97.4 | 33 | 20 | 5 |
| $LaNi_{0.95}Rh_{0.05}O_3$ [21] | 0.06 | 650 | 100 | 0.134 | 97.4 | 51 | 42 | 2 |
| Ni30 [9] | 0.5 | 600 | 110 | 0.446 | 88.0 | 73 | 33 | 5 |
| Ni30 (HPT) [9] | 0.5 | 600 | 110 | 0.446 | 88.0 | 69 | 49 | 5 |
| Ni30 [9] | 1.0 | 600 | 110 | 0.446 | 88.0 | 78 | 76 | 5 |
| Ni30 [9] | 2.5 | 600 | 110 | 0.446 | 88.0 | 83 | 80 | 12 |
| Ni30 [9] | 2.5 | 700 | 110 | 0.446 | 95.9 | 95 | 89 | 5 |
| Ni30Cu50 (TTT) [14] | 1.0 | 600 | 110 | 0.446 | 88.0 | 67 | 60 | 5 |
| Ni30Cu50 (TTT) [14] | 1.0 | 700 | 110 | 0.446 | 95.9 | 89 | 41 | 5 |
| Ni30La | 0.53 | 600 | 110 | 0.446 | 88.0 | 75 | 73 | 5 |
| Ni30La | 0.56 | 600 | 110 | 0.446 | 88.0 | 69 | 67 | 5 |
| Ni30La (HPT) | 0.56 | 600 | 110 | 0.446 | 88.0 | 67 | 65 | 5 |
| NiCuLa (HPT) | 0.224 | 600 | 110 | 0.446 | 88.0 | 43 | 40 | 28 |
| NiCuLa (HPT) | 0.448 | 600 | 110 | 0.446 | 88.0 | 56 | 56 | 19 |
| NiCuLa (HPT) | 1.12 | 600 | 110 | 0.446 | 88.0 | 64 | 63 | 14 |
| NiCuLa (HPT) | 5.6 | 600 | 110 | 0.446 | 88.0 | 79 | 79 | 10 |
| NiCuLa (HPT) | 0.224 | 700 | 10 | 0.446 | 80.8 | 76 | 64 | 16 |
| NiCuLa (HPT) | 1.12 | 700 | 10 | 0.446 | 80.8 | 79 | 79 | 22 |
| NiCuLa (HPT) | 1.12 | 700 | 20 | 0.893 | 80.8 | 79 | 79 | 5 |

$\dot{V}_{total}$ : total volumetric flow rate;

$\dot{n}_{CH_4}$ : molar flow rate of methane;

$X_{CH_4}^{eq}$ : equilibrium methane conversion;

$X_{CH_4}^{max}$ : maximum methane conversion during reaction;

$X_{CH_4}^{t}$ : methane conversion at time t.

## 5.8 Conclusions

Methane decomposition was investigated over Ni and Ni-Cu Raney-type catalysts, which were used as such, after hydrogen pre-treatment, promoted with $La_2O_3$ or hydrogen pre-treated after $La_2O_3$ doping.

$La_2O_3$ was found to be a good promoter for the used Raney-type catalysts. The efficient incorporation of $La_2O_3$ onto the surface of the Raney-type catalysts is mainly dependent on their microstructure.

The isothermal runs show an optimum mass ratio range for the $La_2O_3$ promoter. The lifetime of the catalysts is significantly increased, depending on the operating conditions.

Examination of the carbon deposit morphologies showed that mostly carbon filaments are formed, containing CNF and MWCNT.

From this study, it can be concluded that the NiCuLa (HPT) catalytic system consisting on Ni, Cu, $La_2O_3$ and residual $Al_2O_3$ is one of the most efficient catalysts for CMD ever reported.

## Appendix

Additional results obtained for this Chapter V can be consulted in the Appendix.

## References


[1] M. Zerta, P. R. Schmidt, C. Stiller, H. Landinger, *Int. J. Hydrogen Energy* **33** (2008) 3021.

[2] F. de Bruijin, *Green Chem.* **7** (2005) 132.

[3] J.R. Rostrup-Nielsen, *Catal. Today* **71** (2002) 243.

[4] S. Sircar, W.E. Waldron, M.B. Rao, M. Anand, *Sep. Pur. Tech.* **17** (1999) 11.

[5] N. Muradov, T.N. Veziroglu, *Int. J. Hydrogen Energy* **30** (2005) 225.

[6] N.Z. Muradov, *Energy & Fuels* **12** (1998) 41.

[7] S. Ahmeda, A. Aitani, F. Rahman, A. Al-Dawood, F. Al-Muhaish, *Appl. Catal. A: Gen.* **359** (2009) 1.

[8] J.L. Figueiredo, *Erdöl & Kohle Erdgas Petrochemie* **42** (1989) 294.

[9] A.F. Cunha, J.J.M. Órfão, J.L. Figueiredo, *Appl. Catal. A: Gen.* **348** (2008) 103.

[10] Y. Echegoyen, I. Suelves, M.J. Lázaro, M.L. Sanjuán, R. Moliner, *Appl. Catal. A: Gen.* **333** (2007) 229.

[11] M.J. Lázaro, Y. Echegoyen, I. Suelves, J.M. Palácios, R. Moliner, *Appl. Catal. A: Gen.* **329** (2007) 22.

[12] I. Suelves, M.J. Lázaro, R. Moliner, Y. Echegoyen, J.M. Palácios, *Catal. Today* **116** (2006) 271.

[13] M.J. Lázaro, Y. Echegoyen, C. Alegre, I. Suelves, R. Moliner, J.M. Palácios, *Int. J. Hydrogen Energy* **33** (2008) 3320.

[14] A.F. Cunha, J.J.M. Órfão, J.L. Figueiredo, *Int. J. Hydrogen Energy* (2009), doi:10.1016/j.ijhydene.2009.03.040.

[15] J. Chen, Y. Qiao, Y. Li, *Appl. Catal. A: Gen.* **337** (2008) 148.

[16] K. Otsuka, S. Takenaka, H. Ohtsuki, *Appl. Catal. A: Gen.* **273** (2004) 113.

[17] J. Li, G. Lu, K. Li, W. Wang, *J. Mol. Catal. A: Chem.* **221** (2004) 105.

[18] Y. Li, B. Zhang, X. Tang, Y. Xu, W. Shen, *Catal. Commun.* **7** (2006) 380.

[19] J. Ashok, S.N. Kumar, A. Venugopal, V.D. Kumari, M. Subrahmanyam, *J. Power Sources* **164** (2007) 809.

[20] M.E. Rivas, J.L.G. Fierro, R. Guil-López, M.A. Peña, V. LaParola, M.R. Goldwasser, *Catal. Today* **133-135** (2008) 367.

[21] M.E. Rivas, C.E. Hori, J.L.G. Fierro, M.R. Goldwasser, A. Griboval-Constant, *J. Power Sources* **184** (2008) 265.

[22] M.A. Peña and J.L.G. Fierro, *Chem. Rev.* **101** (2001) 1981.

[23] X.P. Gao, X. Qin, F. Wu, H. Liu, Y. Lan, S.S. Fan, H.T. Yuan, D.Y. Song, P.W. Shen, *Chem. Phys. Lett.* **327** (2000) 271.

[24] Q. Jiang, L.J. Song, Y. Zhao, X.Y. Lu, X.T. Zhu, L. Qian, X.M. Ren, Y.D. Cai, *Mater. Lett.* **61** (2007) 2749.

[25] Y. Kiros, M. Majari, T.A. Nissinen, *J. Alloys and Compounds* **360** (2003) 279.

[26] M. Raney, U.S. Patent 1,628,190 (1927).

[27] U. Birkenstock, J. Scharschmidt, P. Kunert, H. Meinhardt, P. Hausel, P. Maier, U.S. Patent 5,090,997 (1992).

[28] U. Birkenstock, R. Holm, B. Reinfandt, S. Storp, *J. Catal.* **93** (1985) 55.

[29] Y. Cesteros, R. Fernàndez, J. Estellé, P. Salagre, F. Medina, J.E. Sueiras, J.L.G. Fierro, *Appl. Catal. A: Gen.* **152** (1997) 249.

[30] J. Sun, X.-P. Qiu, F. Wu, W.-T. Zhu, *Int. J. Hydrogen Energy* **30** (2005) 437.

[31] S. Natesakhawat, O. Oktar, U.S. Ozkan, *J. Molec. Catal. A: Chem.* **241** (2005) 133.

[32] Á. Slagterm, U. Olsbye, R. Blom, I.M. Dahl, H. Fjellvåg, *Appl. Catal. A: Gen.* **145** (1996) 375.

[33] Y. Jilei, L. Zengxi, D. Huachao, L. Yuan, *J. Rare Earths* **24** (2006) 302.

[34] Á. Slagterm, Y. Schurman, C. Leclercq, X. Verykios, C. Mirodatos, *J. Catal.* **172** (1997) 118.

[35] W.D. Zhang, B.S. Liu, C. Zhu, Y.L. Tia, *Appl. Catal. A: Gen.* **292** (2005) 138.

[36] E.G.M. Kuijpers, J.W. Jansen, A.J. vanDillen, J.W. Geus, *J. Catal.* **72** (1981) 75.

[37] D. Chen, K.O. Christensen, E. Ochoa-Fernández, Z. Yu, B. Tøtdal, N. Latorre, A. Monzón, A. Holmen, *J. Catal.* **229** (2005) 82.

[38] Y. Li, B. Zhang, X. Xie, J. Liu, Y. Xu, W. Shen, *J. Catal.* **238** (2006) 412.

[39] J.L. Figueiredo, in: J.L. Figueiredo (Ed.), Progress in catalyst deactivation, Martinus-Nijhoff, The Hague, 1982, p. 45.

# *Chapter VI*

## Summary

*"Omnium artium catalisis nobilissima est."*

*"Catalysis is the noblest of all arts."*

**A.F. Cunha**

## 6.1 Energy, Materials and Catalysis

Clean sources of energy are currently one of the most important research topics. Fossil fuels are becoming scarce. Permanently increasing greenhouse gas emissions lend support to a catastrophic scenario. In this context, it is predicted that hydrogen may become the fuel of the future, since it is a clean source of energy [1].

Hydrogen can be used in low temperature proton exchange membrane fuel cells (PEMFC). The problem is that PEMFC tolerate CO only in the low ppm range [2].

Traditionally, hydrogen is still produced by steam reforming or partial oxidation [3]. Recently, this process has been used to reform biomass [4]. Unfortunately, separation and purification processes are required. Furthermore, pressure swing adsorption (PSA) has to be coupled in order to achieve complete hydrogen purification [5].

Research on new production processes for hydrogen has attracted a lot of attention [6]. It is known that hydrogen can be synthesized via catalytic methane decomposition (CMD) as an alternative route to avoid $CO_x$ formation. Expensive separation units and environmental concerns are thus minimized, and high value carbon materials can be obtained as by-products.

However, methane is one of the most difficult molecules to activate, since the C-H bond is a strong covalent bond, (435 kJ/mol) [7]. It is known that methane has a rigid tetrahedral structure with ideal bond angles of 109.5º and bond lengths of 110 pm. The strong bond energy and spherical shape of this hydrocarbon makes the molecule resistant towards chemical reactions. Therefore, several issues have to be considered for CMD.

From the literature it is known that carbons perform rather poorly as catalytic materials, and require very high temperatures for acceptable methane conversions. Metal catalysts perform better for CMD and are usually based on Ni, Co or Fe, which is not surprising, since these are well known active phases for hydrocarbon decomposition and carbon formation.

Carbon formation from hydrocarbons on metal catalysts has been extensively studied in the 1970´s [8-10] and has been the subject of several reviews [11-13]. The dissociative adsorption of hydrocarbons leads to the formation of adsorbed carbon atoms, which can diffuse on the surface or through the metal precipitating at the metal-support interface to form carbon filaments. Alternatively the adsorbed carbon atoms can form graphite layers on the surface (encapsulating carbon). A special case is observed for Fe, where phase transitions can occur, and metal carbides can be involved. For instance, as carbon accumulates on the surface of Fe catalysts, the role of iron carbides and other iron phases in the migration of the adsorbed carbon species becomes

more significant. Therefore, filamentous carbon formation has also been explained by a carbide cycle mechanism [14].

To crack the methane molecule, adequate conditions are required. Supported catalysts have moderate activities, but generally they are not very stable. The best results have been obtained with high metal loaded catalytic systems in the presence of textural promoters such as $Al_2O_3$ [15]. Therefore, massive catalysts seem to be a good choice for the proposed task and it was decided in this work to use Raney-type catalysts consisting of Ni, Co or Fe with residual alumina.

In most cases, Raney-type catalysts show enhanced resistance against sinterization. This phenomenon can be attributed to the textural promoting effect of $Al_2O_3$, which separates the metal crystallites. The crystal sizes of the Raney-type metals are also relatively small, and an adequate surface area is available for catalytic reaction.

## 6.2 CMD on Raney-type Catalysts

The results obtained for CMD on Raney-type catalysts are in agreement with the established mechanism for carbon filament growth [11]. The first reaction step is the dissociative adsorption of $CH_{4,(g)}$ into $\rangle\overline{CH_3}$ and $\rangle\overline{H}$ surfaces species. The $\rangle\overline{CH_3}$ species are subsequently dissociated by many possible surface reactions until chemisorbed carbon atoms are formed on the metal surface [16], as shown in Figure 6.1.

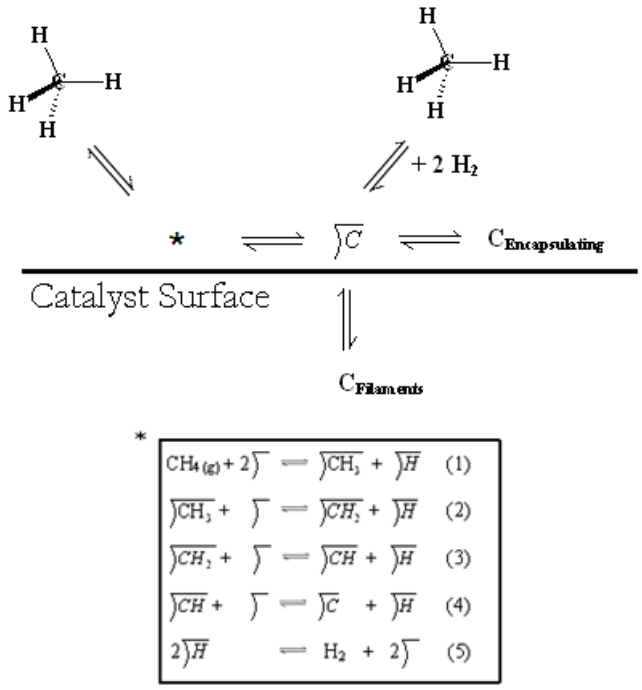



Fig. 6.1 CMD mechanism proposed on Raney-type catalysts.

The chemisorbed carbon atoms migrate on the surface of the metal particles or diffuse through the bulk until they reach the rear side, where they precipitate to form graphene layers, originating the growth of carbon filaments (nanofibers or nanotubes) [8,9,17,18].

Other types of surface carbons (polymers $C_xH_y$ or graphitic layers) may also be formed which encapsulate the metallic particles preventing the access of methane to the active sites and leading to deactivation.

These mechanistic features are common for supported or unsupported metal catalysts. However, there is an important difference, which will affect the stability. In the case of supported catalysts, there will be a fixed number of metal crystallites on the support; each one of them will produce a carbon filament, which will grow until the metal particle is deactivated (by encapsulation). Since this is inevitable [8], the catalyst will soon be dead.

In the case of unsupported metals, there is an initial step (carburization and metal dusting) which leads to disruption of the surface and the production of metal crystallites. The bulk metal acts as an "infinite" source of metal crystallites, thus providing for an extended life of the catalyst [19]. This explains the reported effects of the amount of catalyst and flow rate (contact time) [20].

At this point it is important to mention that two types of Raney catalysts were used; conventional and quenched alloys, which performed better. Pre-treatments with hydrogen on conventional alloys improved also stability. Such treatments, lead to an embrittlement effect. The formation and decomposition of $MeH_2$ bonds lowers the chemical bond energy between the metal atoms. This results in an increased surface roughness. Therefore, additional metal sites become accessible to the methane molecules. The HPT alloys show a surface structure similar to the quenched alloys.

Raney-Fe catalysts show an initial activation period which corresponds to the reduction of $Fe_xO_y$, formed during the preparation of the catalysts (leaching of Al by NaOH). This phenomenon can be minimized by a previous hydrogen treatment.

The effect of the operating conditions on the performance of the used catalytic systems was investigated in detail. The number of filaments formed depends strongly on them.

An increase in temperature is useful for faster kinetics, as described by Arrhenius law. However, parallel reactions also become important at higher temperatures, such as the formation of encapsulating carbon species.

An increase in methane concentration leads to an increase in both the rates of carbon filament formation and also deactivating carbon. However, larger hydrogen amounts are formed during decomposition of methane, which will slow down the formation of encapsulating carbon without going so far as to inhibit filament formation.

The same effect is observed by the introduction of hydrogen in the feed gas during reaction. At high hydrogen partial pressures the decrease in both carbon filaments and encapsulating carbon species is evident. Hence, deactivation will not occur so fast because the carbon species on the surface are gasified. The net amount of hydrogen produced increases.

## 6.3 Carbon deposits on Raney-type Catalysts

An industrial CDM process may become feasible only if the by-products, composite material consisting of carbon deposits and used catalyst, can be used for further purposes. The exceptional properties of filamentous carbon can make it suitable for several applications, such as polymer reinforcement for composites, electronic parts, energy or gas storage and catalysis [21]. The use of CNT/CNF as support material in heterogeneous catalysis is known [22]. Other applications are also of industrial interest [23,24]. Special attention has to be given to the composite materials produced in this work.

The presence of filamentous carbon and metal nanoparticles was achieved by decomposing methane over Raney-type skeletal catalyst. Metal nanoparticles were generated by metal disintegration, and stabilized by filamentous carbon.

The composite materials obtained from CMD show mostly the presence of CNF when produced at low temperatures, and MWCNT when produced at high temperatures. The metal particles on top of the filaments have very small and uniform diameters (in nanometer scale), as shown by SEM, TEM and XRD examinations. Therefore, the high surface area of these particles is useful for successful catalytic properties.

The composite materials were tested as catalysts for hydrogenation reactions [25,26]. They were shown to exhibit excellent catalytic properties for liquid phase hydrogenation reactions (hydrogenation of nitrobenzene and chloro-nitrobenzene). The active phase of the catalysts consists of nickel nanoparticles in reduced form with superficial oxide layers that contribute to protect them from bulk oxidation by air. High activities and selectivities where reached.

## 6.4 Effect of promoters on Raney-type Catalysts

CMD implies in most cases the accumulation of encapsulating carbon, which is responsible for catalyst deactivation. Catalyst regeneration, when possible, can be performed by gasification with steam, oxygen, carbon dioxide or hydrogen. Unfortunately, this step is quite expensive due to the interruption of the production process. Therefore, optimization of the catalyst properties is

required. An elegant solution is to use promoters. In addition to the textural promoter ($Al_2O_3$), which is always present after leaching out Al from the original Raney alloys, two other promoters were tested in this work:

- Structural promoter: Raney-Cu.
- Electronic promoter: $La_2O_3$.

### 6.4.1 Effect of Raney-Cu as structural promoter on Raney-type Catalysts

The need to find adequate catalyst promoters to inhibit encapsulating carbon formation resulted in the development of a Ni catalyst partially poisoned by sulphur [27]. In this case, carbon formation is prevented by "ensemble control". This objective can also be achieved by diluting an active metal phase with an inactive one, such as Cu [28].

This was an important reason to test incipient Me-Cu alloys (Me = Ni, Co and Fe) of Raney-type. The dilution of surface active sites results in ensemble control and determines the stability and selectivity of CMD. The competing reactions of formation of carbon filaments and encapsulating carbon species are strongly influenced. Indeed, the presence of Cu minimizes encapsulating carbon formation on the catalyst surface, and favors CNF/CNT formation.

Experimental results on the performance of Ni-Cu alloyed Raney-type catalysts for the production of hydrogen via CMD were presented [29]. The effects of chemical composition, structure, and resulting catalytic activities of Ni, Cu and Ni-Cu incipient alloys formed by thermal treatment at 600 ºC were studied. The stable performance of Ni-Cu incipient alloys over time intervals exceeding 5 h has been shown. Carbon deposits formed on the catalytic surfaces were characterized. It was shown that CNF/CNT formation occurs on thermally treated Ni-Cu alloy catalysts. The increased stability of Ni-Cu alloy catalysts is explained in terms of an ensemble effect that controls the density of catalytic sites. In return, slightly lower activity is observed. All used operating conditions are reproducible and in good agreement with those tested for the monometallic Raney-type catalysts.

The addition of Raney-Cu to Co Raney system was found to be ineffective. The case of Fe-Cu Raney-type systems can be described as follows. Fe-Cu alloy formation is only possible in certain composition ranges, whereas Ni-Cu alloy formation spans the whole composition range above 700 K. However, good results were obtained when the Fe-Cu Raney-type systems were thermally treated in situ at 600 ºC, as a result of incipient alloy formation. These catalysts showed higher stability than the monometallic Raney-Fe catalysts. The carbon products obtained consist mostly of carbon nanofibers.

### 6.4.2 Effect of $La_2O_3$ as electronic promoter on Raney-type Catalysts

Electronic promoters affect the efficiency of the active sites in a catalyst without being really involved as active phase [30]. In this work the use of $La_2O_3$ as minor component was studied in detail on Raney-type catalysts.

Experimental results on the performance of Ni, Ni-Cu, Co and Fe Raney-type catalysts promoted with $La_2O_3$ for the production of hydrogen via CMD were presented. The effects of chemical composition, and structure in the resulting catalytic activities of the $La_2O_3$ promoted systems formed by hydrogen pre-treatment at 600 ºC were studied. For each catalytic system (Ni, Ni-Cu, Co and Fe) the optimum load of $La_2O_3$ was determined. Excess of $La_2O_3$ was found to deactivate the catalyst. Especially, the stable performance of Ni-$La_2O_3$ and Ni-Cu-$La_2O_3$ mixtures over time intervals exceeding 5 h and 28 h, respectively, was proven experimentally. Carbon deposits formed on the catalytic surfaces were characterized and found to consist of CNF/CNT.

## 6.5 Conclusions and Suggestions for Future Work

The objective of this thesis was to gain knowledge on the behavior of Raney-type catalysts for methane decomposition into $CO_x$-free hydrogen and filamentous carbon formation. This investigation evaluated the nature of the catalytic materials, the influences of the operating conditions, catalyst treatment, promoter effects as well as characteristics of the obtained carbon deposits. The conclusions are as follow:

- It has been proven that Raney-type catalysts are excellent to decompose methane into $CO_x$ - free hydrogen and CNF/CNT. The mechanism proposed in the literature is applicable.

- CMD is strongly dependent on the used active metal phase (Ni, Co and Fe) and on the morphology of the parent alloys (conventional or quenched). Ni catalysts perform better than Co and Fe, and quenched systems perform better than conventional ones.

- CMD shows a strong dependency on catalyst mass and/or flow rate (contact time). The higher the contact time, the more stable is the CMD.

- In general, pre-treatments with hydrogen on conventional alloys increase catalyst activity and mainly stability, thus approaching the performance of the quenched systems.

- Higher temperatures increase the activity, but also the rate of parallel reactions.
- Higher methane concentrations in the feedstream lead to lower conversions and to higher stabilities; hydrogen in the feed has the same effect.
- The presence of CNF and CNT depends largely on the nature of the catalyst and operating conditions. Large amounts of CNF/CNT were observed with Ni and Co, whereas more encapsulating carbon and $Fe_3C$ with Fe.
- Low temperatures favor the formation of CNF, high temperatures favor the formation of CNT and encapsulating carbon species.
- The incipient alloying of Raney-Cu with Ni and Fe Raney-type catalysts increases stability and the formation of CNF/CNT in considerable amounts.
- $La_2O_3$ increases activity and mainly stability coupled with the formation of CNF/CNT.
- The simultaneous promoting effects of Cu and $La_2O_3$ have been observed on Ni30.

Fe, Co and Ni Raney-type catalysts are attractive for methane decomposition into $CO_x$-free hydrogen and CNF/CNT formation.
Exhaustive reaction studies have shown that the process is ripe for larger scale investigations, most probably in a fluidized bed reactor. The reported data show optimal parameter ranges for the development of a larger scale plant. CMD into pure hydrogen and CNF/CNT on Raney-type catalysts was shown to be feasible; however, further studies may be required, as suggested below:

- Optimal Raney-type alloy composition and quenching conditions.
- Trimetallic or tetrametallic Raney-type alloy phases.
- Raney-type alloys with other leachable metals, such as Si, Mg, Ca, Zn, Sn, Pb.
- Raney-type alloys with other active phases, such as Ti.
- Optimal textural promoter quantities on the Raney-type catalysts, controlled by leaching temperature and time.
- Other promoters similar to Cu (ensemble control), such as Zn, Sn.
- Other electronic promoters such as $Na_2O$, $K_2O$, $Cs_2O$, CaO, $CeO_2$.
- Other pre-treating gases such as CO or $CO/H_2$ gas mixtures.
- Sulphur resistant catalyst promoters for direct use of natural gas.

For a successful $CO_x$-free hydrogen production via CMD, the composite materials (carbon + catalyst left) as by-product should find a high-value application.

One thing is the production of CNF/CNT; another is to separate the preferred products from the undesired ones. CMD generates several by-products: metallic catalyst particles, amorphous carbon, metal nanoparticles, and graphitic carbon layers (encapsulating carbon).

Several separation techniques are required for CNF/CNT purification [31], however, the purification of these materials is a quite delicate matter and 100 % purity has not been achieved until now. The field of carbon purification processes requires a lot of attention and has to be explored intensively.

However, the composite materials, consisting on CNF/MWCNT and metal particles, can be used as catalysts in liquid phase hydrogenation reactions. Excellent results were already reported for the hydrogenation of nitrobenzene to aniline [25] and chloronitrobenzenes to chloroanilines [26], with exceptionally high selectivities. The quality of these results deserves further studies. In particular, other hydrogenation reactions should be tested, in order to extend the range of application of the composite materials obtained from CMD in this work.

## References


[1] N. Muradov, T.N. Veziroglu, *Int. J. Hydrogen Energy* **30** (2005) 225.

[2] A.C. Garcia, V. A. Paganin, E.A. Ticianelli, *Electrochimica Acta* **53** (2008) 4309.

[3] J.R. Rostrup-Nielsen, in: J.R. Anderson, M. Boudart (Eds.), Catalytic Steam Reforming Catalysis, Science & Technology, vol. 5, Springer, Berlin, 1984.

[4] D. Wang, S. Czernik, E. Chornet, *Energy & Fuels* **12** (1998) 19.

[5] S. Sircar, W.E. Waldron, M.B. Rao, M. Anand, *Separ. & Purif. Tech.* **17** (1999) 11.

[6] P. Häussinger, R. Lohmüller, A.M. Watson, Hydrogen, Ullmann's Encyclopedia of Industrial Chemistry, 7th Edition (2000).

[7] R.H. Crabtree, *Chem. Rev.* **95** (1995) 987.

[8] R.T.K. Baker, M.A. Barber, P.S. Harris, F.S. Feates, R.J. Waite, *J. Catal.* **26** (1972) 51.

[9] L.S. Lobo, D.L. Trimm, J.L. Figueiredo, in: J.W. Hightower (Ed.), Proceedings of the 5th International Congress on Catalysis 1972, vol. 2, North-Holland, Amsterdam, 1973, pp. 1125.

[10] J.R. Rostrup-Nielsen, *J. Catal.* **27** (1972) 343.

[11] J.L. Figueiredo JL. In: J.L. Figueiredo, editor. Progress in catalyst deactivation. The Hague: Martinus-Nijhoff; 1982. p. 45.

[12] K.P. de Jong and J.W. Geus, *Catal. Rev.-Sci. Eng.* **42** (2000) 481.

[13] J.L. Figueiredo, Filamentous carbon, *Erdöl & Kohle Erdgas Petrochemie* **42** (1989) 294.

[14] V.V. Chesnokov, K.A. Buyanov, *Russ. Chem. Rev.* **69** (2000) 623.

[15] I. Suelves, M.J. Lázaro, R. Moliner, B.M. Corbella, J.M. Palácios, *Inter. J. Hydrogen Energy* **30** (2005) 1555.

[16] J.G. McCarty and H. Wise, *J. Catalysis* **57** (1979) 406.

[17] I. Alstrup, *J. Catal.* **109** (1988) 241.

[18] S. Helveg, P.L. Hansen, *Catal. Today* **111** (2006) 68.

[19] J.L. Figueiredo, D.L. Trimm, *J. Catal.* **40** (1975) 154.

[20] A.F. Cunha, J.J.M. Órfão, J.L. Figueiredo, *Appl. Catal. A: Gen.* **354** (2008) 102.

[21] M. Monthioux, P. Serp, E. Flahaut, C. Laurent, A. Peigney, M. Razafinimanana, W. Bacsa, J.-M. Broto. Introduction to carbon nanotubes. In "Springer handbook of nanotechnology" Second revised and extended Edition B. Bhushan (ed.), Springer-Verlag, Heidelberg, Germany (2007) p. 43.

[22] P. Serp, M. Corrias, P. Kalck, *Appl. Catal. A: Gen.* **253** (2003) 337.

[23] P.M. Ajayan, *Chem. Rev.* **99** (1999) 1787.

[24] A. Krüger, Neue Kohlenstoffmaterialien, Teubner Verlag (2006).

[25] N. Mahata, A.F. Cunha, J.J.M. Órfão, J.L. Figueiredo, *Appl. Catal. A: Gen.* **351** (2008) 204.

[26] N. Mahata, A.F. Cunha, J.J.M. Órfão, J.L. Figueiredo, *Catal. Commun.* **10** (2009) 1203.

[27] J. R. Rostrup-Nielsen, *J. Catal.* **33** (1974) 184.

[28] M.T. Tavares, I. Alstrup, C.A.A. Bernardo, *Mater. & Corr.* **50** (1999) 681.

[29] A.F. Cunha, J.J.M. Órfão, J.L. Figueiredo, *Int. J. Hydrogen Energy*
DOI: 10.1016/j.ijhydene.2009.03.040

[30] H. Idriss, M.A. Barteau, *Advances in Catalysis* **45** (2000) 261.

[31] P.-X. Hou, C. Liu, H.-M. Cheng, *Carbon* **46** (2008) 2003.

## Declaração

Declaro sob juramento que esta tese de doutoramento foi elaborada com os instrumentos indicados, sem ajuda de terceiros e que todos os resultados obtidos correspondem à verdade.

Porto, em 15 de Maio de 2009

_____

Dipl. -Ing. Filipe Cunha

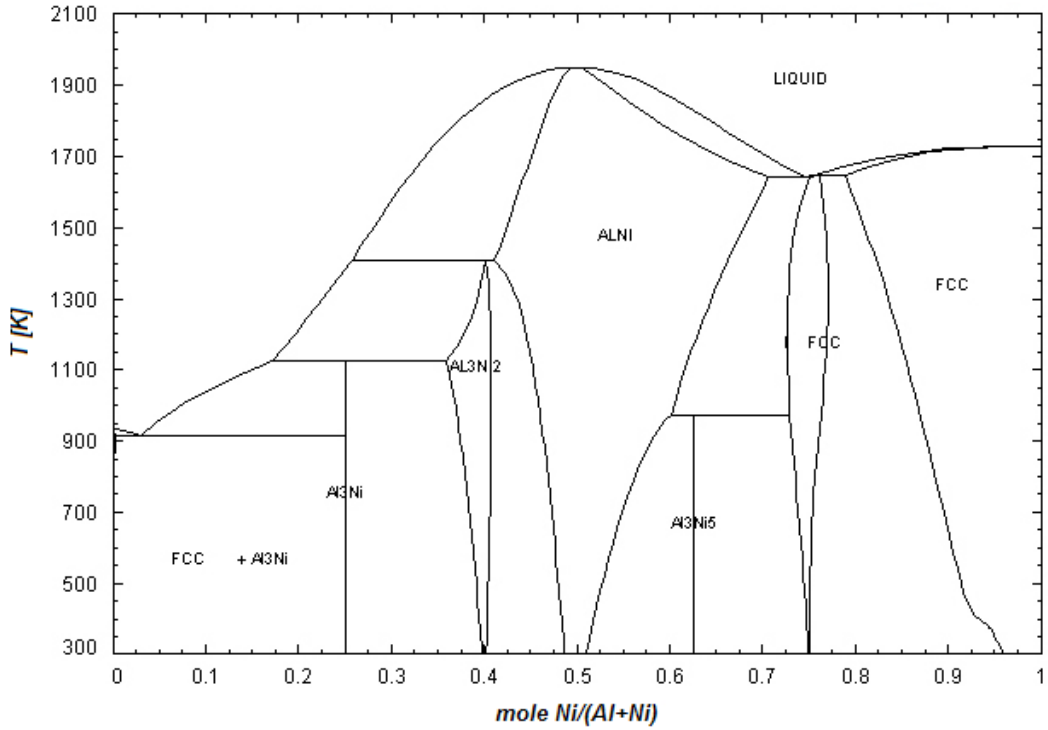



Fig. 0-0 SEM micrograph obtained on Ph.D. student Filipe Cunha ☺

# *Appendix*

**0. Phase Diagrams** 215
**I. Laser particle size analysis (LPSA)** 222
**II. Isotherms** 245
**III. Scanning electron microscopy (SEM)** 252
**IV. Energy dispersive X-ray Spectroscopy (EDX)** 272
**V. X-Ray Photoelectron Spectroscopy** 278
**VI. X-Ray Diffraction** 332
**VII. Thermodynamic calculations** 342
**VIII. Reaction studies and Kinetics** 347
**IX. Theoretical Calculation of Carbon Mass formation** 351
**X. Temperature programmed studies** 352
**XI. Isothermal reaction studies** 366
**XII. SEM, TEM and XRD analysis of the composite materials** 376

## 0. Phase Diagrams




0.1 Phase diagram of the bimetallic Ni-Al system.

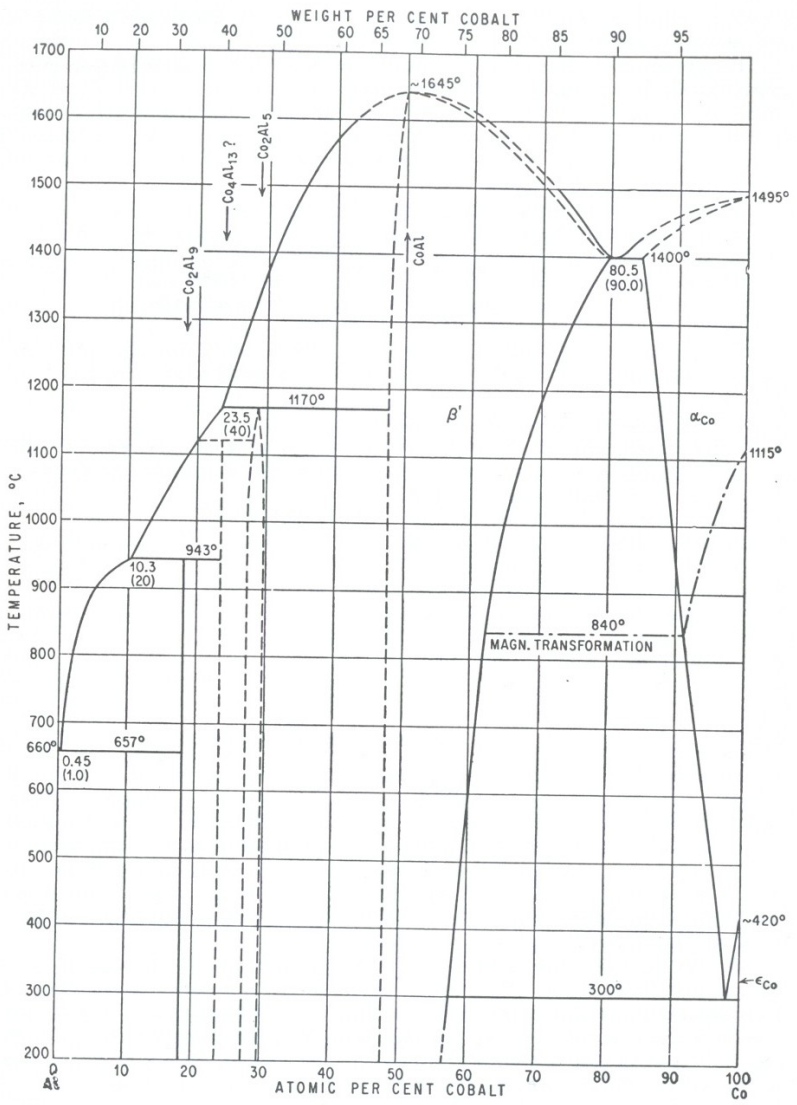



Fig. 50. Al-Co

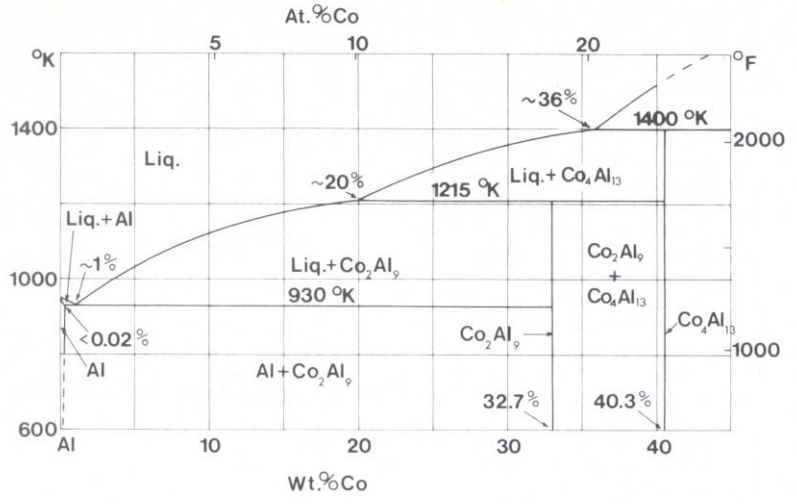
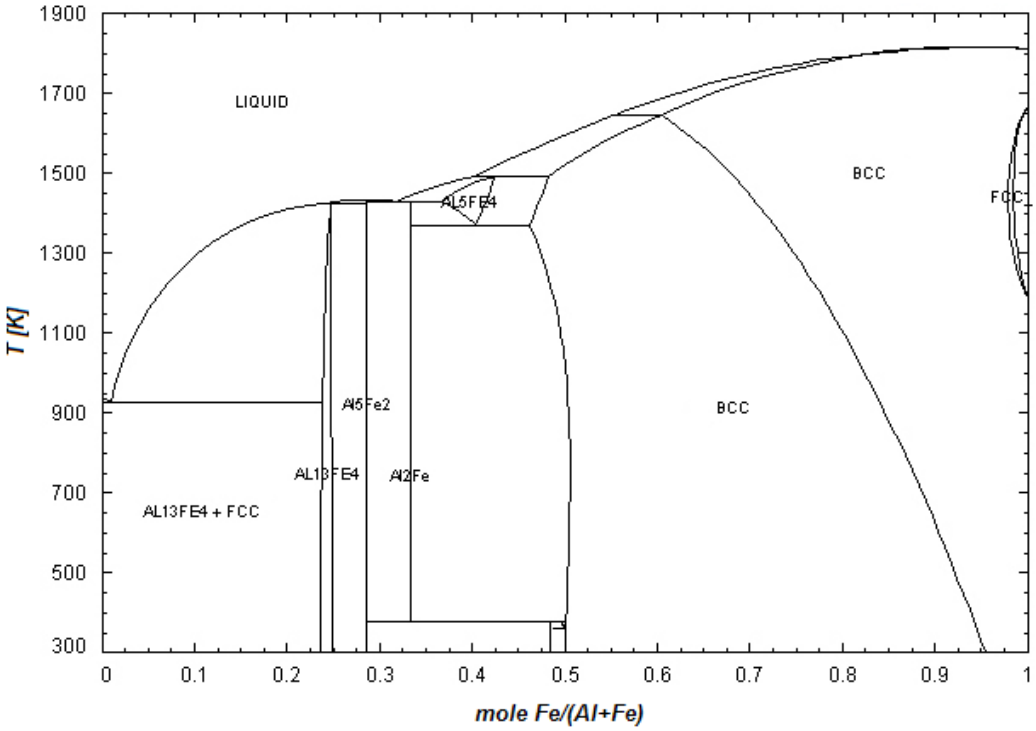
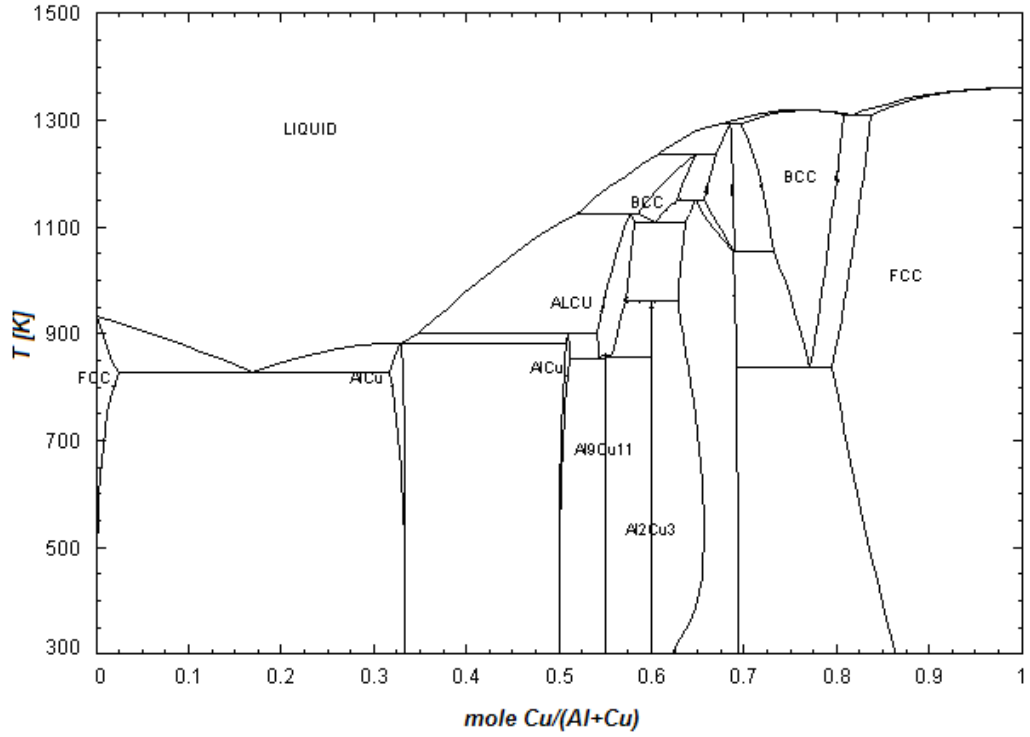



*Figure 2.15. The aluminum end of the aluminum–cobalt equilibrium diagram*

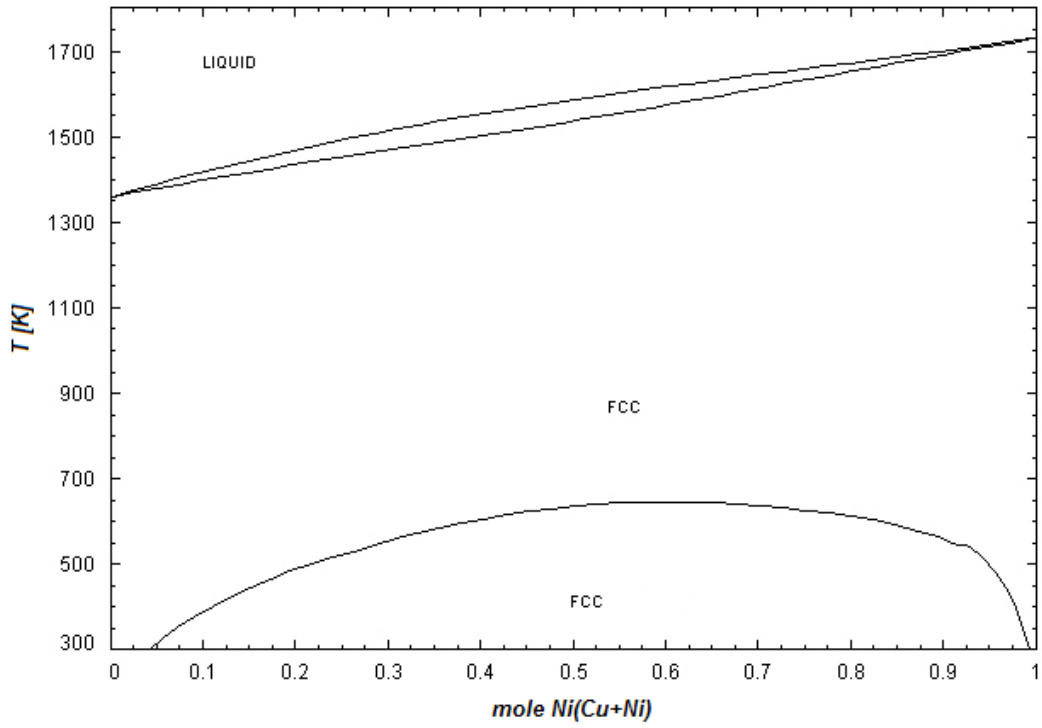
0.2 Phase diagram of the bimetallic Co-Al system.



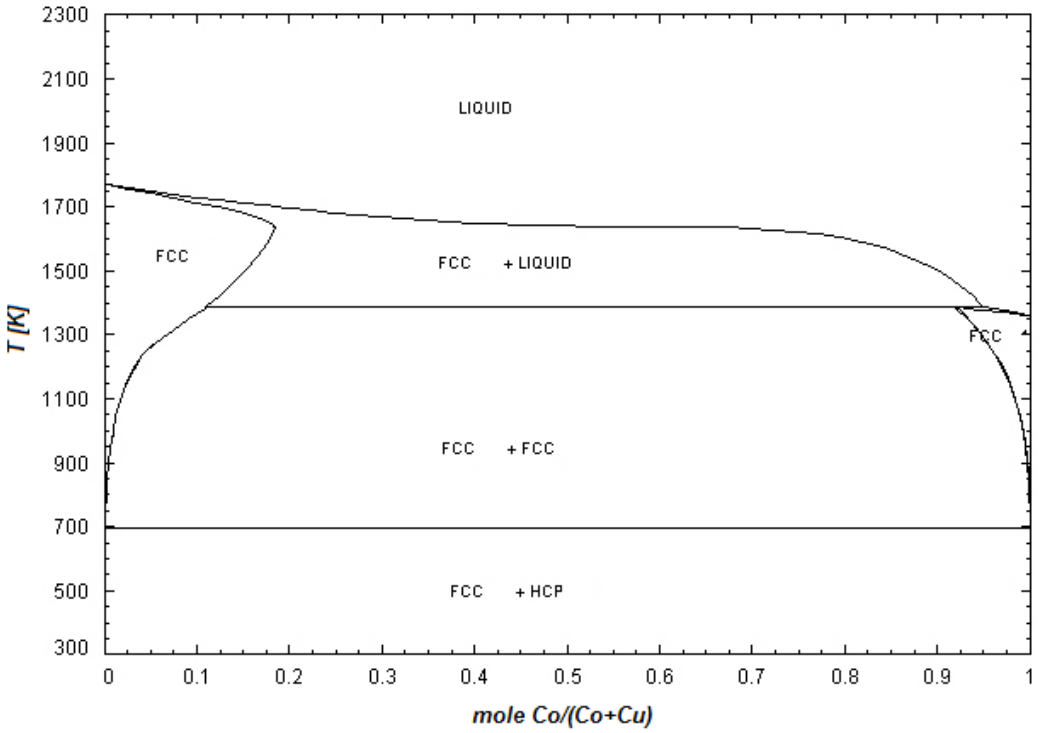

0.3 Phase diagram of the bimetallic Fe-Al system.



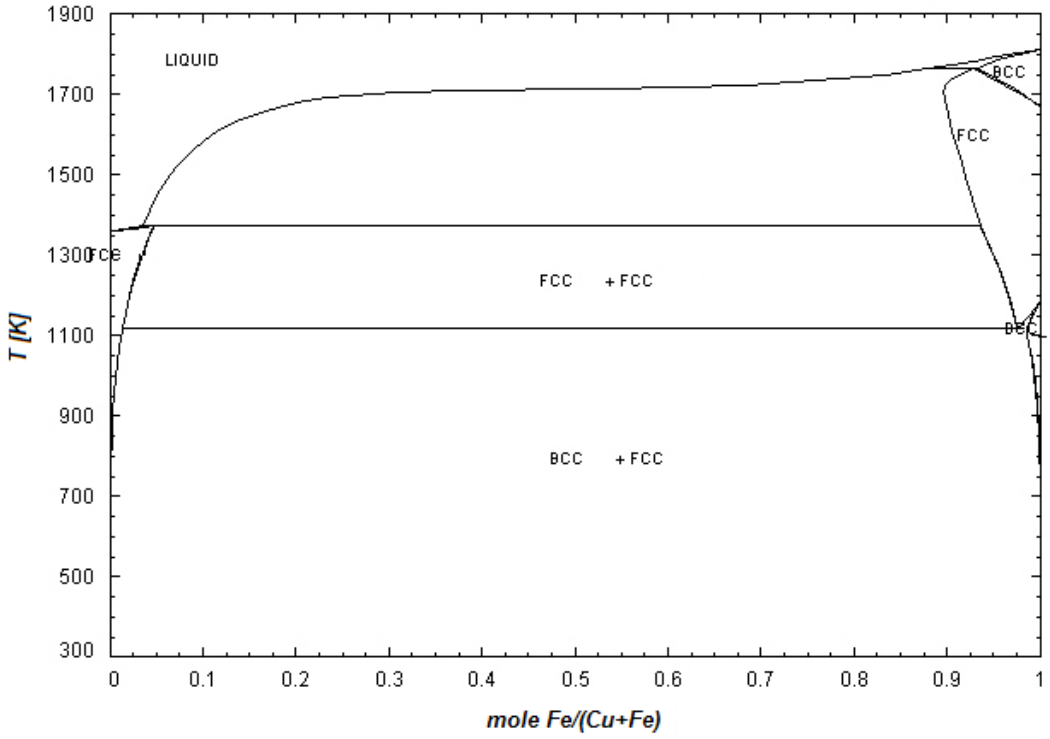

0.4 Phase diagram of the bimetallic Cu-Al system.



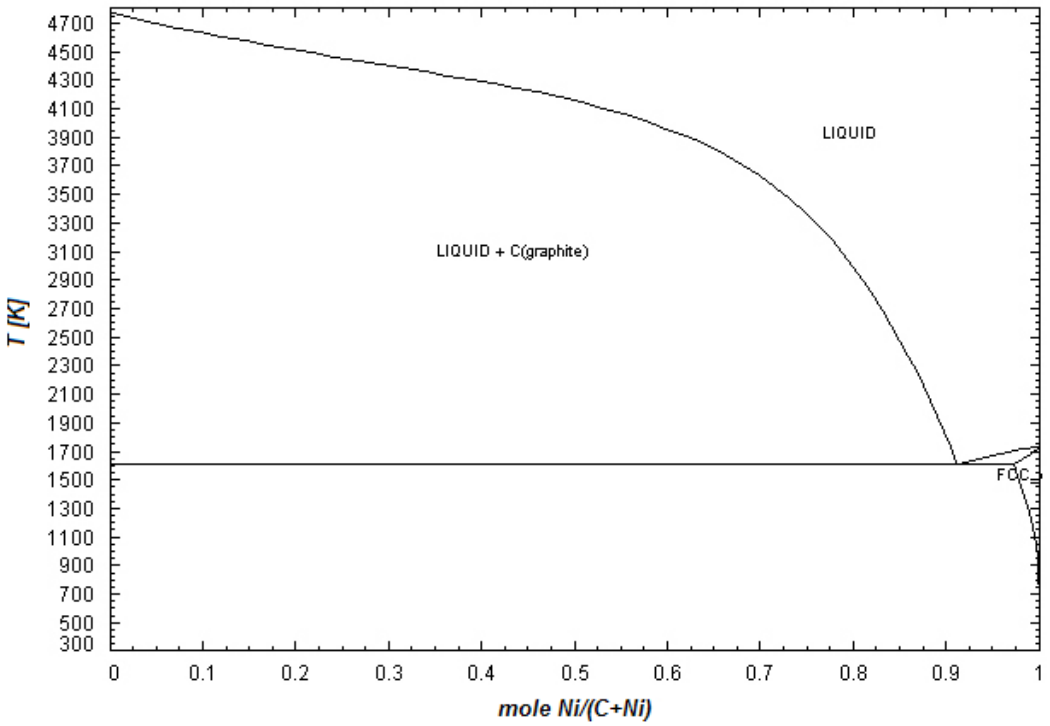

0.5 Phase diagram of the bimetallic Ni-Cu system.



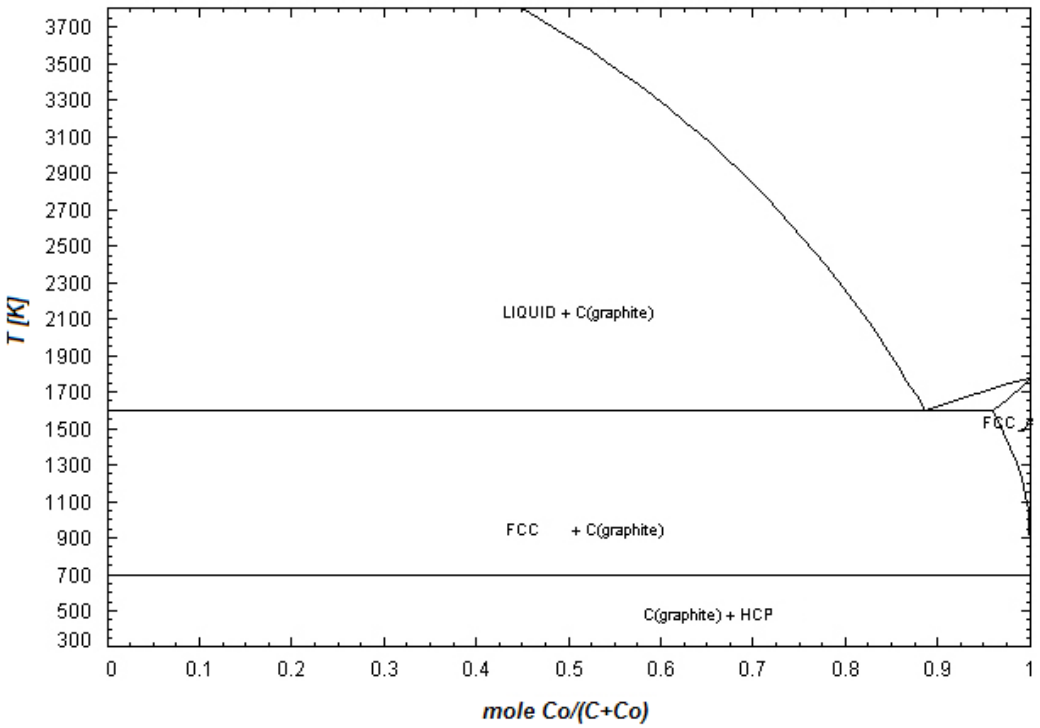

0.6 Phase diagram of the bimetallic Co-Cu system.



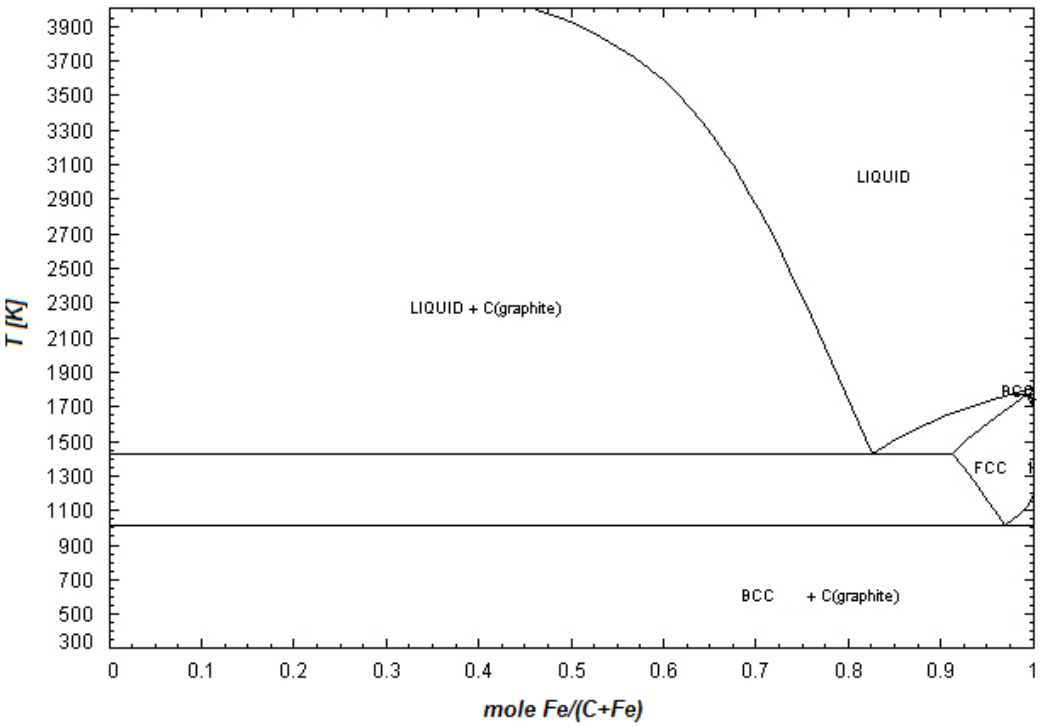

0.7 Phase diagram of the bimetallic Fe-Cu system.



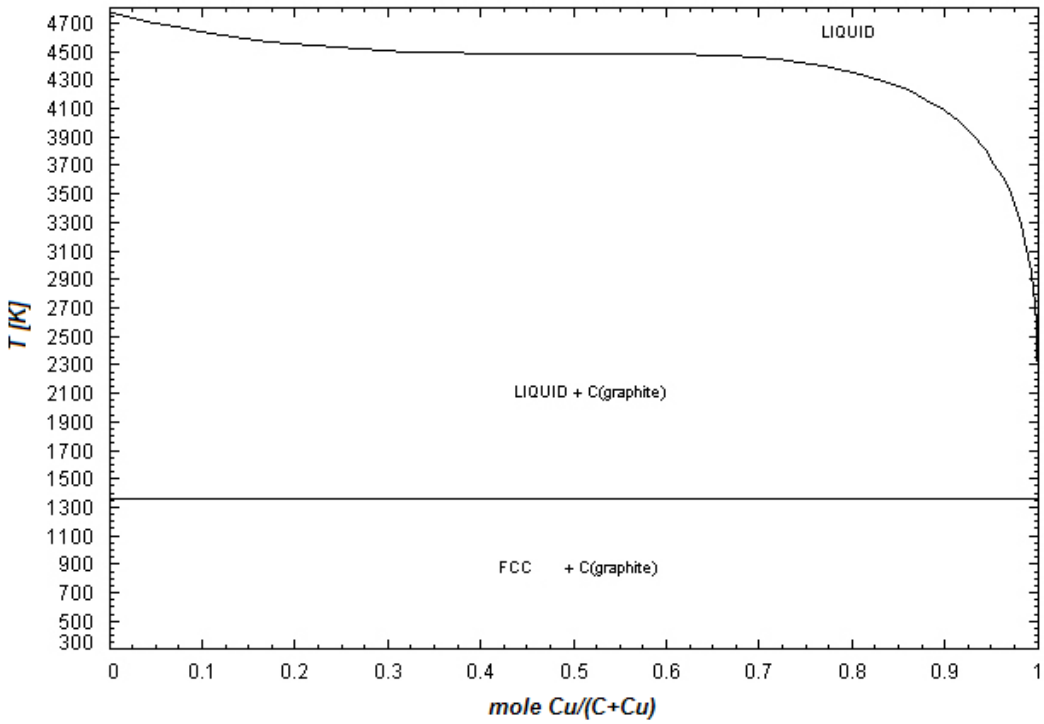

0.8 Phase diagram of the Ni-C system.




0.9 Phase diagram of the Co-C system.




0.10 Phase diagram of the Fe-C system.




0.11 Phase diagram of the Cu-C system.

## I. Laser particle size analysis (LPSA)

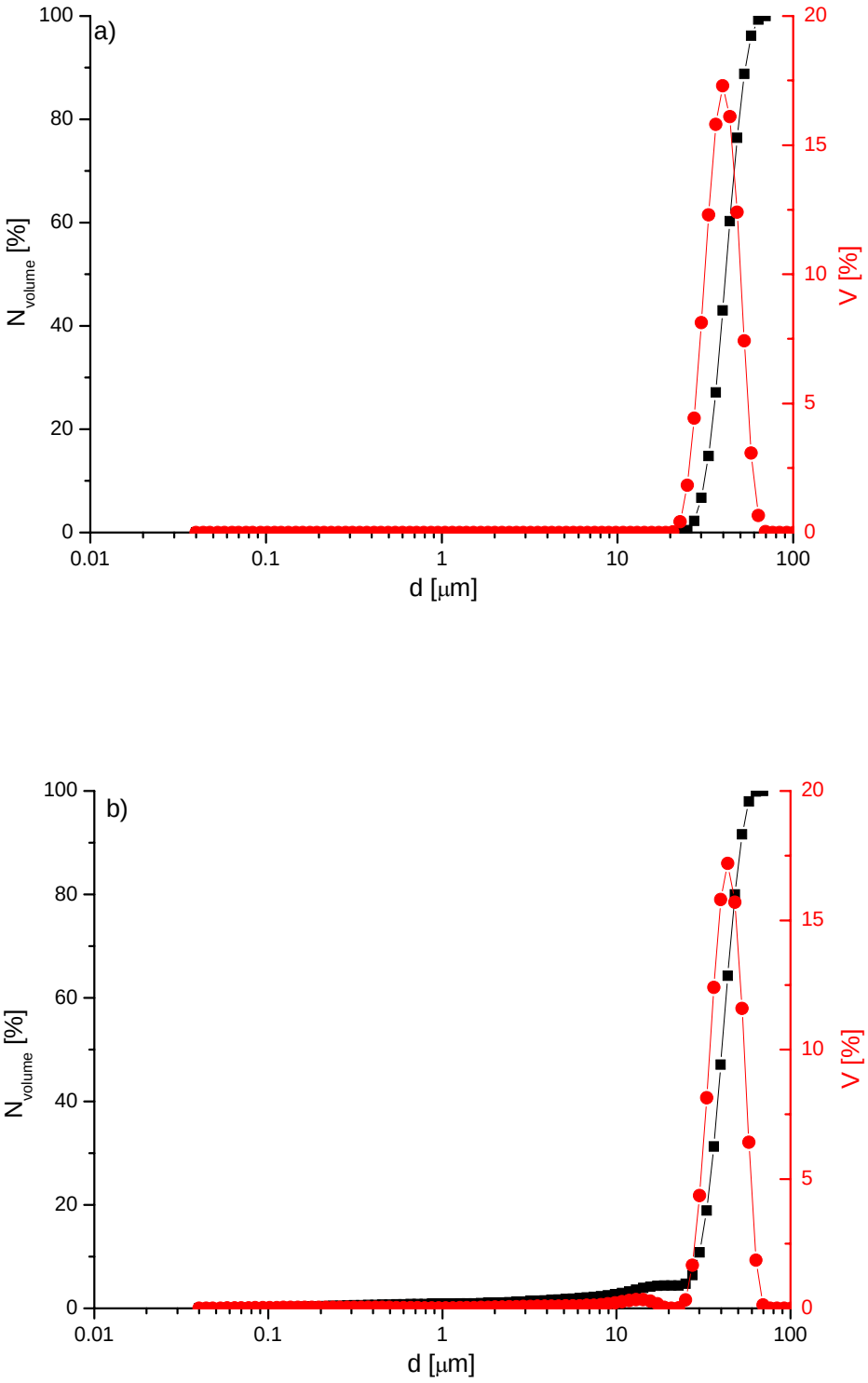



Fig. I-1 Integral & Differential arithmetic volume statistics on Ni69 alloy particles (a) and catalyst particles (b).

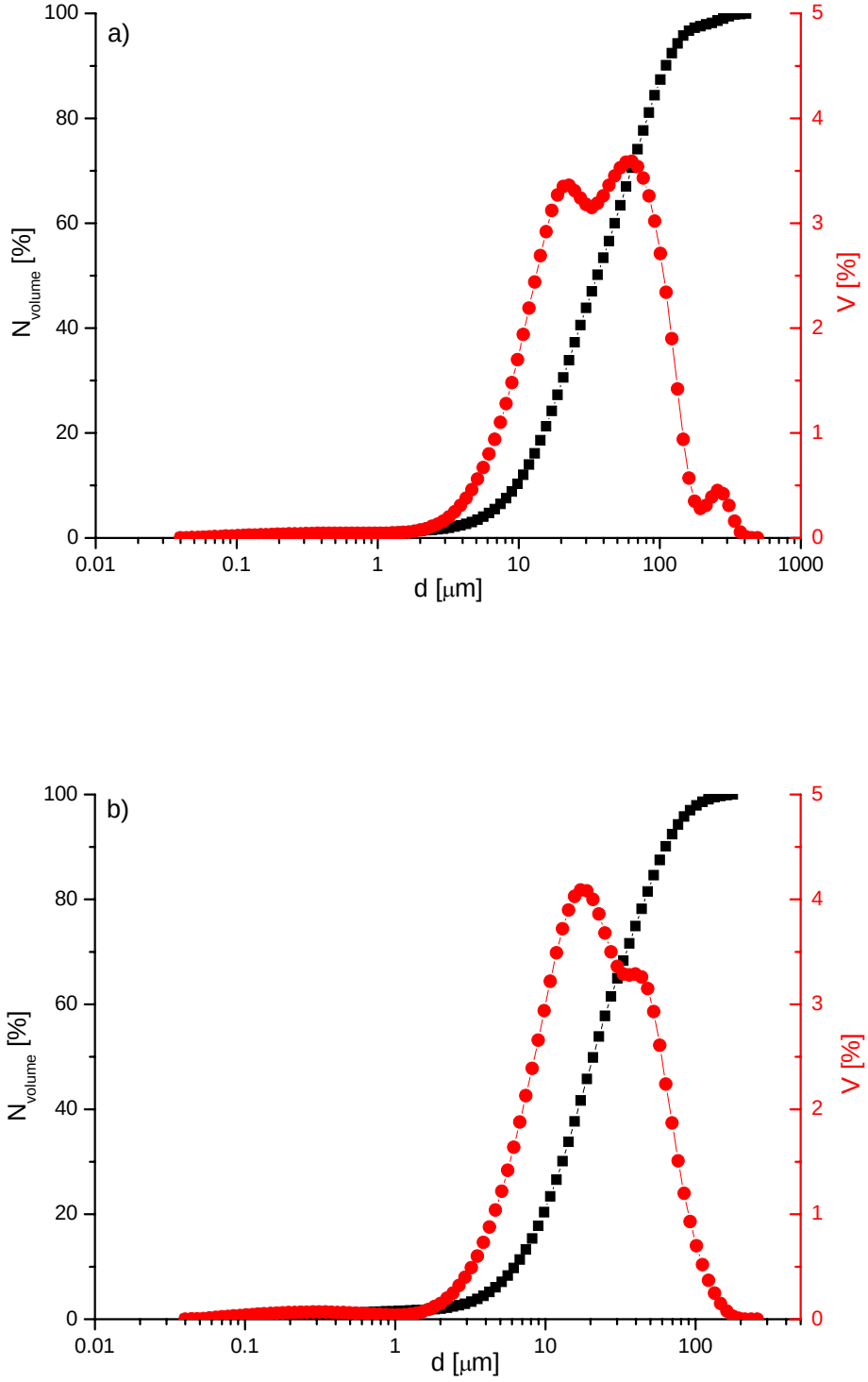



Fig. I-2 Integral & Differential arithmetic volume statistics on Ni50 alloy particles (a) and catalyst particles (b).

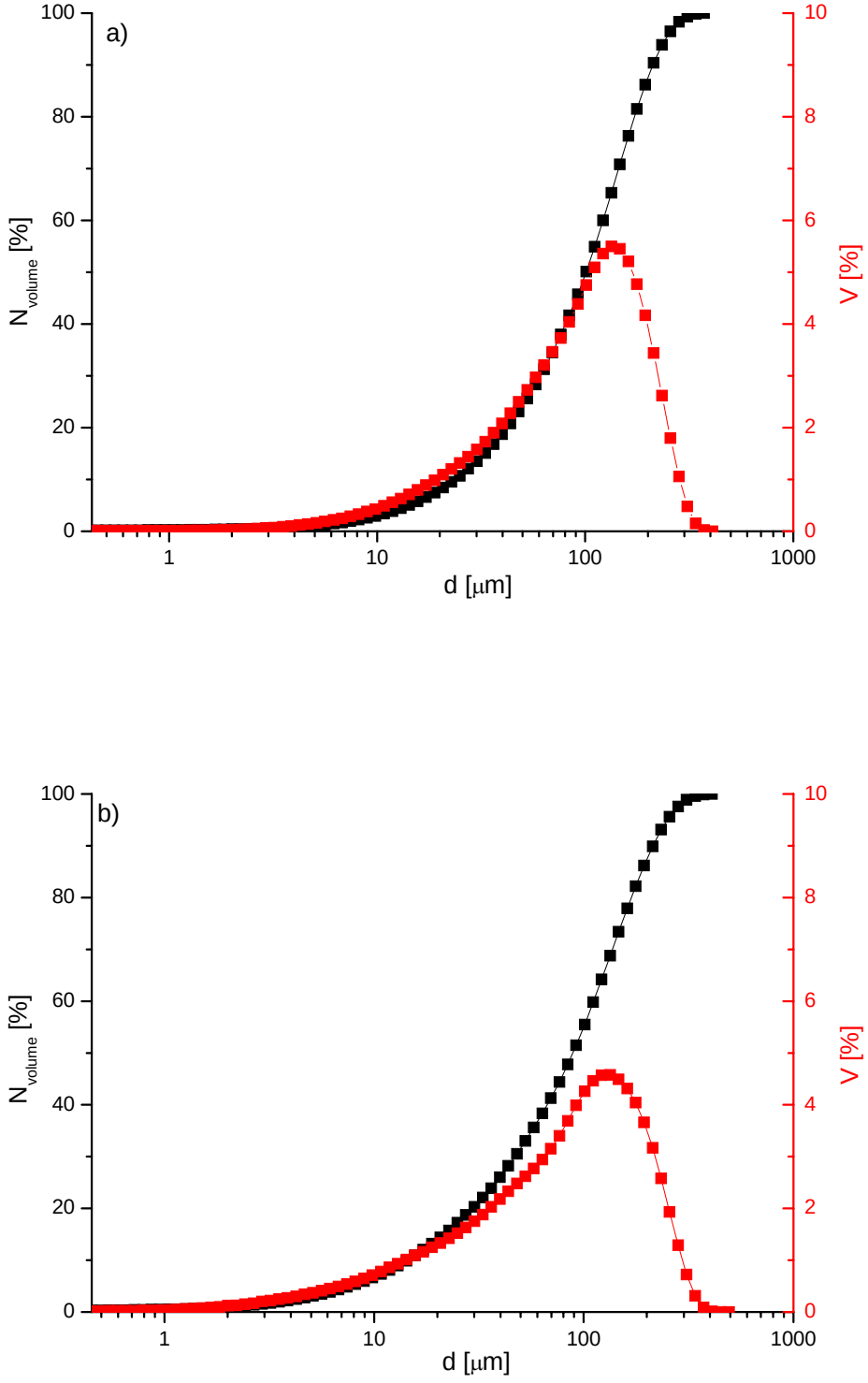



Fig. I-3 Integral & Differential arithmetic volume statistics on Ni47-Mo6 alloy (a) and catalyst particles (b).

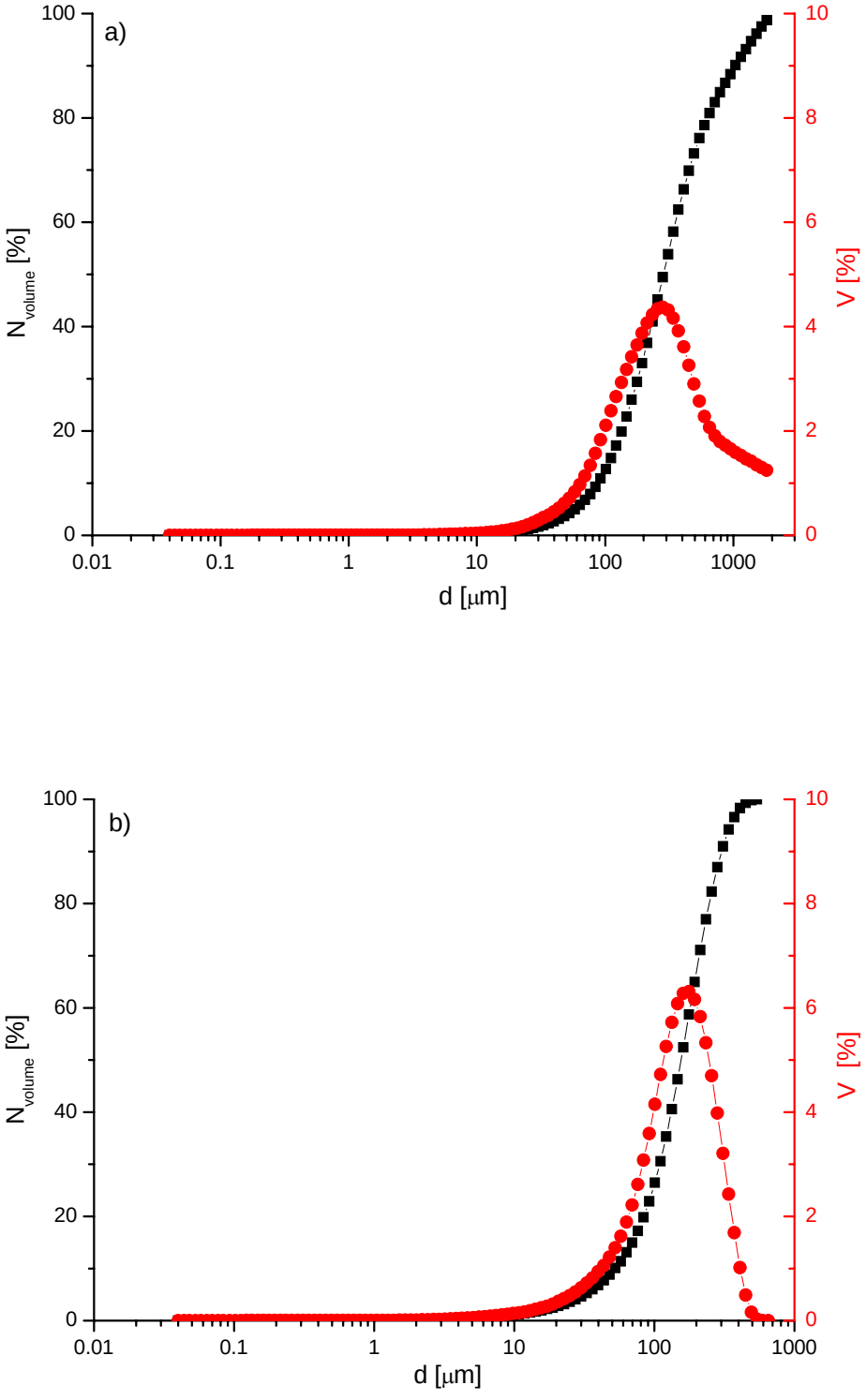



Fig. I-4 Integral & Differential arithmetic volume statistics on Ni30(a) alloy particles and catalyst particles (b).

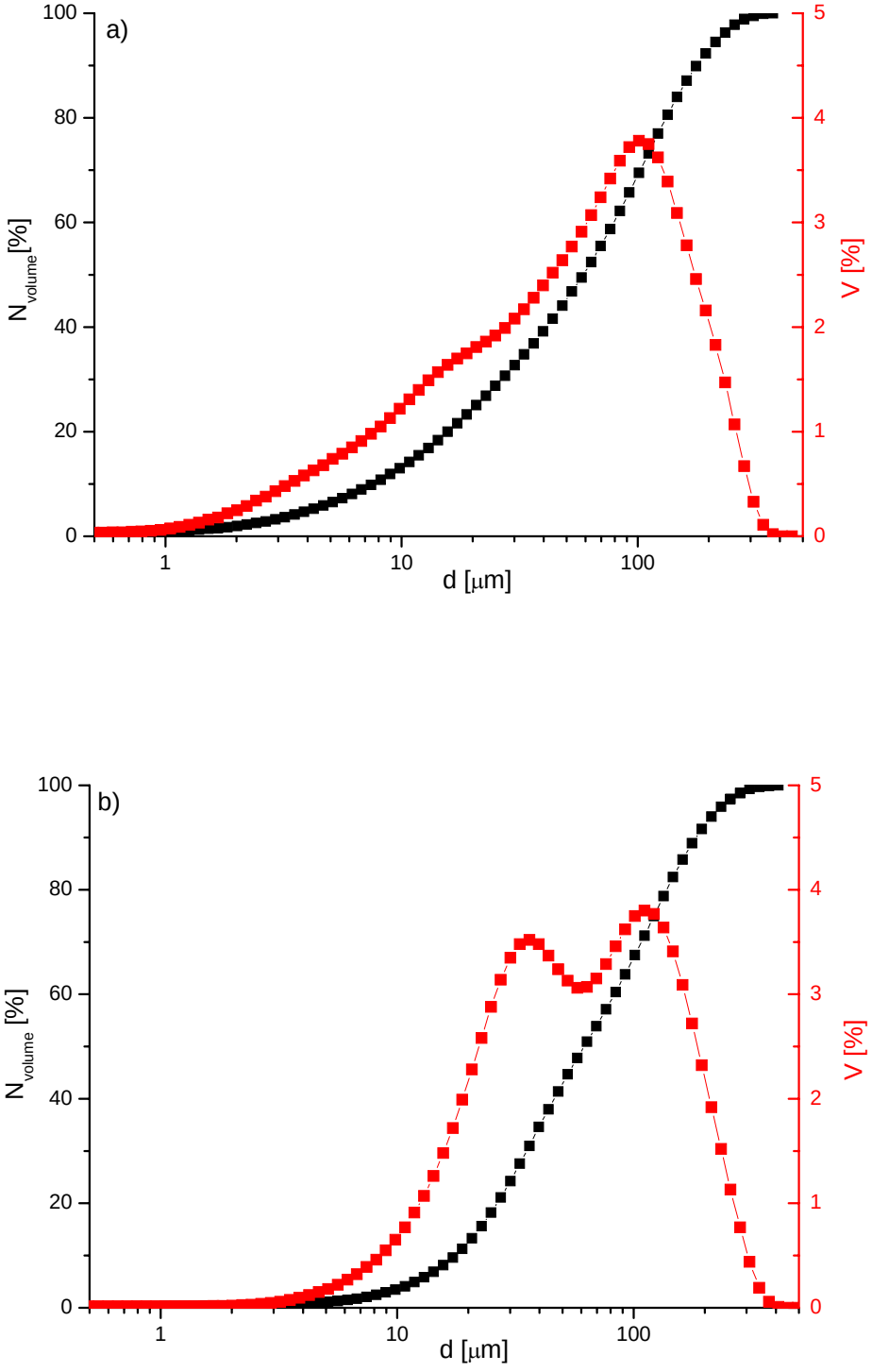



Fig. I-5 Integral & Differential arithmetic volume statistics on Co50 (a) alloy particles and catalyst particles (b).

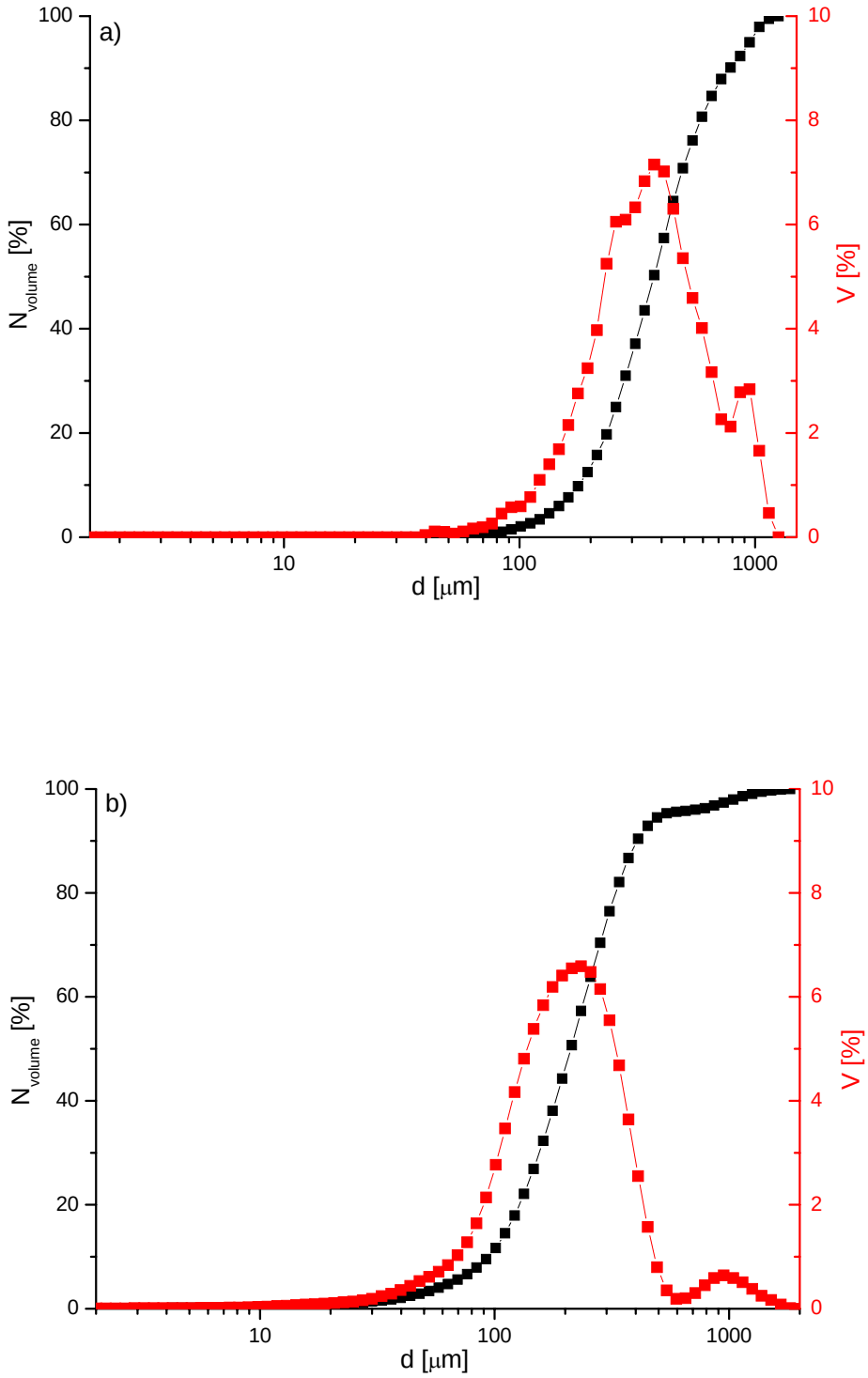



Fig. I-6 Integral & Differential arithmetic volume statistics on Co30 (a) alloy particles and catalyst particles (b).

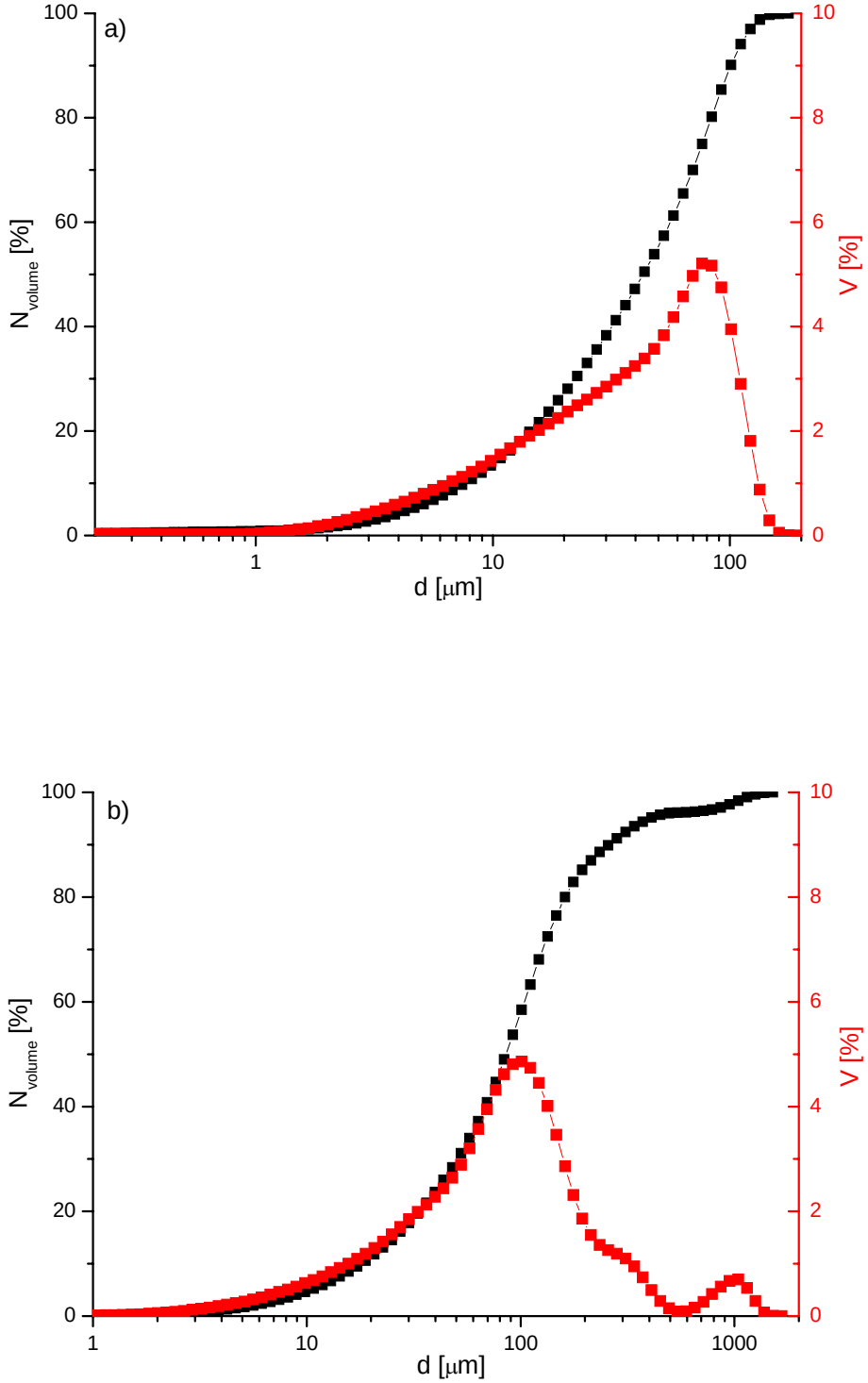



Fig. I-7 Integral & Differential arithmetic volume statistics on Fe50 (a) alloy particles and catalyst particles (b).

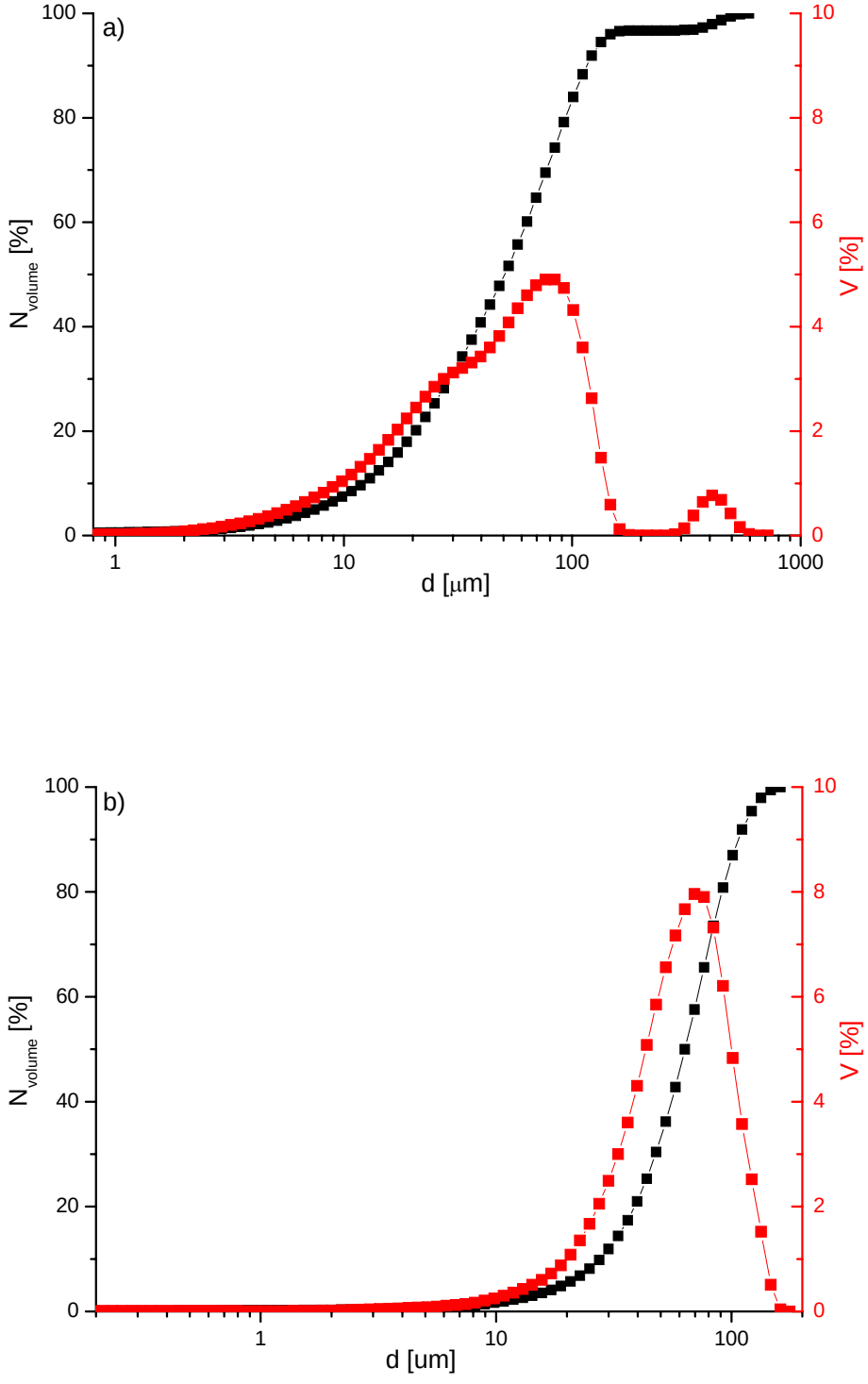



Fig. I-8 Integral & Differential arithmetic volume statistics on Fe 35 (a) alloy particles and catalyst particles (b).

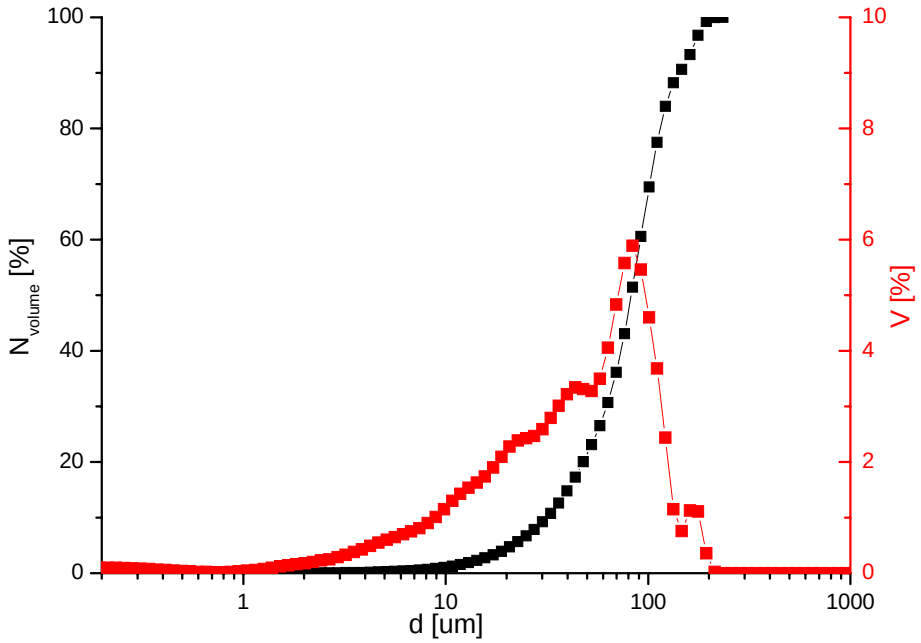



Fig. I-9 Integral & Differential arithmetic volume statistics on Cu50 alloy particles.

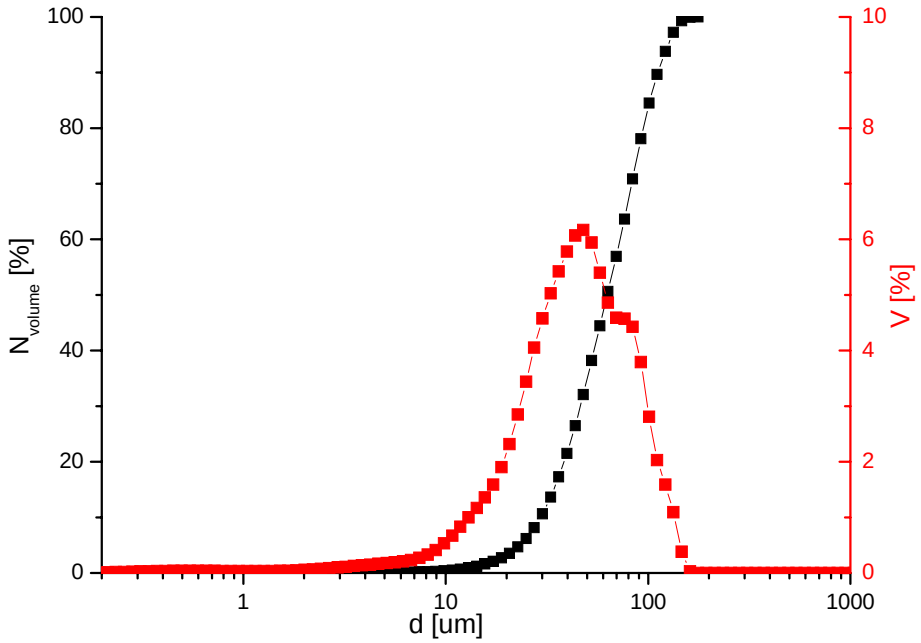



Fig. I-10 Integral & Differential arithmetic volume statistics on Cu50 catalyst particles.

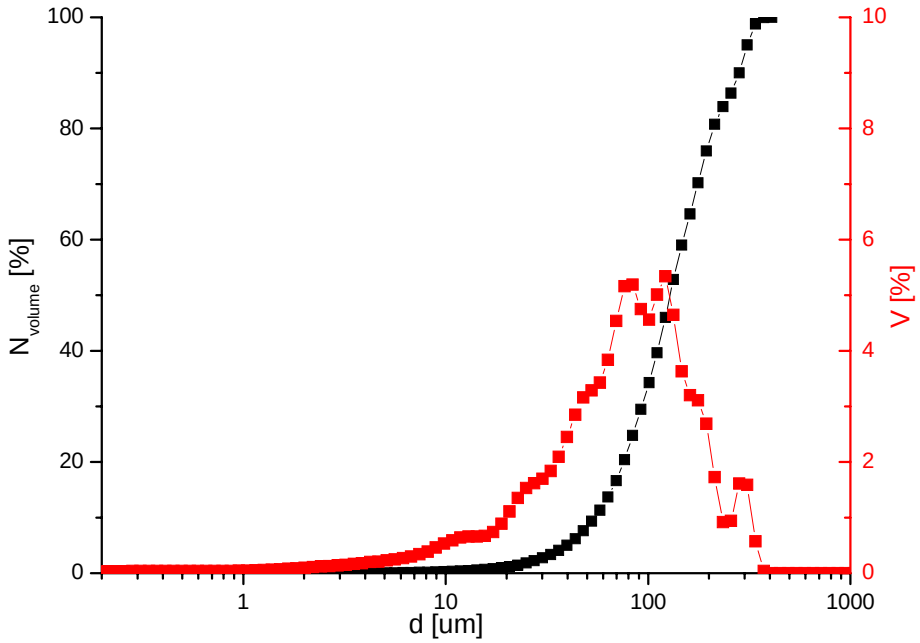



Fig. I-11 Integral & Differential arithmetic volume statistics on Ni30Cu50 (ITT) catalyst particles.

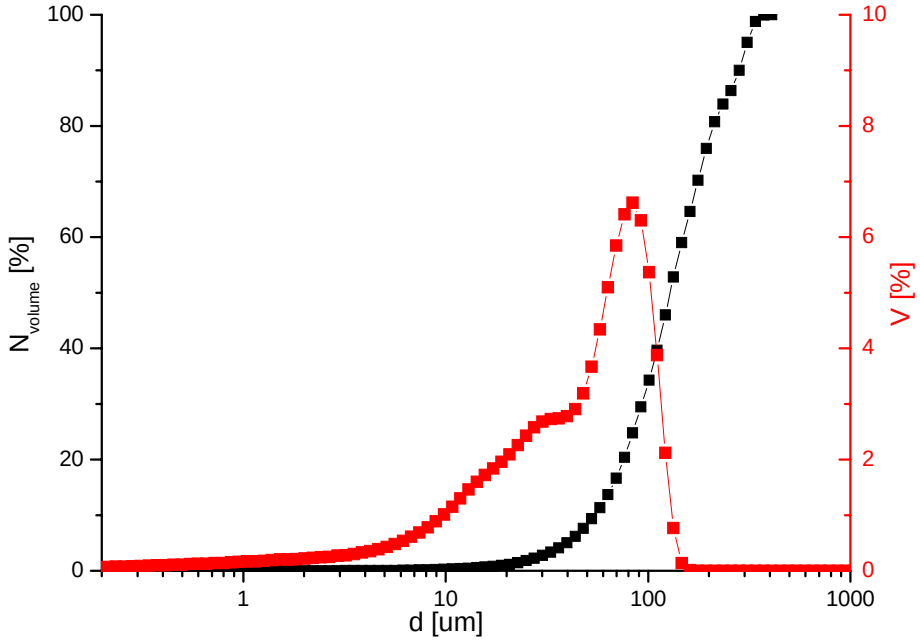



Fig. I-12 Integral & Differential arithmetic volume statistics on Ni50Cu50 (ITT) catalyst particles.

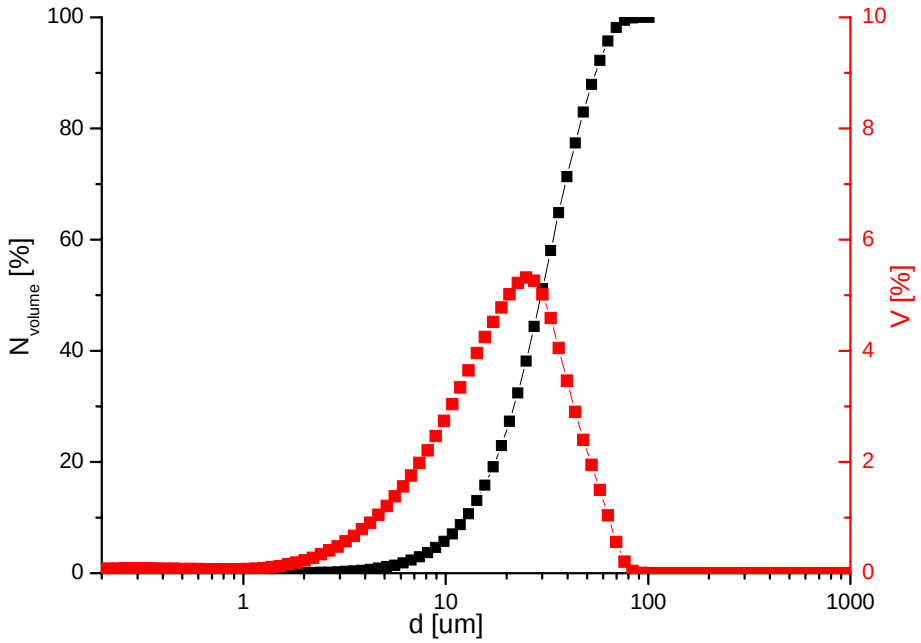



Fig. I-13 Integral & Differential arithmetic volume statistics on Co30Cu50 (ITT) catalyst particles.

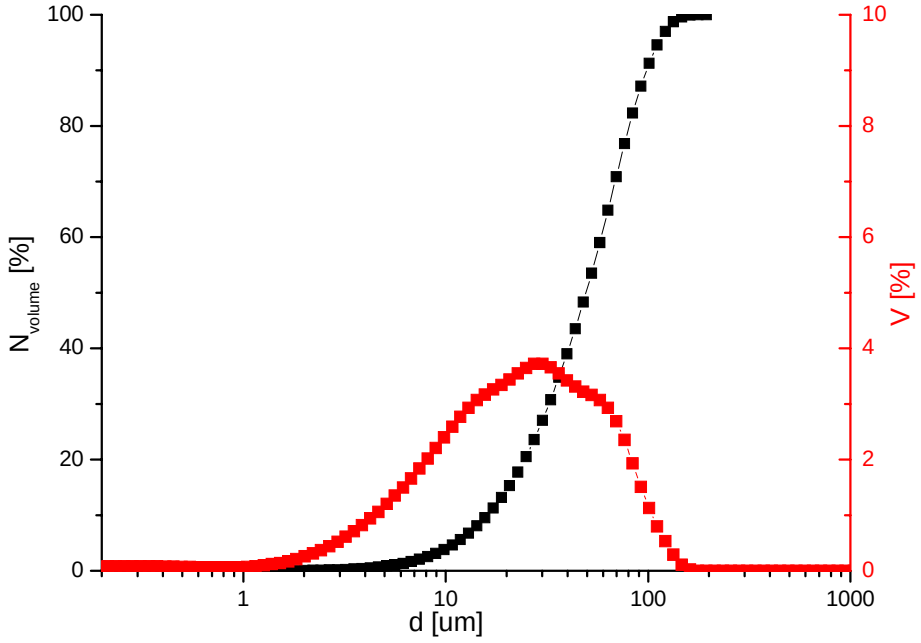



Fig. I-14 Integral & Differential arithmetic volume statistics on Co50Cu50 (ITT) catalyst particles.

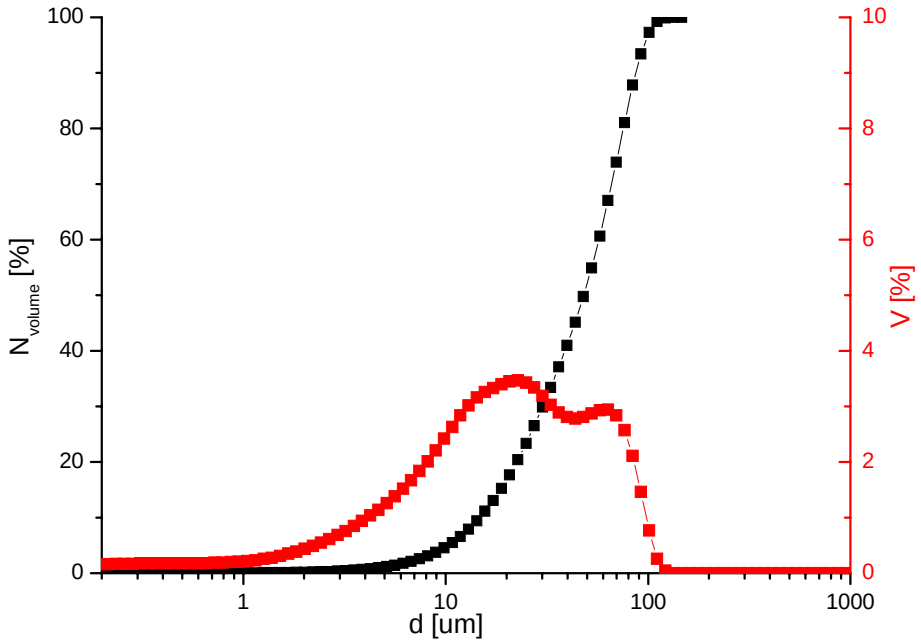



Fig. I-15 Integral & Differential arithmetic volume statistics on Fe50Cu50 (ITT) catalyst particles.

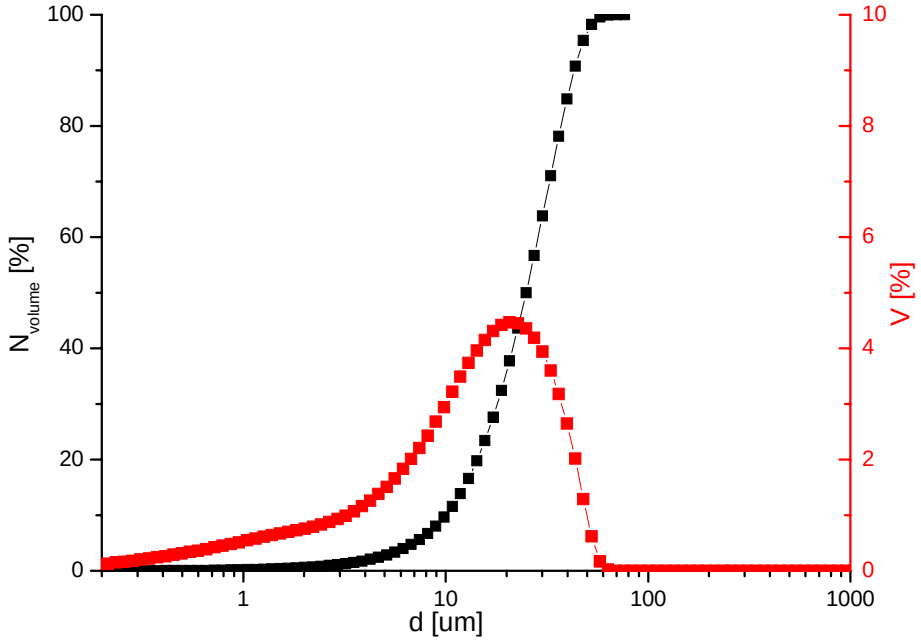



Fig. I-16 Integral & Differential arithmetic volume statistics on Fe35Cu50 (ITT) catalyst particles.

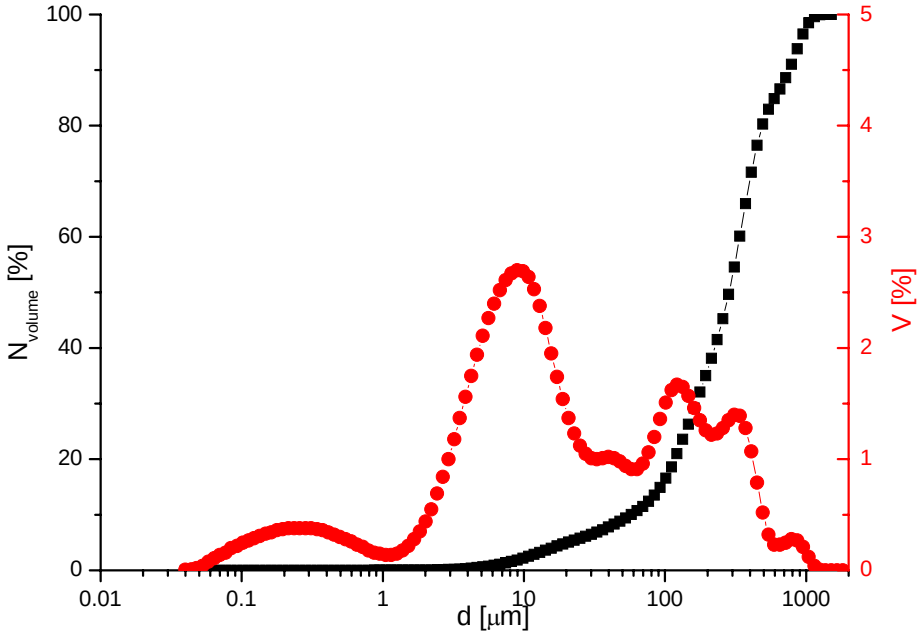



Fig. I-17 Integral & Differential arithmetic volume statistics on $La_2O_3$ particles.

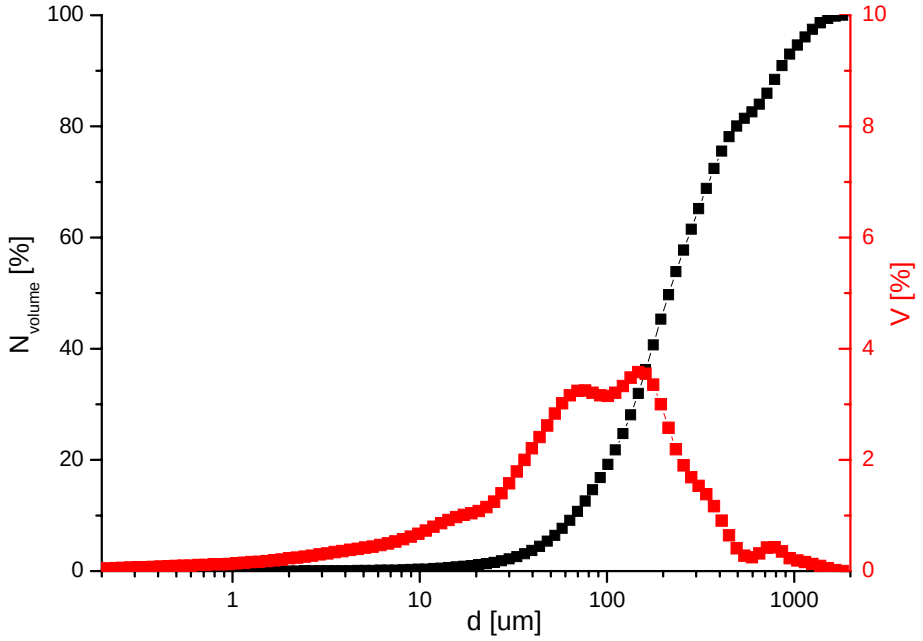



Fig. I-18 Integral & Differential arithmetic volume statistics on Ni50 (HPT) catalyst particles.

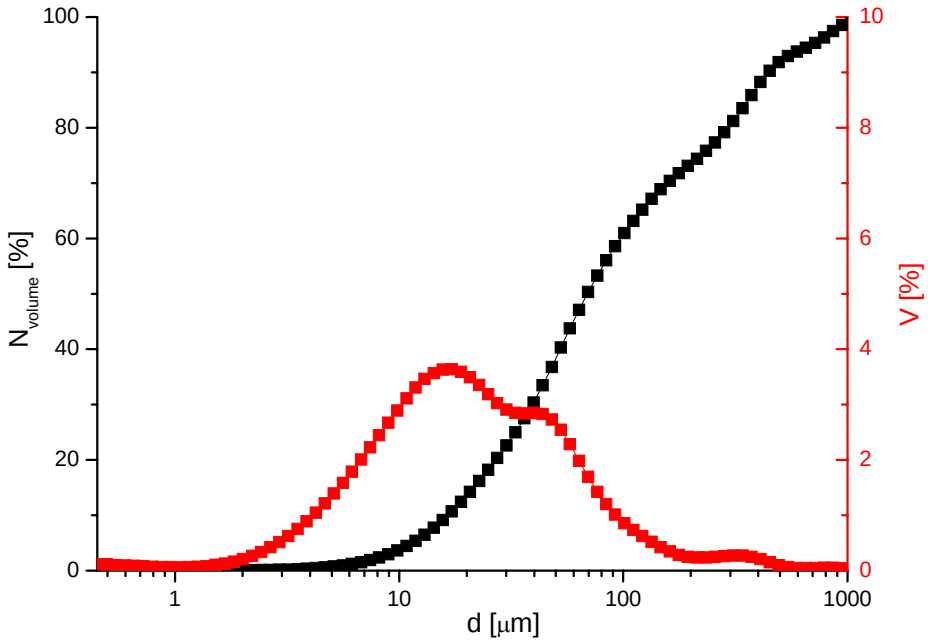



Fig. I-19 Integral & Differential arithmetic volume statistics on Ni50-$La_2O_3$ catalyst particles.

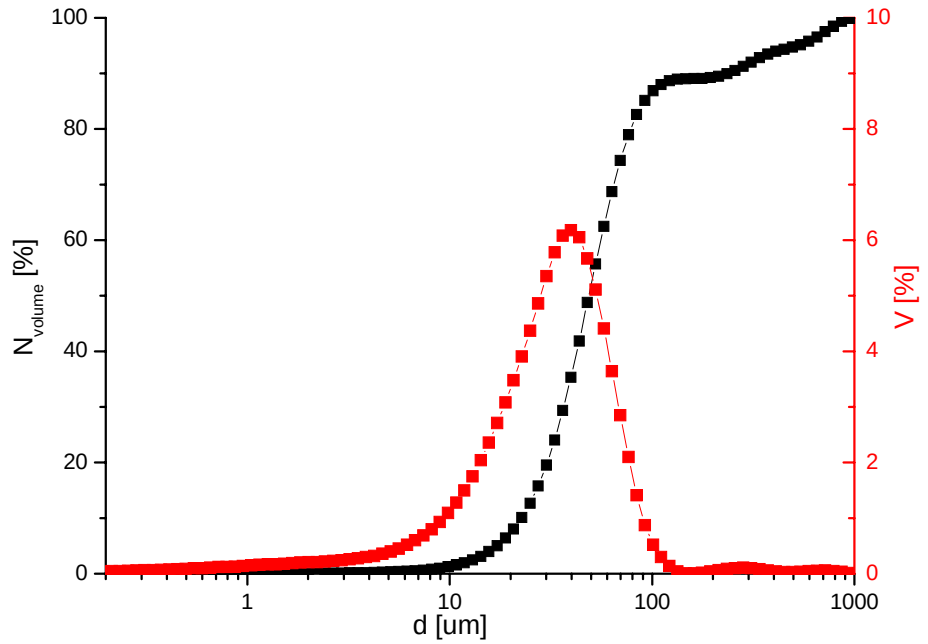



Fig. I-20 Integral & Differential arithmetic volume statistics on Ni50-$La_2O_3$ (HPT) catalyst particles.

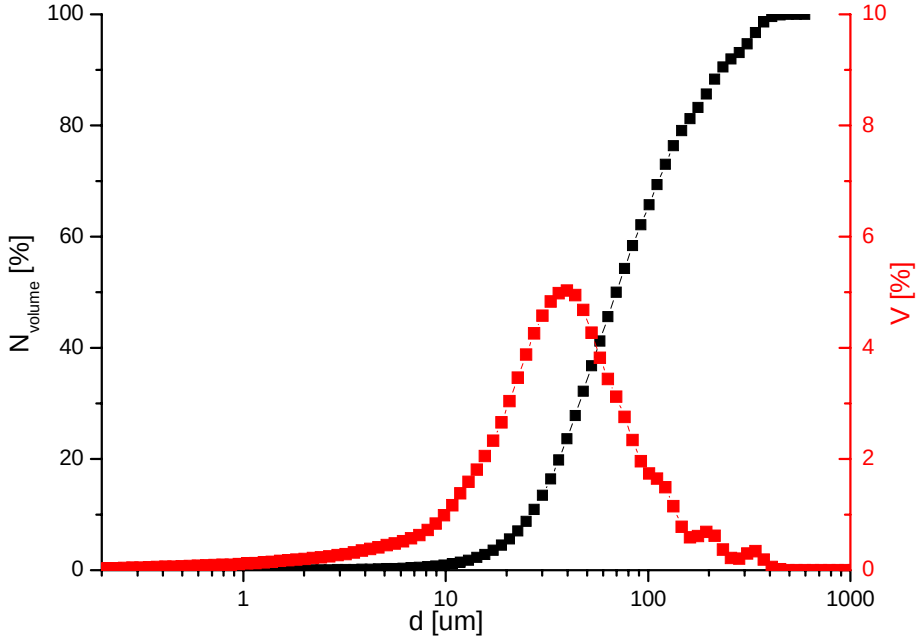



Fig. I-21 Integral & Differential arithmetic volume statistics on Ni30 (HPT) catalyst particles.

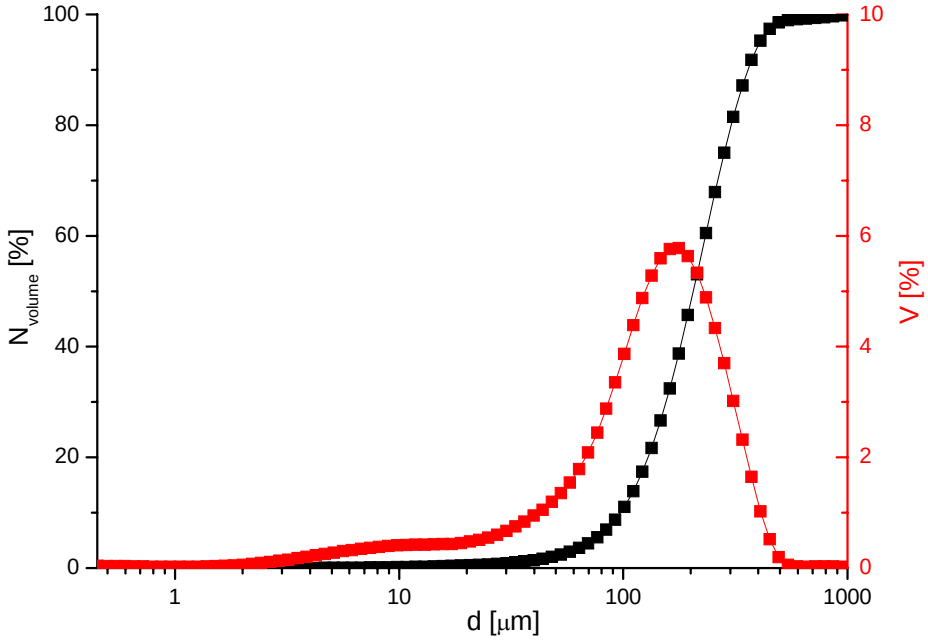



Fig. I-22 Integral & Differential arithmetic volume statistics on Ni30-$La_2O_3$ catalyst particles.

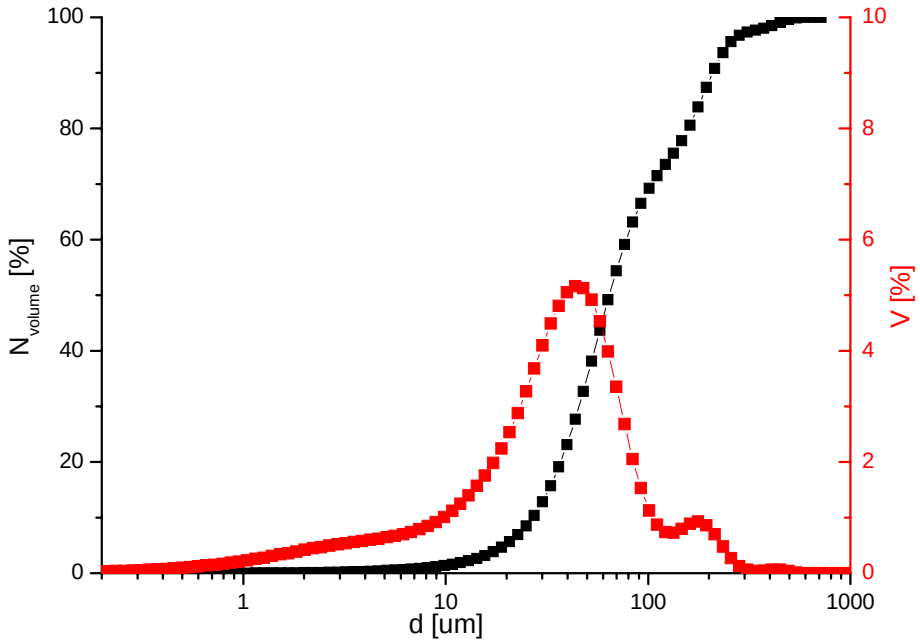



Fig. I-23 Integral & Differential arithmetic volume statistics on Ni30-$La_2O_3$ (HPT) catalyst particles.

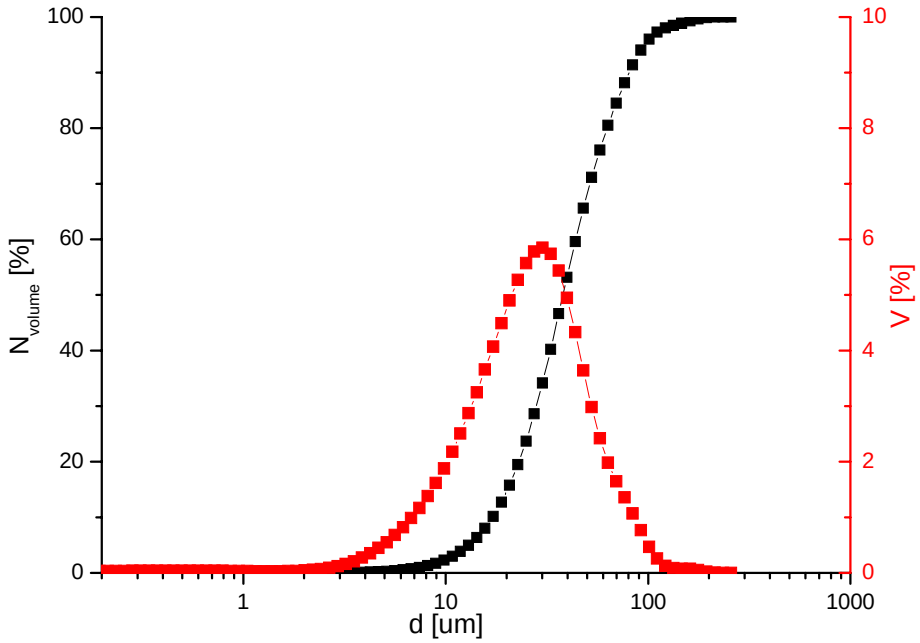



Fig. I-24 Integral & Differential arithmetic volume statistics on Co30 (HPT) catalyst particles.

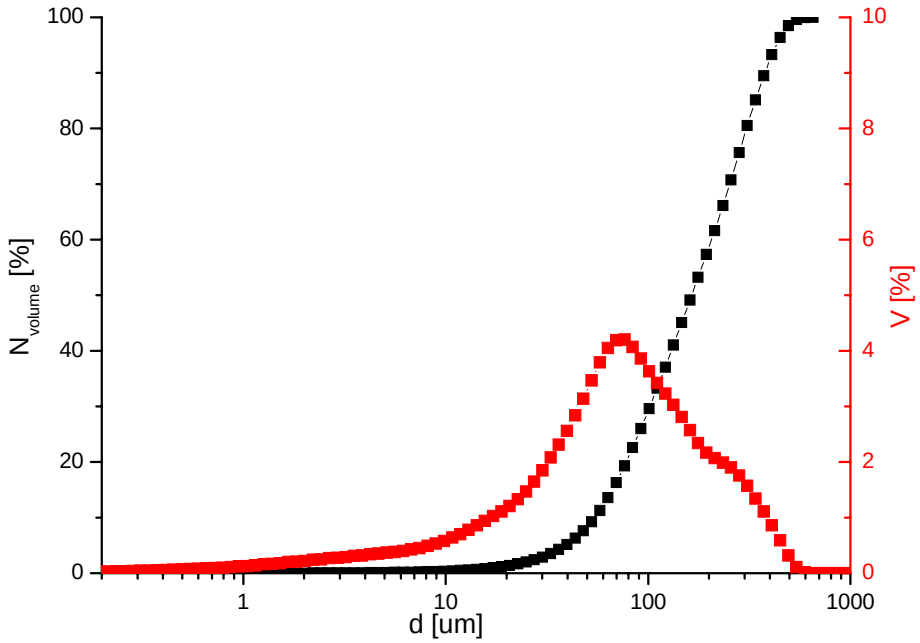



Fig. I-25 Integral & Differential arithmetic volume statistics on Co30-$La_2O_3$ catalyst particles.

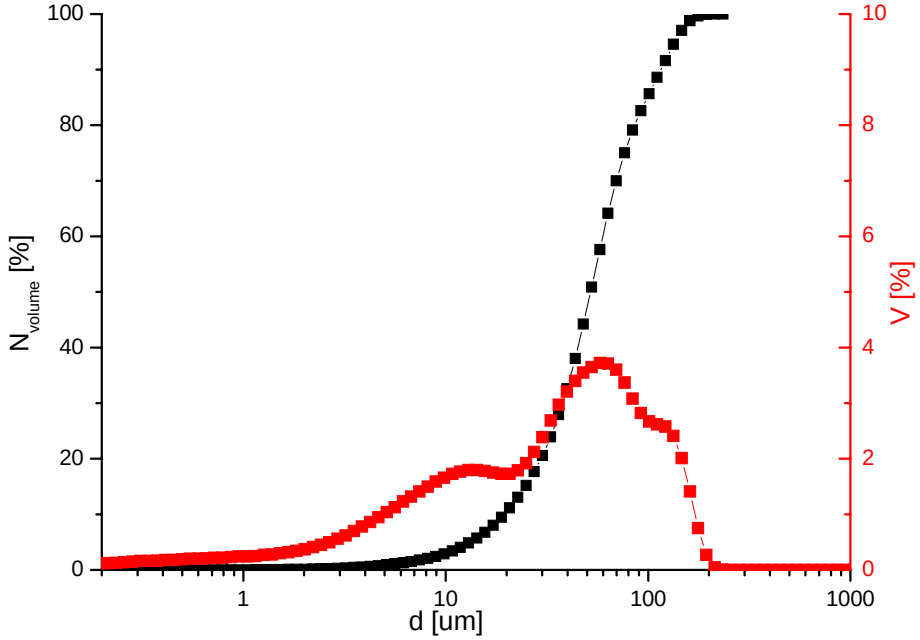



Fig. I-26 Integral & Differential arithmetic volume statistics on Co30-$La_2O_3$ (HPT) catalyst particles.

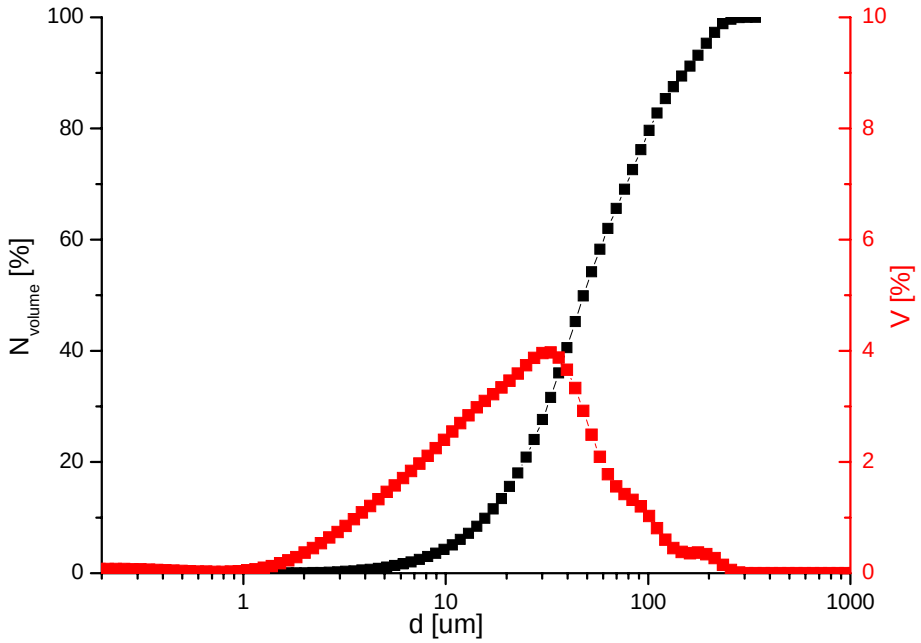



Fig. I-27 Integral & Differential arithmetic volume statistics on Co50 (HPT) catalyst particles.

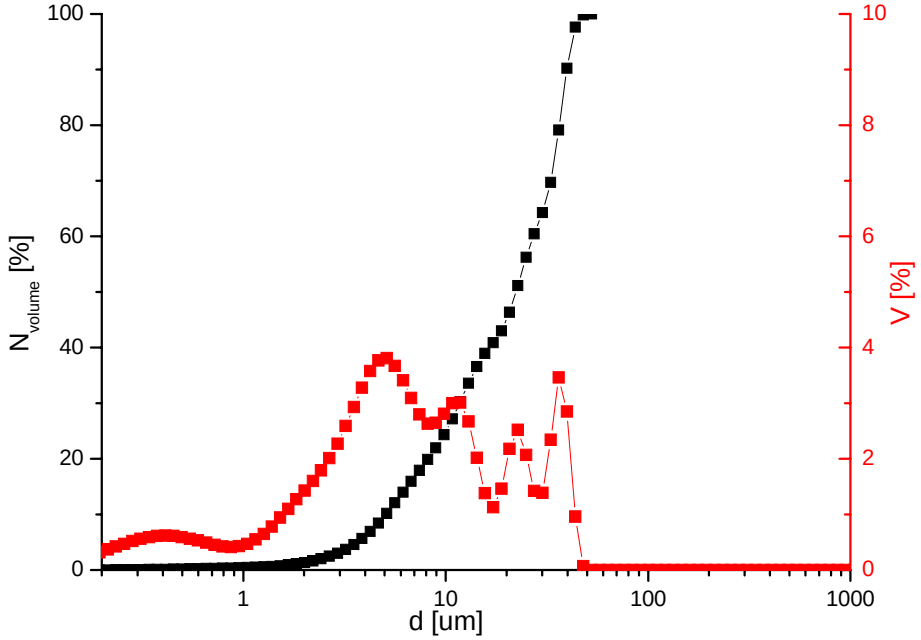



Fig. I-28 Integral & Differential arithmetic volume statistics on Co50-$La_2O_3$ catalyst particles.

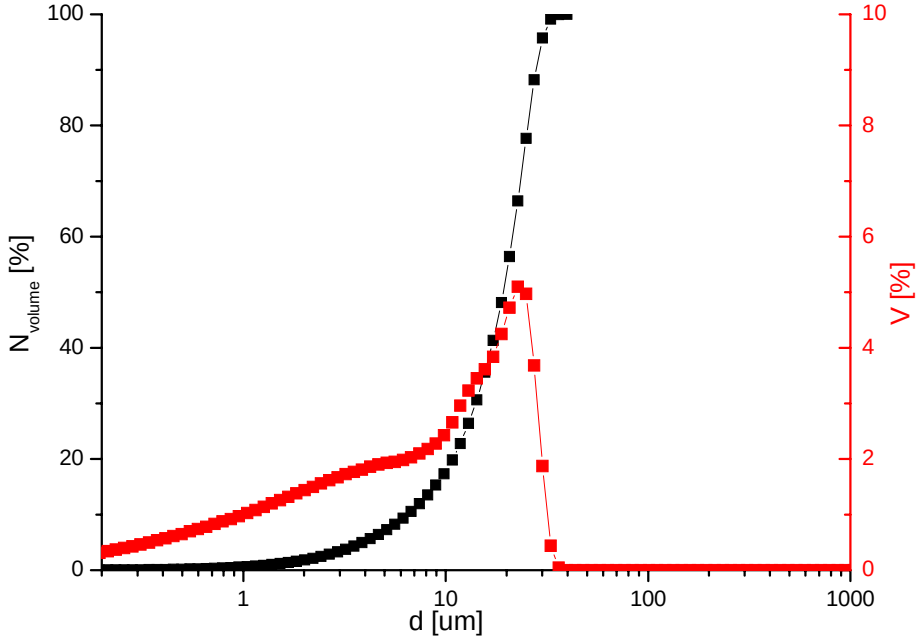



Fig. I-29 Integral & Differential arithmetic volume statistics on Co50-$La_2O_3$ (HPT) catalyst particles.

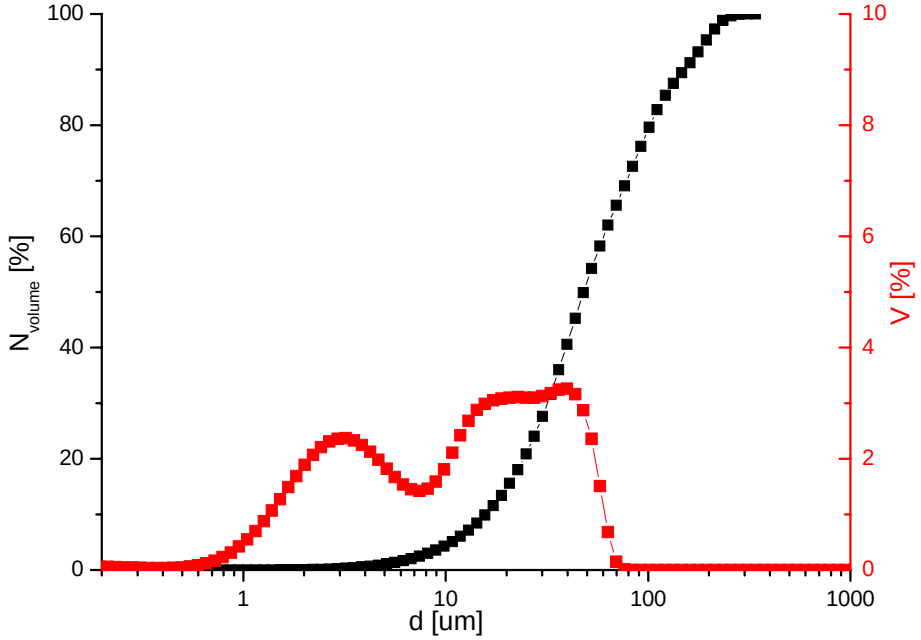



Fig. I-30 Integral & Differential arithmetic volume statistics on Fe50 (HPT) catalyst particles.

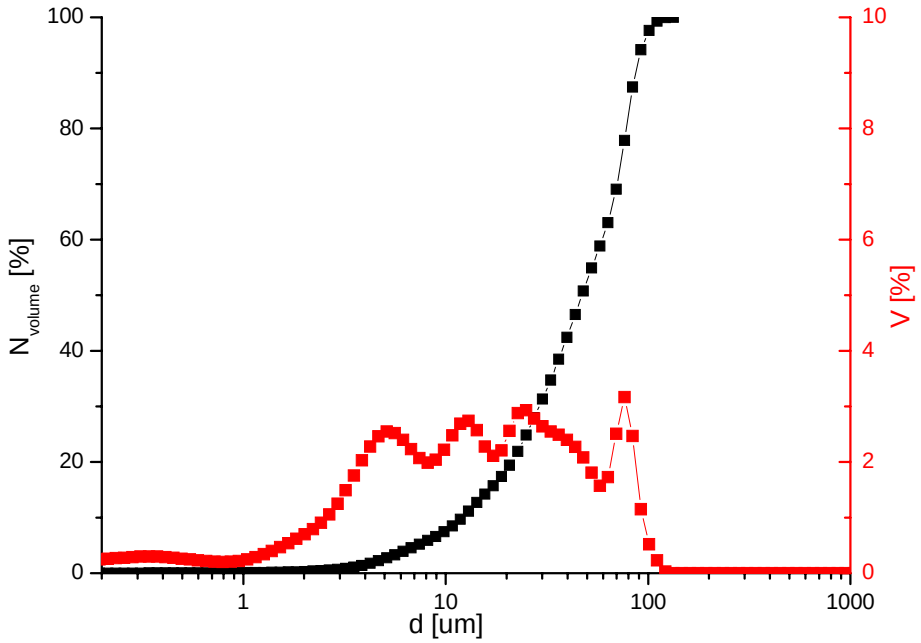



Fig. I-31 Integral & Differential arithmetic volume statistics on Fe50-$La_2O_3$ catalyst particles.

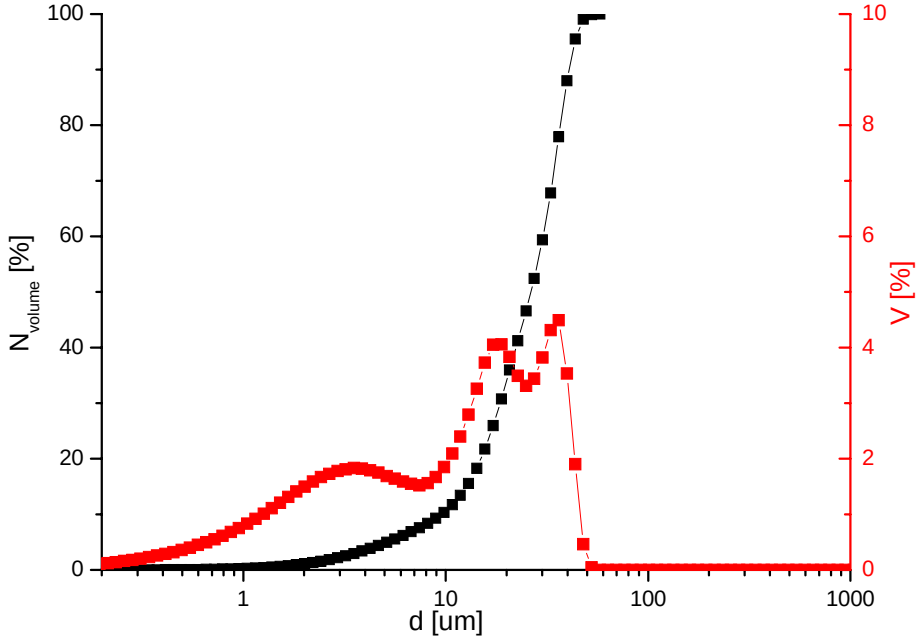



Fig. I-32 Integral & Differential arithmetic volume statistics on Fe50-$La_2O_3$ (HPT) catalyst particles.

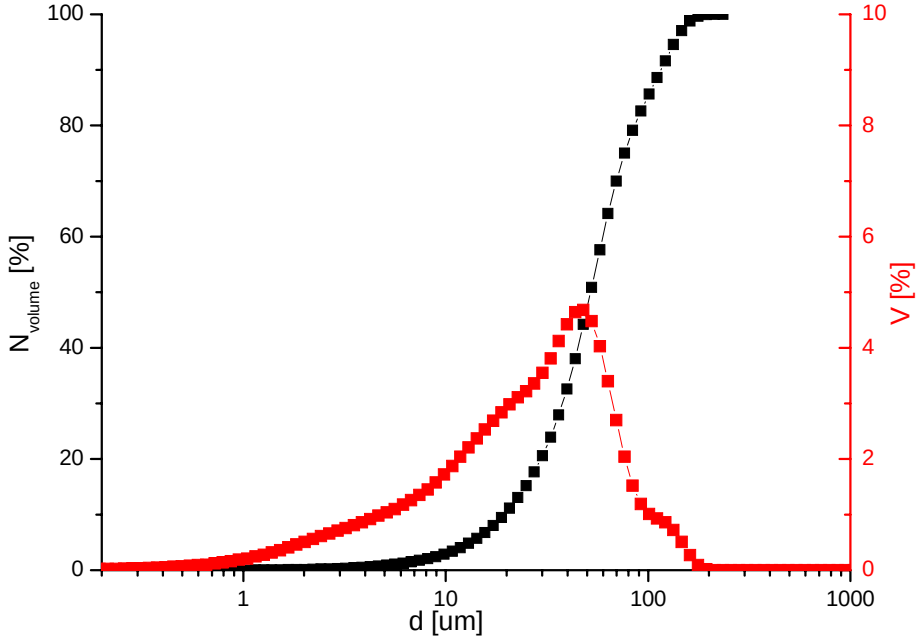



Fig. I-33 Integral & Differential arithmetic volume statistics on Fe35 (HPT) catalyst particles.

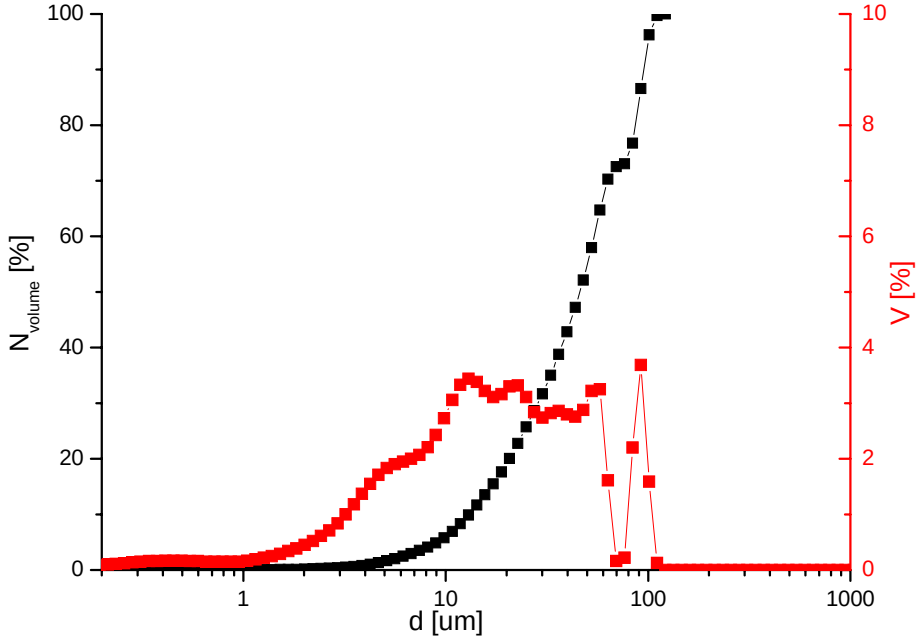



Fig. I-34 Integral & Differential arithmetic volume statistics on Fe35-$La_2O_3$ catalyst particles.

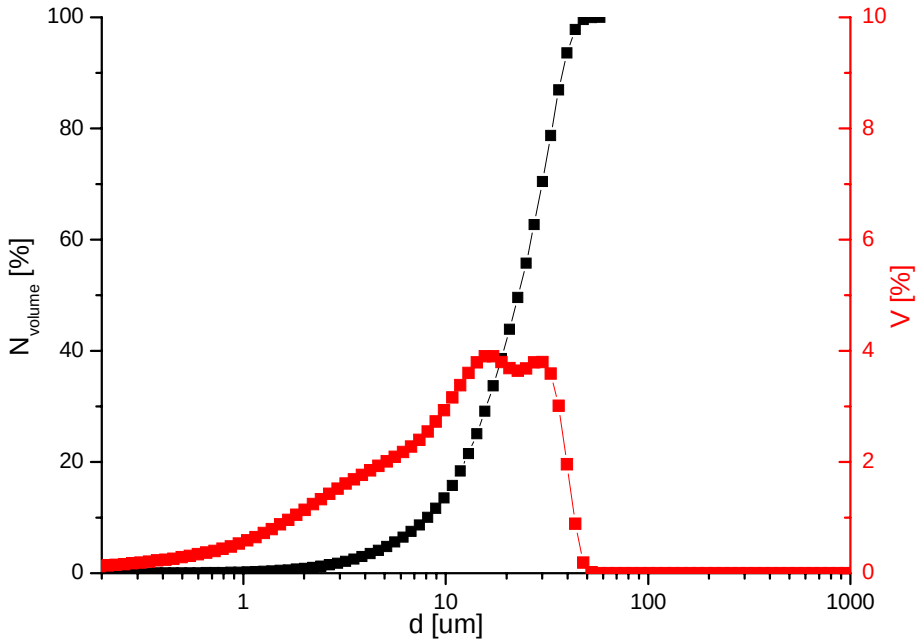



Fig. I-35 Integral & Differential arithmetic volume statistics on Fe35-$La_2O_3$ (HPT) catalyst particles.

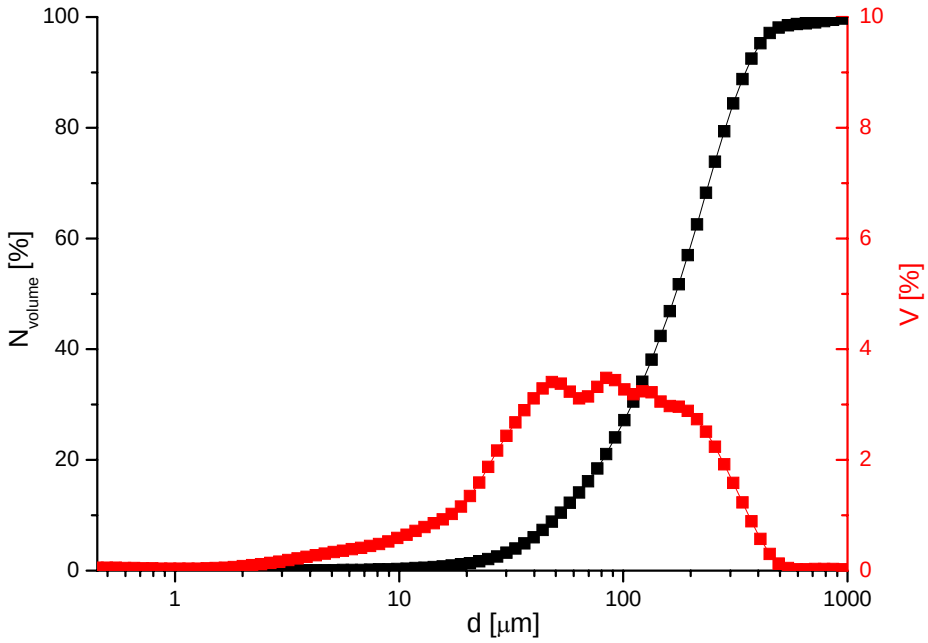



Fig. I-36 Integral & Differential arithmetic volume statistics on Ni30-Cu50-$La_2O_3$ catalyst particles.

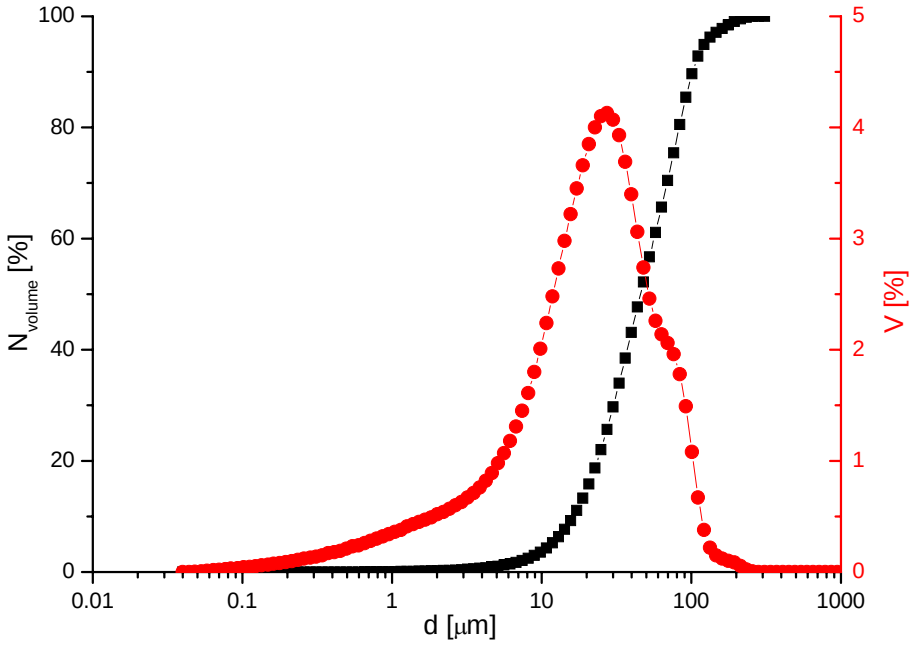
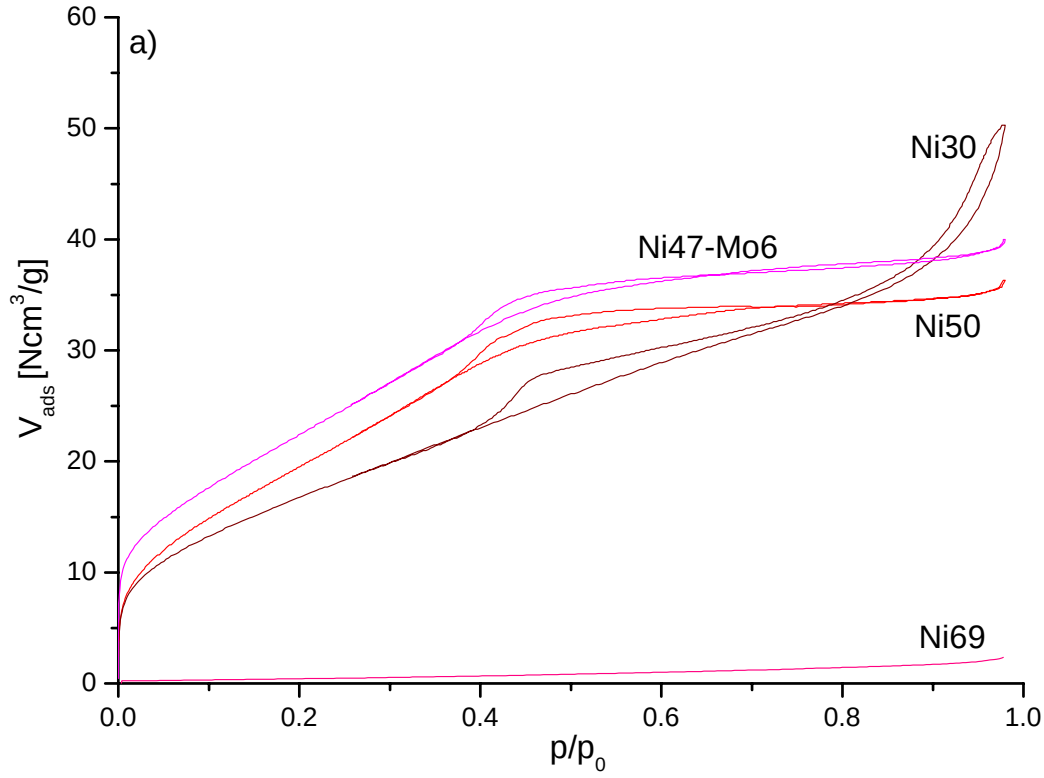
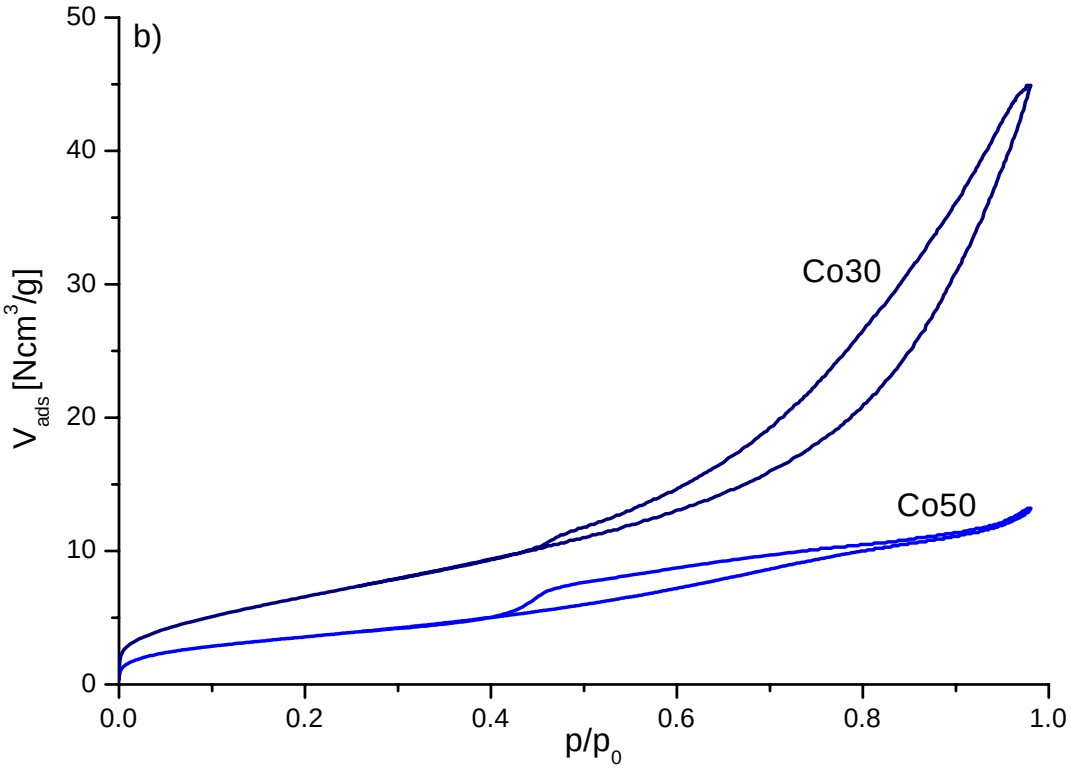



Fig. I-37 Integral & Differential arithmetic volume statistics on Ni30Cu50$La_2O_3$ (HPT) catalyst particles.

## II. Isotherms



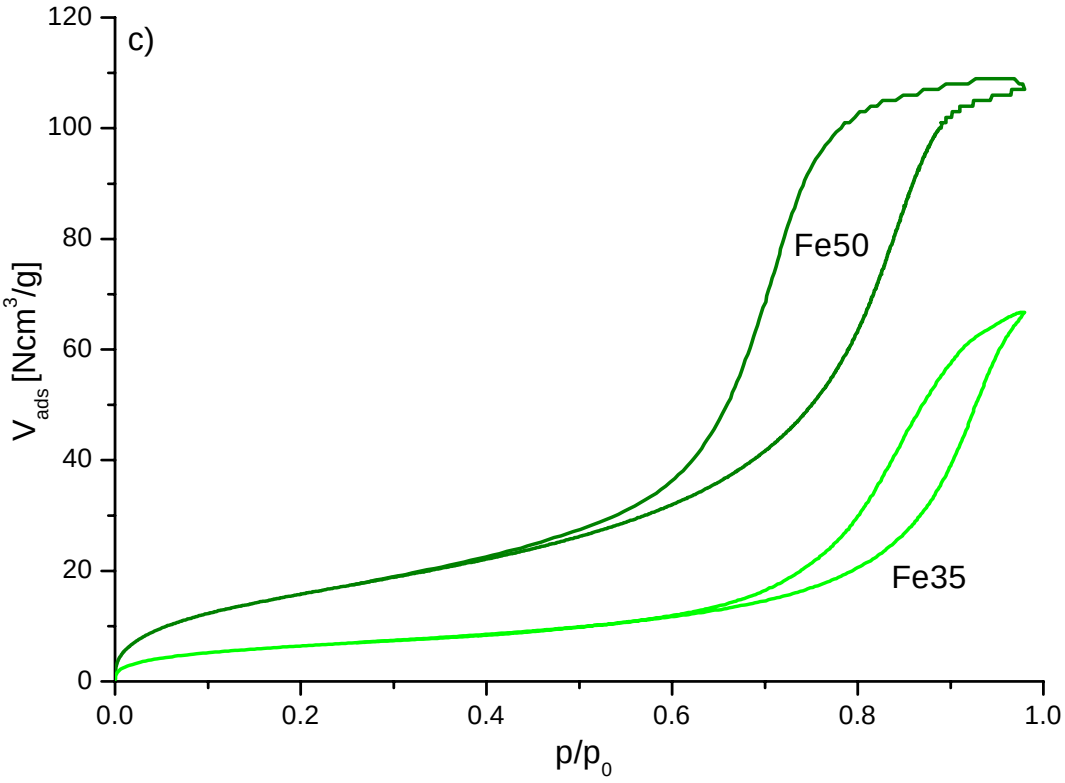



Fig. II.1 $N_2$ equilibrium adsorption-desorption isotherms at 77.35K:

a) on Ni69, Ni50, Ni47-Mo6 and Ni30;

b) on Co30 and Co50;

c) on Fe50 and Fe35.

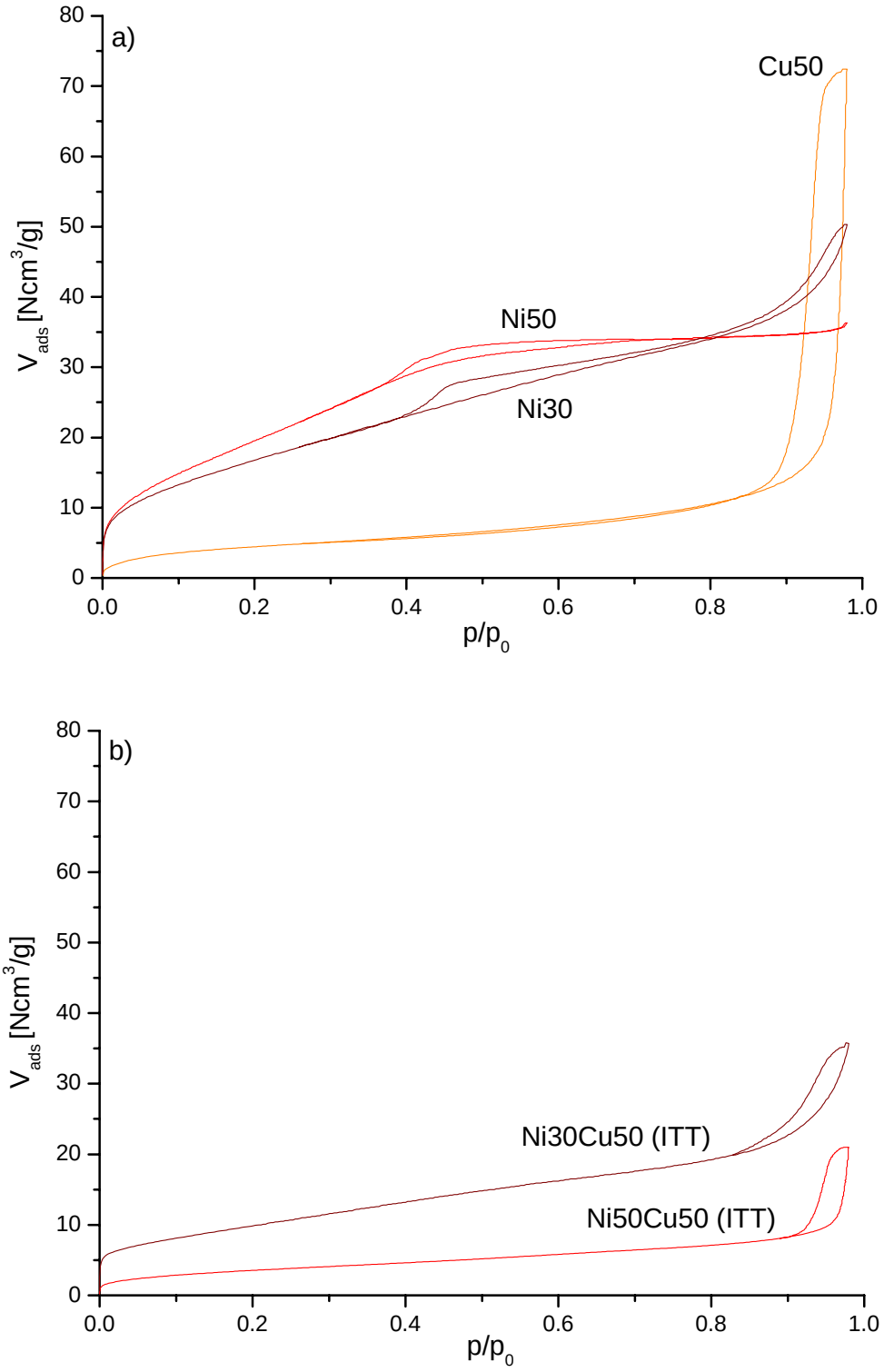



Fig. II.2 $N_2$ equilibrium adsorption-desorption isotherms at 77.35K:

a) on Ni30, Ni50 and Cu50;

b) on Ni30Cu50 (ITT) and Ni50Cu50 (ITT).

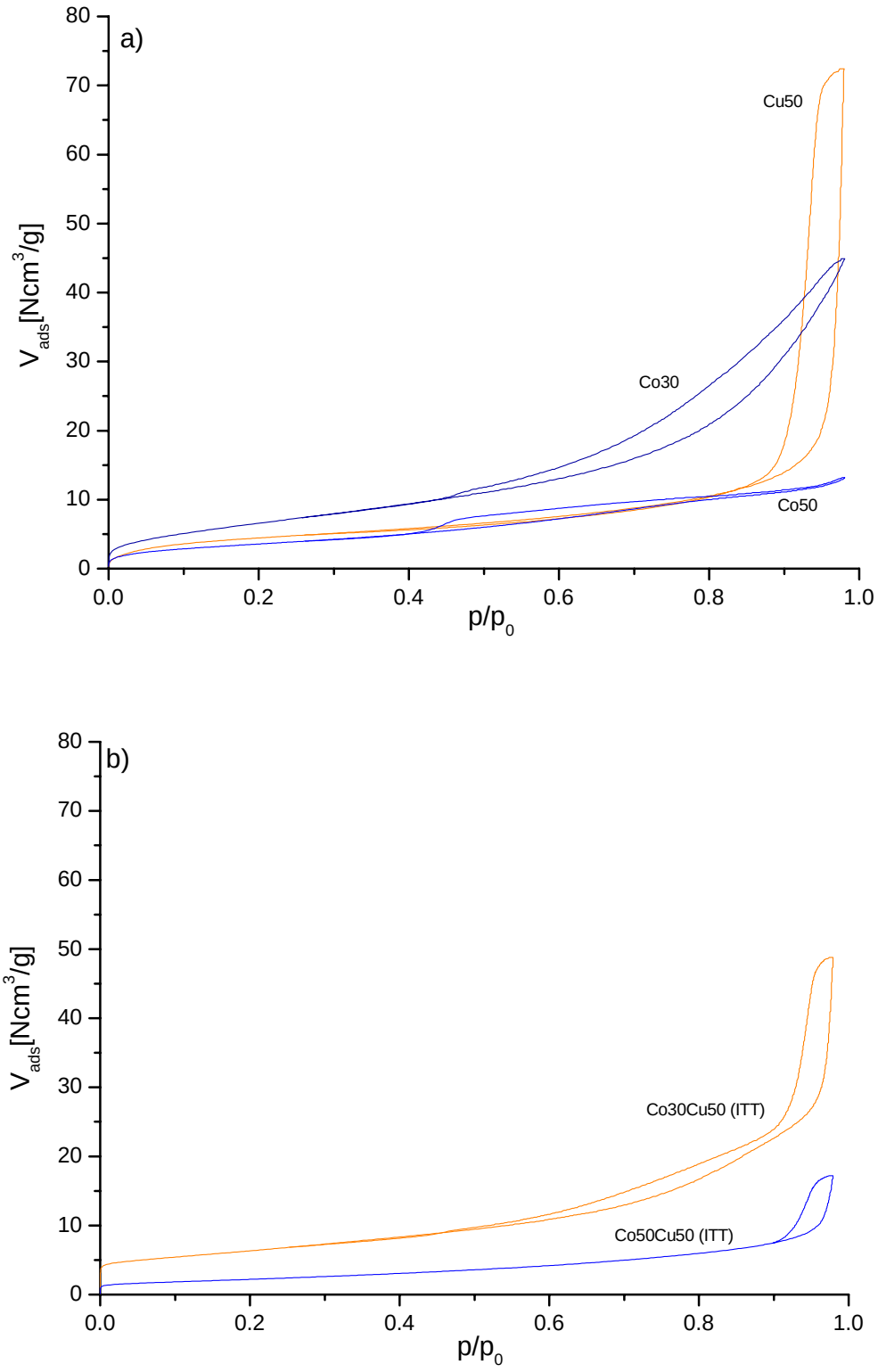



Fig. II.3 $N_2$ Equilibrium adsorption-desorption isotherms at 77.35K:
a) on Co30, Co50 and Cu50;
b) on Co30Cu50 (ITT) and Co50Cu50 (ITT).

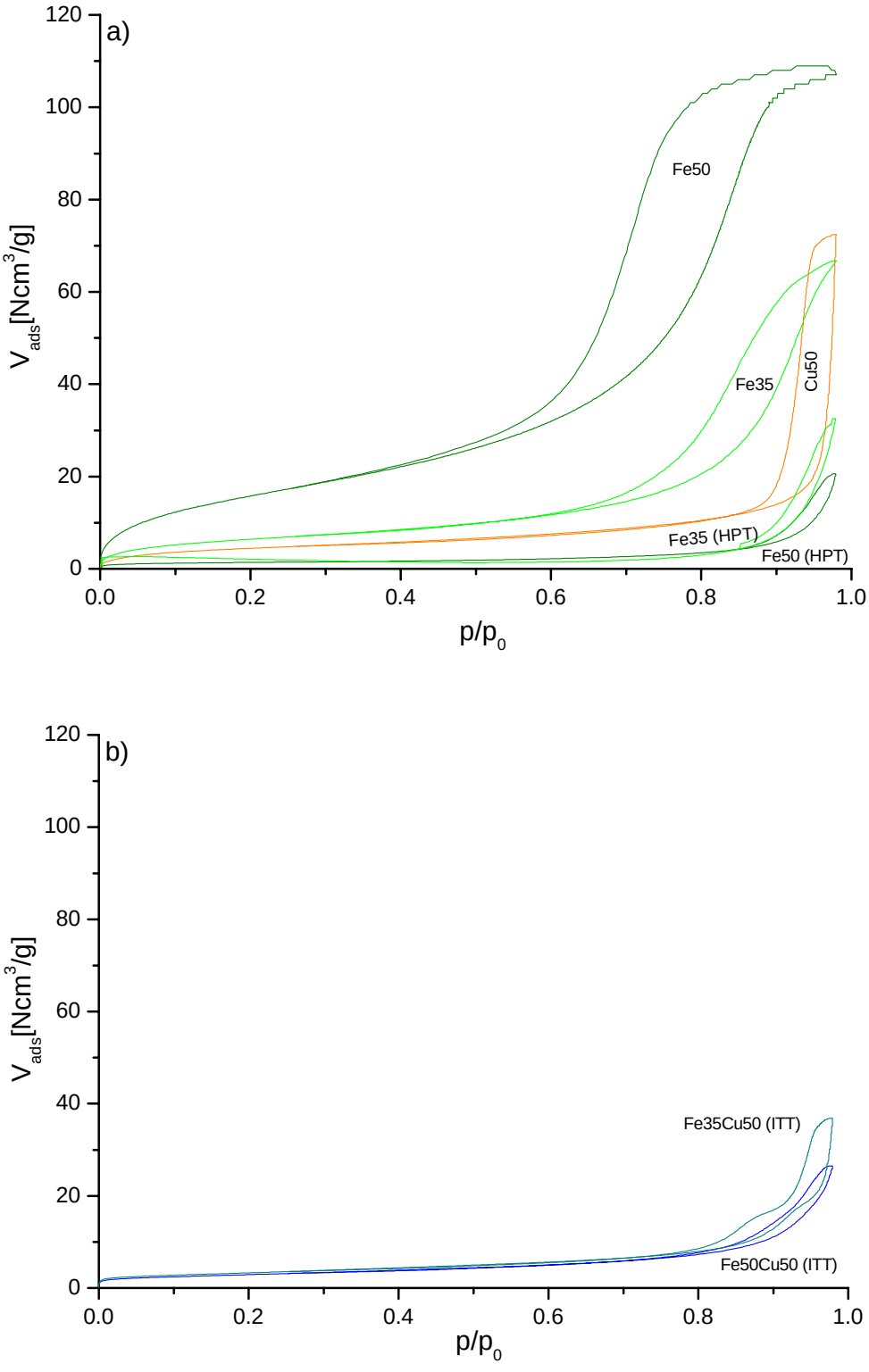



Fig. II.4 $N_2$ equilibrium adsorption-desorption isotherms at 77.35K:
a) on Fe50, Fe35 and Cu50;
b) on Fe50Cu50 (ITT) and Fe35Cu50 (ITT).

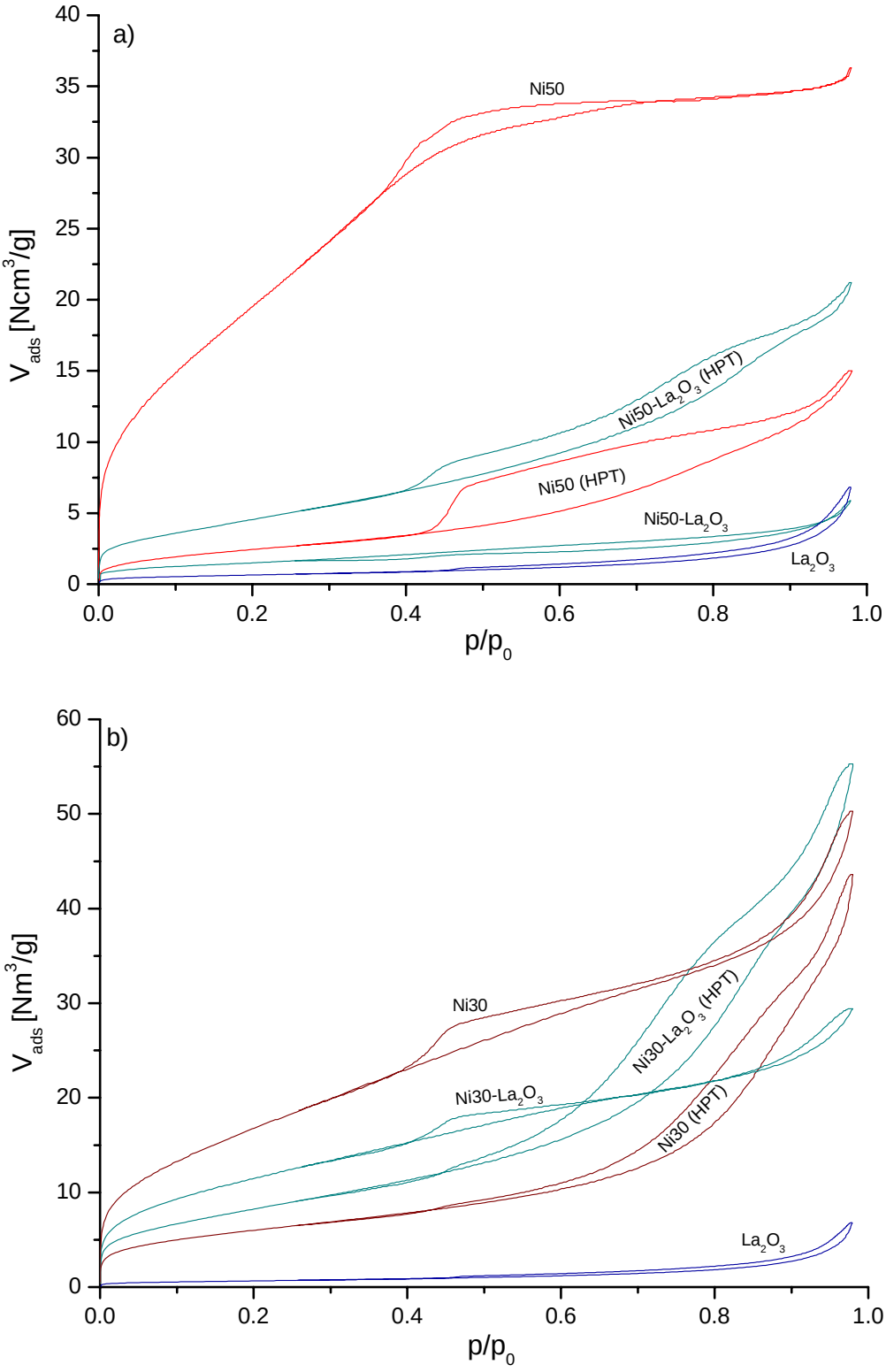



Fig. II.5 $N_2$ equilibrium adsorption-desorption isotherms at 77.35 K:
a) of $La_2O_3$, Ni50, Ni50-$La_2O_3$, Ni50 (HPT) and Ni50-$La_2O_3$ (HPT);
b) of $La_2O_3$, Ni30, Ni30-$La_2O_3$, Ni30 (HPT) and Ni30-$La_2O_3$ (HPT).

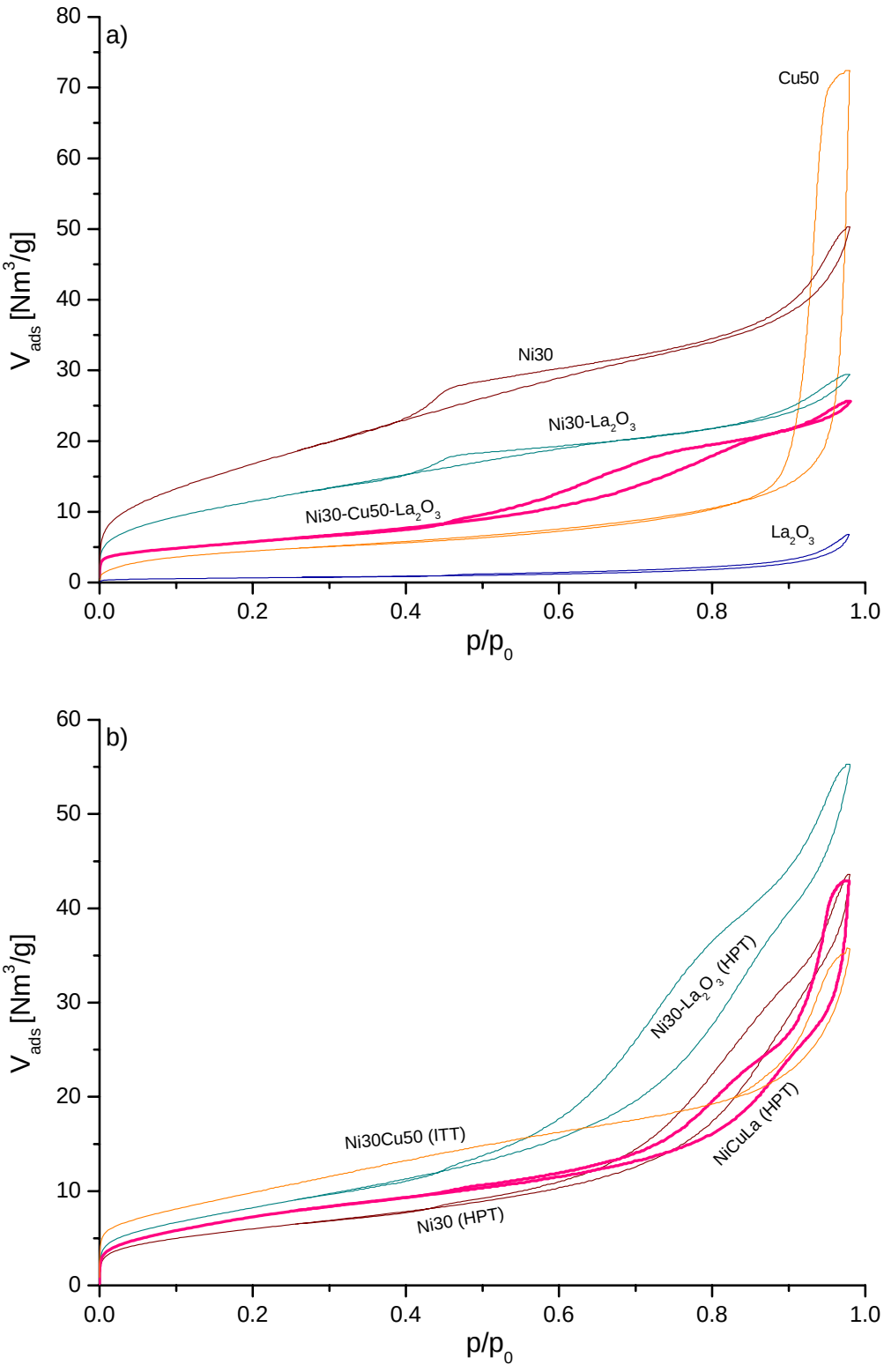



Fig. II.6 Equilibrium adsorption-desorption isotherms with $N_2$ at 77.35 K:
a) on Ni30, Cu50, $La_2O_3$, Ni30-$La_2O_3$ and Ni30-Cu50-$La_2O_3$
b) on Ni30 (HPT), Ni30-$La_2O_3$ (HPT), Ni30Cu50 (ITT) and NiCuLa (HPT).

## III. Scanning electron microscopy (SEM)

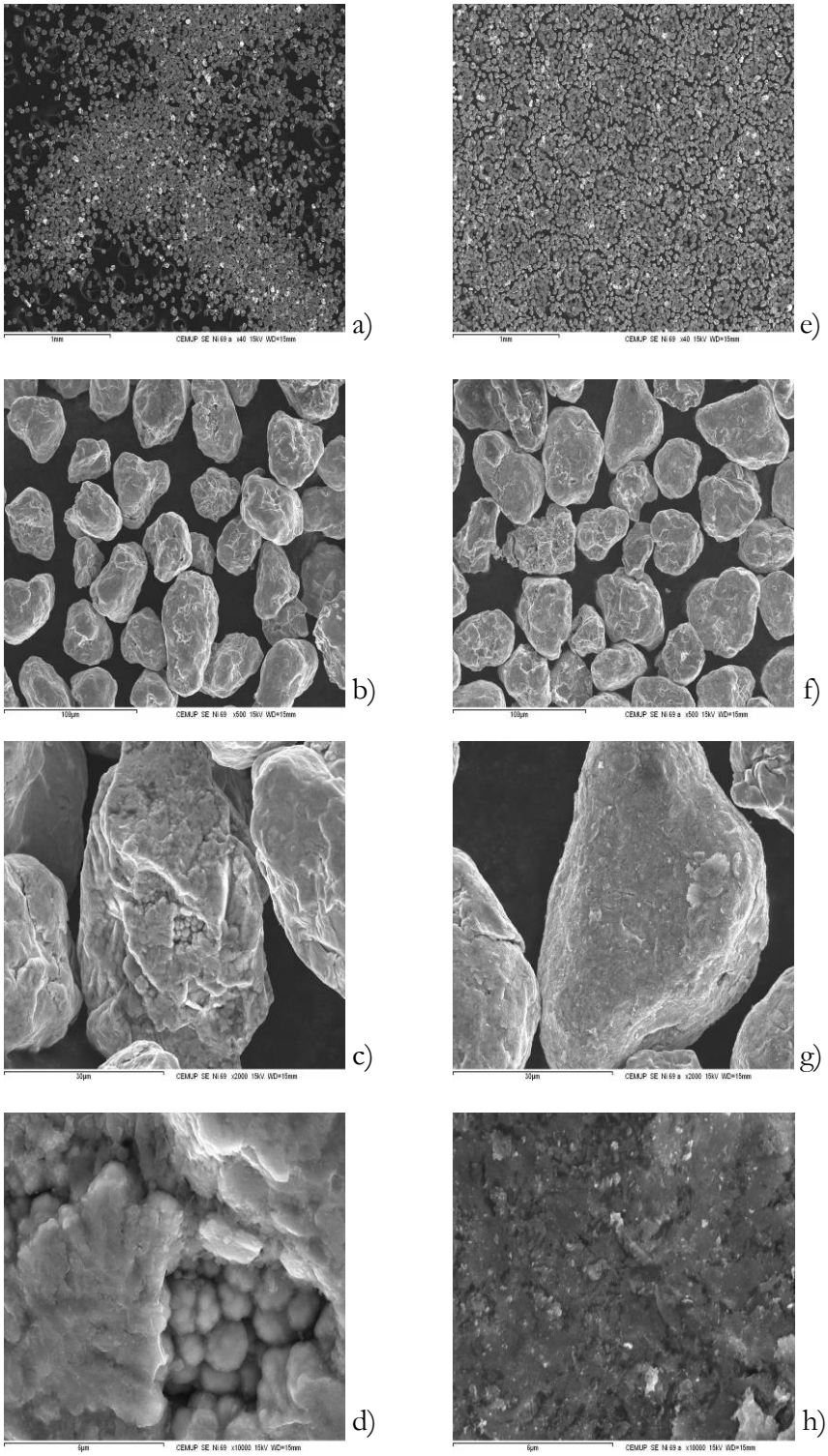



Fig. III.1 SEM micrographs on Ni69 alloy (a-d) and catalyst (e-h).

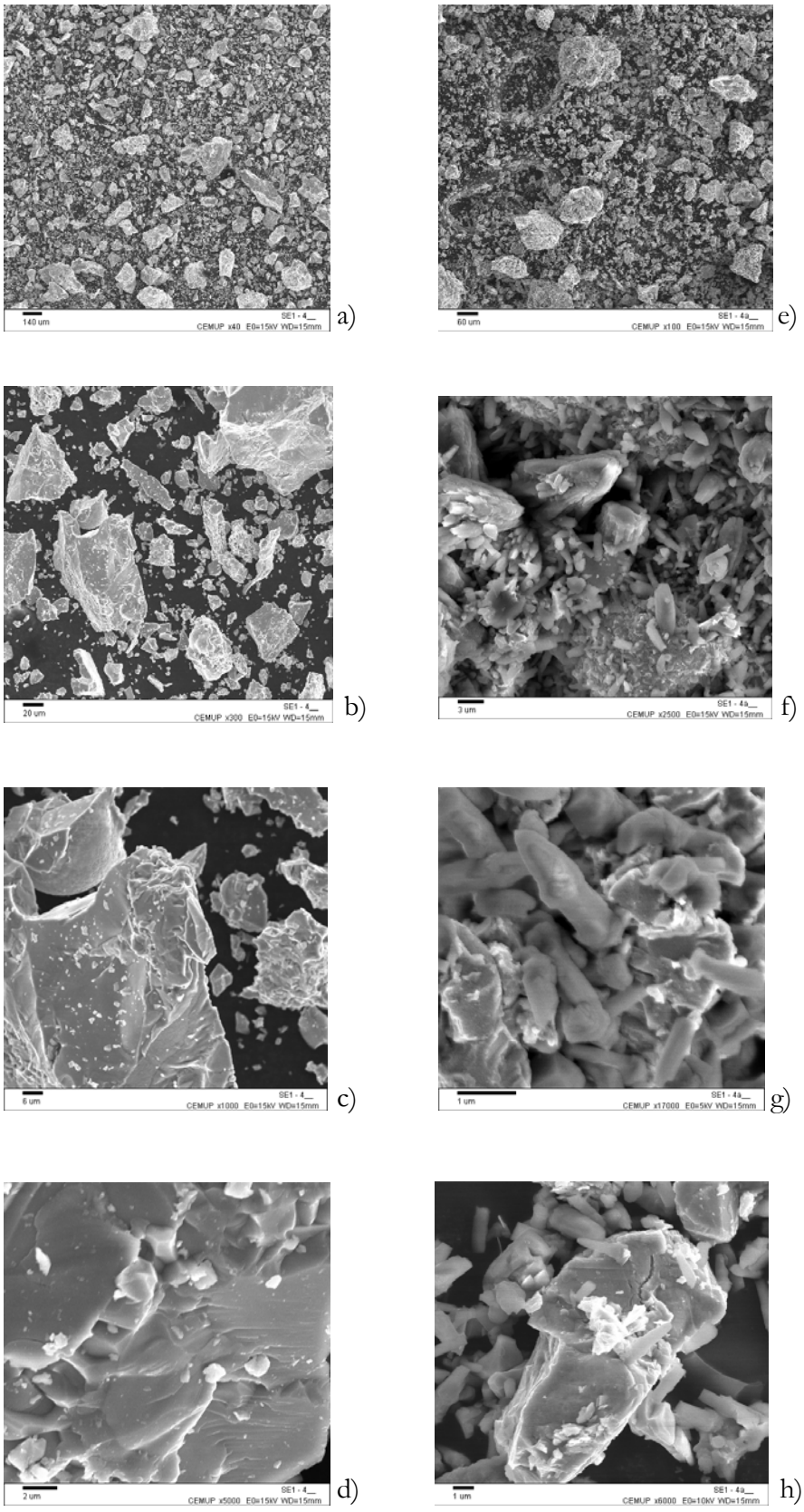



Fig. III.2 SEM micrographs on Ni47-Mo6 alloy (a-c) and catalyst (d-f).

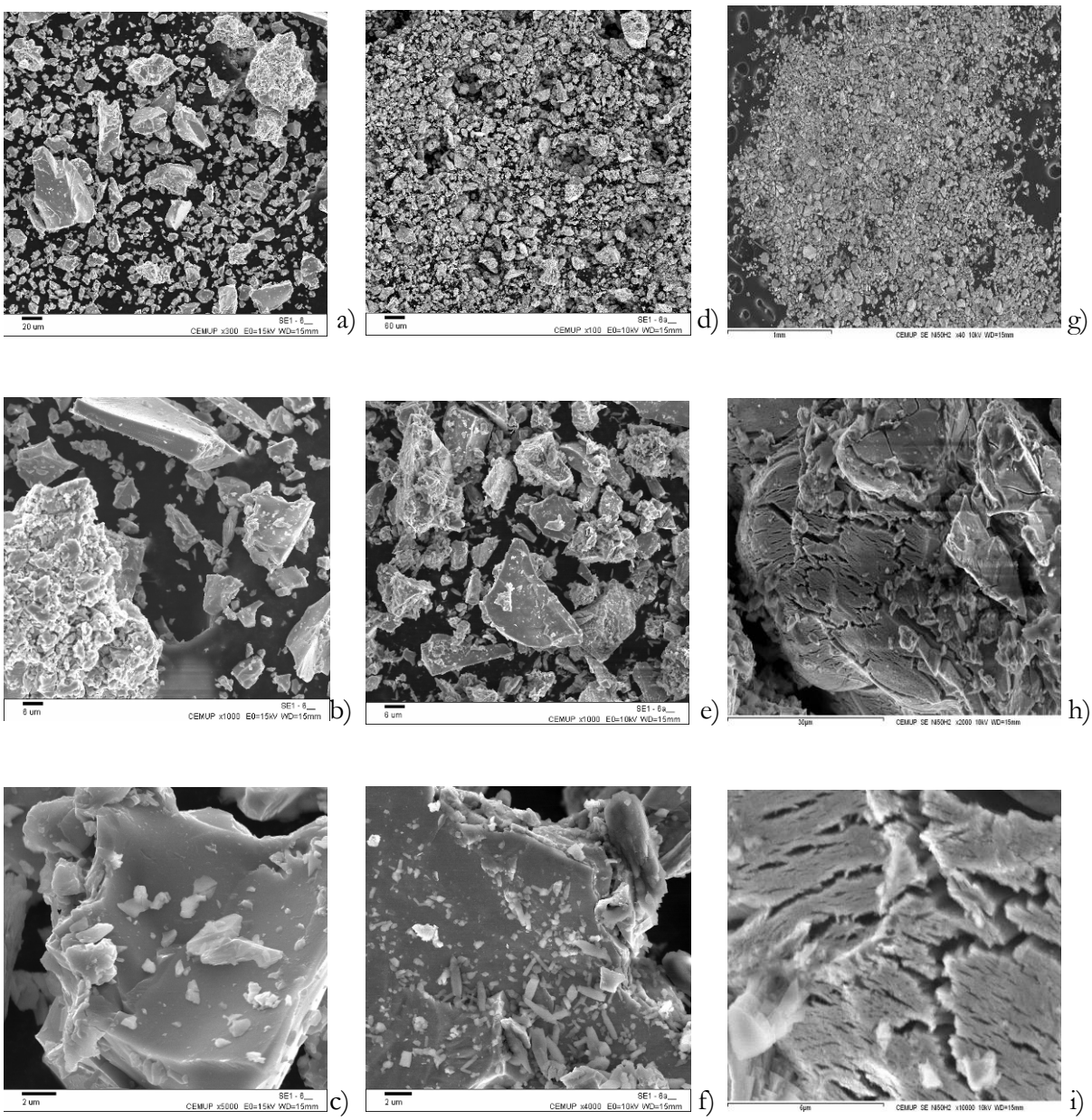



Fig. III.3 SEM micrographs on Ni50 alloy (a-c), catalyst (d-f) and hydrogen pre-treated catalyst (g-i).

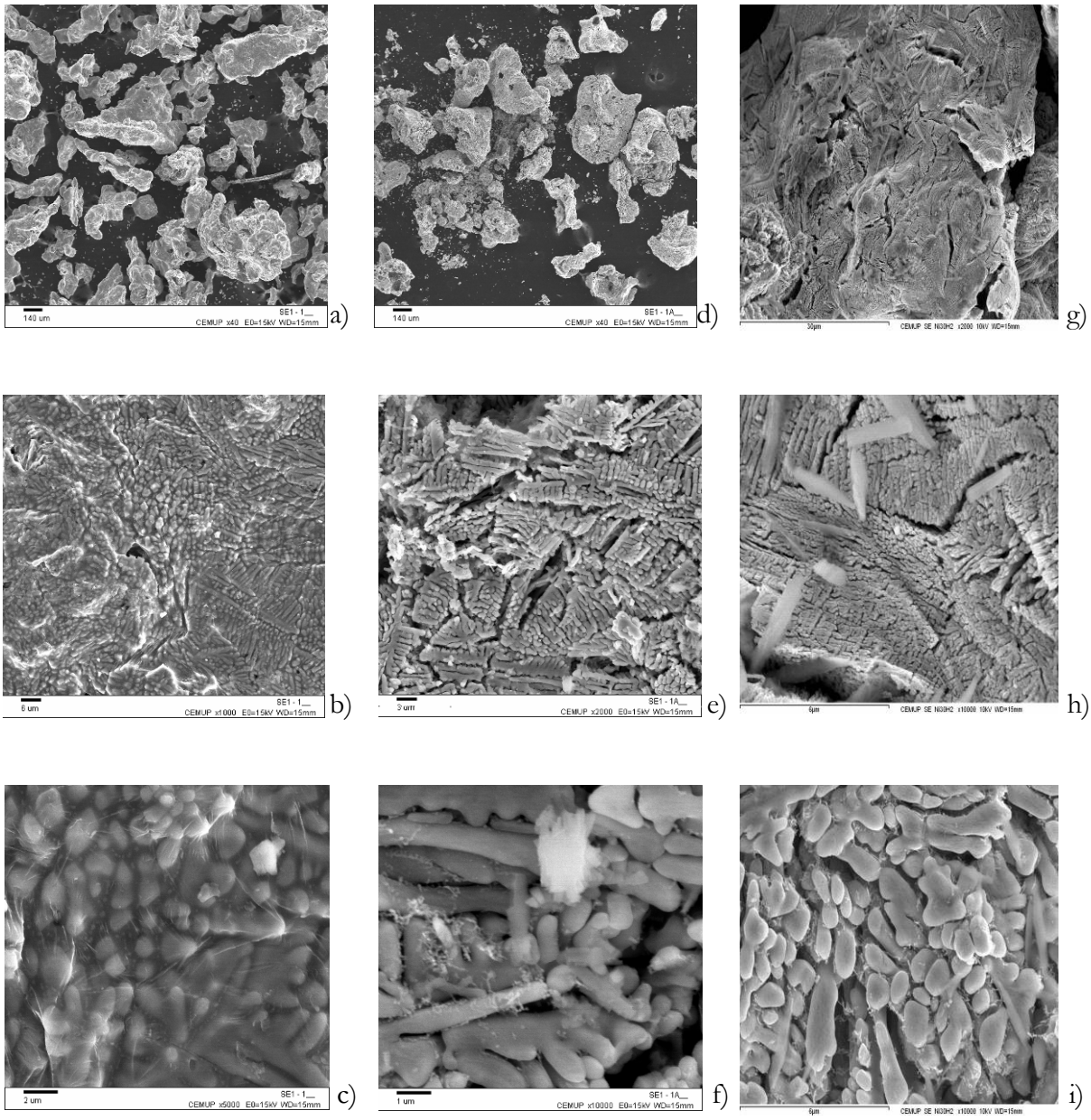



Fig. III.4 SEM micrographs on Ni30 alloy (a-c), catalyst (d-f) and hydrogen pre-treated catalyst (g-i).

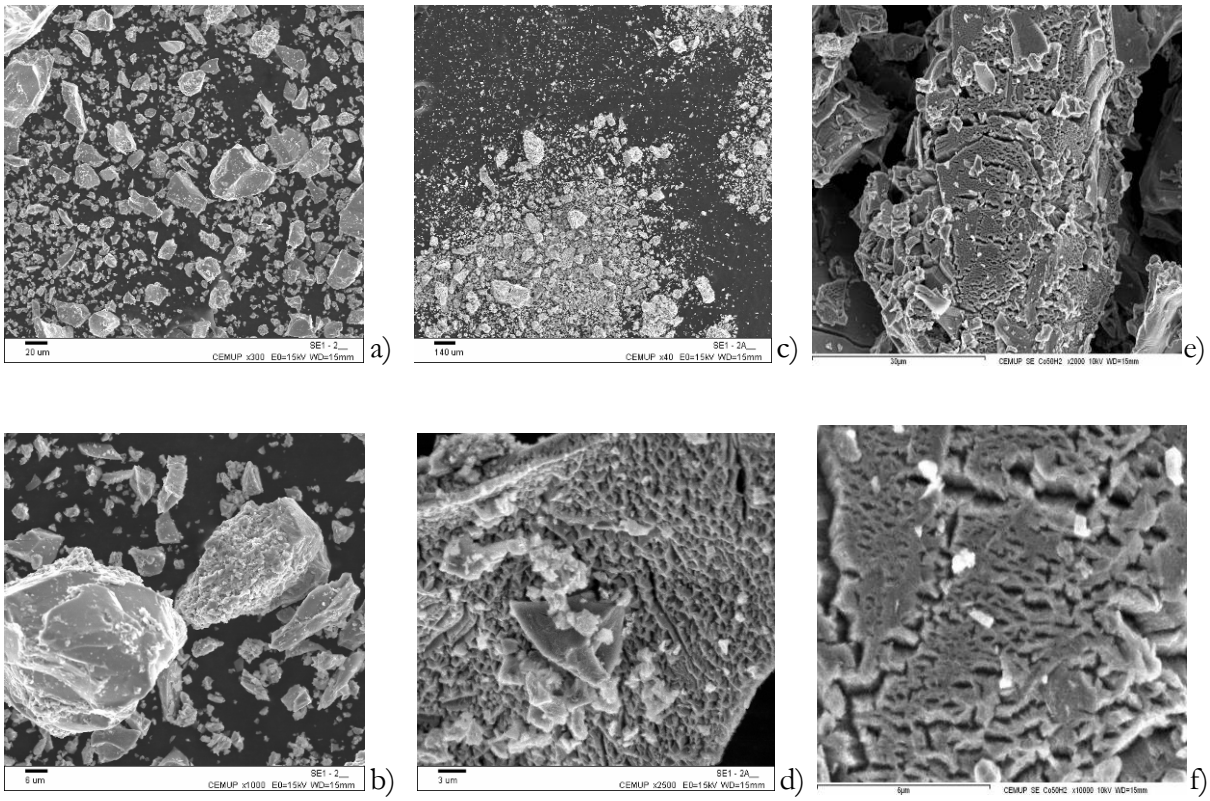



Fig. III.5 SEM micrographs on Co50 alloy (a-b), catalyst (c-d) and hydrogen pre-treated catalyst (e-f).

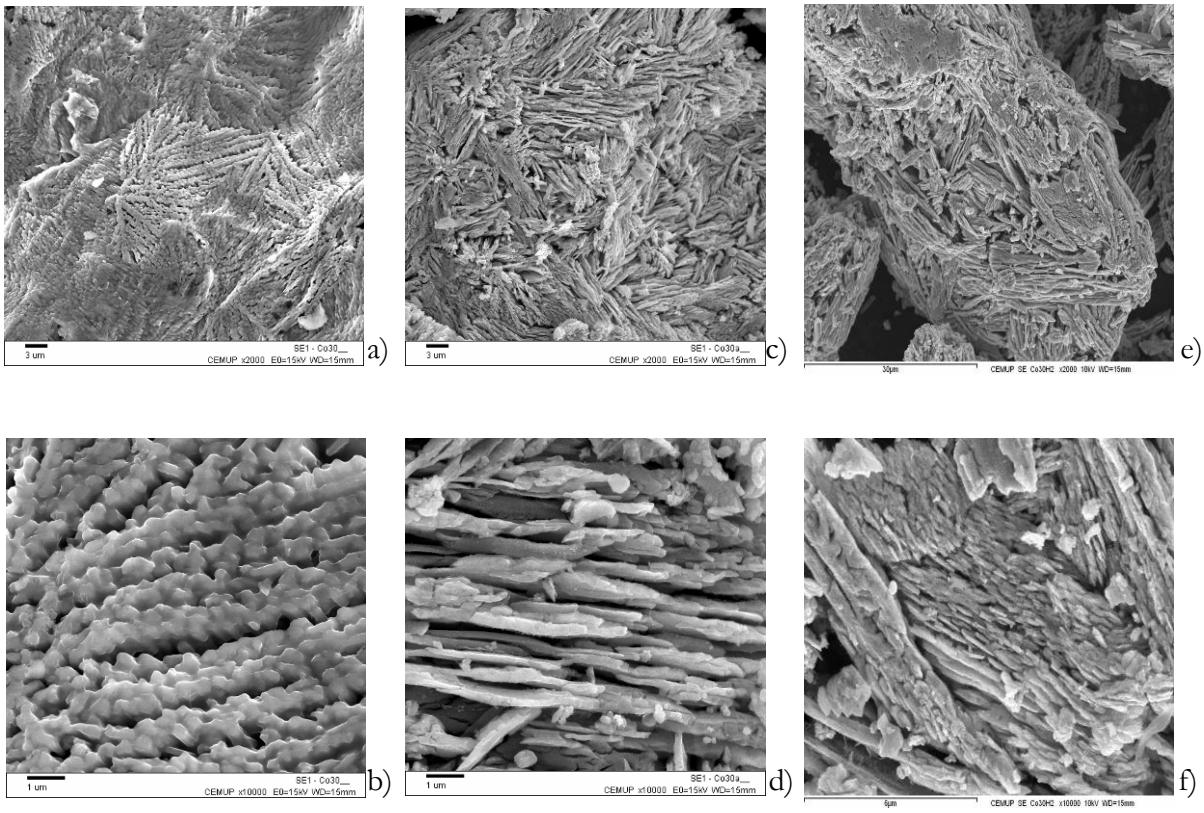



Fig. III.6 SEM micrographs on Co30 alloy (a-b), catalyst (c-d) and hydrogen pre-treated catalyst (e-f).

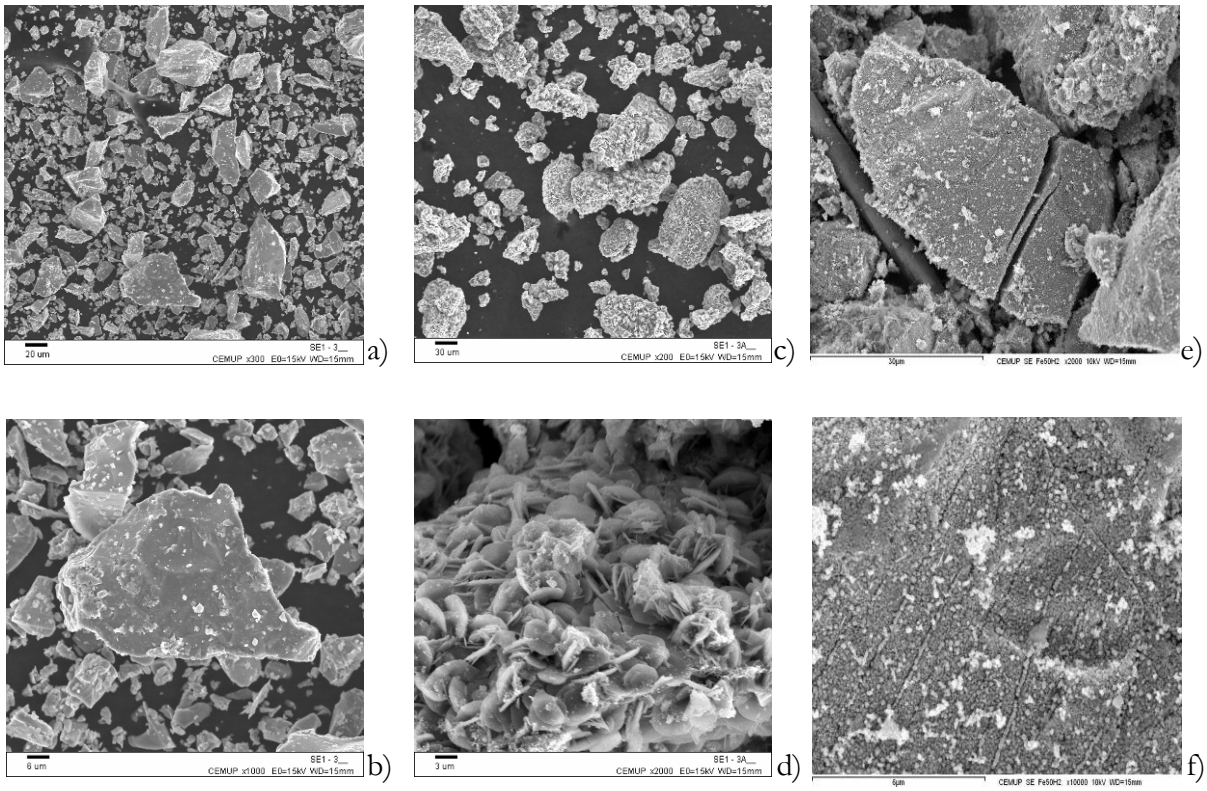



Fig. III.7 SEM micrographs on Fe50 alloy (a-b), Fe50 catalyst (c-d) and hydrogen pre-treated catalyst (e-f).

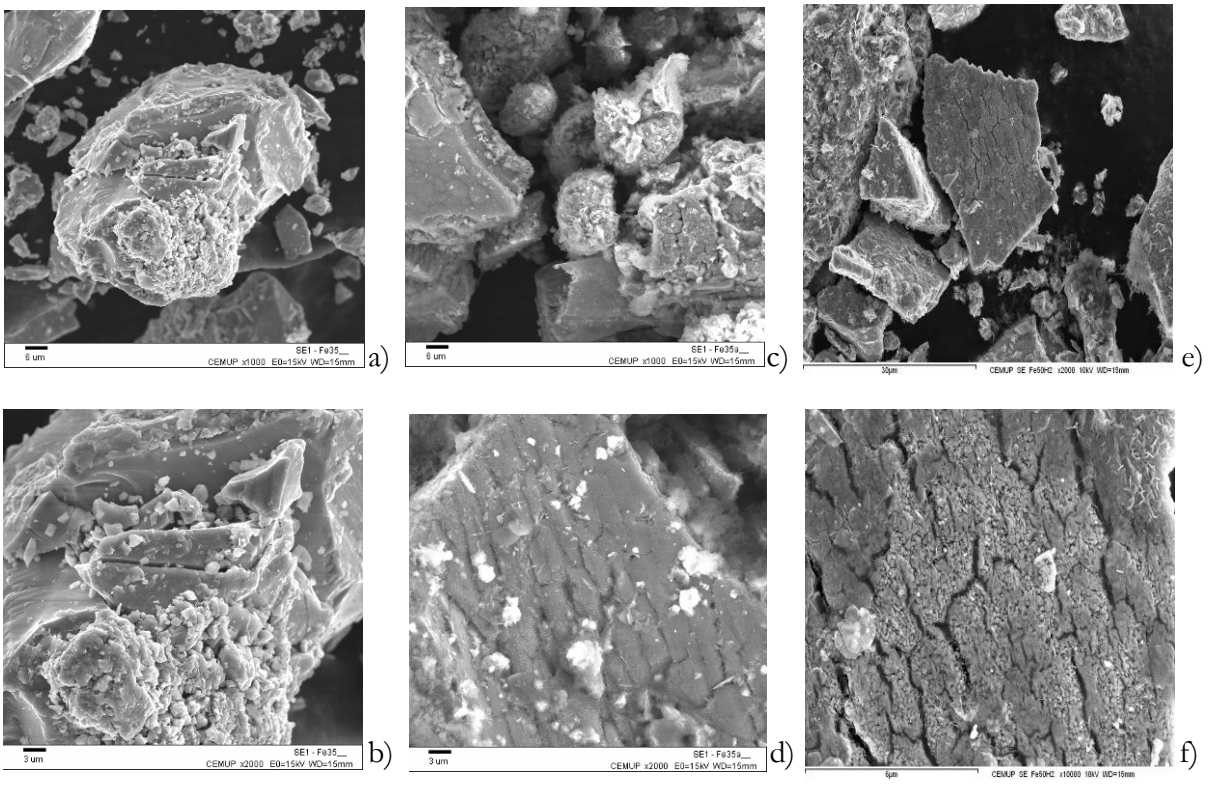
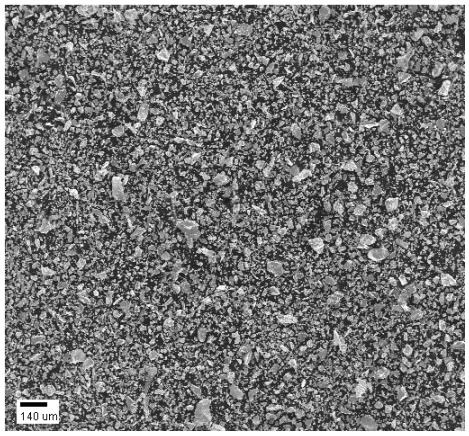
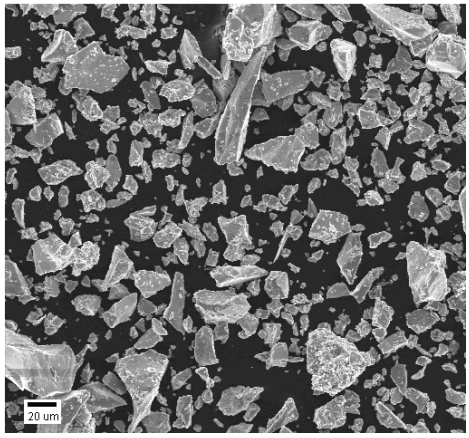


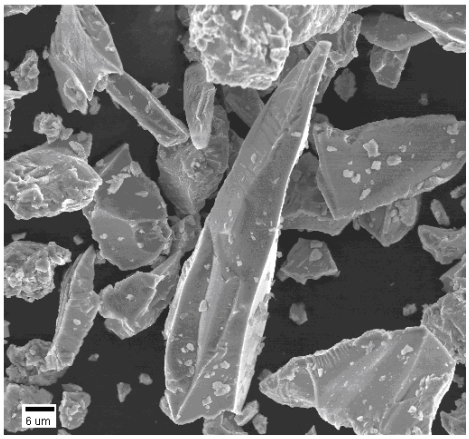

Fig. III.8 SEM micrographs on Fe35 alloy (a-b), catalyst (c-d) and hydrogen pre-treated catalyst (e-f).



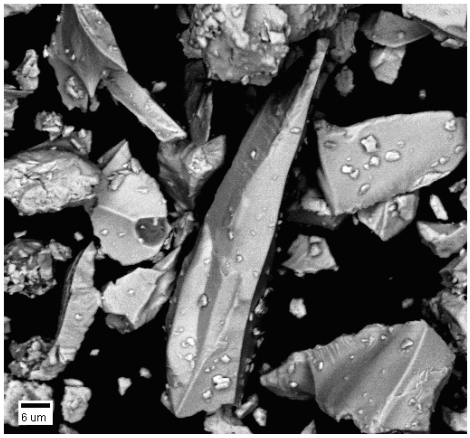

a)




b)

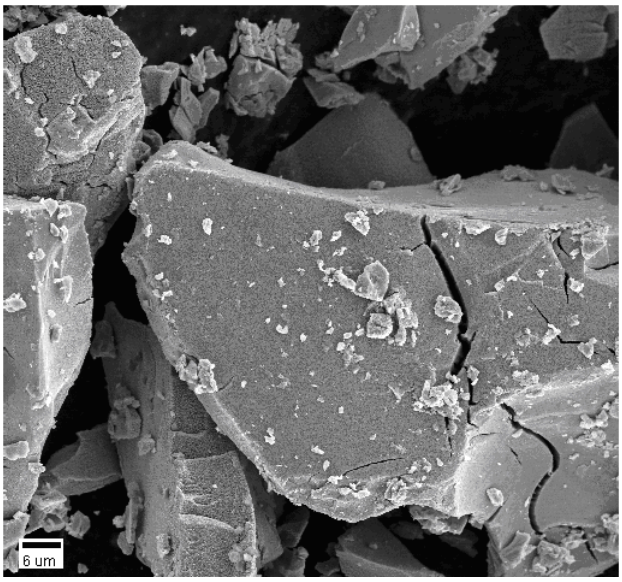



c)

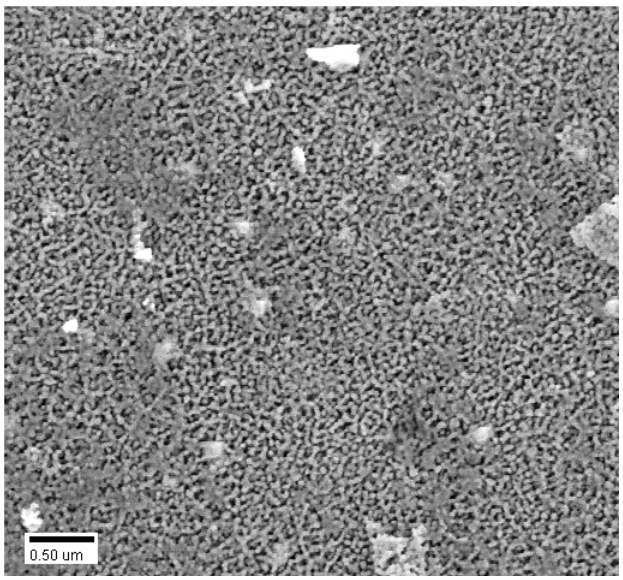



d)

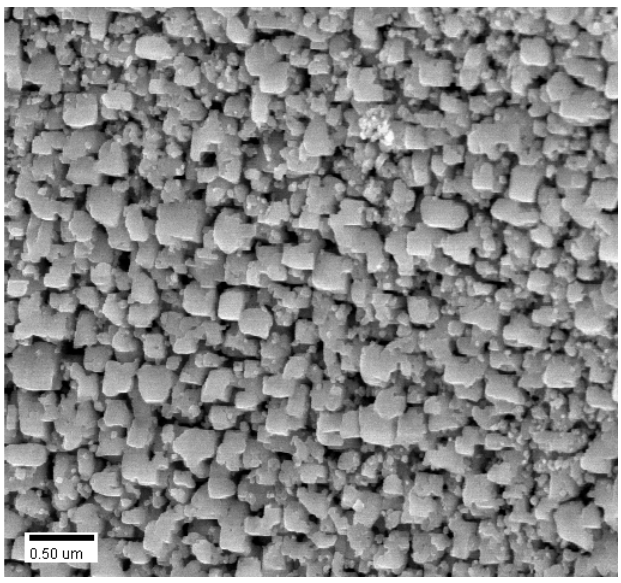
Fig. III.9 SEM micrographs on Cu50 alloy.



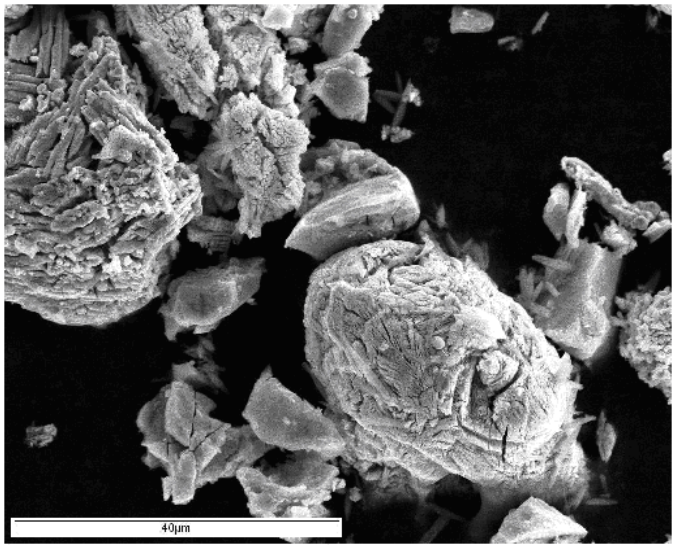

a)



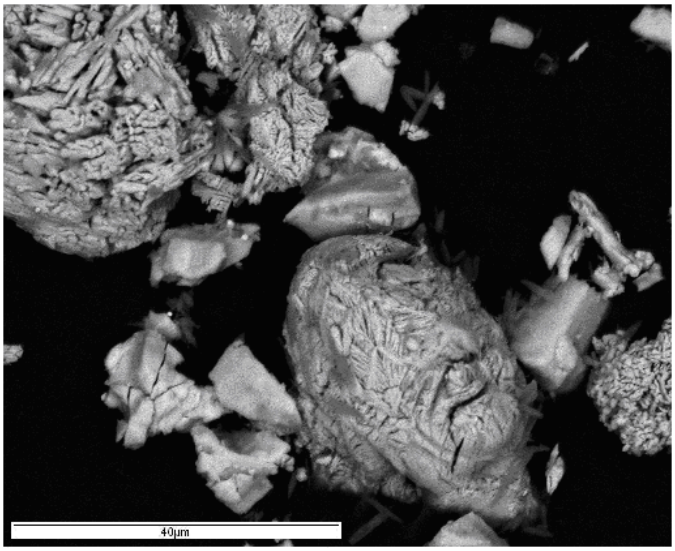

b)



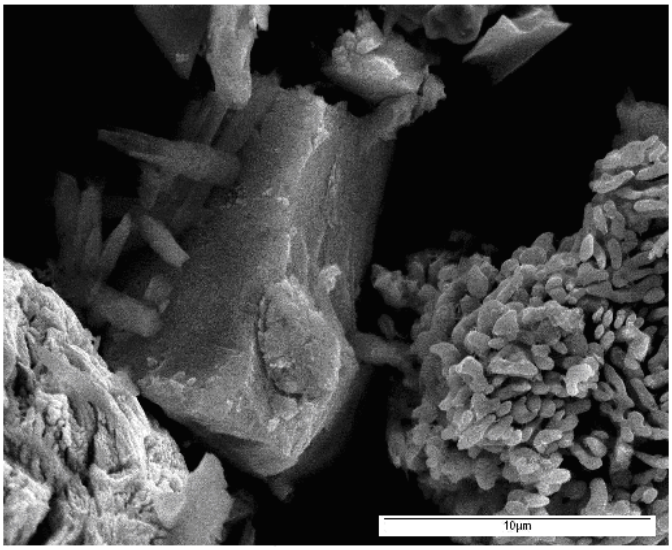

c)



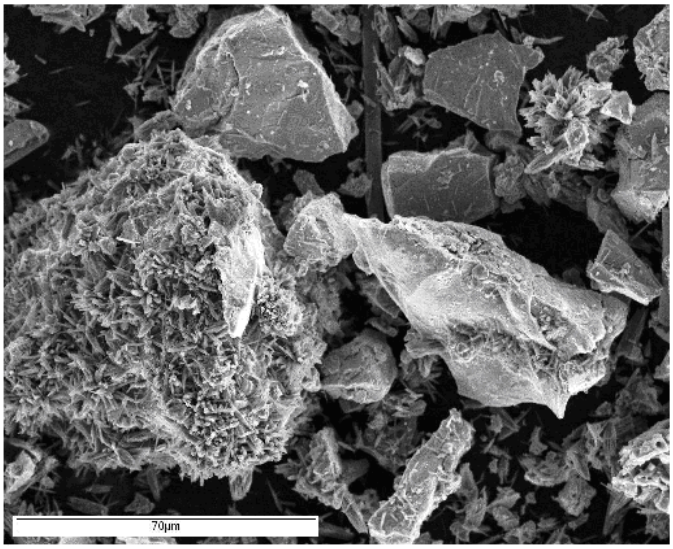

d)



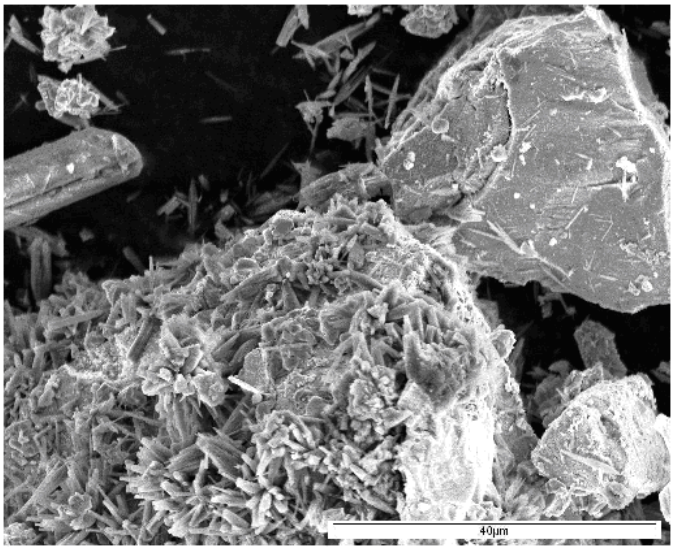

e)



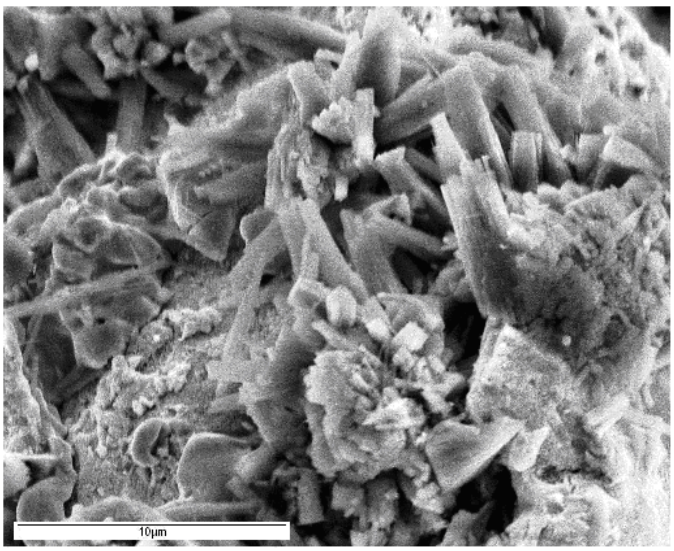

f)




g)

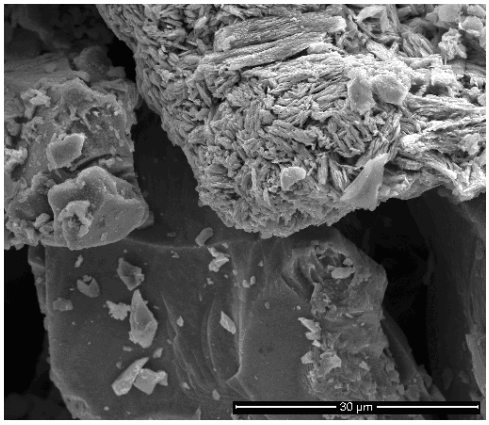



h)

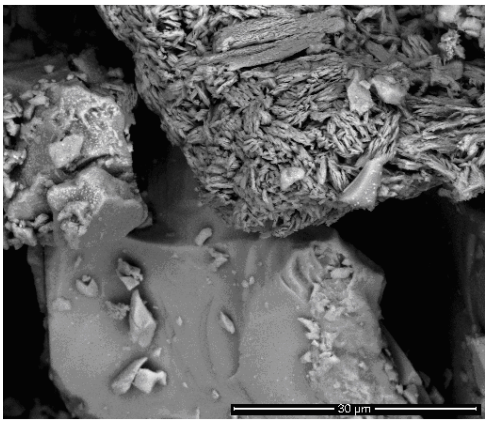



i)

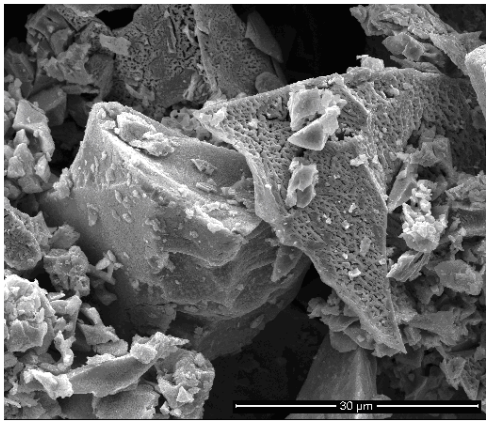
Fig. III.10 SEM micrographs of Cu50 (a-c), Ni30Cu50 (ITT) (d-f) and Ni50Cu50 (ITT) (g-i) catalysts.



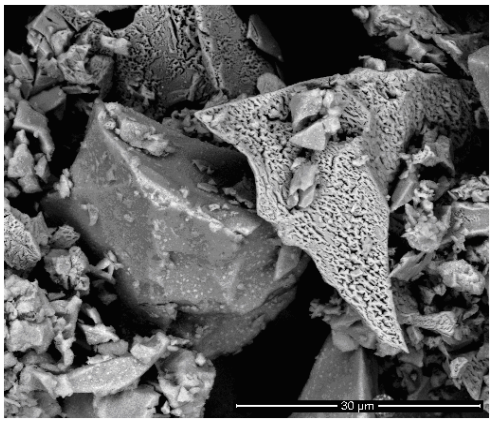
a)



b)

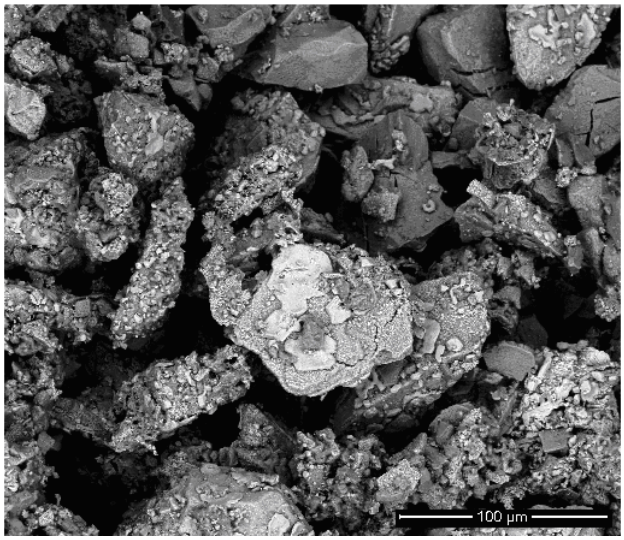


c)

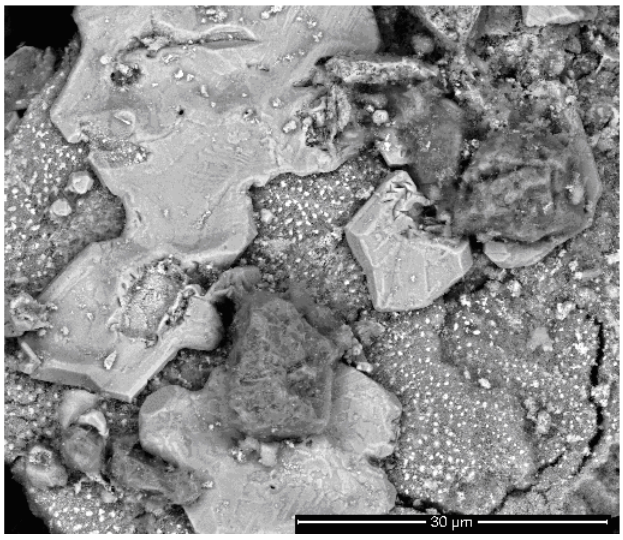


d)

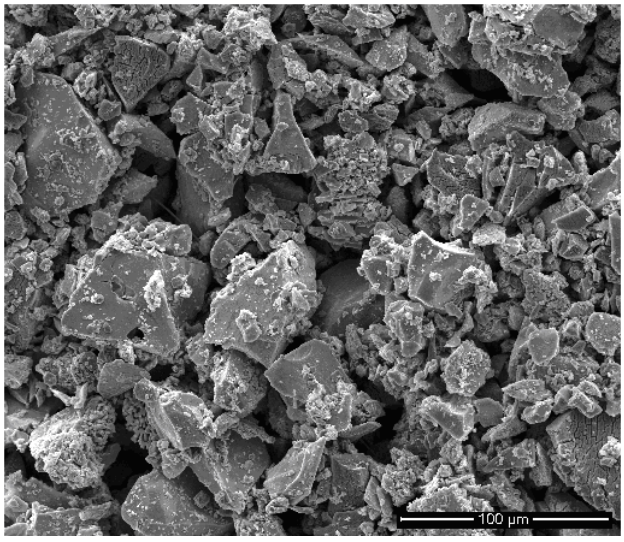
Fig. III.11 SEM micrographs on Co30Cu50 (ITT) (a-b) and Co50Cu50 (ITT) (c-d) catalysts.



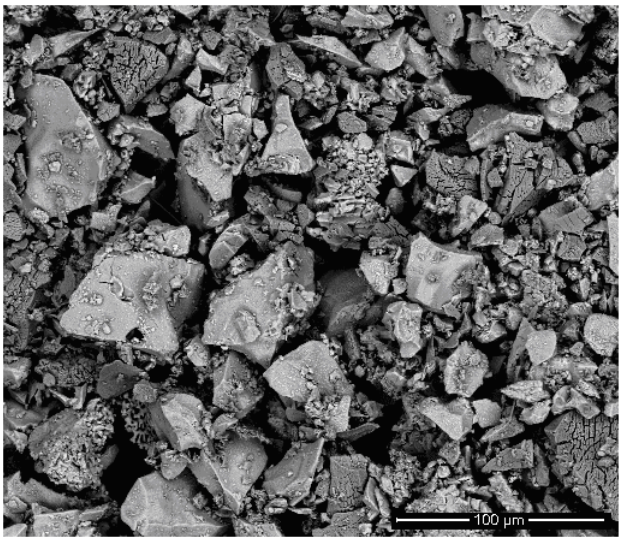
a)



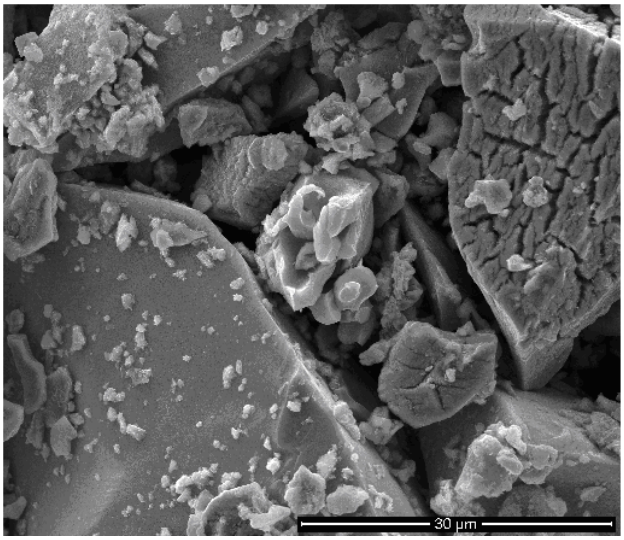
b)



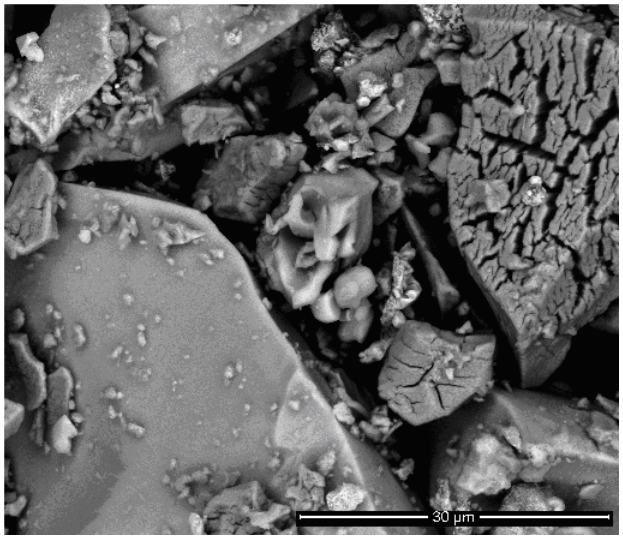
c)



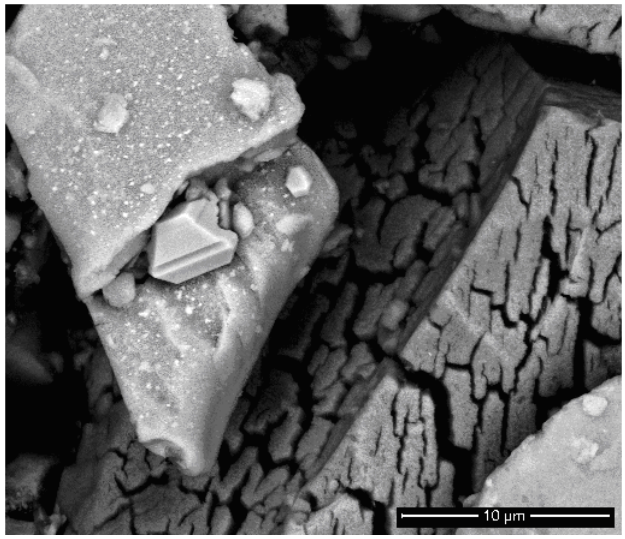

d)




e)

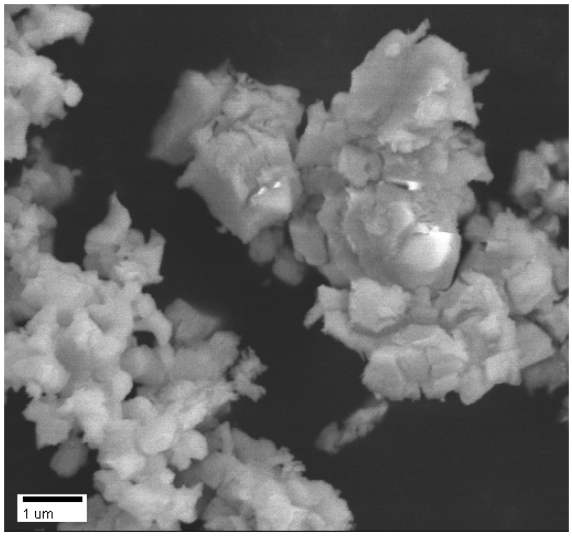



f)

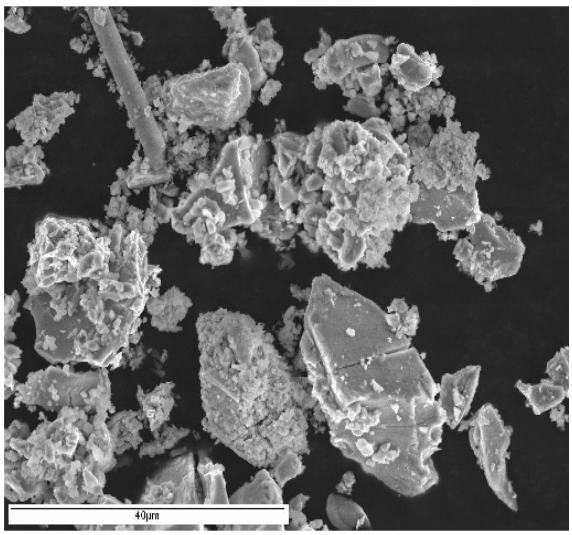


g)

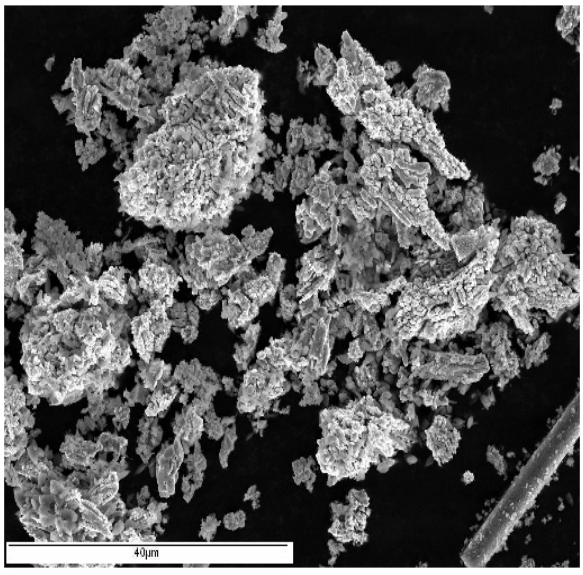
Fig. III.12 SEM micrographs on Fe50Cu50 (ITT) (a-b) and Fe35Cu50 (ITT) (c-g) catalysts.




a)

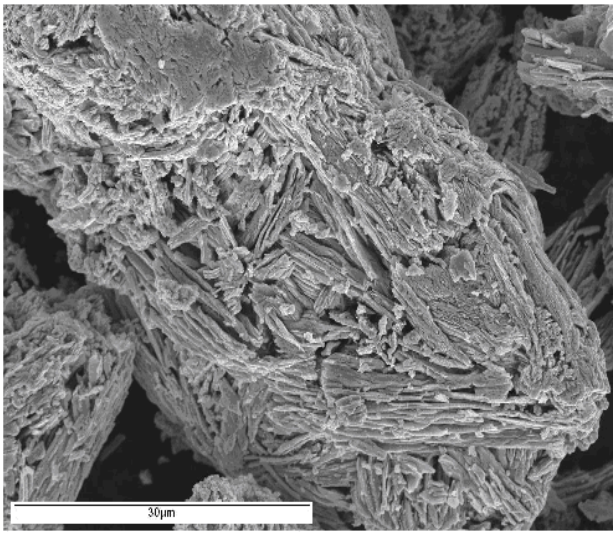



b)

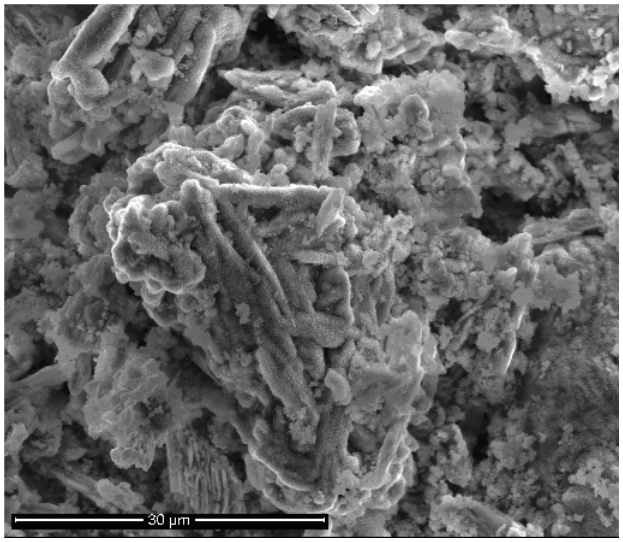



c)

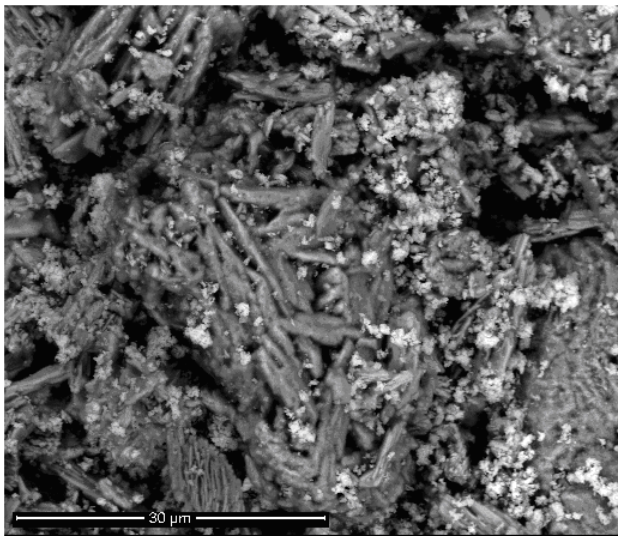
Fig. III.13 SEM micrographs of $La_2O_3$ (a), Ni50-$La_2O_3$ (HPT) (b) and Ni30-$La_2O_3$ (HPT) (c) catalysts.



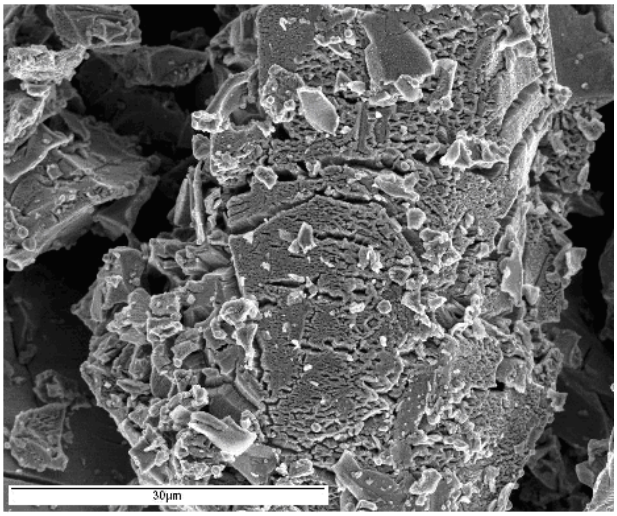

a)



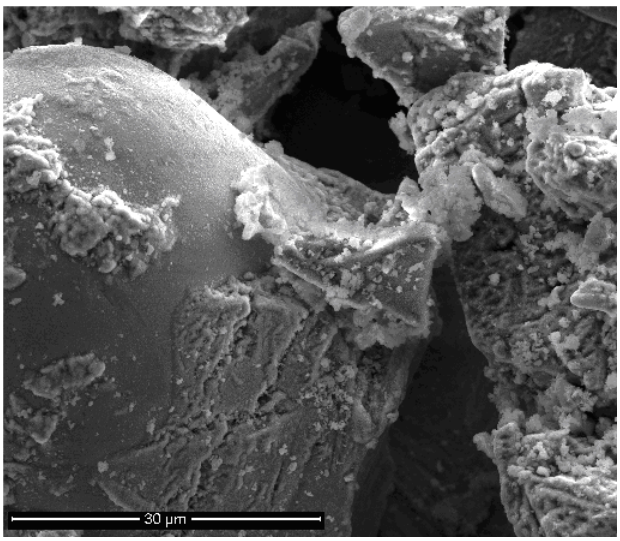

b)



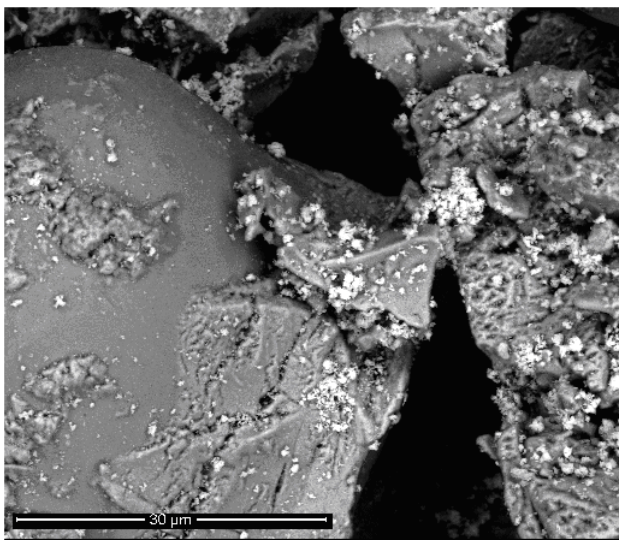

c)




d)

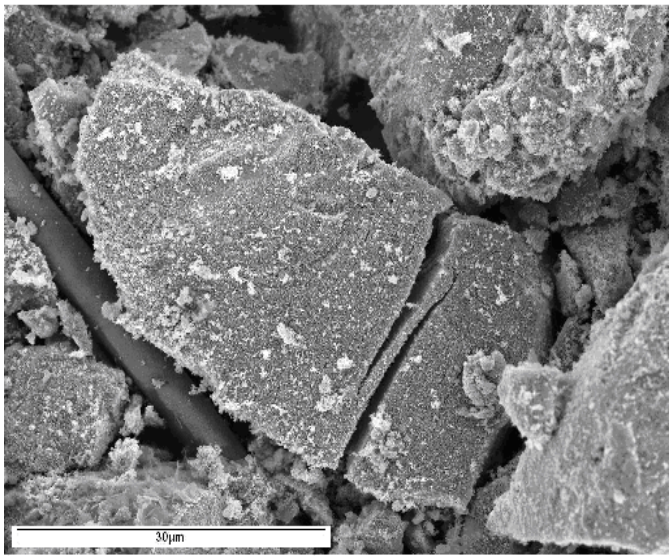



e)

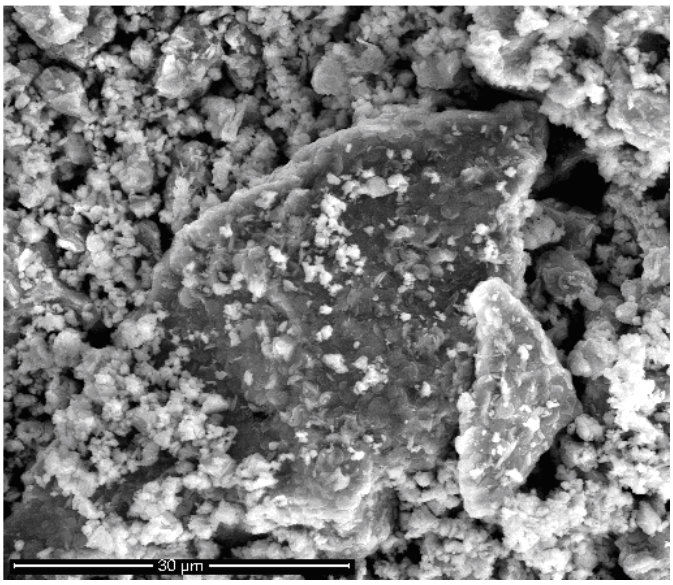



f)

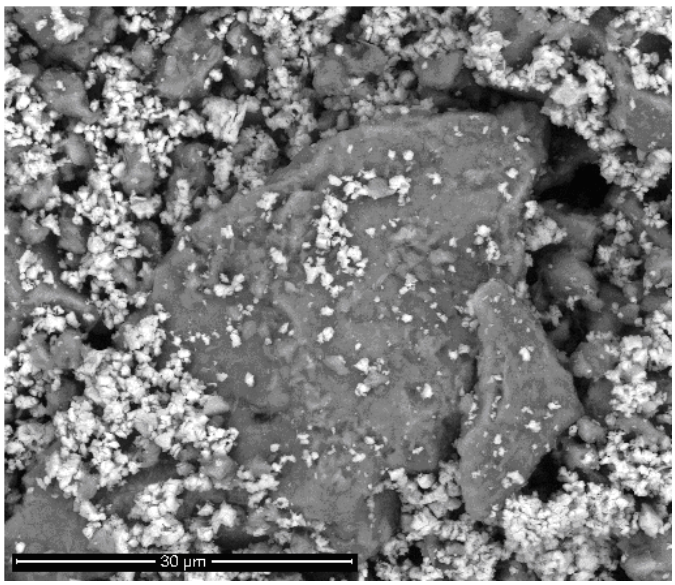
Fig. III.14 SEM micrographs of Co30 (HPT) (a), Co30-$La_2O_3$ (HPT) (b-c), Co50 (HPT) (d), Co50-$La_2O_3$ (HPT) (e-f) catalysts.



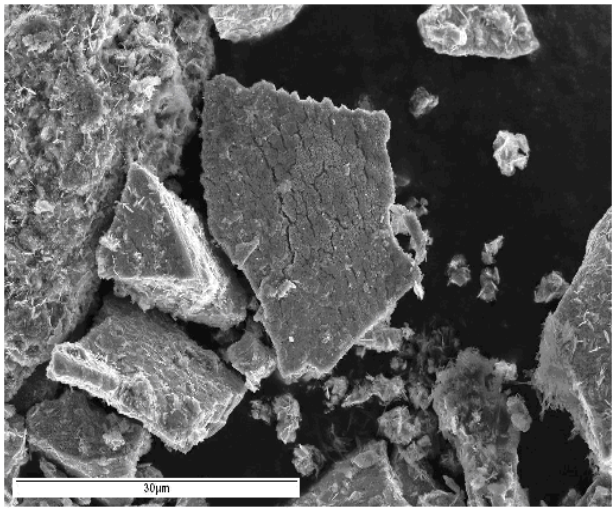

a)



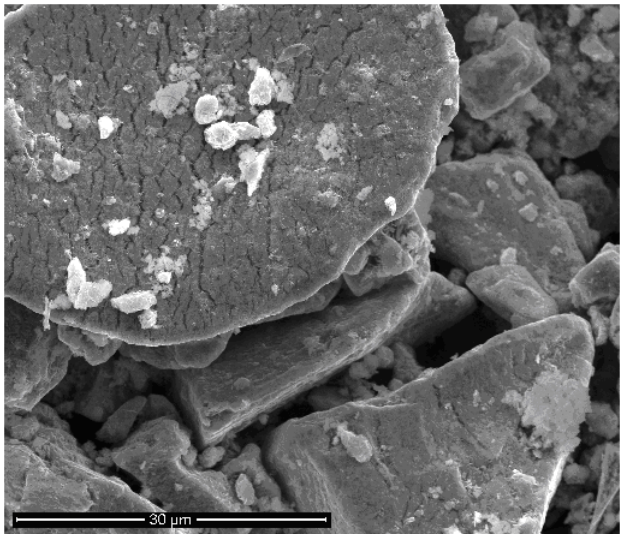

b)



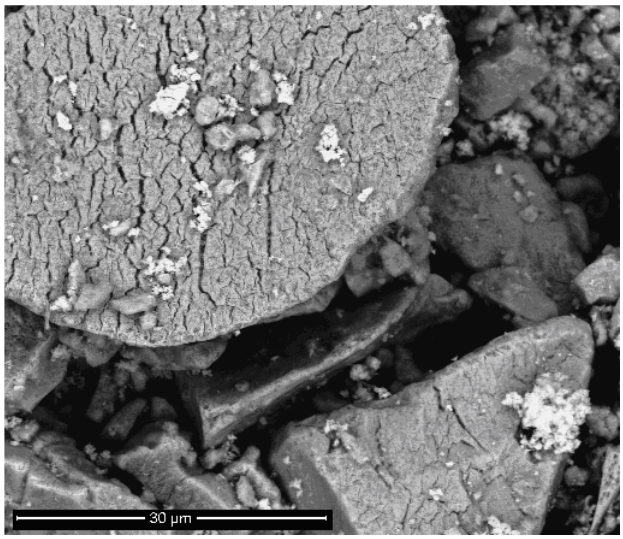

c)




d)

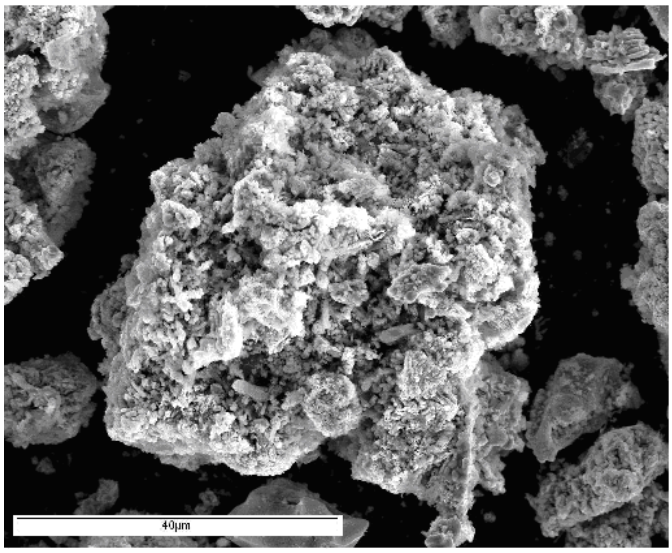



e)

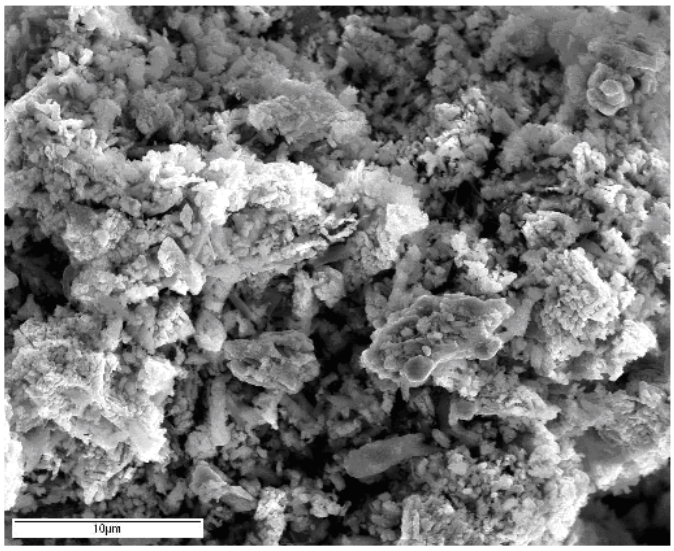



f)

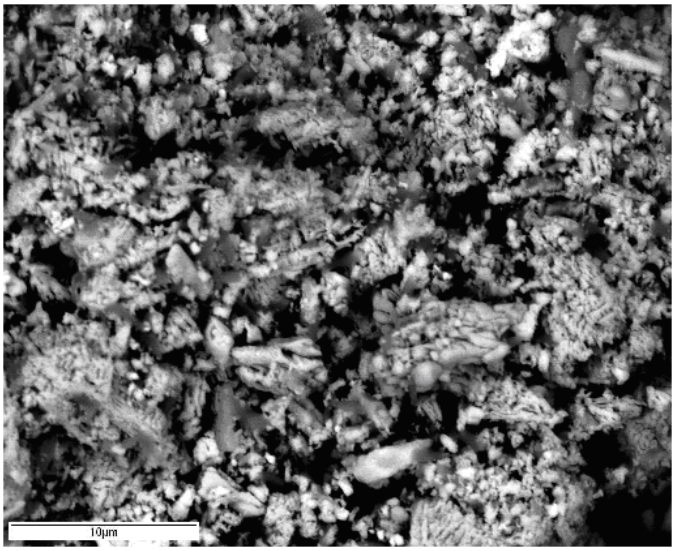
Fig. III.15 SEM micrographs of Fe50 (HPT) (a), Fe50-$La_2O_3$ (HPT) (b-c), Fe35 (HPT) (d) and Fe35-$La_2O_3$ (HPT) (e-f) catalysts.




a)




b)




c)

Fig. III.16 SEM micrographs on NiCu-$La_2O_3$ (HPT) catalyst.

## IV. Energy dispersive X-ray Spectroscopy (EDX)

Table IV.1

EDX values for the Ni-Al Raney-type alloy powders

| Alloy | Ni | | Mo | | Al | | $R_{atomic}$ | ± error |
|---|---|---|---|---|---|---|---|---|
| | Atom [%] | Element [wt. %] | Atom [%] | Element [wt. %] | Atom [%] | Element [wt. %] | | |
| Ni69 | 50.89 | 69.27 | / | / | 49.11 | 30.73 | | |
| | 49.56 | 68.13 | / | / | 50.44 | 31.87 | | |
| | 54.06 | 71.91 | / | / | 45.94 | 28.09 | | |
| | 49.79 | 68.33 | / | / | 50.21 | 31.67 | | |
| | 48.91 | 67.56 | / | / | 51.09 | 32.44 | | |
| $\overline{X}$ | 50.62 | 69.04 | / | / | 49.38 | 30.96 | **0.51** | **0.16** |
| S | 2.04 | 1.72 | / | / | 2.04 | 1.72 | | |
| $\pm k$ | 2.12 | 1.79 | / | / | 2.12 | 1.79 | | |
| Ni50 | 37.18 | 56.29 | / | / | 62.82 | 43.71 | | |
| | 37.25 | 56.37 | / | / | 62.75 | 43.63 | | |
| | 41.30 | 60.49 | / | / | 58.70 | 39.51 | | |
| | 38.21 | 57.37 | / | / | 61.79 | 42.63 | | |
| | 40.12 | 59.32 | / | / | 59.88 | 40.68 | | |
| $\overline{X}$ | 38.81 | 57.97 | / | / | 61.19 | 42.03 | **0.39** | **0.03** |
| S | 1.83 | 1.87 | / | / | 1.83 | 1.87 | | |
| $\pm k$ | 1.90 | 1.90 | / | / | 1.90 | 1.90 | | |
| Ni47-Mo6 | 38.77 | 57.10 | 0.84 | 2.02 | 60.40 | 40.88 | | |
| | 36.32 | 55.20 | 0.18 | 0.46 | 63.49 | 44.34 | | |
| | 26.39 | 38.76 | 6.70 | 16.08 | 66.91 | 45.16 | | |
| | 28.85 | 42.94 | 4.80 | 11.68 | 66.35 | 45.38 | | |
| | 37.43 | 56.40 | 0.15 | 0.38 | 62.42 | 43.23 | **0.34** | **0.10** |
| $\overline{X}$ | 33.55 | 50.08 | 2.53 | 6.12 | 63.91 | 43.80 | | |
| S | 5.55 | 8.58 | 3.02 | 7.28 | 2.72 | 1.84 | | |
| $\pm k$ | 5.77 | 8.93 | 3.15 | 7.57 | 2.83 | 1.91 | | |
| Ni30 | 17.82 | 32.05 | / | / | 82.18 | 67.95 | | |
| | 17.92 | 32.20 | / | / | 82.08 | 67.80 | | |
| | 16.30 | 29.76 | / | / | 83.70 | 70.24 | | |
| | 17.47 | 31.54 | / | / | 82.53 | 68.46 | | |
| | 17.68 | 31.85 | / | / | 82.32 | 68.15 | | |
| $\overline{X}$ | 17.44 | 31.48 | / | / | 82.56 | 68.52 | **0.17** | **0.01** |
| S | 0.66 | 0.99 | / | / | 0.66 | 0.99 | | |
| $\pm k$ | 0.68 | 1.03 | / | / | 0.68 | 1.03 | | |

Table IV.2

EDX values for Raney-Ni catalyst powders

| Catalyst | Ni | | Mo | | Al | | $R_{atomic}$ | ± error |
|---|---|---|---|---|---|---|---|---|
| | Atom [%] | Element [wt. %] | Atom [%] | Element [wt. %] | Atom [%] | Element [wt. %] | | |
| Ni69 | 54.06 | 77.20 | / | / | 18.41 | 12.08 | | |
| | 50.83 | 74.84 | / | / | 19.70 | 13.33 | | |
| | 59.14 | 80.64 | / | / | 16.37 | 10.26 | | |
| | 44.63 | 69.87 | / | / | 22.19 | 15.97 | | |
| | 50.32 | 74.45 | / | / | 19.91 | 13.54 | | |
| $\overline{X}$ | 51.58 | 75.40 | / | / | 19.40 | 13.04 | **0.59** | **0.03** |
| S | 5.33 | 3.95 | / | / | 2.14 | 2.10 | | |
| $\pm k$ | 5.54 | 4.11 | / | / | 2.23 | 2.18 | | |
| Ni50 | 48.96 | 73.42 | / | / | 20.42 | 14.07 | | |
| | 50.30 | 74.45 | / | / | 19.88 | 13.52 | | |
| | 48.66 | 73.18 | / | / | 20.54 | 14.19 | | |
| | 50.68 | 74.74 | / | / | 19.73 | 13.37 | | |
| | 54.24 | 77.34 | / | / | 18.30 | 11.99 | | |
| $\overline{X}$ | 50.57 | 74.63 | / | / | 19.77 | 13.43 | **0.72** | **0.07** |
| S | 2.22 | 1.65 | / | / | 0.89 | 0.88 | | |
| $\pm k$ | 2.31 | 1.72 | / | / | 0.93 | 0.91 | | |
| Ni47-Mo6 | 49.04 | 73.15 | 0.23 | 0.56 | 20.29 | 13.91 | | |
| | 48.06 | 72.26 | 0.32 | 0.79 | 20.65 | 14.27 | | |
| | 54.84 | 76.76 | 0.72 | 1.64 | 17.78 | 11.43 | | |
| | 47.11 | 71.16 | 0.56 | 1.39 | 20.93 | 14.53 | | |
| | 58.80 | 80.18 | 0.18 | 0.40 | 16.41 | 10.28 | **0.73** | **0.15** |
| $\overline{X}$ | 51.57 | 74.70 | 0.40 | 0.96 | 19.21 | 12.88 | | |
| S | 5.04 | 3.71 | 0.23 | 0.54 | 2.01 | 1.91 | | |
| $\pm k$ | 5.24 | 3.86 | 0.24 | 0.56 | 2.09 | 1.99 | | |
| Ni30 | 68.03 | 85.96 | / | / | 12.79 | 7.43 | | |
| | 71.81 | 88.00 | / | / | 11.28 | 6.35 | | |
| | 68.23 | 86.08 | / | / | 12.71 | 7.37 | | |
| | 72.00 | 88.10 | / | / | 11.20 | 6.30 | | |
| | 66.86 | 85.31 | / | / | 13.25 | 7.77 | | |
| $\overline{X}$ | 69.39 | 86.69 | / | / | 12.25 | 7.04 | **0.85** | **0.07** |
| S | 2.36 | 1.28 | / | / | 0.94 | 0.67 | | |
| $\pm k$ | 2.45 | 1.33 | / | / | 0.98 | 0.70 | | |

Table IV.3

EDX values on Co-Al Raney-type alloy powders

| Alloy | Co Atom [%] | Co Element [wt. %] | Al Atom [%] | Al Element [wt. %] | $R_{atomic}$ | ± error |
|---|---|---|---|---|---|---|
| Co50 | 52.23 | 70.49 | 47.77 | 29.51 | | |
| | 29.98 | 48.33 | 70.02 | 51.67 | | |
| | 31.61 | 50.24 | 68.39 | 49.76 | | |
| | 27.54 | 45.36 | 72.46 | 54.64 | | |
| | 29.33 | 47.55 | 70.67 | 52.45 | | |
| $\overline{X}$ | 34.14 | 52.39 | 65.86 | 47.61 | **0.34** | **0.11** |
| S | 10.22 | 10.27 | 10.22 | 10.27 | | |
| $\pm k$ | 10.63 | 10.68 | 10.63 | 10.68 | | |
| | | | | | | |
| Co30 | 17.05 | 30.99 | 82.95 | 69.01 | | |
| | 17.78 | 32.07 | 82.22 | 67.93 | | |
| | 17.71 | 31.98 | 82.29 | 68.02 | | |
| | 18.43 | 33.04 | 81.57 | 66.96 | | |
| | 16.20 | 29.69 | 83.80 | 70.31 | | |
| $\overline{X}$ | 17.43 | 31.55 | 82.57 | 68.45 | **0.17** | **0.01** |
| S | 0.85 | 1.27 | 0.85 | 1.27 | | |
| $\pm k$ | 0.88 | 1.32 | 0.88 | 1.32 | | |

Table IV.4

EDX values on Co-Al Raney-type catalyst powders

| Catalyst | Co Atom [%] | Co Element [wt. %] | Al Atom [%] | Al Element [wt. %] | $R_{atomic}$ | ± error |
|---|---|---|---|---|---|---|
| Co50 | 72.87 | 77.95 | 23.76 | 11.67 | | |
| | 68.51 | 86.28 | 12.59 | 7.26 | | |
| | 80.35 | 92.20 | 7.86 | 4.13 | | |
| | 74.45 | 89.39 | 10.22 | 5.62 | | |
| | 76.39 | 90.34 | 9.45 | 5.11 | | |
| $\overline{X}$ | 74.51 | 87.23 | 12.78 | 6.76 | **0.85** | **0.16** |
| S | 4.37 | 5.61 | 6.37 | 2.97 | | |
| $\pm k$ | 4.54 | 5.84 | 6.63 | 3.09 | | |
| | | | | | | |
| Co30 | 85.91 | 94.63 | 5.63 | 2.84 | | |
| | 86.71 | 94.96 | 5.32 | 2.67 | | |
| | 83.78 | 93.72 | 6.49 | 3.32 | | |
| | 89.26 | 96.00 | 4.30 | 2.12 | | |
| | 83.30 | 93.51 | 6.68 | 3.43 | | |
| $\overline{X}$ | 85.79 | 94.56 | 5.68 | 2.88 | **0.94** | **0.06** |
| S | 2.41 | 1.01 | 0.96 | 0.53 | | |
| $\pm k$ | 2.50 | 1.05 | 1.00 | 0.55 | | |

Table IV.5

EDX values on Fe-Al Raney-type alloy powders

| Alloy | Fe Atom [%] | Fe Element [wt. %] | Al Atom [%] | Al Element [wt. %] | $R_{atomic}$ | ± error |
|---|---|---|---|---|---|---|
| Fe50 | 45.78 | 63.61 | 54.22 | 36.39 | | |
| | 31.85 | 49.17 | 68.15 | 50.83 | | |
| | 34.82 | 52.51 | 65.18 | 47.49 | | |
| | 34.68 | 52.35 | 65.32 | 47.65 | | |
| | 38.02 | 55.94 | 61.98 | 44.06 | | |
| $\overline{X}$ | 37.03 | 54.72 | 62.97 | 45.28 | **0.37** | **0.10** |
| S | 5.36 | 5.52 | 5.36 | 5.52 | | |
| $\pm k$ | 5.58 | 5.74 | 5.58 | 5.74 | | |
| | | | | | | |
| Fe35 | 24.26 | 39.87 | 75.74 | 60.13 | | |
| | 24.20 | 39.79 | 75.80 | 60.21 | | |
| | 23.87 | 39.36 | 76.13 | 60.64 | | |
| | 29.32 | 46.19 | 70.68 | 53.81 | | |
| | 20.32 | 34.55 | 79.68 | 65.45 | | |
| $\overline{X}$ | 24.39 | 39.95 | 75.61 | 60.05 | **0.24** | **0.05** |
| S | 3.21 | 4.14 | 3.21 | 4.14 | | |
| $\pm k$ | 3.34 | 4.30 | 3.34 | 4.30 | | |

Table IV.6

EDX values on Fe-Al Raney-type catalyst powders

| Catalyst | Fe Atom [%] | Fe Element [wt. %] | Al Atom [%] | Al Element [wt. %] | $R_{atomic}$ | ± error |
|---|---|---|---|---|---|---|
| Fe 50 | 87.50 | 95.04 | 5.00 | 2.62 | | |
| | 87.44 | 95.02 | 5.02 | 2.64 | | |
| | 90.07 | 96.13 | 3.97 | 2.05 | | |
| | 89.70 | 95.98 | 4.12 | 2.13 | | |
| | 91.64 | 96.78 | 3.34 | 1.71 | | |
| $\overline{X}$ | 89.27 | 95.79 | 4.29 | 2.23 | **0.95** | **0.05** |
| S | 1.80 | 0.76 | 0.72 | 0.40 | | |
| $\pm k$ | 1.87 | 0.79 | 0.75 | 0.41 | | |
| | | | | | | |
| Fe 35 | 97.49 | 99.07 | 1.00 | 0.49 | | |
| | 86.14 | 94.45 | 5.54 | 2.94 | | |
| | 89.81 | 96.02 | 4.07 | 2.10 | | |
| | 87.82 | 95.18 | 4.87 | 2.55 | | |
| | 76.52 | 89.93 | 7.32 | 5.33 | | |
| $\overline{X}$ | 87.56 | 94.93 | 4.56 | 2.68 | **0.95** | **0.19** |
| S | 7.54 | 3.30 | 2.32 | 1.75 | | |
| $\pm k$ | 7.85 | 3.44 | 2.42 | 1.82 | | |

Table IV.7

EDX values on Cu50 Raney-type alloy powder

| Alloy | Cu | | Al | | $R_{atomic}$ | ± error |
|---|---|---|---|---|---|---|
| | Atom [%] | Element [wt. %] | Atom [%] | Element [wt. %] | | |
| Cu50 | 35.62 | 56.58 | 64.38 | 43.42 | | |
| | 35.33 | 56.27 | 64.67 | 43.73 | | |
| | 33.64 | 54.42 | 66.36 | 45.58 | | |
| | 40.18 | 61.27 | 59.82 | 38.73 | | |
| | 32.40 | 53.02 | 67.60 | 46.98 | | |
| $\overline{X}$ | 35.43 | 56.31 | 64.57 | 43.69 | **0.35** | **0.05** |
| S | 2.96 | 3.13 | 2.96 | 3.13 | | |
| $\pm k$ | 3.08 | 3.25 | 3.08 | 3.25 | | |

Table IV.8

EDX values on Cu50 Raney-type catalyst powder

| Catalyst | Cu | | Al | | $R_{atomic}$ | ± error |
|---|---|---|---|---|---|---|
| | Atom [%] | Element [wt. %] | Atom [%] | Element [wt. %] | | |
| Cu50 | 92.69 | 97.53 | 2.92 | 1.31 | | |
| | 89.75 | 96.46 | 4.10 | 1.87 | | |
| | 82.83 | 93.76 | 6.87 | 3.30 | | |
| | 91.26 | 97.02 | 3.49 | 1.58 | | |
| | 88.25 | 95.90 | 4.70 | 2.17 | | |
| $\overline{X}$ | 88.96 | 96.13 | 4.42 | 2.05 | **0.95** | **0.10** |
| S | 3.80 | 1.46 | 1.52 | 0.77 | | |
| $\pm k$ | 3.96 | 1.52 | 1.59 | 0.80 | | |

**Summary of the results**

Table IV.9

Characterization of the catalysts

| Sample | Alloy | | | Catalyst | | |
|---|---|---|---|---|---|---|
| | $\bar{d}$ [μm] | $R^a_{n,alloy}$ | $R^a_{eff,alloy}$ | $\bar{d}$ [μm] | $R^a_{eff,catalyst}$ | $S_{BET}$ [$m^2/g$] |
| Ni69 | 41 | 0.506 | 0.51 ± 0.16 | 40 | 0.59 ± 0.03 | 2 |
| Ni47-Mo6 | 101 | 0.307 | 0.34 ± 0.10 | 101 | 0.73 ± 0.15 | 86 |
| Co30 | 372 | 0.164 | 0.17 ± 0.02 | 211 | 0.94 ± 0.06 | 26 |
| Co50 | 62 | 0.314 | 0.30 ± 0.05 | 59 | 0.85 ± 0.16 | 41 |
| Co30Cu50 (ITT) | / | / | / | 20 | 0.95 ± 0.08 | 23 |
| Co50Cu50 (ITT) | / | / | / | 24 | 0.90 ± 0.13 | 8 |

Table IV.10

Characterization of the catalysts

| Catalyst | $\bar{d}$ [μm] | $R^a_{eff,catalyst}$ | $S_{BET}$ [$m^2/g$] |
|---|---|---|---|
| Co30 | 211 | 0.94±0.06 | 26 |
| Co30 (HPT) | 27 | 0.94±0.06 | 63 |
| Co30-$La_2O_3$ | 75 | 0.93±0.06 | 14 |
| Co30-$La_2O_3$ (HPT) | 38 | 0.93±0.06 | 68 |
| Co50 | 59 | 0.85±0.16 | 41 |
| Co50 (HPT) | 23 | 0.85±0.16 | 9 |
| Co50-$La_2O_3$ | 6 | 0.83±0.16 | 5 |
| Co50-$La_2O_3$ (HPT) | 9 | 0.83±0.16 | 14 |
| Fe50 | 43 | 0.95±0.05 | 62 |
| Fe50 (HPT) | 13 | 0.95±0.05 | 5 |
| Fe50-$La_2O_3$ | 14 | 0.93±0.05 | 15 |
| Fe50-$La_2O_3$ (HPT) | 13 | 0.93±0.05 | 11 |
| Fe35 | 63 | 0.95±0.19 | 24 |
| Fe35 (HPT) | 29 | 0.95±0.19 | 6 |
| Fe35-$La_2O_3$ | 18 | 0.93±0.19 | 20 |
| Fe35-$La_2O_3$ (HPT) | 12 | 0.93±0.19 | 11 |

## V. X-Ray Photoelectron Spectroscopy

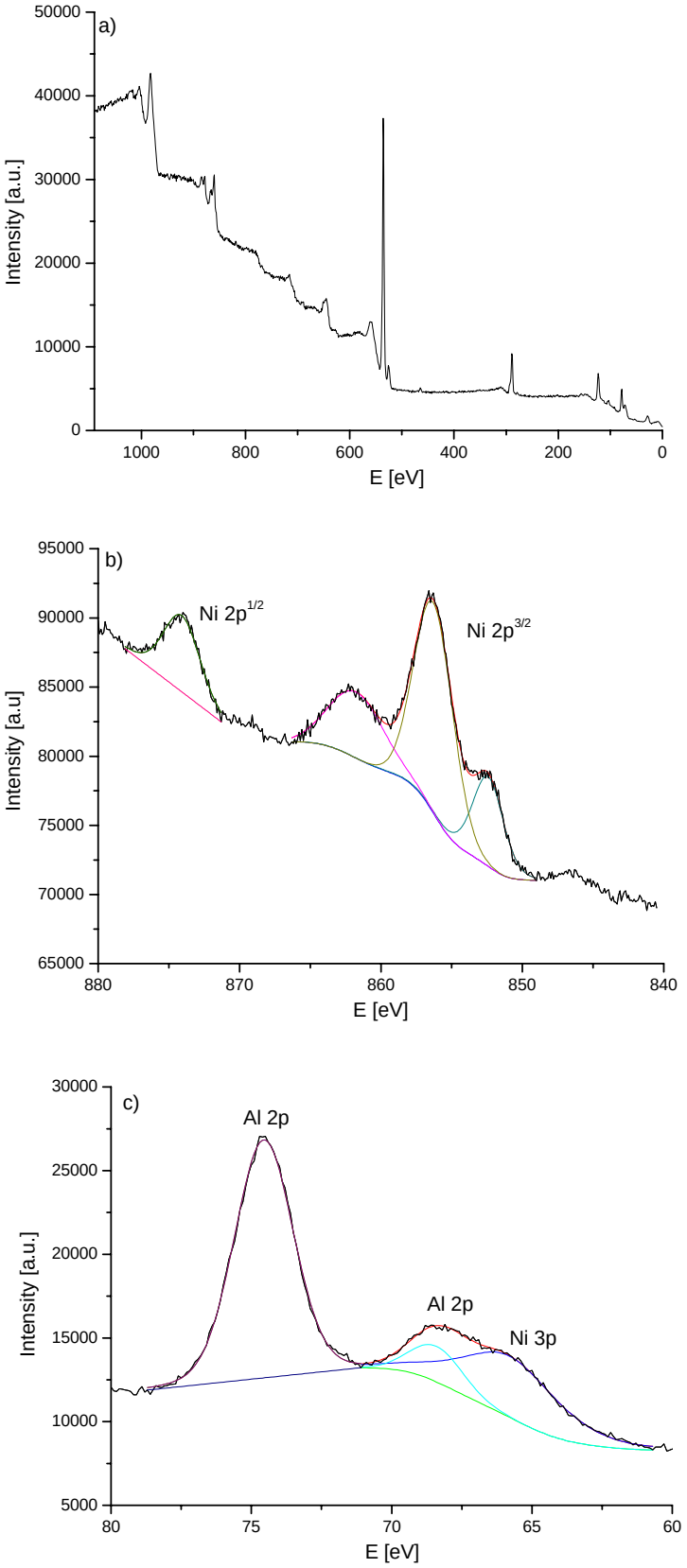



Fig. V.1 XPS survey spectrum (a) and narrow scan (b-c) on Ni69 alloy.

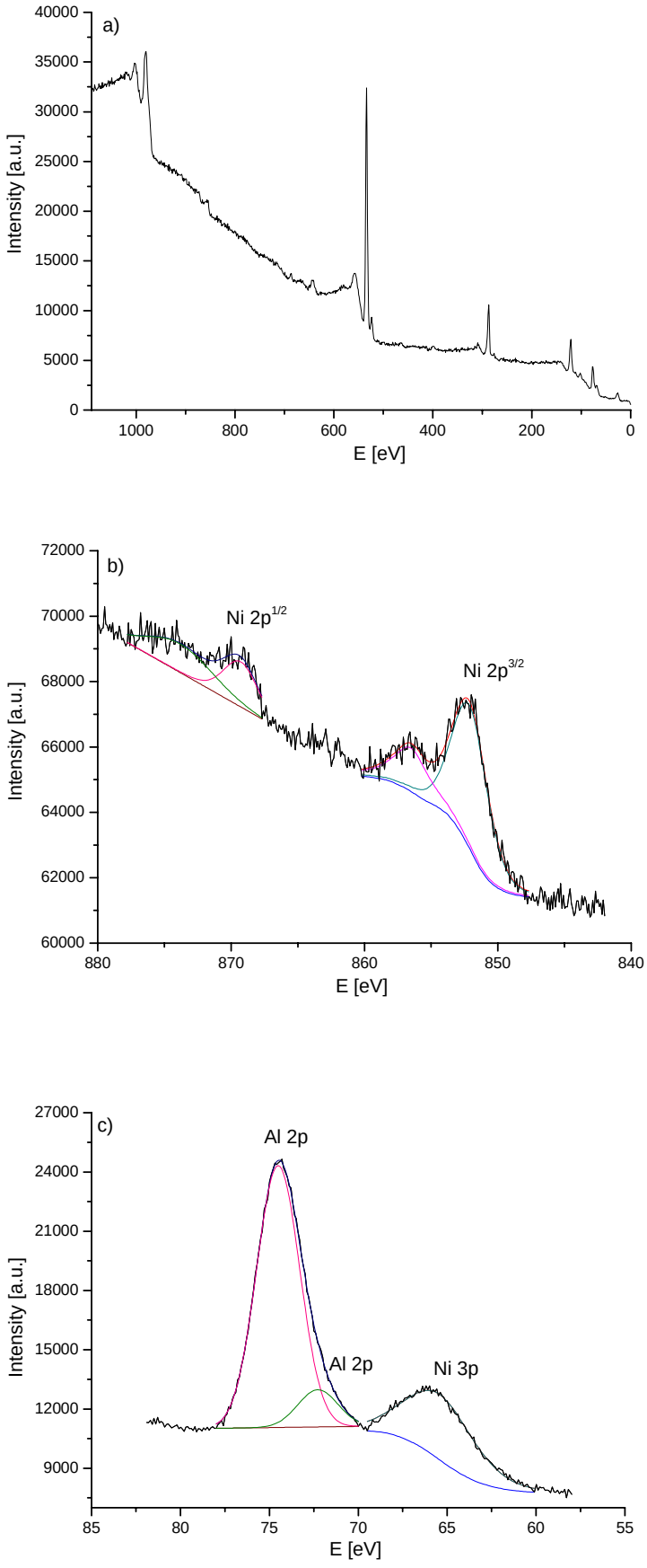



Fig. V.2 XPS survey spectrum (a) and narrow scan (b-c) on Ni47-Mo6 alloy.

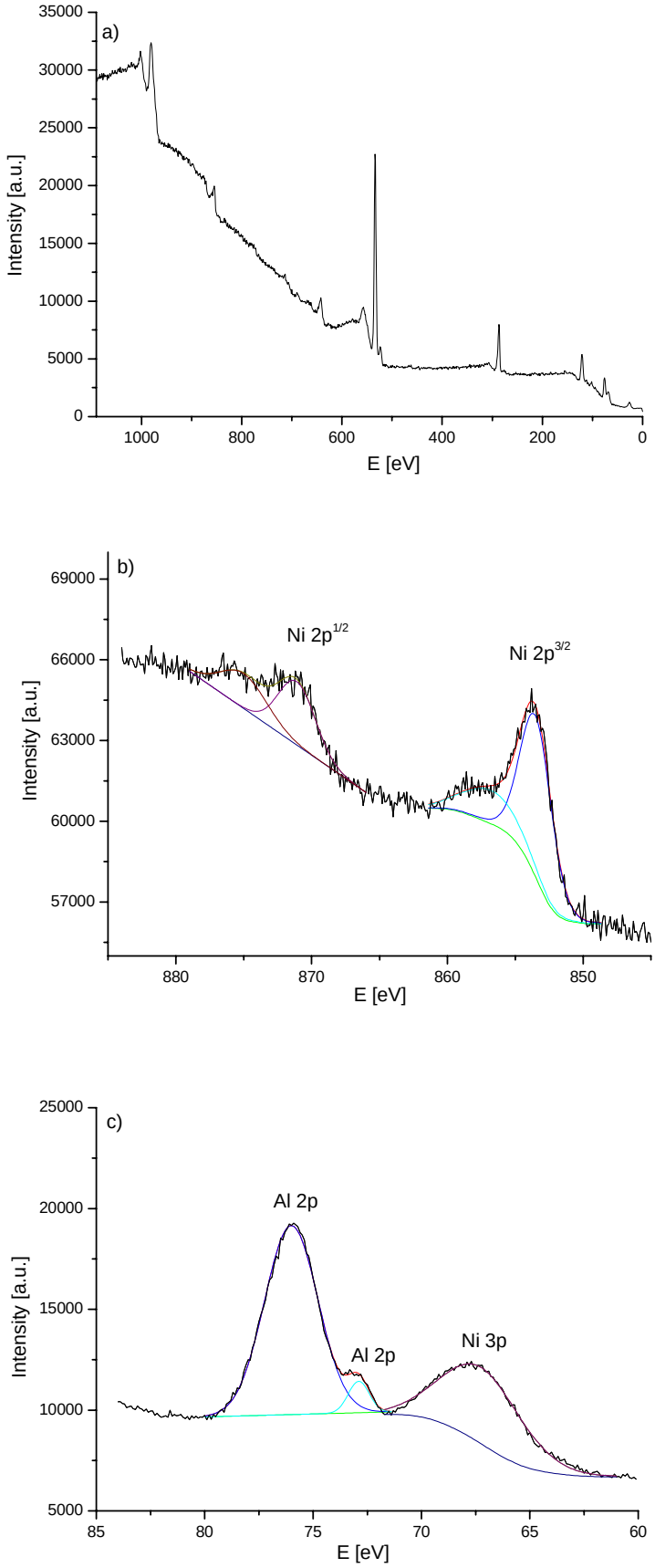



Fig. V.3 XPS survey spectrum (a) and narrow scan (b-c) on Ni50 alloy.

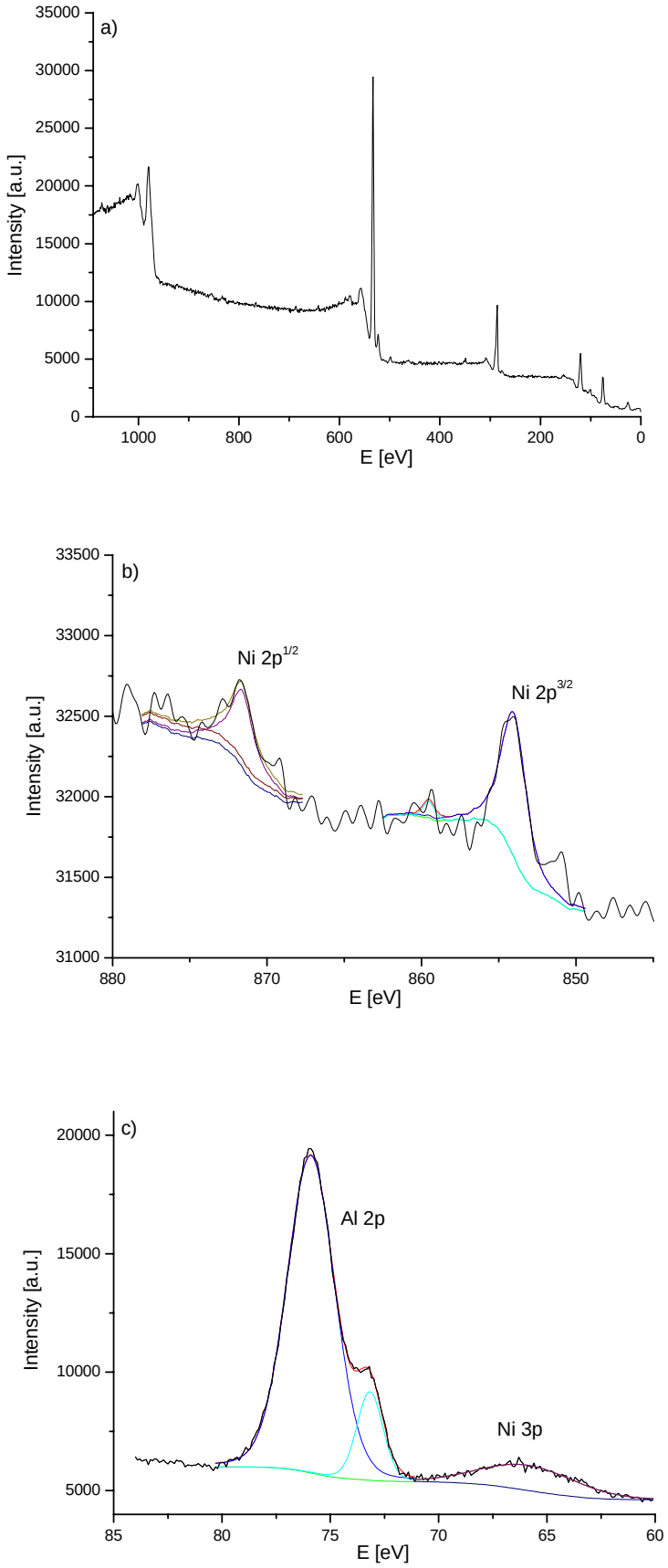



Fig. V.4 XPS survey spectrum (a) and narrow scan (b-c) on Ni30 alloy.

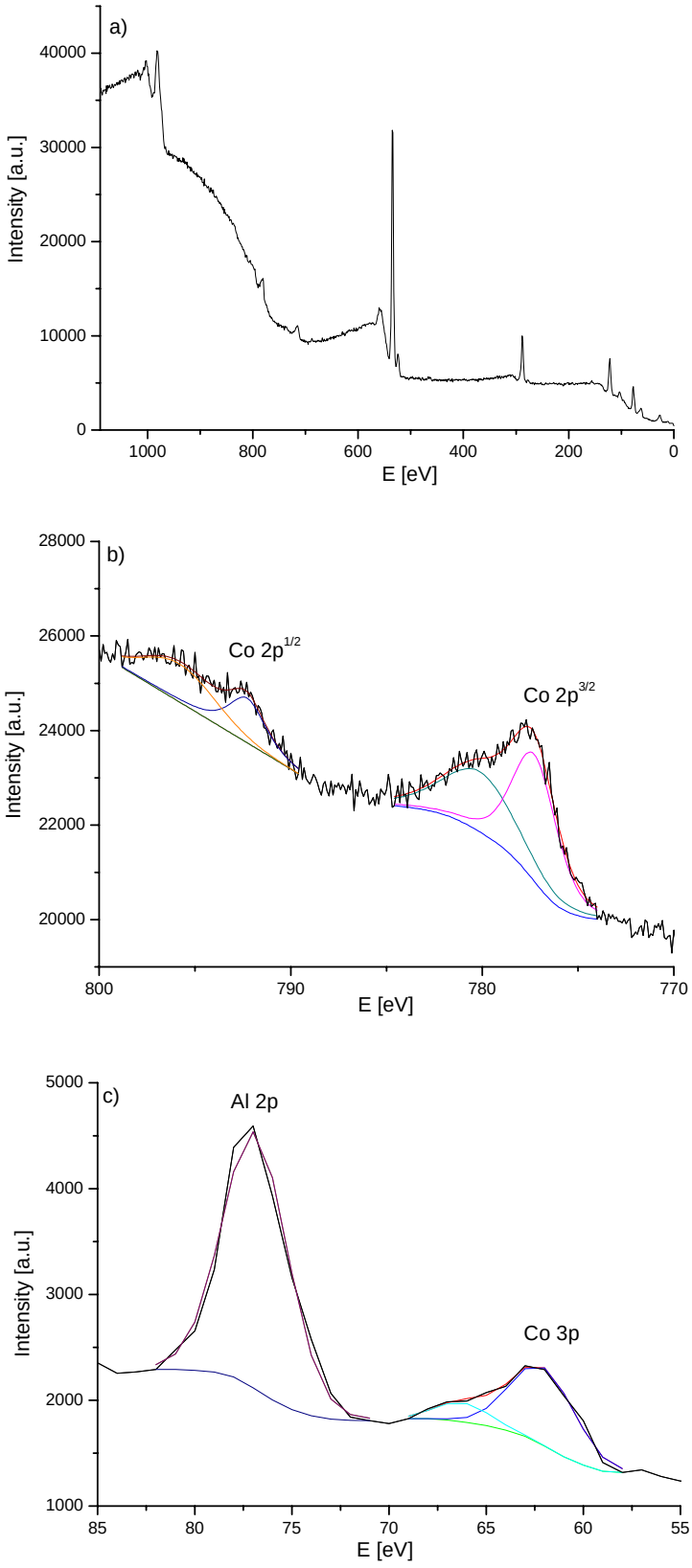



Fig. V.5 XPS survey spectrum (a) and narrow scan (b-c) on Co50 alloy.

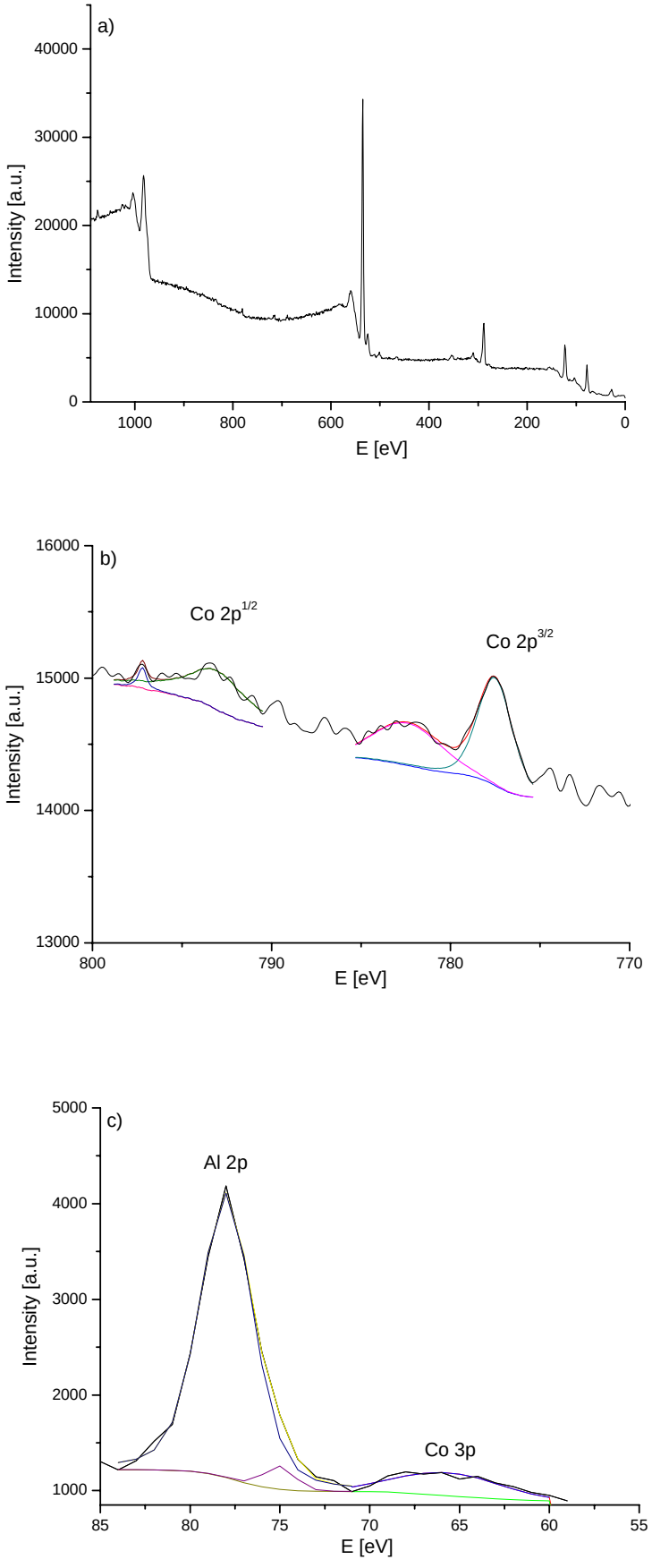



Fig. V.6 XPS survey spectrum (a) and narrow scan (b-c) on Co30 alloy.

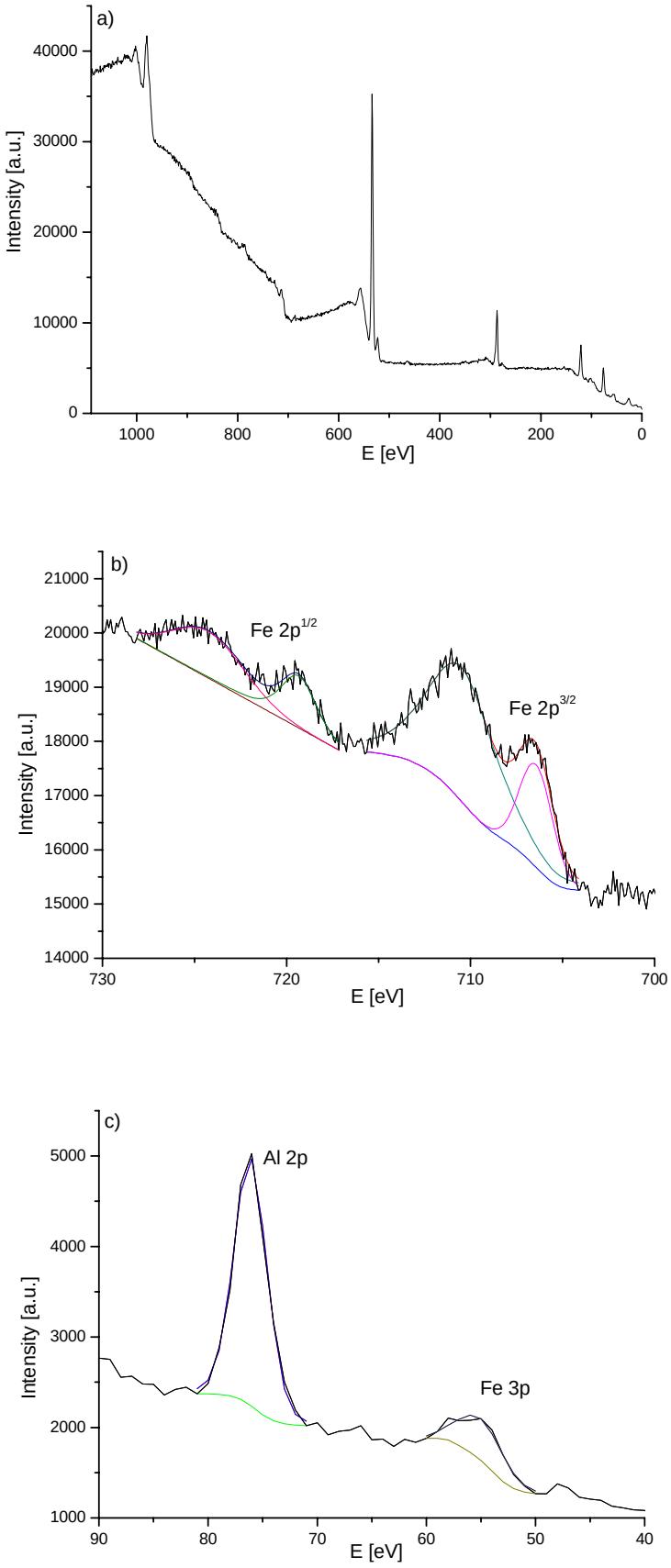



Fig. V.7 XPS survey spectrum (a) and narrow scan (b-c) on Fe50 alloy.

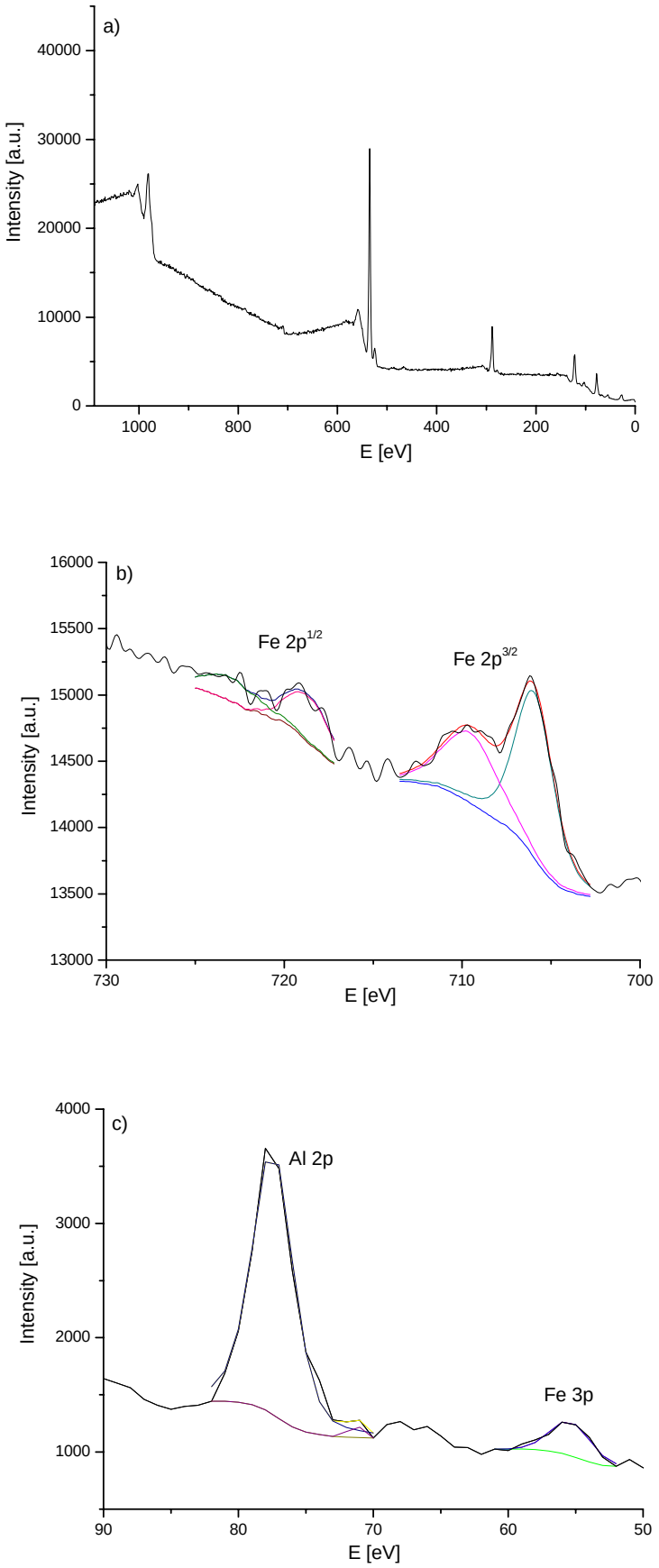



Fig. V.8 XPS survey spectrum (a) and narrow scan (b-c) on Fe35 alloy.

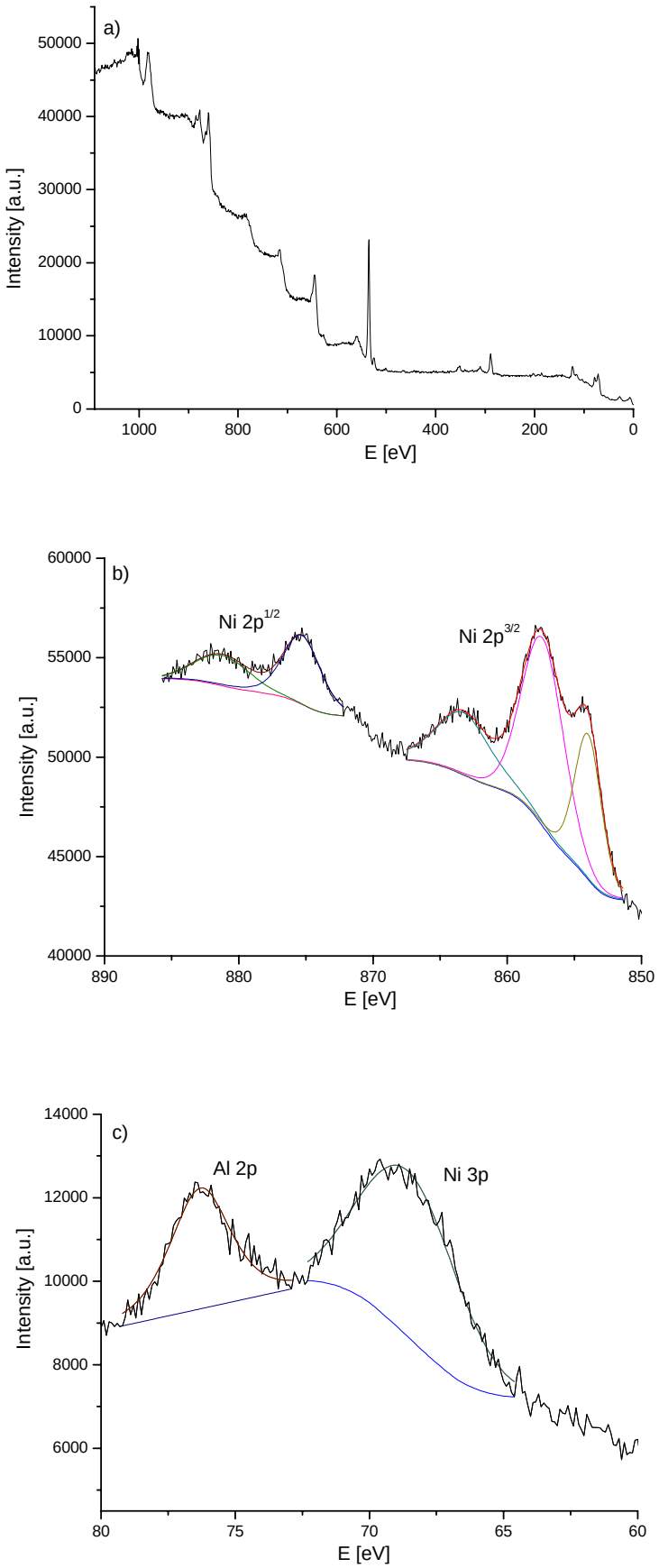



Fig. V.9 XPS survey spectrum (a) and narrow scan (b-c) on Ni69 catalyst.

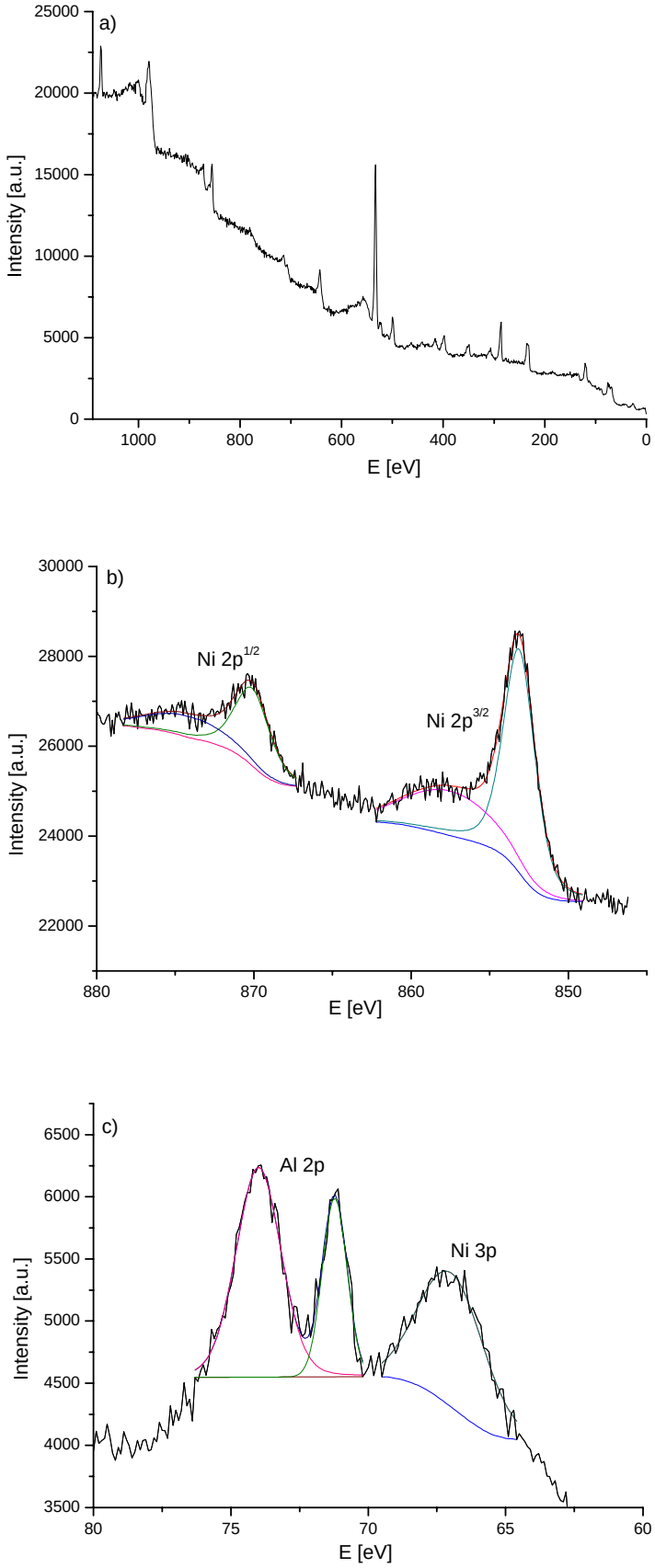



Fig. V.10 XPS survey spectrum (a) and narrow scan (b-c) on Ni47-Mo6 catalyst.

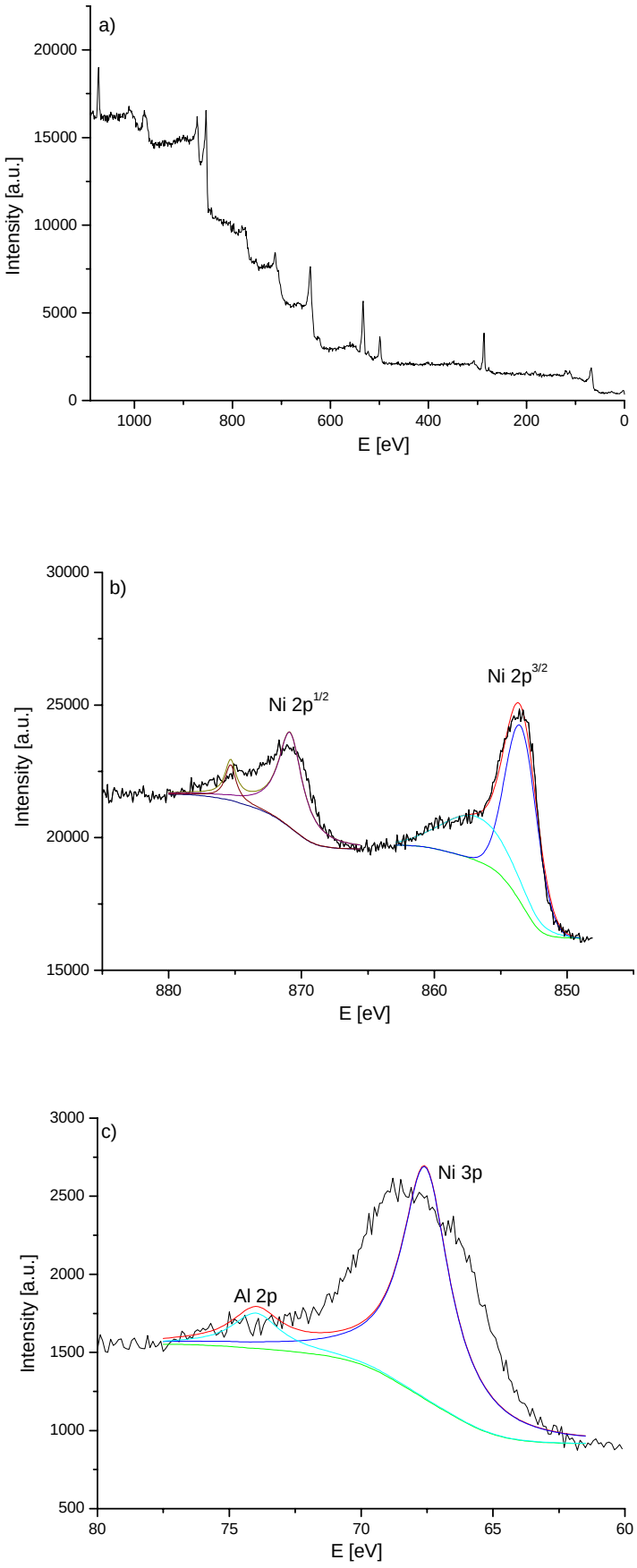



Fig. V.11 XPS survey spectrum (a) and narrow scan (b-c) on Ni50 catalyst.

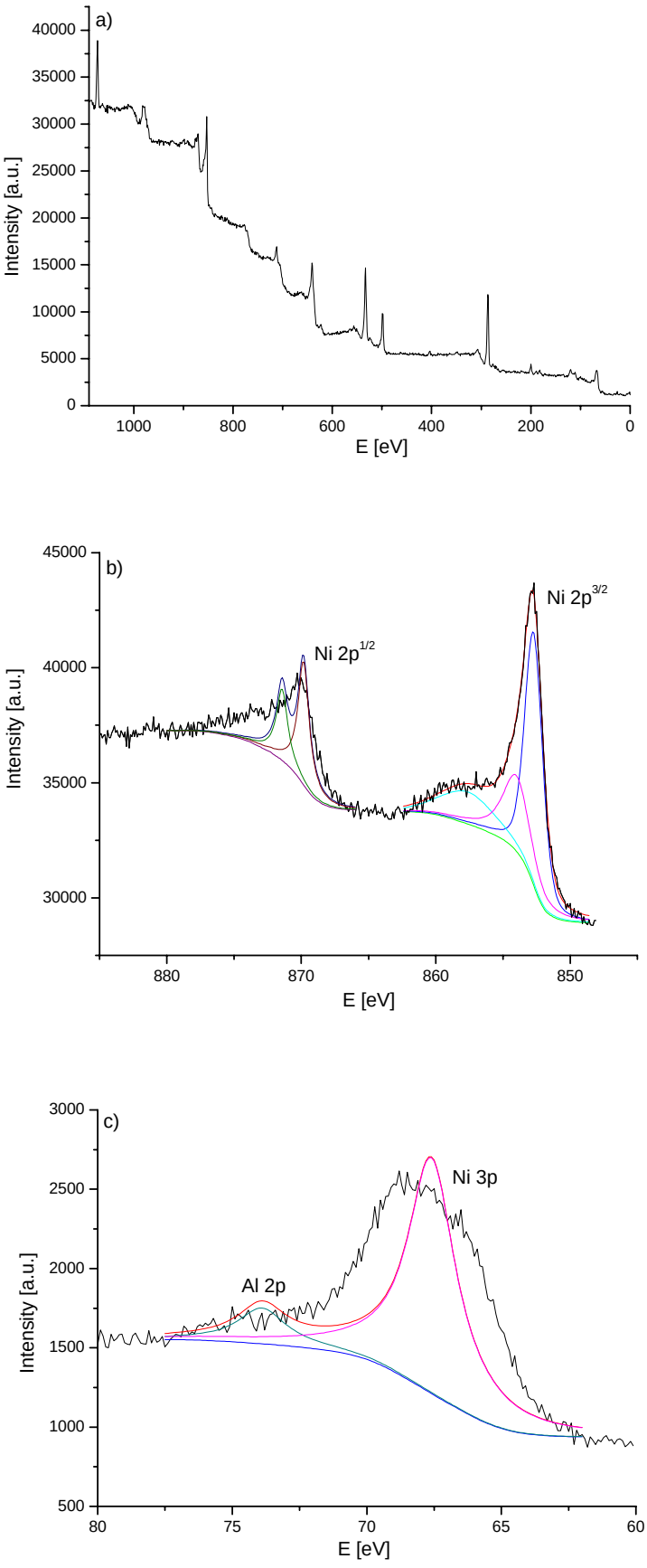



Fig. V.12 XPS survey spectrum (a) and narrow scan (b-c) on Ni30 catalyst.

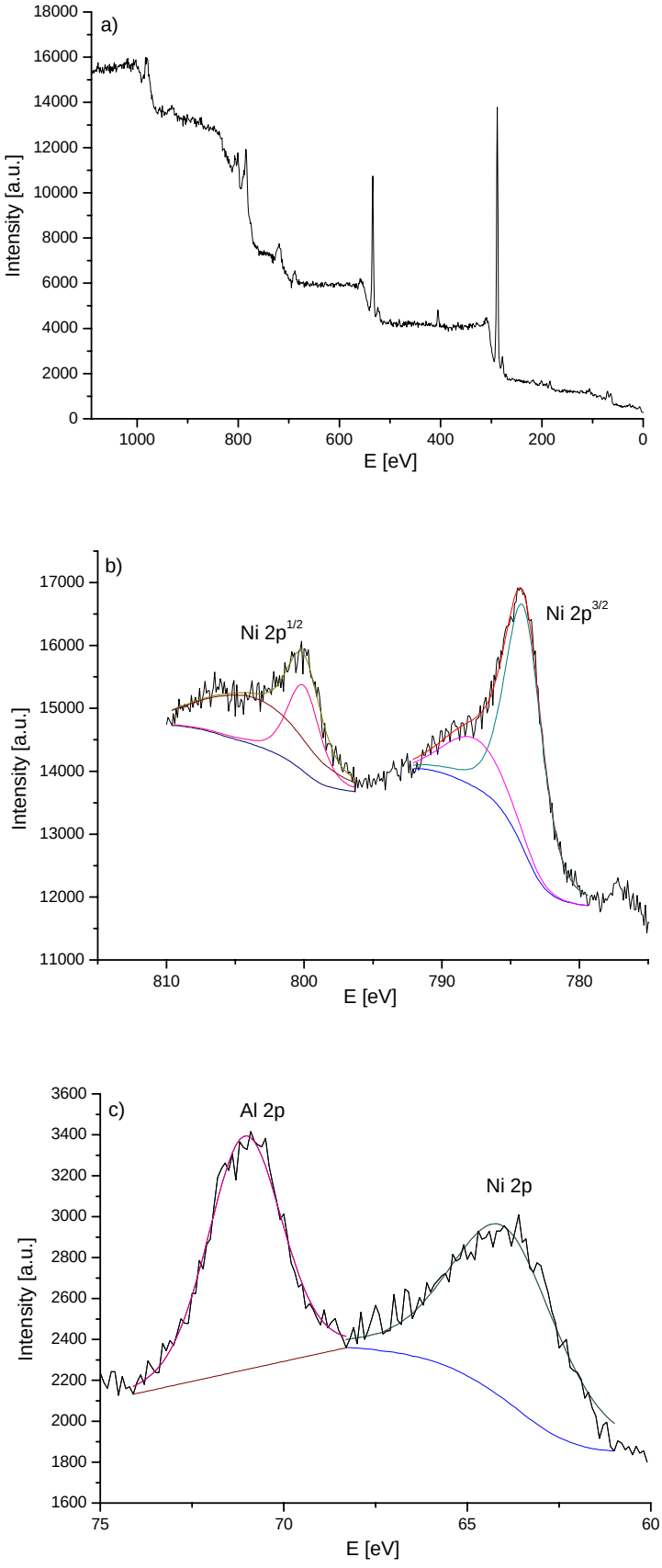



Fig. V.13 XPS survey spectrum (a) and narrow scan (b-c) on Co50 catalyst.

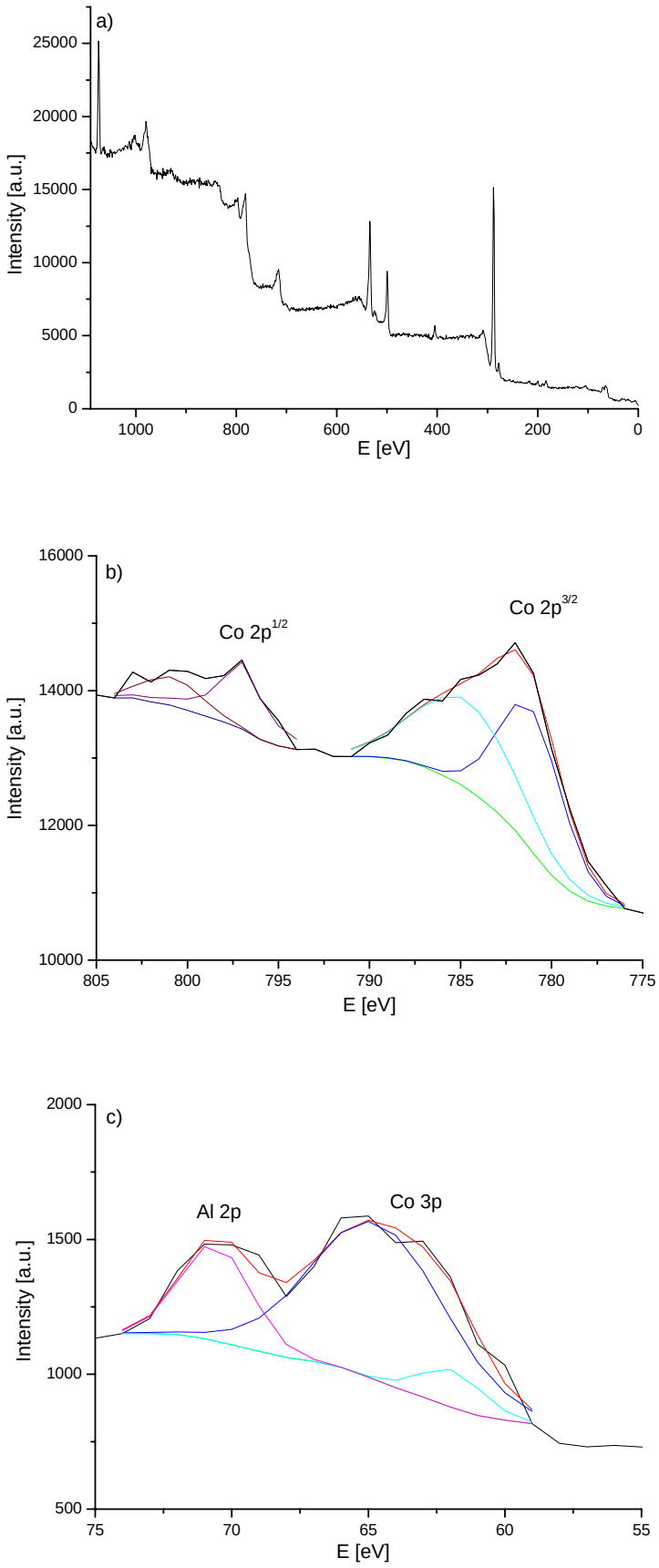



Fig. V.14 XPS survey spectrum (a) and narrow scan (b-c) on Co30 catalyst.

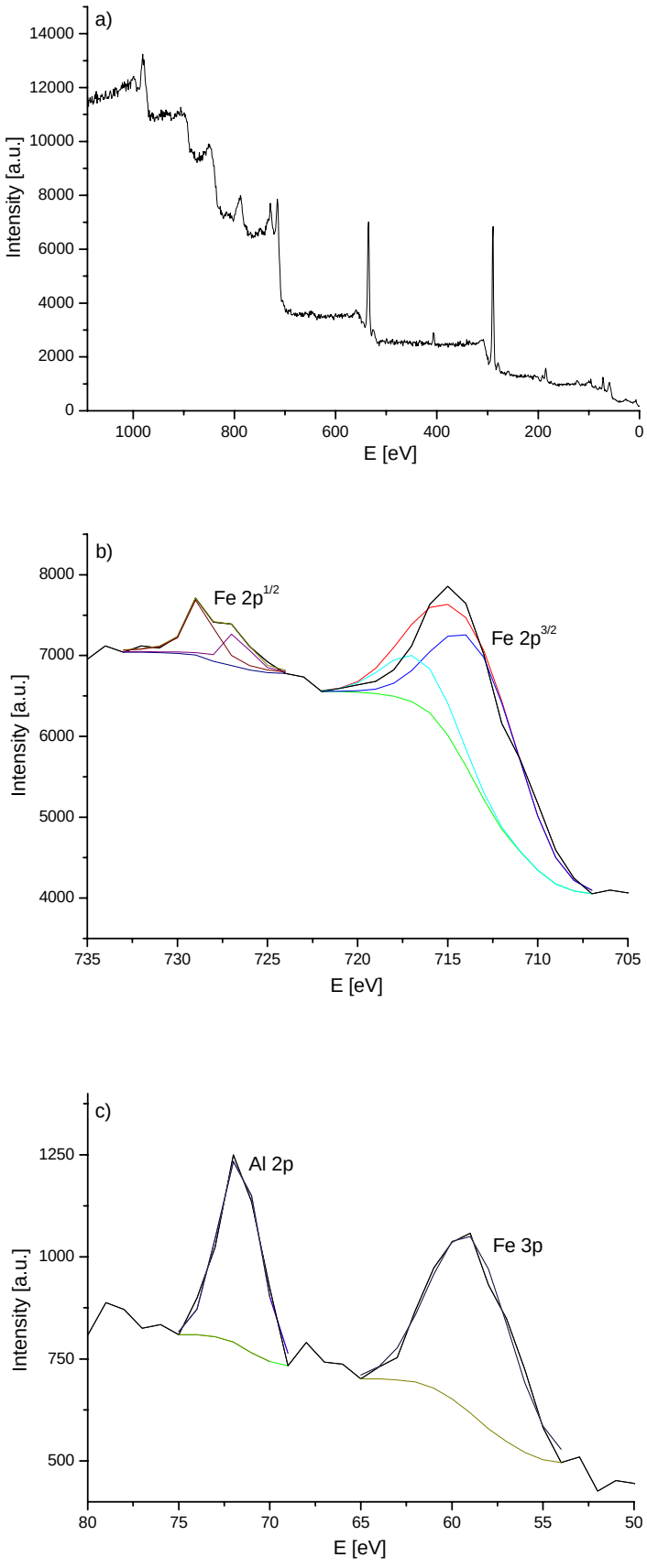



Fig. V.15 XPS survey spectrum (a) and narrow scan (b-c) on Fe50 catalyst.

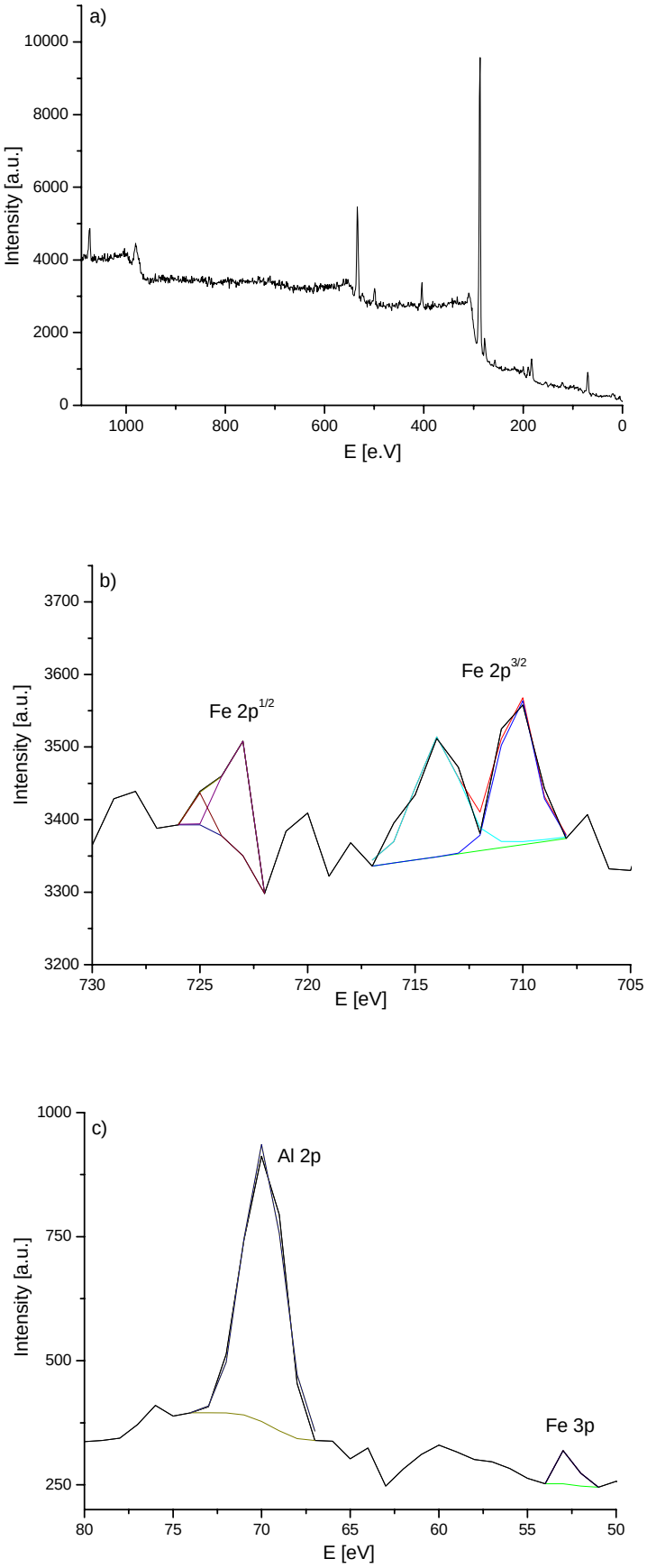



Fig. V.16 XPS survey spectrum (a) and narrow scan (b-c) on Fe35 catalyst.

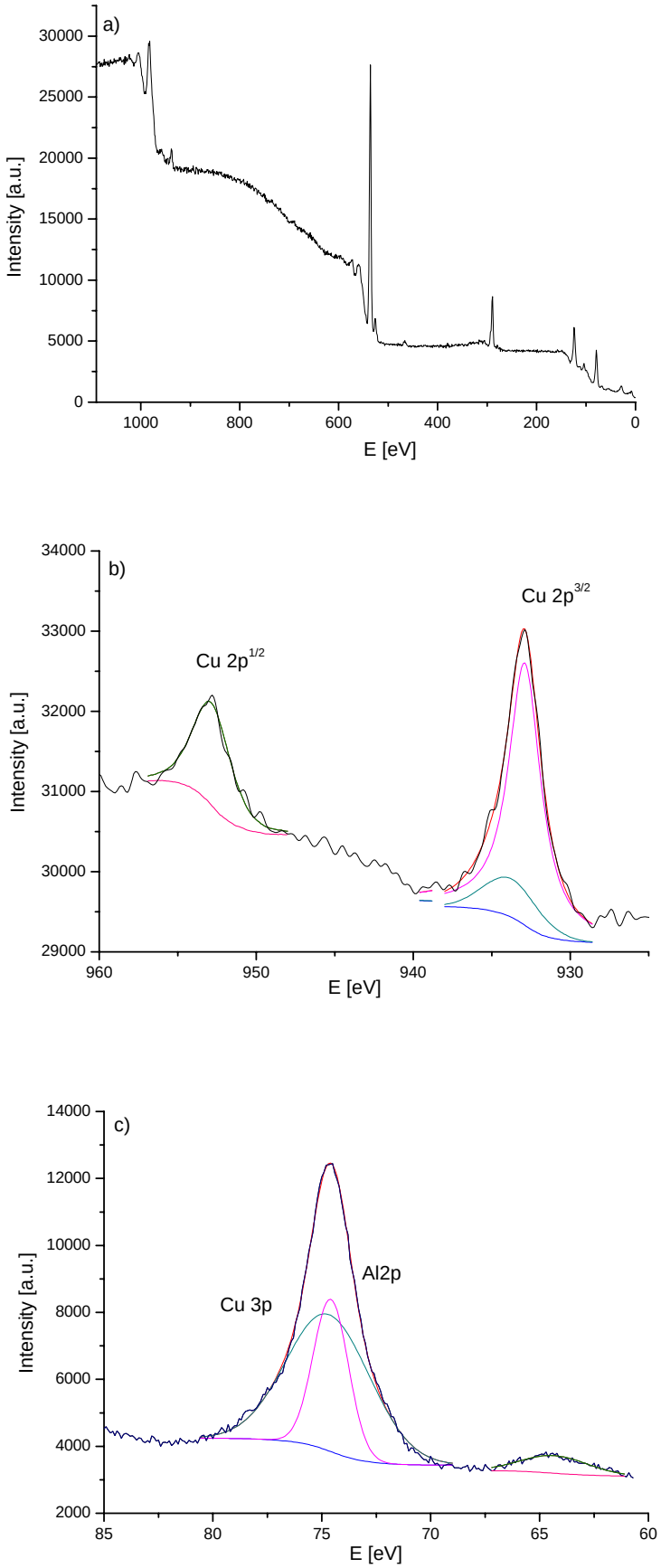



Fig. V.17 XPS survey spectrum (a) and narrow scan (b-c) on Cu50 alloy.

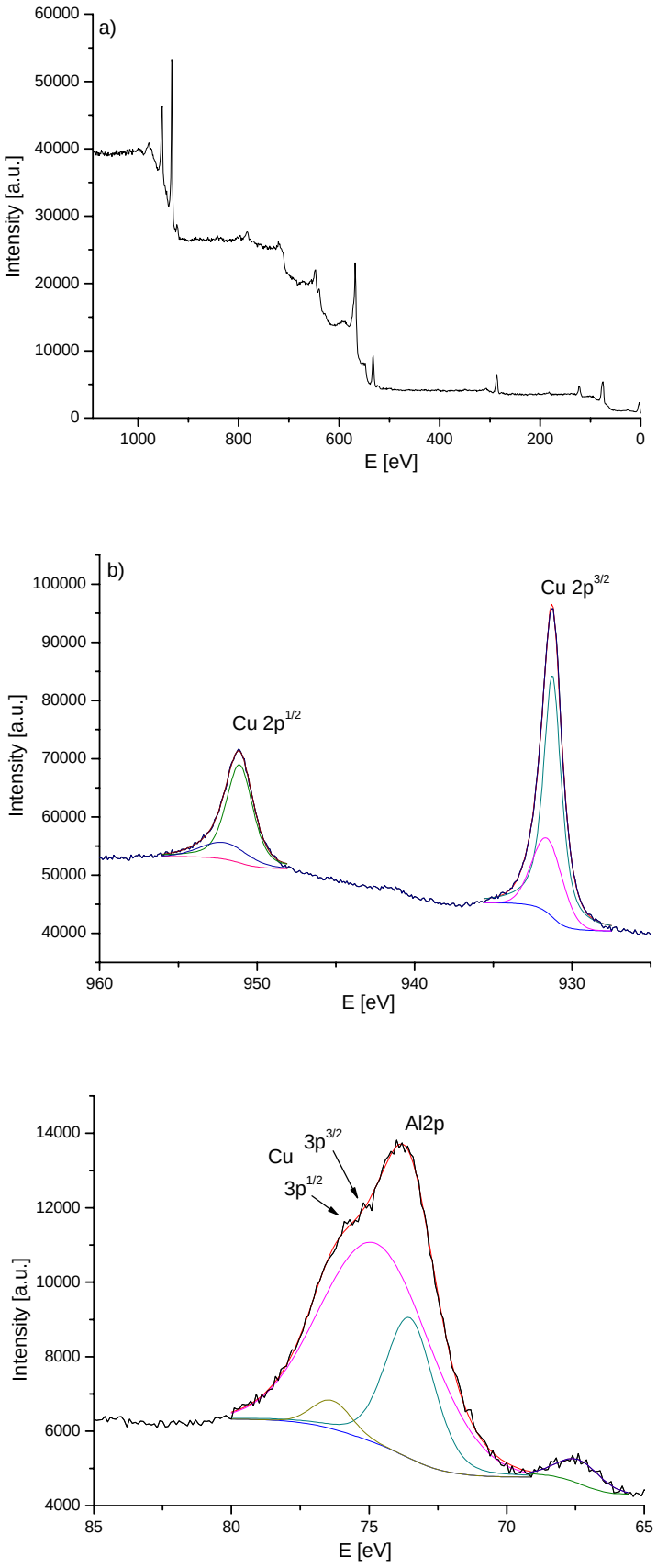
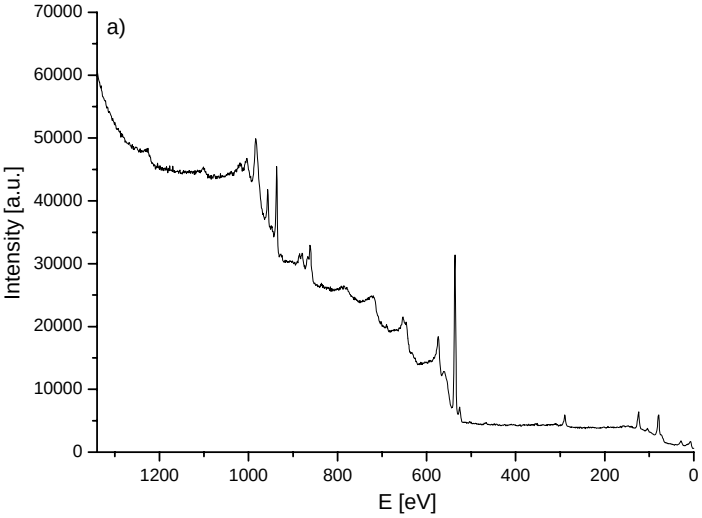
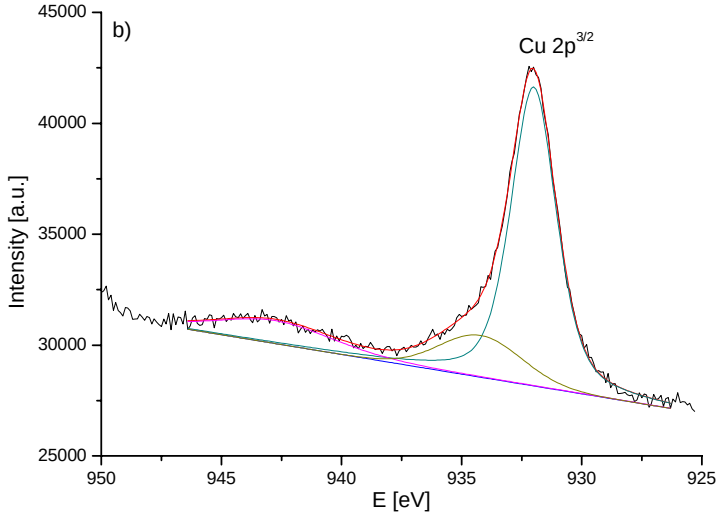
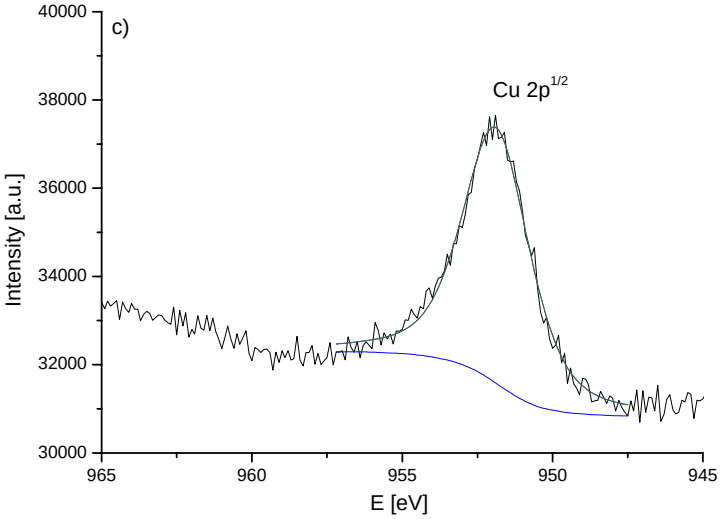



Fig. V.18 XPS survey spectrum (a) and narrow scan (b-c) on Cu50 catalyst.


a)
Intensity [a.u.]
E [eV]
70000
60000
50000
40000
30000
20000
10000
0
1200
1000
800
600
400
200
0


b)
Cu 2p3/2
Intensity [a.u.]
E [eV]
45000
40000
35000
30000
25000
950
945
940
935
930
925


c)
Cu 2p1/2
Intensity [a.u.]
E [eV]
40000
38000
36000
34000
32000
30000
965
960
955
950
945

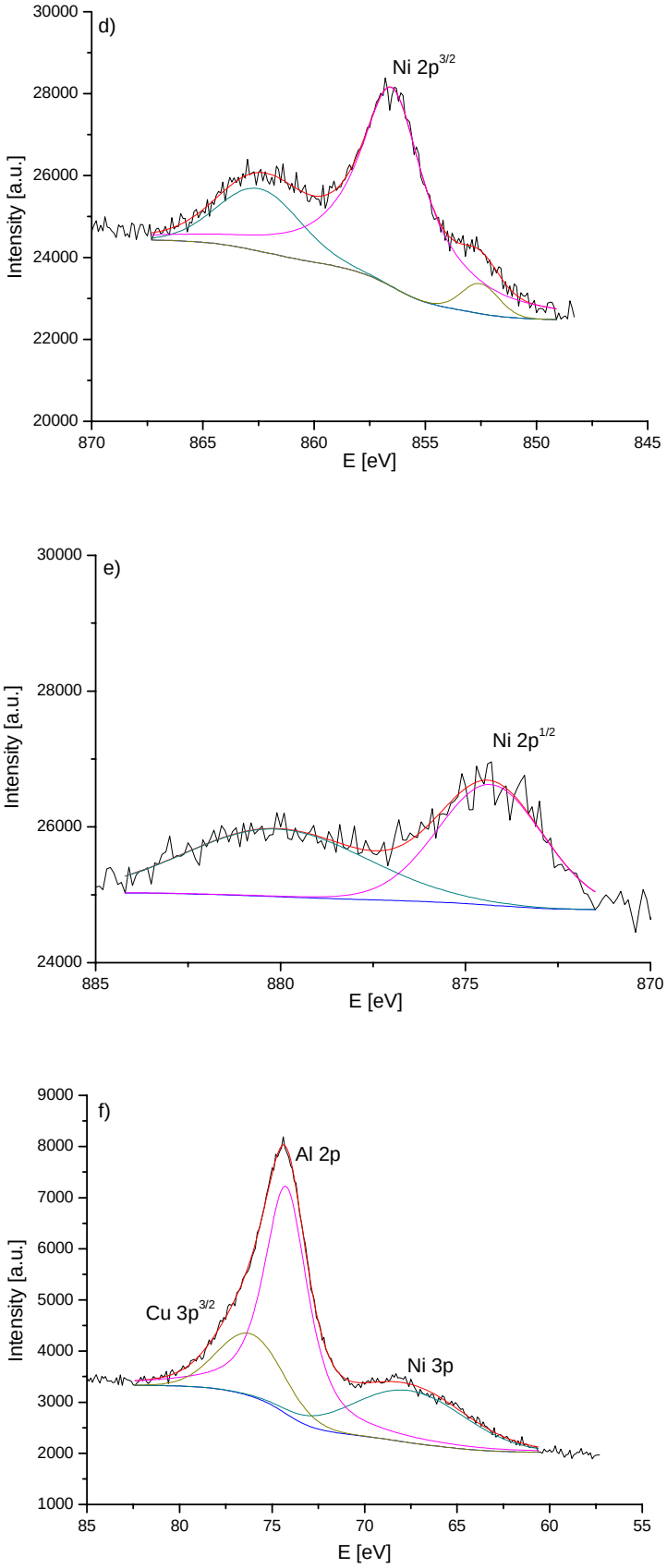
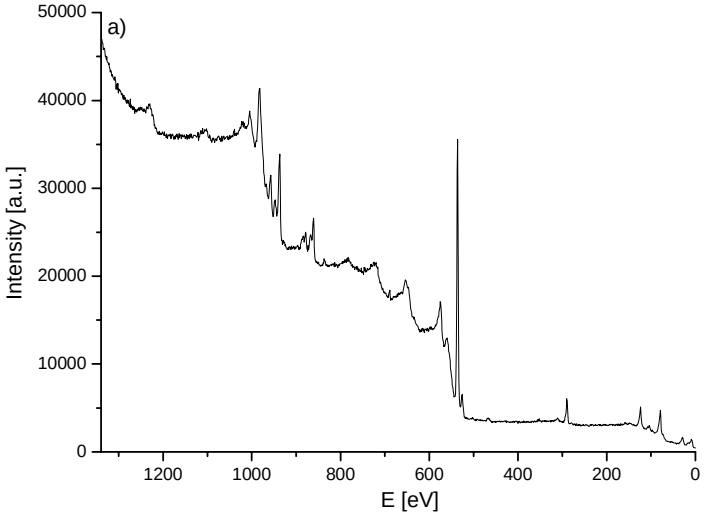
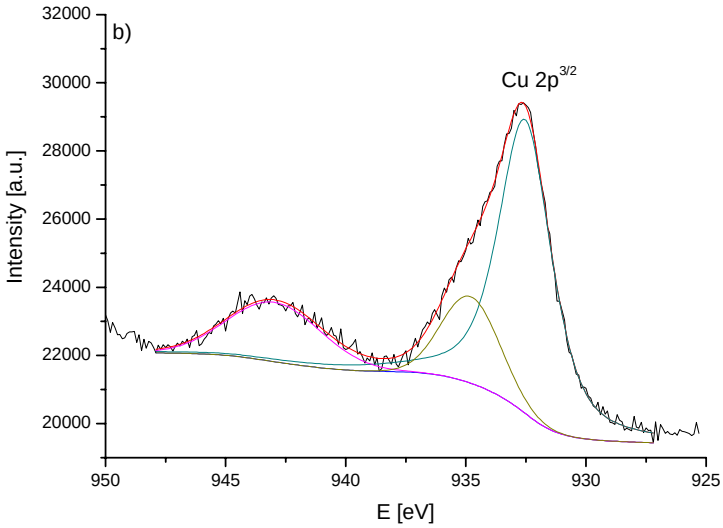
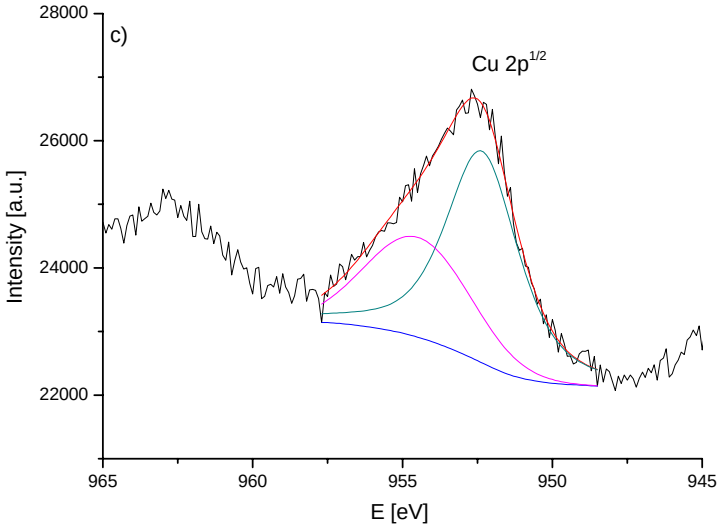



Fig. V.19 XPS survey spectrum (a) and narrow scan (b-c) on Ni30Cu50 (ITT).


a)
Intensity [a.u.]
E [eV]
50000
40000
30000
20000
10000
0
1200
1000
800
600
400
200
0


b)
Cu 2p3/2
Intensity [a.u.]
E [eV]
32000
30000
28000
26000
24000
22000
20000
950
945
940
935
930
925


c)
Cu 2p1/2
Intensity [a.u.]
E [eV]
28000
26000
24000
22000
965
960
955
950
945

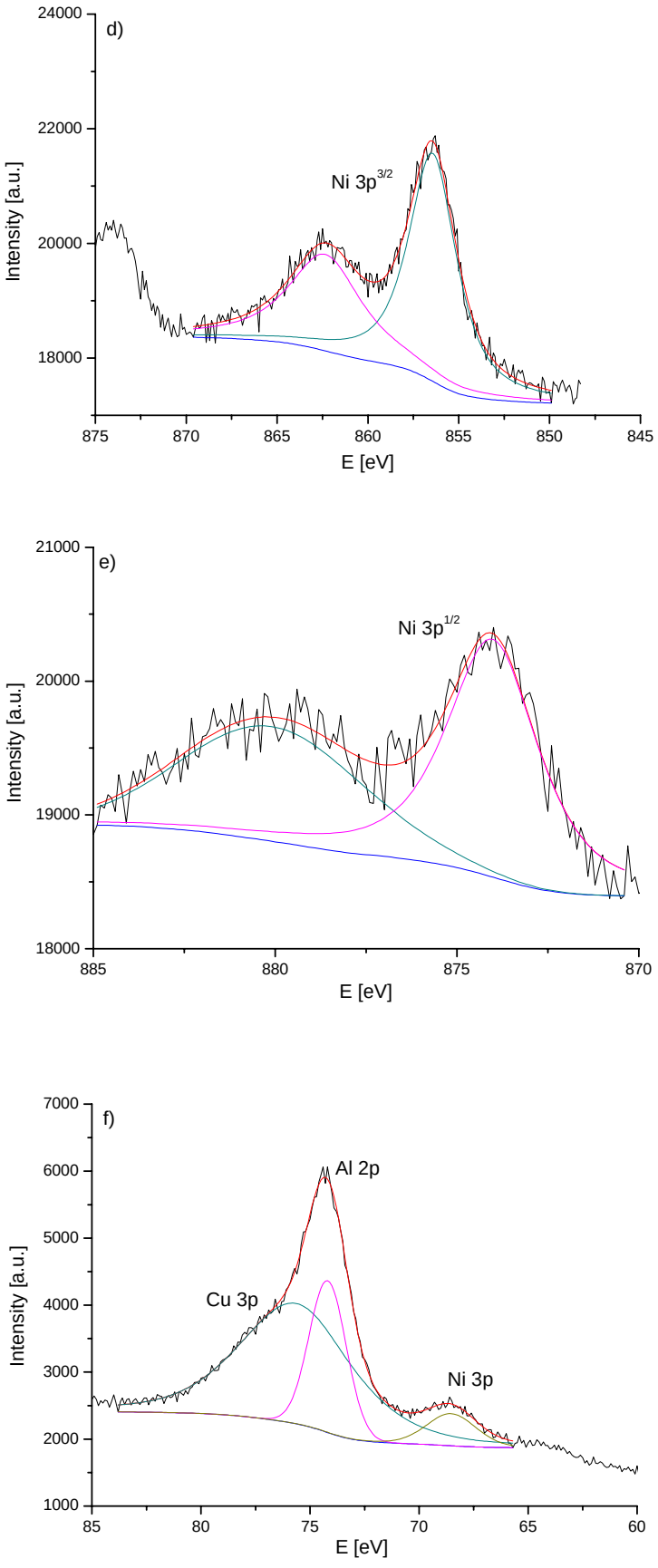
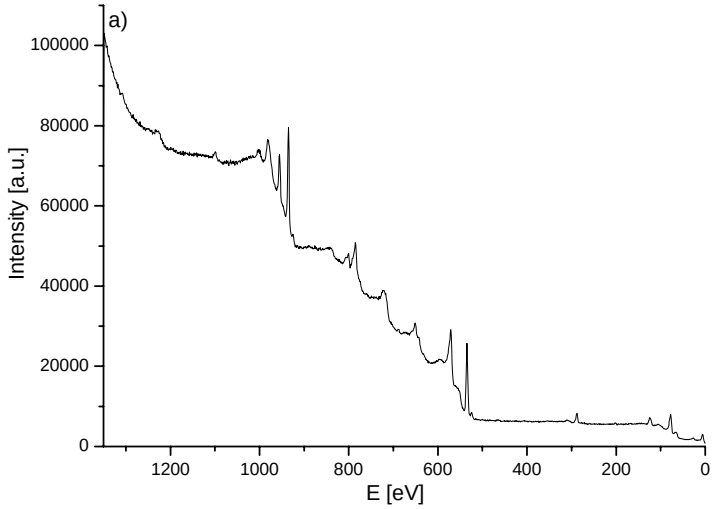
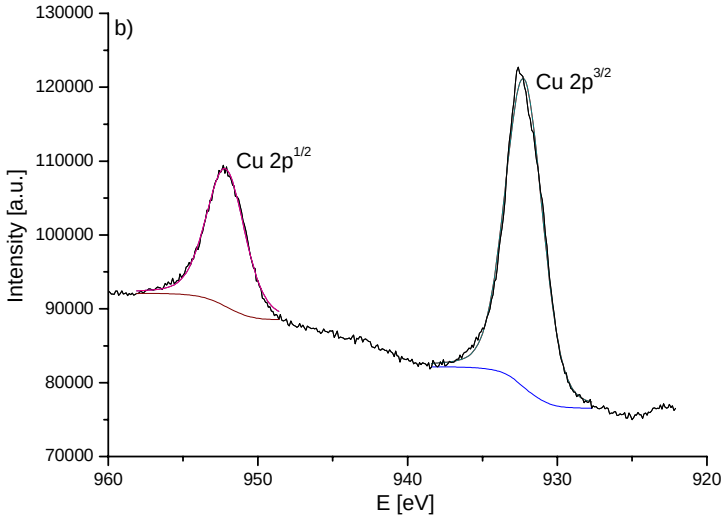
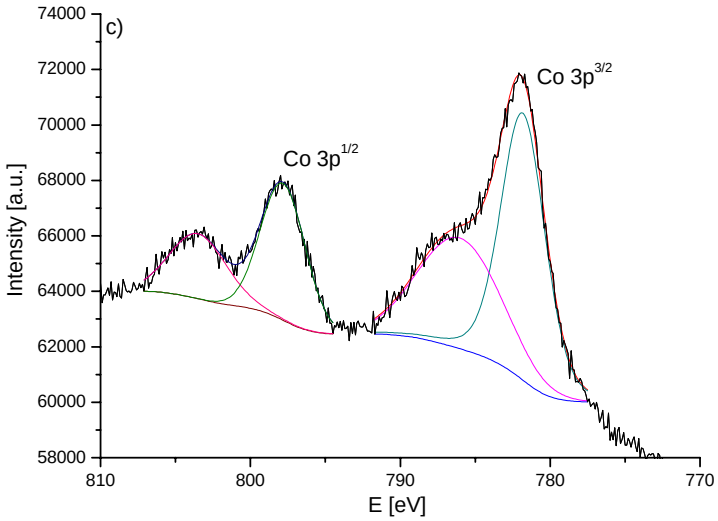



Fig. V.20 XPS survey spectrum (a) and narrow scan (b-c) on Ni50Cu50 (ITT).


a)
Intensity [a.u.]
E [eV]


b)
Cu 2p3/2
Cu 2p1/2
Intensity [a.u.]
E [eV]


c)
Co 3p3/2
Co 3p1/2
Intensity [a.u.]
E [eV]

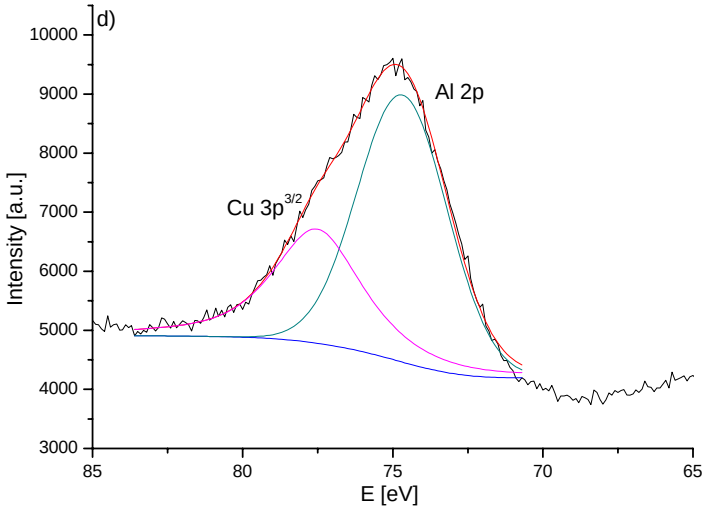
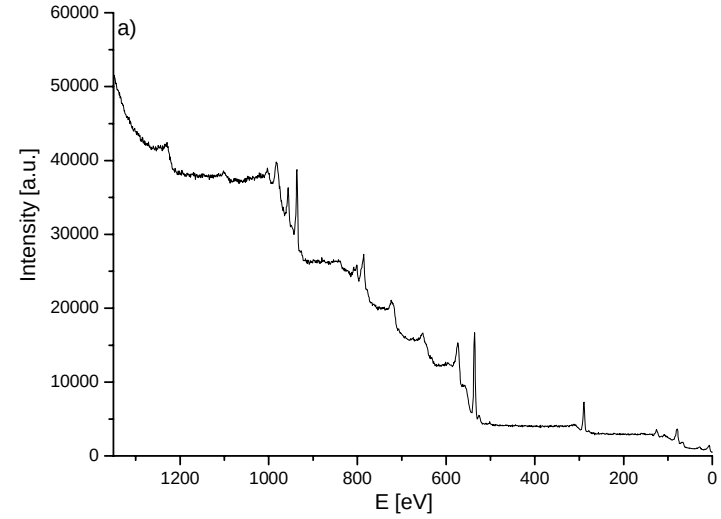
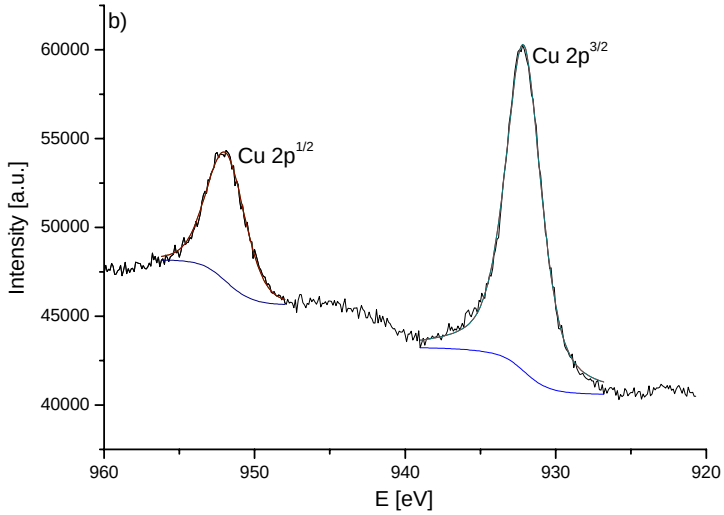
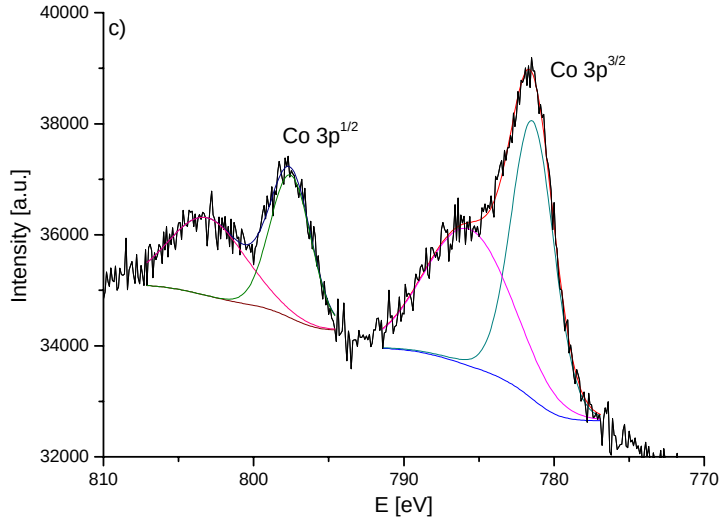



Fig. V.21 XPS survey spectrum (a) and narrow scan (b-d) on Co30Cu50 (ITT).


a)
Intensity [a.u.]
E [eV]
60000
50000
40000
30000
20000
10000
0
1200
1000
800
600
400
200
0


b)
Cu 2p3/2
Cu 2p1/2
Intensity [a.u.]
E [eV]
60000
55000
50000
45000
40000
960
950
940
930
920


c)
Co 3p3/2
Co 3p1/2
Intensity [a.u.]
E [eV]
40000
38000
36000
34000
32000
810
800
790
780
770

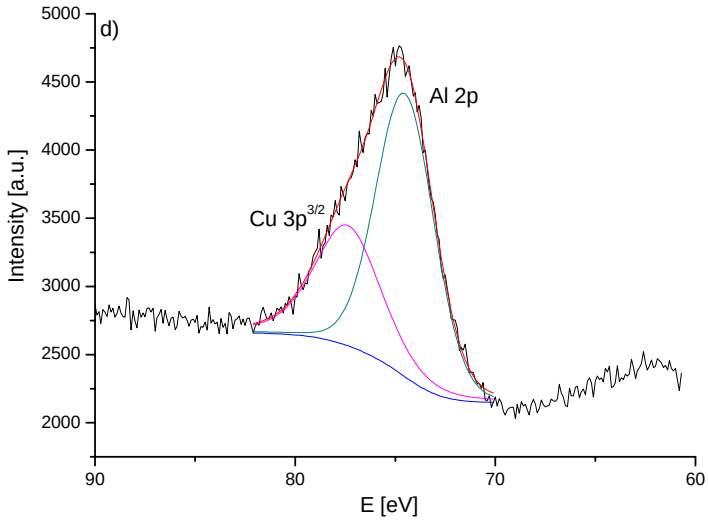
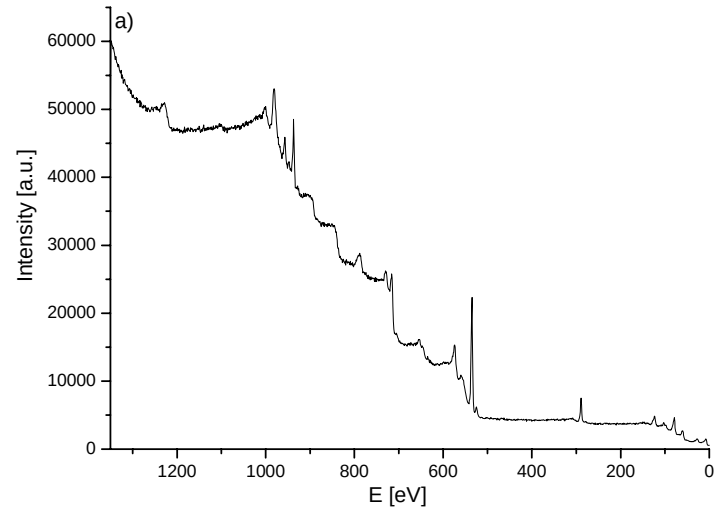
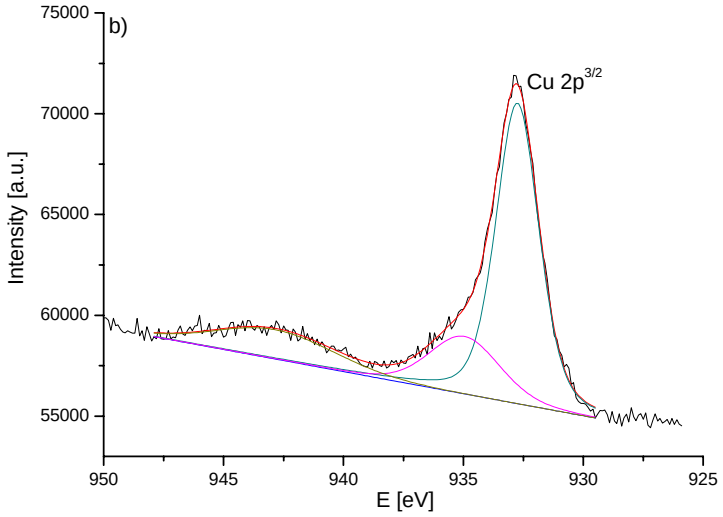
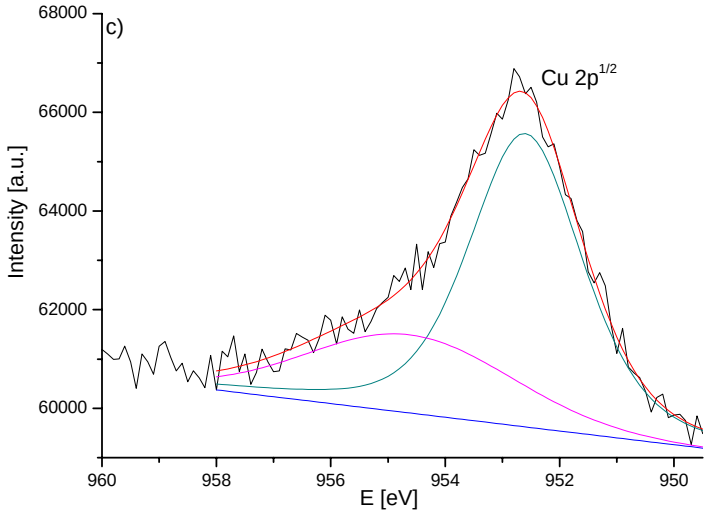



Fig. V.22 XPS survey spectrum (a) and narrow scan (b-d) on Co50Cu50 (ITT).


a)
Intensity [a.u.]
E [eV]


b)
Cu 2p3/2
Intensity [a.u.]
E [eV]


c)
Cu 2p1/2
Intensity [a.u.]
E [eV]

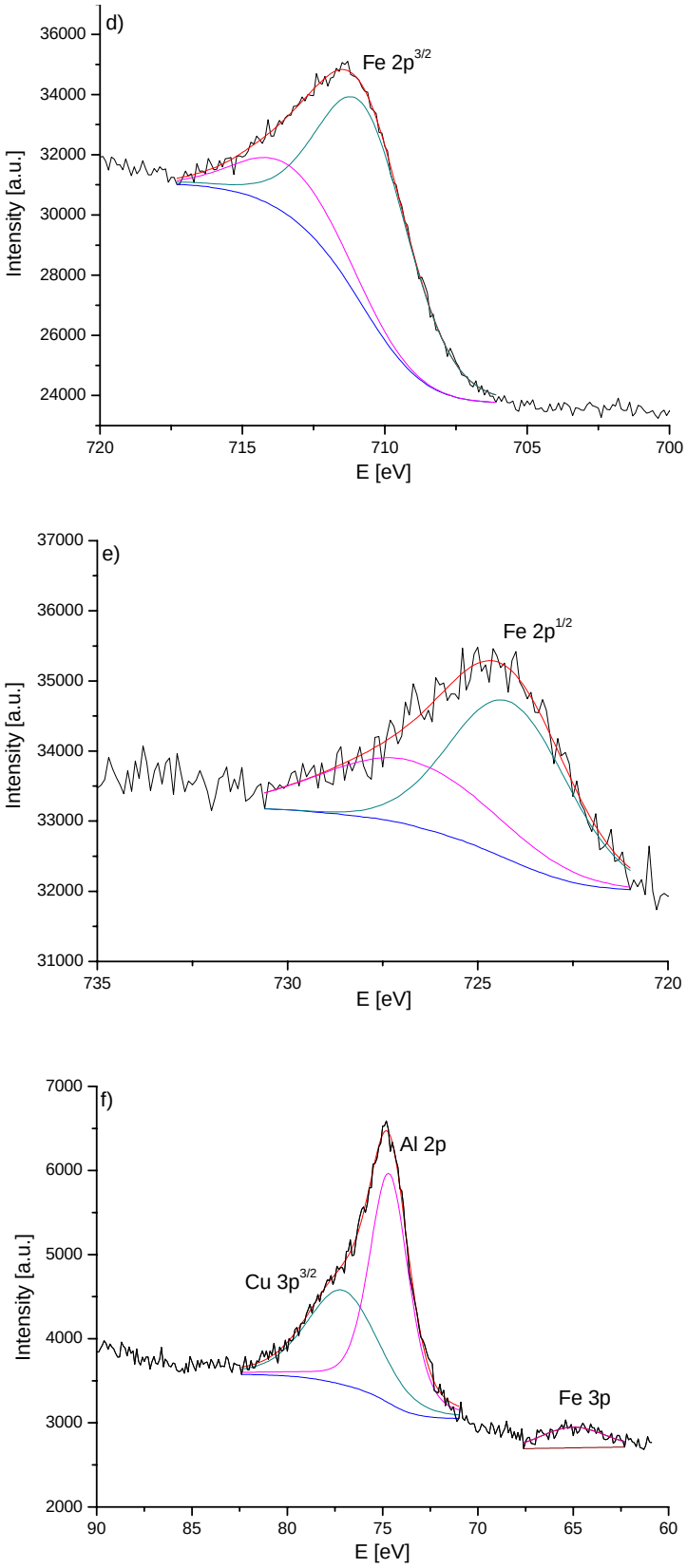
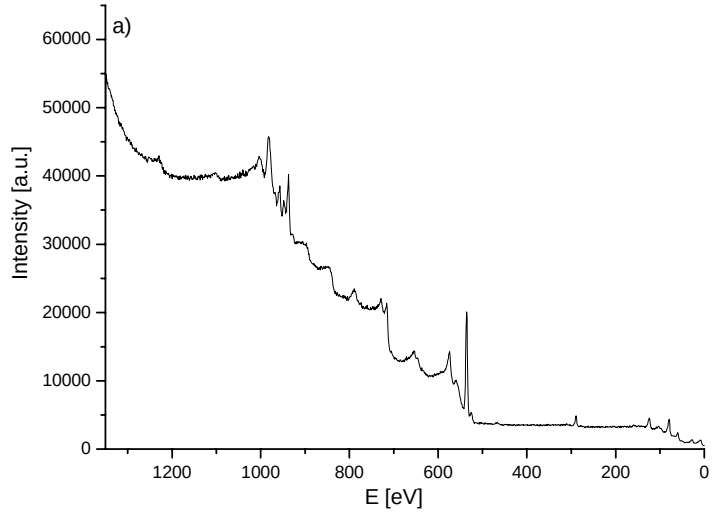
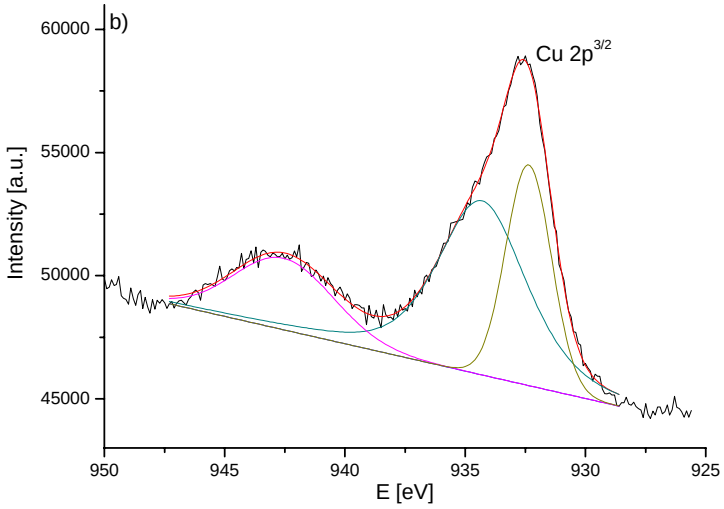
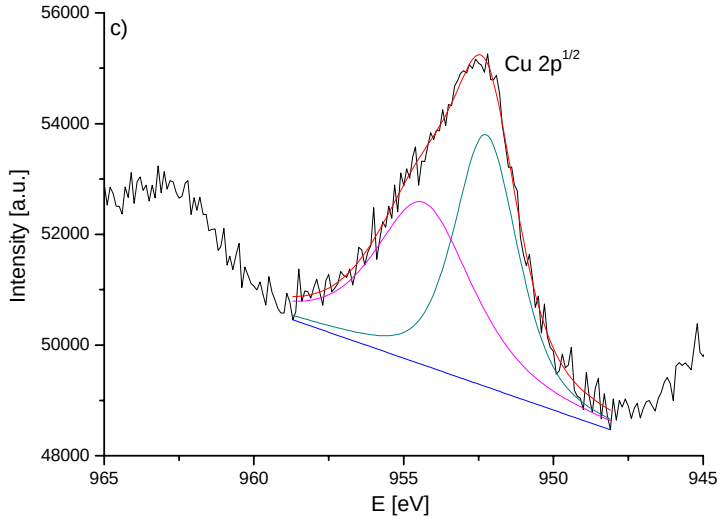



Fig. V.23 XPS survey spectrum (a) and narrow scan (b-f) on Fe50Cu50 (ITT).


a)
Intensity [a.u.]
60000
50000
40000
30000
20000
10000
0
1200
1000
800
600
400
200
0
E [eV]


b)
Cu 2p3/2
Intensity [a.u.]
60000
55000
50000
45000
950
945
940
935
930
925
E [eV]


c)
Cu 2p1/2
Intensity [a.u.]
56000
54000
52000
50000
48000
965
960
955
950
945
E [eV]

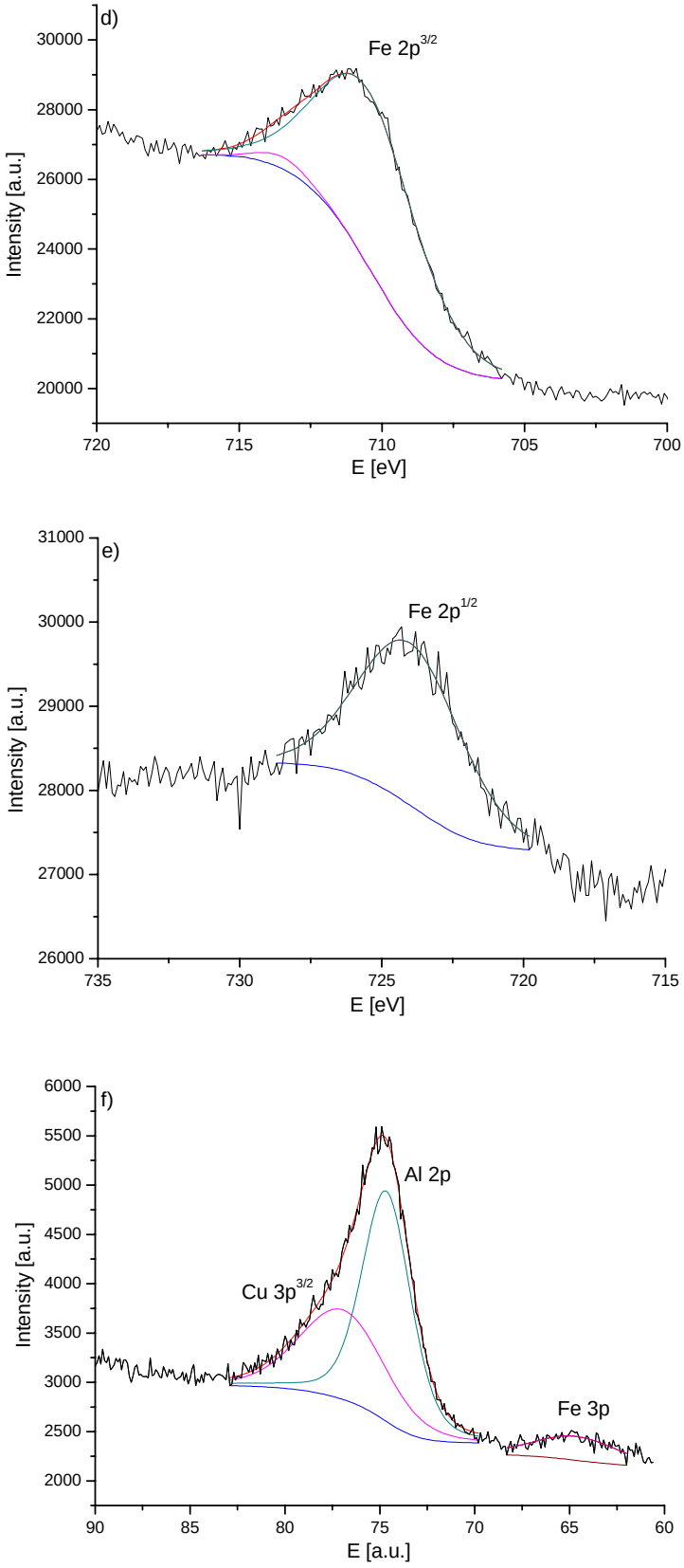



Fig. V.24 XPS survey spectrum (a) and narrow scan (b-f) on Fe35Cu50 (ITT).

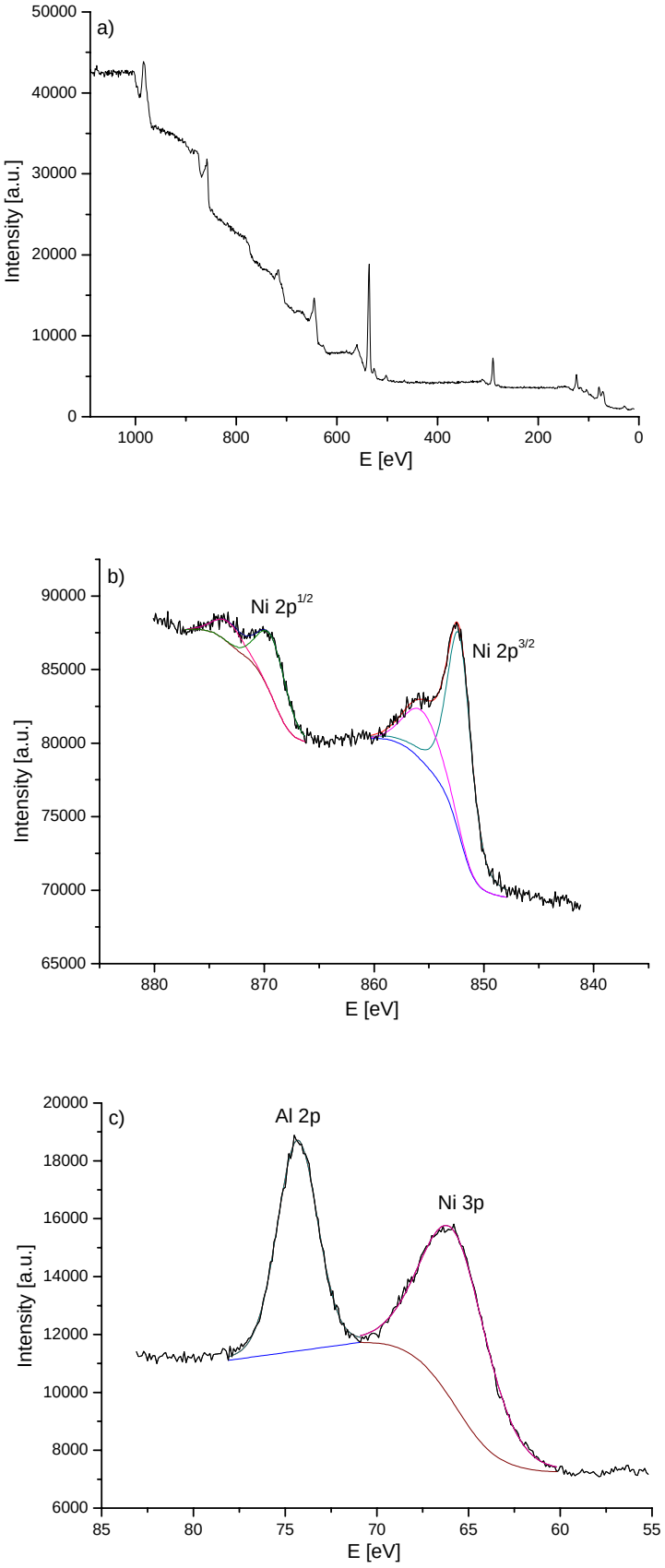



Fig. V.25 XPS survey spectrum (a) and narrow scan (b-c) on Ni30 (HPT).

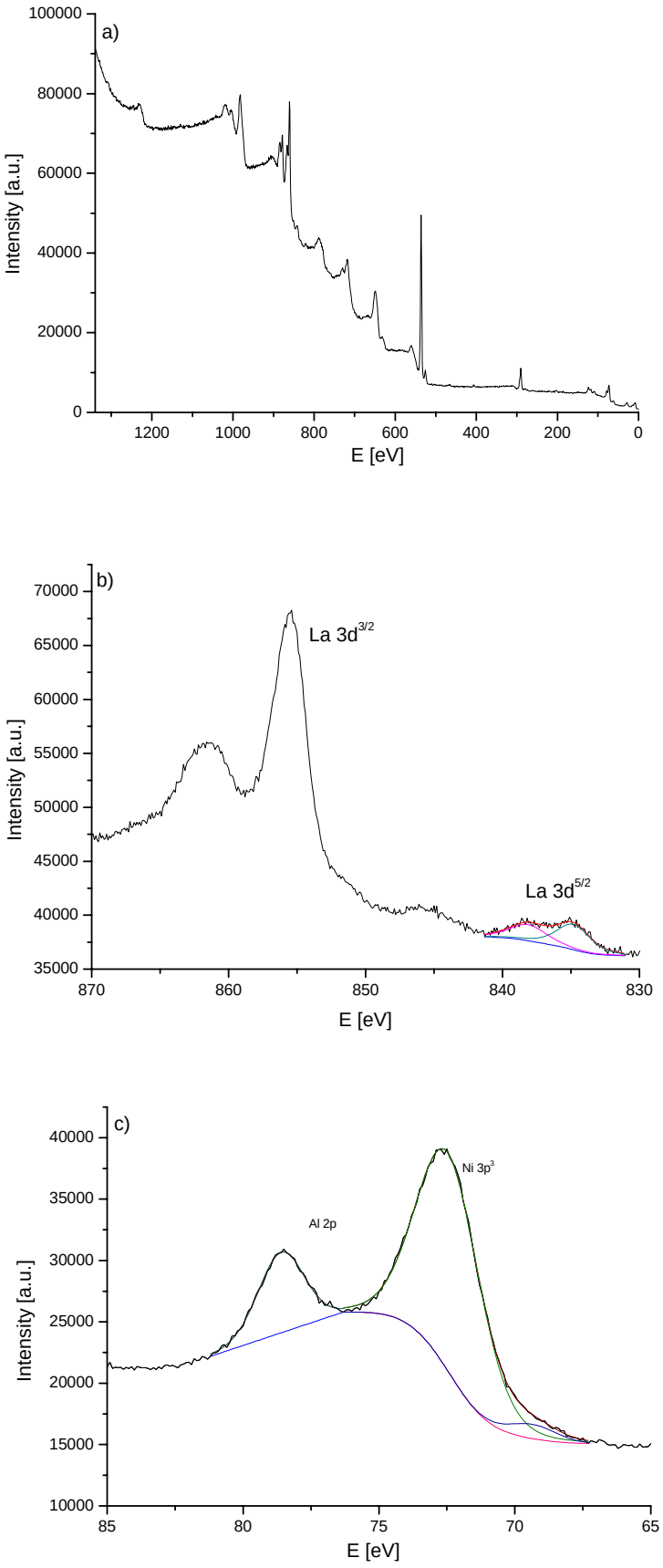



Fig. V.26 XPS survey spectrum (a) and narrow scan (b-c) on Ni30-$La_2O_3$.

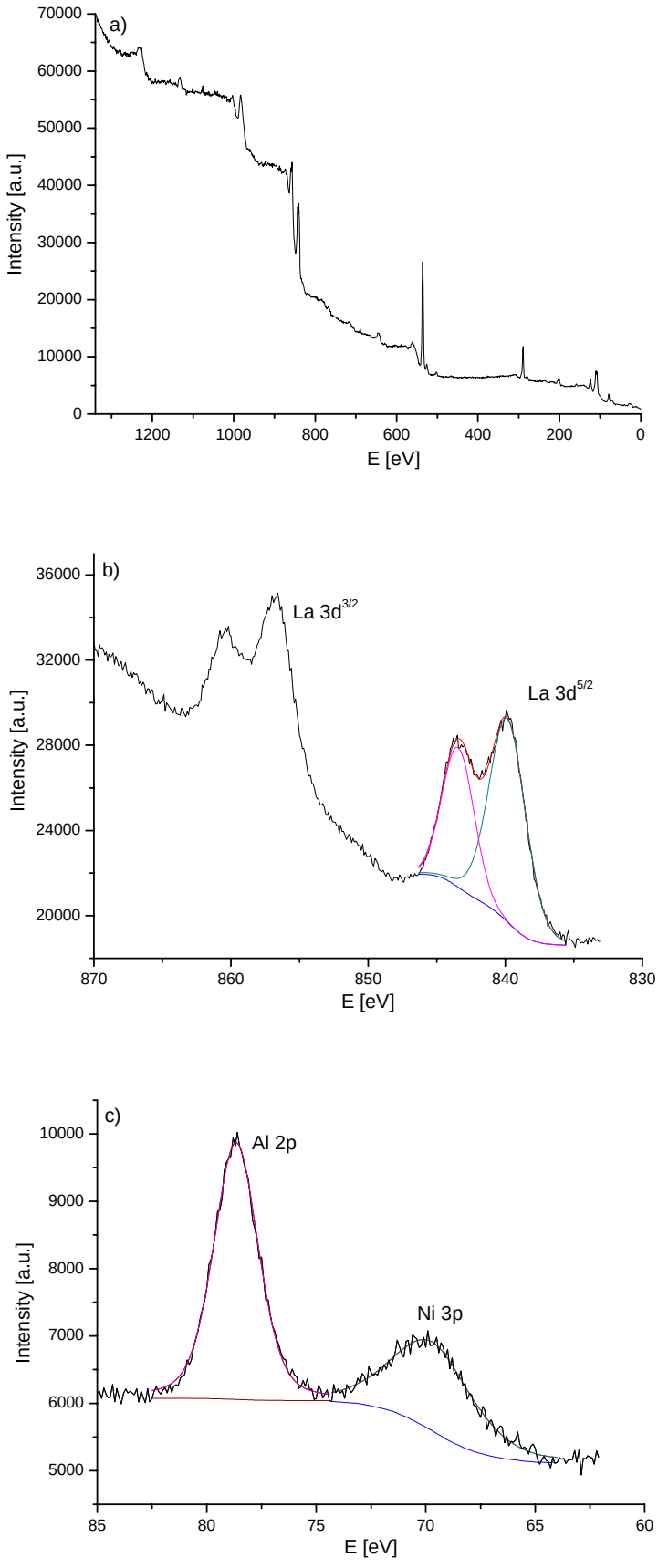



Fig. V.27 XPS survey spectrum (a) and narrow scan (b-c) on Ni30-$La_2O_3$ (HPT).

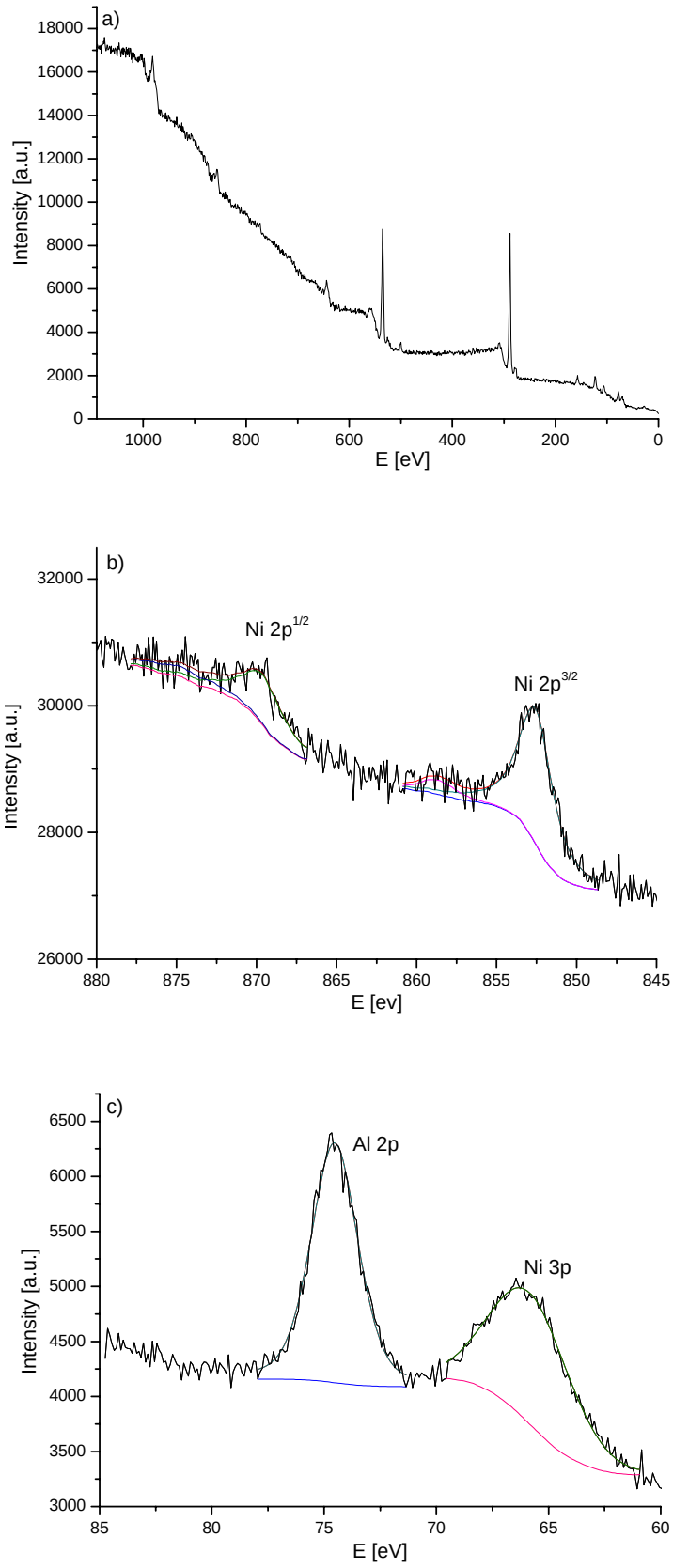



Fig. V.28 XPS survey spectrum (a) and narrow scan (b-c) on Ni50 (HPT).

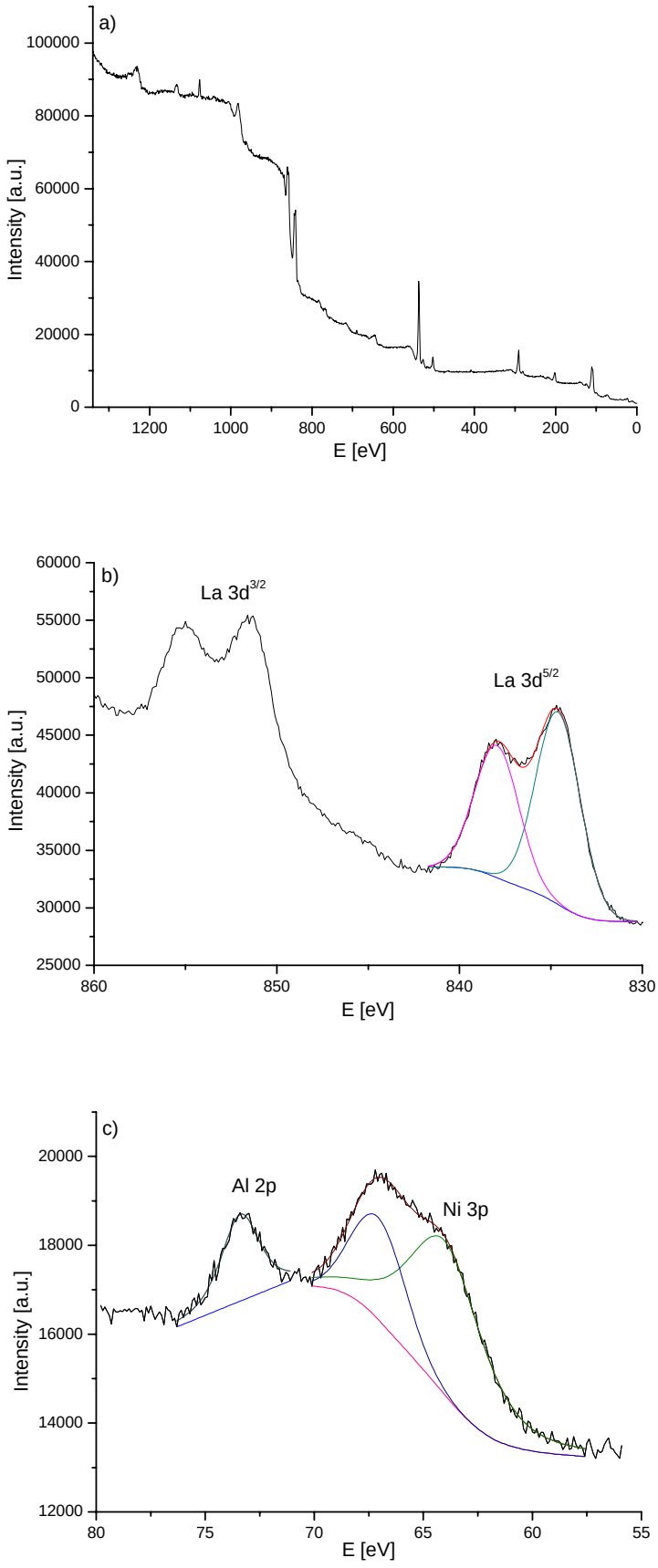



Fig. V.29 XPS survey spectrum (a) and narrow scan (b-c) on Ni50-$La_2O_3$.

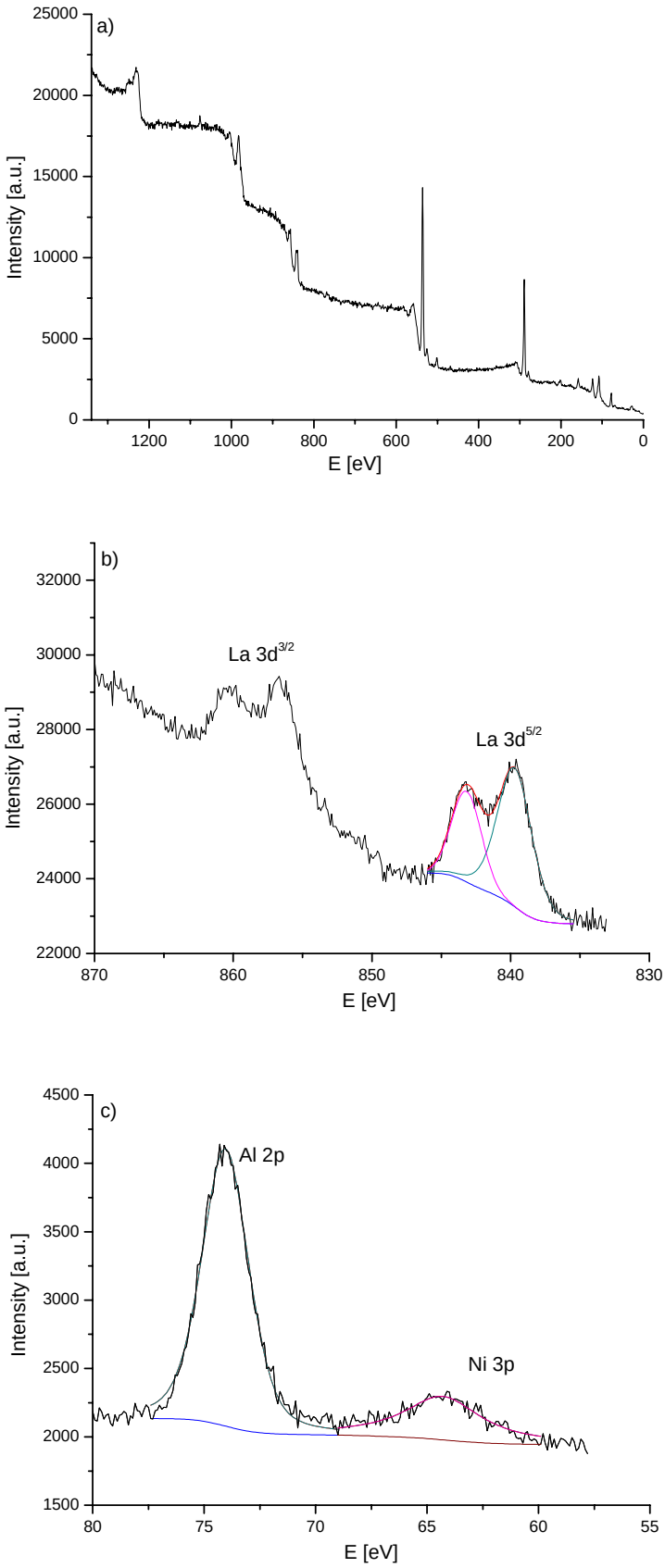



Fig. V.30 XPS survey spectrum (a) and narrow scan (b-c) on Ni50-$La_2O_3$ (HPT).

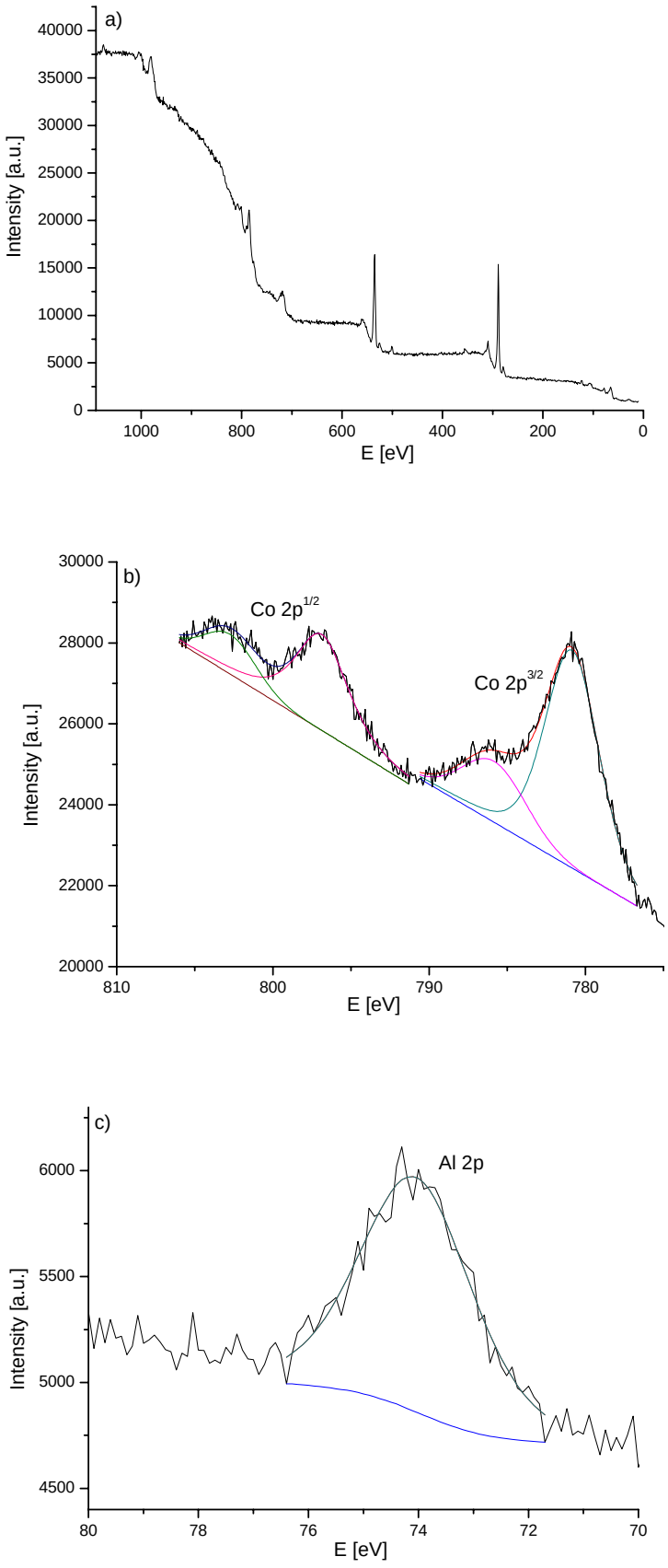



Fig. V.31 XPS survey spectrum (a) and narrow scan (b-c) on Co30 (HPT).

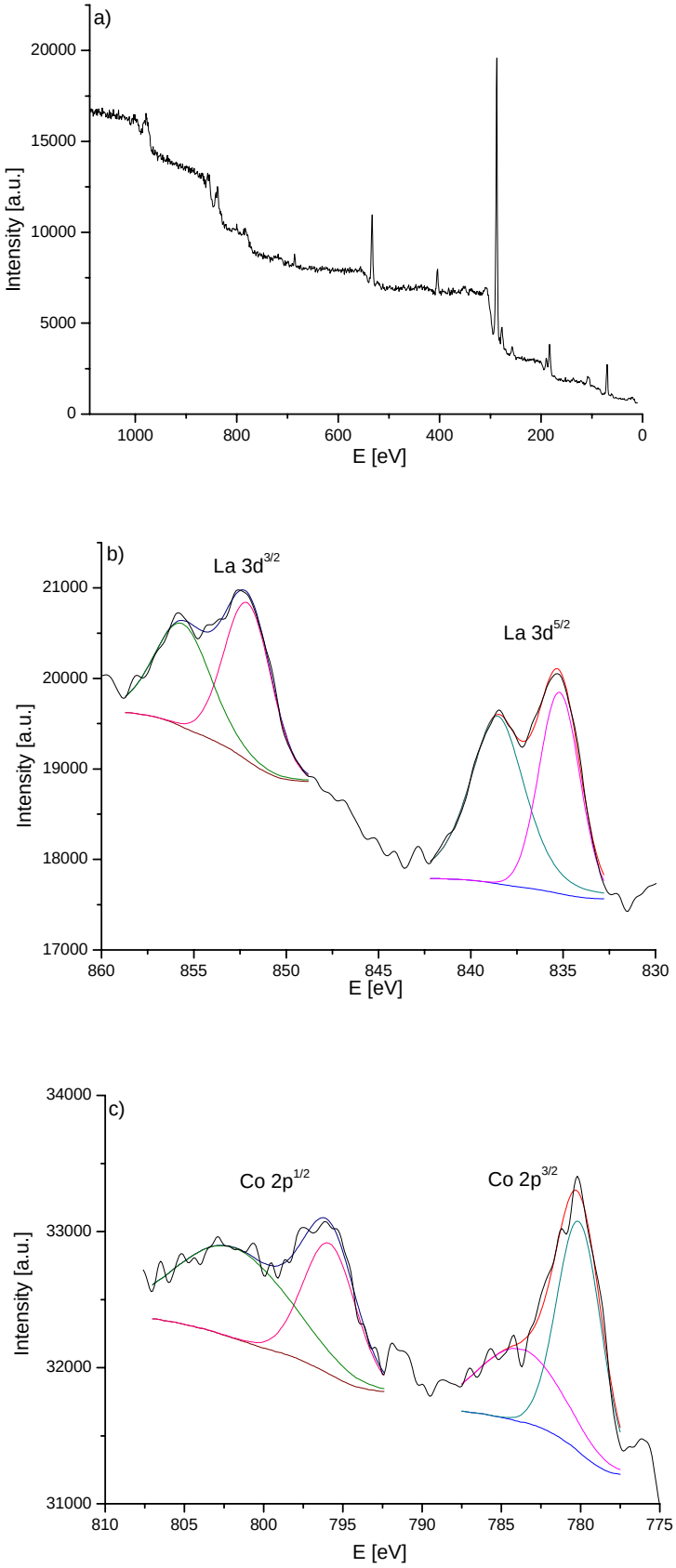
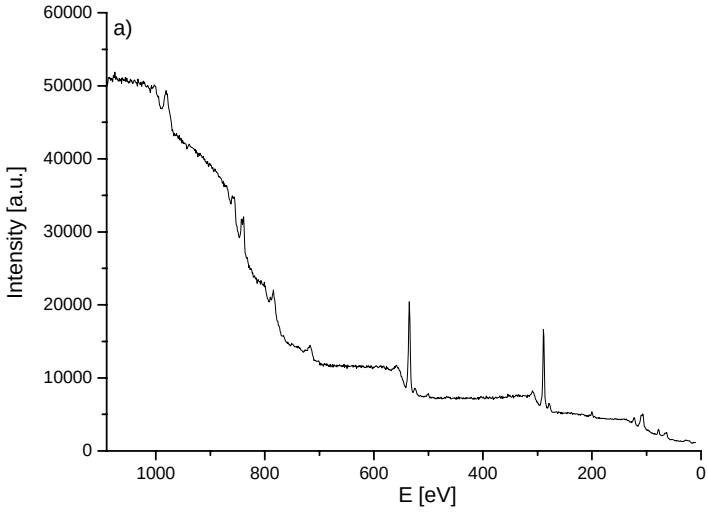
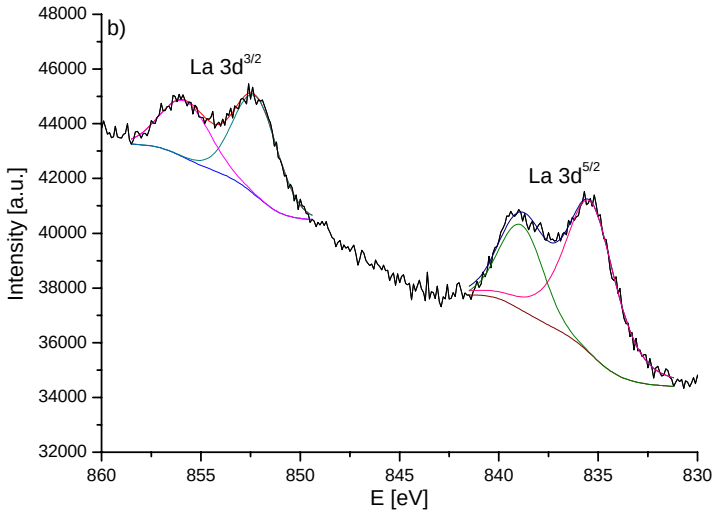
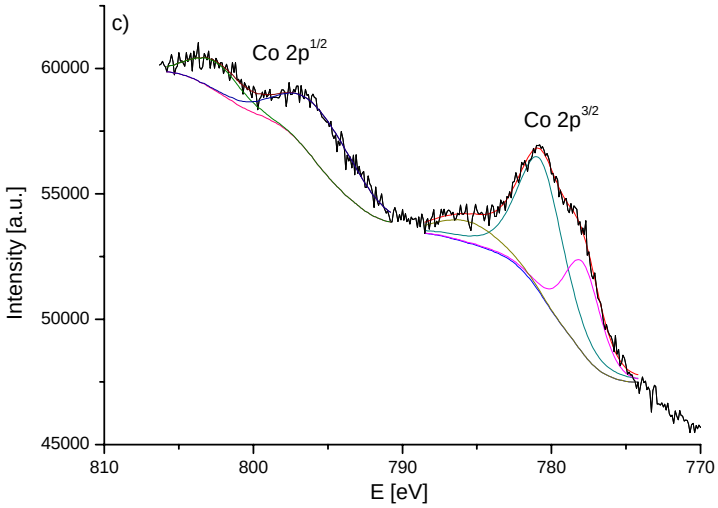



Fig. V.32 XPS survey spectrum (a) and narrow scan (b-d) on Co30-$La_2O_3$.


a)
Intensity [a.u.]
E [eV]
60000
50000
40000
30000
20000
10000
0
1000
800
600
400
200
0


b)
La 3d3/2
La 3d5/2
Intensity [a.u.]
E [eV]
48000
46000
44000
42000
40000
38000
36000
34000
32000
860
855
850
845
840
835
830


c)
Co 2p1/2
Co 2p3/2
Intensity [a.u.]
E [eV]
60000
55000
50000
45000
810
800
790
780
770

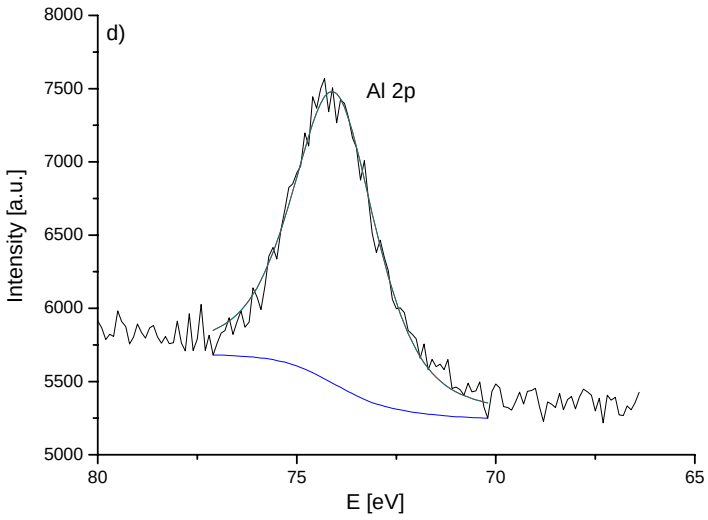



Fig. V.33 XPS survey spectrum (a) and narrow scan (b-d) on Co30-$La_2O_3$ (HPT).

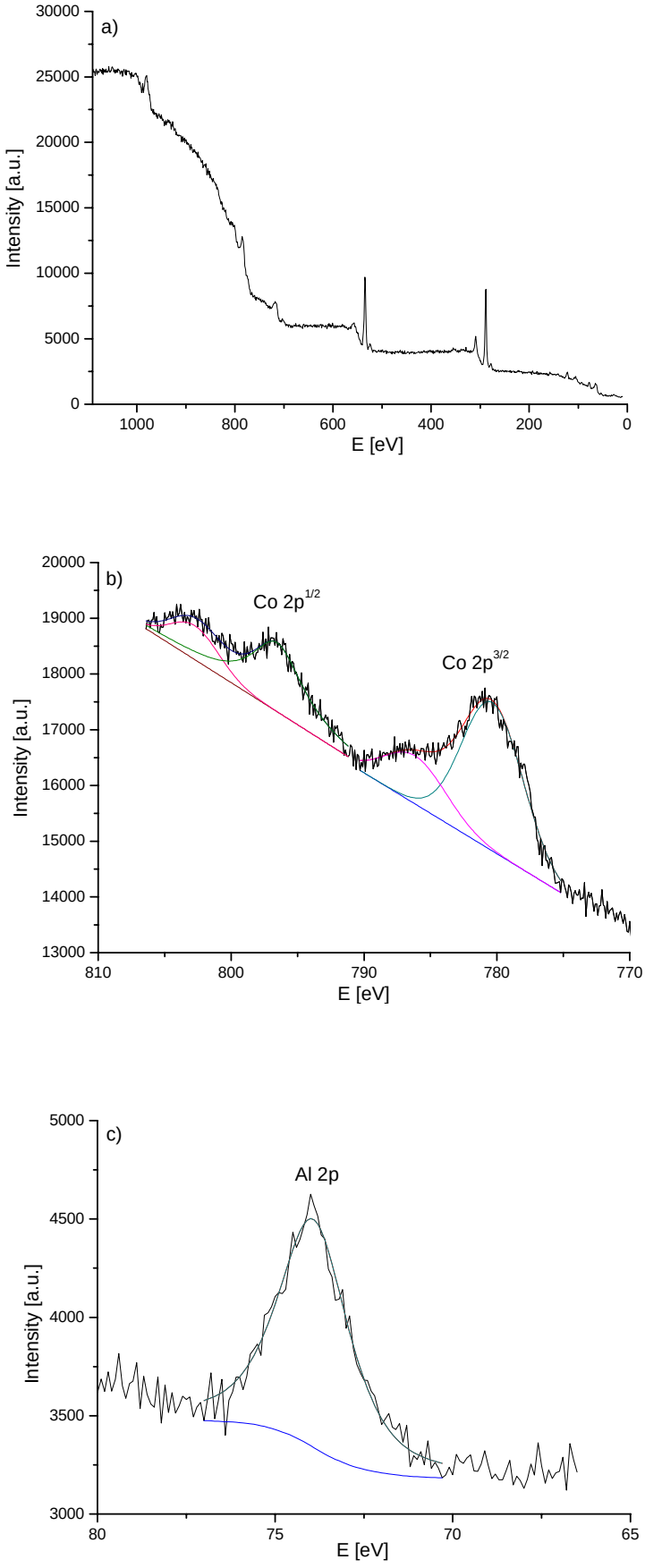



Fig. V.34 XPS survey spectrum (a) and narrow scan (b-c) on Co50 (HPT).

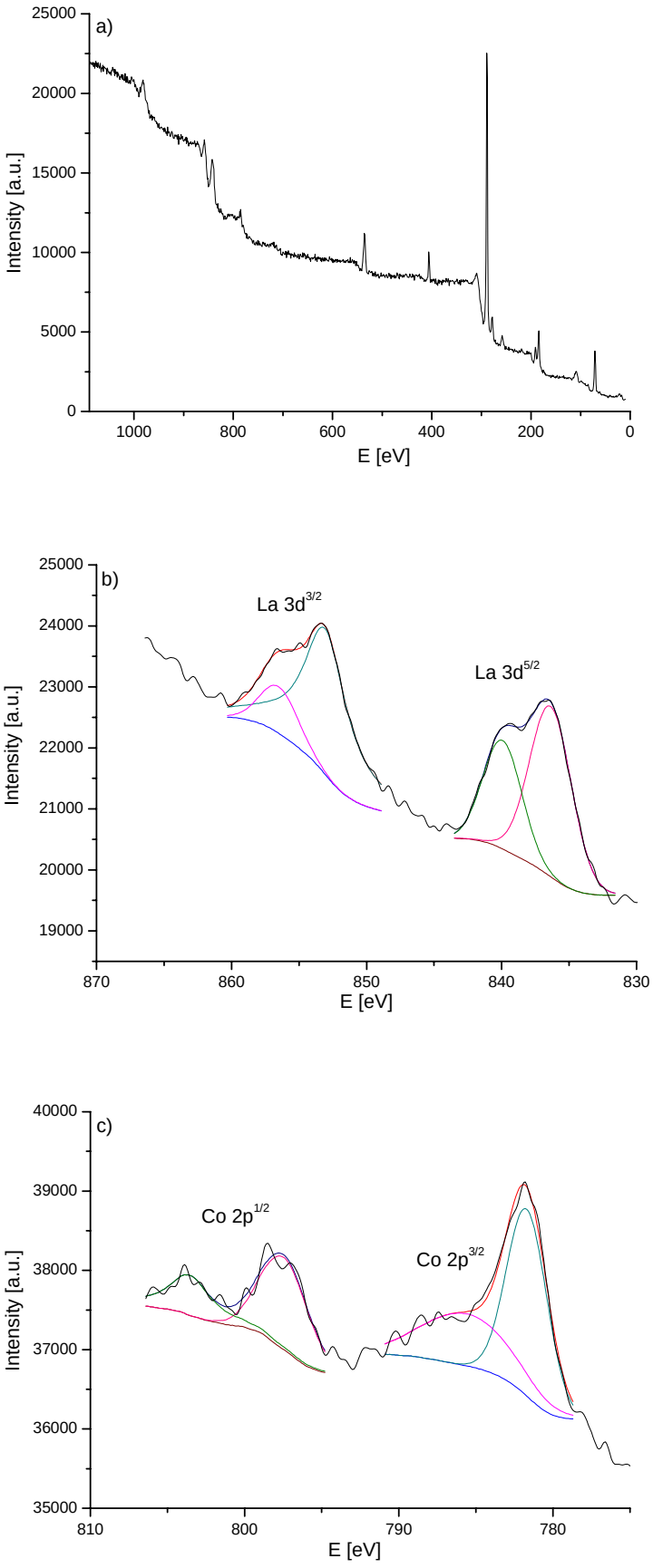
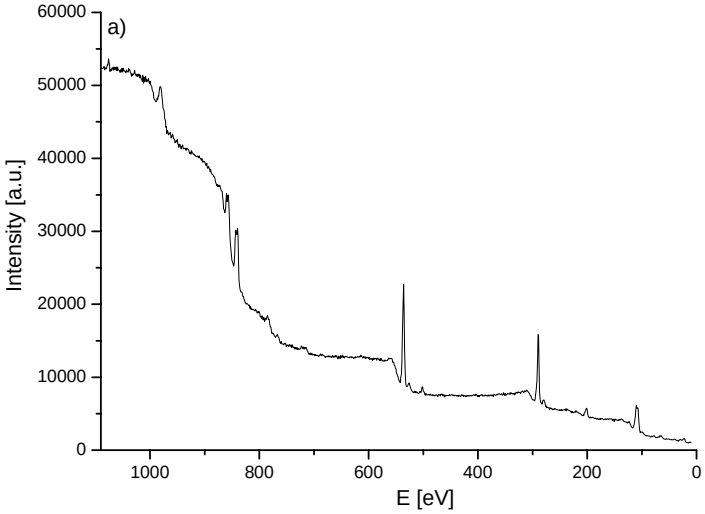
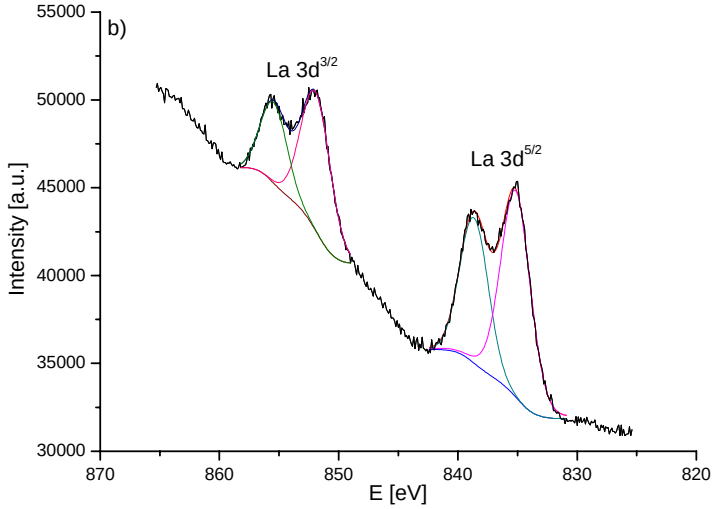
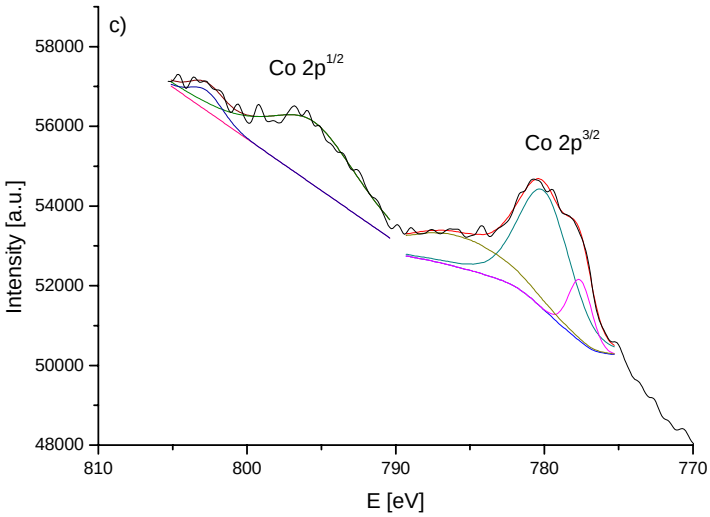



Fig. V.35 XPS survey spectrum (a) and narrow scan (b-d) on Co50-$La_2O_3$.


a)
Intensity [a.u.]
E [eV]
60000
50000
40000
30000
20000
10000
0
1000
800
600
400
200
0


b)
La 3d3/2
La 3d5/2
Intensity [a.u.]
E [eV]
55000
50000
45000
40000
35000
30000
870
860
850
840
830
820


c)
Co 2p1/2
Co 2p3/2
Intensity [a.u.]
E [eV]
58000
56000
54000
52000
50000
48000
810
800
790
780
770

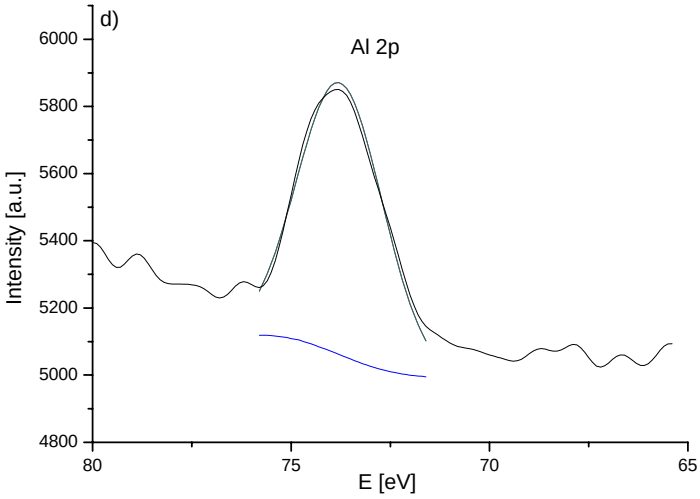



Fig. V.36 XPS survey spectrum (a) and narrow scan (b-d) on Co50-$La_2O_3$ (HPT).

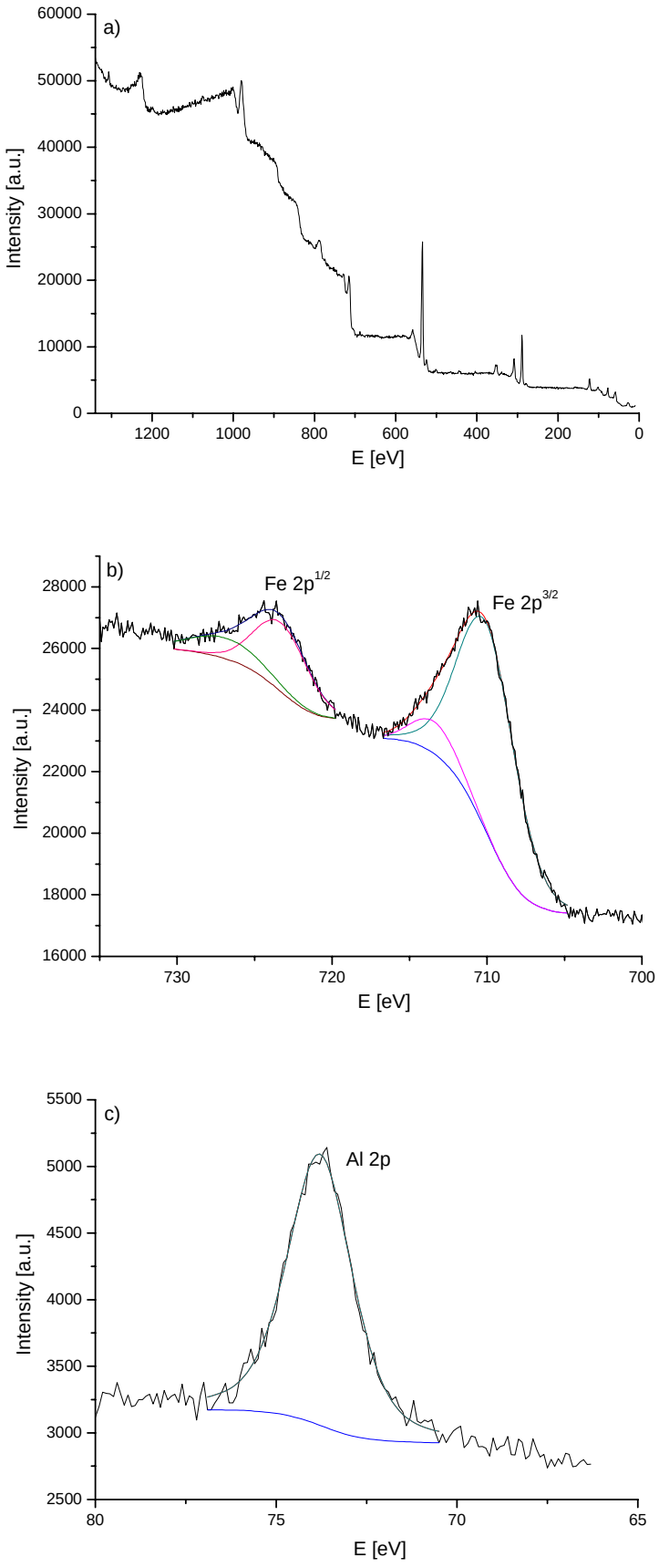



Fig. V.37 XPS survey spectrum (a) and narrow scan (b-c) on Fe50 (HPT).

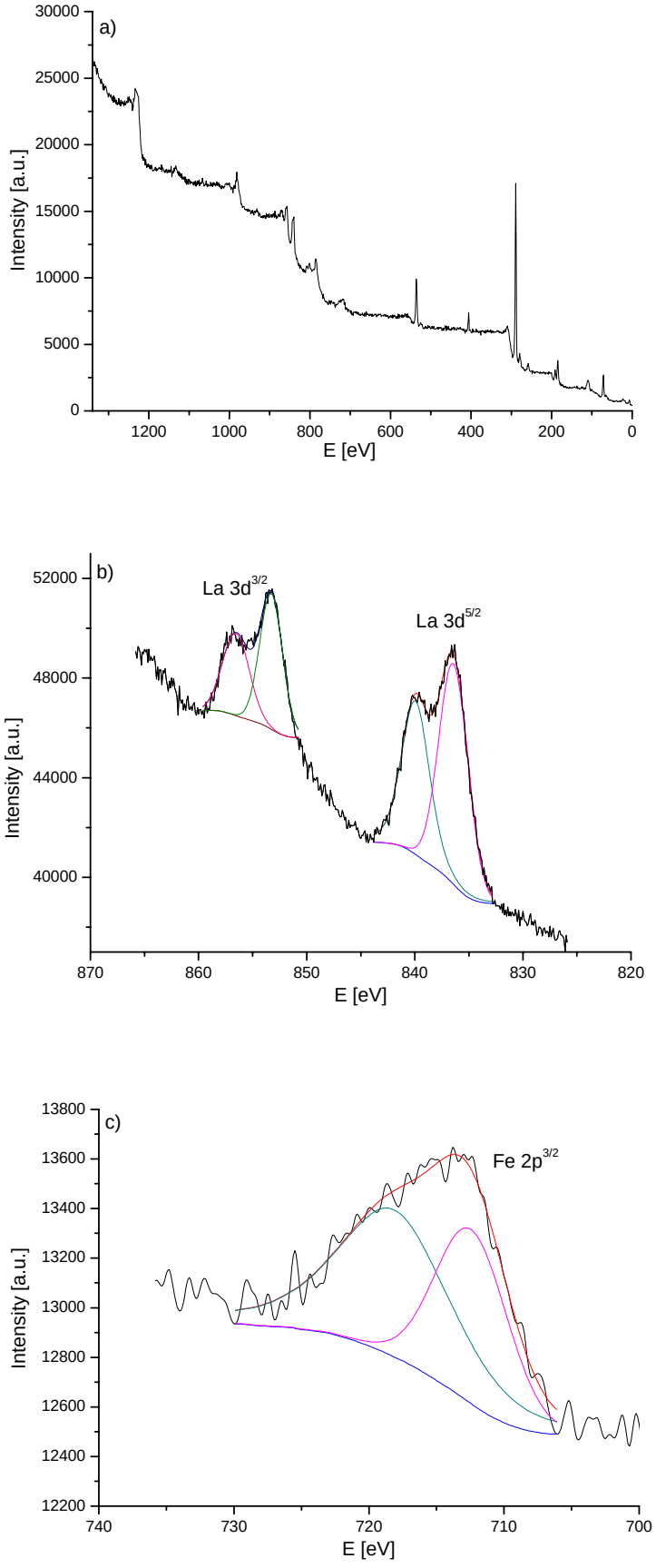
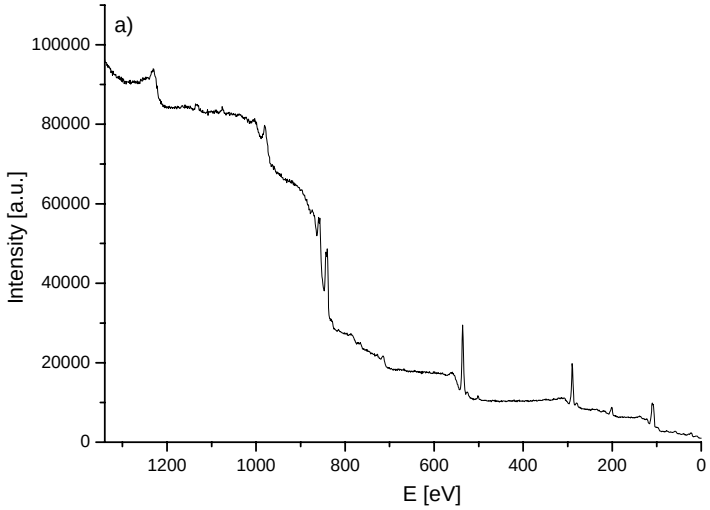
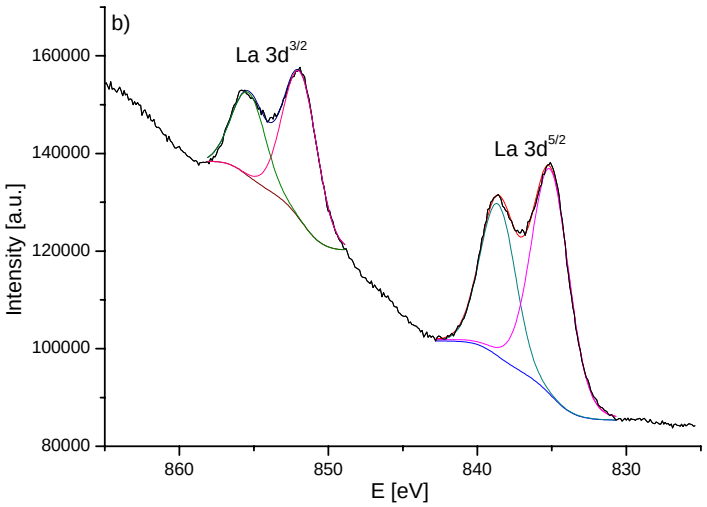
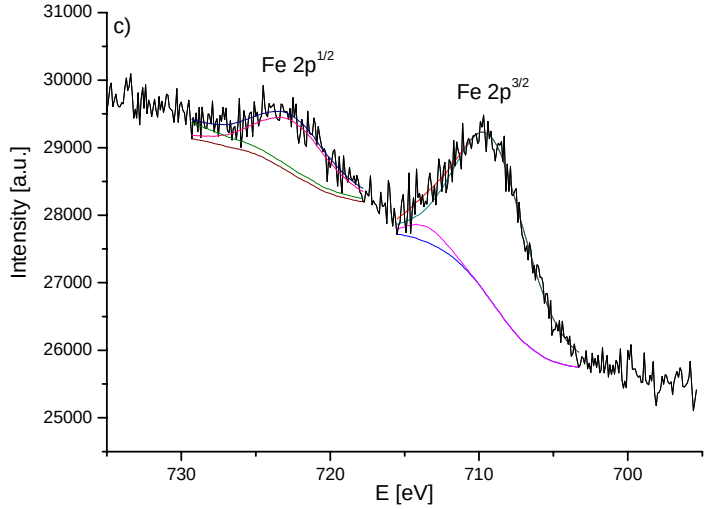



Fig. V.37 XPS survey spectrum (a) and narrow scan (b-c) on Fe50-$La_2O_3$.


a)
Intensity [a.u.]
E [eV]


b)
La 3d3/2
La 3d5/2
Intensity [a.u.]
E [eV]


c)
Fe 2p1/2
Fe 2p3/2
Intensity [a.u.]
E [eV]

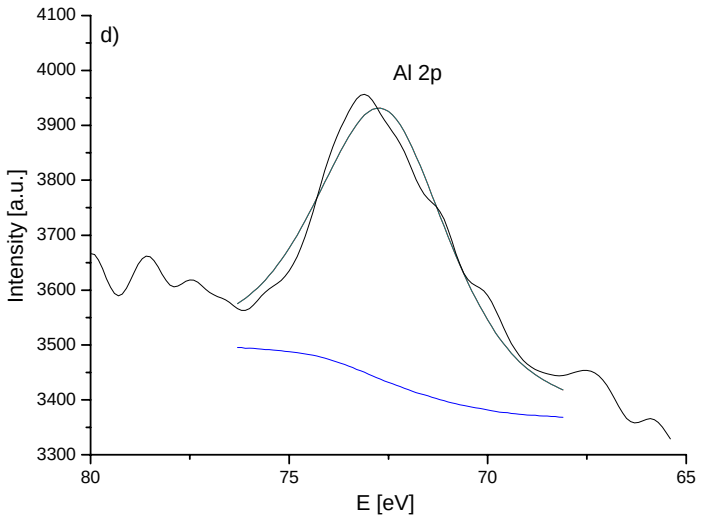



Fig. V.38 XPS survey spectrum (a) and narrow scan (b-d) on Fe50-$La_2O_3$ (HPT).

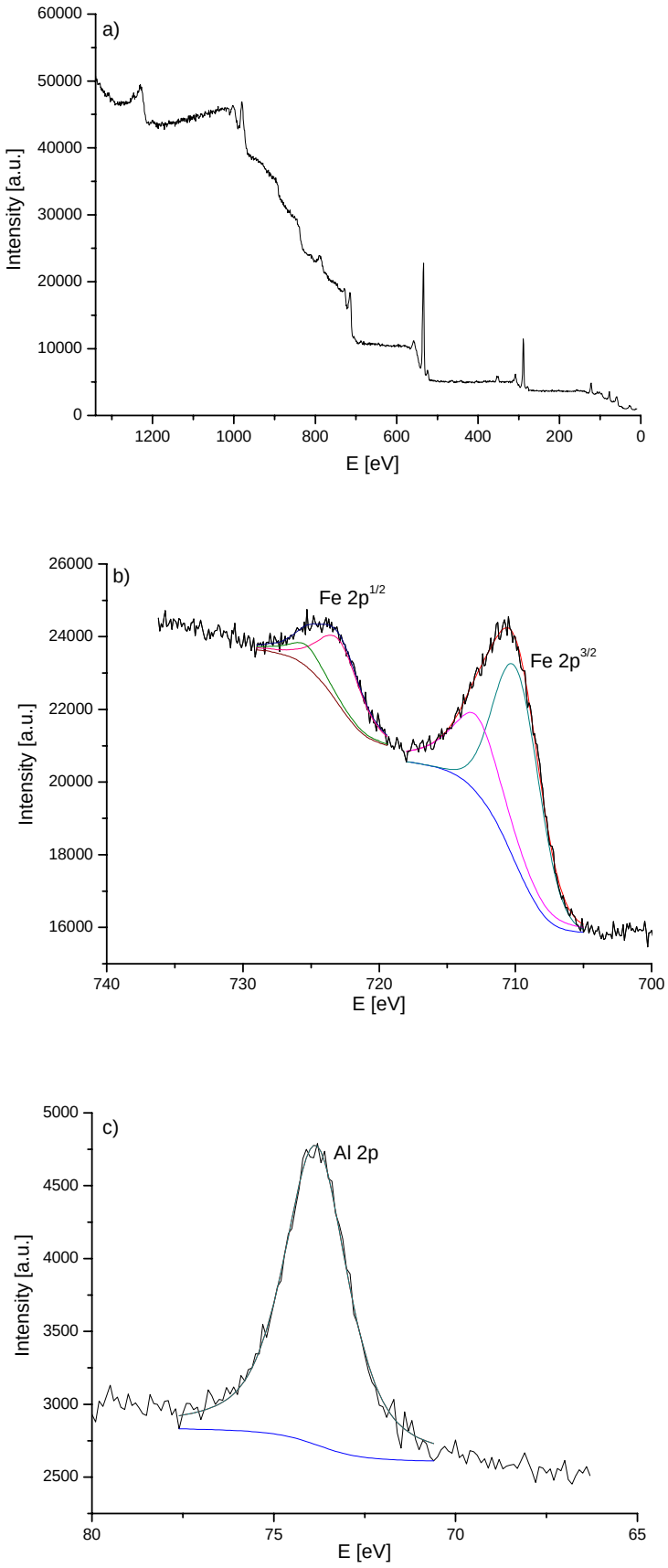



Fig. V.39 XPS survey spectrum (a) and narrow scan (b-c) on Fe35 (HPT).

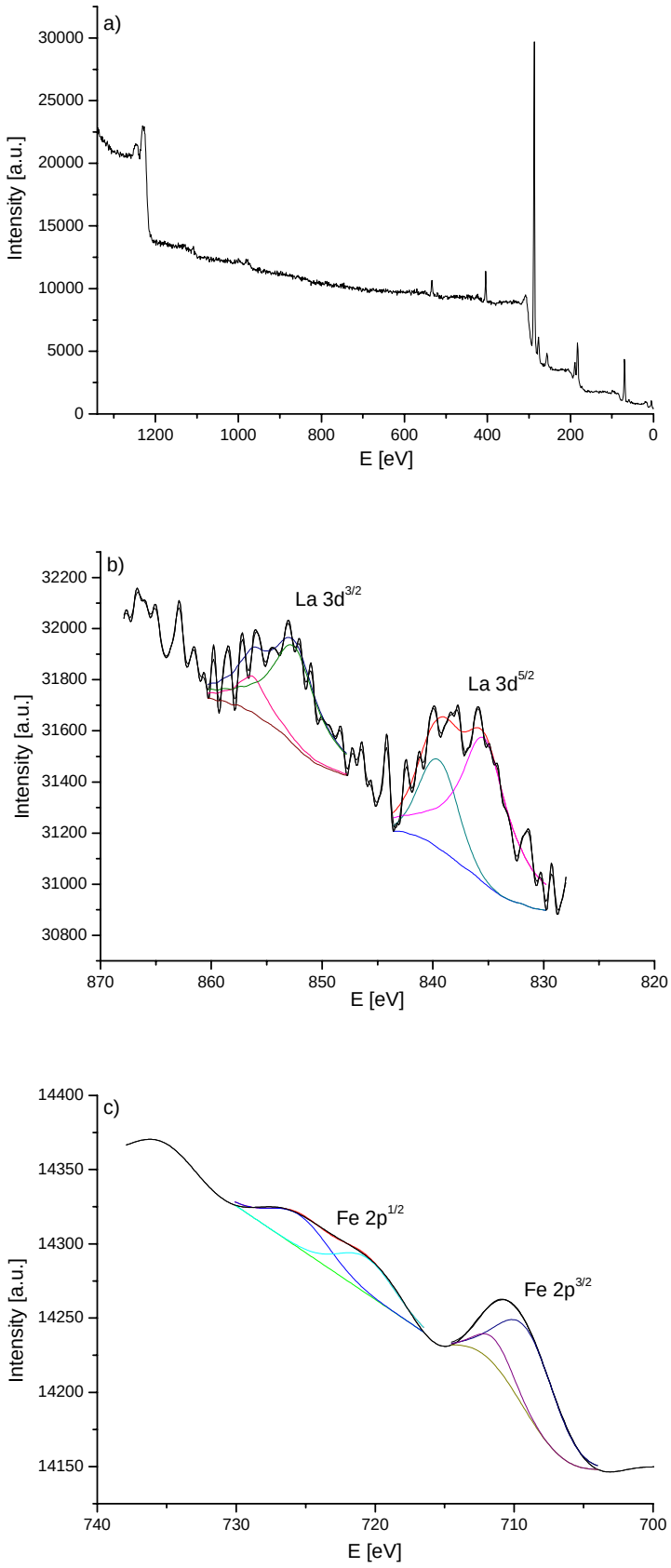
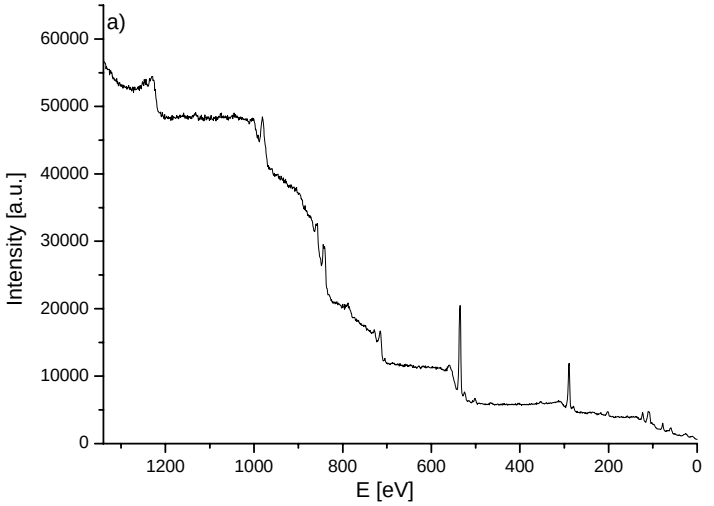
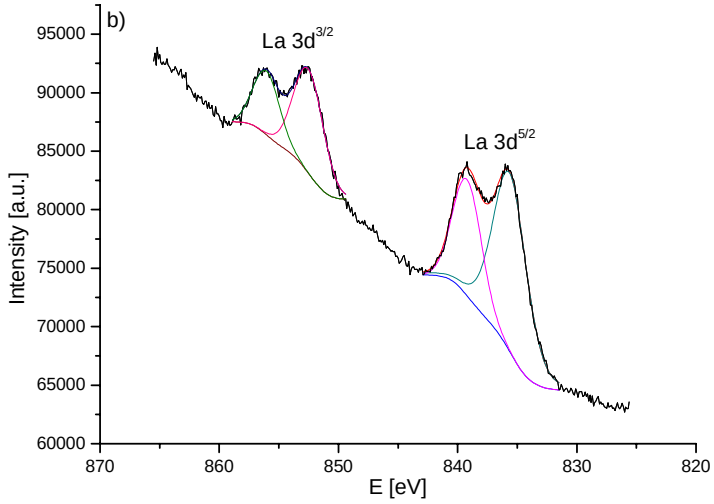
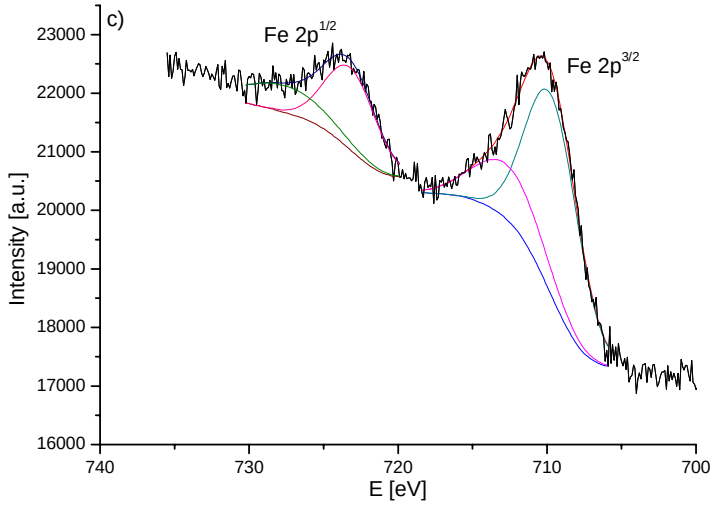



Fig. V.40 XPS survey spectrum (a) and narrow scan (b-c) on Fe35-$La_2O_3$.


a)
Intensity [a.u.]
E [eV]


b)
La 3d3/2
La 3d5/2
Intensity [a.u.]
E [eV]


c)
Fe 2p1/2
Fe 2p3/2
Intensity [a.u.]
E [eV]

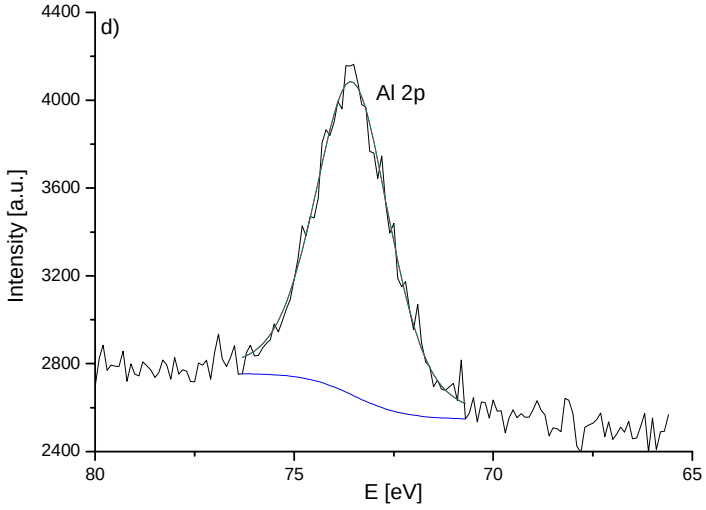



Fig. V.41 XPS survey spectrum (a) and narrow scan (b-d) on Fe35-$La_2O_3$ (HPT).

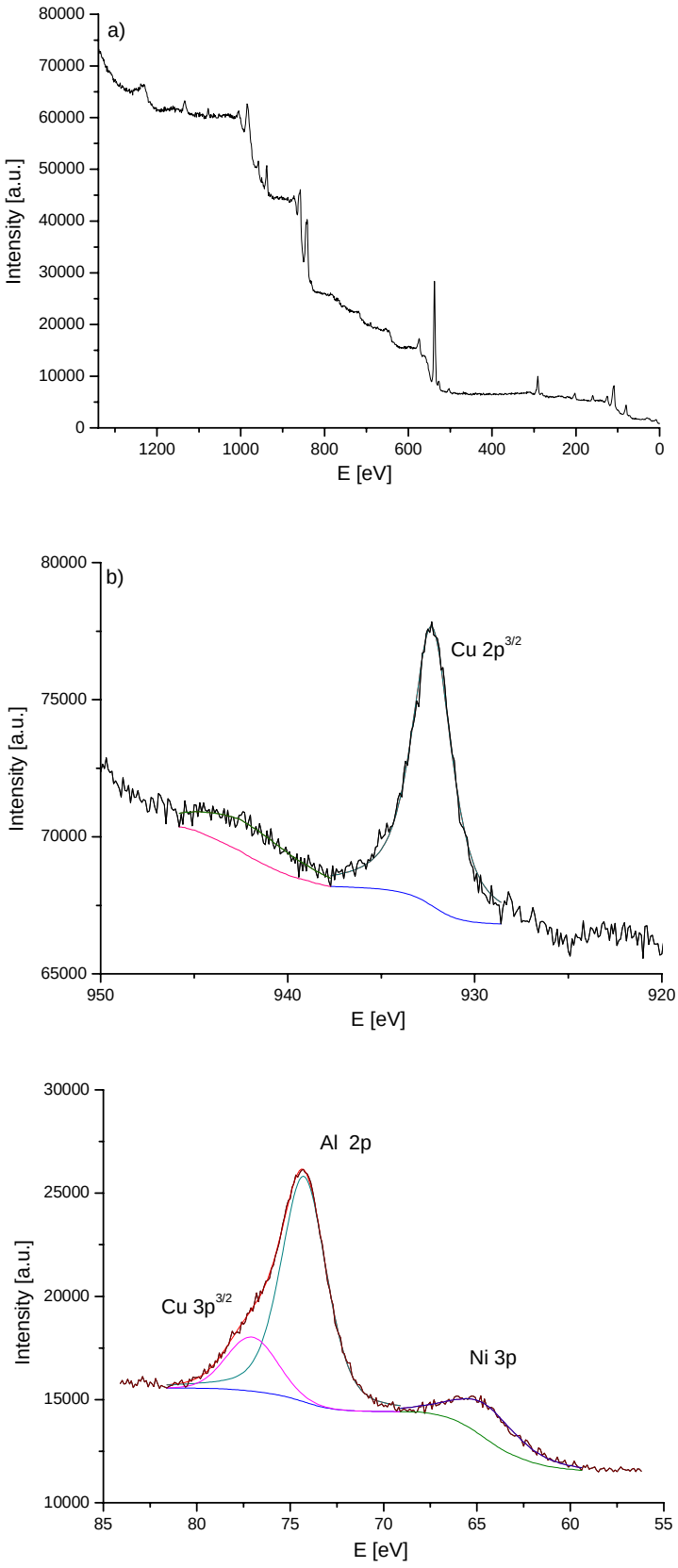



Fig. V.42 XPS survey spectrum (a) and narrow scan (b-d) on Ni30Cu50-$La_2O_3$ (HPT).

Table V.1

Surface characterization

| | Me $2p^{3/2}$ [eV] | Me 3p [eV] | $Al/Al_2O_3$ 2p [eV] | $R^a_{surface}$ |
|---|---|---|---|---|
| Alloy | | | | |
| Ni69 | 852.4 | 68.3 | 74.6 | 0.16 |
| Ni47-Mo6 | 852.1 | 65.4 | 74.5 | 0.04 |
| Catalyst | | | | |
| Ni69 | 854.0 | 68.5 | 76.3 | 0.36 |
| Ni47-Mo6 | 853.1 | 67.0 | 74.0 | 0.38 |

| Sample | Co $2p^3$ [eV] | Cu $2p^3$ [eV] | $Al/Al_2O_3$ 2p [eV] | $R^a_{Co}$ | $R^a_{Cu}$ |
|---|---|---|---|---|---|
| Alloy | | | | | |
| Co30 | 780.7 | / | 78.0 | 0.01 | / |
| Co50 | 779.6 | / | 76.9 | 0.03 | / |
| Catalyst | | | | | |
| Co30 | 781.1 | / | 70.6 | 0.58 | / |
| Co50 | 784.0 | / | 71.1 | 0.43 | / |
| Co30Cu50 (IIT) | 781.8 | 932.2 | 74.7 | 0.17 | 0.27 |
| Co50Cu50 (IIT) | 781.4 | 932.1 | 74.5 | 0.13 | 0.19 |

| Catalyst | $La_2O_3$ [wt. %] | Co $2p^3$ [eV] | La $3p^5$ [eV] | $Al/Al_2O_3$ 2p [eV] | $R^a_{Co}$ | $R^a_{La}$ |
|---|---|---|---|---|---|---|
| Co30 | / | 781.1 | / | 70.6 | 0.58 | / |
| Co30 (HPT) | / | 780.9 | / | 74.0 | 0.47 | / |
| Co30-$La_2O_3$ | 10.7 | 780.1 | 835.2 | n.a. | 0.43 | 0.57 |
| Co30-$La_2O_3$ (HPT) | 10.7 | 780.7 | 835.4 | 74.0 | 0.14 | 0.13 |
| | | | | | | |
| Co50 | / | 784.0 | / | 71.1 | 0.43 | / |
| Co50 (HPT) | / | 780.3 | / | 73.9 | 0.31 | / |
| Co50-$La_2O_3$ | 19.4 | 781.7 | 836.4 | n.a. | 0.45 | 0.55 |
| Co50-$La_2O_3$ (HPT) | 19.4 | 780.0 | 835.2 | 73.8 | 0.17 | 0.44 |

| Catalyst | $La_2O_3$ [wt %] | Fe $2p^3$ [eV] | La $3p^5$ [eV] | $Al/Al_2O_3$ 2p [eV] | $R^a_{Fe}$ | $R^a_{La}$ |
|---|---|---|---|---|---|---|
| Fe50 | / | 713.1 | / | 71.7 | 0.49 | / |
| Fe50 (HPT) | / | 710.0 | / | 73.8 | 0.25 | / |
| Fe50-$La_2O_3$ | 19.4 | 712.4 | 836.4 | 72.7 | 0.51 | 0.41 |
| Fe50-$La_2O_3$ (HPT) | 19.4 | 709.1 | 835.1 | 72.6 | 0.15 | 0.41 |
| | | | | | | |
| Fe35 | / | 710.3 | / | 69.9 | 0.05 | / |
| Fe35 (HPT) | / | 709.9 | / | 73.8 | 0.24 | / |
| Fe35-$La_2O_3$ | 19.4 | 708.9 | 835.4 | n.a. | 0.00 | 1.00 |
| Fe35-$La_2O_3$ (HPT) | 19.4 | 709.7 | 835.6 | 73.5 | 0.18 | 0.22 |

## VI. X-Ray Diffraction

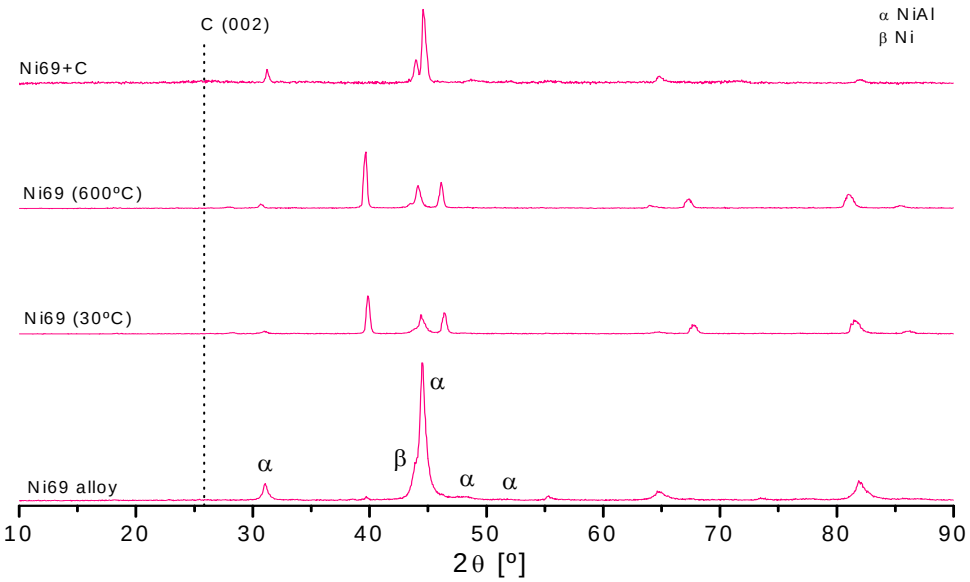



Fig. VI.1 XRD patterns of the Ni69 alloy, catalyst and catalyst with carbon deposits produced at 600ºC.

Table VI.1

Average crystal sizes and interplanar distance of carbon

| Sample | $T^{measured}$ [ºC] | $T^{reaction}$ [ºC] | $d_{Ni}$ [nm] | $d_{NiAl}$ [nm] | $d_C$ [nm] | $D_{(002)}$ [nm] |
|---|---|---|---|---|---|---|
| Ni69 alloy | 30 | / | 17.9 | / | / | / |
| Ni69 catalyst | 30 | / | / | 19.1 | / | / |
| Ni69 catalyst | 600 | / | / | 20.0 | / | / |
| Ni69+C | 30 | 600 | / | 41.4 | 6.3 | 0.340 |

The Ni69 alloy was identified with the following phases: $Ni_2Al_3$ (2θ = 31.1º, 44.5º, 48.5º, 51.8º and 55.3º), $NiAl_3$ (2θ = 33.6º, 35.2º, 37.5º, 38.7º, 44.1º, 48.5º, 70.5º and 86.9º) and Ni (2θ = 44.5º, 77.9º, 85.8º and 87.7º). The Ni69 catalyst shows the presence of a $Ni_{0.97}Al_{1.03}$ phase, detected at 2θ = 30.7º, 44.2º, 54.7º, 64.0º and 81.1º. The Ni69 catalyst with carbon deposits shows the presence of graphite at 2θ = 26.2º, a NiAl phase (2θ = 31.2º, 44.6º, 48.7º and 51.8º) and a $Ni_5Al_3$ phase (2θ = 44.0º, 55.5º, 71.9º and 82.0º).

The used Co-Al alloys were identified. For the Co30 alloy, a monoclinic $Co_4Al_{13}$ phase with segregated cubic centred packed (ccp) Al was found. For the Co50 alloy the identified phase are ccp CoAl and hexagonal centred packed (hcp) $Co_2Al_5$.

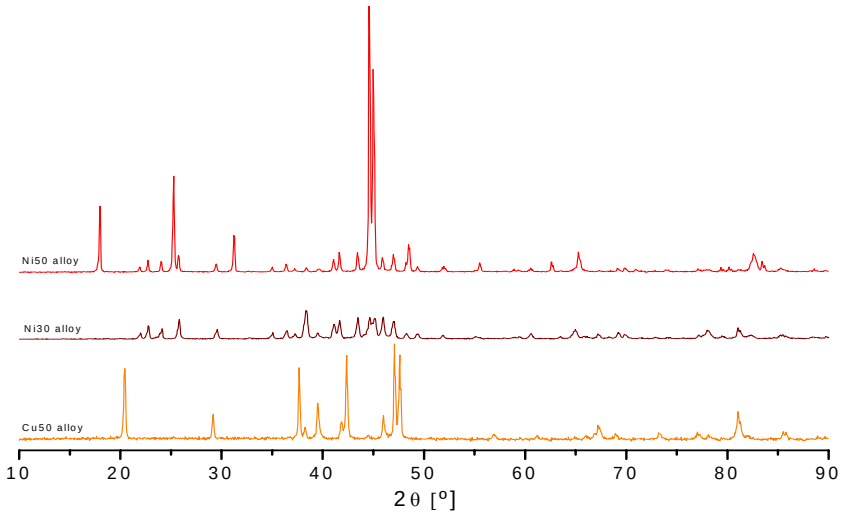



Fig. VI.2 XRD patterns of the Cu50, Ni30 and Ni50 alloy powders.

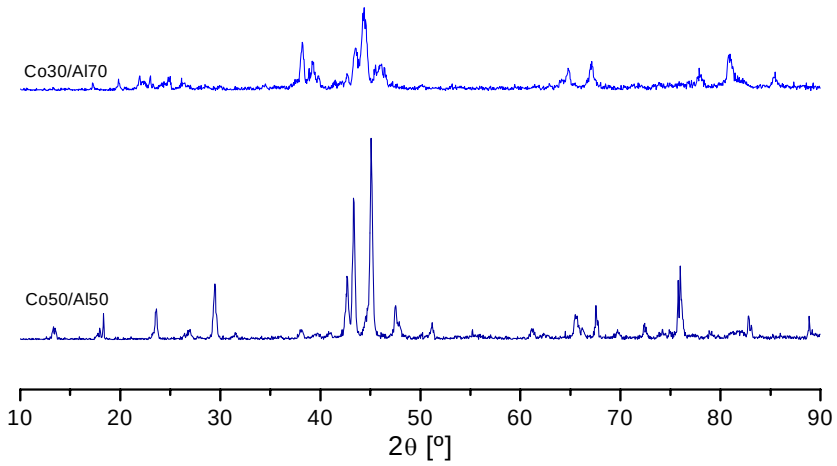



Fig. VI.3 XRD patterns of the Co30 and Co50 alloys.

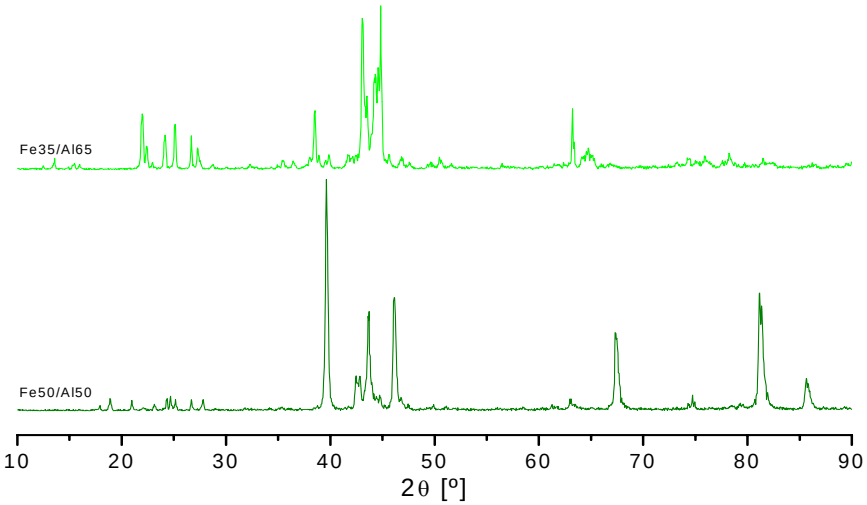



Fig. VI.4 XRD patterns of the Fe50 and Fe35 alloys.

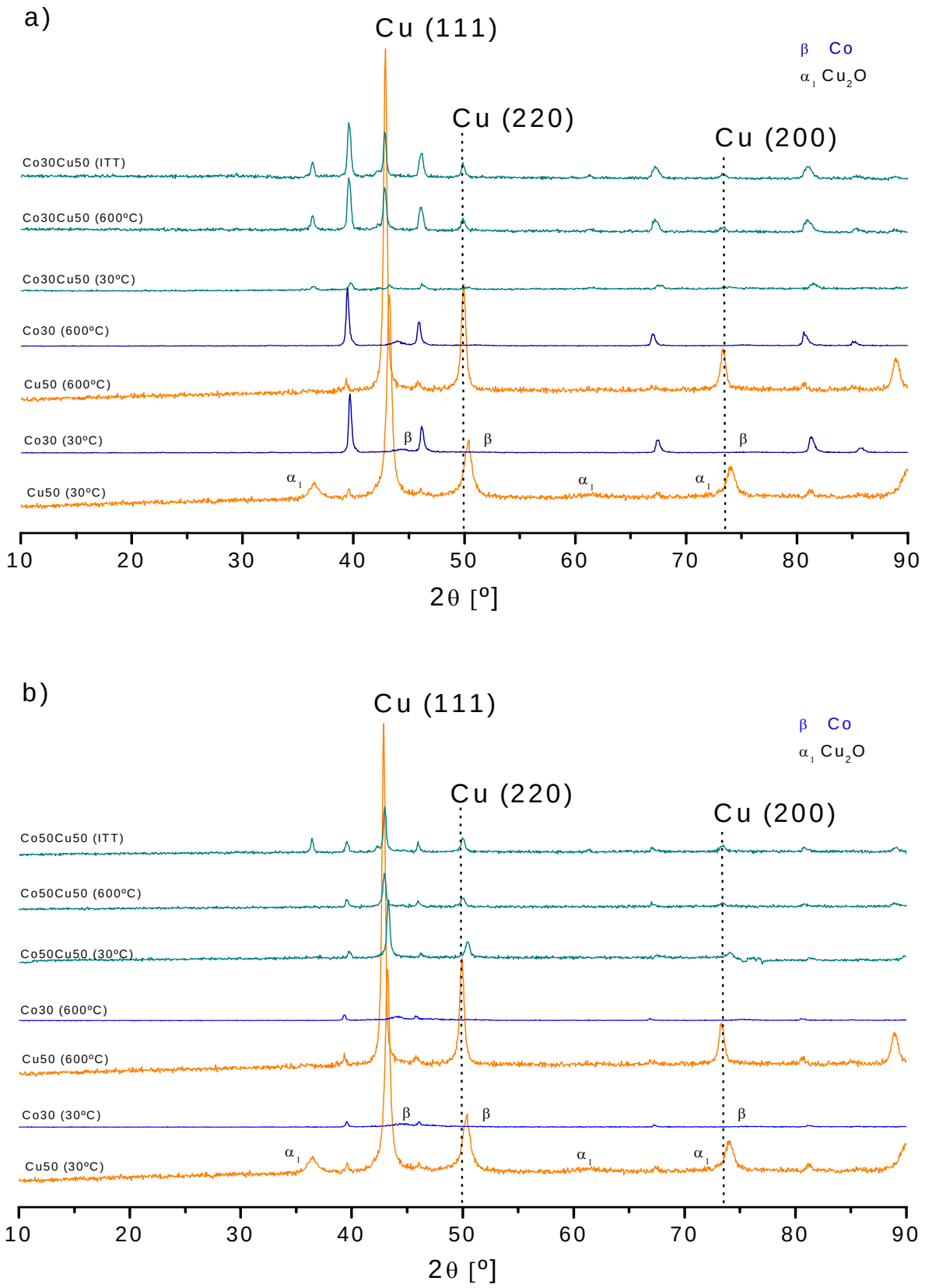


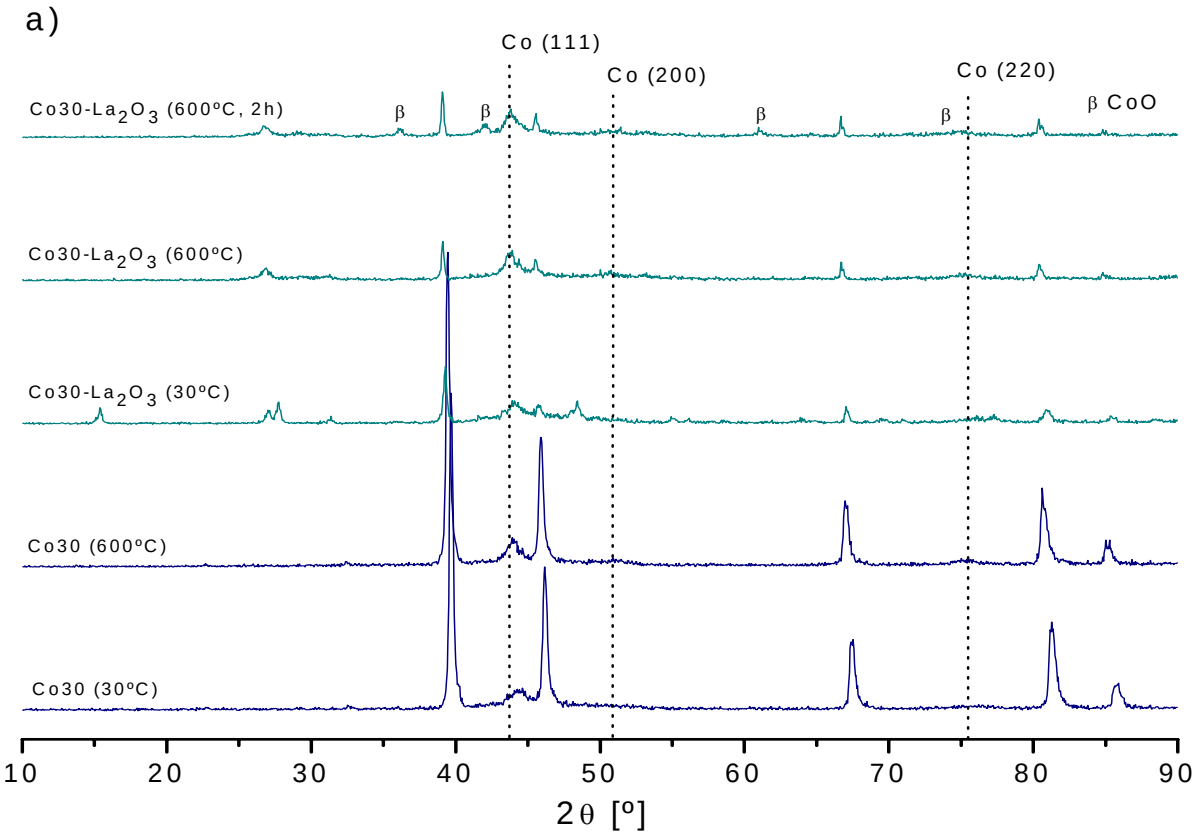

Fig. VI.5 XRD patterns of the Co30-Cu50 (a) and Co50-Cu50 (b) mono- and bimetallic catalysts measured at 30 ºC, 600 ºC and after 2h of thermal treatment at 600 ºC.

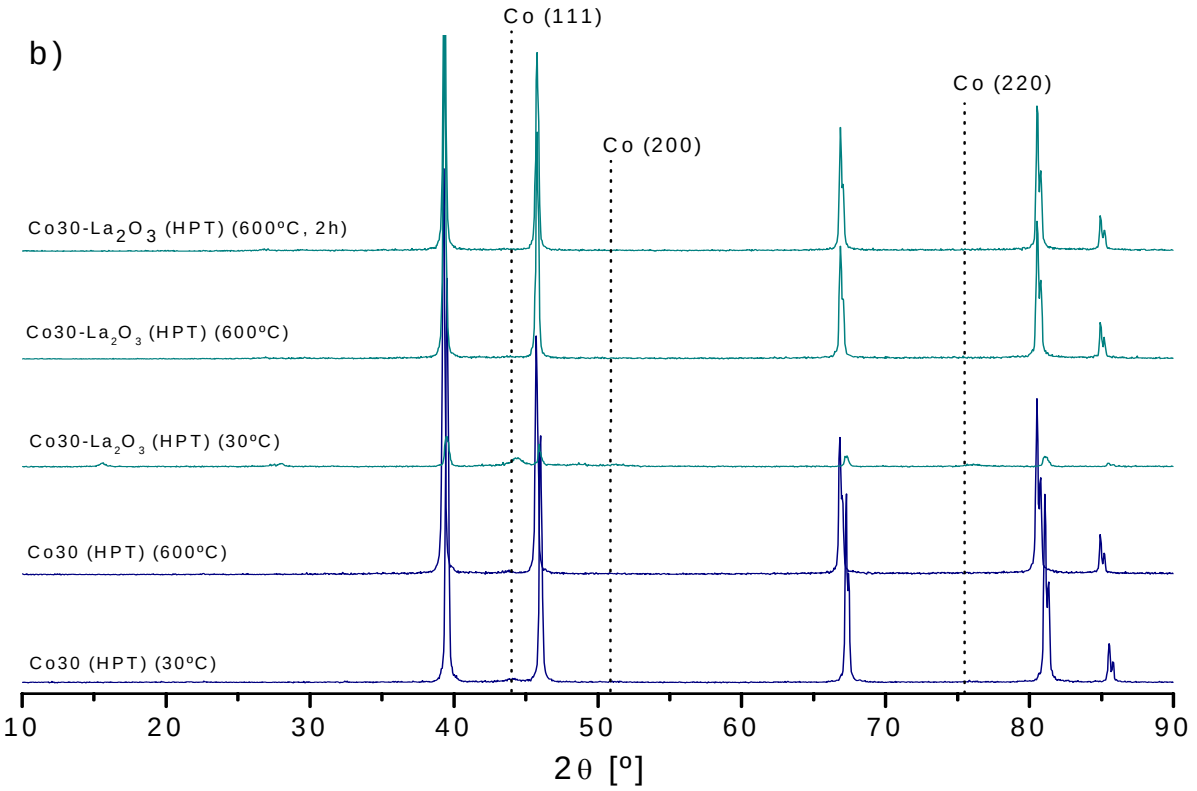
Table VI.2

Average Co and Cu crystal sizes

| Sample | $T^{measured}$ [°C] | $d_{Co}$ [nm] | $d_{Cu}$ [nm] |
|---|---|---|---|
| Alloy | | | |
| Cu50 | | / | 53.8 |
| Co30 | 30 | 12.9 | / |
| Co50 | 30 | 35.8 | / |
| Monometallic Catalyst | | | |
| Cu50 | 30 | / | 17.2 |
| Cu50 | 600 | / | 23.8 |
| Co30 | 30 | 8.2 | / |
| Co30 | 600 | 8.5 | / |
| Co50 | 30 | 15.1 | / |
| Co50 | 600 | 19.0 | / |
| Bimetallic Catalyst | | | |
| Co30Cu50 | 30 | n.a. | 22.1 |
| Co30Cu50 | 600 | n.a. | 33.0 |
| Co30Cu50 (ITT) | 600[2h] | n.a. | 34.0 |
| Co50Cu50 | 30 | n.a. | 15.8 |
| Co50Cu50 | 600 | n.a. | 28.3 |
| Co50Cu50 (ITT) | 600[2h] | n.a. | 31.6 |

[2h]in situ thermal treated under vacuum during 2h before measurement.


a)
Co (111)
Co (200)
Co (220)
Co30-La2O3 (600ºC, 2h)
β
β
β
β
β CoO
Co30-La2O3 (600ºC)
Co30-La2O3 (30ºC)
Co30 (600ºC)
Co30 (30ºC)
10
20
30
40
50
60
70
80
90
2θ [º]


b)
Co (111)
Co (200)
Co (220)
Co30-La2O3 (HPT) (600ºC, 2h)
Co30-La2O3 (HPT) (600ºC)
Co30-La2O3 (HPT) (30ºC)
Co30 (HPT) (600ºC)
Co30 (HPT) (30ºC)
10
20
30
40
50
60
70
80
90
2θ [º]

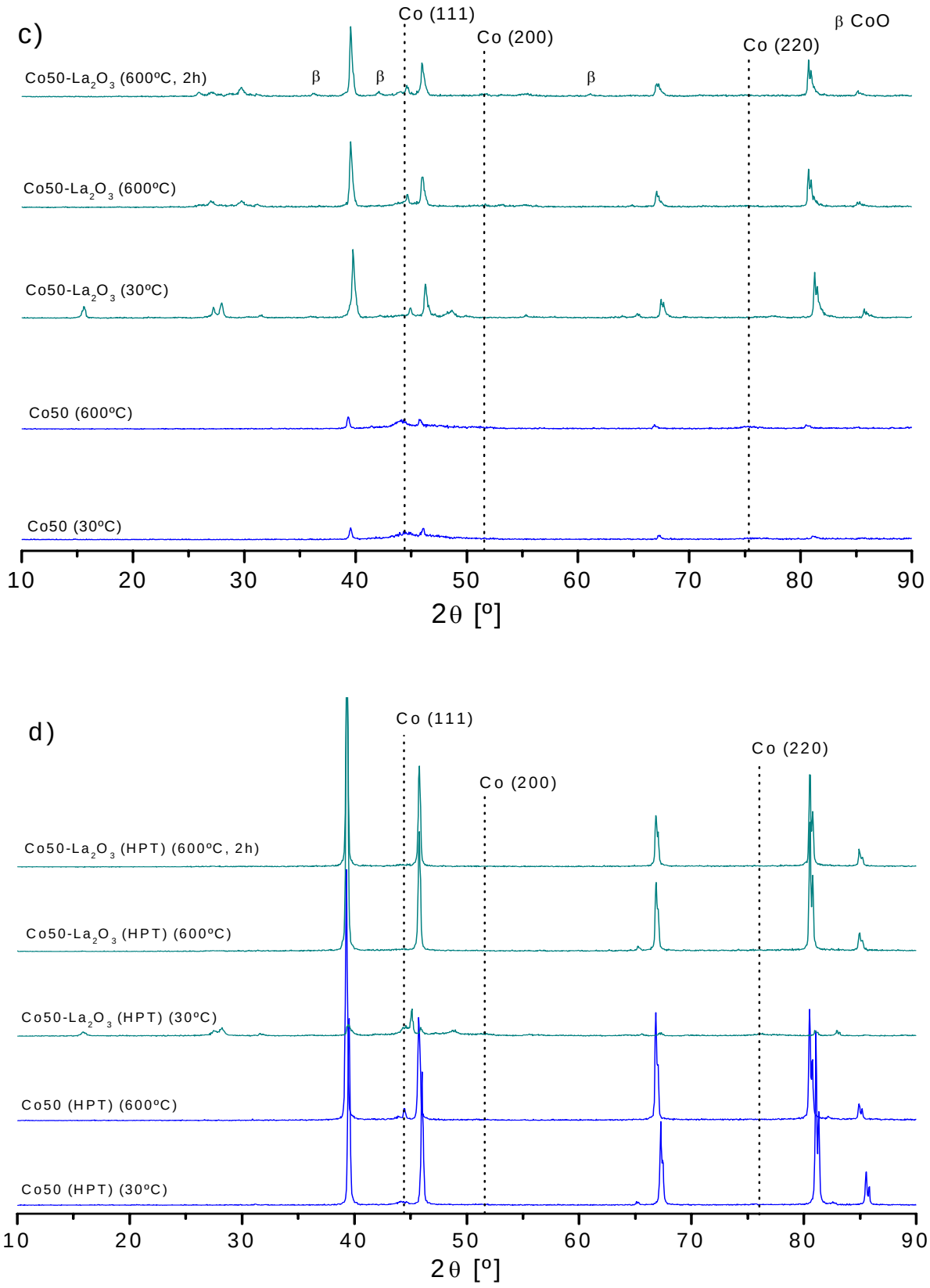


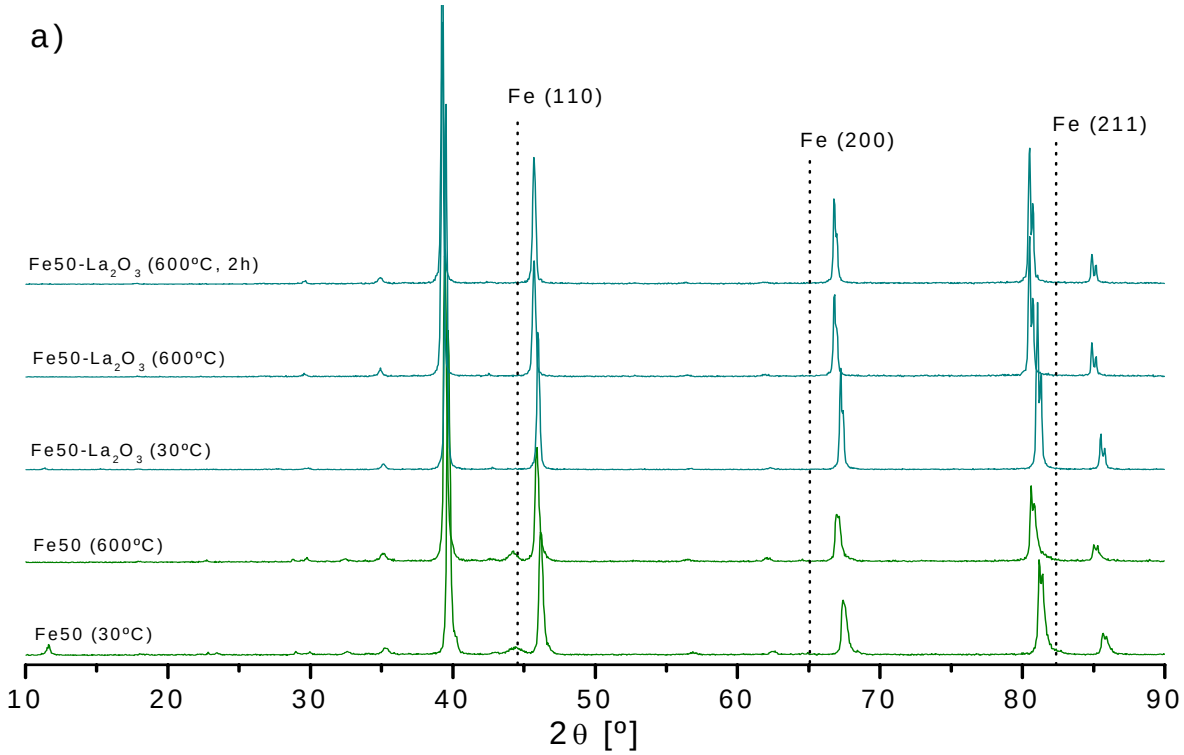

Fig. VI.6 XRD patterns of Co30-$La_2O_3$ (a), Co30-$La_2O_3$ (HPT) (b), Co50-$La_2O_3$ (c) and Co50-$La_2O_3$ (HPT) (d) measured at 30 ºC, 600 ºC and after 2h of thermal treatment at 600 ºC.

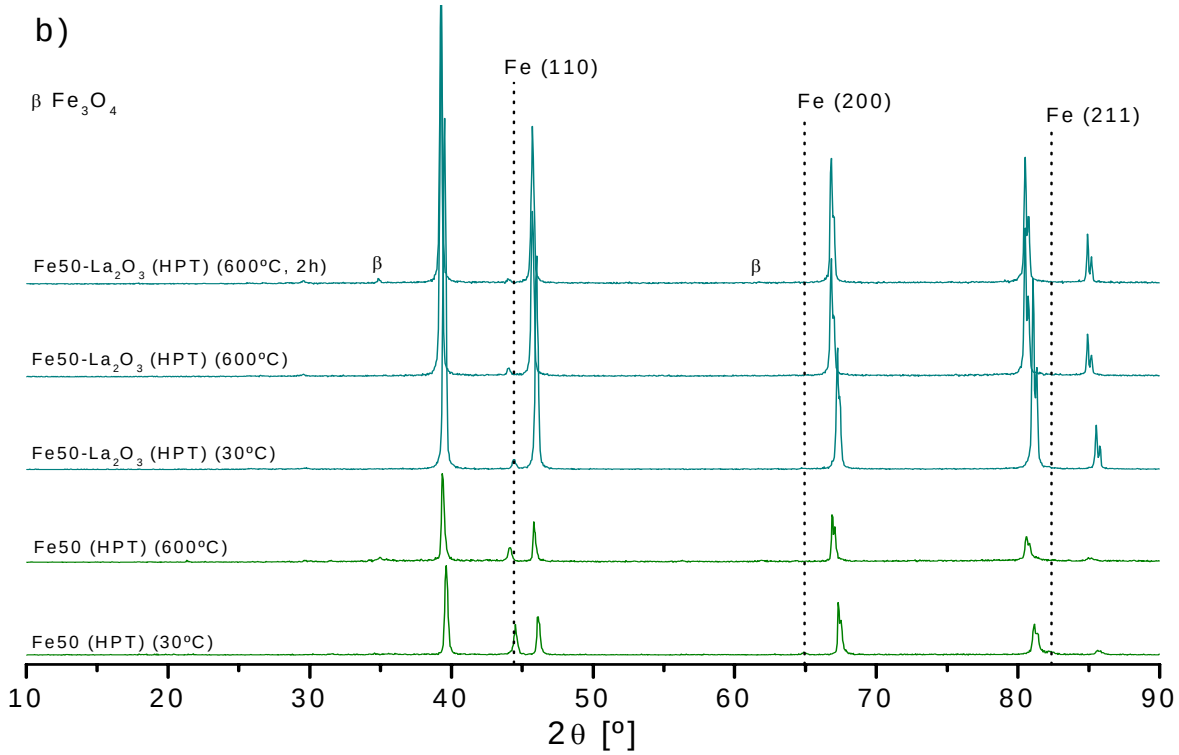
Table VI.3

Average Co, CoO and $La_2O_3$ crystal sizes

| Catalyst | T [ºC] | $d_{Co}$ [nm] | $d_{CoO}$ [nm] | $d_{La_2O_3}$ [nm] |
|---|---|---|---|---|
| Co catalysts | | | | |
| Co30 | 30 | 8.2 | / | / |
| Co30 | 600 | 8.5 | / | / |
| Co30 (HPT) | 30 | 7.4 | / | / |
| Co30 (HPT) | 600 | 9.2 | / | / |
| Co50 | 30 | 15.1 | / | / |
| Co50 | 600 | 19.0 | / | / |
| Co50 (HPT) | 30 | 10.0 | / | / |
| Co50 (HPT) | 600 | 35.0 | / | / |
| $La_2O_3$ doped Co catalysts | | | | |
| Co30-$La_2O_3$ | 30 | 20.6 | / | 44.1 |
| Co30-$La_2O_3$ | 600 | 26.1 | / | 21.2 |
| Co30-$La_2O_3$ | 600[2h] | 19.5 | 42.8 | 10.4 |
| Co30-$La_2O_3$ (HPT) | 30 | 11.0 | / | 29.4 |
| Co30-$La_2O_3$ (HPT) | 600 | 14.5 | / | 4.5 |
| Co30-$La_2O_3$ (HPT) | 600[2h] | 11.1 | / | 21.4 |
| Co50-$La_2O_3$ | 30 | 14.6 | / | 43.0 |
| Co50-$La_2O_3$ | 600 | 25.9 | / | 20.2 |
| Co50-$La_2O_3$ | 600[2h] | 22.5 | 9.7 | 15.4 |
| Co50-$La_2O_3$ (HPT) | 30 | 14.4 | / | 34.7 |
| Co50-$La_2O_3$ (HPT) | 600 | 16.3 | / | 5.1 |
| Co50-$La_2O_3$ (HPT) | 600[2h] | 10.8 | / | 18.0 |

[2h]in situ thermal treated under vacuum during 2h before measurement.


a)
Fe (110)
Fe (200)
Fe (211)
Fe50-La2O3 (600ºC, 2h)
Fe50-La2O3 (600ºC)
Fe50-La2O3 (30ºC)
Fe50 (600ºC)
Fe50 (30ºC)
10
20
30
40
50
60
70
80
90
2θ [º]


b)
β Fe3O4
Fe (110)
Fe (200)
Fe (211)
Fe50-La2O3 (HPT) (600ºC, 2h)
β
β
Fe50-La2O3 (HPT) (600ºC)
Fe50-La2O3 (HPT) (30ºC)
Fe50 (HPT) (600ºC)
Fe50 (HPT) (30ºC)
10
20
30
40
50
60
70
80
90
2θ [º]

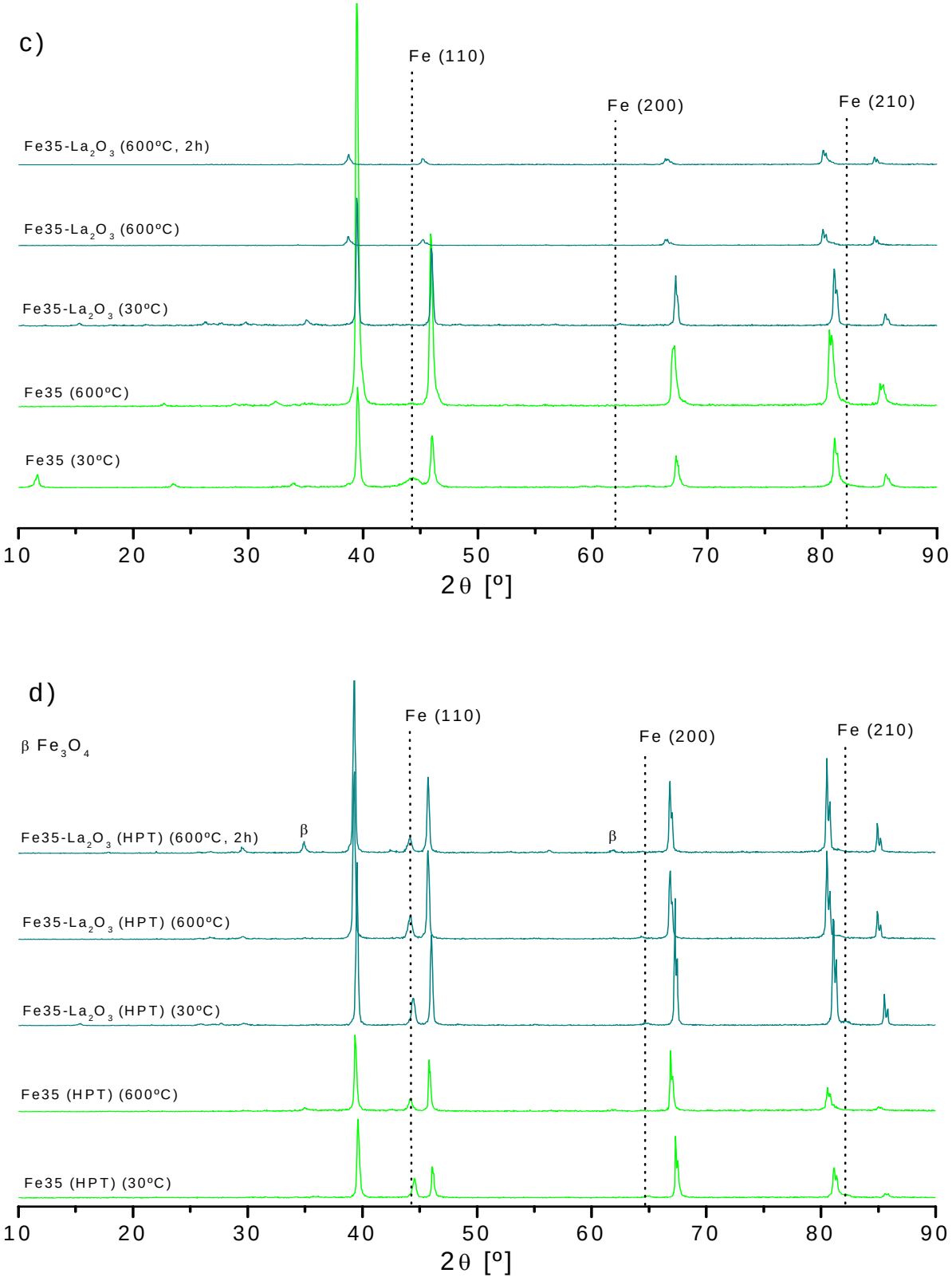



Fig. VI.7 XRD patterns of Fe50-$La_2O_3$ (a), Fe50-$La_2O_3$ (HPT) (b), Fe35-$La_2O_3$ (c) and Fe35-$La_2O_3$ (HPT) (d) measured at 30ºC, 600ºC and after 2h of thermal treatment at 600ºC.

Table VI.4

Average Fe, $Fe_2O_3$, $Fe_3O_4$ and $La_2O_3$ crystal sizes

| Catalyst | $T^{measured}$ [°C] | $d_{Fe}$ [nm] | $d_{La_2O_3}$ [nm] |
|---|---|---|---|
| Fe catalysts | | | |
| Fe50 | 30 | 17.9 | / |
| Fe50 | 600 | 34.2 | / |
| Fe50 (HPT) | 30 | 14.8 | / |
| Fe50 (HPT) | 600 | 30.6 | / |
| Fe35 | 30 | 7.6 | / |
| Fe35 | 600 | / | / |
| Fe35 (HPT) | 30 | 25.3 | / |
| Fe35 (HPT) | 600 | 28.7 | / |
| $La_2O_3$ doped Fe catalysts | | | |
| Fe50-$La_2O_3$ | 30 | / | 22.9 |
| Fe50-$La_2O_3$ | 600 | / | 23.8 |
| Fe50-$La_2O_3$ | 600[2h] | / | 18.5 |
| Fe50-$La_2O_3$ (HPT) | 30 | 16.0 | 8.9 |
| Fe50-$La_2O_3$ (HPT) | 600 | 24.0 | 23.5 |
| Fe50-$La_2O_3$ (HPT) | 600[2h] | 23.6 | 8.3 |
| Fe35-$La_2O_3$ | 30 | / | 21.9 |
| Fe35-$La_2O_3$ | 600 | | 22.8 |
| Fe35-$La_2O_3$ | 600[2h] | | 17.8 |
| Fe35-$La_2O_3$ (HPT) | 30 | 24.5 | 9.1 |
| Fe35-$La_2O_3$ (HPT) | 600 | 25.1 | 27.3 |
| Fe35-$La_2O_3$ (HPT) | 600[2h] | 24.5 | 8.3 |

[2h]in situ thermal treated under vacuum during 2h before measurement.

## VII. Thermodynamic calculations

The following thermodynamic calculations were made for methane decomposition into hydrogen and graphitic carbon in order to obtain the maximum possible methane conversion as a function of the corresponding reaction temperature.

$$CH_4 \rightleftharpoons 2\,H_2 + C; \qquad \Delta_r H = 74.6\ kJ/mol \qquad \text{(eq. VII.1)}$$

Equilibrium equation:

$$K = \frac{a_c \cdot a_{H_2}^2}{a_{CH_4}} \quad ; p = 1\ atm \qquad \text{(eq. VII.2)}$$

The activity in the gas phase is:

$$a_i = \frac{p_i}{p_i^{\circ}} \qquad \text{(eq. VII.3)}$$

Supposing that the activity of the formed carbon (graphite) is unitary $a_{carbon} = 1$,

$$K = \frac{p_{H_2}^2}{p_{CH_4}} \qquad \text{(eq. VII.4)}$$

the mole fraction in the gas phase is,

$$y_i = \frac{n_i}{n} = \frac{p_i}{p}, \qquad \text{(eq. VII.5)}$$

and

$$K = \frac{y_{H_2}^2}{y_{CH_4}} \cdot p \qquad \text{(eq. VII.6)}$$

The $CH_4$ flow is,

$$\dot{n}_{CH_4} = \dot{n}_{CH_4,0}(1 - X) \qquad \text{(eq. VII.7)}$$

and the $H_2$ flow

$$\dot{n}_{H_2} = \dot{n}_{H_2,0} + 2\dot{n}_{CH_4,0} X = \dot{n}_{CH_4}(M + 2X) \qquad \text{(eq. VII.8)}$$

in which, M is defined as

$$M \equiv \frac{\dot{n}_{H_2}}{\dot{n}_{CH_4}} \qquad \text{(eq. VII.9)}$$

The $N_2$ inert-flow is

$$\dot{n}_{N_2} = \dot{n}_{N_2} = N \cdot \dot{n}_{CH_4,0} \qquad \text{(eq. VII.10)}$$

and N is defined as

$$N \equiv \frac{\dot{n}_{N_2}}{\dot{n}_{CH_4}} \qquad \text{(eq. VII.11)}$$

The total flow is

$$\dot{n}_{total} = \dot{n}_{CH_4,0}(1 + M + N + X) \qquad \text{(eq. VII.12)}$$

According to equation VII.6 we get the following relation:

$$K = \frac{(M + 2X_{CH_4})^2}{(1 - X_{CH_4}) \cdot (1 + M + N + X_{CH_4})} \cdot p \qquad \text{(eq. VII.13)}$$

The exchange of equation into the Conversion X leads to the definitive mathematic relation;

$$X = -\frac{4M + \frac{K}{p}(M + N)}{2(\frac{K}{p} + 4)} \pm \sqrt{\left[\frac{4M + \frac{K}{p}(M + N)}{2(\frac{K}{p} + 4)}\right]^2 + \frac{\frac{K}{p}(1 + M + N)}{\frac{K}{p} + 4}} \qquad \text{(eq. VII.14)}$$

As observed, the Conversion depends also on the equilibrium constant which is determined by the van´t Hoff relation;

$$\left(\frac{\partial \ln K}{\partial T}\right)_p = \frac{\Delta_r H^o}{RT^2} \qquad \text{(eq. VII.15)}$$

Integrating the equation, in which K is a function of the Temperature, we get

$$\ln K = \frac{1}{R}\int_{T_0}^{T} \frac{\Delta_r H^\circ(T)}{T^2} \cdot dT + \ln K_0 \qquad \text{(eq. VII.16)}$$

The equilibrium constant at standard conditions (298,15 K; 1 bar) is expressed as

$$K_p^{298,15K} = e^{-\frac{\Delta_r G^\circ}{RT}} \qquad \text{(eq. VII.17)}$$

The free reaction Energy or Gibbs Energy $\Delta_r G^0$ at standard conditions is

$$\Delta_r G^0 = \Delta_r H^0 - T\,\Delta_r S^0 \qquad \text{(eq. VII.18)}$$

where the reaction Entropy at standard conditions is

$$\Delta_r S^0 = \Sigma\, \Delta_r S_p^{\,0} - \Sigma\, \Delta_r S_e^{\,0} \qquad \text{(eq. VII.19)}$$

and the reaction Enthalpy at standard conditions is

$$\Delta_r H^0 = \Sigma\, \Delta_r H_p^{\,0} - \Sigma\, \Delta_r H_e^{\,0} \qquad \text{(eq. VII.20)}$$

It is visible that the reaction Enthalpy is a function of the temperature, for the conclusion of the van´t Hoff equation, another physical relation which is expressed in the law of Kirchhoff is needed. The heat capacity $c_p$ is also defined as function of the temperature

$$\left(\frac{\partial H}{\partial T}\right)_p = c_p \qquad \text{(eq. VII.21)}$$

So, we get the Kirchhoff law expressed as

$$\Delta_r H_{T_1} = \Delta_r H_{T_0} + \int_{T_0}^{T_1} \Delta c_{p_i} \cdot dT \qquad \text{(eq. VII.22)}$$

and with the definition of the heat capacity in (VII.21)

$$\Delta c_p = \sum_0^i \nu_i c_{p,i} \qquad \text{(eq. VII.23)}$$

we get the equation:

$$\Delta_r H^o(T) = \Delta_r H^o(T_0) + \int_{T_0}^{T_1} \nu_i \cdot c_{p_i}(T) \cdot dT \qquad \text{(eq. VII.24)}$$

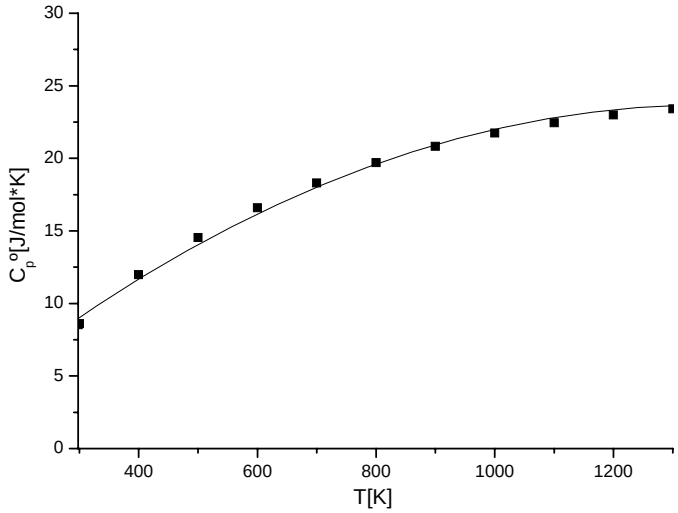



Fig. VII.1 Heat capacity vs. temperature of graphitic carbon.

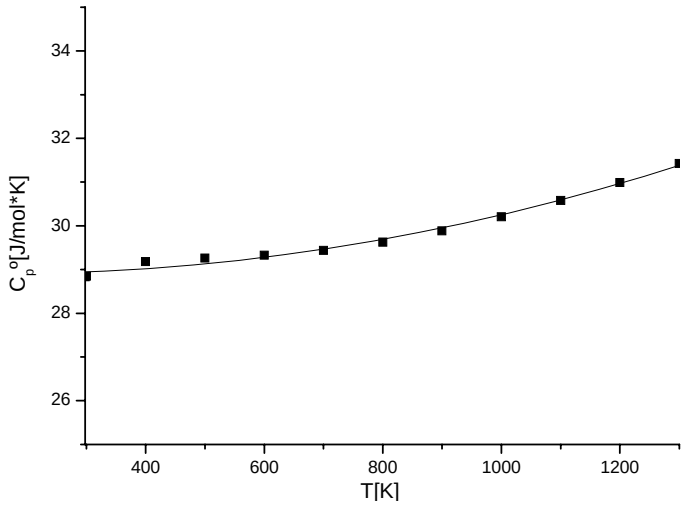



Fig. VII.2 Heat capacity vs. temperature of gaseous hydrogen.

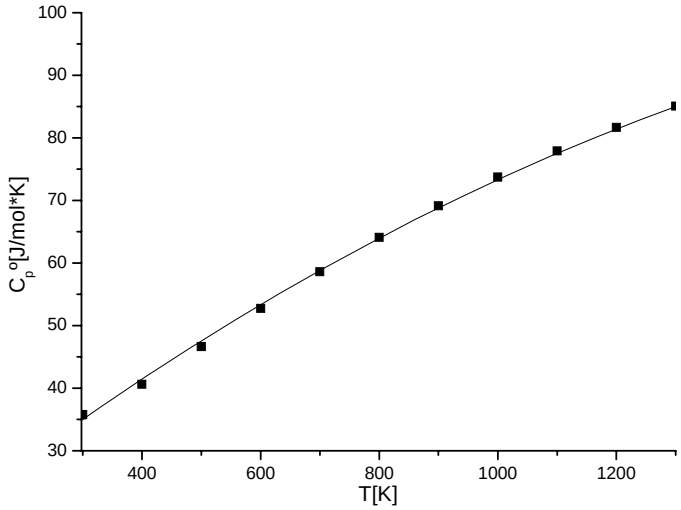



Fig. VII.3 Heat capacity vs. temperature of gaseous methane.

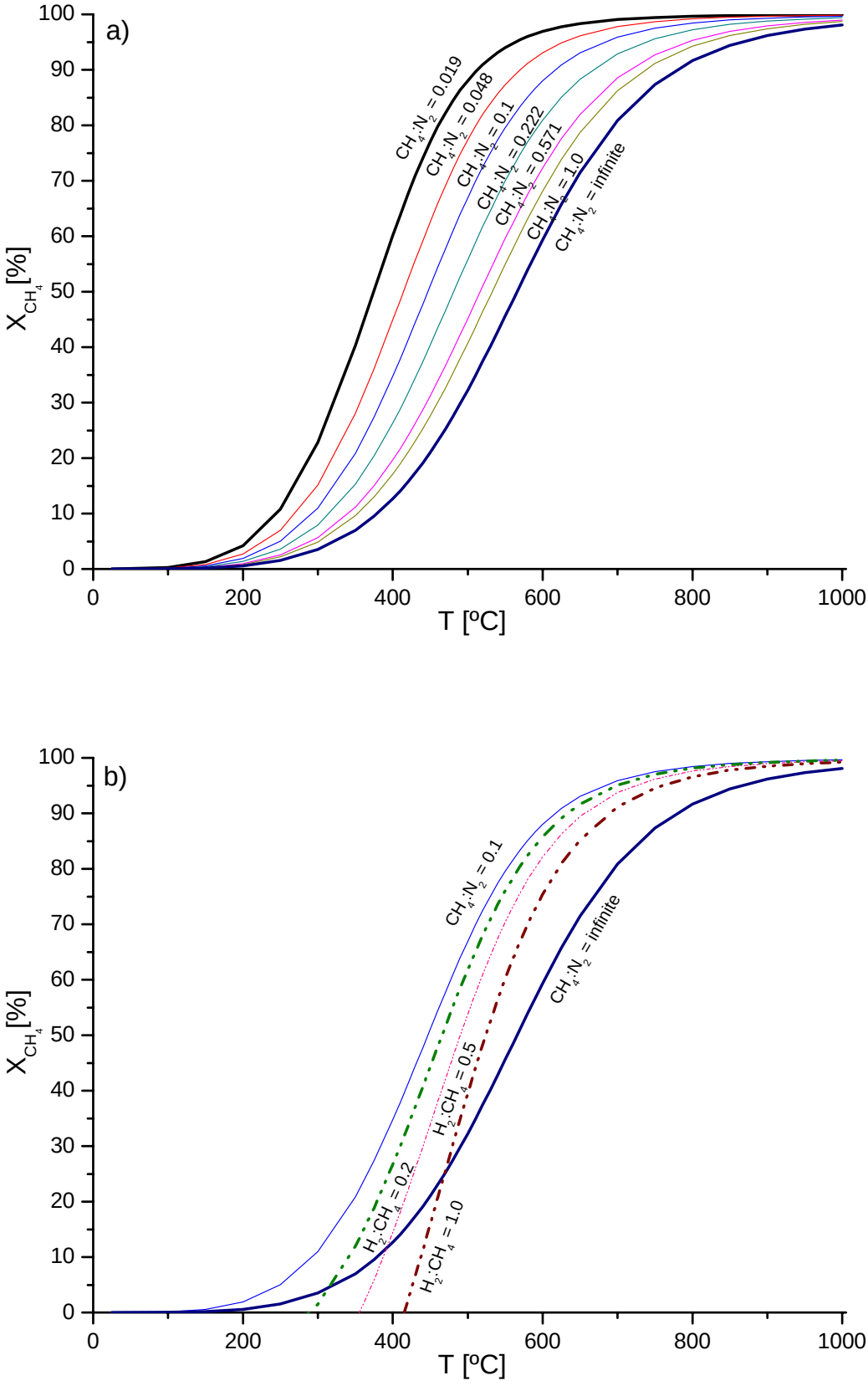



Fig. VII.4 Thermodynamic equilibrium of $CH_4$ decomposition diluted in $N_2$ (a) or $H_2/N_2$ (b).

Temperature dependent heat capacity of graphitic carbon, gaseous hydrogen and methane, respectively:

$$c_{p,c}^{o}(T) = -0.44935 + 0.03553T - 1.30788 \cdot 10^{-5} T^{2} \quad \text{(eq. VII.25)}$$

$$c_{p,H_2}^{o}(T) = 28.94811 - 5.83906 \cdot 10^{-4} T + 1.88773 \cdot 10^{-6} T^{2} \quad \text{(eq. VII.26)}$$

$$c_{p,CH_4}^{o}(T) = 13.9245 + 0.07511T - 1.57173 \cdot 10^{-5} T^{2} \quad \text{(eq. VII.27)}$$

The polynomial regressions are introduced in equation VII.24

$$\Delta_r H^{\circ} = 63378.247 + 43.522T - 0.021T^{2} + 2.138 \cdot 10^{-6} T^{3} \quad \text{(eq. VII.28)}$$

The new equation and the calculated value is introduced in the van´t Hoff equation, and results in the desired equilibrium constant K(T);

$$\ln K(T) = -20.387 - 7622.71T^{-1} + 5{,}234 \cdot \ln T - 0.003T + 1.286 \cdot 10^{-7} T^{2} - 3.521 \quad \text{(eq. VII.29)}$$

**VIII. Reaction studies and Kinetics**

- differential (flow) reactors,
- integral (plug flow) reactors,
- and mixed flow reactors (recycle reactor).

Table VIII.1

Comparison of differential circulating reactor vs. integral reactor

| | differential | Integral |
|---|---|---|
| Behaviour | $\frac{\partial c}{\partial x} = 0 \,;\, \frac{\partial T}{\partial x} = 0$ gradientless | $\frac{\partial c}{\partial x} \neq 0 \,,\, \frac{\partial T}{\partial x} \neq 0$ T and C profile |
| Information's | r, kinetic parameters | $r_{eff}$, Activity ($X_i$), Selectivity ($S_p$), Lifetime (t) |
| Transport phenomena | no | possible |

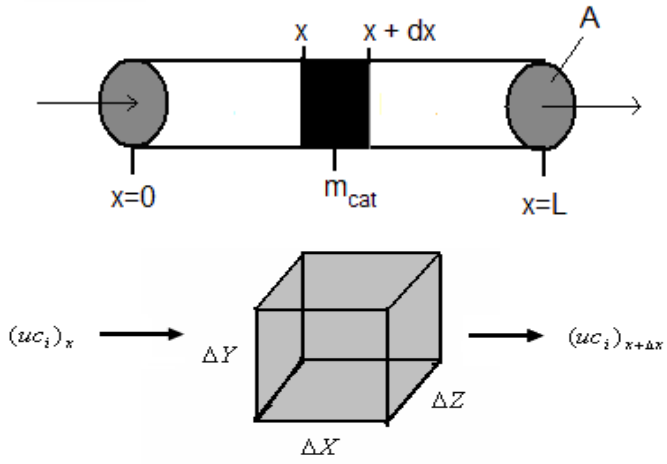



Fig. VIII.1 Integral reactor with a fixed catalyst bed

Tri-dimensional equation:

$$\frac{\partial C}{\partial t}\cdot\Delta x\cdot\Delta y\cdot\Delta z=[(uc_i)_x-(uc_i)_{x+\Delta x}]\cdot\Delta y\cdot\Delta z\ \pm r\cdot\Delta x\cdot\Delta y\cdot\Delta z \qquad \text{(eq. VIII.1)}$$

Linear equation:

$$(uc_i)_{x+\Delta x}=(uc_i)_x+\frac{\partial(uc_i)}{\partial x}\Delta x+\frac{\partial^2(uc_i)}{\partial x^2}\Delta x^2+..... \qquad \text{(eq. VIII.2)}$$

Mass balance:

$$\frac{\partial c}{\partial t}=-\frac{\partial(uc_i)}{\partial x}\pm r \qquad \text{(eq. VIII.3)}$$

In a stationary plug-flow system (u≠0) and $\frac{\partial c}{\partial t}=0$, the equation is than

$$r=\frac{d(uc_i)}{dx}=\frac{d\left(\frac{n_i}{t}\right)}{dV}=\frac{d\dot{n}_i}{dV} \qquad \text{(eq. VIII.4)}$$

where $\dot{n}_i=\dot{n}_{total}\cdot X_i$, if $\dot{n}_{total}=const.$, and resulting in the following expression

$$r=\dot{n}_{total}\frac{dy_i}{dV} \qquad \text{(eq. VIII.5)}$$

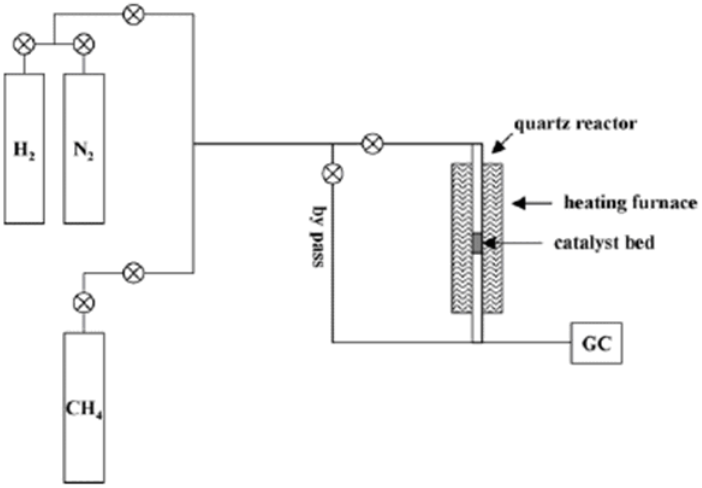
In a heterogeneous reaction the reaction velocity is related to the catalyst mass, thus

$$m_{cat}=\rho_{cat}\cdot V=\rho_{cat}\cdot A\cdot\partial x \qquad \text{(eq. 0 VIII.6)}$$

and introducing this relation into eq. VIII.5, then

$$r_i=\dot{n}_{total}\cdot\rho_{cat}\cdot\frac{dX_i}{dm_{cat}} \qquad \text{(eq. VIII.7)}$$

is obtained.





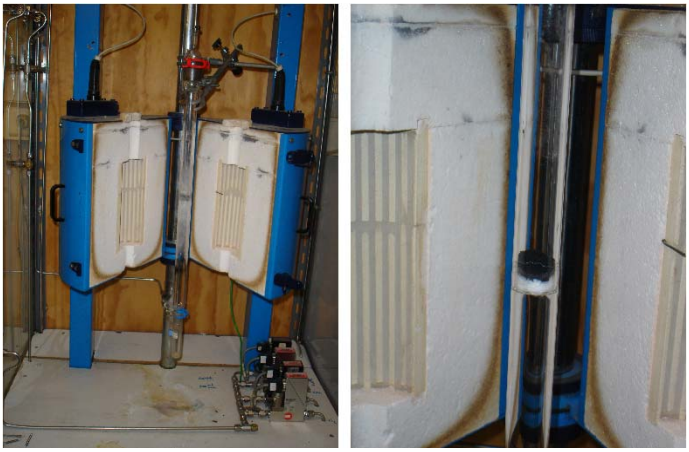



Fig. VIII.2 Used integral plug flow fixed bed catalyst test reactor

The slope of the reaction rate is given by the plot of conversion X versus $m_{cat}/\dot{n}_{i,0}$ (so-called time factor) in the curve.

$$r_i' = -\frac{dX_i}{d\left(\frac{m_{cat}}{\dot{n}_{total}}\right)} \qquad \left[\frac{mol}{kg \cdot s}\right] \tag{eq. VIII.8}$$

If the catalyst mass is required, then

$$m_{cat} = \dot{n}_{total} \cdot \rho_{cat} \cdot \int_{x}^{x_L} \frac{dX_i}{r(X_i, T)} \tag{eq. VIII.9}$$

has to be used.

The measurements are made under standard experimental conditions. Screening processes and the influences which can be studied:

- ❖ Catalyst mass
- ❖ Temperature
- ❖ Mole ratio
- ❖ Volumetric flow rate
- ❖ Catalyst pre-treatment
- ❖ Effect of adding reagents
- ❖ Dependence of the reaction solvent
- ❖ Lifetime estimation

$$r = k \cdot c_{CH_4}^n \tag{eq. VIII.10}$$

$$X_{CH_4} = a + b\frac{m_{cat}}{\dot{n}_{CH_4,0}} + c\left(\frac{m_{cat}}{\dot{n}_{CH_4,0}}\right)^2 + d\left(\frac{m_{cat}}{\dot{n}_{CH_4,0}}\right)^3 \tag{eq. VIII.11}$$

$$r = \frac{dX_{CH_4}}{d\left(\frac{m_{cat}}{\dot{n}_{CH_4,0}}\right)} = b + 2c\left(\frac{m_{cat}}{\dot{n}_{CH_4,0}}\right) + 3d\left(\frac{m_{cat}}{\dot{n}_{CH_4,0}}\right)^2 \tag{eq. VIII.12}$$

## IX. Theoretical Calculation of Carbon Mass formation

Numerical Simpson Integration:

Limits border values:

$$n_1 = \sum_0 (y_0 + y_{2n}) \quad \text{(eq. IX.1)}$$

Inner unpaired values:

$$n_2 = 4\sum_1 (y_1 + y_3 + ... + 2y_{2n-1}) \quad \text{(eq. IX.2)}$$

Inner paired values:

$$n_3 = 2\sum_2 (y_2 + y_4 + ... + y_{2n-2}) \quad \text{(eq. IX.3)}$$

The pathway is defined as

$$h = \frac{y_{2n} - y_0}{2n} \quad \text{(eq. IX.4)}$$

so that the final equation is

$$\int_a^b f(x) \cdot dx \approx [n_1 + n_2 + n_3]\frac{h}{3} \quad \text{(eq. IX.5)}$$

The theoretical carbon mass is, then

$$n_{carbon} = \dot{n}_{CH_4} \cdot X_{CH_4} \cdot t \quad \text{(eq. IX.6)}$$

$$\partial n_{carbon} = \dot{n}_{CH_4} \cdot X_{CH_4} \cdot \partial t \quad \text{(eq. IX.7)}$$

$$\int_{n_{carbon,0}}^{n_{carbon}} dn_{carbon} = \dot{n}_{CH_4} \cdot \int_0^t X_{CH_4} \cdot dt \quad \text{(eq. IX.8)}$$

$$n_{carbon} - n_{carbon,0} = \dot{n}_{CH_4} \cdot \int_0^t X_{CH_4} \cdot dt \quad \text{(eq. IX.9)}$$

$$m_{carbon} = \dot{n}_{CH_4} \cdot M_{carbon} \cdot \int_0^t X_{CH_4} \cdot dt \quad \text{(eq. IX.10)}$$

$$m_{carbon} = \rho_{CH_4} \cdot \dot{V}_{CH_4} \cdot \dot{M}_{carbon} \cdot \int_0^t X_{CH_4} \cdot dt \quad \text{(eq. IX.11)}$$

## X. Temperature programmed studies

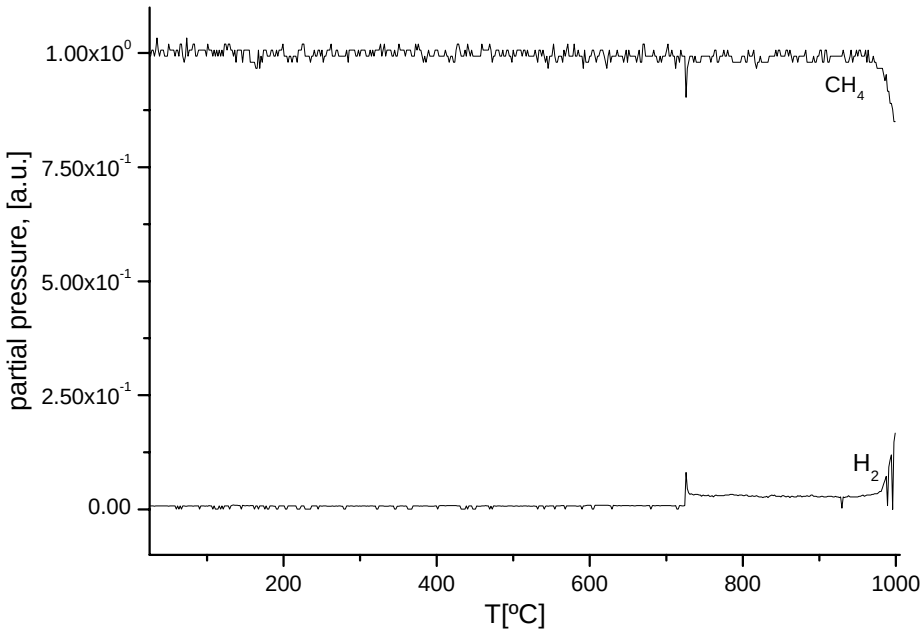
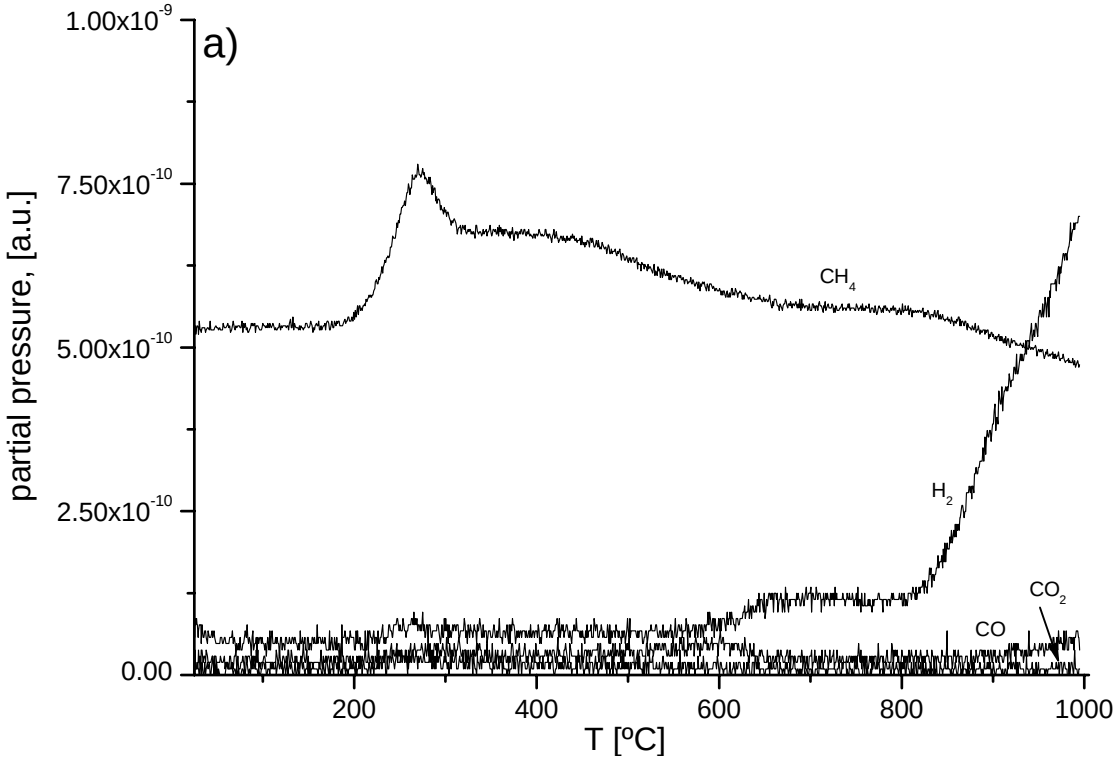
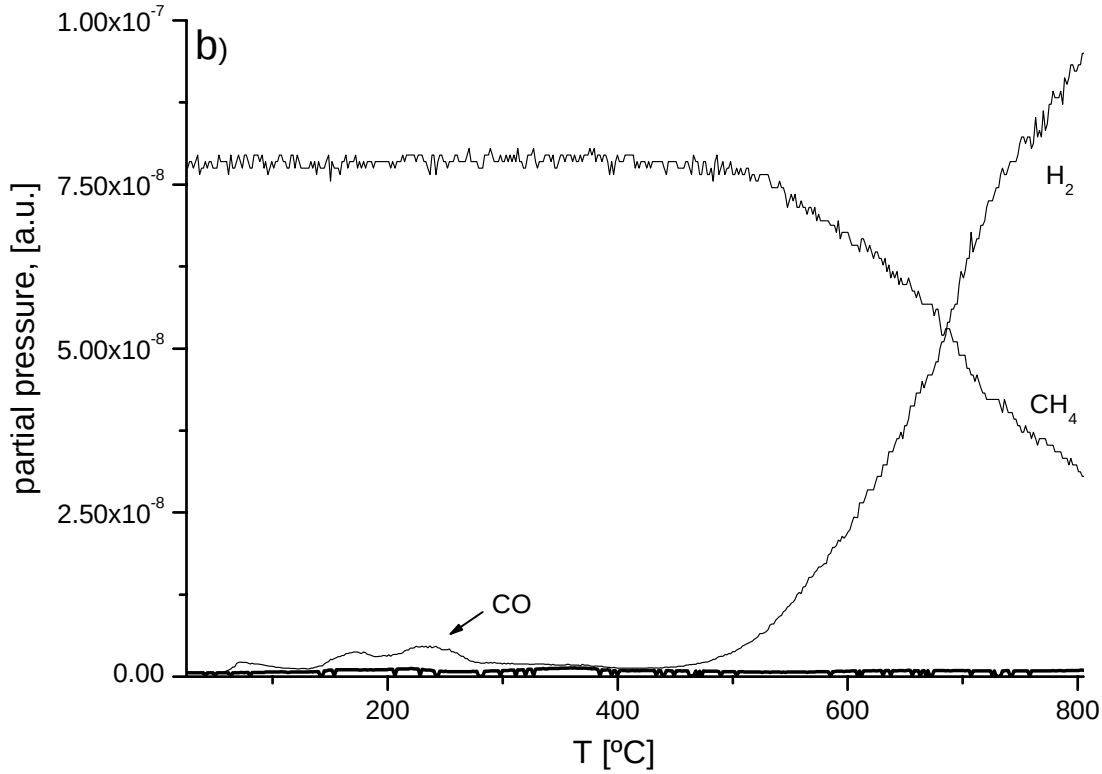



Fig. X.1 TPRe without catalyst. Experimental conditions: heating rate 5 ºC/min, temperature range 25-1000 ºC and a flow rate of 27.5 $Ncm^3$/min ($CH_4$/He = 0.1).


a)
1.00x10-9
7.50x10-10
5.00x10-10
2.50x10-10
0.00
partial pressure, [a.u.]
CH4
H2
CO2
CO
200
400
600
800
1000
T [ºC]


b)
1.00x10-7
7.50x10-8
5.00x10-8
2.50x10-8
0.00
partial pressure, [a.u.]
H2
CH4
CO
200
400
600
800
T [ºC]

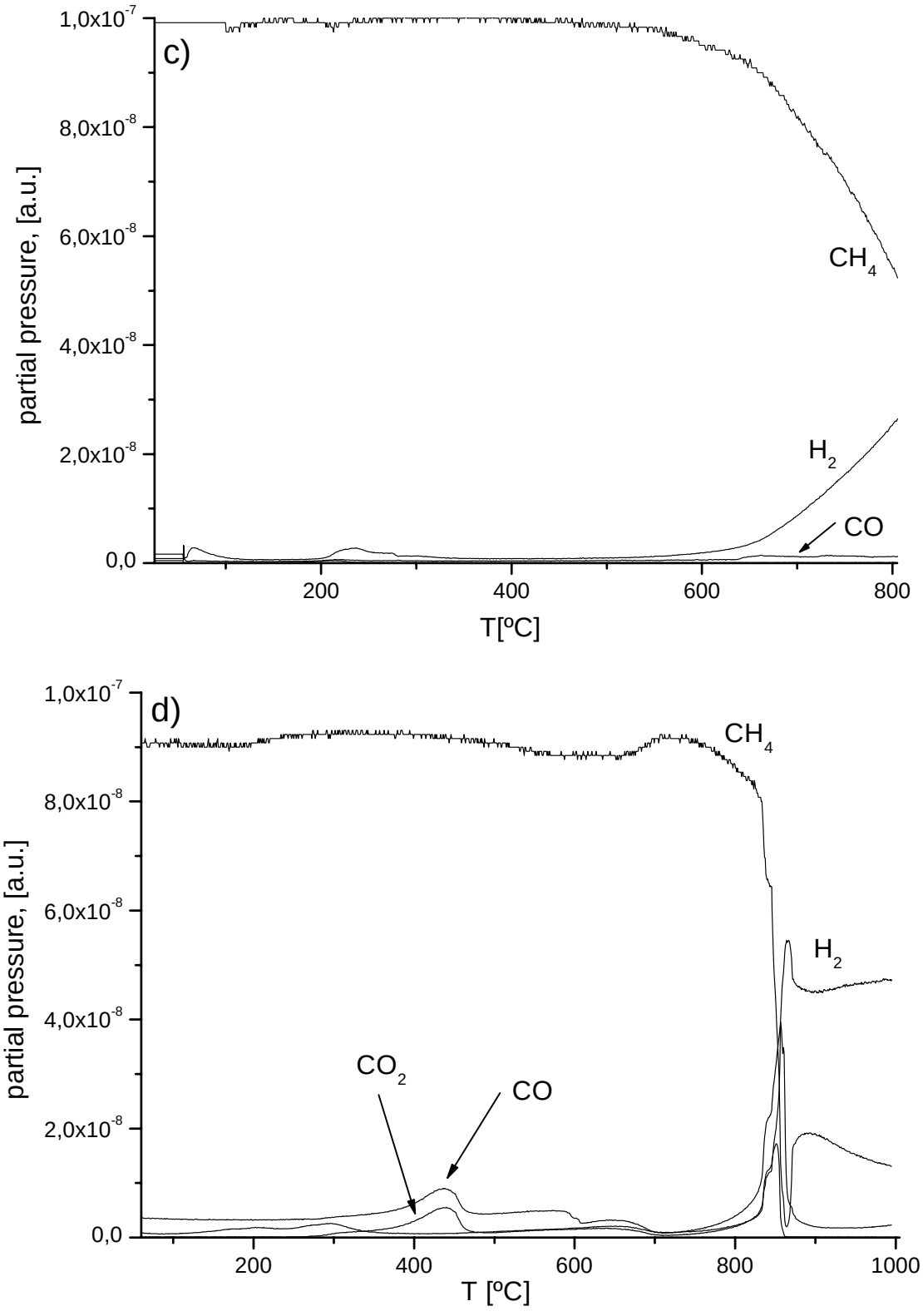



Fig. X.2 TPRe on Ni69 (a), Ni50 (b), Co50 (c) and Fe35 (d). Experimental conditions: 0.1 g catalyst, heating rate 5ºC/min, temperature range 25-1000 ºC and a flow rate of 27.5 $Ncm^3/min$ ($CH_4$/He = 0.1).

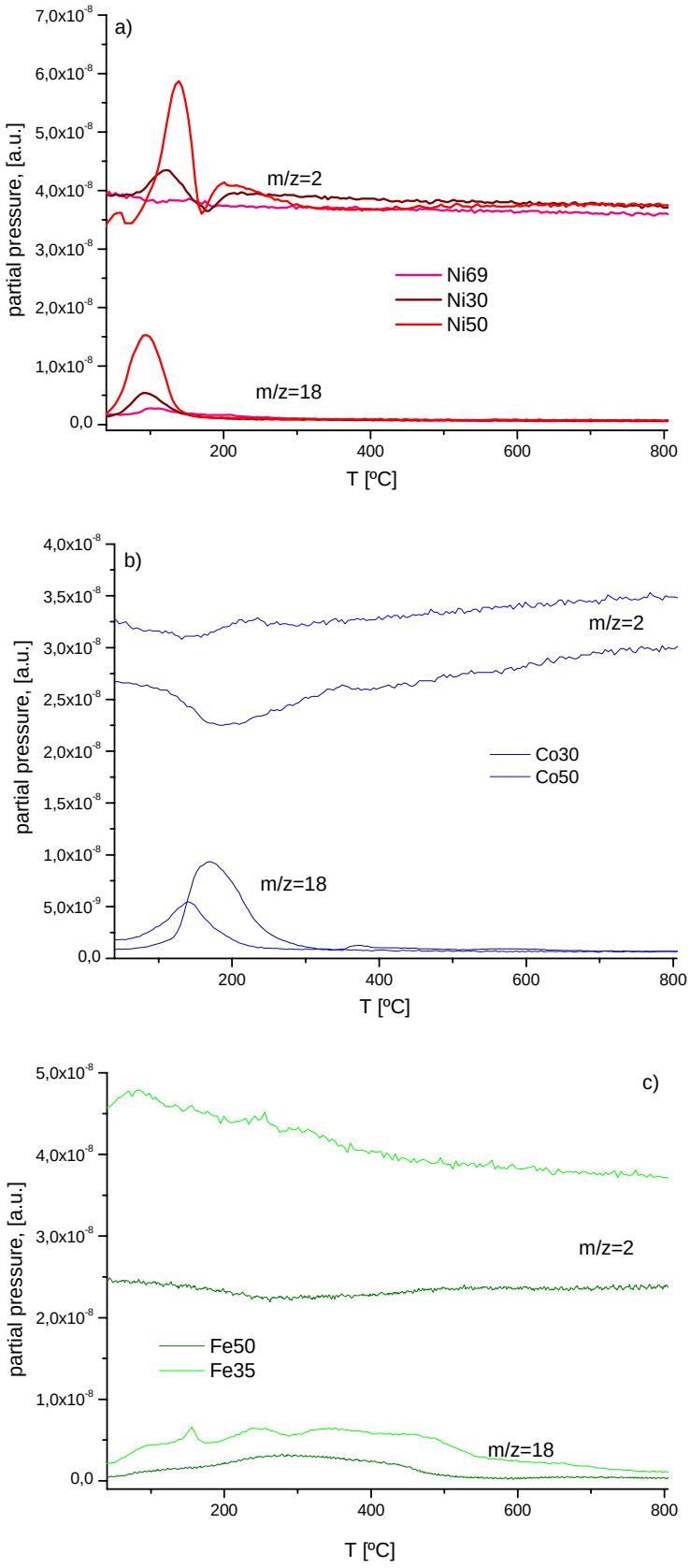
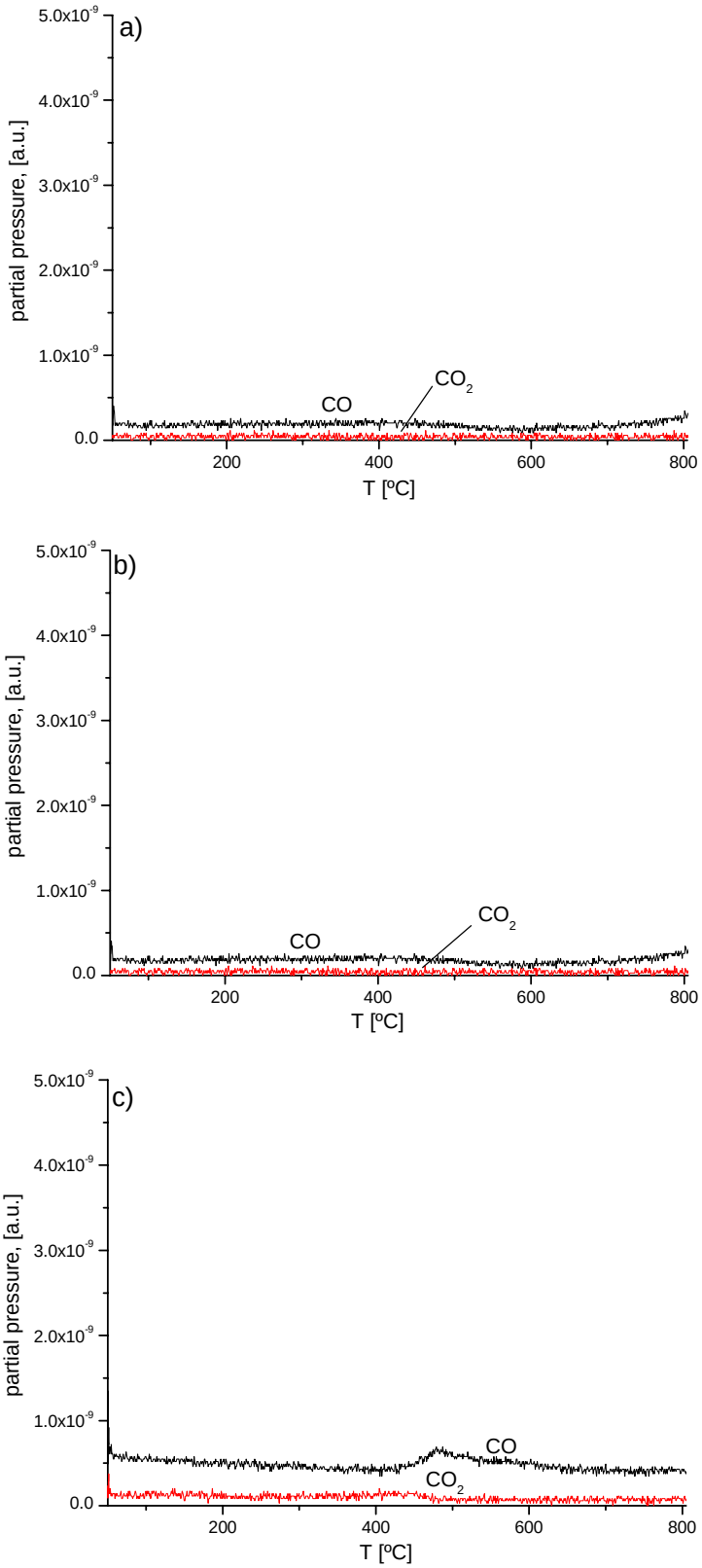



Fig. X.3 TPR on Ni69, Ni50, Ni30 (a), Co50, Co30 (b), Fe50 and Fe35 (c). Experimental conditions: 0.1 g catalyst, heating rate of 5 ºC/min, temperature range 25-800 ºC and a flow rate of 27.5 $Ncm^3/min$ ($H_2/He$ = 0.1).


a)
b)
c)
partial pressure, [a.u.]
T [ºC]
CO
CO2
5.0x10-9
4.0x10-9
3.0x10-9
2.0x10-9
1.0x10-9
0.0
200
400
600
800

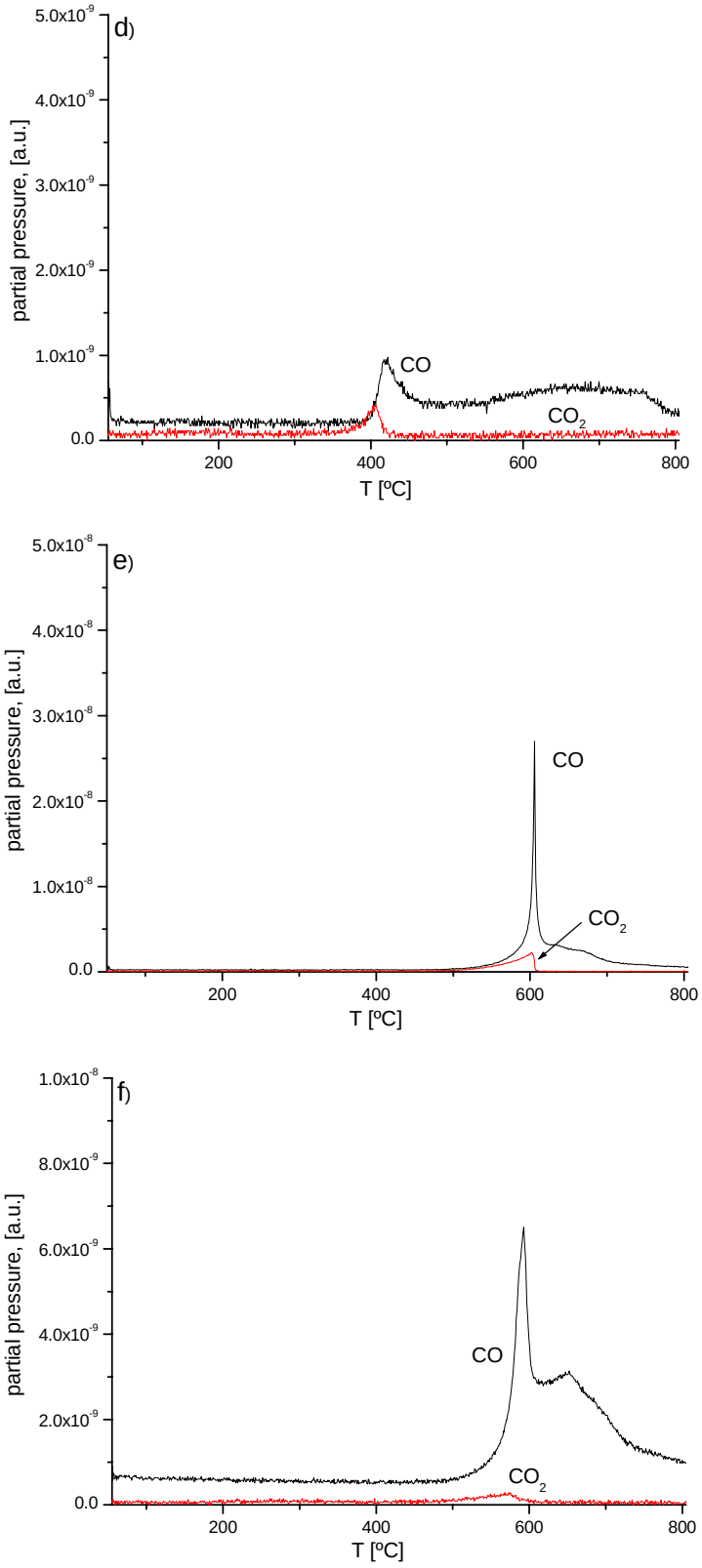



Fig. X.4 TPRe on HPT Ni50 (a), Ni30 (b), Co50 (c), Co30 (d), Fe50 (e) and Fe35 (g). Experimental conditions: 0.1 g catalyst, heating rate of 5ºC/min, temperature range 25-800ºC and a flow rate of 27.5 $Ncm^3/min$ ($CH_4$/He = 0.1).

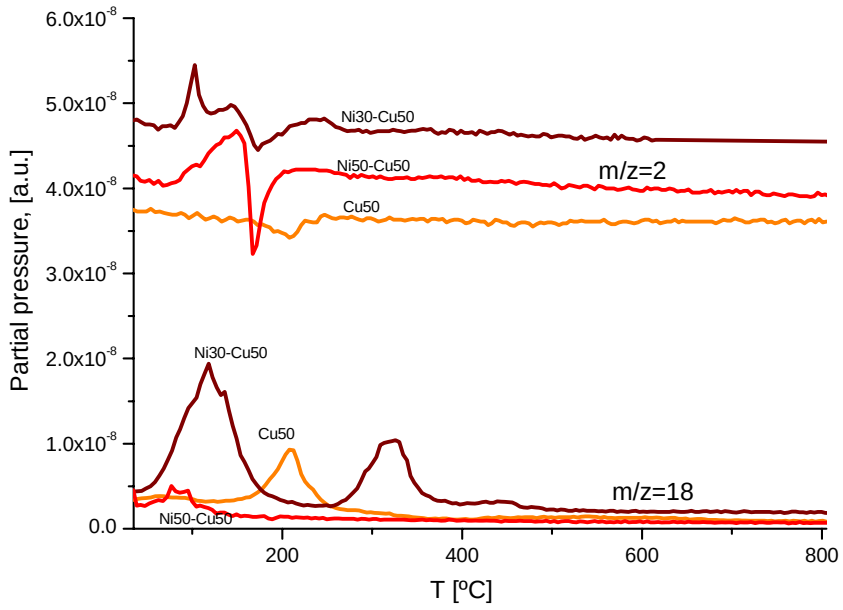



Fig. X.5 TPR on Cu50 (a), Ni30Cu50 (ITT) (b) and Ni50Cu50 (ITT) (c). Experimental conditions: 0.2 g catalyst, heating rate of 5 ºC/min, temperature range 30-800 ºC and a flow rate of 27.5 $Ncm^3$/min ($CH_4$/He = 0.1).

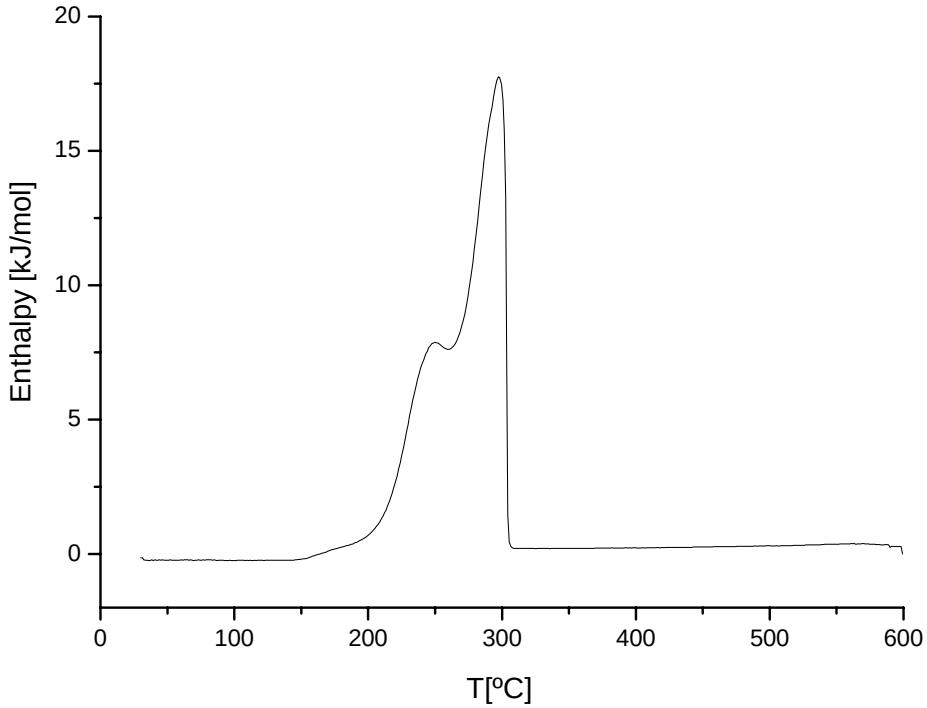



Fig. X.6 DSC on Cu50 catalyst. Experimental conditions: 0.5 g catalyst, heating rate of 5 ºC/min, temperature range 30-600 ºC and a flow-rate of 27.5 $Ncm^3$/min ($H_2$/He = 0.1).

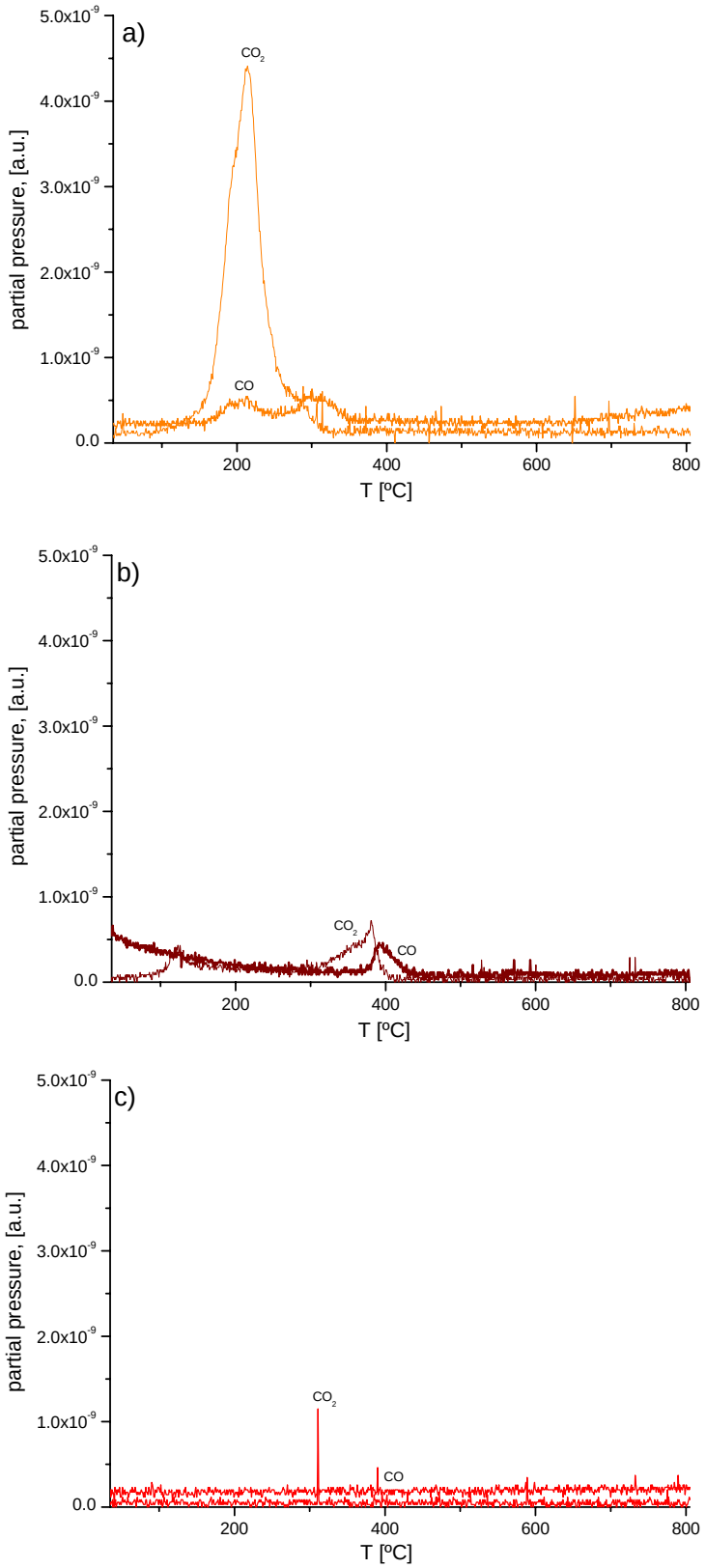



Fig. X.7 TPRe on Cu50 (a), Ni30Cu50 (IT*T) (b) and Ni50Cu50 (IT*T) (c). Experimental conditions: 0.2 g catalyst, heating rate of 5 ºC/min, temperature range 30-800 ºC and a flow rate of 27.5 $Ncm^3/min$ ($CH_4$/He = 0.1).

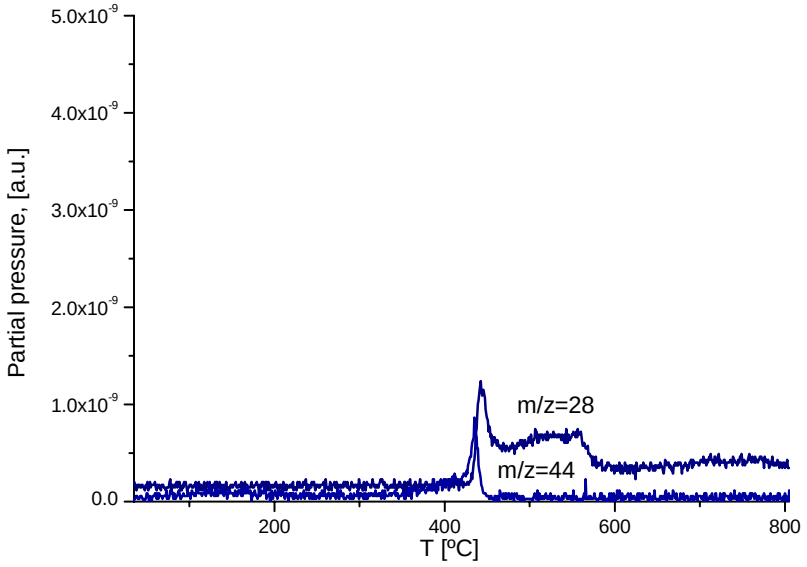



Fig. X.8 TPRe on Co30Cu50 (ITT). Experimental conditions: 0.2g catalyst, heating rate of 5 ºC/min, temperature range 30-800 ºC and a flow rate of 27.5 $Ncm^3/min$ ($CH_4$/He = 0.1).

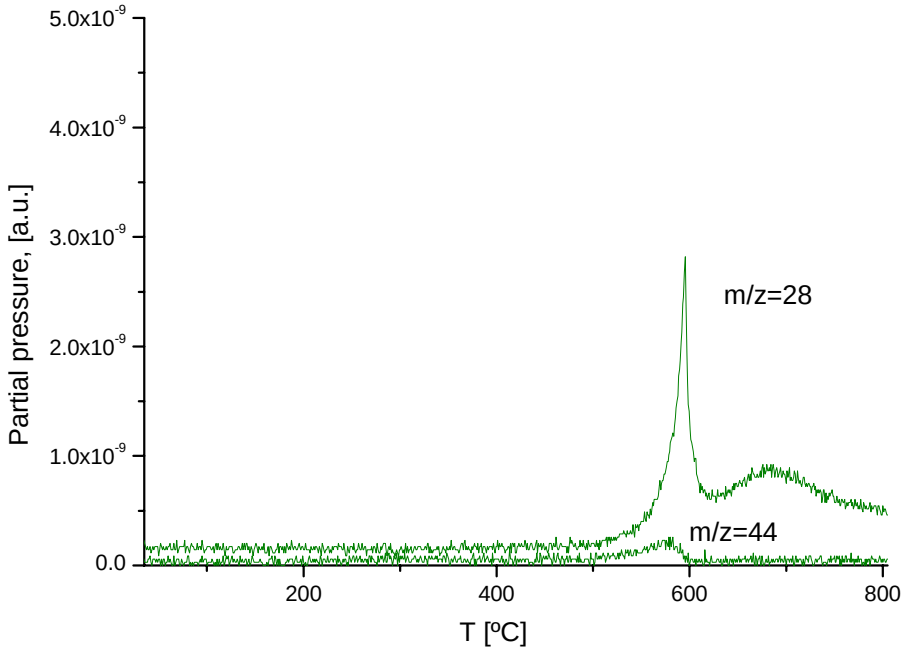



Fig. X.9 TPRe with Fe50Cu50 (ITT). Experimental conditions: 0.2g catalyst, heating rate of 5 ºC/min, temperature range 30-800 ºC and a flow rate of 27.5 $Ncm^3/min$ ($CH_4$/He = 0.1)

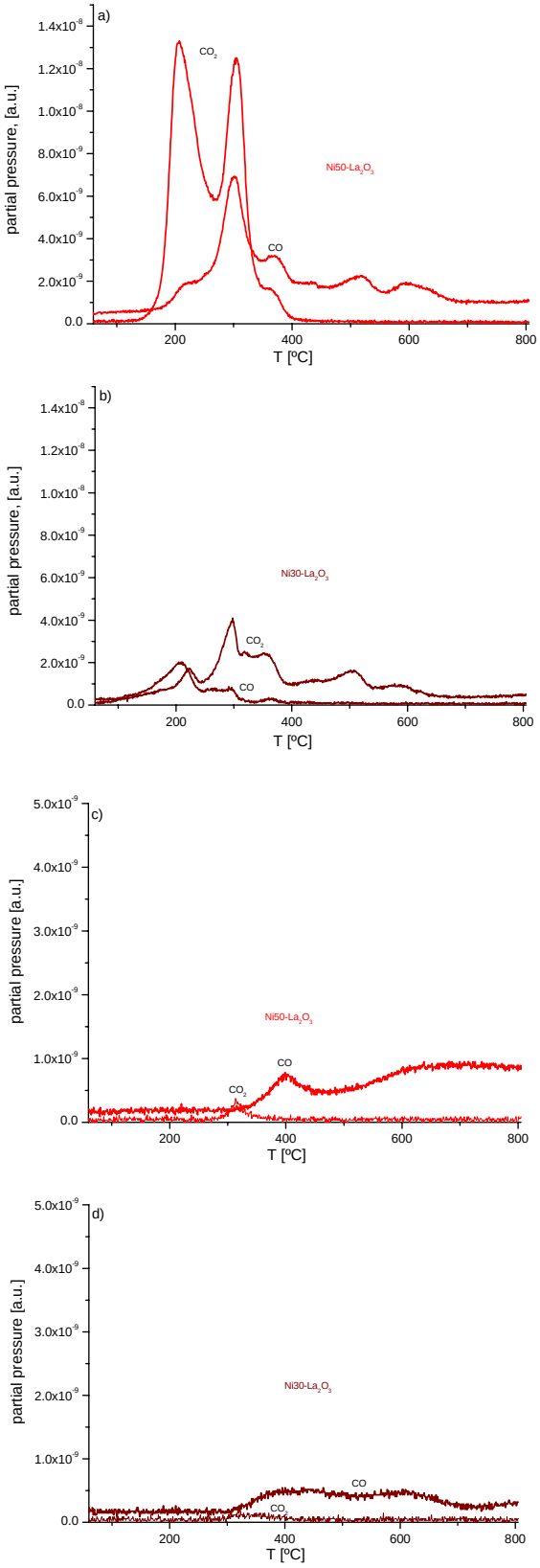



Fig. X.10 TPRe on Ni50-$La_2O_3$ (a), Ni50-$La_2O_3$ (HPT) (b), Ni30-$La_2O_3$ (c) and Ni30-$La_2O_3$ (HPT) (d). Experimental conditions: 0.62 g (a-b) and 0.56 g (c-d) of catalyst, heating rate of 5 ºC/min, temperature range 30-800 ºC and a flow-rate of 27.5 $Ncm^3$/min ($CH_4$/He = 0.1).

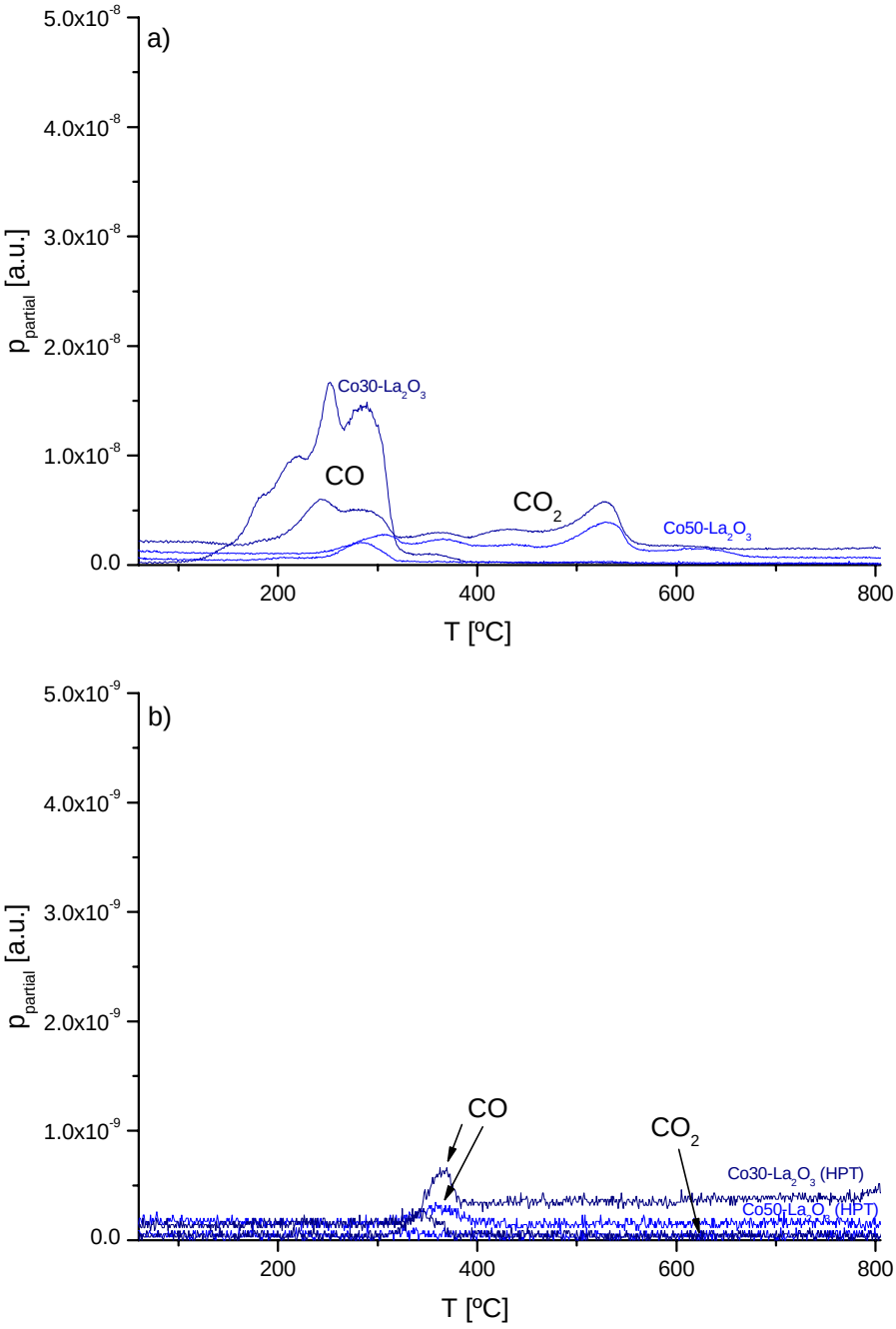



Fig. X.11 TPRe on Co30-$La_2O_3$, Co50-$La_2O_3$ (a) and Co30-$La_2O_3$ (HPT), Co50-$La_2O_3$ (HPT) (b). Experimental conditions: 0.62 g (0.12 g $La_2O_3$) of catalyst, heating rate of 5 ºC/min, temperature range 30-1000 ºC and a flow-rate of 27.5 $Ncm^3$/min ($CH_4$/He = 0.1).

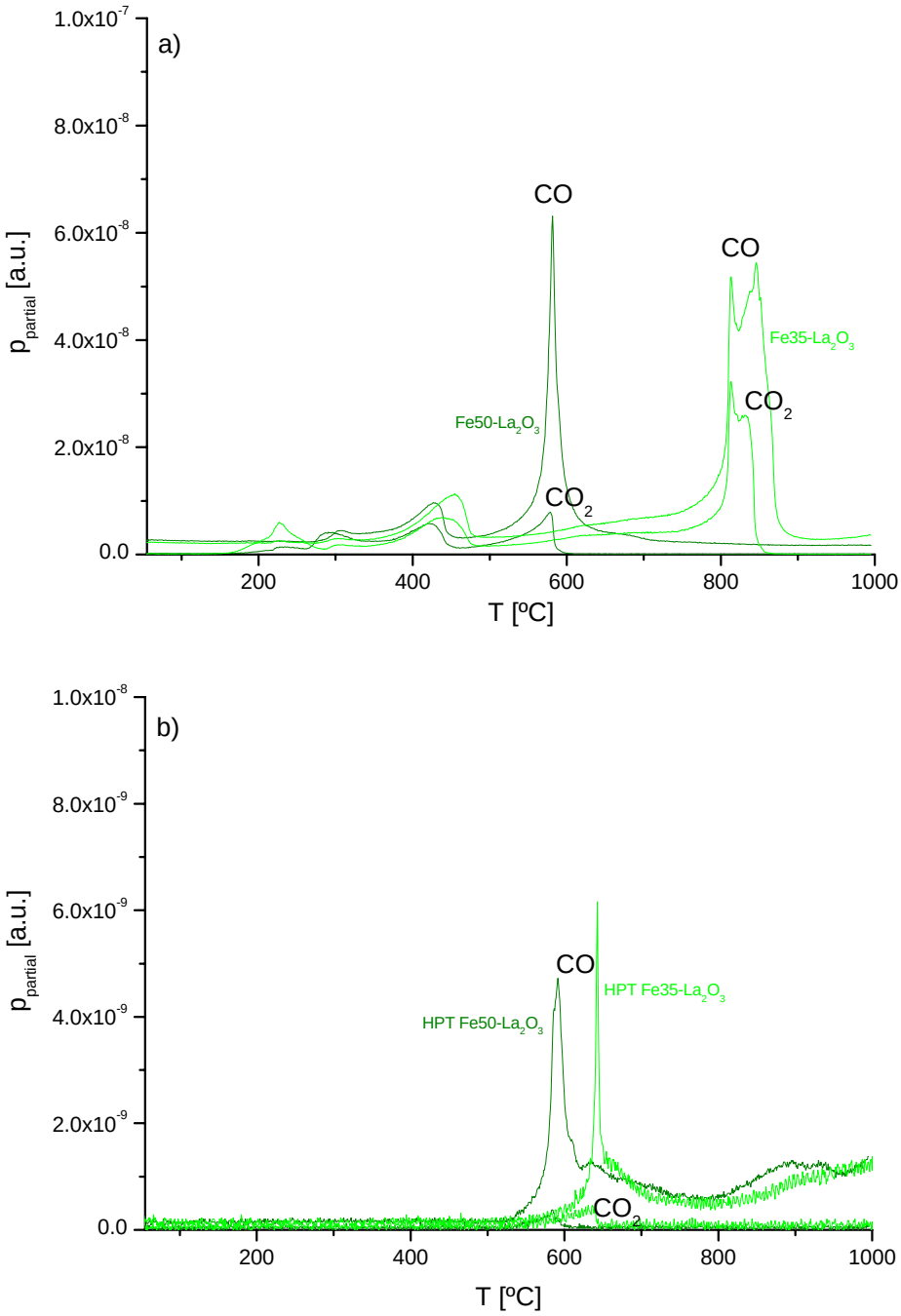



Fig. X.12 TPRe on Fe50-$La_2O_3$, Fe35-$La_2O_3$ (a) and Fe50-$La_2O_3$ (HPT), Fe35-$La_2O_3$ (HPT) (b). Experimental conditions: 0.62 g (0.12 g $La_2O_3$) of catalyst, heating rate of 5ºC/min, temperature range 30-1000ºC and a flow-rate of 27.5 $Ncm^3$/min ($CH_4$/He = 0.1).

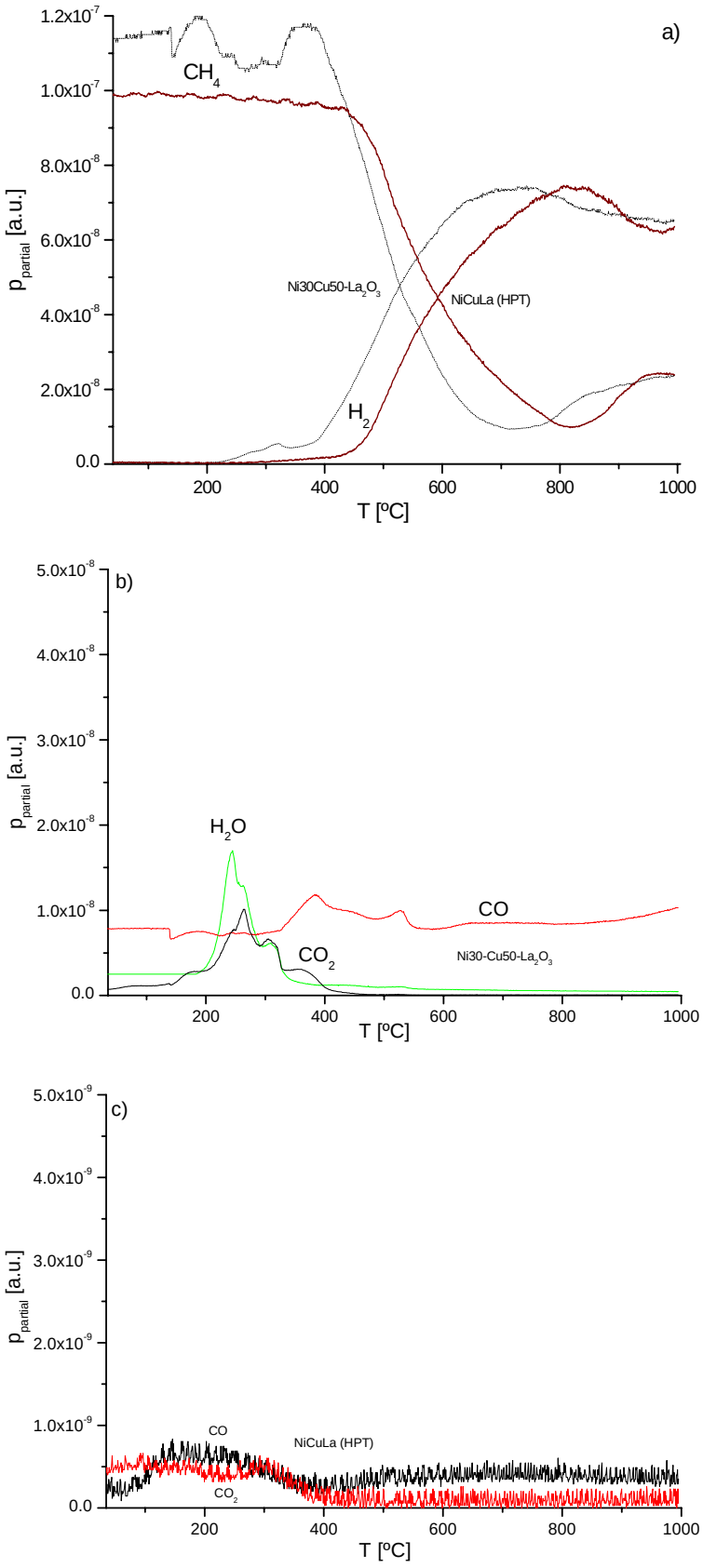



Fig. X.13 TPRe on $Ni30Cu50\text{-}La_2O_3$ (a,b) and NiCuLa (HPT) (a,c). Experimental conditions: 0.112 g of catalyst, heating rate of 5ºC/min, temperature range 30-1000 ºC and a flow-rate of 27.5 $Ncm^3$/min ($CH_4$/He = 0.1).

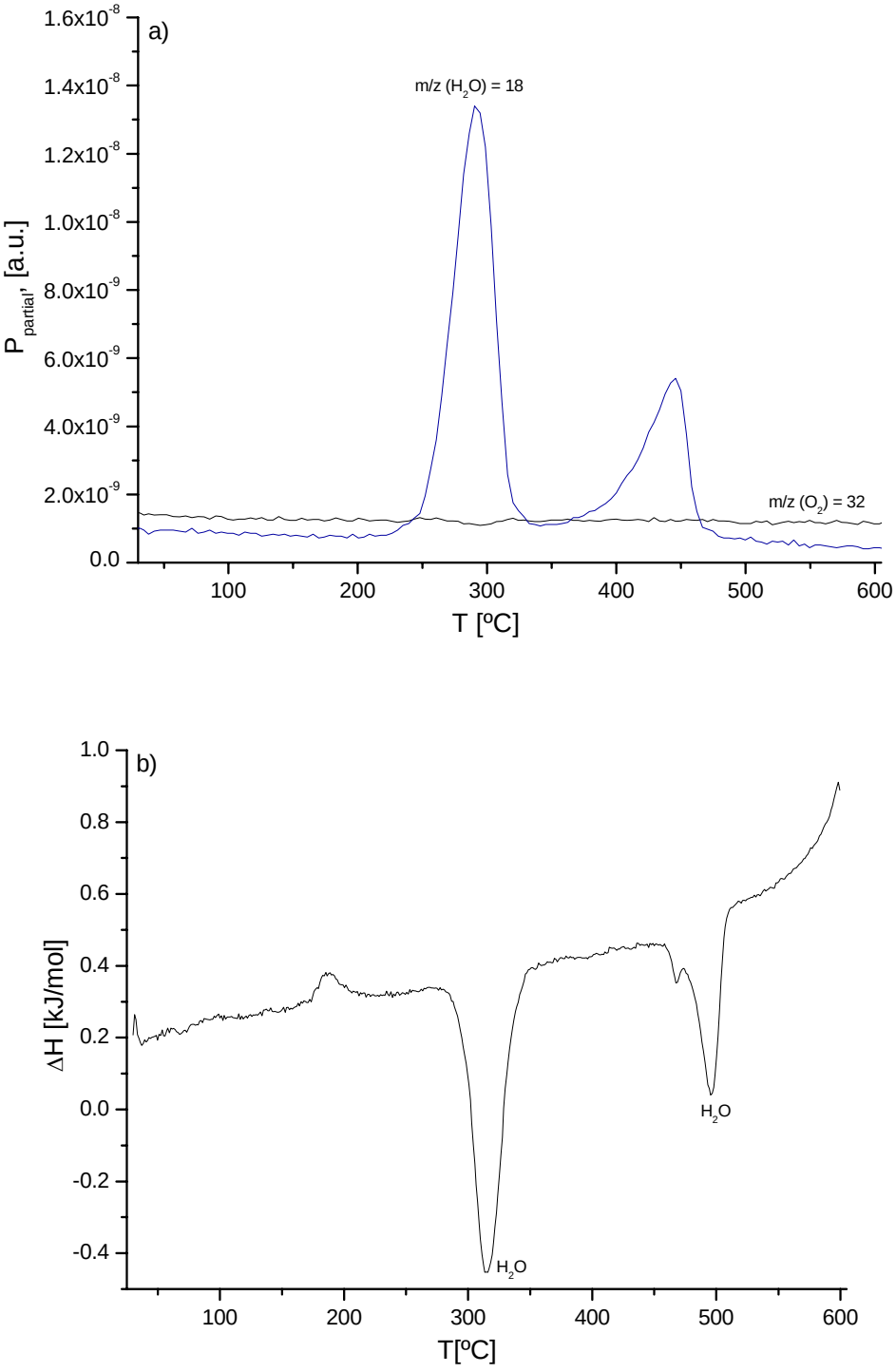



Fig. X.14 TPD (a) and DSC (b) on $La_2O_3$. Experimental conditions: 0.586 g, heating rate of 5 ºC/min, temperature range 30-600 ºC and a flow-rate of 27.5 $Ncm^3$/min ($H_2$/He = 0.1).

**XI. Isothermal reaction studies**

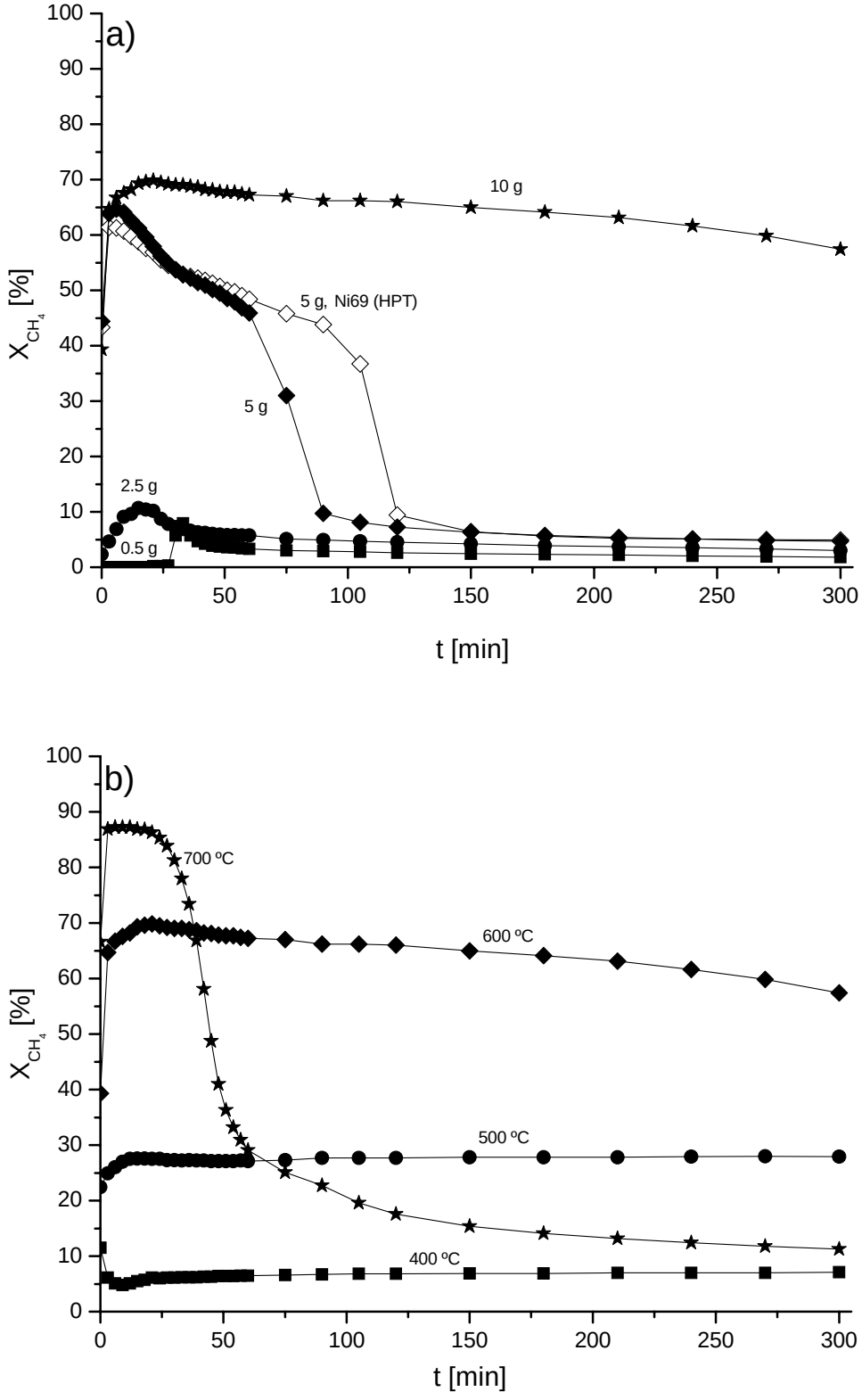



Fig. XI.1 Methane conversion as function of reaction time with Ni69 catalyst and a flow rate of 110 $Ncm^3/min$ ($CH_4/N_2$ = 0.1): Catalyst mass effect at 600 ºC (a), and temperature effect with 10 g of catalyst mass (b).

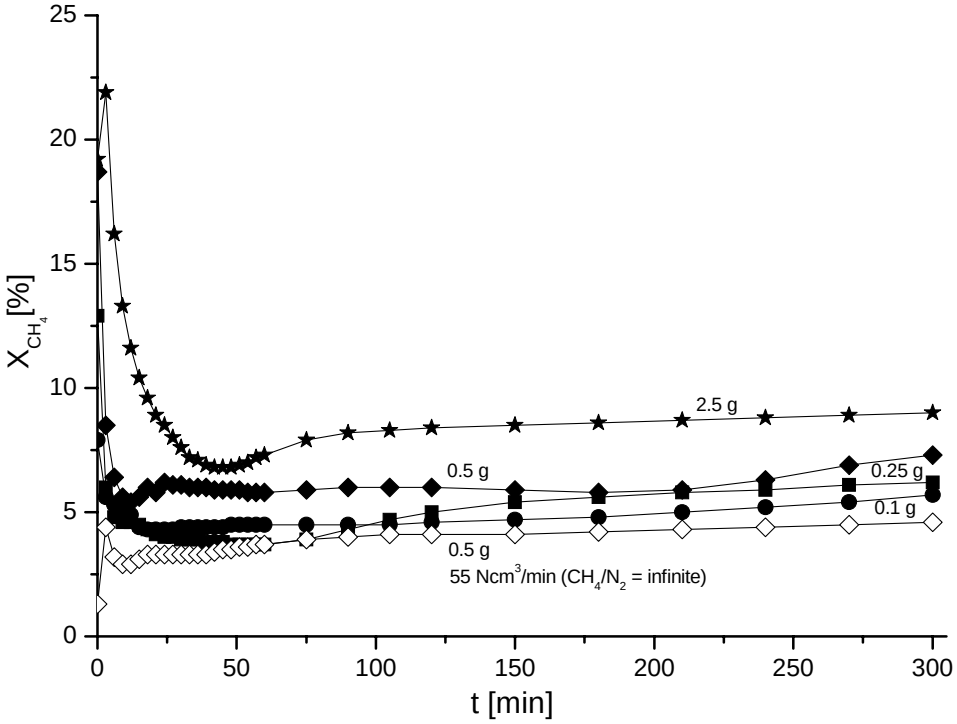



Fig. XI.2 Methane conversion as function of reaction time with Ni50 catalyst: Catalyst mass effect at 400 ºC and flow rate of 110 Ncm$^3$/min ($CH_4/N_2$ = 0.1).

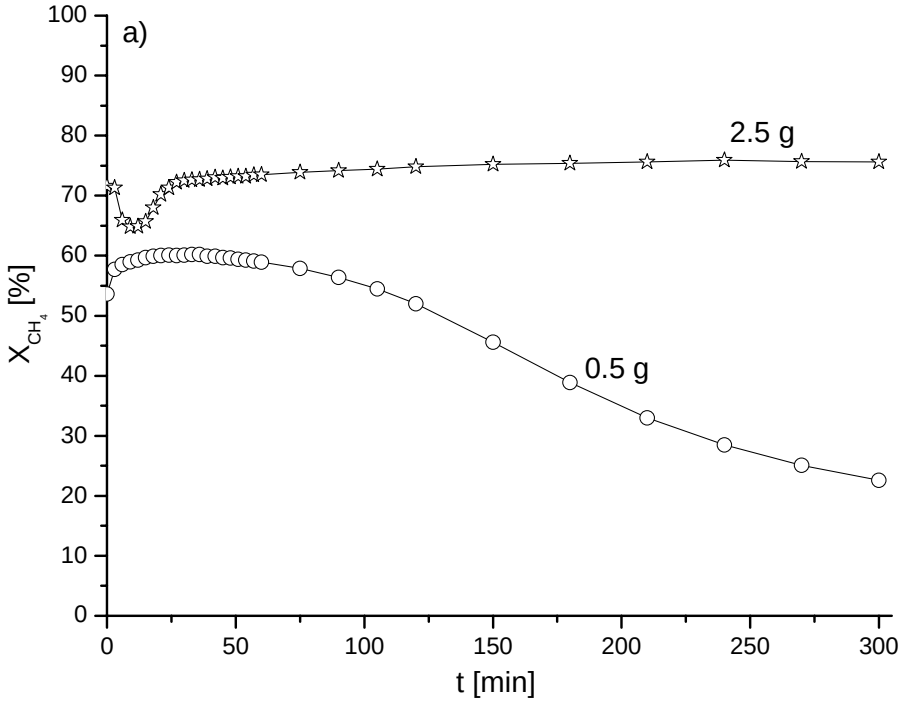



Fig. XI.3 Methane conversion as function of reaction time: Catalyst mass effect on Ni47-Mo6 at 600ºC and a flow rate of 110 Ncm$^3$/min ($CH_4/N_2$ = 0.1).

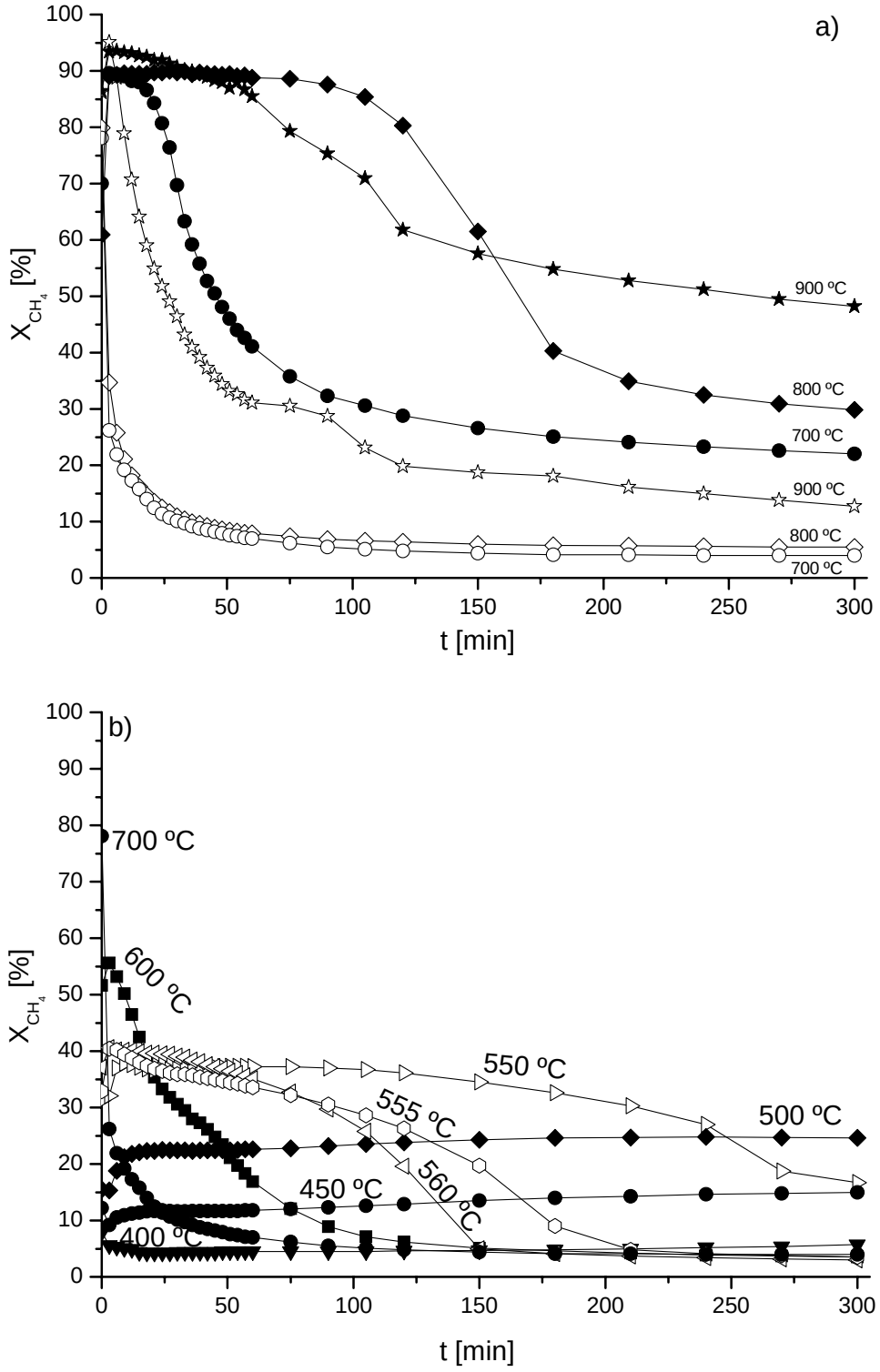



Fig. XI.4 Methane conversion as function of reaction time with Ni50 catalyst and a flow rate of 110 $Ncm^3/min$ ($CH_4/N_2$ = 0.1): a) Temperature effect with 0.5 g of catalyst mass; b) Temperature effect with 0.1 g of catalyst mass.

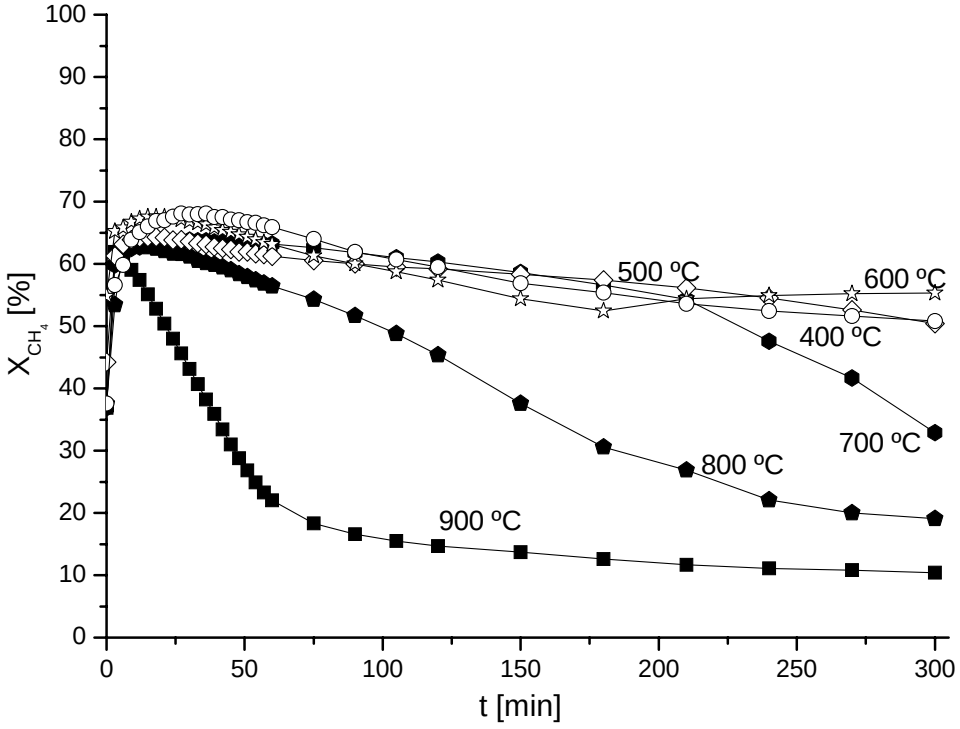



Fig. XI.5 Methane conversion as function of reaction time with Ni50 catalyst: Hydrogen pre-treatment effect with 0.5 g of catalyst mass at 600ºC and a flow rate of 110 $Ncm^3/min$ ($CH_4/N_2$ = 0.1).

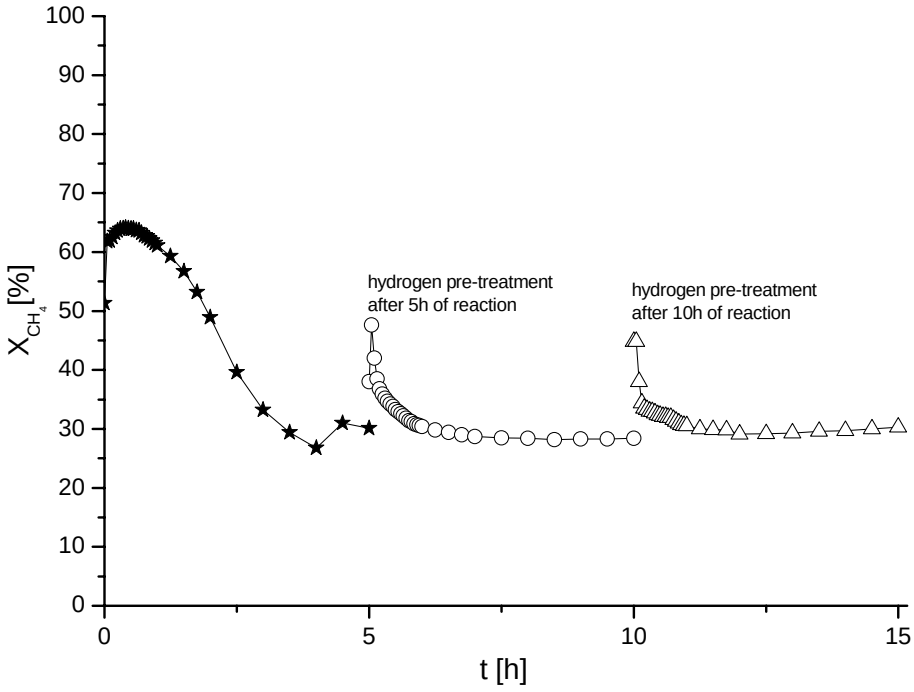



Fig. XI.6 Methane conversion as function of reaction time with Ni50 catalyst: Hydrogen re-generation effect after 5 h and 10 h of reaction on 0.5 g of catalyst mass at 600ºC and a flow rate of 110 $Ncm^3/min$ ($CH_4/N_2$ = 0.1).

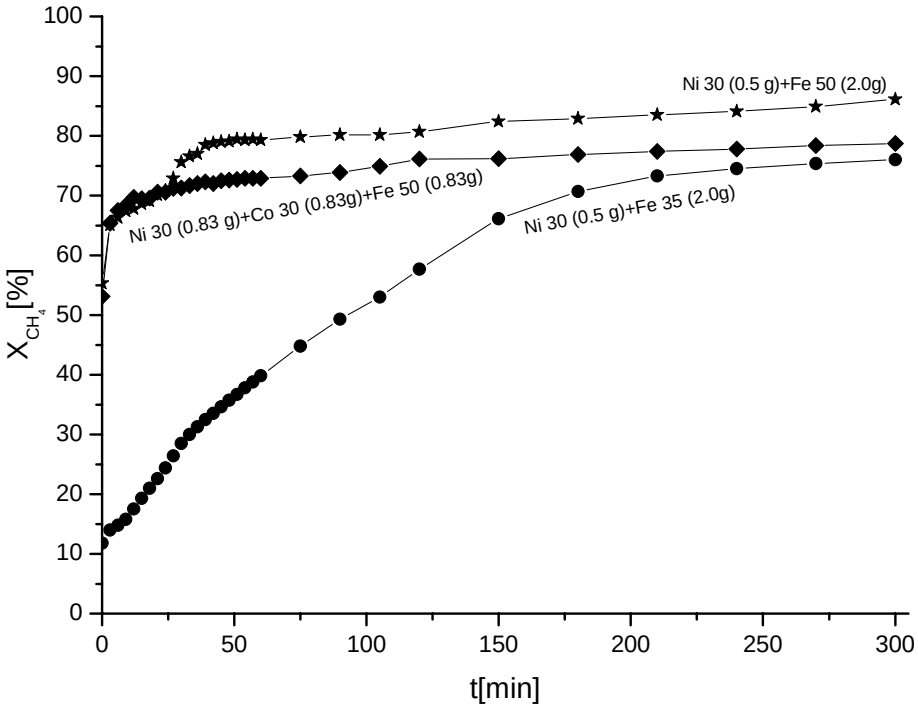



Fig. XI.7 Methane conversion as function of reaction time: Effect of catalyst mixtures at 600 ºC, with 2.5 g of catalyst mass and a flow rate of 110 $Ncm^3/min$ ($CH_4/N_2$ = 0.1).

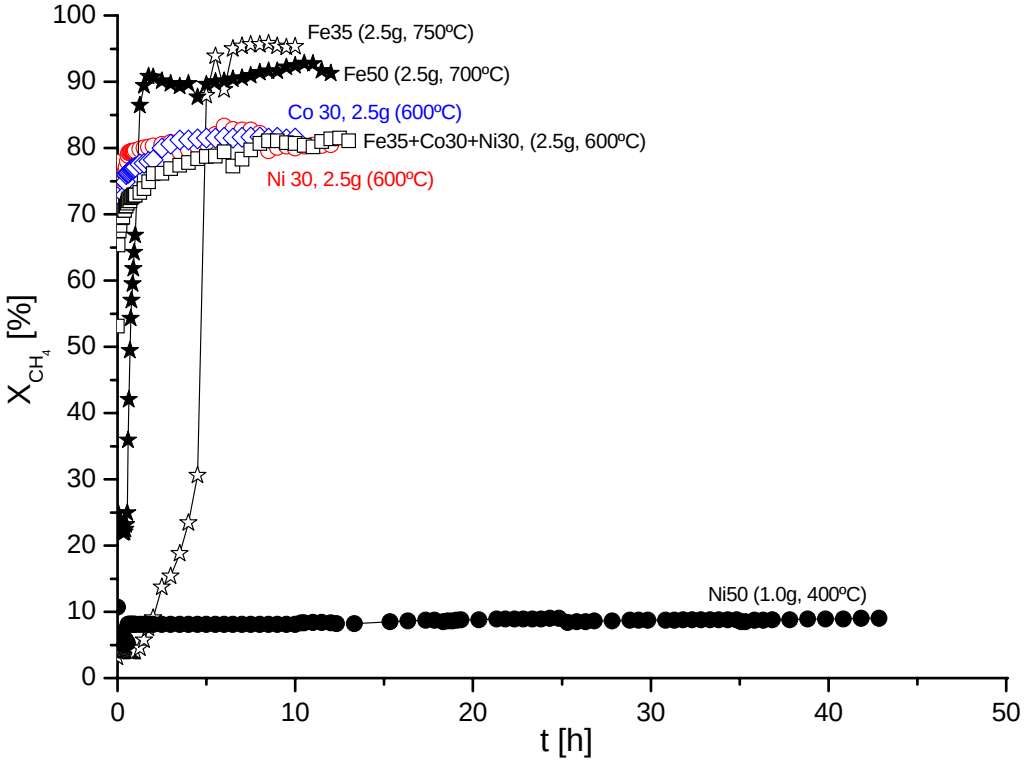



Fig. XI.8 Methane conversion as function of reaction time: Long time measurements at a flow rate of 110 $Ncm^3/min$ ($CH_4/N_2$ = 0.1).

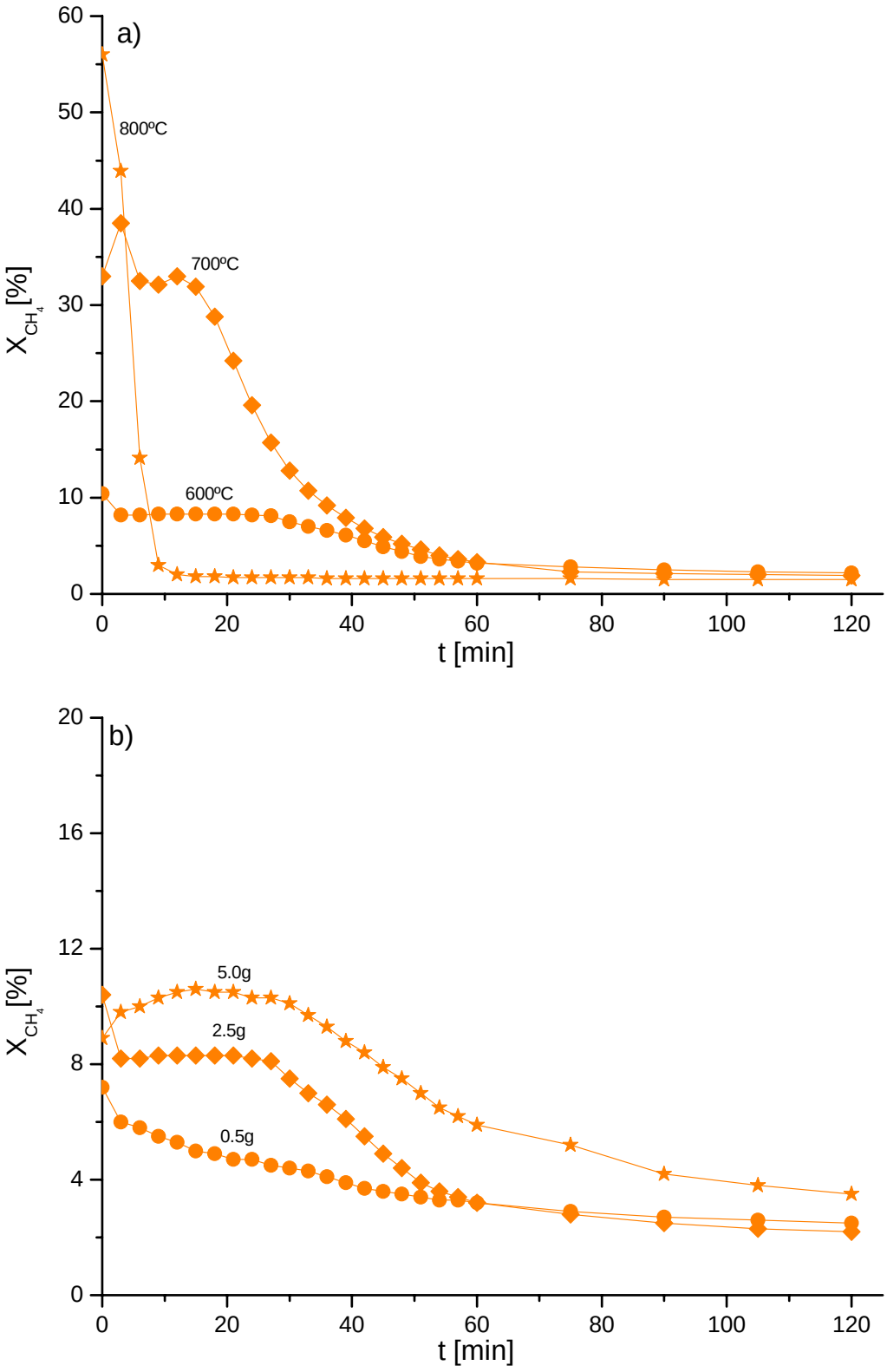



Fig. XI.9 Methane conversion as function of reaction time with a flow rate of 110 $Ncm^3/min$: a) Temperature effect with 2.5 g of catalyst mass; b) Catalyst mass effect at 600ºC.

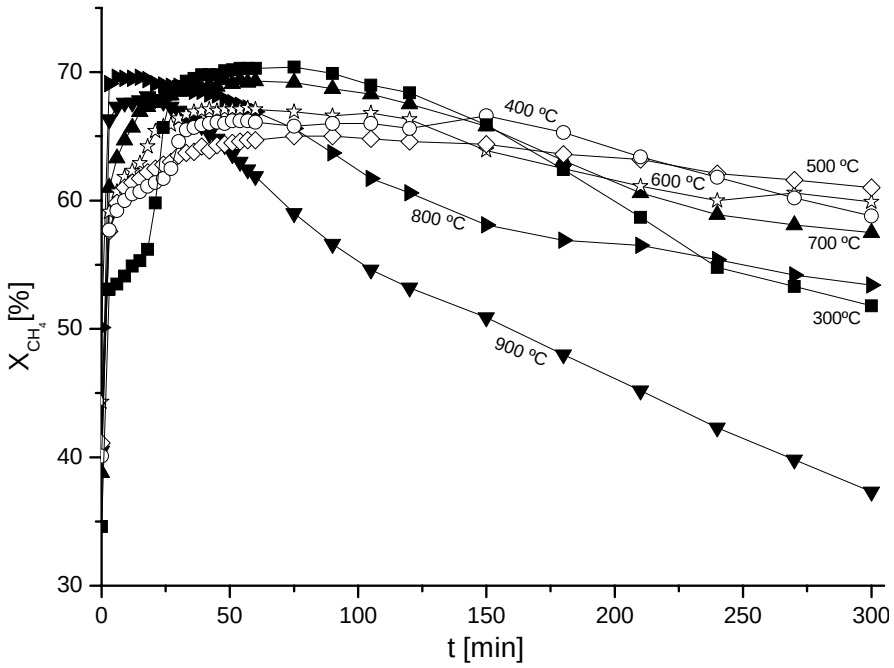



Fig. XI.10 Methane conversion as function of reaction time with 1.0 g (0.5 g Cu50) of catalyst mass at 600ºC and a flow rate of 110 $Ncm^3$/min: Effect of the thermal treatment temperature on Ni30Cu50 (ITT).

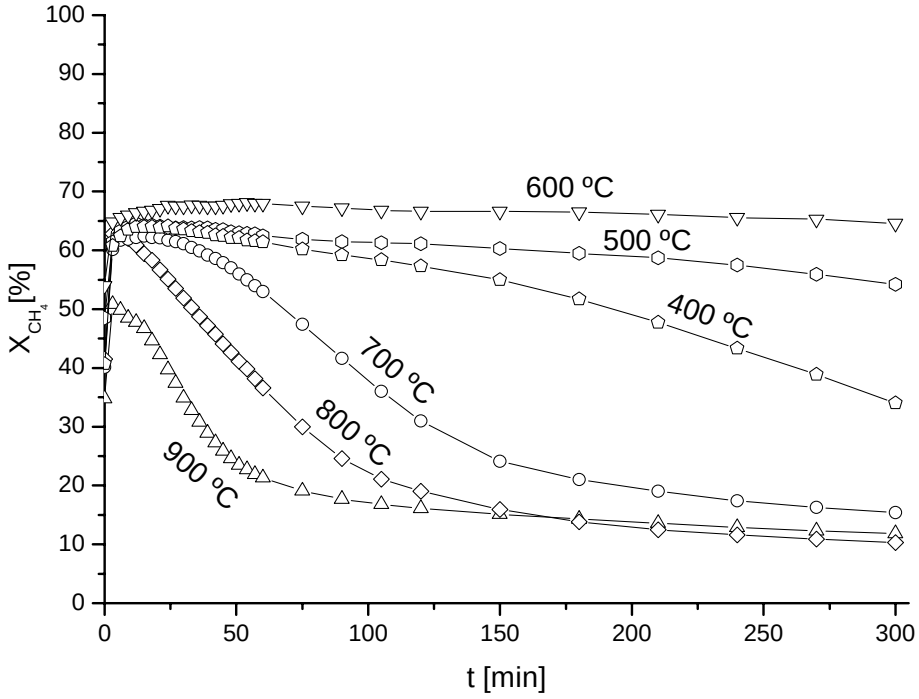



Fig. XI.11 Methane conversion as function of reaction time with Ni50-$La_2O_3$: Effect of hydrogen pre-treating temperature with 0.62 g (0.12 g $La_2O_3$) of catalyst mass and a flow-rate of 110 $Ncm^3$/min ($CH_4/N_2$ = 0.1).

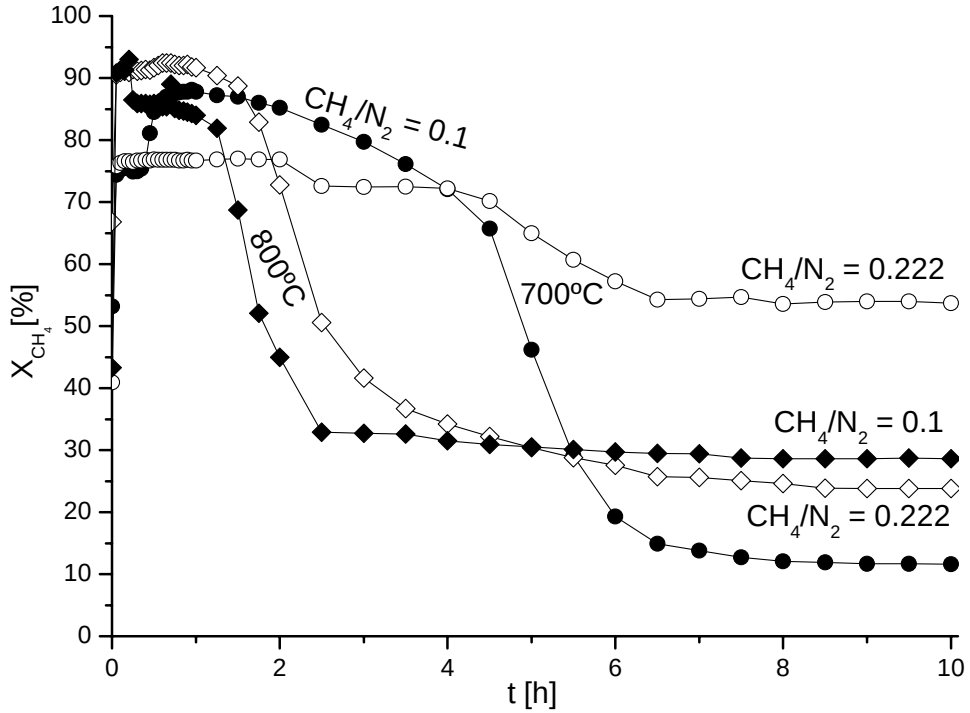



Fig. XI.12 Methane conversion as function of reaction time with NiCuLa (HPT): Feed composition effect with 1.12g of catalyst and and a total flow-rate of 110 $Ncm^3/min$.

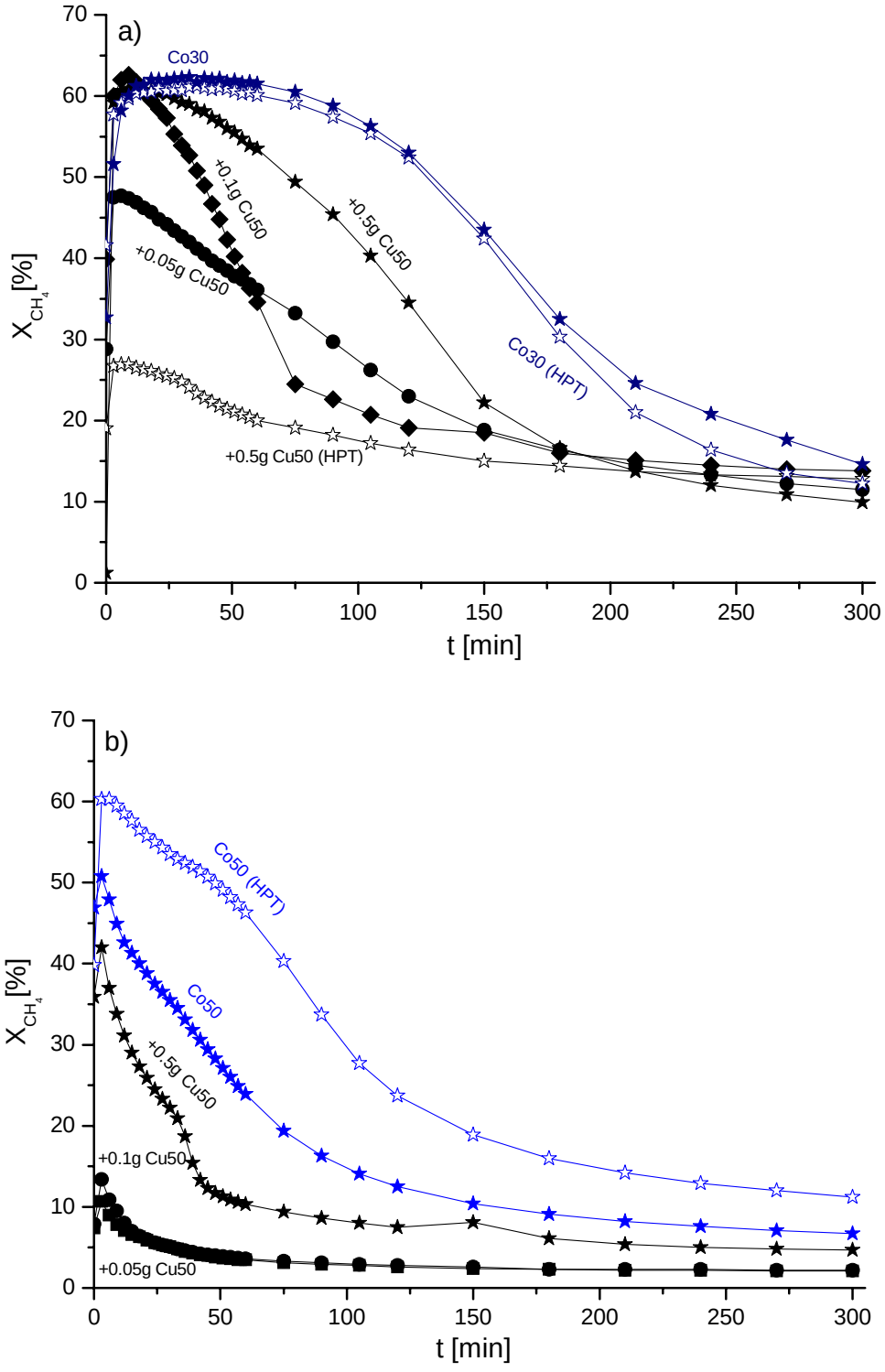



Fig. XI.13 Methane conversion as function of reaction time at 600ºC and a flow rate of 110 $Ncm^3$/min: a) Mass composition effect on Co30Cu50 (ITT) (filled symbols) and Co30Cu50 (HPT) (open symbols) catalyst mixtures with 0.5 g of Co30; b) Mass composition effect on Co50Cu50 (ITT) catalyst mixtures with 0.5 g of Co50.

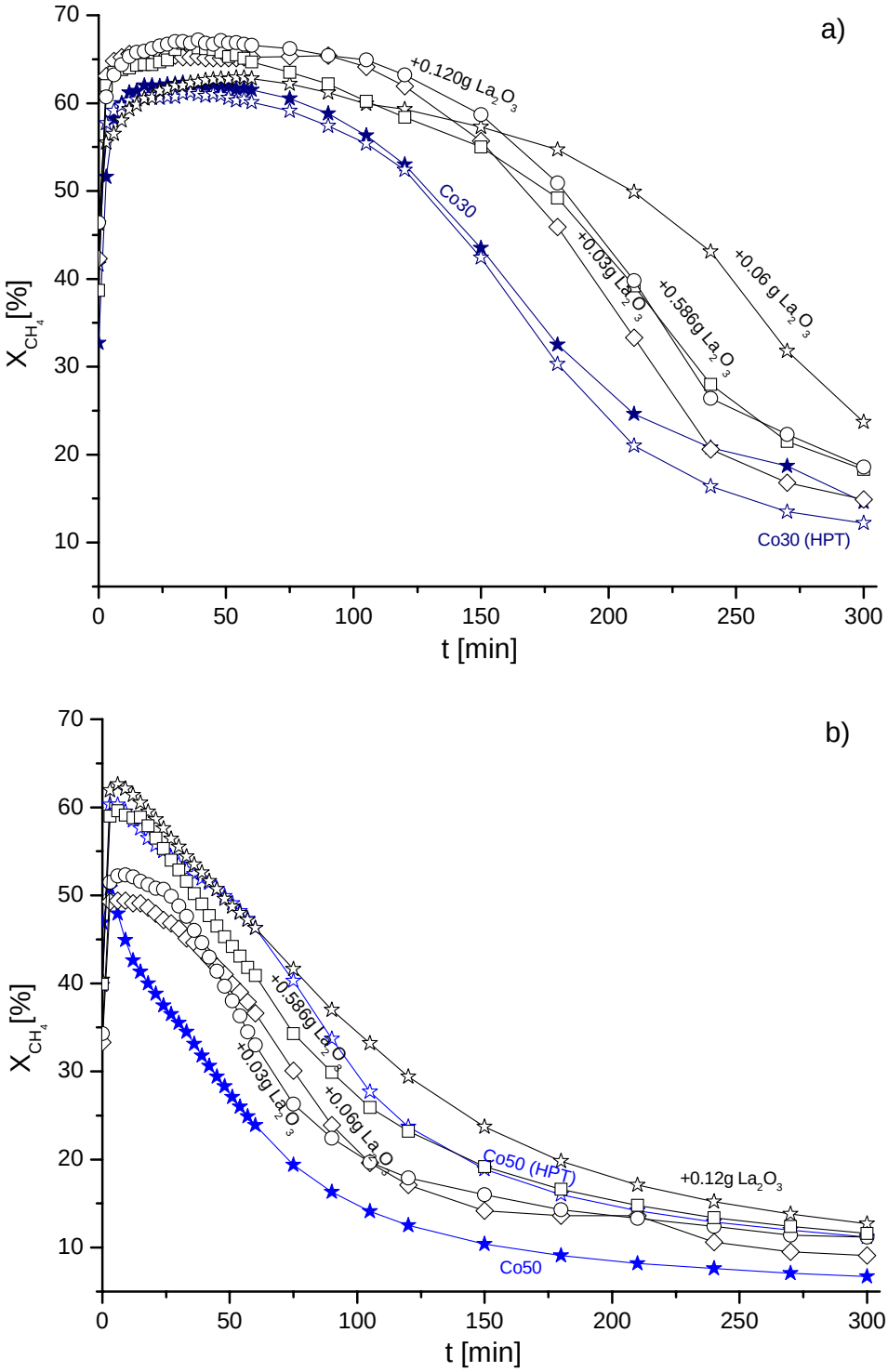



Fig. XI.14 Methane conversion as function of reaction time with Co-$La_2O_3$ (HPT) at 600 ºC and flow-rate of 110 $Ncm^3/min$ ($CH_4/N_2$ = 0.1): a) Mass composition effect with 0.5 g Co30. b) Mass composition effect with 0.5 g Co50.

## XII. SEM, TEM and XRD analysis of the composite materials

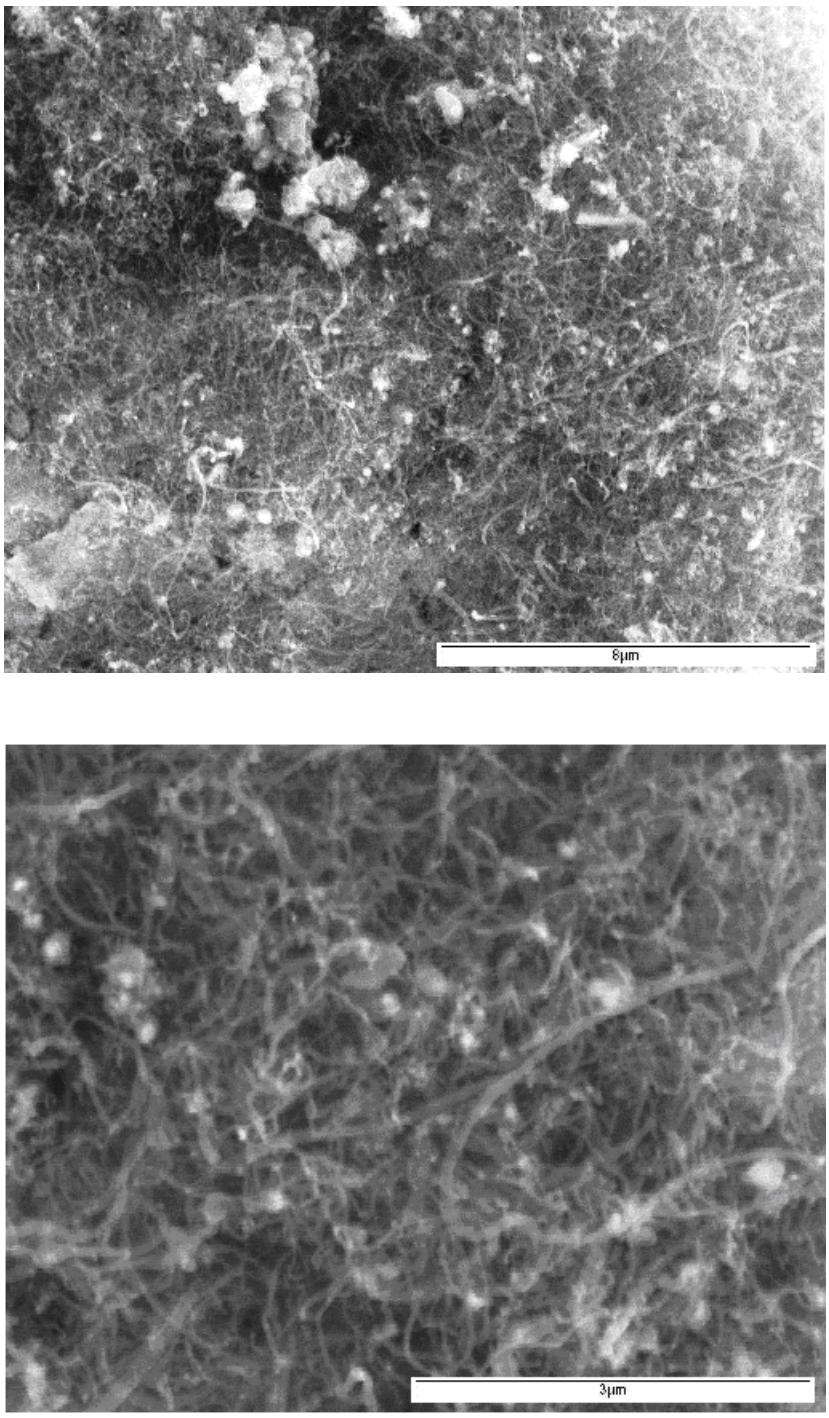



Fig. XII.1 SEM micrographs of carbon deposits obtained on Ni69 catalyst: 600 ºC of reaction temperature, 10 g of catalyst mass and a flow rate of 110 $cm^3$/min ($CH_4/N_2$ = 0.1).

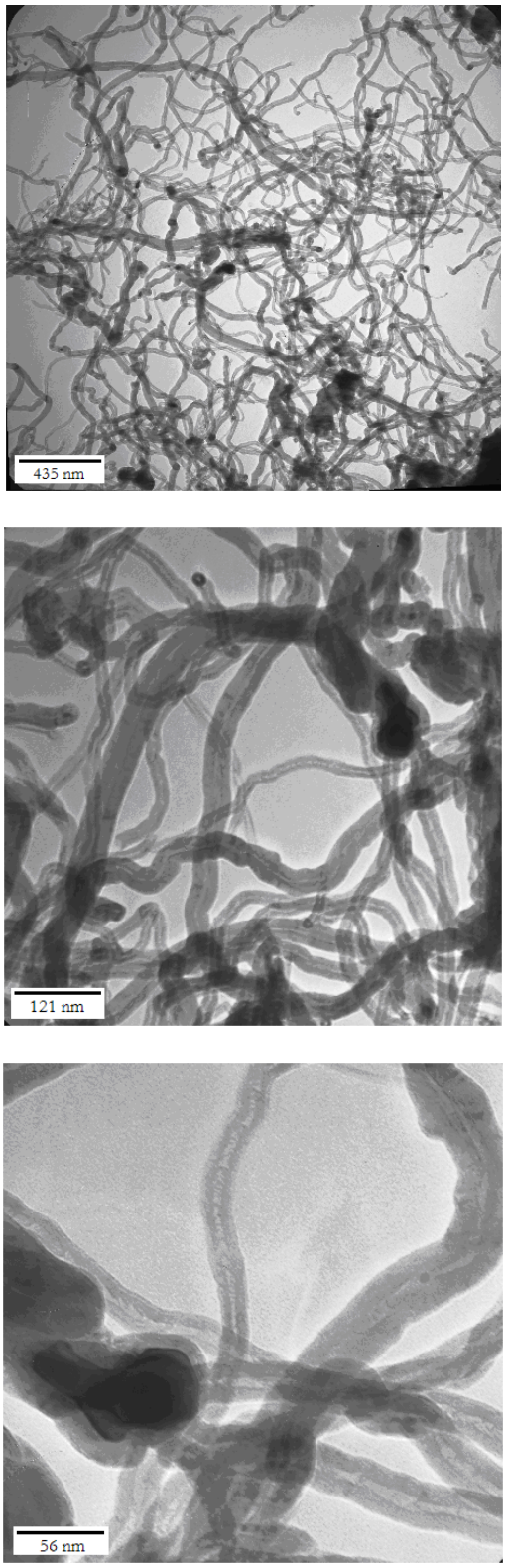
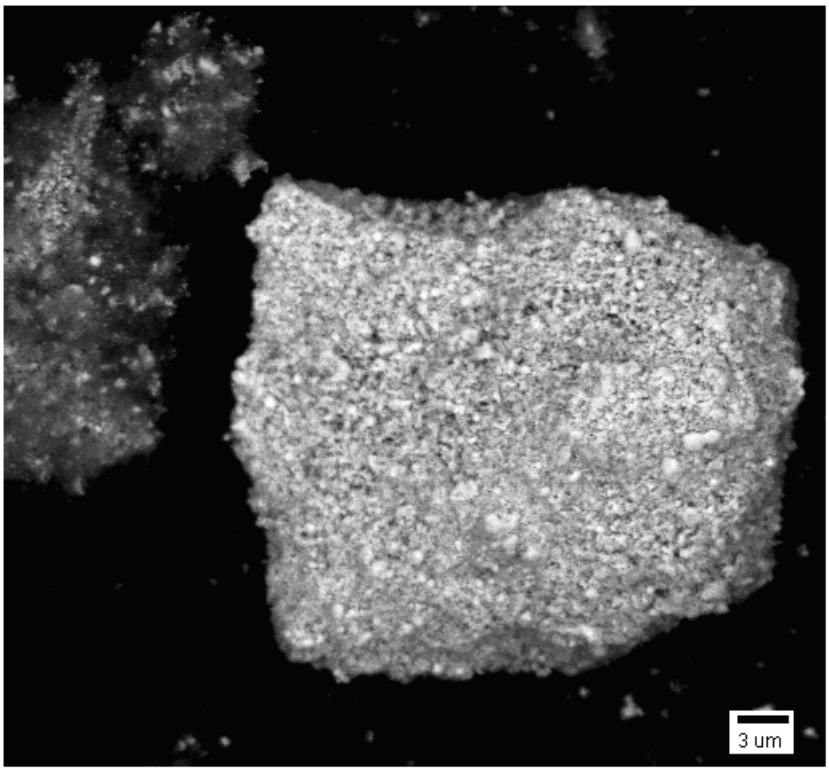
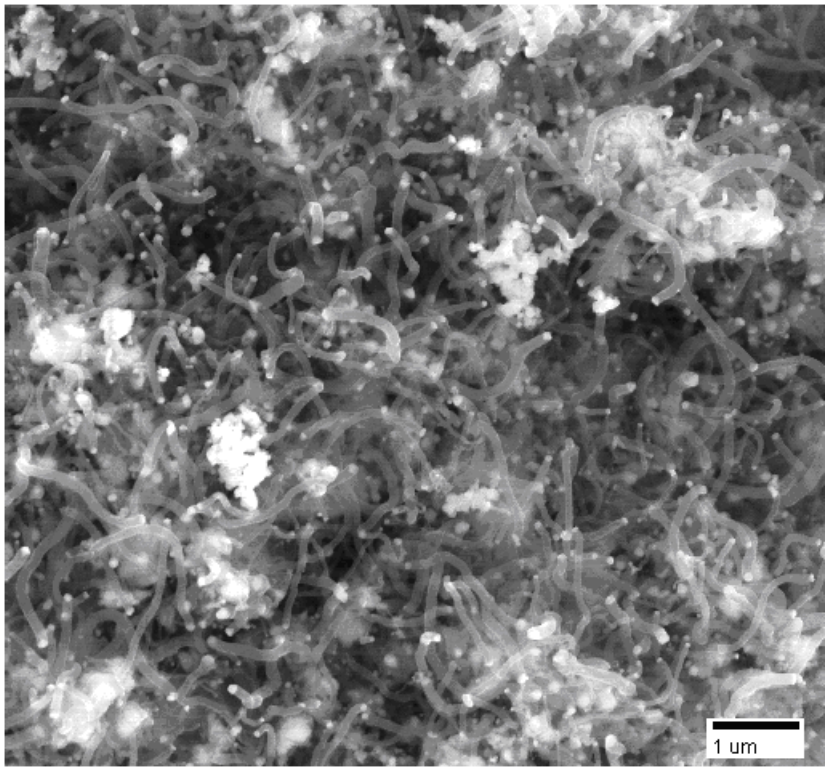


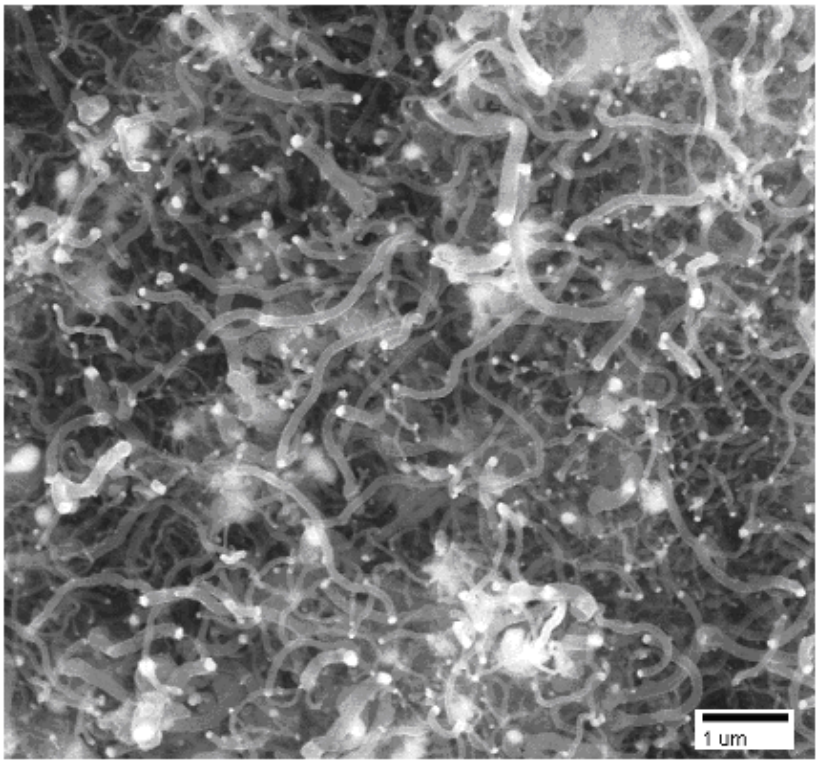

Fig. XII.2 TEM micrographs of carbon deposits obtained on Ni69 catalyst: 600 ºC of reaction temperature, 10 g of catalyst mass and a flow rate of 110 $cm^3$/min ($CH_4/N_2$ = 0.1).



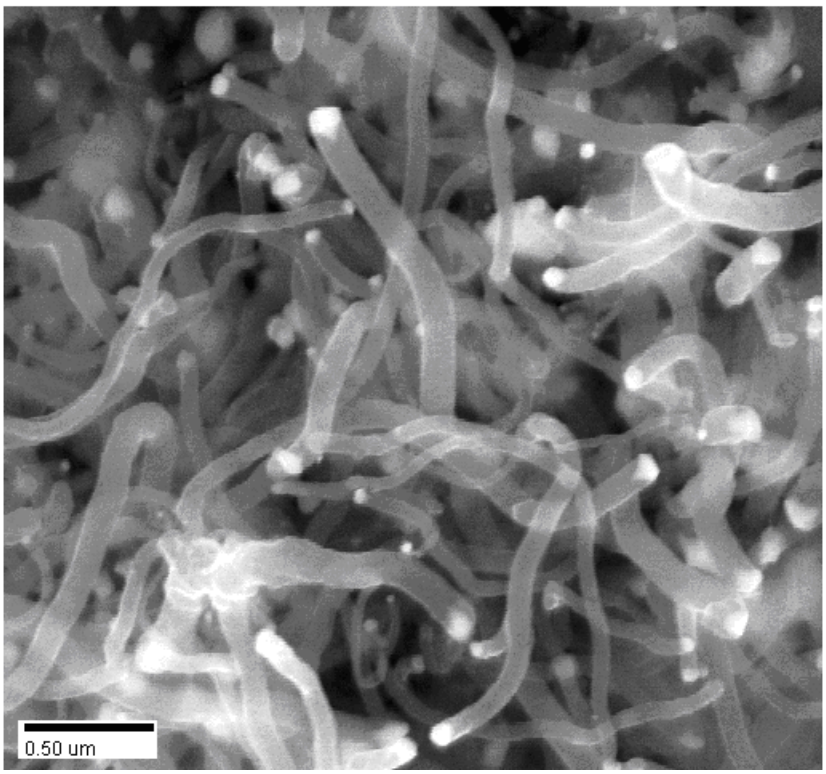

a)




b)

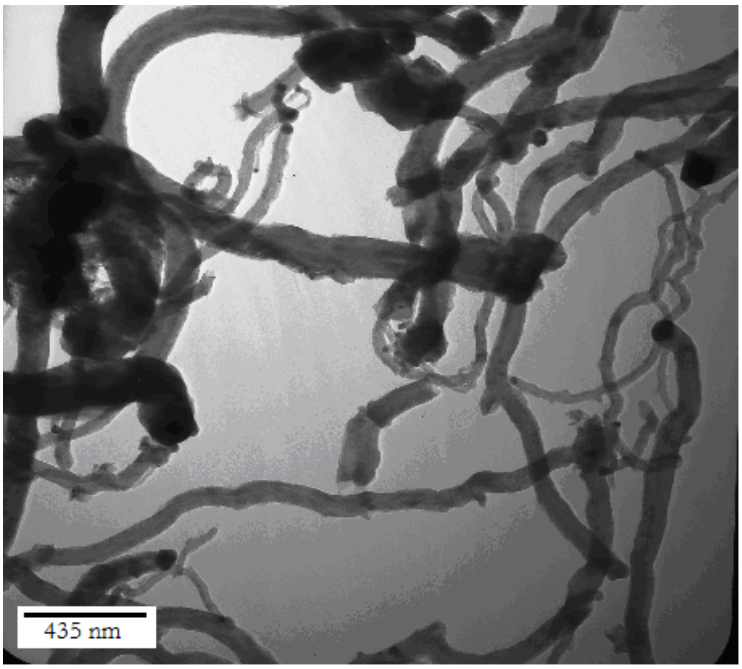



c)




d)

Fig. XII.3 SEM micrographs of carbon deposits obtained on Ni50 catalyst: 400 ºC of reaction temperature, (a-b) 0.5 g and (c-d) 1.0 g of catalyst mass and a flow rate of 110 $cm^3$/min ($CH_4/N_2$ = 0.1).



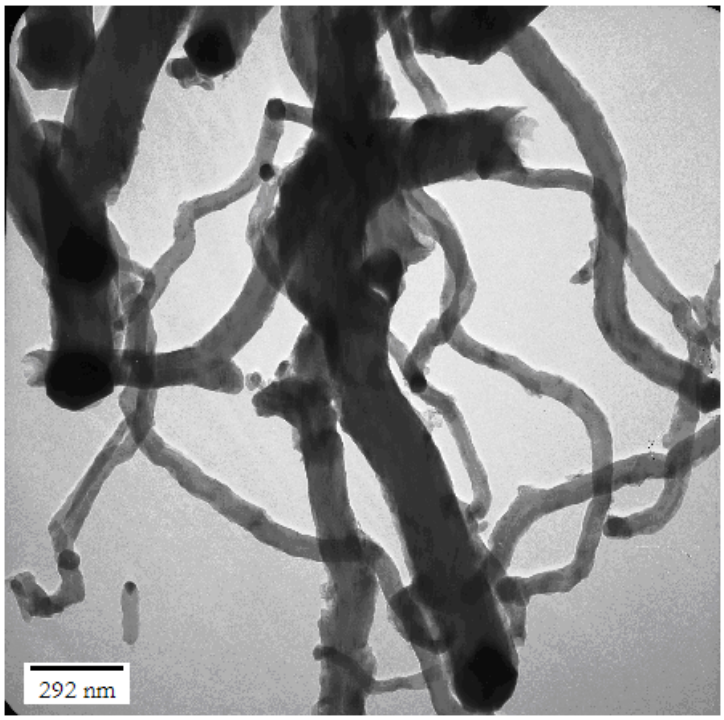




Fig. XII.4 TEM micrograph of carbon deposits obtained on Ni50 catalyst: 400 ºC of reaction temperature, 0.5 g of catalyst mass and a flow rate of 110 $cm^3$/min ($CH_4/N_2$ = 0.1).

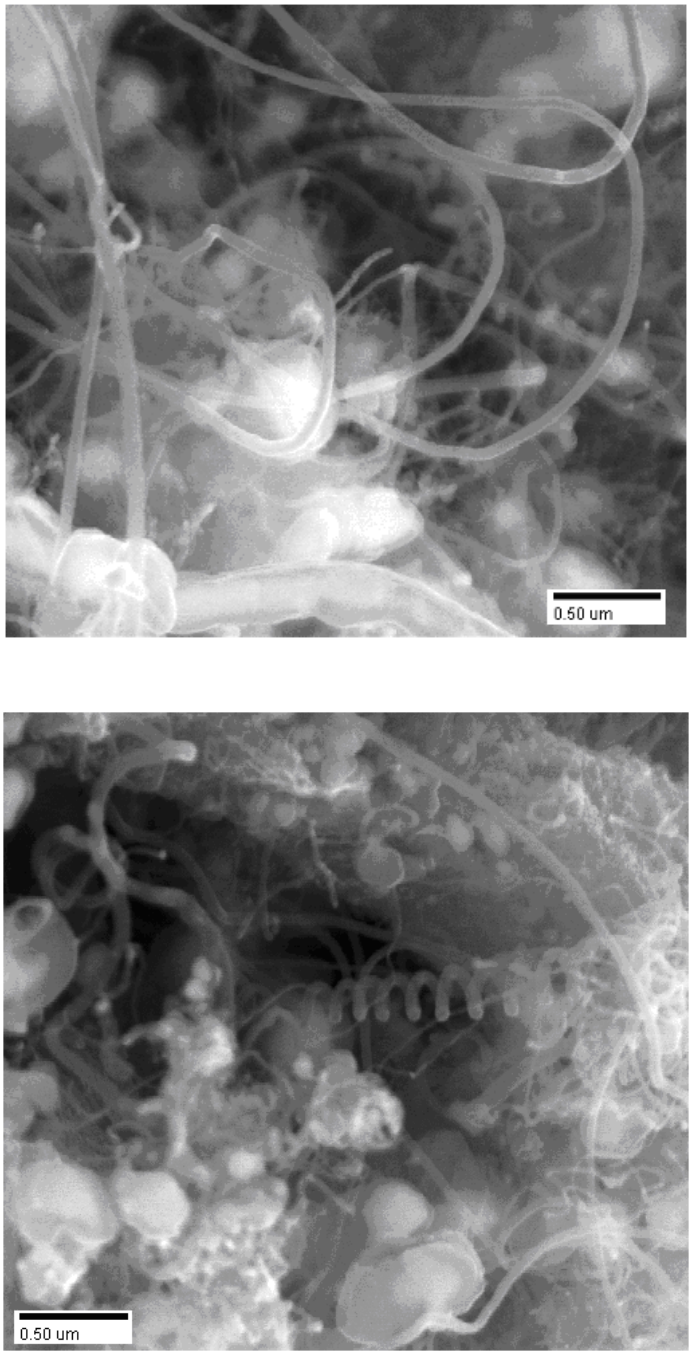
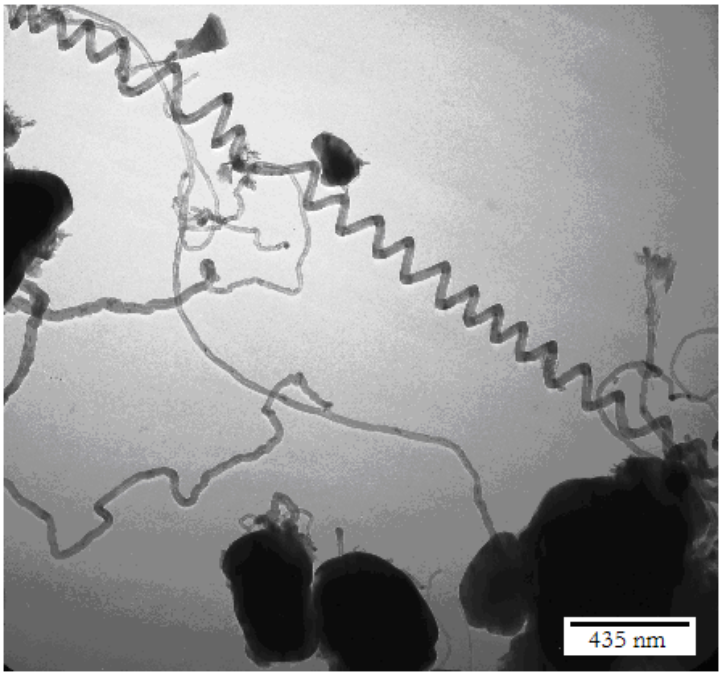



Fig. XII.5 SEM micrographs of carbon deposits obtained on Ni50 catalyst: 600 ºC of reaction temperature, 0.5 g of catalyst mass and a flow rate of 110 $cm^3$/min ($CH_4/N_2$ = 0.1).



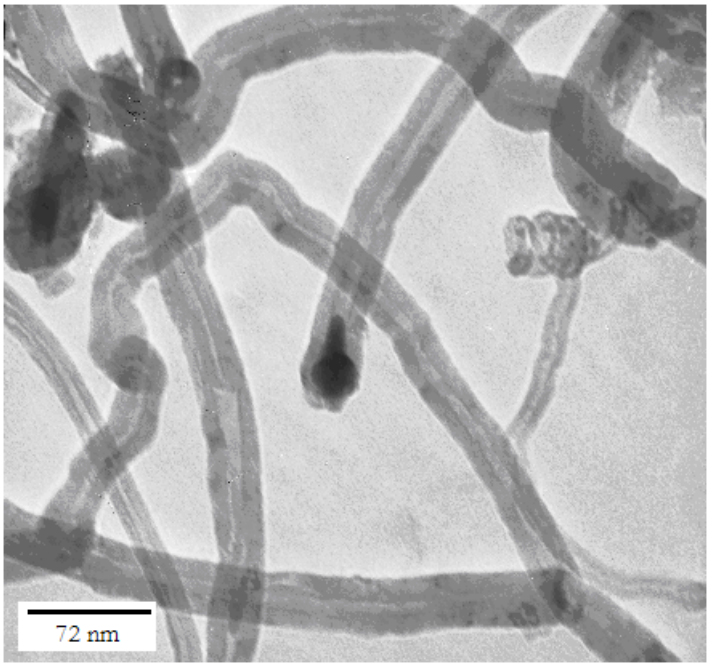




Fig. XII.6 TEM micrographs of carbon deposits obtained on Ni50 catalyst: 600 ºC of reaction temperature, 0.5 g of catalyst mass and a flow rate of 110 $cm^3$/min ($CH_4/N_2$ = 0.1).

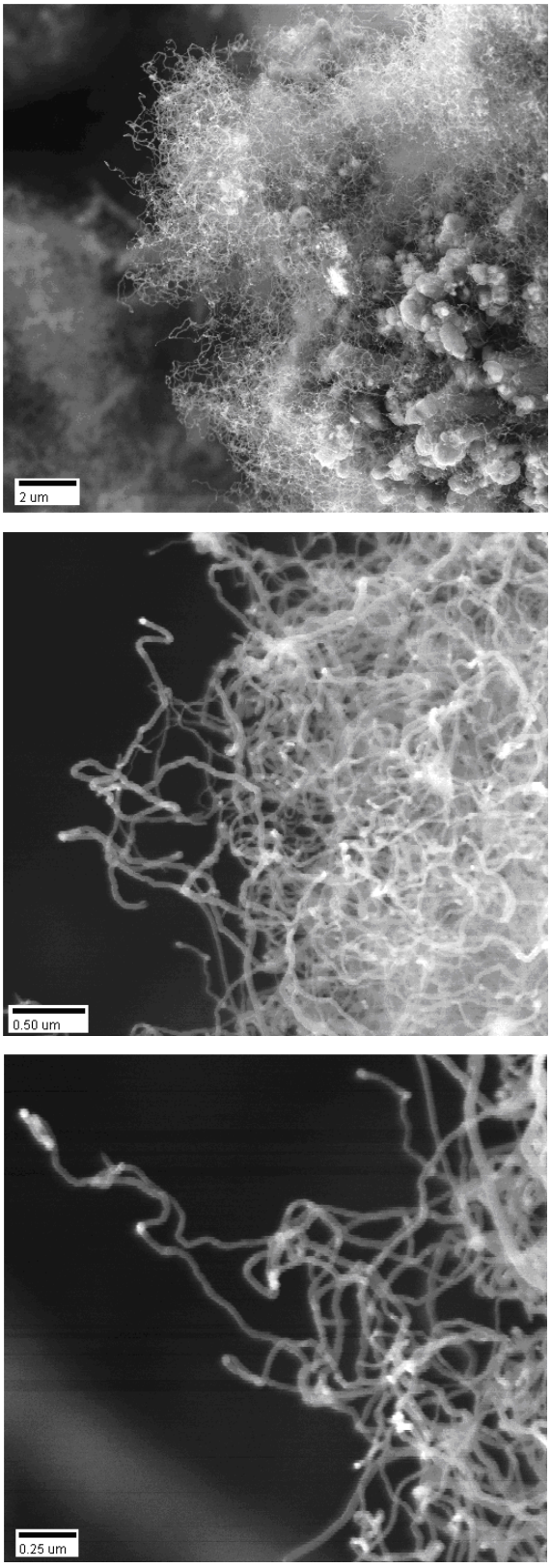
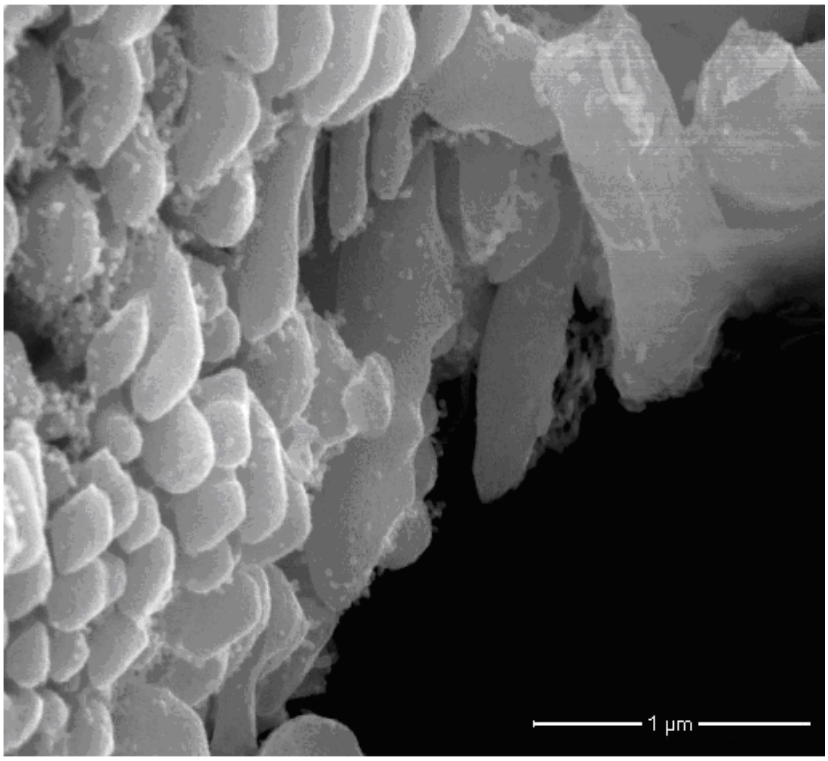
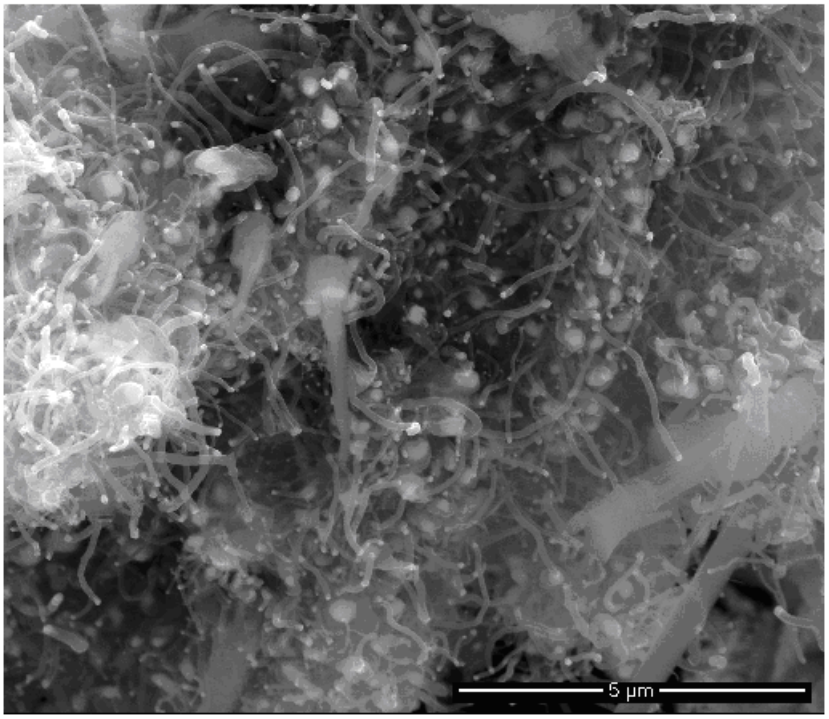


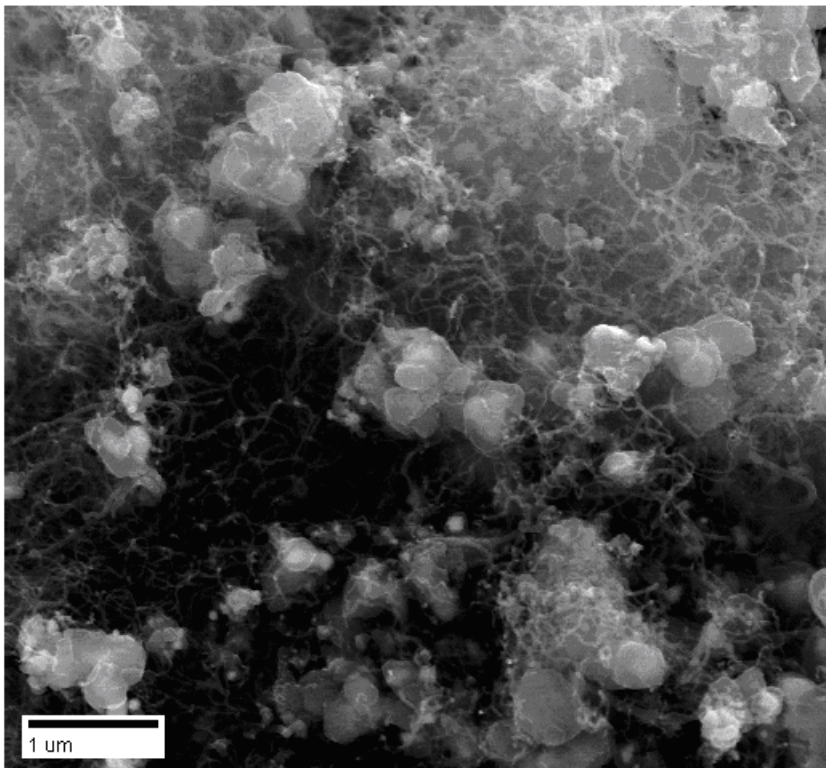

Fig. XII.7 SEM micrographs of carbon deposits obtained on Ni50 catalyst: 600 ºC of reaction temperature, 0.5 g of catalyst mass and a flow rate of 110 $cm^3$/min ($CH_4/N_2$ = 0.1 and $H_2/N_2$ = 0.1).



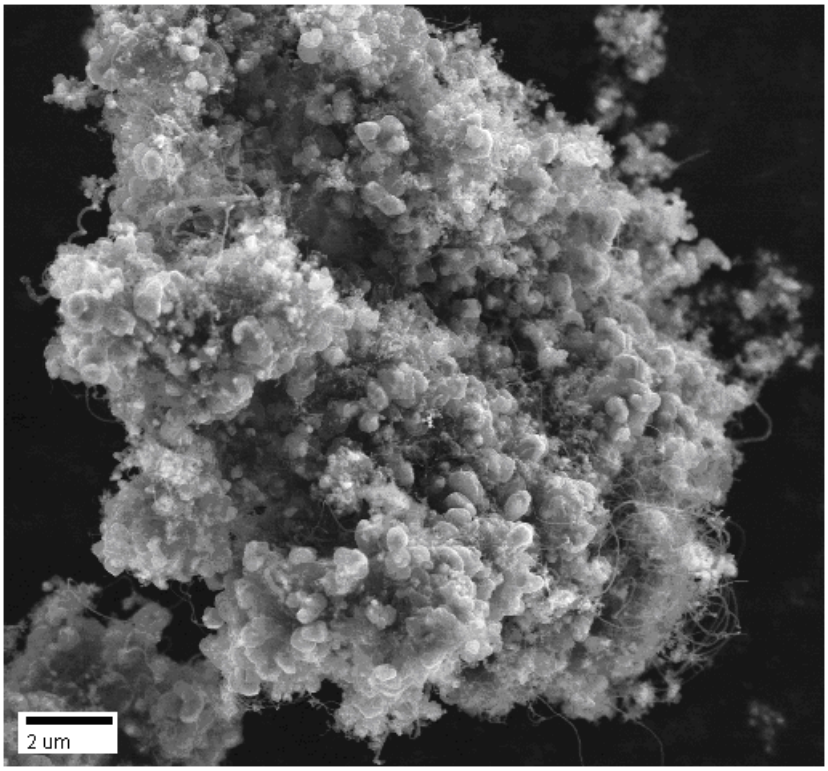

a)




b)

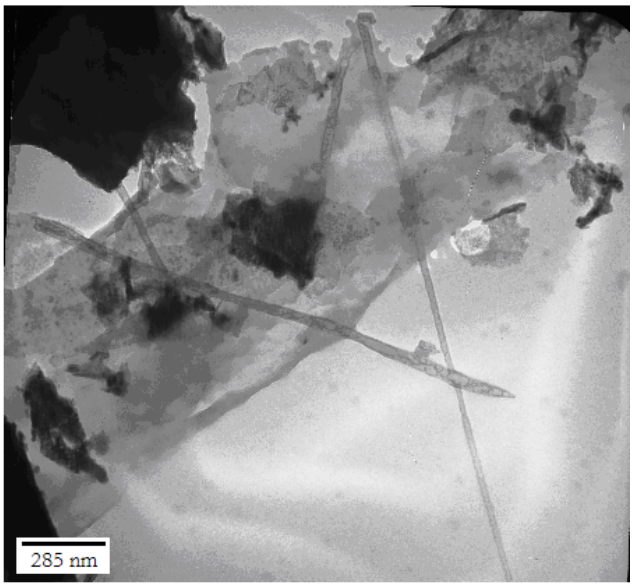



c)

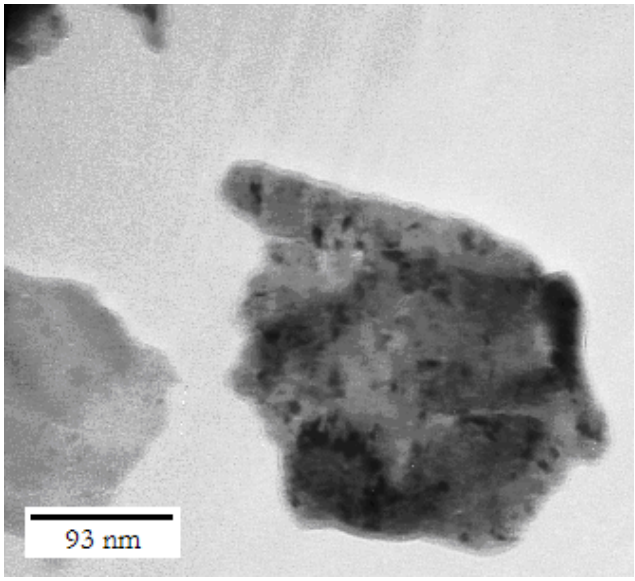



d)

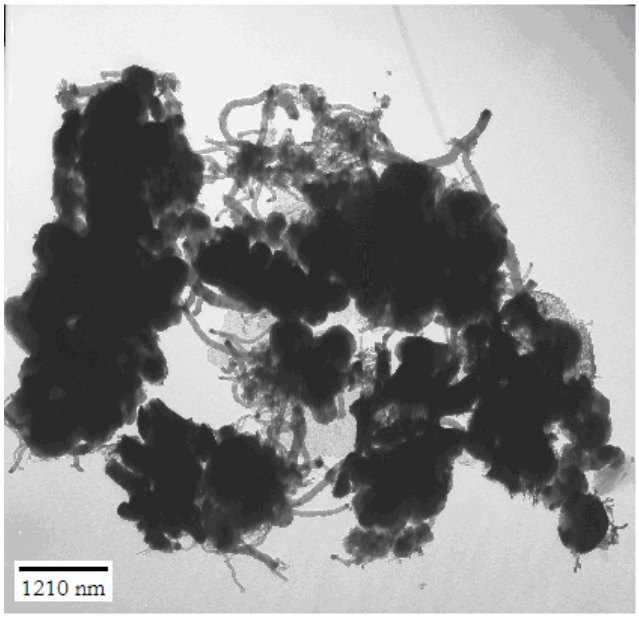
Fig. XII.8 SEM micrographs of carbon deposits obtained on Ni30 catalyst: (a) 400 ºC, (b) 500 ºC, (c) 600 ºC and (d) 700 ºC of reaction temperature, 2.5 g of catalyst mass and a flow rate of 110 $cm^3$/min ($CH_4/N_2$ = 0.1).



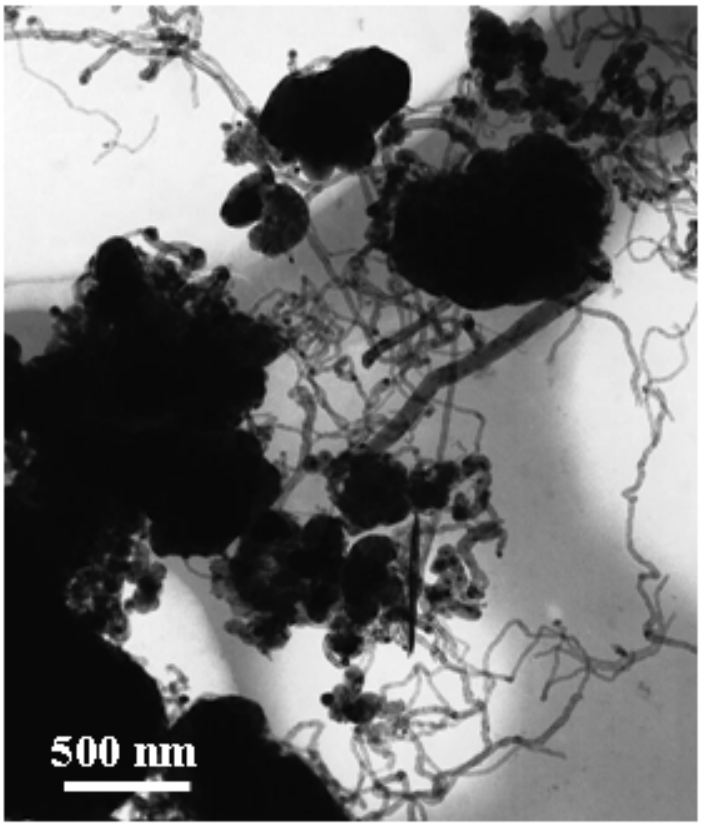

a)



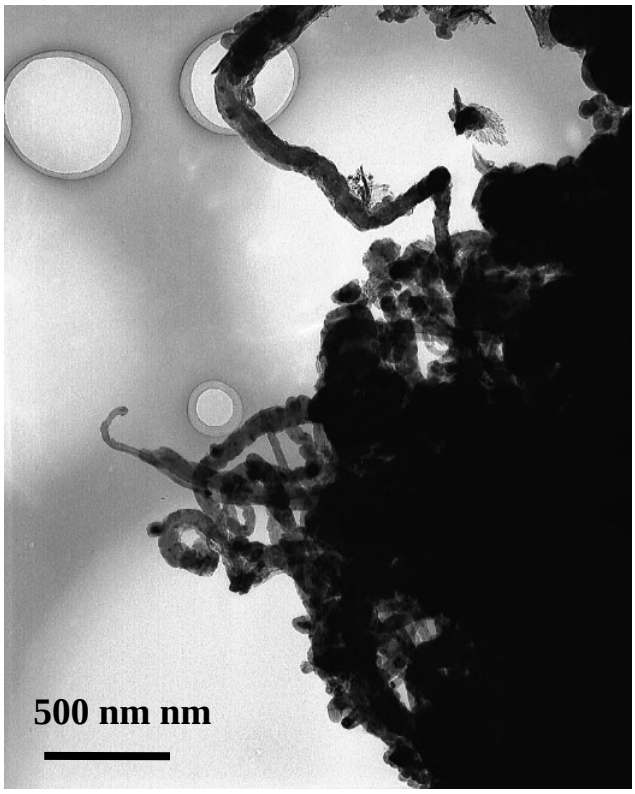

b)




c)

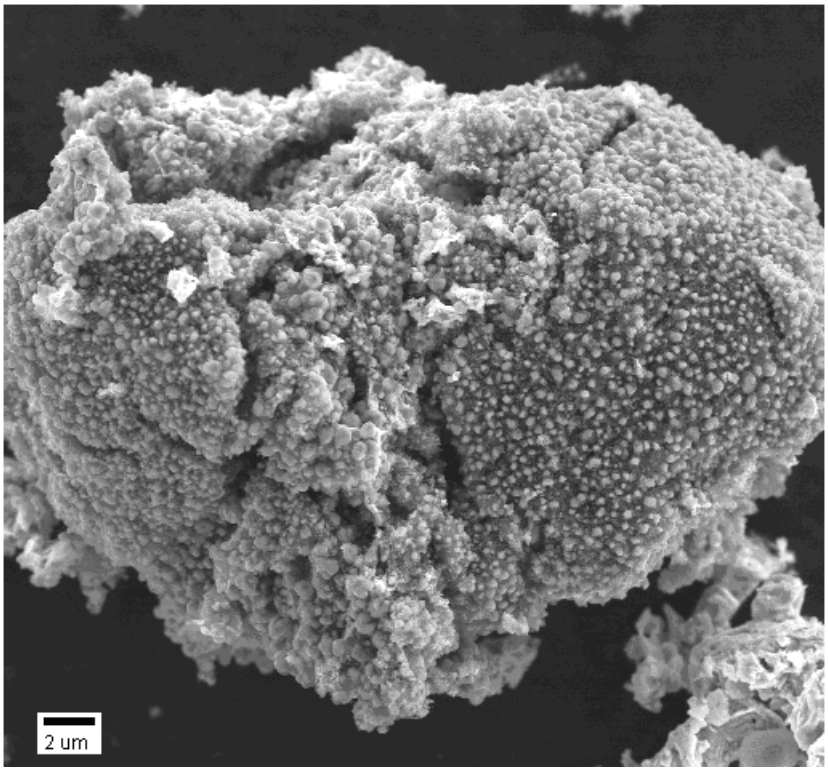



d)

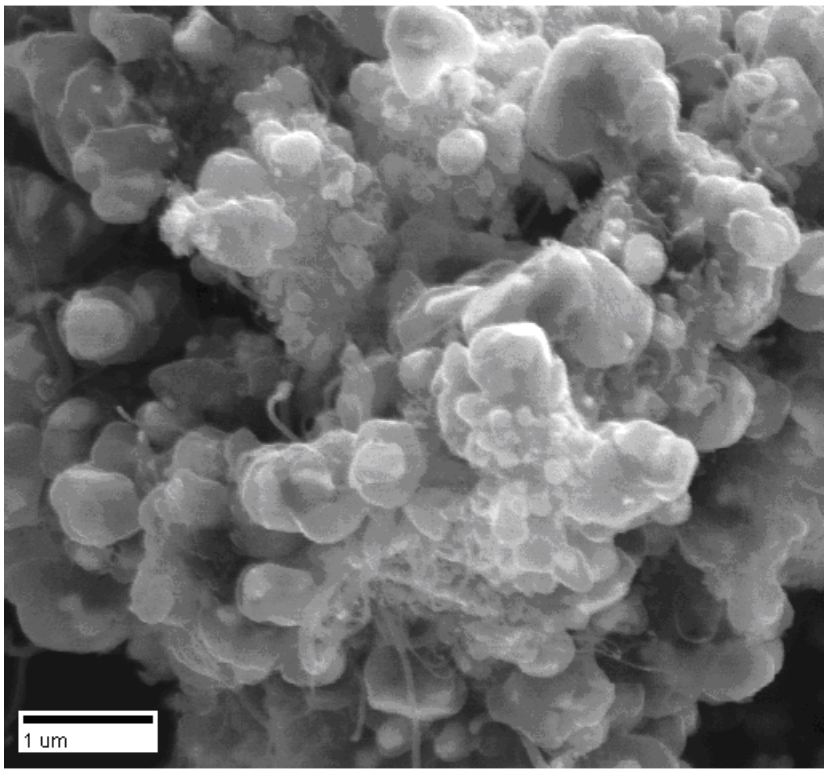



e)

Fig. XII.9 TEM micrograph of carbon deposits obtained on Ni30 catalyst: (a-b) 400 ºC, (c) 500 ºC, (d) 600 ºC and (e) 700 ºC of reaction temperature, 2.5 g of catalyst mass and a flow rate of 110 $cm^3$/min ($CH_4/N_2$ = 0.1).




a)




b)

Fig. XII.10 SEM micrographs of carbon deposits obtained on Co50 catalyst: (a) 500 ºC and (b) 700 ºC of reaction temperature, 2.5g of catalyst mass and a flow rate of 110 $cm^3$/min ($CH_4/N_2$ = 0.1).

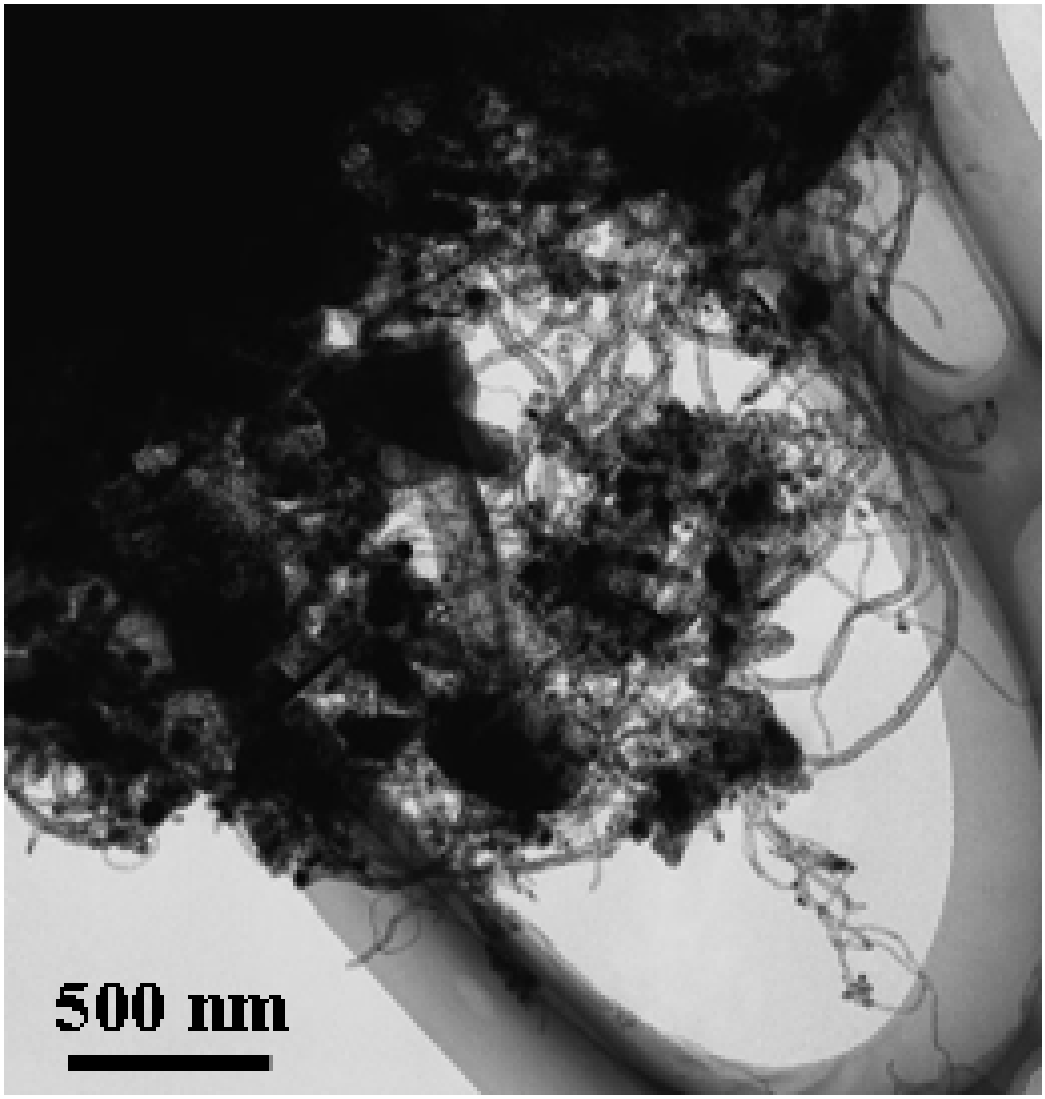
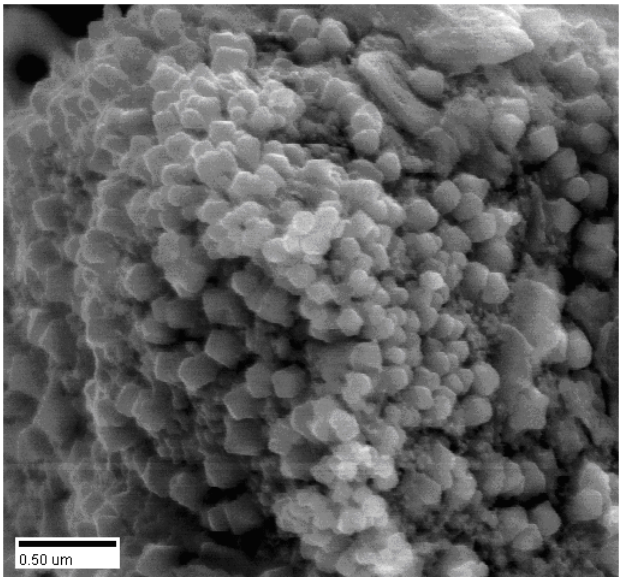
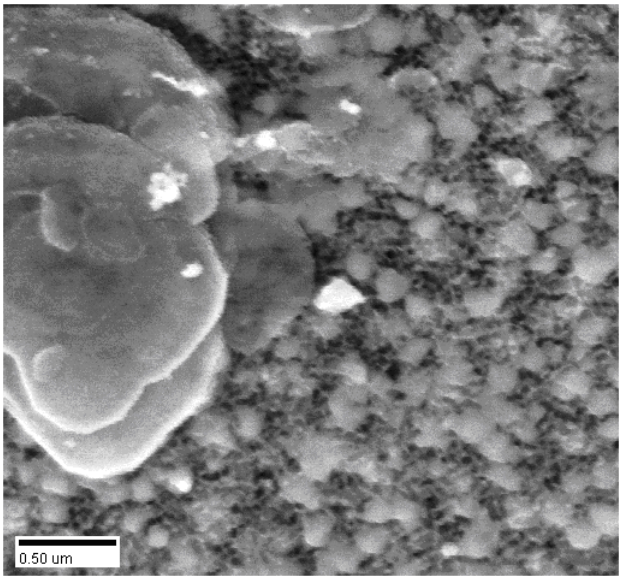


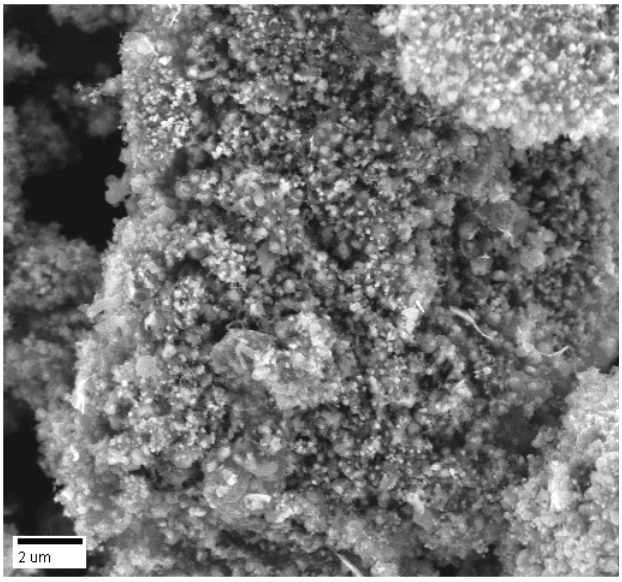

Fig. XII.11 TEM micrograph of carbon deposits obtained on Co30 catalyst: 600 ºC of reaction temperature, 2.5 g of catalyst mass and a flow rate of 110 $cm^3$/min ($CH_4/N_2$ = 0.1).



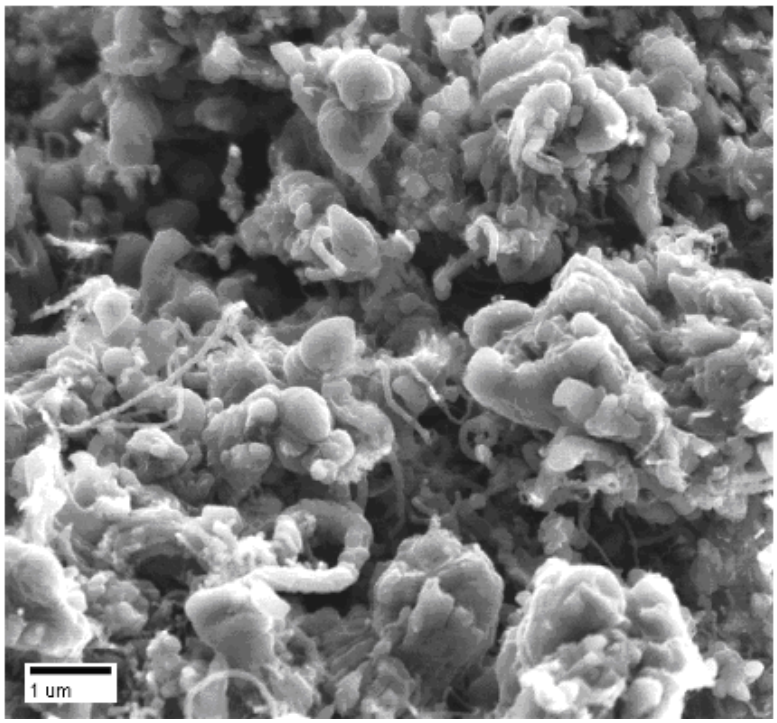

a)



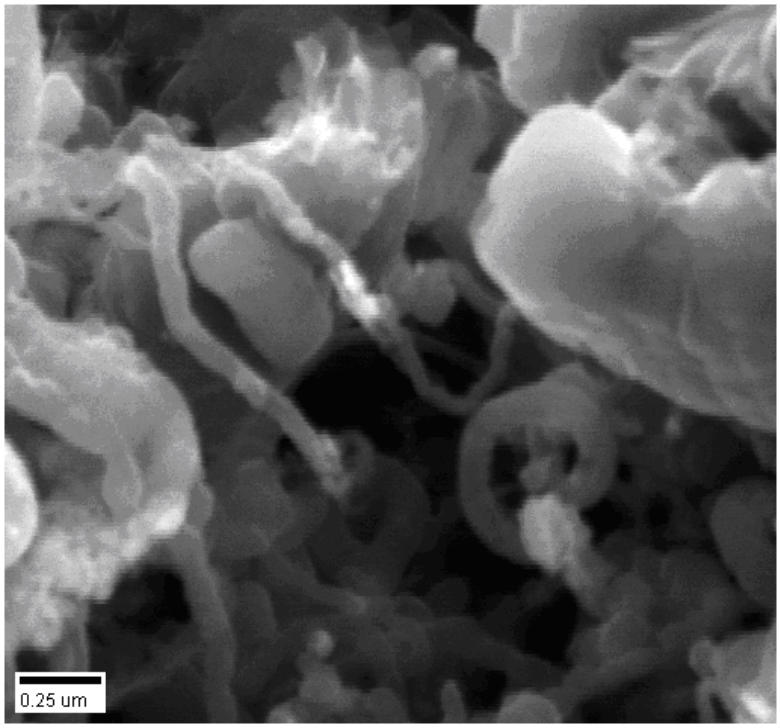

b)




c)

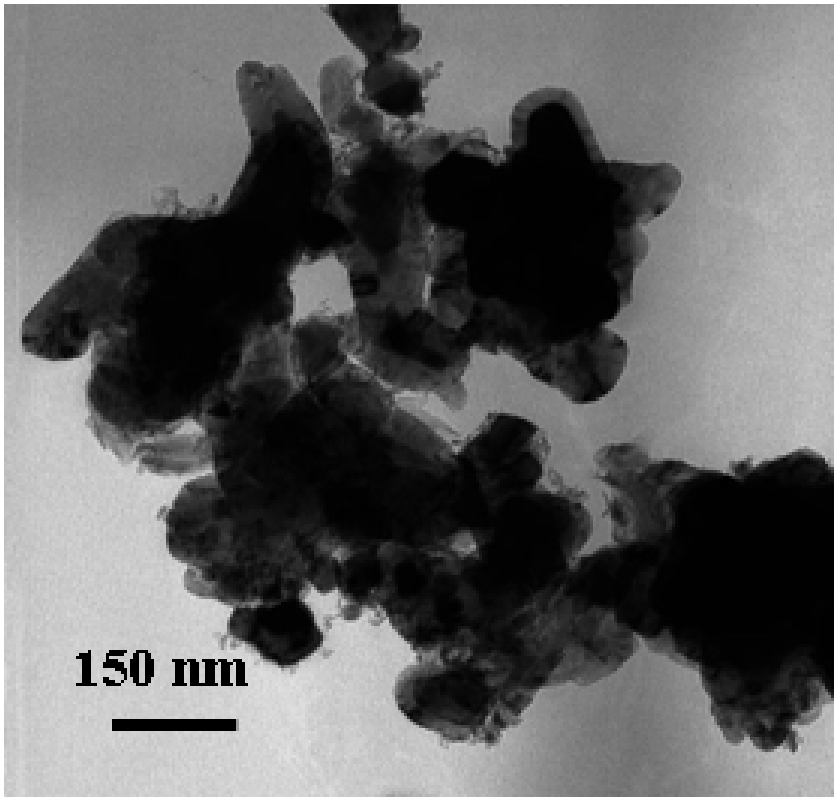



d)

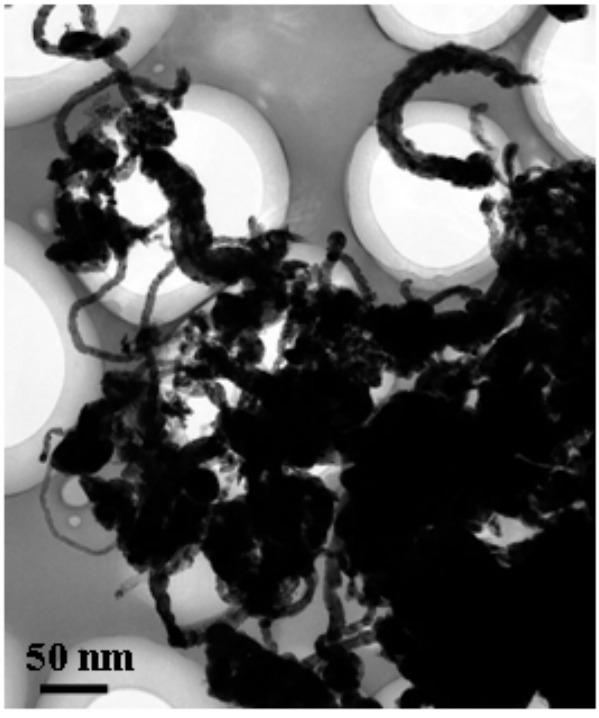



e)

Fig. XII.12 SEM micrographs of carbon deposits obtained on Fe50 catalyst: (a-b) 550 ºC, (c) 600 ºC and (d-e) 700 ºC of reaction temperature, 2.5 g of catalyst mass and a flow rate of 110 $cm^3$/min ($CH_4/N_2$ = 0.1).

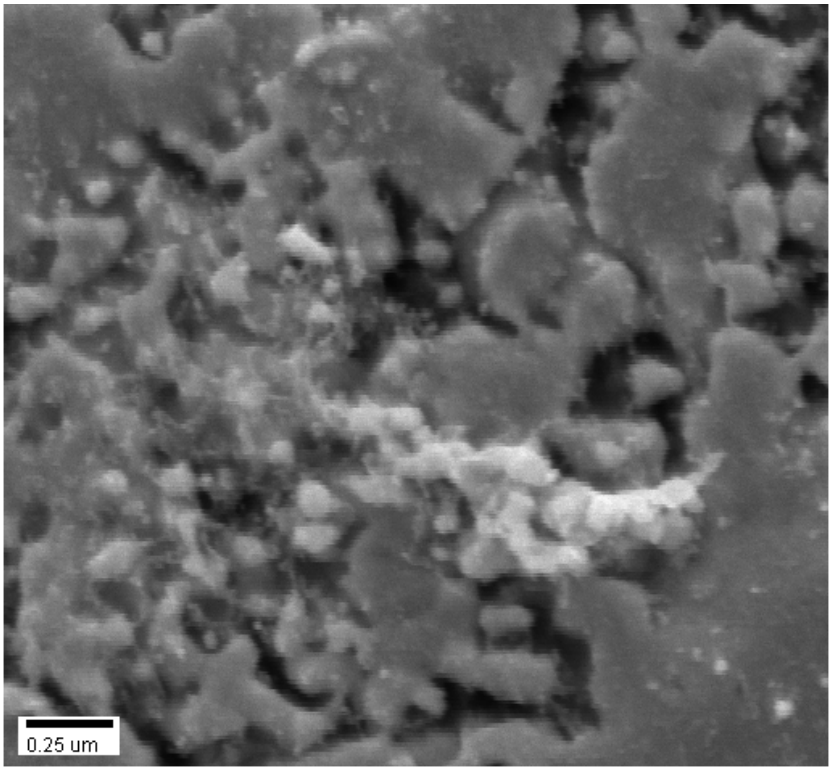



a)

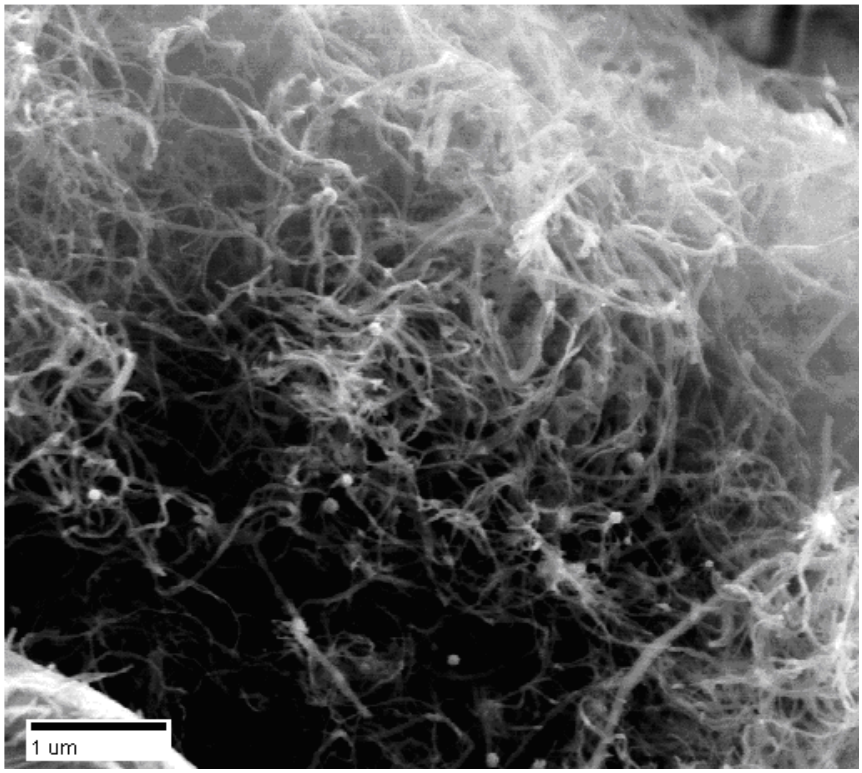



b)

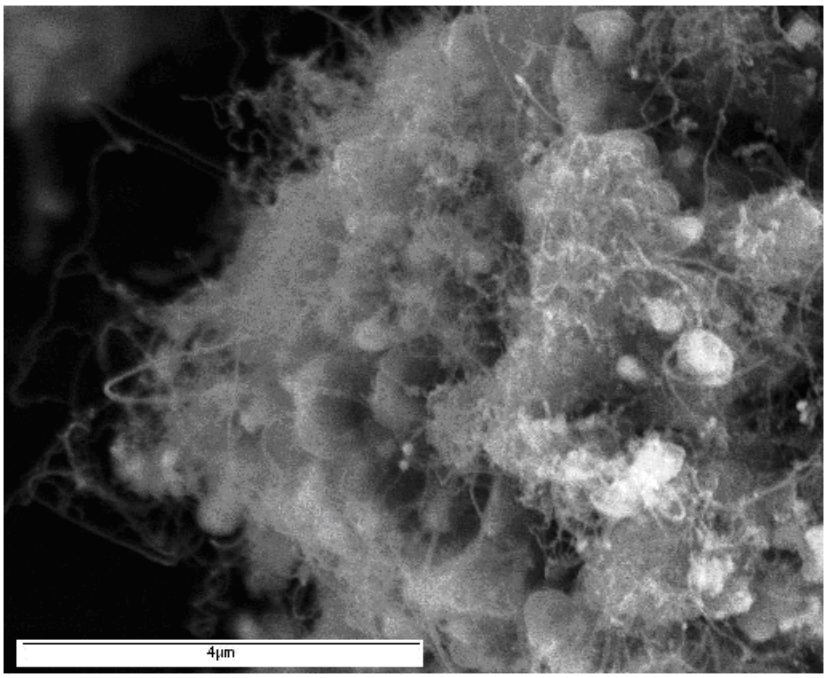
Fig. XII.13 TEM micrographs of carbon deposits obtained on Fe50 catalyst: (a) 600 ºC and (b) 700 ºC of reaction temperature, 2.5 g of catalyst mass and a flow rate of 110 $cm^3$/min ($CH_4/N_2$ = 0.1).



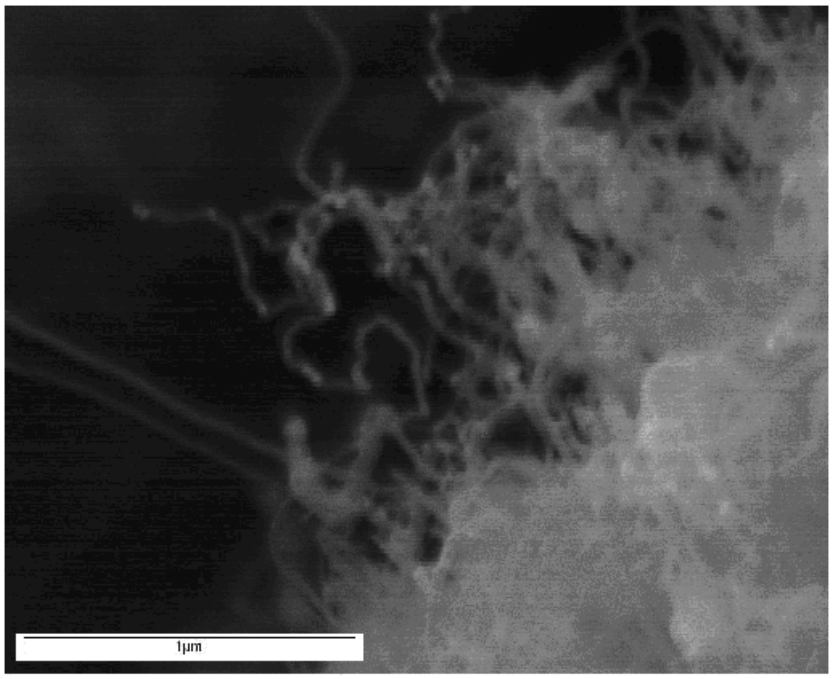

a)



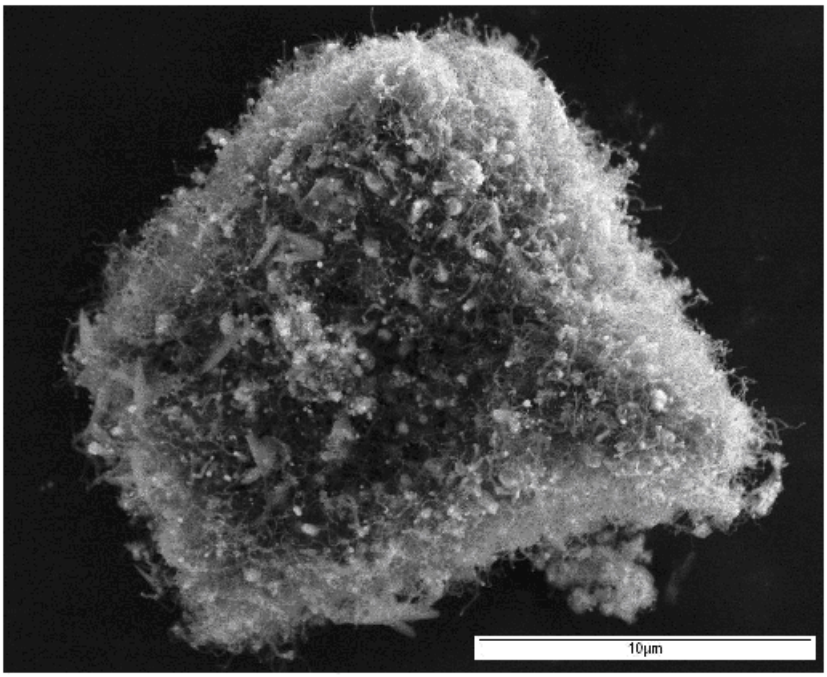

b)



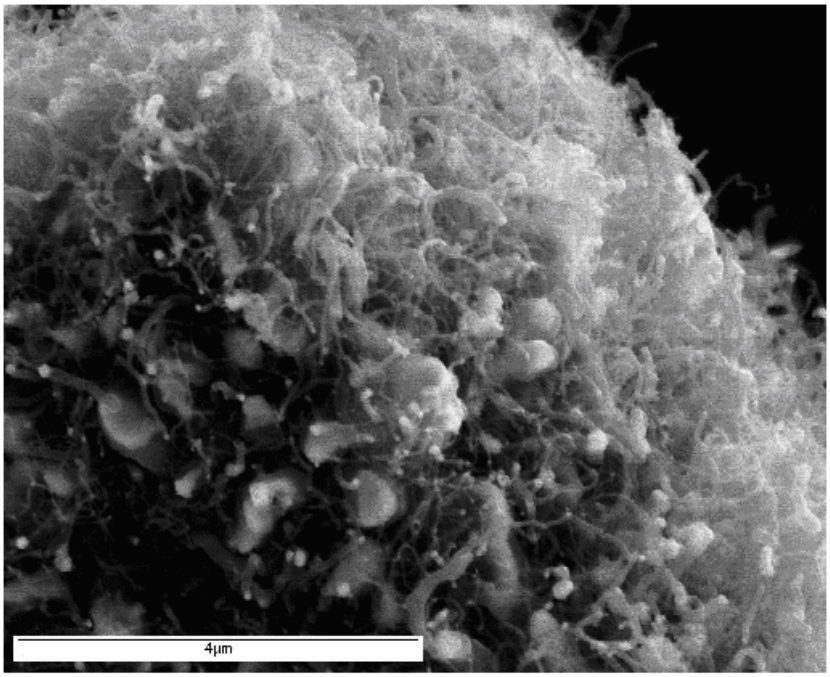

c)



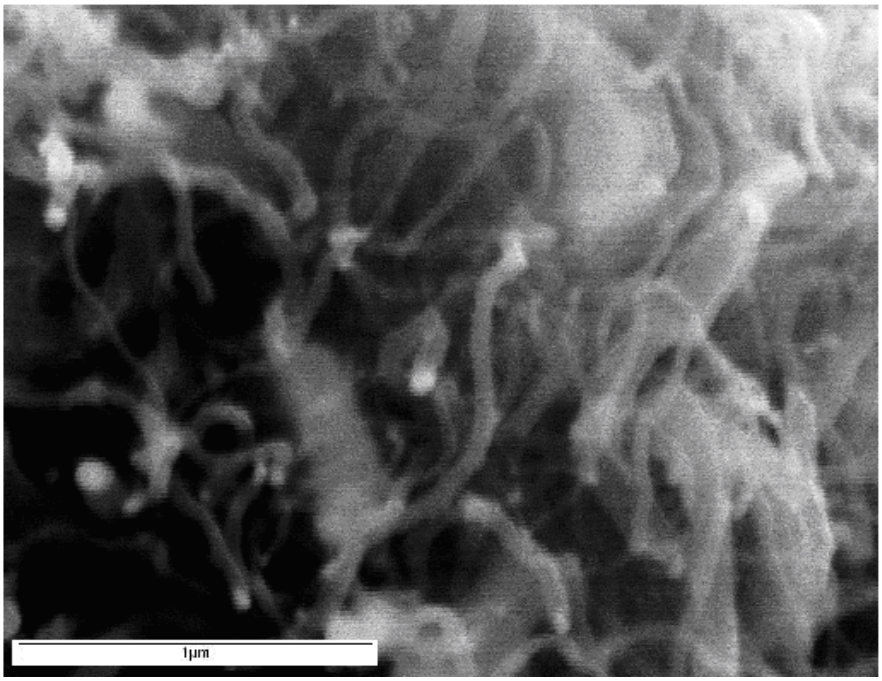

d)




e)




f)



g)

Fig. XII.14 SEM micrographs of carbon deposits obtained on Cu50 (a), Ni30Cu50 (b), Ni50Cu50 (ITT) (c-d) and Ni30Cu50 (ITT) at 600ºC (e-g) at 600ºC.

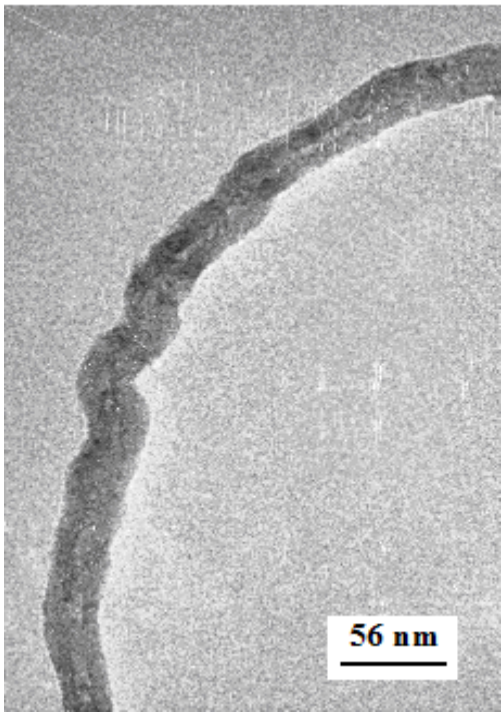
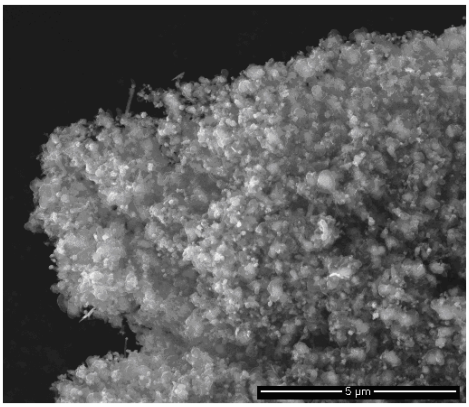
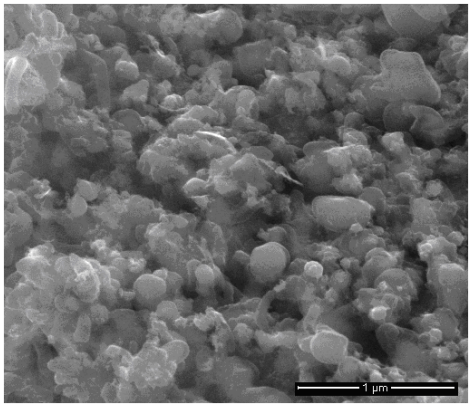


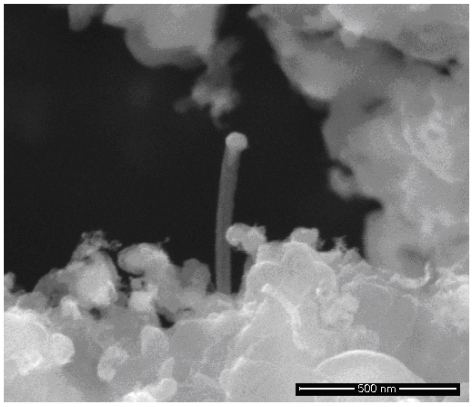

Fig. XII.15 TEM micrograph of carbon deposits obtained on Ni30Cu50 (ITT) at 600ºC.



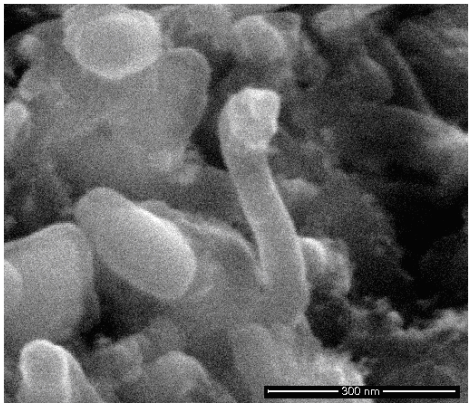

a)



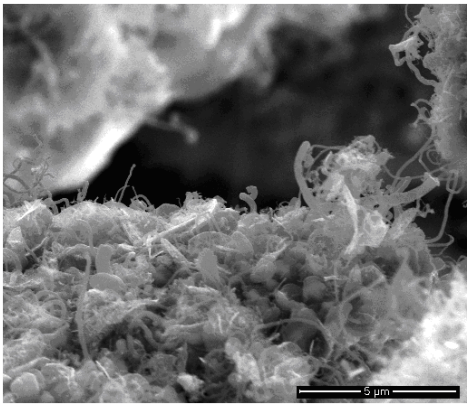

b)



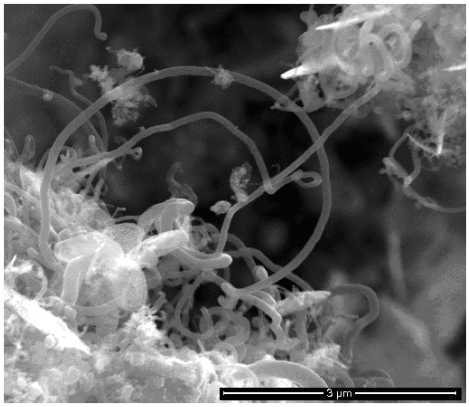

c)



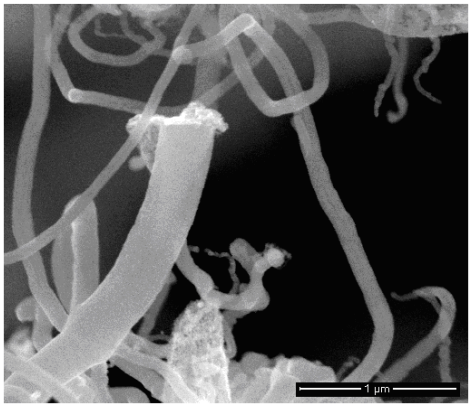

d)



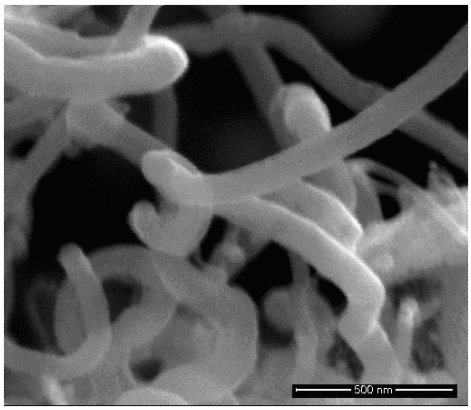

e)




f)

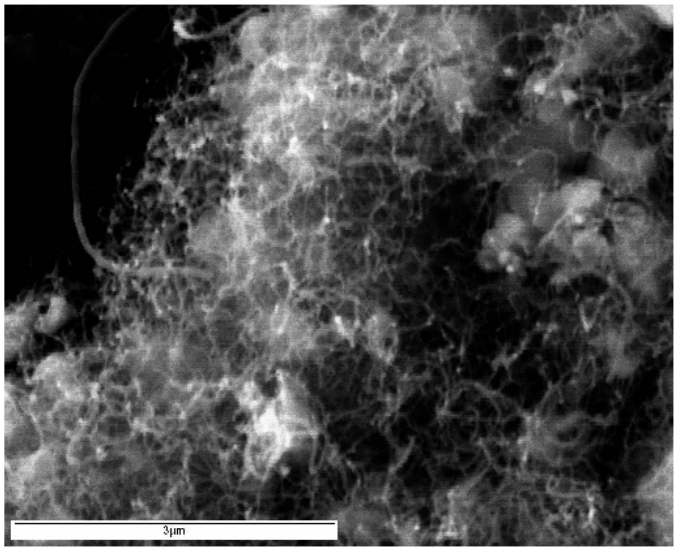



g)

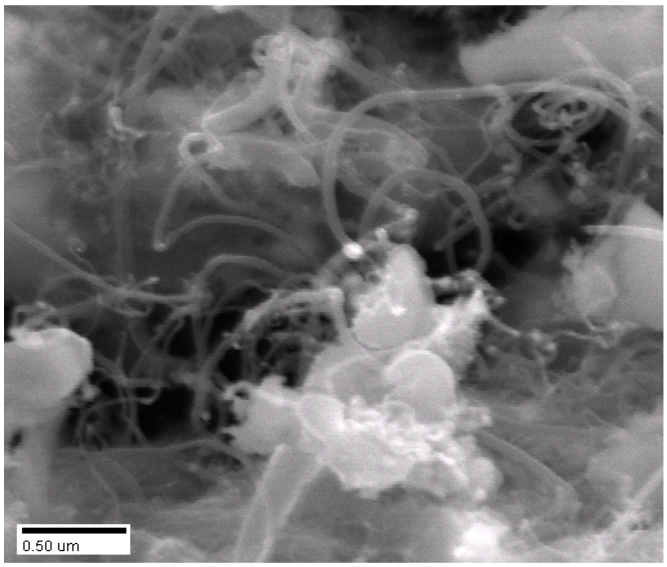



h)

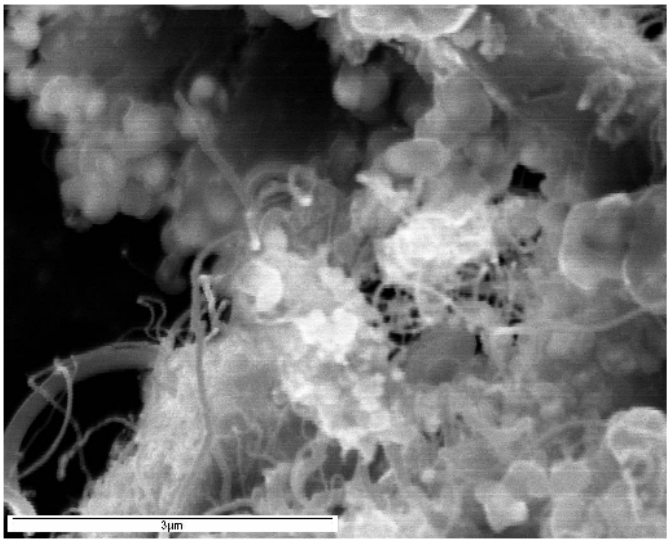
Fig. XII.16 SEM micrographs of carbon deposits obtained on Fe50Cu50 (IT˙T) (a-d) and Fe35Cu50 (IT˙T) (e-h), at 600 ºC.



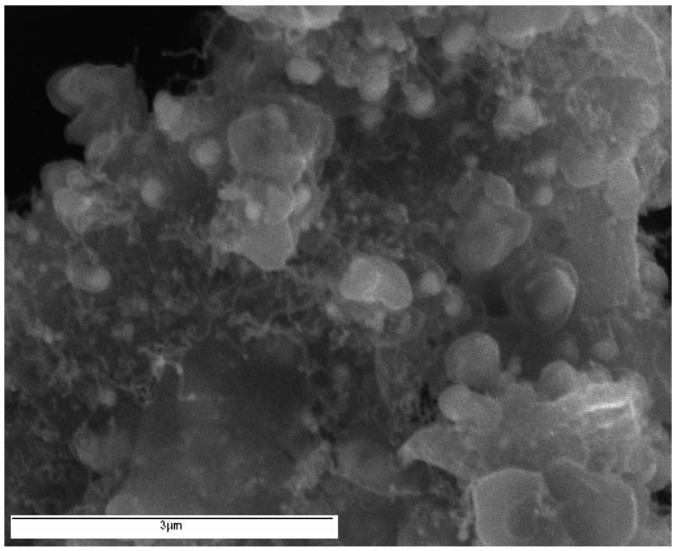

a)



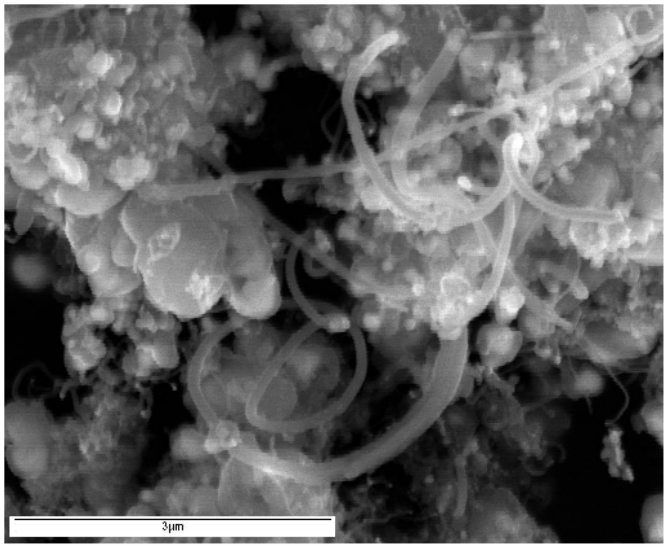

b)



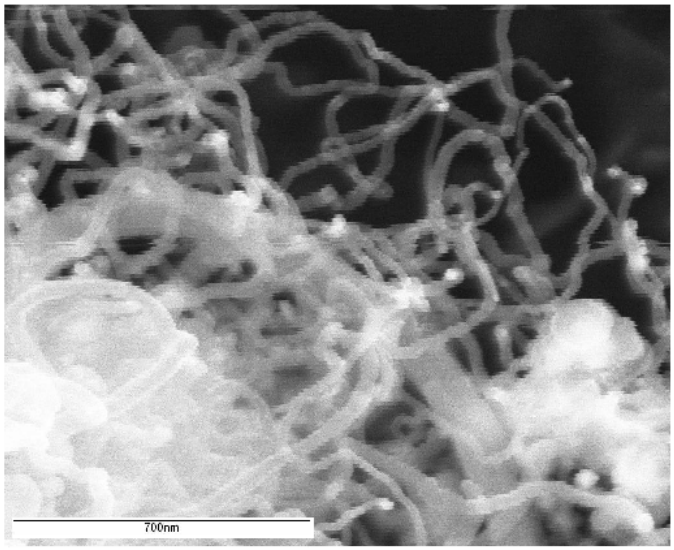

c)




d)

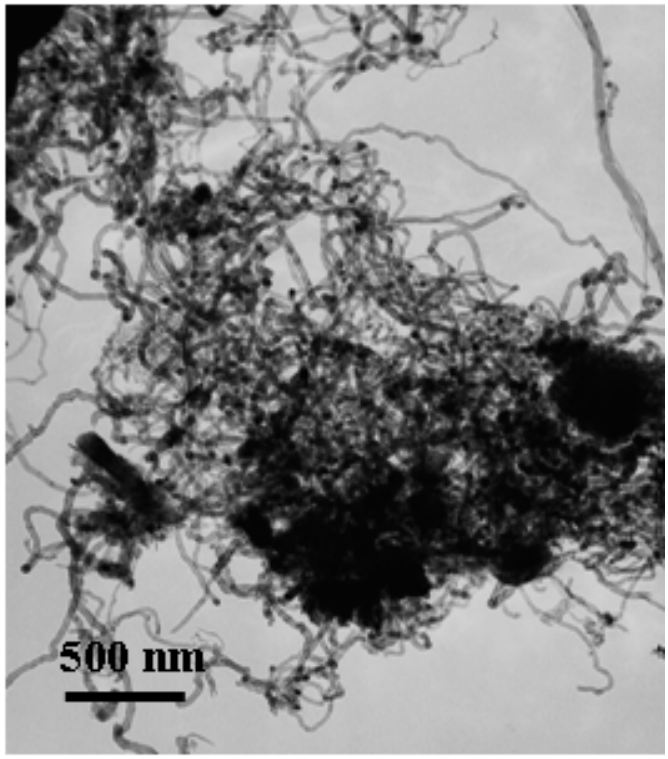



e)

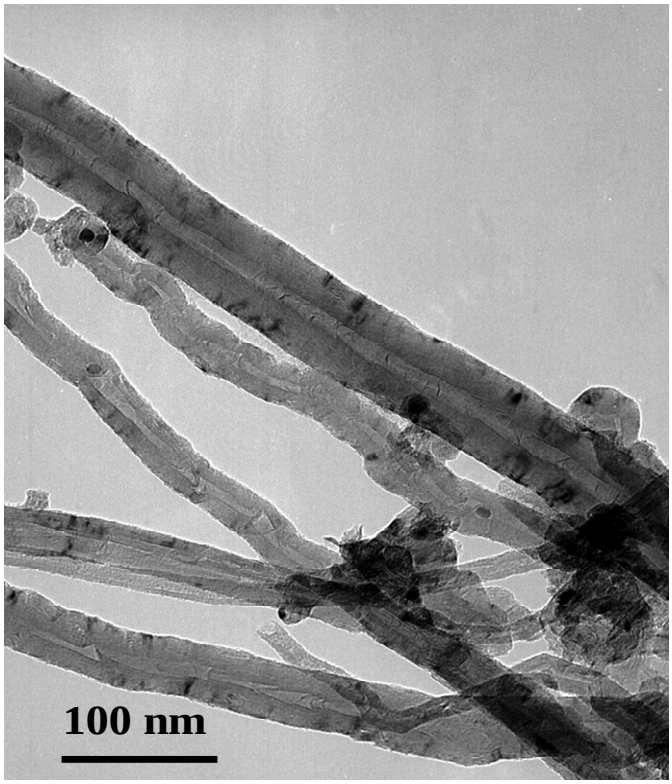



f)

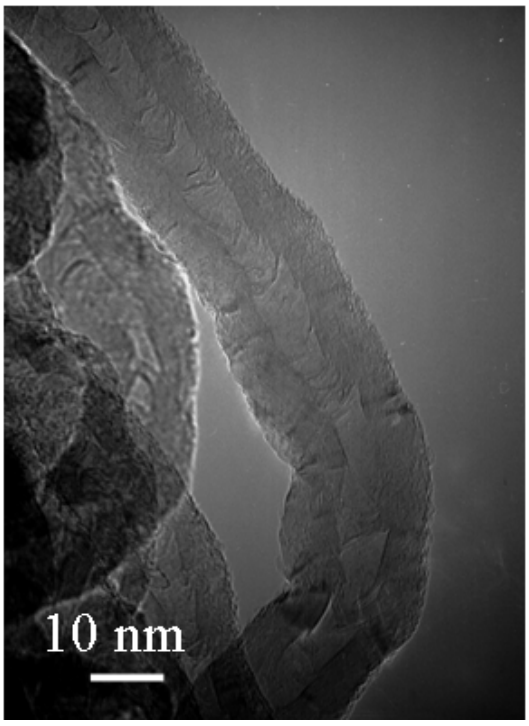
Fig. XII.17 SEM micrographs of carbon deposits obtained at 600ºC on Ni50 (HPT) (a), Ni50-$La_2O_3$ (HPT) (b), Ni50-$La_2O_3$ (HPT) at 700ºC (c), Ni30 (HPT) (d), Ni30-$La_2O_3$ (HPT) (e) and Ni30-$La_2O_3$ (f).



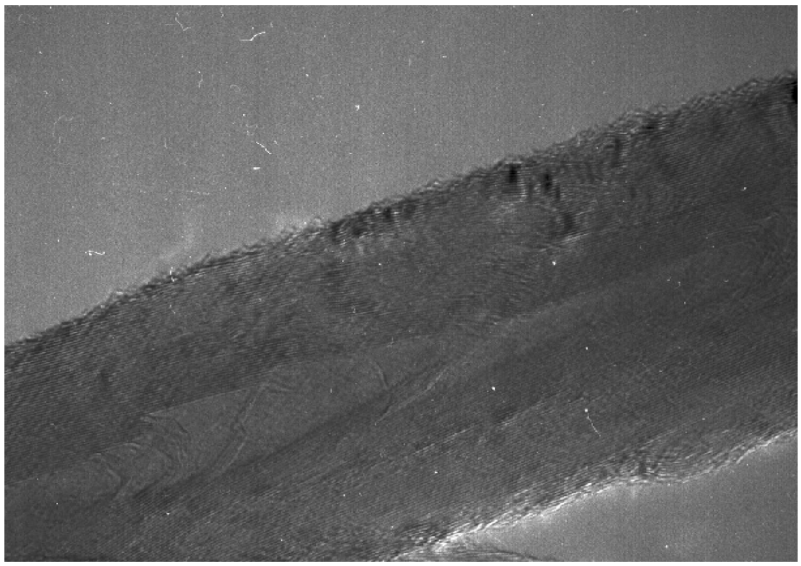

a)

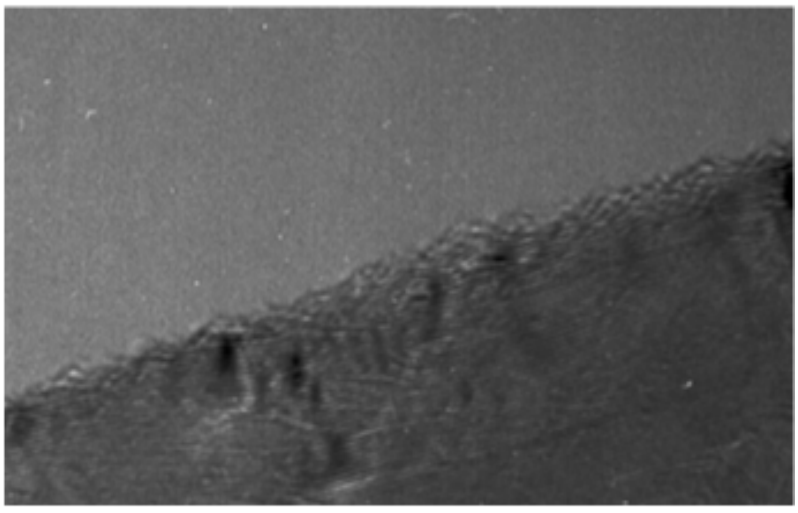


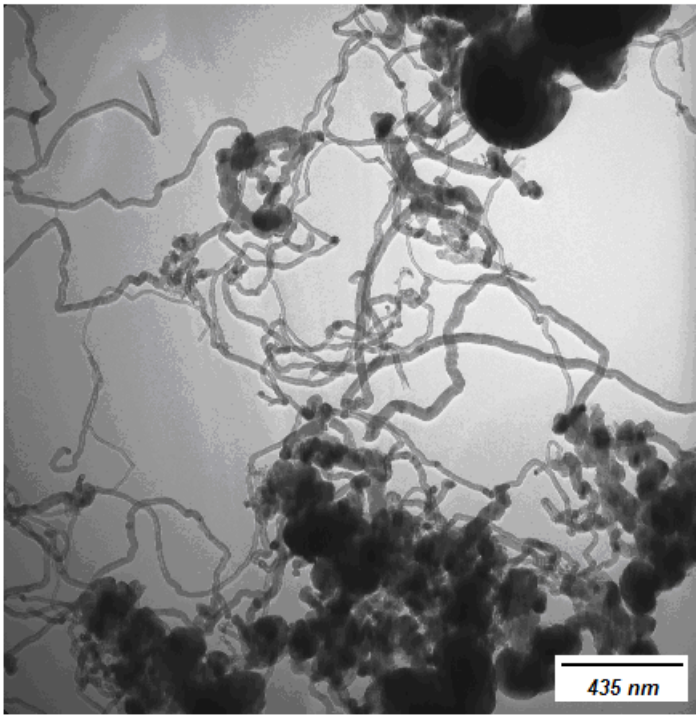

b)



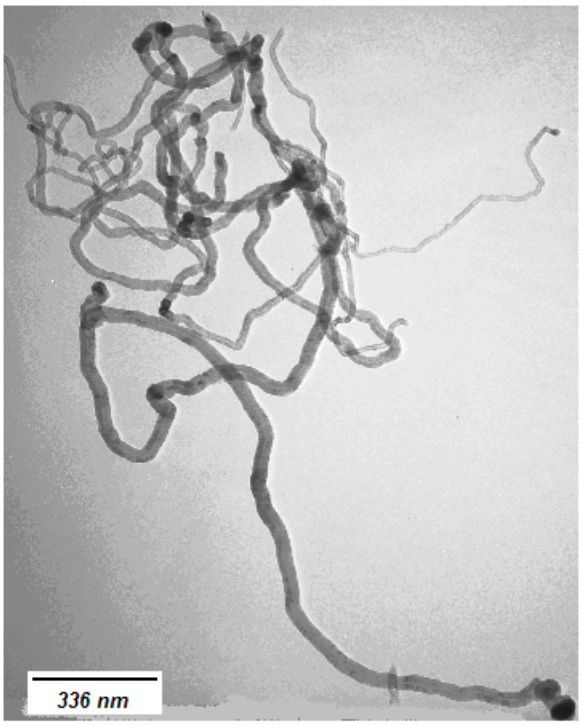
c)


d)

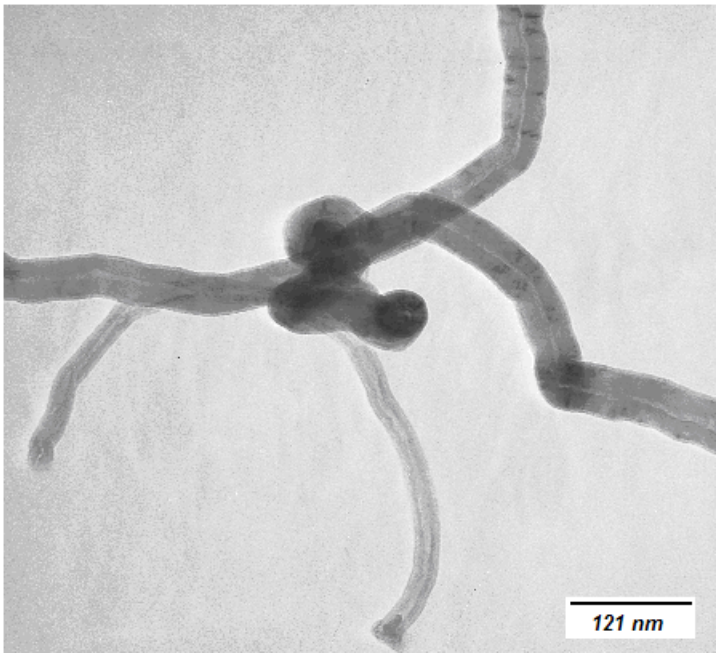

e)



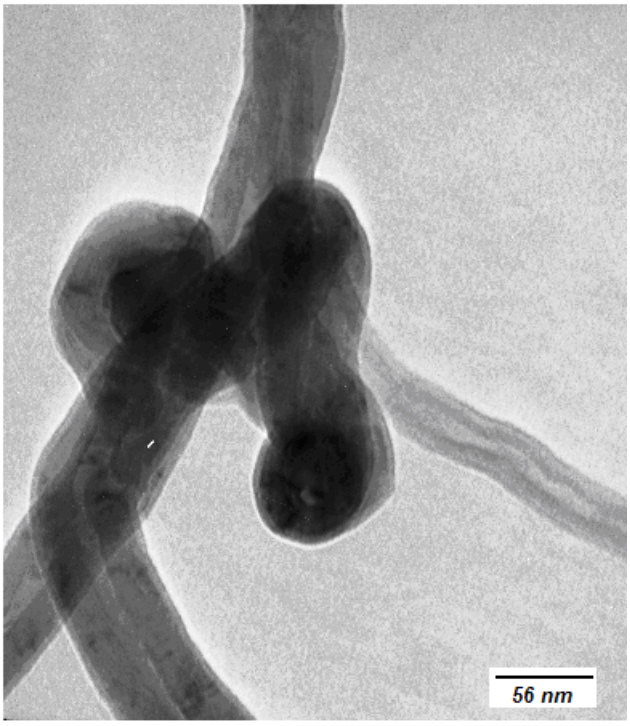

f)




g)

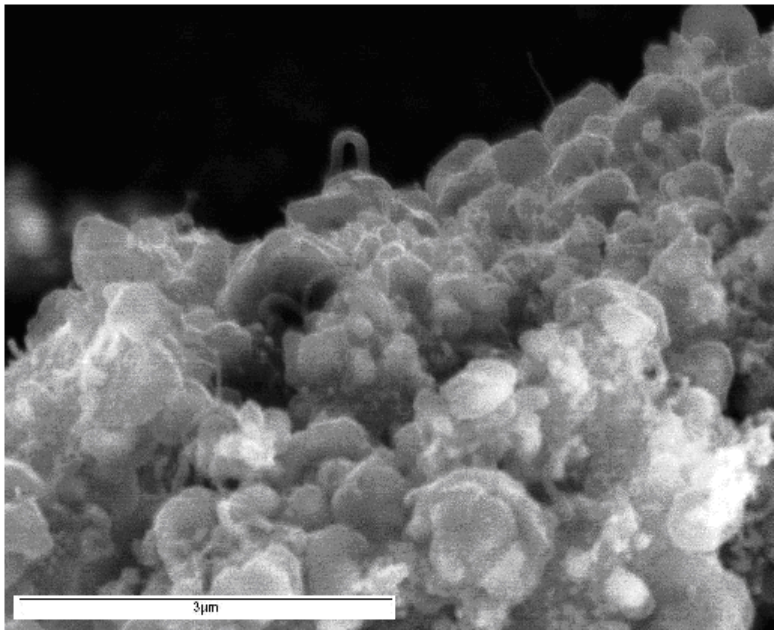



h)

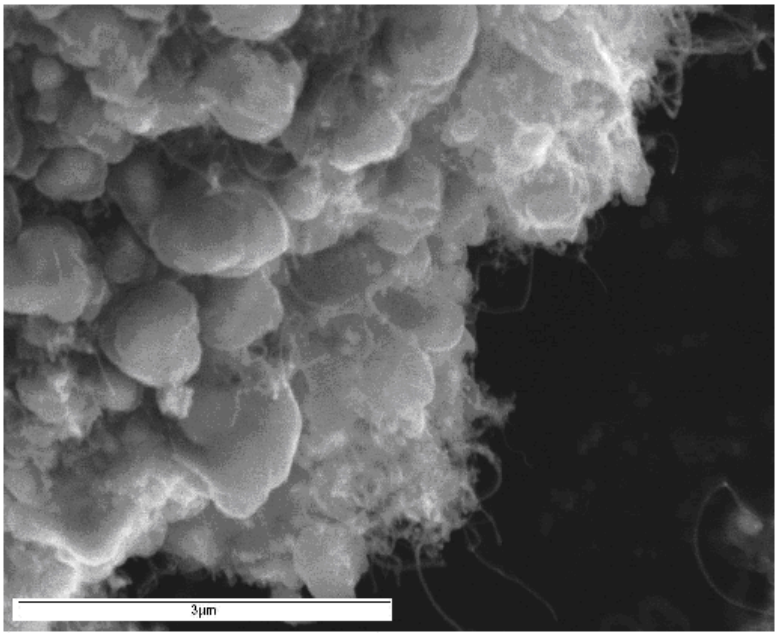



i)

Fig. XII.18 TEM micrographs of carbon deposits obtained on Ni50-$La_2O_3$ (HPT) (a-e) and Ni30-$La_2O_3$ (f-i) at 600 °C.




a)




b)

Fig. XII.19 SEM micrographs of carbon deposits obtained at 600 ºC on Co30 (HPT) (a) and Co30-$La_2O_3$ (HPT) (b).

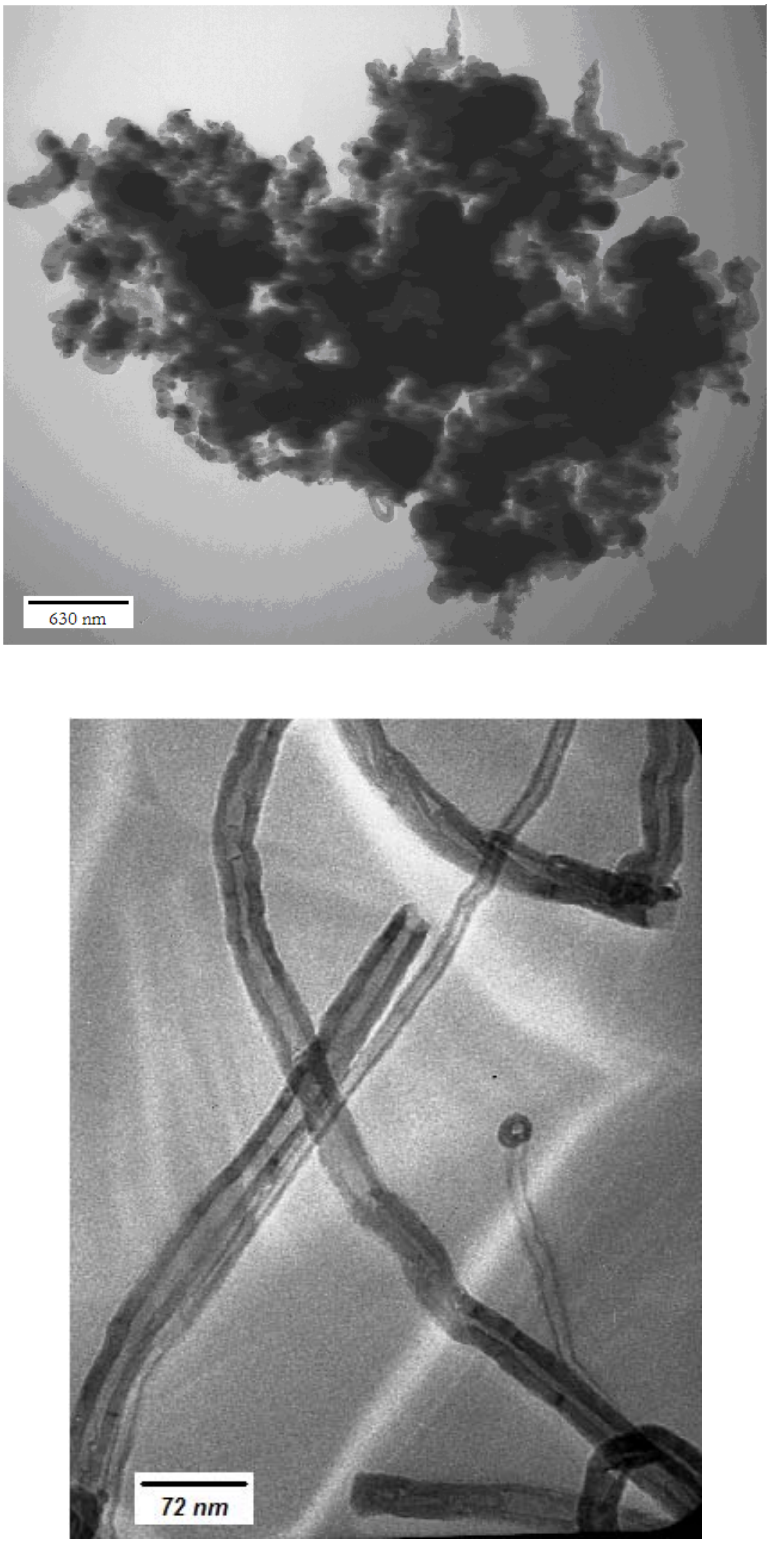



Fig. XII.20 TEM micrographs on carbon deposits obtained at 600 ºC on Co30-$La_2O_3$ (HPT).

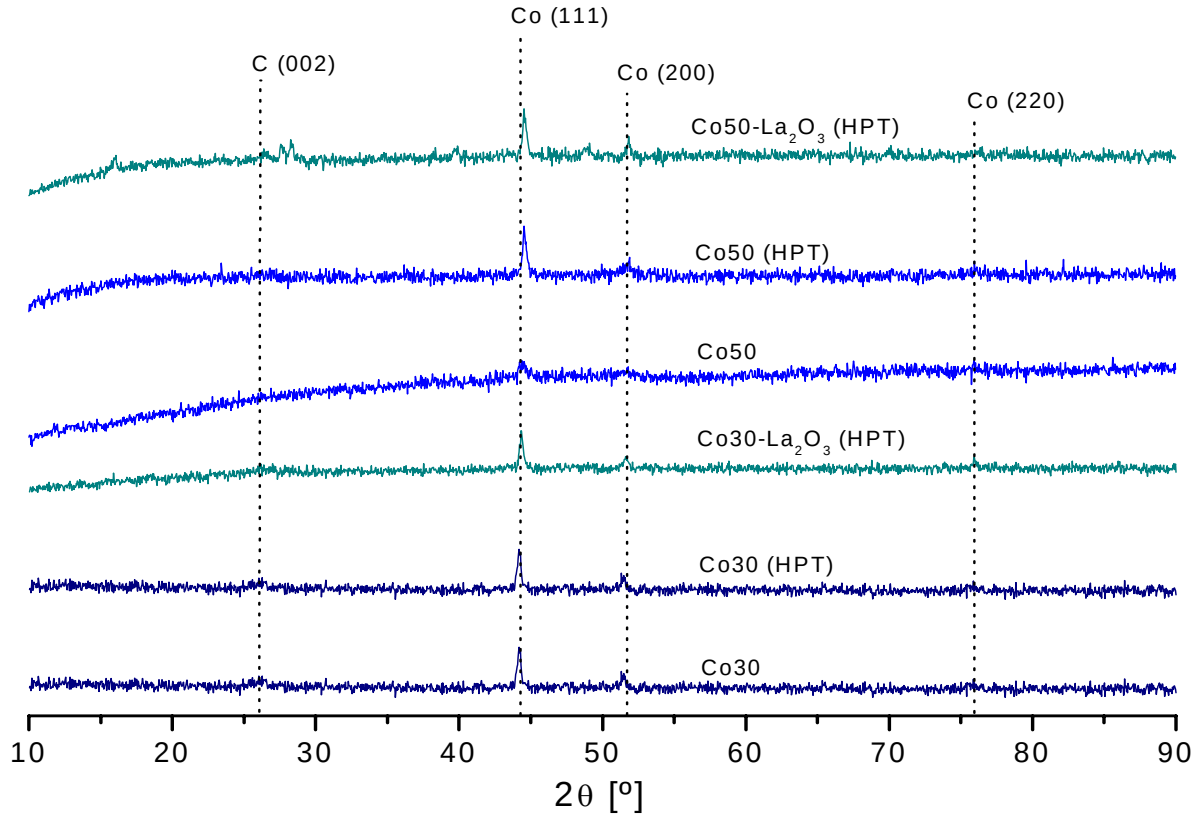
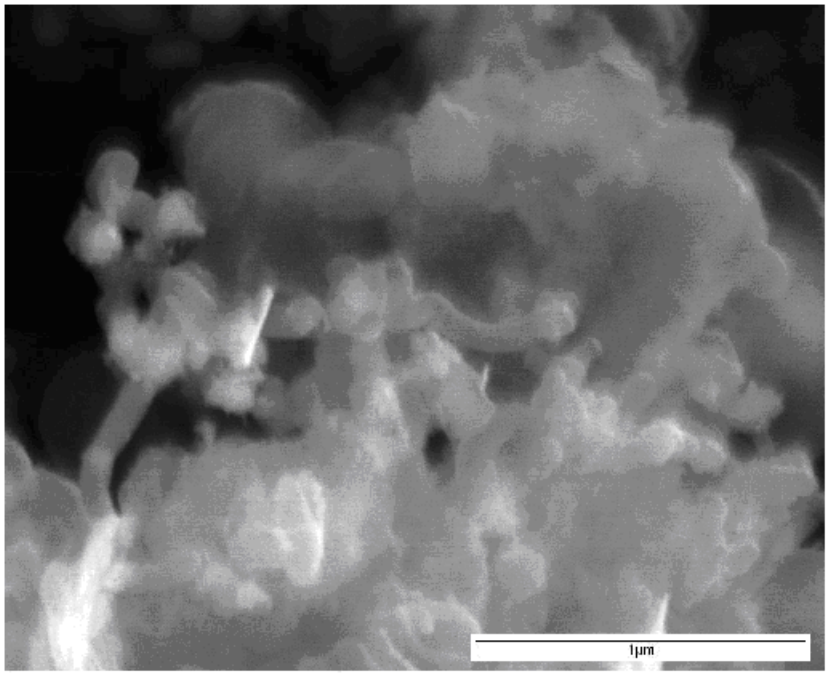



Fig. XII.21 XRD patterns of carbon deposits obtained on Co and Co-$La_2O_3$ catalysts at 600 ºC.

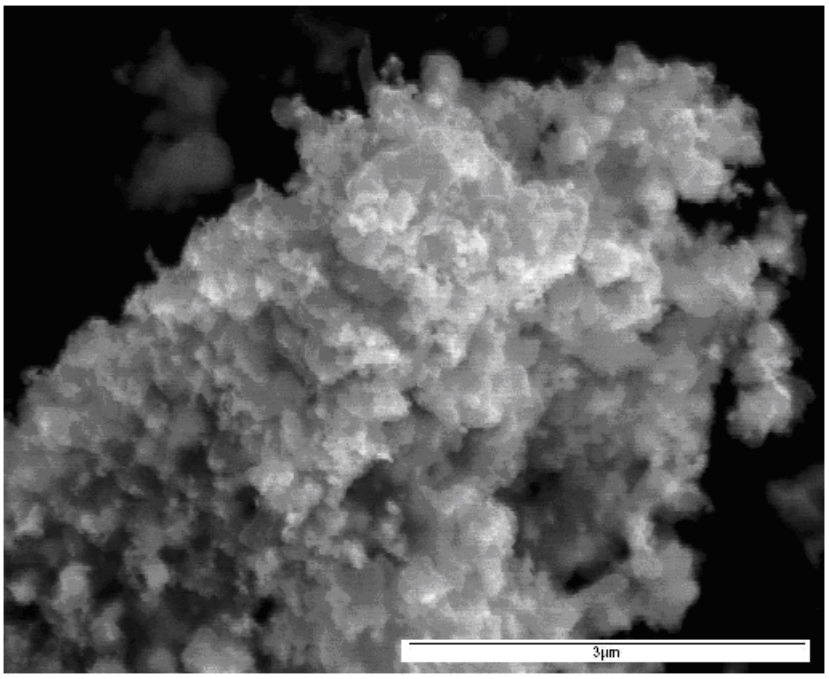
Table XII.1

Average Co and C crystal sizes

| Catalyst | $d_{Co}$ [nm] | $d_C$ [nm] | $D_{(002)}$ [nm] |
|---|---|---|---|
| Co30 | 17 | 17 | 0.337 |
| Co30 (HPT) | 32 | / | 0.340 |
| Co30-$La_2O_3$ (HPT) | 32 | 19 | 0.337 |
| Co50 | 16 | 15 | 0.340 |
| Co50 (HPT) | 20 | / | 0.341 |
| Co50-$La_2O_3$ (HPT) | 17 | 10 | 0.340 |




a)




b)

Fig. XII.22 SEM micrographs of carbon deposits obtained at 600 ºC on Fe50 (HPT) (a) and Fe50-$La_2O_3$ (HPT) (b).

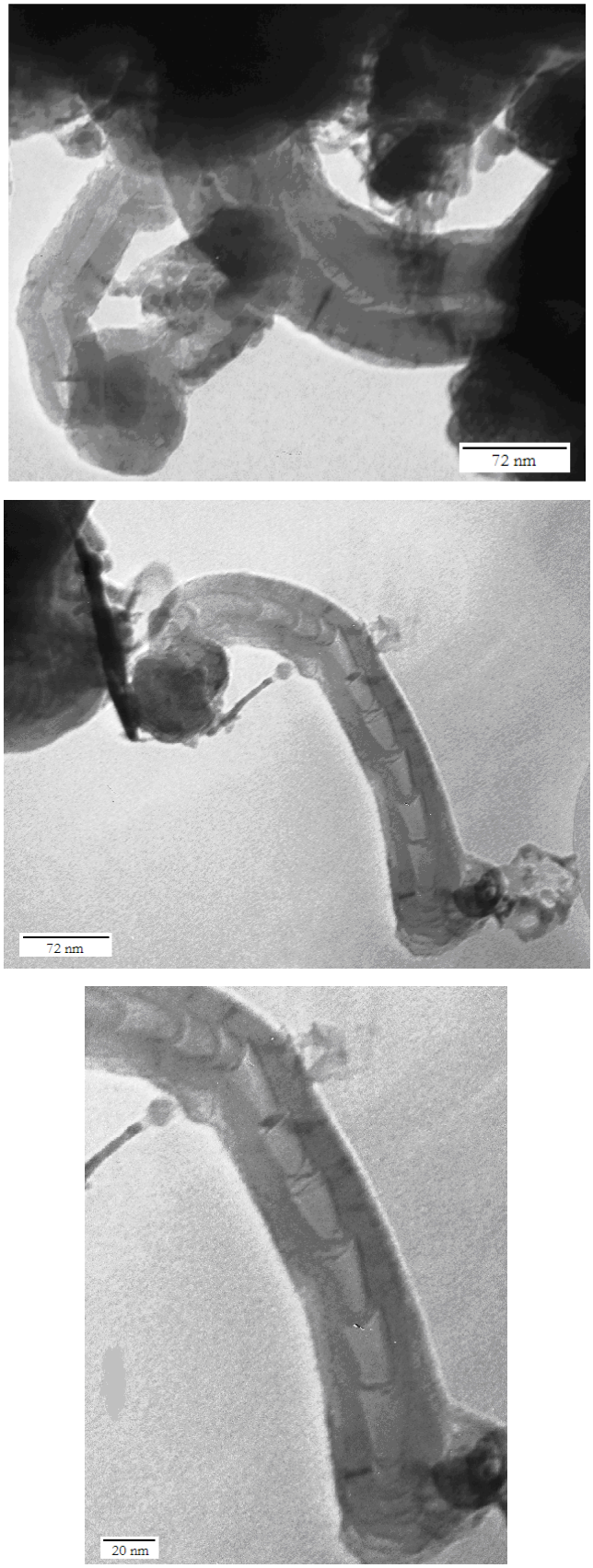



Fig. XII.23 TEM micrographs on carbon deposits obtained at 600 ºC on Fe50-$La_2O_3$ (HPT).

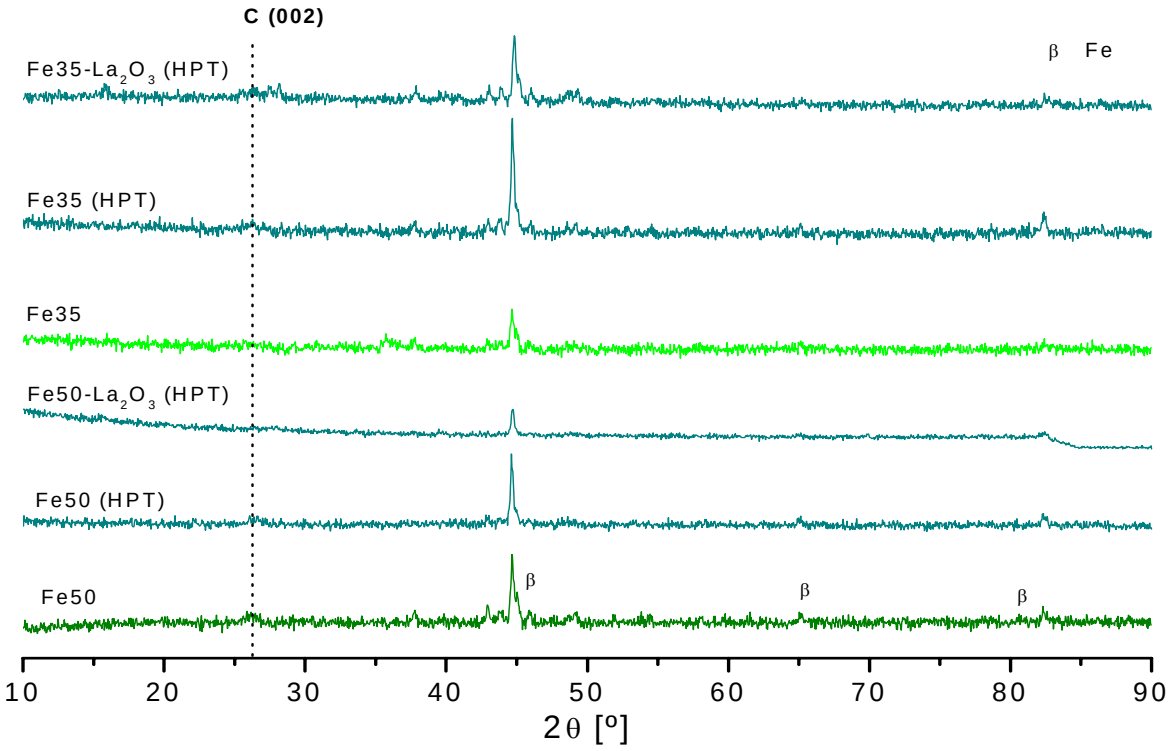



Fig. XII.24 XRD patterns of carbon deposits obtained on Fe and Fe-$La_2O_3$ catalysts at 600 ºC.

Table XII.2

Average Fe and C crystal sizes

| Catalyst | $d_{Fe}$ [nm] | $d_C$ [nm] | $D_{(002)}$ [nm] |
|---|---|---|---|
| Fe50 | 33 | 42 | 0.341 |
| Fe50 (HPT) | 41 | / | 0.339 |
| Fe50-$La_2O_3$ (HPT) | 32 | / | 0.338 |
| Fe35 | 33 | 46 | 0.346 |
| Fe35 (HPT) | 52 | / | 0.339 |
| Fe35-$La_2O_3$ (HPT) | 40 | 35 | 0.341 |

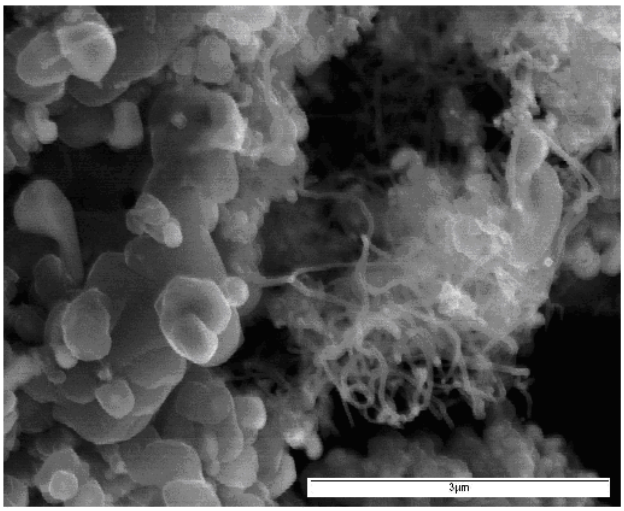
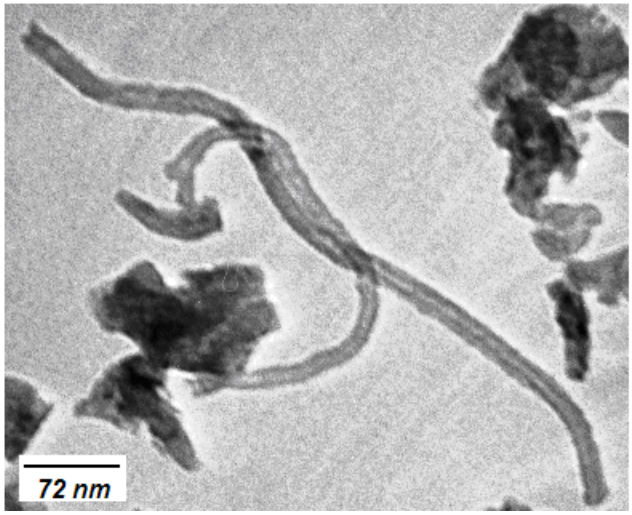
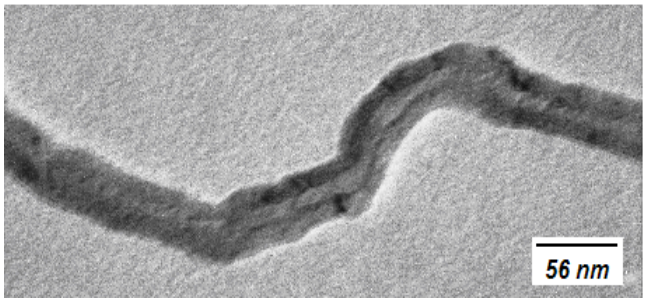



Fig. XII.25 SEM micrograph of carbon deposits obtained on NiCuLa (HPT) at 700 ºC and with a total flow-rate of 110 $Ncm^3$/min.




a)




b)

Fig. XII.26 TEM micrographs on carbon deposits obtained on NiCuLa (HPT) at 600 ºC (a), and at 700 ºC with a pure methane flow (b).